Electrically–Transduced Chemical Sensors Based on Two–Dimensional Nanomaterials

Zheng Meng,[1,†] Robert M. Stolz,[1,†] Lukasz Mendecki,[1,†] Katherine A. Mirica[1,*]

[1]Department of Chemistry, Dartmouth College, Hanover, NH 03755

ABSTRACT: Electrically–transduced sensors, with their simplicity and compatibility with standard electronic technologies, produce signals that can be efficiently acquired, processed, stored, and analyzed. Two dimensional (2D) nanomaterials, including graphene, phosphorene (BP), transition metal dichalcogenides (TMDCs), and others, have proven to be attractive for the fabrication of high–performance electrically–transduced chemical sensors due to their remarkable electronic and physical properties originated from their 2D structure. This review highlights the advances in electrically–transduced chemical sensing that rely on 2D materials. The structural components of such sensors are described, and the underlying operating principles for different types of architectures are discussed. The structural features, electronic properties, and surface chemistry of 2D nanostructures that dictate their sensing performance are reviewed. Key advances in the application of 2D materials, from both a historical and analytical perspective, are summarized for four different groups of analytes: gases, volatile compounds, ions, and biomolecules. The sensing performance is discussed in the context of the molecular design, structure–property relationships, and device fabrication technology. The outlook of challenges and opportunities for 2D nanomaterials for the future development of electrically–transduced sensors is also presented.

Contents

1. Introduction

1.1. Unique Features of Electrically–Transduced Detection

The senses of smell, taste, sight, touch, and hearing are some of the most elegant and powerful mechanisms through which living systems interact with their surroundings.[1] Each sense has a specific function to help living systems collect chemical or physical information from the surrounding environment. Physical organs have developed sensing systems that leverage thermodynamics, Nernstian potentials, photochemical processes, and molecular recognition to interpret exterior perturbations into neuronal impulses. The remarkable success of natural sensing systems continues to inspire the development of analytical, biochemical, and technological sensing systems. Building upon the principles of molecular recognition has propelled the development of analytical instrumentation that can probe physical parameters, such as temperature, pressure, or light intensity, and obtain chemical information about a sample.[2] The desire to create technologies that enhance the perception of the surrounding environment further drove the progress in the development of physical and chemical sensors.[2]

Since the second half of the 20th century, chemical sensors and biosensors have become an indispensable part of modern society with broad applications in industrial chemical production processes, pharmaceuticals, food products, environmental monitoring, security, industrial safety, healthcare, and indoor monitoring applications **(Figure 1)**.[3-4] Portable chemical sensors, that are easy to-operate, economical, sensitive, and simple to construct, have become an effective tool in situations where the use of more precise analytical techniques and equipment is restricted by sample pretreatment requirements, the need for using hazardous reagents, or qualified personnel.[5] Portable chemical sensors can be broadly classified into gas, liquid, and solid particulate sensors, depending on the nature/phase of the targeted analytes.[6] These groups of sensors can be further subdivided according to their underlying principles of signal transduction into either optical, electrochemical, thermometric, or gravimetric sensors.[4] Of these, a class of electrically–transduced devices has gained a significant role in the sensing field owing to the simplicity, compatibility with wireless transmission, non-line-of-sight detection, possibility of continuous monitoring, portability, and compatibility with standard electronic equipment (**Figure 2**).[7-10, 11-15] These features have the potential to enable highly interconnected networks of physical, chemical, and biological sensors with the ability to link different realms of human experience with measurements of causality that are currently unavailable.[16] In particular, wireless sensing networks can enhance spatial and temporal resolution of acquired information, and thus permit continuous monitoring at otherwise highly inaccessible locations.[17-18] Realizing next-generation transformation in electronic-sensor science necessitates access to high quality conductive materials capable of converting physical and chemical stimuli into electronic signal, as well as development of methods of their integration into functional sensing devices.

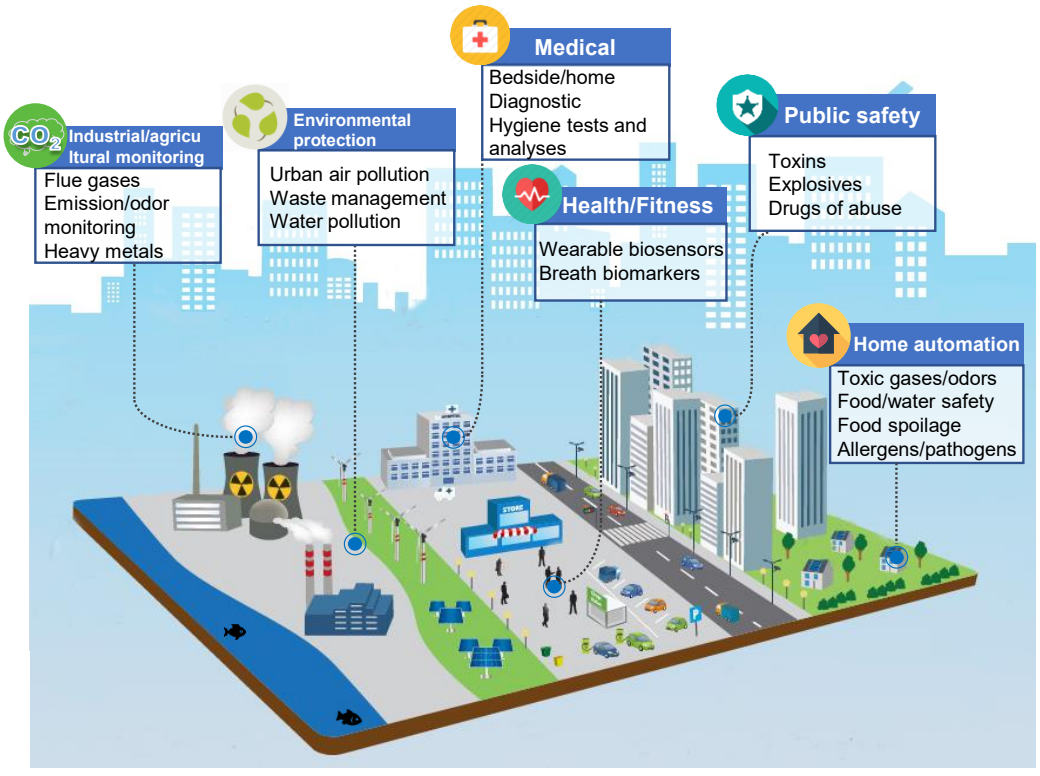

Figure 1. Chemical sensors are widely used in different aspects of human life. (Figure is adapted under permission, Copright Monicaodo | Dreamstime.com.)

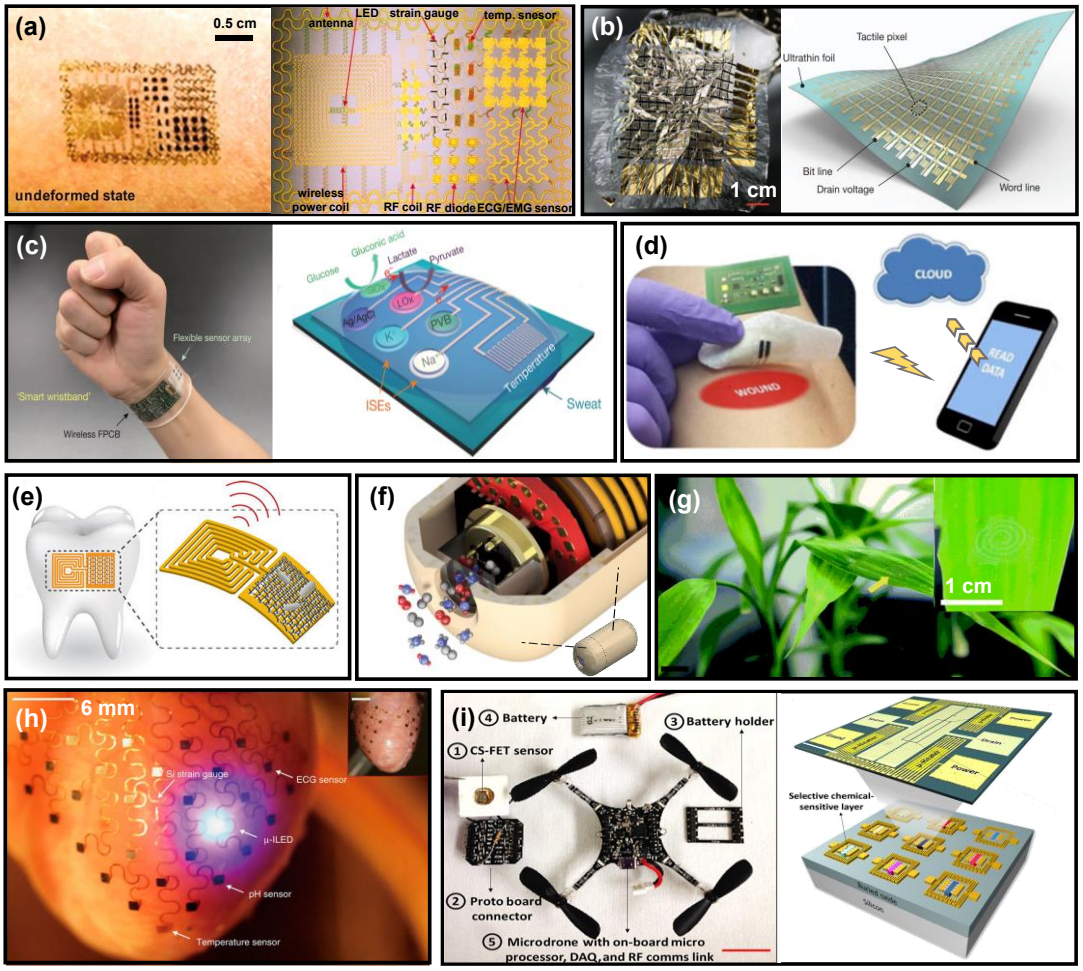

Figure 2. Electrically–transduced sensors can be used in a diverse range of applications and sensor architectures. (a) Multifunctional epidermal electronic system (EES) on compressed skin for the measurement of physiological activities (left). The physical EES integrates electrophysiological, temperature, strain sensors, and other electronic components (right).[19] (b) Illustration of a thin large-area field-effect transistor (FET) based bolometer sensor with 12 × 12 tactile pixels (left). The devices are ultra-flexible, extremely lightweight (3 g m^{-2}, left), and can be crumpled like a sheet of paper (right).[20] Adapted with permission from Ref. [20]. Copyright 2013 Springer Nature. (c) Photograph of a wearable flexible integrated sensing array (FISA) on a subject's wrist, integrating multiplexed sweat sensor array with a wireless (flexible printed circuit board) FPCB (left). Schematic of the sensor array (including glucose, lactate, sodium, potassium, and temperature sensors) for multiplexed perspiration analysis (right).[21] Adapted with permission from Ref. [21]. Copyright 2016 Springer Nature. (d) Bandage-based uric acid sensor for monitoring wound healing. Demonstrated wireless communication with a computer and smartphone.[22] Adapted with permission from Ref. [22]. Copyright 2015 Elsevier B.V. (e) Graphene-based wireless resistive sensor integrated on tooth enamel for bacteria monitoring.[23] Adapted with permission from Ref. [23]. Copyright 2012 Springer Nature. (f) An ingestible electronic capsules capable of sensing gases in the gut.[24] Adapted with permission from Ref. [24]. Copyright 2018 Springer Nature. (g) A graphene-based FET sensor transferred onto leaf for nerve gas simulant dimethyl methylphosphonate sensing.[25] Scale bar, 1 cm. Adapted with permission from Ref. [25]. Copyright 2016 The Royal Society of Chemistry. (h) Images of a representative 3D multifunctional integumentary membrane integrated on a Langendorff-perfused rabbit heart. The white arrows highlight various function elements in this system. The electronics can cover both anterior and posterior surfaces of the heart (inset). Scale bars, 6 mm.[26] Adapted with permission from Ref. [26]. Copyright 2014 Springer Nature. (i) A microdrone equipped with a CS-FET and data acquisition components for environmental pollution mapping and personal air-quality monitoring(left). Schematic illustration of a single-chip CS-FET array functionalized with different selective sensing layers (bottom, right) and optical microscope image of a single chemical-sensitive FET (CS-FET) functionalized with a Pd-Au sensing layer integrated with microheaters (top, right).[27] Adapted with permission from Ref. [27]. Copyright 2017 Science/AAAS.

1.2. The Role of Sensing Material in Electrically–Transduced Chemical Sensing

A sensing device typically comprises two main components: the sensing material and the transducer.[4] The sensing material is responsible for interacting with the stimuli, either in the form of a physical perturbation (e.g., temperature or pressure change) or a chemical entity, inducing a change in one or several of its properties, which are then transformed into readable signals by the transducer (**Figure 3**).[28-30] Sensors that probe the physical change have been attained by synergistic breakthroughs in material development through the engineering of their physical properties and the refinement in the methods of integrating these materials into devices.[31-32] The physical sensors, which have been widely used in various fields—such as in wearable consumer electronics, soft robotics, smart medical prosthetics and electronic skins, and real-time healthcare monitoring[33-34]—function on a direct cause-effect relationship.[35] For example, the touch screen of a cellphone changes its capacitance upon the contact with a finger due to the alterations in the dielectric characteristics of the screen, thus producing a measurable response to a touch stimulus.[36]

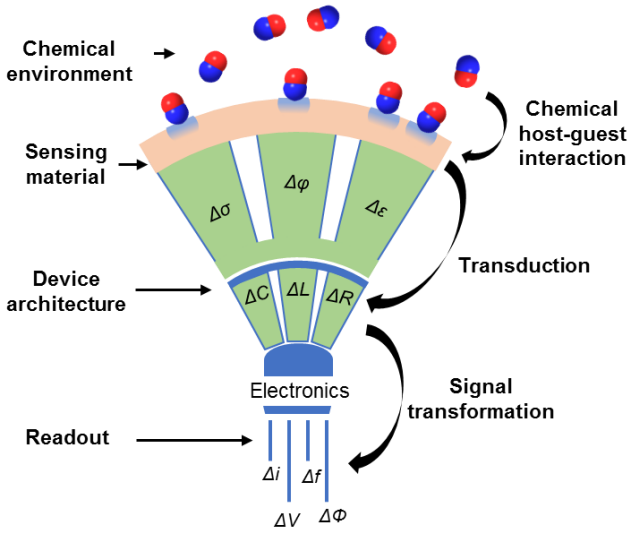

Figure 3. Logical structure of a chemical sensor.[29] Analytes interact with the sensing material changing some of its physical properties including conductivity (σ), work function (φ), and permittivity (ε). The transducer converts one of these physical quantities into the variation of its electric parameters (here, capacitance C, inductance L, and resistance R are mentioned).[37] The circuit to which the device is connected gives rise to the sensing signal. Electrical signals are current (I), voltage (V)/electrical potential (E), and capacitance with measurable changes in magnitude, frequency (f), and phase (Φ). Reproduced from Ref. [29]. Copyright 2017 American Chemical Society.

In contrast to physical sensors, progress in electrically–transduced chemical sensing requires an additional level of complexity posed by the chemical interfaces between the material and the analyte (**Figure 3**).[4] These interfaces play a key role in determining the sensitivity, selectivity, stability, and biocompatibility of chemical sensing devices.[38-40] The role of the sensing material is two-fold.[29] First, it must (be able to) interact covalently or non-covalently with the analyte on its surface. Second, it must respond to this interaction in a form of changing its electrically related physical properties. The transduction mechanism can be a function of conductivity, work function, or electrical permittivity, and can be transduced as a change in capacitance, resistance, or inductance.[41] Using standard electronic equipment, generally including resistor,[42] diode,[43] field-effect transistor,[44] capacitor,[45] and electrochemical sensor[9] configuration, these transduction events can be measured as changes in the resistance/impedance, current, voltage/electrical potential, and capacitance, where magnitude, frequency, and phase of the signal can provide valuable information regarding the sensing event (**Figure 3**).[46] Therefore, the design of sensing material must consider its ability to selectively interact with targeted analytes, and consequently undergo a change in its electrical property.

Ideally, a sensing material should have a large exposed surface available for the material-analyte interaction, suitable active sites for effective and selective analyte binding, the ability to transduce the binding events into a detectable signal, as well as good mechanical and processing properties. Advances in the development of modified carbon-based electrode,[47-48] boron-doped diamond[49] coupled with the discoveries of conductive polymers,[12, 50] fullerenes,[51-52] carbon nanotubes,[53-56] metallic and semi-conductive nanoparticles,[57-59] have led to extensive applications of these materials in electrically–transduced chemical sensing. These materials have their own distinct advantages and disadvantages in context of the chemical sensing.[7] For example, conductive polymers are straightforward to synthesize and integrate into electrical devices and they exhibit high sensitivity to a broad range of analytes.[11] However, conductive polymers need to be doped to obtain substantial electrical conductivity for chemical sensing applications.[12, 50, 60] Metallic nanoparticles can achieve high sensitivity through feasible functionalization, however, they may be hard to fabricate into functional devices due to the aggregation effects on the surface of a substrate that can lead to their dissolution or even material degradation.[61] A good candidate for electrically–transduced sensing should have a synergistic combination of its surface chemistry, desired electronical properties as well as fabrication with control over dimensionality, flexibility, mechanical stability, and lattice matching with the device substrate. It should also possess the ability to respond to the recognition event by changing its electrical properties that could be further transformed into a readable signal.

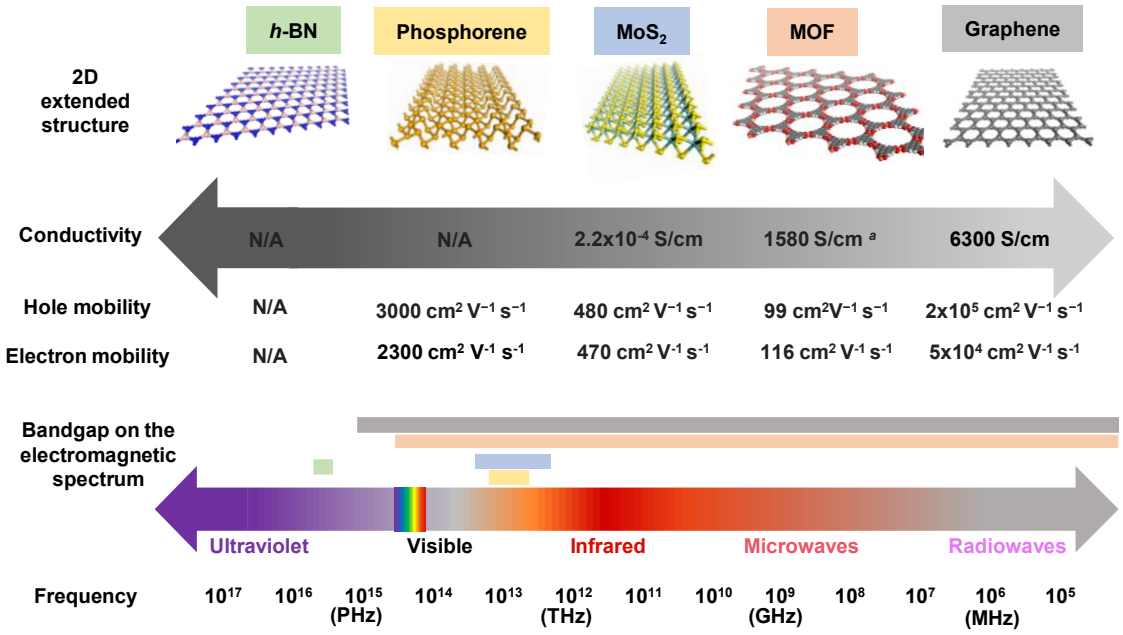

Figure 4. Atomically thin 2D materials span a wide range of chemical structures, conductivities, carrier mobilities, and bandgaps.[62] Chemical structures of 2D materials have been discovered with mixed elemental structure such as *h*-BN,[63] 2D-MOFs,[64] and MoS_2,[65] as well as well as pure elemental sheets such as black phosphorous[66-67] and graphene.[68-69] The electronic structure of 2D materials covers a wide range from insulating *h*-BN, to the metallic conductivity of graphene. This wide range of properties exhibited by diverse 2D materials is the key to their success in sensing applications. [a] Value reported from material Cu-BHT, Ref. [64]. N/A: no known reports of this value exist.

1.3. Unique Features of 2D Materials in Chemical Sensing

Two-dimensional (2D) materials,[70-73] with thicknesses ranging from few to tens of nanometers and lateral dimension reaching up to many centimeters,[74-75] possess remarkable physical and chemical properties with promising potential utility in electrically–transduced chemical sensing. Graphene (Gr),[76] a one-atom-thick sheet of carbon atoms with a 2D hexagonal crystal structure, has shown great promise for applications in electronics, photonics, energy conversion and storage, medicine, and chemical/biological sensing due to its unique physical, chemical, electrical, optical, thermal, and mechanical properties.[77-79 80] The diversity of 2D materials has grown appreciably to include phosphorene,[67, 81] hexagonal boron nitride (*h*-BN),[82-83] transition metal dichalcogenides (TMDC),[84-85] layered metal oxides,[86-87] 2D metal-organic frameworks (MOFs),[88-89] covalent organic frameworks (COFs),[90-91] and other 2D compounds.[73] These materials exhibit exceptional properties— large surface-to-volume ratio, rich surface chemistry, atomic-level thickness, exceptional electrical properties—that are distinct from their 3D bulk counterparts, which make them uniquely suited to detect and transduce chemical events. Table 1 compares the unique features of using 2D materials with other materials of different dimensionality (0D, 1D and 3D) in the context of potential utility in electrically–transduced sensing.

Compared with their 0D, 1D, and 3D analogs, the large surface-to-volume ratio of most 2D materials[92] ensures tremendous surface area available for the material-analyte interactions, which are beneficial in realizing high sensitivity even at extremely low concentrations of the analyte. For example, the occupancy by highly reactive surface Sn and O atoms with low coordination numbers of five-atomic-layer-thick SnO_2 sheets (0.66 nm) is as high as 40%.[93] The rich surface chemistry is manifested by the presence of active sites that could effectively and selectively interact with targeted species.[94] The surface of the materials can also act as a molecular scaffold for the immobilization of additional recognition components (e.g., metallic nanoparticles, metal oxides, enzymes), which can further improve the sensing performance of a device including its sensitivity and selectivity.[95-97] For example, each P atom on the surface of phosphorene can potentially function as an active site for the chemical adsorption of gaseous analyte.[98] Theoretical studies demonstrated that chemical doping of heteroatoms of phosphorene can tune its bandgap, and also enhance the strength and selectivity of the phosphorene-analyte interactions.[99-100] 2D materials also exhibit a rich variety of electrical properties. Their conductivities encompass metals, semimetals, insulators, and semiconductors with direct and indirect bandgaps ranging from ultraviolet to infrared throughout the visible absorption range (**Figure 4**).[62] The fine structural and compositional tuning can also improve the electrical characteristics of 2D nanomaterials enabling efficient signal transduction as a result of molecular binding event.[101]

The charge transport in 2D materials is strongly confined in the 2D plane, leading to remarkable changes in their electronic properties upon analyte binding. In contrast to

1D nanostructures, 2D nanomaterials can offer good conformal and intimate electrical contact with metal electrodes due to their relatively large lateral sizes.[102] The geometry of 2D materials also shows excellent compatibility with current thin film manufacturing techniques in the semiconductor industry, which can facilitate the coupling of 2D structure with traditional electronic materials, such as Si.[102] 2D materials, such as graphene, also demonstrate other excellent physical properties, such as an ultra-large Young's modulus (≈1000 GPa), high strain limit (≈25%), and good optical transparency (> 90%).[103] Compared to conventional inorganic semiconductors that heavily rely on mechanical design to minimize intrinsic strain below 1% to prevent material breakage, the large modulus and strain limit of 2D materials reinforce their potential in fabricating sensing devices with good stability and flexibility.[8, 104]

Table 1. Representative structure of materials from 0 to 3 dimensions and the comparison of their features in context of electrically–transduced sensing materials.

Dimension	Example	Advantage	Disadvantage
0D	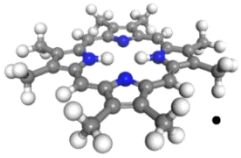	• Regio- and stereo- selective functionalization[96] • Atomic control of structure–property relationship • Large area-to-volume ratio • Single-molecular electronic based sensing[105] • Tunable size and shape[106-108]	• Low conductivity • Difficulty with device integration • Limited stability of devices • Potential toxicity[109]
1D	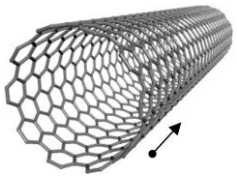	• High surface-to-volume ratio[110] • High aspect ratio • Excellent stability • High density of reactive sites • Good thermal stability • Compatible with device miniaturization[111-112]	• Required chemical modification to enhance selectivity • Difficulty in establishing reliable electrical contacts • Difficult purification • Limited structure and precision control[53, 112]
2D	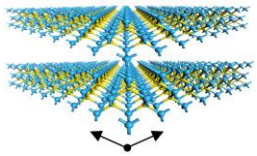	• Wide tunability of conductivity • Large surface-to-volume ratio • Thickness dependent electronic properties • Good optical transparency • Excellent mechanical flexibility • Good functionalization ability • Potential for good processability • Compatible with ultra-thin silicon channel technology[73, 94, 113-114]	• Lack of mass production of materials with large area, high and uniform quality • Lack of facile, effective, and reliable strategies for device integration • Limited stability of some forms at ambient conditions[73, 94]
3D	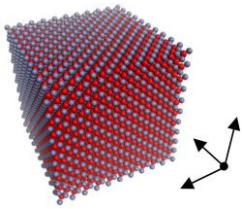	• Strong analyte adsorption/binding • Good mechanical strength • Good thermal stability • Easy to interface with solid-state devices • Good designability to improve selectivity[115]	• Low surface area (for non-porous materials) • Difficulty with miniaturization[116] • Slow dynamics of analyte transport[115]

1.4. Scope and Organization of this Review

This review provides a comprehensive discussion of the recent advancements in the fundamental and applied research on 2D nanomaterials in the context of electrically–transduced chemical sensing. We outline the components necessary for the fabrication of functional devices, and the transduction principles underlying their operation. Subsequently, we discuss the device architectures of the current and emerging electrically–transduced sensing platforms, and then highlight the fundamental detection principles governing their response. We describe the structural and compositional features of 2D nanostructures that determin their electrical properties, ultimately leading to applications in the development of sensors. We then highlight key advances in the application of 2D materials in electrically–transduced sensors, both from a historical and analytical perspectives with respect to four major groups of analytes: gases, volatile organic compounds (VOCs), ions, and biomolecules. We conclude by offering insights on the challenges and opportunities facing the development and application of 2D materials within the electrically–transduced sensing platforms.

The increasing exploration of the electronic properties of 2D nanostructures has burgeoned into the new field of chemical sensors. Although excellent reviews on the broad subject of electronic transduction of chemical sensing using nanomaterials,[7] the synthesis and structure of 2D materials,[117-118] their physio-chemical properties,[71, 119] and their application in energy, electrocatalysis, and electronics,[102, 120-121] are separately available, a comprehensive review focusing on the progress and challenges of 2D materials that act as electronic sensors and transducers does not exist. This review focuses on facilitating insights into the connection between the low dimensionality, surface chemistry, electronic properties, and the analytical response of electrically–transduced sensors based on 2D nanomaterials. The organization of this review is structured to introduce the readers to key component, sensing mechanisms, performance parameters, and device architectures of the electrically-transduced sensors that are based on the 2D materials. Although certain aspects of these topics have been reviewed forr general class of nanomaterials,[7, 29, 122] carbon nanotubes,[53] graphene,[78, 123-126] and metal oxide semconductors,[127-129] we offer a comprehensive overview based on the latest literature pertinent to the broad topic of 2D materials.

The organization of the review is intended not only to help the readers grasp and assess the latest advancements in the surface chemistry and structural characterization of 2 materials, but also to compare the important characteristics across the broad range of materials in this review. By organizing this review with a focus on four major classes of analytes enables cross-cutting examination of how the structural features of 2D materials and the strategic modifications of their surface promote the sensitivity and selectivity of target-oriented electroanalysis.

2. Electrically–Transduced Sensors

2.1. Components of Electrically–Transduced Chemical Sensors

Chemical sensors consist of a chemical recognition element coupled with a transducing element that together can detect changes in chemical environment and translate that information into a readable signal.[4] In the recognition step, the sensing material identifies a chemical parameter—the identity and concentration of a gas, ion or biomolecule—and undergoes a change in a physical parameter of the sensing material as a function of concentration of the sensed analytes. Electrically–transduced sensors rely on a few key physical parameters that can be altered in response to an analyte, including electrical conductivity (σ), work function (φ), and permittivity (ε) (**Figure 3**). The transducer then converts the change produced by the sensory material into a measurable electrical signal, including current (I), capacitance (C), resistance (R)/impedance (Z), voltage (V) or electrical potential (E).[7] These electrical signals, or data, can undergo further processing, including amplification, filtering, analysis or display to generate information about the identity of the analyte and its concentration.[130] Each of the components is responsible for a specific step in the sensing process that stems from initial molecular recognition between the analyte and the active 2D material, and the readout signal for application. Specific choice of sensing material, transducer, and the method of integration into a device dictates the behavior and performance characteristics of sensing devices. In the following section we discuss the function of sensing materials, transducers, and data processors in the context of electrically–transduced sensing.

2.1.1. Sensing Materials and Their Variable Electronic Properties

The role of a sensing material is to interact with analytes and to respond to this interaction by changing its internal physical parameters.[131] Firstly, this process necessitates the presence of active sites capable of binding guest analytes. These active sites can be either inherently imbedded in the material during their synthesis, or deliberately incorporated via post–synthetic modifications, after the material is formed.[3] Bottom–up approaches often provide more precise control over the spatial distribution of incorporated host–sites in the final structure of the 2D nanomaterials.[132-133] However, these approaches may be difficult to realize as they requires the compatibility of host–site chemistry with available material synthetic methods. Alternatively, the active sites necessary for host–guest interactions can be incorporated onto the surface of 2D material through post–synthetic modifications.[134-136] This method relies on the decoration of surfaces with covalent or non–covalent modifiers that act as host sites.[97, 137] Because the materials are synthesized prior to the chemical modifications, a diverse range of methods is available for the incorporation of desired recognition elements. However, in certain situations harsh experimental conditions may unfavorably alter the physical, chemical, and electronic properties of 2D materials.[73, 138-139] Typically, post–synthetic modification methods cannot offer the same level of organization of host sites in the 2D nanostructure as can be obtained by bottom–up methods.

Secondly, the interaction between analyte and sensing material must induce an observable change in the conductivity, work function, or permittivity of the material. Conductivity of a material (σ) is governed by the charge carrier mobility μ_i and charge carrier population n_i as given in **eq 1.**[140]

$$\sigma = e(\mu_e n_e + \mu_h n_h) \quad \textbf{(1)}$$

where μ_e and μ_h are the mobility of electrons and holes, n_h and n_e are the electron and hole populations, and e is the fundamental charge. In 2D materials, both electrons in the conduction band or electron holes in the valence band may act as charge carriers.[141] The mobility of these carriers is related to the drift velocity under the influence of an electric field. Changes in conductivity, according to **eq1**, stem from the modifications in the mobility or population of charge carriers. The population of charge carriers n_i (n_e *or* n_h) is further related to the bandgap of the conductive material (E_g) by a constant (C), and temperature (T) (**eq 2**). **Equation 2** shows that changes in temperature can alter conductivity of the 2D material by changing the population of electrons in the conduction band. This equation also demonstrates that increasing bandgap also reduces carriers at a given

temperature, leading to a decrease in overall conductivity. In the band theory of conductivity, the bandgap is the energetic difference between an electron in the conduction band (E_c) and in the valence band (E_v) (**eq 3**).[142]

$$n_i = CT^{3/2} e^{\frac{-E_g}{2k_B T}} \quad \textbf{(2)}$$

$$E_g = E_c - E_v \quad \textbf{(3)}$$

The work function (W) of a material measures how much thermodynamic work is required to remove an electron from the Fermi level (E_F) to the vacuum level, or directly outside the material surface (**eq 4**).[143]

$$W = -e\varphi - E_F \quad \textbf{(4)}$$

The work function dependence on the electrostatic potential (φ) shows that W is dependent on the bias potential applied to the material. When the relationship is rewritten to consider externally applied potentials (V, **eq 5**), one can understand phenomena such as Schottky barriers and band–bending.[144]

$$\varphi = V - \frac{W}{e} \quad \textbf{(5)}$$

The permittivity of a material is a measure of how easily electric fields, and electromagnetic radiation, such as radio waves, can travel through materials. The permittivity of a material is directly related to the permittivity of a vacuum (ε_0), and the material property of relative static permittivity (ε_r) which is a function of the electric susceptibility (χ) (**eq 6**).[145]

$$\varepsilon = \varepsilon_r \varepsilon_o = (1 + \chi)\varepsilon_o \quad \textbf{(6)}$$

Together, perturbation of conductivity, electrostatic potential, and permittivity are responsible for the changes in electronic properties of a material. Analyte binding may influence one or all of these factors, which in turn will be translated by a transducer into a readable electrical signal.

2.1.2. Transducers

Transduction refers to converting the changes in electronic properties of the sensing materials to a specific electrical signal.[3] This signal conversion is realized by integrating the sensing materials into an electronic device. A material–analyte interaction may induce more than one physical property change (e.g., permittivity, work function or conductivity) in the sensing material.[146] However, one of these alterations in physical parameters can be more prominent than others, meaning that the resulting physical property change induced by the chemical binding event should be properly transduced to obtain higher sensing performance.[41] For example, the adsorption of gaseous analytes on graphene can theoretically alter both conductivity and permittivity in the material, while sensing of these types of analytes is mostly realized by monitoring changes in current/resistance, as the associated capacitance changes (resulting from the permittivity change upon graphene–gas interaction) can be relatively small.[147-148] Based on the electronic properties of different 2D materials and the nature of sensed analytes, 2D materials can be integrated into a diverse range of devices to transduce the chemical interaction into a readable electrical signal. These aspects will be discussed in **section 2.4**.

2.1.3. Data Processing

All readouts obtained from a sensing device must undergo processing into a visual form for manual interpretation, or into a signal that can be utilized for various process–specific applications. Algorithmic processing of raw sensor data is a method of analyzing selectivity of a sensor without modifying device chemistry or architecture.[149] Methods such as principle component analysis (PCA) and linear discriminant analysis (LDA) can be applied to multiple devices to distinguish classes of analytes.[130] PCA uses linear combinations of correlated parameters to describe the greatest amount of variation in a data set. Such methods of data processing in arrays have been applied in numerous examples to successfully distinguish broad patterns such as functional group recognition from single–analyte mixtures. As sensors become increasingly mobilized by miniaturization, important design criteria, like portability and cost of data processing units, must be taken into consideration. Different techniques for conditioning individual outputs from a multivariable sensor are also being explored with the goal of providing more reliable sensor performance.[150] The best practices in data analytics of dynamic and steady–state features should be shared proactively across different types of platforms and sensors. In recent years, technologies for integrating 2D materials into new generation of highly integrated devices have begin to develop,[102] making it possible to leverage the compact and powerful computing ability of smart terminals for sharing and analyzing data online.[104]

2.2. Sensing Mechanisms

The underlying principles of most chemical sensors that enable their operation rely on two consecutive parts: molecular recognition and transduction of the recognition event.[4] In the recognition step, an analyte molecule interacts with the active site or receptor molecule present in the structure of the sensing material. These interactions either change the chemical structure, and composition of the sensory materials or the chemical environmental around it, resulting in a characteristic alteration in one or more physical parameters. This change is then reported by means of an integrated transducer that generates the output signal.[29] These two principles behind the sensing mechanism of the electrically–transduced sensor, namely analyte–material interaction and the mechanism of transduction, will be further discussed in the following sections.

2.2.1. Mechanisms of Analyte–Material Interactions

The interaction between analyte and material is a prerequisite for the operation of any chemical sensor. We can distinguish two types of interactions between the chemical species and the sensory material: (i) non–covalent interactions between the targeted analyte and the sensing material, including van der Waals forces, hydrogen bonding, coordination, and π–π interactions; and (ii) covalent

bonding through chemical reaction, due to the high reactivity of a sensory material to the analyte. Non–covalent interactions usually lead to a reversible or partially reversible response. Covalent bonding, although can provide high selectivity and sensitivity, often leads to an irreversible response. The specific type of interaction is determined by the chemical structure of analyte and sensing material, which together are the key factors that define sensitivity, selectivity, and reversibility of sensing devices. Different 2D materials possess distinct structural features, surface chemistries, and contain active sites for analyte–material interactions that are unique from each type of 2D material. For example, graphene has a large, electron-rich π-surface which enables interactions with targeted analytes through van der Waals forces, charge transfer, and π–π interaction. Metal oxides contain chemically adsorbed oxygen molecules on their surface, which are responsible for the interaction with gaseous analytes through oxygen involved chemical reactions.[151-152] The potential active sites existing in each type of 2D material and the nature of the resulting interactions are summarized in **Table 2**.

Table 2. Typical analyte–material interaction in electrically–transduced sensing using 2D materials.

Material	Active sites	Resulting Interactions
Graphene	sp^2 orbital of carbon (large π system), defects[153-154]	π–π interaction,[155-156] Van der Waals,[153]charge transfer[157]
Black Phosphorous	p_z orbital of P atom[158]	charge transfer[98, 159-160]
Xenes	unstable sp^2 orbital, defects[161]	charge transfer,[162] dispersive interaction, chemical reaction[163]
Metals	zero–valent metal atom,[164] pre–adsorbed oxygen species[165]	charge transfer, chemical reaction
TMDCs	p orbital of chalcogenide atoms[166-167], defects [168-169]	charge transfer[170]
Metal Oxides	pre–adsorbed oxygen species[152, 171-172]	redox reaction
2D MOFs	d orbital of metal node,[173-175] absorbed water/oxygen	charger transfer, coordination, H–bond[176]
MXene	O, OH, and F on surface,[177-178]	Van der Waals, H–bond, charge transfer[179]
h–BN, *g*–CN	electron deficient π system,[180] defects,[181] absorbed O_2[182]	π–π interaction, Van der Waals, oxidation reaction

Active sites with specific and stronger binding abilities can be strategically introduced through the controlled incorporation of defects, doping, and functionalization, which together can lead to improvements in the selectivity and sensitivity of sensing devices. For example, Al–doped Gr showed stronger response to CO than the pristine Gr due to the formation of Al–CO bonds.[183] In another example, the surface of MoS_2 functionalized with bio–recognition receptors can induce selectivity for targeted biomolecules.[184]

2.2.2. Mechanisms of Transduction

In order to complete electrically–transduced sensing, the analyte–material interaction should induce change in one or several of the physical parameters including conductivity, work function, and/or permittivity, which are usually realized through the fundamental mechanisms listed below: modulation of doping level and Schottky barrier, as well as the formation of dipole and interfacial layer.

Modulation of doping level. During the interaction of an analyte with the material, the distance between the target molecule and sensory material becomes close enough to allow for electron transfer between them.[185] Based on the relative energy levels of the material and analyte, the analyte can act either as an electron donor (n–type dopant) or acceptor (p–type–dopant) resulting in augmentation or compensation of the doping charge density (**Figure 5**). This process is often described as a secondary doping of the sensing material. The primary doping (inherent doping) is carried out during the synthesis of the materials by incorporating doping ions, or during the chemical or electrochemical preparation processes.[186] In some instances, the doping induced by an approximal analyte can drastically change doping effects inherent to the material. The primary doping effect of the material can be minimized or undergo complete deactivation due to analyte–dopant interactions. The modification of the doping density thus alters the density of states, in the barrier region, and consequently, the conductivity of the sensor. The conductance change of the device, through the modulation of doping level, is closely related to the sensing material surface occupancy of the analyte molecules. This mechanism is described by the site–binding hypothesis, where atoms on the surface of the sensing material can act as binding sites for molecule adsorption.[80, 187] The large specific surface area of most 2D materials, which is beneficial in obtaining a high–density surface occupancy, makes them very sensitive to these chemical environmental perturbations.

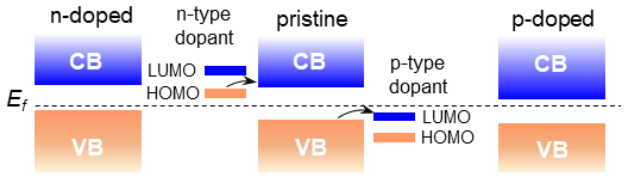

Figure 5. A scheme showing the n– and p–type doping of a semiconductor. The arrows denote the direction of electron transfer.[188]

Modulation of Schottky barrier (ϕ_b). Metal–semiconductor junctions are involved in many types of electronic devices. When a metal and a semiconductor are in contact, a potential barrier is built due to the mismatch in their work functions (ϕ_M, ϕ_S, **Figure 6a**). This energy

barrier prevents efficient transport of charge carriers (electrons or holes) between the two adjacent materials. Only a small number of carriers have enough energy to overcome this barrier and cross through the metal–semiconductor junction. When a bias is applied to the junction, it can bend the barrier lower or higher from the semiconductor side, depending on the type of the semiconductor, but it does not change the barrier height from the metal side. This effect leads to the formation of a Schottky barrier (rectifying contact), in which the junction conducts charges for one bias polarity, but not the other.[189-190] **Figure 6b** depicts that a Schottky barrier is created upon the contact of n–type semiconductor MoS_2 with the electrode (Ti/Au). Almost all metal–semiconductor junctions will exhibit some rectifying behavior. The height of Schottky barrier depends on the work function difference of the two materials in electrical contact.[191]

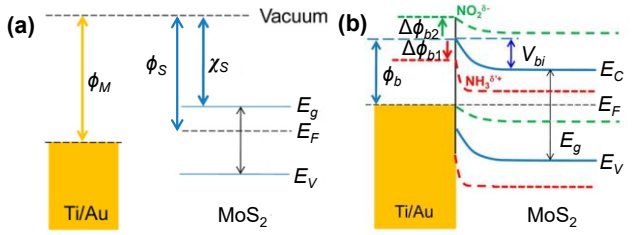

Figure 6. (a) Energy diagram of the Ti/Au and MoS_2 before contact. ϕ_M and ϕ_S are work functions of the metal and semiconductor, respectively, and χ_S is the electron affinity of the semiconductor. E_C, E_F and E_V represent the energy level of conduction band and Valence band, and Fermi level, respectively. E_g is the band gap. (b) Band realignment and energy diagram of the Ti/Au and MoS_2 after contact and the formation of Schottky barrier. Blue, green, and red lines indicate the energy band of the pristine MoS_2 (solid blue), after exposure to NO_2 (dashed green), and after exposure to NH_3 (dashed red), respectively. V_{bi} is the built–in voltage.[191] Reproduced from Ref. [191]. Copyright 2014 American Chemical Society.

In sensing, the adsorption of analytes causes a change in the doping level of the material, altering the Fermi level and work function, which successively modulates the barrier height at the metal/semiconductor junction. Donor and acceptor type analytes change the Schottky barrier height in the opposite directions according to the specific location of the work function and primary doping type of the semiconductor. For instance, in a MoS_2/(Ti/Au) device, the exposure to NH_3 gas (n–type dopant) lowers the Schottky barrier height, while NO (p–type dopant) leads to an increased energy barrier.[191] In electrically–transduced devices, where Schottky barriers contribute significantly to the total electron transport, the modulation of barrier height will be an important factor for measurements of conductivity change. Under these conditions, the sensing device operates as a junction–controlled device.[192] In an ohmic contact where a metal–semiconductor junction conducts current in both directions, without rectification, the modulation of Schottky barrier is negligible and does not affect the conductance of the device.

Formation of dipole and interfacial layer. The interactions of analytes with the material can cause two effects: (1) polarization or ionization of the analytes at the surface of material (pinning or unpinning of the Fermi level), giving rise to a dipole layer that changes the interface state density;[193] (2) an excess of charge states at the metal electrode/material interface, formed in the presence of analytes, that modulates the Schottky barrier height. In the first situation, the analyte polarized/ionized layer redistributes the electrical charges in the depletion region and abates the degree of the band bending at the material/metal surface. The corresponding output signal, such as current, would be correlated to the quantity of the analyte that was adsorbed at the interface of the material. This sensing mechanism is evident in the n–type metal oxides semiconductors in which the oxygen molecules are usually adsorbed on the surface of metal oxide when exposed to an oxygen–rich atmosphere. The adsorbed oxygen species accept electrons from the inside of the metal oxide film to form negative charged ions, including O_2^-, O^-, and O^{2-}. These negatively charged species build a space–charge region on the surface of the metal oxide, also known as a depletion layer (**Figure 7a**), which results in the formation of a potential barrier for the electronic conduction between each grain boundary. When the sensor is exposed to reducing gases, like alcohols, the negatively charged oxygen species are consumed by the reaction with the analytes. During this process, the electrons previously trapped by the adsorbed oxygen species will be transferred back to the metal oxide film, leading to a decrease in the potential barrier height, and thus an increase in conductivity.[127, 151-152] This effect becomes dominant when crystal size of the materials are close to the scale of the depth of the depletion layer.[194-195]

When an analyte is adsorbed on the surface of the material, an equilibrium between the concentration of charge carriers at the material surface, and metal electrode/material interface is reached resulting in the modulation of the device double layer. If the exposure to the targeted analytes can alter the degree of the double layer formation, this effect would lead to the modification of the barrier height, and consequently in the current flowing across the metal/semiconductor interface. The analytes that cause the barrier height to increase will enhance the rectifying current–voltage behavior, while the species that can reduce the energy barrier will improve the ohmic current–voltage behavior (**Figure 7b**).[192] In addition, the interfacial layer should be capable of supporting the transport of electrons or holes through the interface. If the layer is considered as an electrical insulator, the transport of charge carriers must proceed through tunneling which requires the thickness of the interfacial layer to be lower than 50 Å.[196-197]

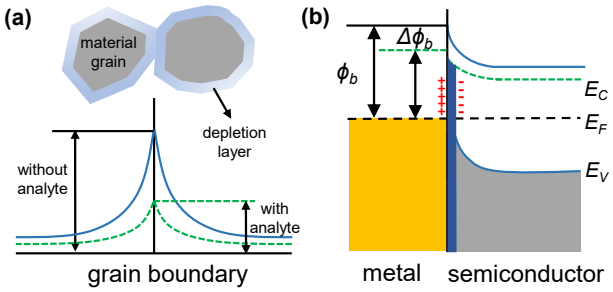

Figure 7. Band diagrams of a metal/semiconductor Schottky contact (a) without and (b) with formation of an interfacial layer after the analyte adsorption.[152, 186]

2.3. Performance Parameters

Sensitivity of a sensor can be defined as the slope of the output characteristic curve or, more generally, the minimum perturbation of physical parameters that will create a detectable output change.[4, 198-199] In some sensors, the sensitivity is also defined as the input parameter change required to produce a standardized output signal. Site-binding hypothesis assumes that atoms on the surface of the sensing materials can act as binding sites for analyte adsorption, thus the conductance change of the device would be related to the surface occupancy of the analyte molecules on sensing materials.[187] High sensitivity to analytes in electrically–transduced sensors based on 2D materials can be ascribed to large available surface area and large abundance of active sites on their surface for analyte-material interactions. Strategies for improving sensitivity can be further realized through indroducing analyte-specific acceptor that have high bidning affinityies to analytes, which will be discussed in more details in **Chapter 4**.

Limit of detection (LOD) is the smallest concentration of an analyte that can be reliably distinguished from its absence in a sample (blank) with a specified precision and reproducibility (99% confidence interval).[198] One of the commonly-used experimental methods to determine LODs utilizes the exposure of a sensing device to known concentrations of the analyte of interest to generate a calibration curve.[200-201] The detection limit can be obtained by dividing the sensor resolution with its sensitivity. Numerous analytical specifications depending on the techniques (e.g., the concentration at signal that is 3 times of noise level) have been used to ensure that the recorded analytical signal is indeed meaningful and distinguishable from the baseline. As LOD is dictated by sensitivity and the resolution of the sensor, it can be targeted through improving material–analyte interactions, available surface area, surface functionalization, and signal amplifications.[202] The high coverage of functional groups of 2D materials can allow effective and strong interactions with targeted analytes to afford high sensitivity; meanwhile the high intrinsically conductivities found in this group of materias and their good contact lead to a low signal noise. This combination has already rendered 2D materials attractive in gas sensing development with low LODs.[203]

Selectivity describes the extent to which an analytical method can discriminate between the analytes of interest, in multicomponent mixtures, without interference from other components.[198, 204] In the current literature, selectivity can be estimated directly from analytical measurements by comparing signal resolution between the obtained analytical signals or/and through means of statistical analysis (e.g., principle component analysis) or computational modelling. In addition, the reported selectivity values/coefficients should only be directly compared if the experimental conditions, used for their determination, were standardized to eliminate bias. Selectivity of analytical devices is usually induced by the presence of recognition elements capable of producing selective interactions with a targeted analyte. Depending on the sensor, selectivity can be further improved through the alterations in experimental conditions such as temperature, or pressure or via use of alternative materials that can, for example exclude interferents based on their size, or affinity of binding. Specificity is the ability of an analytical technique to distinguish the targeted analyte from other compounds that are present within the analyzed sample and is often considered as ultimate selectivity. Obtaining selectivity in complex mixtures of interferents is a primary goal of sensor research and a driving force in the exploration of new materials that may provide new selective host–guest surface chemistries.[205]

The diversity of surface chemistries of different types of 2D materials is well poised for targeted molecular design of selective interactions. For instance, black phosphorus can be oxidized to phosphorus oxides or phosphoric acid upon exposure to water molecules under oxygen, which has been applied to develop efficient humidity sensor (**section 4.2**). The oxygen-rich surface of metal oxides makes them usually sensitive toward reducing analytes (**section 4.1-4.2**). Selectivity to targeted analytes can be achieved/modulated by either installing different functional groups on the surface of 2D materials using post-synthetic modifications or/and through incorporating molecular building blocks with high affinity to species of interested. For example, graphene functionalized with aptamer molecules can exert great selectivity to small biomolecules (e.g. dopamine) in the presence of interferants such as ascorbic acid or uric acid.[206] Alternatively, the incorporation of different metallic nodes within a conductive MOF can lead to tunable selectivity to volatile organic compounds and small gaseous molecules (e.g., NH_3).[174]

Response time is the time required to reach a stable output reading upon the exposure to analytes.[207] Typically, it is referred as the time at which the analytical signal reaches a certain percentage (e.g., 90–95%) of its final value, in response to a step change of the input.[208] The response time is strongly dependent on the device architecture, recognition components, and analytical techniques used to generate the signal. The specific requirement for the response time is often dictated by the final application of the analytical device, for example, the response time required to monitor changes in physiological concentrations of analytes in human body is usually at ms scale.[9] Recovery time is considered as the converse of the response time and it is

defined as the time required for the sensor signal to return to its initial value after a step concentration change from a certain value to zero. Reversibility is extent to which the signal is restored to its initial state prior to analyte exposure.[209-210] Full recovery of the analytical device is paramount for practical applications of sensors for continuous sample monitoring. However, in the case of fabrication of one–measurement disposable devices, semi–reversible or irreversible interactions between the recognition element and the analyte may be utilized. Because the electron confinement in 2D materials with very small lateral size down to atomic scale, the chemical perturbation on their surface is enough to result a detectable change of the bulk property.[114, 211] Meanwhile, the unique dimensionality of 2D materials is advantageous for the ananlyte to quickly difusse to the surfae the materials, where the anlyte-materials interaction can subsequently happen to trigger the change of electronic parameter of the materials.[212] Quick diffusion rates are also expected in porous 2D materials, for example, 2D MOFs, whose inherent channel-like strucute can serve as the analyte diffusion pathway.[115]

Dynamic response range is defined as the concentration range that corresponds to the maximum usable readout (e.g., upper detection limits) and the minimum operable analytical signal (LOD) that can be measured by a sensing system.[204] An ideal sensor would give responses that can be correlated to specific concentrations at a range wide enough to meet the sensing requirement. This range results in a meaningful and accurate output for the sensing system. All sensing systems are designed to perform over a specified range. Output signals that fall outside of the response range may cause large inaccuracies in recorded data, and possibly result in an irreversible damage to the sensing system. The response range of a sensing system is determined experimentally through repetitive measurements of the response of the sensor over the range of concentrations of targeted analyte. Linear response range of the sensing system refers to the part of the recorded calibration curve through which a fitted linear regression demonstrates either no or minimal deviation from linearity. The dynamic response range of sensors comprising of 2D materials, as in the case of their low detection limits, is dependent on the material-analyte interactions, available surface area, and surface modifications. The role of incorporated nanostructures on the dynamic response range and low detection limits in the context of electrically–transduced sensing of gases, volatile organic compounds, ions, and biomolecules is further emphasized in **Chapter 4**.

Drift is the slow, non–random change of analytical signal with time while the concentration of measured analyte remains constant.[213-214] It can be caused by mechanical or thermal instability, contamination, or degradation of materials used for the fabrication of an analytical device. The contribution of drift to the analytical response may be minimized by frequent device recalibration, or through computational data processing. Signal drift can be overcome through careful device design in which the influence of external environment is reduced by application of protective coatings or encapsulating layers.[53]

Reproducibility is the ability of the analytical device to produce the same signal output after the experimental conditions have been altered.[204] It can be quantified by measuring the variation in calibration data obtained for different devices, using the same test protocols and test equipment. Reproducibility should be reported together with specification of experimental conditions. In sensors comprising of 2D materials, the device–to–device reproducibility is primarily dictated by the ability to synthesize the nanomaterial in well–defined and controllable fashion as well as its integration into a functional device. For instance, chemical vapor deposition was realized as suitable method for large–scale manufacturing of graphene or MoS_2 with good control over the structure of synthesized materials (see also in **Chapter 3**). Development of synthetic method that permits deposition of the 2D nanostructures directly onto the sensing device can promote and improve the signal reproducibility in analytical measurements.[215]

Stability is the ability of a sensor to produce the same output signal when performing the same analytical measurement over a period of time.[199] This includes a retention of the device parameters such as sensitivity, selectivity, response, and recovery time. It can be quantified by comparing the response produced by an aged device with a new analytical sensor. Stability is particularly important for the fabrication of devices that are employed for continuous and prolonged monitoring of analytes as in the case of environmental analysis. Ideally, the fabricated device should remain unchanged over the lifespan of the device. The lifetime of analytical devices based on 2D nanostructures is primarily dictated by the stability of the sensing material to external stimuli such as applied potential, temperature, or mechanical/physical stress.[216]

The requirements for specific parameters of the sensing system are primarily dictated by its final application. For instance, sensors used for continuous sample monitoring need to exhibit exceptional signal stability, minimal drift, and no degradation in the selectivity and sensitivity over prolonged period of time. Furthermore, systems used for *in vivo* clinical analysis should be able to respond to sensed analyte within the shortest time possible to ensure that the measured sample did not undergo degradation/contamination due the presence of numerous biological process. In this case, the stability of analytical device can be compensated for by short response times to targeted analytes.

2.4. Electrically–Transduced Sensing Architectures

The architectures of electrically–transduced chemical sensors, with few expectations, will fall into five categories, including chemiresistor, chemical diode, field–effect transistor, chemical capacitor, and electrochemical sensor.[7] In the following sections, the general configuration and operation mechanism of each type of architectures will be discussed.

2.4.1. Chemiresistors

A chemiresistor consists of two electrodes connected with a chemiresistive material deposited onto an insulating support (**Figure 8a**).[217-218] The sensing materials used for chemiresistor fabrication can be either semi–conductive as in the case of metal oxides or TMDC or possess metallic conductivity (e.g., graphene). The resistance of a chemiresistive material, which are sandwiched between the two electrodes, can be altered by exposure to gaseous analytes. By measuring the change in resistance or current of the sensor device, the concentration of analytes can be measured.

The resistance of the device can be mainly divided into two components:

$$R = R_{mat} + R_{contact} \quad \textbf{(7)}$$

Here, the R, R_{mat}, and $R_{contact}$ are the total resistance of the device, the resistance of the sensing material, and the sum of contact resistance originating from the metal electrode/sensing material junctions and junctions of the material grains, respectively. The response (S) of the sensor is given by **eq 8**:

$$S = \frac{\Delta R}{R_0} = \frac{R_{analyte} - R_0}{R_0} \times 100\% \quad \textbf{(8)}$$

or,

$$S = \frac{\Delta I}{I_0} = \frac{I_{analyte} - I_0}{I_0} \times 100\% \quad \textbf{(9)}$$

where I_0, R_0 are the current and resistance of the circuit in the device under an applied voltage, V, and $I_{analyte}$, $R_{analyte}$ are the current and resistance upon exposure to analyte, respectively.

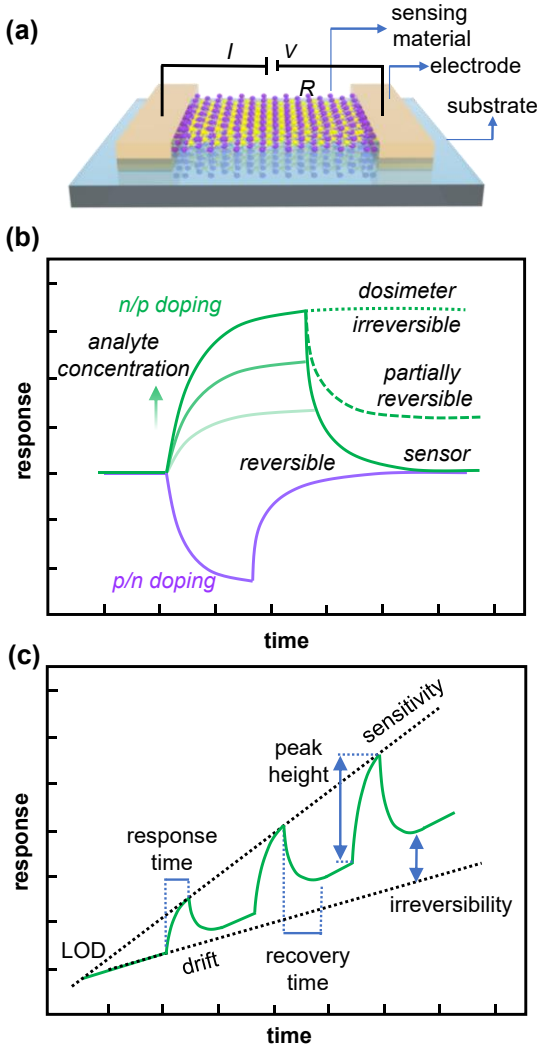

Figure 8. (a) Scheme diagram of a typical chemiresistor–based sensor made of metal chalcogenide. V is the voltage applied to the device, I is the current flowing through the device. (b) A typical response curve of a sensor exposed to analyte with opposite type (green and purple line) of electronic character at different concentration. Depending on the reversibility of interaction between analyte and sensing material, the response of the sensor can be irreversible, partially or fully reversible. (c) Graphical representation of selected performance parameters in a device successively exposed to increasing concentrations of analyte.[53] Adapted with permission from Ref. [53]. Copyright 2016 WILEY - VCH Verlag GmbH & Co. KGaA, Weinheim.

The sensing process of chemiresistive devices is mainly dictated by three distinct mechanisms, including change of doping level, modulation of Schottky barrier, and modulation of junction distance, which can work independently or synergistically, to alter the resistance of the device.[53, 219] In the case of p–type semiconductors like reduced graphene oxide (rGO), the exposure to electron donating analytes (e.g., NH_3) results in electron transfer to the valence band of the rGO semiconductor, diminishing the concentration of holes, and subsequently causing a

decrease in the conductance; conversely, an electron withdrawing gases such as NO_2, will trigger the electron transfer from the p–type semiconductor material to the analyte, increasing the hole concentration, and thus improving its conductance (**Figure 8b**).[157] The adsorption of analyte can alter the work function (ϕ_s, ϕ_m) of the material layer, successively modifying the height of Schottky barrier of the material–electrode contact. In addition, the adsorption of the analytes at the junctions between the crystallinities or particles of the material can cause the grains of the chemiresistive material to separate from each other, which increases the hopping distance for charge transport, thus leading to an increase in the resistance.[220-221] **Figure 8c** shows a representative sensing trace of chemiresistive sensor upon three successive exposures to increasing analyte concentrations, that graphically represent the key features of the sensing performance, including sensitivity, LOD, response/recovery time, drift, and reversibility.

Chemiresistive sensors are one of the most widely applied device architectures for electronic sensing of gaseous analytes due to their simplicity, compatibility with conventional DC circuits, low cost, predictable electrical properties, and the ease of high precision measurement.[217-218] Chemiresistive architectures are best employed in systems where rapid prototyping is necessary. The straight-forward design and operation of this type of device make them attractive starting platforms for investigating chemical sensitivity of new materials. The wide variety of techniques for incorporating sensing materials, and the macroscale features typically used, make this architecture highly suitable for initial testing when the morphology of materials has not been optimized, or to reduce device fabrication costs. In addition, chemiresistors typically exhibit good sensitivity, good reproducibility, and low power consumption.[54]

2.4.2. Chemical Diodes

A diode is a two–terminal electronic component that exhibits low resistance to passing current in one direction, and high resistance in the opposite direction.[222] There are two types of diodes, the p–n junction diodes and Schottky diodes. The p–n junction type diode is formed by joining a p–type semiconductor with a n–type semiconductor, while the Schottky diode is composed of only one type of a semiconductor (p or n) material that is in contact with a metal or semi-metal electrode (**Figure 9a**).[223] Schottky barrier diode sensors are simple to fabricate, obviating the need for photolithography or high–temperature diffusion/oxidation steps.[224-225]

The current–voltage (I–V) characteristic of Schottky diode can be explained by charge carrier transport mechanism,[186]

$$I = I_S[\exp\left(\frac{eV}{kT}\right) - 1] \quad \textbf{(10)}$$

where V is the forward bias voltage, k is the Boltzmann constant, T is temperature. The reverse bias saturation current (or scale current) I_S is defined by **eq 11**.

$$I_S = eN_c\mu_e E_{max} \exp\left(-\frac{\emptyset_b}{kT}\right) \quad \textbf{(11)}$$

In **eq 11** ϕ_b is the Schottky barrier height for an ideal contact between a metal and a semiconductor, N_c is the effective density of states in the conduction band, μ_e is the electron mobility, and E_{max} is the maximum field strength at the metal/semiconductor interface. The current density–voltage (J–V) curve is also widely used to describe the characteristics of a diode, which follows the similar relation as that of I–V curve.

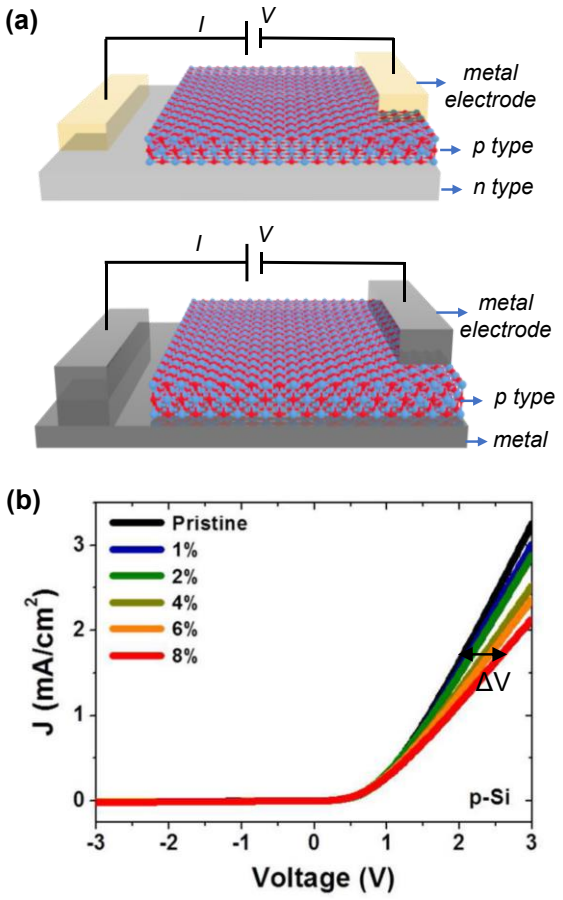

Figure 9. (a) Scheme diagram of a typical PN diode sensor (top) and a typical Schottky diode sensor (bottom); (b) Typical response curves of a Schottky diode–based sensor expressed by I–V curve upon exposure to analyte. ΔV indicates the gas or vapor induced voltage shift at constant current density.[226] Reproduced from Ref. [226] Copyright 2013 American Chemical Society.

A typical change in the J–V characteristic of a Schottky barrier diode due to analyte–material interactions is shown in **Figure 9b**. The sensitivity of diodes is represented by the analyte–induced voltage shift at a given diode current I (or current density J), ΔV, extracted from current voltage characteristics and is defined as the following equation,

$$S = \frac{\Delta V}{V_0} = \frac{V_{analyte} - V_0}{V_0} \times 100\% \quad \textbf{(12)}$$

where $V_{analyte}$ and V_0 are the applied voltages at a constant current density with and without the exposure to analyte,

respectively. If the devices are operated at constant voltage, then the sensitivity can also be given by $\Delta I/I$.

The generation of signal in Schottky barrier diodes originates from the change of junction characteristics (i.e., I–V or J–V characteristics) by alternating the Schottky barrier height, Φ_b, or modifying the built–in voltage, V_{bi}.[186, 227] The response can be due to either the adsorption of species at the surface of a metal that affects the interfacial polarization by formation of a dipole layer or caused by the absorption of analytes onto the semiconductor, which changes its work function and, hence, the contact potential or built–in voltage of the diode. The former is mostly encountered in Schottky barrier diodes based on inorganic semiconductors, whereas the latter is related to diodes based on organic semiconductors.[186]

Chemical diodes are effective sensors that are comparable in sensitivity and power consumption to chemiresistors. Device integration is more involved than chemiresistors since the connection between the semiconductive material and metal must be precisely controlled. Lithographic techniques are often used to ensure placement of 2D materials with respect to electrodes. A disadvantage of chemical diodes is that sensitivity is dependent on the applied voltage, and this requires that materials must be stable under bias voltages higher than those typically required by chemiresistors.[226-227]

2.4.3. Field–Effect Transistors

Field–effect transistor (FET) is another type of device which has attracted a lot of research interest for chemical sensing applications.[228-229] FET devices consist of source and drain electrodes, a semiconductive channel material, an insulating gate oxide, and a gate electrode (**Figure 10**).[230] The current–flows through the contact terminals via the channel (called the drain current, I_{DS}) which can be modulated by an electric field perpendicular to the semiconductor originating from a voltage (V_{GS}) applied to the metal electrode (called the gate) and the source. The electric field acts upon the number of mobile charge carriers in the semiconductor, and consequently, controls the current, I_{DS}. The conductivity of the channel is a function of the potential applied across the gate and source terminals. The drain current I_{DS} is given by:

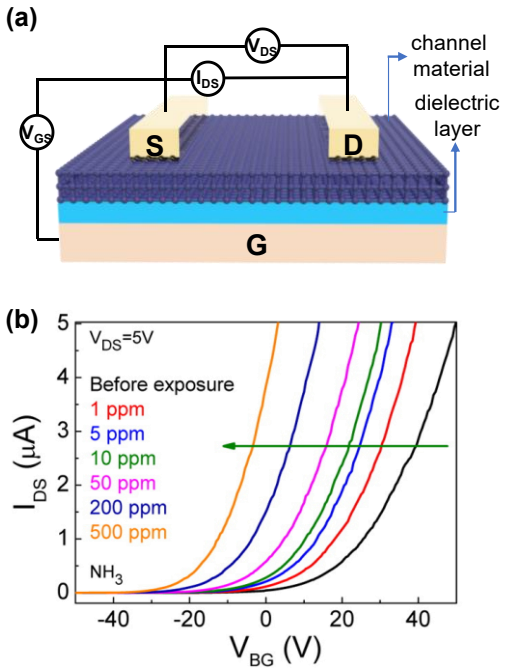

Figure 10. (a) Scheme diagram of a typical bottom–gated FET sensor made of metal oxides. (b) Typical response curves (I_{ds}–V_g) of a MoS_2 FET upon exposure to NH_3 with different concentrations.[191] Reproduced from Ref. [191] Copyright 2014 American Chemical Socety.

$$I_{DS} = \frac{C_i \mu W}{L}\left[(V_{GS} - V_{th}) - \frac{1}{2}V_{DS}\right]V_{DS} \qquad \textbf{(13)}$$

where C_i is the capacitance of the gate insulator per unit area, μ is the charge carrier mobility in the channel, W/L is the width–to–length ratio of the channel, V_{GS} and V_{DS} are the applied gate–source and drain–source voltage, and V_{th} is the threshold voltage defined as the (minimum) voltage required on the gate to create a layer of minority charge carriers under the insulate layer.[231] The curves are characterized by a linear region when $V_{DS} << (V_{GS}–V_{th})$ and a saturation region when $V_{DS} > (V_{GS}–V_{th})$. At low drain–source voltages the I_{DS} current follows Ohm's law and is proportional to V_{DS} at a fixed V_{GS} (linear regime).

In a FET based chemical sensor, the channel is usually composed of a semiconducting bulk material that is sensitive to analyte molecules.[229] It operates by monitoring current change in the channel material before and after the adsorption of target analytes.[229] Most FET sensors operate in the linear range of I_{DS} and act as resistive type sensors. Their performance is governed by the intrinsic properties of the channel material, such as the work function, carrier mobility, and band gap, of which, band gap is the most important parameter in engineering sensor performance.[229] Depending on the geometry of the devices, the type of a semiconductor (p–type vs. n–type), the nature of the analyte (reducing vs. oxidizing), the quality/morphology of the sensing materials, and physio–chemical interactions, including hydrogen bonding, charge transfer, hydrophobic interactions, and dipole–dipole interactions, can contribute to the

modulation of electrical conductivity in the 2D nanomaterial.[228, 232] The interactions between the analyte and semiconductor can induce a change in Fermi–level, and thus alter the height of a Schottky barrier. These interactions can also involve a change in electronic coupling along the charge carrier transfer path in the semiconductor, which is attributed to morphological changes or interactions at grain boundaries.[233] As a consequence, a change in conductance occurs upon exposure to a targeted analyte.

The response of the FET–based sensor can thus be expressed by $\Delta I_{DS}/I_{DS}$ at the given gate–source and drain–source voltage:

$$S = \frac{\Delta I_{DS}}{I_{DS}} = \frac{I_{DS}' - I_{DS}}{I_{DS}} \times 100\% \quad \textbf{(14)}$$

where I_{DS}' is the current upon exposure to analyte.

FET sensors have attracted considerable attention because of their potential for miniaturization in nanoscale, parallel sensing. Additionally, they can be engineered to exhibit fast response and are easily integrated with electronic manufacturing processes. FET sensor platform can work in both gas and liquid environments permitting detection of a wide range of analytes including gases, ions, and biomolecules.[228-229] FET devices are commonly used to increase sensitivity compared with other device architectures because charge carrier mobility can be modulated by controlling gate voltage. FET devices can be manipulated into microscale or nanoscale features and present a useful means of providing strong device characterization (charge carrier mobility, conductivity, major carrier species) and subsequently being used for chemical sensing. However, the integration of materials into FET devices requires advanced techniques such as lithography, and a high degree of control over material morphology to incorporate the material as the channel in FET devices. Therefore, most FETs are limited to materials that are well understood. In addition, the application of FET for in-solution sensing has been limited primarily to measurements in non-physiological or/and low–ionic strength solutions due to the charge screening effects (Debye screening length).[234-236] The charge of targeted molecules in solution (e.g., DNA, proteins) is screened by dissolved solution electrolytes (cations and anions). Current methods to overcome these limitations primarily rely on solution desalting (decrease in ionic-strength),[237] incorporation of antibody receptors,[238] and aptamers[239], which can minimize the distance between analytes and the FET surface, and application of permeable polymer coatings that increase the effective Debye length immediately adjacent to the FET surface.[240]

2.4.4. Chemical Capacitors

A capacitor is a device that consists of two conducting electrodes separated by a non–conducting substance called a dielectric (**Figure 11a**).[241] The dielectric may be either air, mica, ceramic, organic solvent, or other suitable insulating material. Electrical energy charge is stored as a build–up of charge on the opposing electrodes. In general, the capacitance value is determined by the dielectric material (ε_r), distance between the electrodes (d), and the area of each plate. The capacitance of a system can be expressed in terms of its geometry and dielectric constant as[242]

$$C = \varepsilon_r \frac{\varepsilon_o A}{d} \quad \textbf{(15)}$$

where C is the capacitance in farads (F), ε_r is the relative static permittivity (dielectric constant) of the material between the plates, and ε_0 represents the permittivity of free space (8.854×10^{-12} F/m), A is the area of each plate, in square meters and d, corresponds to the separation distance (in meters) of the two plates.

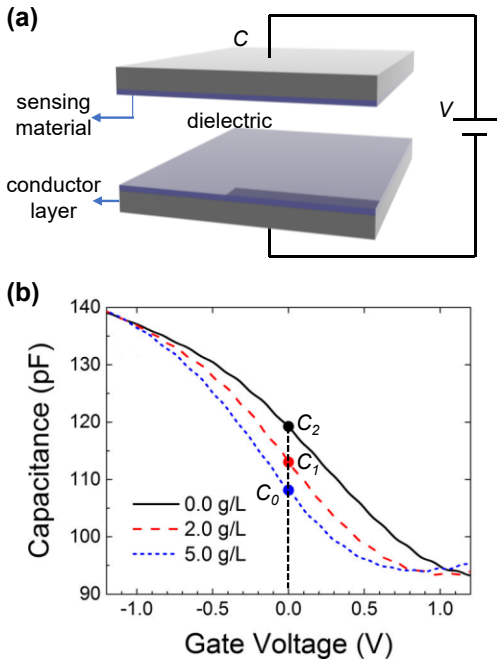

Figure 11. (a) Scheme diagram of a typical chemicapacitor-based sensor. (b) Response of a graphene based chemicapacitor under different concentrations of glucose as expressed by the shift of the C–V curve toward negative gate voltages with increase in glucose concentration.[243] Reproduced from Ref. [243] Copyright 2017 American Chemical Society.

Any adsorption or binding of analytes onto the dielectric layer will change the thickness (d) and/or dielectric behavior (ε_r), and consequently the capacitance of the system. The binding event between the sensing material and analyte further induces alterations in the electrical properties or dimensions of the material resulting in a measurable analytical signal.[244] For example, changes in the dielectric constant (ε_r) due to the interactions between an immobilized antibody and antigen on a surface of 2D material are frequently utilized in biomolecules sensing. Dielectric–variable chemical capacitors are generally not applied to gas sensing applications because the relative permittivity of most inorganic gases (except H_2O) are similar. Instead, changes in dielectric layer thickness (d) are more frequently found in gas sensing.[148] For humidity sensing, the change in

the electrode area is also possible.[245] **Figure 11b** shows the C–V characteristic of a capacitor–based sensor before and after interacting with an analyte. The sensitivity can be defined in terms of the change in capacitance ΔC at a fixed voltage V.[243]

$$S = \frac{\Delta C}{C_0} = \frac{C_{analyte} - C_0}{C_0} \times 100\% \quad \textbf{(16)}$$

It could also be defined as $\Delta V/V$ at a given C value. Often the sensitivity is simply given as is the change of the flat band potential (ΔV_{FB}), the bias needed to force the surface potential (ψ_s) of the semiconductor in the capacitor to zero.[246]

Capacitive–type sensors are characterized by low cost and simple device configuration that enables their miniaturization for sensing applications. Multiple capacitive sensors containing different recognition elements can be integrated onto a single-chip platform, to form a compact array of micro–sensors for targeting different molecules. Since chemical capacitor devices do not require static power consumption, they are suitable for use in energy–constrained applications, including wireless sensor networks and low power battery–operated technologies. (as low as a few μW)[247]. The amplification of capacitance signal can be readily performed by using oscillator circuits thus enabling sensitive detection of analytes.[148, 244] A wide scope of 2D materials can be sued for electronic transduction of chemical sensing, because adsorption of chemical analytes can lead to a permittivity change. However, chemical capacitors are generally less selective than other sensing architectures. They are more often sensitive to humidity and swelling effects.

2.4.5. Electrochemical Sensors

Electrochemical sensors are one of the largest groups of chemical sensors. They are comprised of integrated receptor–transducer devices capable of providing selective and quantitative analytical information regarding the investigated system (**Figure 12a**).[10] Electrochemical sensing measurements typically generate a measurable response in the form of current potential, charge accumulation, or impedance change of a medium between electrodes.[9]

Potentiometric sensors. Potentiometric sensing devices measure the difference in electrical potential between the connecting leads of the working electrodes relative to the potential of a suitable reference electrode.[248] Potentiometric measurements are carried out in a two–electrode galvanic cell under ideally zero current conditions.[249] In this situation the measured potential is defined by the charge distribution of ions and electrons, at the solution/working electrode interface, as a function of ion activity in a measured sample.[249] This relationship is defined by the Nernst equation indicating that, at room temperature, a 10–fold increase in the activity of measured ions is followed by an increase in the potential/electromotive force (EMF) of 59.2 mV/z_i.[204]

$$E_{PB} = E_i^0 + \frac{RT}{z_i F} \ln \frac{a_I\,(aq)}{a_i\,(org)} \quad \textbf{(17)}$$

E_{PB} is the electrical potential developed between the working and reference electrode, E_i^0 is a cell potential under standard conditions (273.15 K and 100 kPa), $a_I\ (aq)$ are the activities of primary ions in the aqueous and organic phase, respectively. z_i is the ionic charge of the ion i, F, R, T are the Faraday constant, the universal gas constant, and the absolute temperature, respectively.[204]

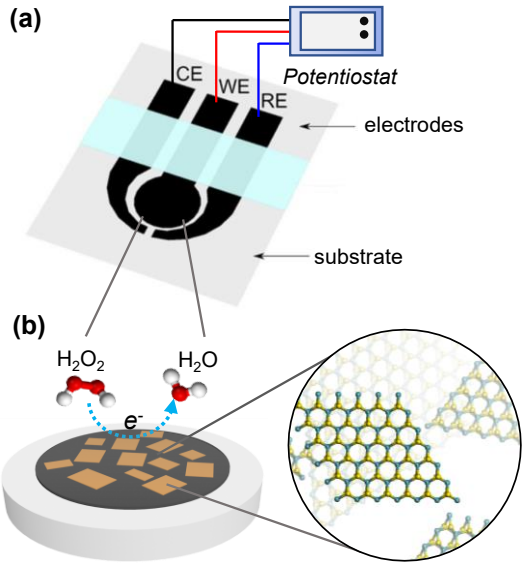

Figure 12. (a) A typical configuration of electrochemical sensor with counter, working, and reference electrodes connected to a potentiostat. CE, counter electrode, WE, working electrode, RE, reference electrode. (b) A working electrode that consists of a glassy carbon electrode functionalized with redox active MoS_2.[250] Adapted from Ref. [250] Copyright 2013 American Chemical Society.

In direct potentiometry, the measured phase boundary potential is ideally a function of the activity of only one specific analyte ion due to the charge separation at the water/water immiscible interface, allowing selective detection of targeted analytes even in the presence of ionic interferants.[248] Therefore, selectivity of ion selective electrode (ISE) is directly related to the equilibrium constant of the exchange reaction of targeted and interfering ions between the organic and aqueous phases.[251] Many modern potentiometric sensors rely on the presence of either ionically conductive mono–or poly–crystalline solids (e.g., lanthanum trifluoride) or ion–selective membranes (ISM), whose nature/composition dictates the sensing properties of the electrodes. Typically, an ISM is composed of an ionophore (ion ligand), lipophilic salt (ion exchanger), polymer, and plasticizer which together form the matrix of the membrane.[252] These polymeric membranes have proven to be suitable for numerous sensing applications because their electrochemical response and sensing properties (e.g., selectivity and sensitivity) can be relatively easily modulated by using different components during the ISE fabrication.[252]

Since the input signal in potentiometric measurements refers to the activity of a target ion, while the output

is an electrical potential, the effective conversion of the charge carriers from ions to electrons is needed. This signal conversion can be achieved using transducers.[253] To achieve stable electrode potential, it is required to obtain sufficiently fast and reversible ion–to–electron transduction across the ionically active polymeric ion–selective membrane and the electrochemically active transducer, and the electrical contact, without any contribution from side reactions.[254] In conventional liquid contact ISEs, usually AgCl coated Ag wire serves as inner reference electrode submerged in the internal electrolyte containing fixed concentration of Cl^-ions. In this situation, the ion–to–electron transduction proceeds through the reversible redox reaction between $AgCl_{(s)} + e^- \rightleftarrows Ag_{(s)} + Cl^-(aq)$, which provides stable interfacial potential between the AgCl/Ag electrode and the inner filling solution.[252]

Advancements in the development of potentiometric ion–selective sensors led to the elimination of internal filling solution giving rise to solid–contact ISE, which are more durable and easier to miniaturize than their conventional counterparts.[254] Although first reports of solid contact ISEs emerged in early 1970s with the invention of the coated–wire electrodes (CWE), the poor potential stability of resulting CWEs due to the blocked interface between ISM and electrical conducted strongly inhibited their further analytical applications.[254] Solid–contact electrodes with enhanced potential stability have been produced by using numerous electroactive materials with both mixed electronic and ionic conductivities that can work as ion–to–electron transducers when sandwiched in between the ISM and underlying conductor.[253] Among these materials, electroactive conductive polymers (e.g. poly(3,4–ethylenedioxythiophene)-poly(styrenesulfonate) (PEDOT-PSS), poly(3–octyl)thiophene or polyaniline (PANI)[255-256]), carbon materials,[257-260] and 2D nanomaterials including graphene[261-263] were recognized as one of the most promising ion–to–electron transducers for solid–contact ISEs.

Potentiometric sensing has three beneficial characteristics that allow these types of sensors to perform well for chemical detection. *First*, potentiometric sensors use only two electrodes, allowing simplified device design. *Second*, analysis happens at thermodynamic equilibrium meaning observation of the system may be performed without applying a potential that may motivate chemical reactions to occur. *Third*, potentiometry is able to detect chemical species without redox processes occurring, meaning redox-inert species are possible analytes. A few drawbacks of potentiometry exist. As devices, potentiometric sensors are more sensitive to mechanical disturbances such as stirring., which hiders their use in mobile applications. Also, since only the potential of the system is measured, information about reversibility and this subsequent boost to selectivity, is not obtained.

Voltammetric Sensors and Amperometric Sensors. Voltammetry and amperometry are the most utilized transducing methods in the development of electrochemical sensing platforms due to their overall simplicity, low–cost instrumentation, and significant sensitivity to targeted analytes.[9-10, 264-266] In both methods, the applied potential is a driving force for electron transfer reactions, which produce a measurable change in current.[267] Since the magnitude of measured current is proportional to the number of oxidized/reduced molecules in the solution, it is possible to monitor relative concentrations of molecules at physiological timelines.[267] Voltammetric and amperometric measurements typically utilize a three–electrode set–up comprising of working electrode, counter electrode and reference electrode.[204] The zero or 'reference' potential is set by the presence of reference electrode. The third electrode is the counter electrode, which acts as an electron source/sink[268]. In the development of sensing devices, the surface of a working electrode (e.g., Au, Pt, or GCE) is most commonly functionalized with an electroactive layer to induce selectivity to targeted analytes as shown in **Figure 12b**.[9-10, 269-270] Electrodes modified with redox active polymers, ionic liquids, carbons, metals, and 2D nanomaterials are only a small representation of available modifications that led to the development of excellent sensing platforms for applications spanning across many disciplines and industries.[8, 11, 266, 271-275]

In amperometry, the electrode is held at a fixed potential and the current is monitored over time.[276] Current magnitude is then related to the concentration of the analyte present.[277] Amperometric sensors typically have response times, dynamic ranges and sensitivities similar to potentiometric sensors.[278-279] The main limitation of amperometry is, that it is difficult to confirm the identity of detected molecules solely by the shape of recorded current.[9, 280]

In cyclic voltammetry (CV), the applied potential at the working electrode is ramped linearly with time and the current flowing between the working electrode and an auxiliary electrode is measured.[267] When the CV scan, in either cathodic or anodic direction, reaches the set potential, the potential ramp is reversed to bring the potential of the working electrode back to its initial value.[281] This potential inversion can occur multiple times during a single experiment, until a desired number of electrochemical cycles is obtained. Because many biologically important molecules undergo redox transformations at different potentials, a cyclic voltammogram can be used as a fingerprint technique to identify the presence of targeted biomolecules.[10, 266, 270, 278] Besides cyclic voltammetry, numerous other voltammetric techniques have been employed in electrochemical detection of biomolecules to further enhance the sensitivity of sensing platforms in the context of quantitative analysis.[8-11, 14, 59, 264-266, 270, 272-275, 278-279, 282] Typically, pulse voltammetry techniques such as differential pulse voltammetry (DPV), square–wave voltammetry (SWV), and normal pulse voltammetry (NPV) are encompassed within this category.[10, 266, 283] Recent review articles have focused on specific applications or methods for voltammetric sensors.[8-10, 13, 121, 273]

Voltammetry and amperometry-based sensors access a regime of chemical sensing that provides exceptional selectivity and sensitivity. The advantage of voltammetry is that a positive or negative bias can be applied to assess the

redox profile of a solution. Specific redox couples can be observed to give information about the reversibility of reactions, the nature of the species present, and how they interact with 2D surfaces. Amperometry has many of the same benefits of voltammetry, and like voltammetry, can only detect redox active species. Amperometry can be performed with stirring or other disturbances with no ill effect on sensing performance. This is beneficial to mobile applications of these sensors such as wearable sensors, or installations for environmental monitoring.

Impedance sensors. Electrochemical impedance spectroscopy (EIS) is a non–destructive steady–state technique capable of probing the relaxation phenomena over a wide range of frequencies typically spanning from 10^6 to 10^{-4} Hz.[284] Similarly, as to voltammetric/amperometric techniques, EIS predominantly utilizes a three–electrode configuration for electroanalytical measurements in solutions. During the EIS experiments a small AC perturbation signal (2–10 mV) is imposed to the electrochemical cell and the resulting current is measured.[285] The current response to the AC potential is a sin wave with the same frequency but with different amplitude and phase.[286] The in–phase current response determines the real component (resistive) of the impedance, while the out–of–phase current response determines the imaginary component (capacitive).[287] The magnitude of the recorded phase shift depends on the nature of the electrolyte, diffusion process, electrode kinetics and chemical reactions that may take place in the electrochemical cell.[267] In general, impedance data can be represented using either Cartesian or polar coordinates. The plot of real part of the impedance–ReZ(jω) (x axis) versus the imaginary part of the impedance–ImZ(jω) (y axis) is typically referred as a Nyquist plot. A Bode plot is a log–log plot of the magnitude $|Z(j\omega)|$ and phase (ϕ) of the impedance $Z(j\omega)$ as a function of the frequency of a sinusoidal excitation ($\omega \; or \; f = \omega/2\pi$).[286] Since the Nyquist plot combines gain (magnitude) and phase into one plot in the complex plane, the information regarding frequency is thus unavailable, and needs to be extracted from the Bode plot.[267] EIS results are most often fitted, through modelling, into equivalent circuits made up of resistors, capacitors or inductors, which can be used to describe most of the electrochemical systems.[287] Impedance methods are thus capable of characterizing physicochemical processes of widely differing time constants such as sampling the electron transfer at high frequency and mass transfer at low frequencies.[288] Since EIS is particularly sensitive to changes caused by either surface or bulk phenomena, its prominence as an analytical tool for electrochemical research and sensor applications have been on a rise.[289-296]

In the context of 2D materials, EIS is a powerful technique for investigating the properties and phenomina at different stages of development and integration of materials into targeted applications. Interfacial phenomia important for sensing, energy storage, and electronic applications can be characterized.[297] For example, EIS can offer information about double layer capacitance of materials in solution. EIS can be used to help characterize the conductive junction between electrode and 2D material. Finally, chemical proceses enabled by 2D materials that are essencial to sensing and catalysis, such as rate constants and diffusion coefficients, can be characterized using EIS techniques.[298]

3. Structure and Surface Chemistry of 2D Materials

3.1. Graphene and Graphene Oxides

Graphene is a single layer of sp^2–hybridized carbon atoms covalently bound together in a honeycomb lattice (**Figure 13a**).[77] It is the basic building block of other carbon-based allotropes, such as graphite, carbon nanotubes (CNTs), and fullerenes.[299] The distance between two neighboring carbon atoms in a single sheet of graphene is about 1.42 Å. Individual layers are held together by the van der Waals interactions to form graphite (**Figure 13d, e**), in which the distance between the adjacent layers is about 3.35 Å (**Figure 13b**). Graphene was first successfully isolated at 2004 by Geim and Novoselov by exfoliation from graphite.[76] Since then, it has become one of the most published topics for material scientists due to its extraordinary thermal, optical, electrical, mechanical, and physiochemical properties arising from its two–dimensional crystal structure.[73] Graphene displays extremely high carrier mobility of 2×10^5 cm^2 V^{-1} s^{-1} and high carrier density of 1012 cm^{-2} at room temperature, which corresponds to a resistivity of 10^{-6} Ω.[300-301] Its bandgap and conductivity is dependent on the number of layers in the stack and approach those of graphite when the number of layers is increased.[302] Graphene exhibits a large theoretical specific surface area of 2630 m^2 g^{-1}, which is twice as high as that of single–walled CNTs.[303] It also has remarkable mechanical properties, and it is considered as one of the strongest materials available, with an intrinsic tensile strength of 130.5 GPa and a Young's modulus of 1 TPa.[304]

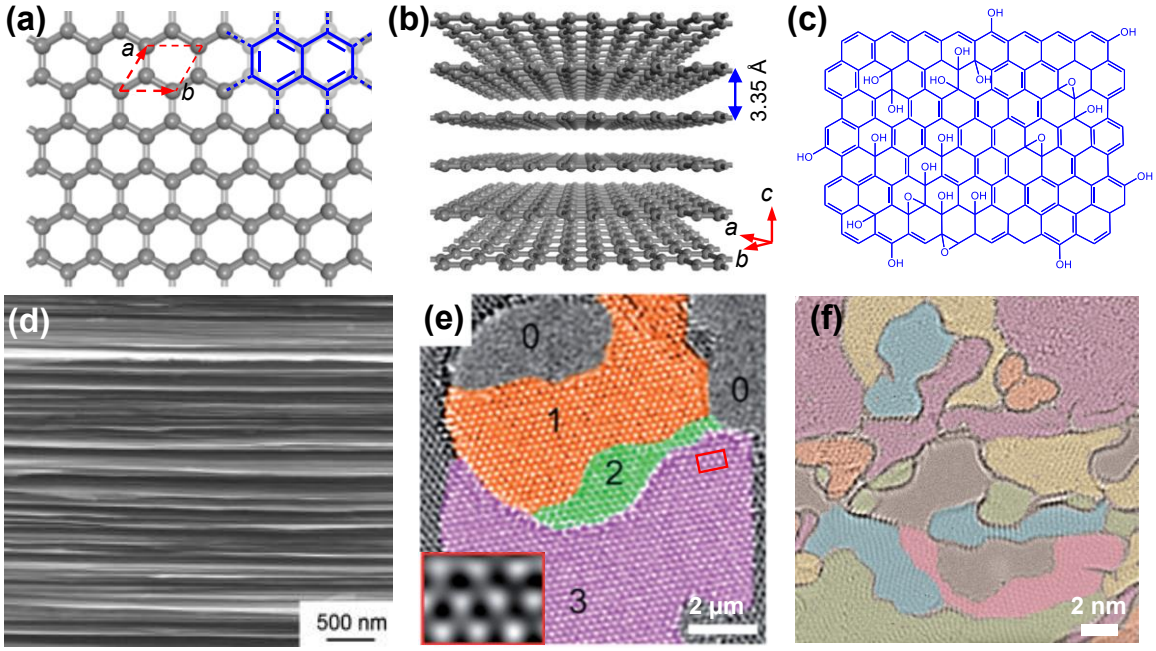

Figure 13. (a) The ideal structure of a sheet of graphene that consist of atomic–scale hexagonal lattice made of carbon atoms. (b) Structure of graphene layers. (c) Chemical structure of Graphene oxide based on the Lerf–Klinowski model.[305] Epoxy and hydroxyl groups functionalize the surface. (d) SEM images of highly ordered pyrolytic graphite consisting of many layers of graphene.[306] Reproduced with permission from Ref. [306] Copyright 2013 Elsevier Ltd. (e) HRTEM image of a region containing 0, 1, 2, and 3 layers of graphene. Scale bar, 2 μm.[307] Reproduced with permission from Ref.[307] Copyright 2010 IOP Publishing Ltd. (f) Overlaid color representation of few–layer graphene oxide at 700 °C imaged with an in situ TEM heating holder. Scale bar, 2 nm.[308] Adapted from Ref. [308] Copyright 2016 American Chemical Society.

Well–established methods to produce graphene include micromechanical cleaving,[76] solution-phase exfoliation from graphite,[309-310] chemical vapor deposition (CVD)[311-314] and organic synthesis based methods.[315-316] Micromechanical cleaving technique, also known as the 'Scotch tape' or peel–off method, tends to produce graphene with the best quality with the least amount of structural and compositional defects.[317] However, this method offers only limited control over the number of mechanically peeled–off layers, and it is not suitable for mass manufacturing of graphene. Solution-phase exfoliation usually involves the oxidation of graphite under strongly acidic conditions (e.g., Brodie,[318] Staudenmaier,[319] and Hummer's methods[320]) and leads to the formation of graphene oxide (GO), which has many oxygen–containing functional groups on the surface, such as carboxyls, epoxides, and hydroxyls (**Figure 13c**).[73, 321-322] GO retains a layered structure (**Figure 13f**), but in contrast to graphene, it is an electrical insulator due to the existence of a large proportion of sp^3 C–C bonds. To regain the structural features of graphene, that define its unique electrical properties, GO can be reduced either by thermal, electrical or chemical treatments.[322] The resulting product–reduced graphene oxide (rGO)–contains a significant amount of C–O bonds. This method allows the low–cost and high–volume production of rGO; however, it results in the incorporation of structural and compositional defects with limited control over their spatial distribution. CVD relies on the epitaxial growth of graphene layers on the surface of other single–crystal substrate (e.g., SiC, Ni and Cu) under high temperatures (> 600 °C) in the presence of hydrocarbon vapors as a source of carbon.[323] CVD is suitable for producing macroscale areas/quantities of graphene, which then can be readily transferred onto desired surfaces after the dissolution of the single–crystal supporting substrate. However, the uniform growth of single–layer graphene sheet, using CVD methods, remains challenging, and requires further development.[75, 117]

The high electrical conductivity of graphene, together with its large specific surface area, high mechanical strength, and potential for mass production, makes it an excellent platform for applications in chemical sensing.[78, 123, 125, 232, 272, 324-325] *First*, graphene exhibits remarkably high carrier mobility and high carrier density, at room temperature.[299] These outstanding electronic properties make graphene a good candidate for the fabrication of high–performance electrically–transduced analytical devices.[102, 317] *Second,* the surface of graphene can interact with a broad range of analytes through van der Waals force, electron transfer or covalent bonding.[77, 326] These interactions can result in the perturbation of electronic properties of graphene, usually reflected in a conductivity change.[264] Theoretical studies indicate that the adsorption of different gas molecules on graphene can also modulate electrical conductivity through changes in doping states.[327-330] Electron density within graphene-based materials can be localized around its edges and structural defects giving rise to much faster electron transfer rates than encountered on its basal plane, thus demonstrating a versatile nature of graphene as electrocatalyst for electrically–transduced sensing applications.[331] *Third*, graphene possesses high surface–to–volume ratio, meaning that every carbon atom in graphene is a surface atom, providing the greatest possible surface area per unit volume. Therefore, the charge transport through

graphene is highly sensitive to its chemical environment.[80, 125] *Fourth*, graphene has inherently low electrical noise due to the high quality of its crystal lattice, making it capable of screening charge fluctuation compared to one–dimensional counterparts (e.g., CNTs).[76, 332-333] Only one electron change in the local carrier concentration in graphene can lead to a step–like alterations in its resistance resulting in single–molecule sensitivity.[157] *Fifth*, graphene offers an outstanding mechanical strength and flexibility, which are well–suited with electronic devices that have the form of flexible, stretchable, or even conformal features.[124, 324, 334] These extraordinary properties enable graphene to be considered as a promising material for wearable electronics.[124]

Because the surface of graphene plays a crucial role in intermolecular interactions, tuning the surface chemistry of graphene materials is the most primary and direct approach to adjust its sensing properties. To provide enhanced specificity and strength of the interactions, the surface of graphene can be modified through various covalent and noncovalent methods.[97, 335] *Firstly*, molecular level tuning of graphene surfaces through either post–synthetic incorporation of functional groups or dopants as well as by achieving a high level of control over the structural and compositional defects may enhance its sensing properties for the fabrication of functional devices. Theoretical and experimental studies on graphene–based gas sensors revealed that defects and dopants make the graphitic sheets more sensitive to gas molecules if compared to the intact graphitic domains in graphene–based materials.[336-339] Introducing electron–withdrawing groups (e.g., epoxide and carboxylic groups) generates holes in the valence band of rGO, and consequently improves the response towards reducing molecules. Conversely, surface modifications with functional groups containing lone–pair electrons (e.g., ethylenediamine or sulfonate) can improve the response towards oxidizing molecules. *Secondly*, the sensing properties of graphene materials, such as sensitivity and selectivity, can be further improved by creating graphene hybrid materials with other functional nanostructures, including metal[340-341] and metal oxide nanoparticles, [342-344] organic receptor,[345] conducting polymers,[346] proteins or nucleic acids.[272] The optimized performance arises from the synergistic effects of different components.[78, 123, 125, 264, 283, 334, 347] For example, modification with conductive polymers can enhance carrier scattering of graphene, leading to the formation of an adsorbent layer on the graphene providing additional electrochemical or acid–base interactions with a range of molecules,[348] while modifications with enzymes can induce selectivity to biomolecules.[349] A holistic understanding of the surface chemistry and modified surface species, lattice defects, electronic properties, and how each attribute can be tailored, should be considered when applying graphene to chemical sensing applications.

3.2. Black Phosphorous

The most stable allotrope of phosphorous — black phosphorous (BP) — was first synthesized by Bridgman in 1914 by subjecting white phosphorus to high temperature (200 °C) and pressure (1.2 GP).[350] A century later, Ji and co–workers used mechanical exfoliation to isolate single and few atomic layers of 2D BP–phosphorene–through micro-mechanical exfoliation. The resulting 2D materials exhibits unique properties such as hinge–like structure, structural anisotropy, quasi–one–dimensional excitonic nature, and layer dependent band gap–features that often contrast those found in other 2D materials.[67, 351-352] 2D BP exists as a single–elemental layered crystalline material composed solely of sp^3 hybridized phosphorus atoms, arranged in a layered orthorhombic crystal structure with the *Cmca* space group.[353] It forms a honeycomb lattice structure with notable non–planarity in the shape of structural ridges, with lattice constants of a = 3.31, b = 10.50, and c = 4.38 Å.[354] BP also displays a puckered conformation along the armchair direction, with a bilayer structure being dominant along the zigzag direction (**Figure 14a**). Stacks of 2D layered BP are held together by interlayer van der Waals interactions with the distance of 5.5 Å between the adjacent layers (**Figure 14b–c**). In each phosphorene layer, P atoms display triangular pyramidal structure due to the presence of three covalently coordinated phosphorous atoms with one lone pair of electrons; while defects may exist in the single layer duo to the loss of the P atoms (**Figure 14d**).[355]

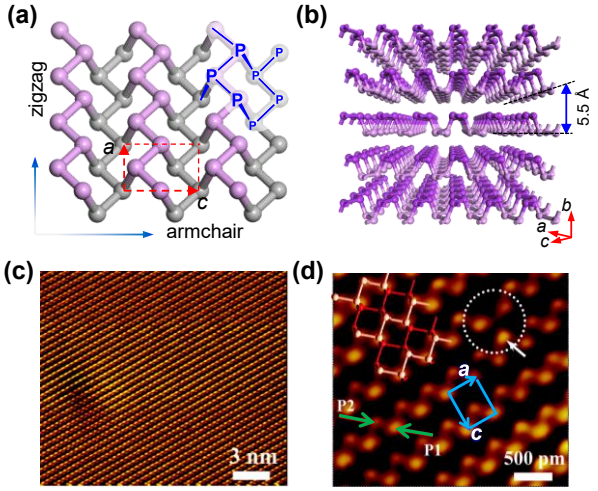

Figure 14. (a) Schematic diagram and chemical structure of single–layer phosphorene. (b) Few layers of phosphorene stacked by van der Waals force. (c) Large–scale STM image of BP surface with atomic resolution. (d) Close–up STM image showing that only the upper atoms of the topmost puckered layer can be seen with no reconstructions. The unit cell is indicated by blue dashed lines and a vacancy is marked by a green dashed circle. There is a contrast between the two rows in the same zigzag chain, indicated by red arrows and labeled as P1 and P2, respectively.[355] Adapted from Ref. [355] Copyright 2009 American Chemical Society.

In addition to the tunable direct bandgap of BP, which can be modulated by increasing the layer multiplicity, from 1.51 eV for a monolayer to 0.59 eV for a five–layer system[356] BP also possesses the drain current modulation up to 10^5 and carrier mobility up to 1000 cm^2 /V s,[351] which makes it attractive for electronics applications. Recent theoretical studies showed that the band gap of BP can be further engineered by controlling the direction of the edges

(e.g., zigzag or armchair), as well as controlling the functional groups at the edges.[357] For example, Tran et al. demonstrated that the magnitude of the band gap for BP nanoribbons is also dependent on the width of the nanoribbons due to quantum confinement effect.[358] Peng et al. further demonstrated that the armchair P–nanoribbons exhibited semi–conductive behavior for all investigated edge functionalized groups (H, F, Cl, OH, O, S, and Se), while the zigzag nanoribbons displayed either semiconductor or metallic behavior depending on their edge chemical groups.[359]

The increasing use of BP in electrically–transduced sensing technologies arises from the combination of its unique electronic properties such as a direct bandgap regardless of the number layers, a small intrinsic band gap, and anisotropic electrical conductance, with its unique surface chemistry.[159] In particular, BP possesses high chemical adsorption energy, as well as large abundance of available adsorption sites for analyte interactions as a result of its puckered surface structure, [98, 159] which can lead to high sensitivity in electrically–transduced sensing. Charge transfer between analyte and BP, and consequently sensitivity, can be further improved by introducing structural ripples into the surface of BP.[360] Recent DFT calculations demonstrated that the molecular adsorption energy of BP exceeds that of other 2D materials, including graphene and MoS_2, [98] further confirming suitability of BP for chemical sensing applications. In addition, large surface–to–volume ratio of BP could be utilized as a scaffold for the immobilization of known molecular receptors to induce selectivity to targeted analytes.[361-363]The introduction of dopants is another approach to improve ability of BP to sense analytes.[364] BP also exhibits faster heterogeneous electron transfer rates at the edge plane sites than on its basal plane, in similar fashion to that of graphene. Thus with the future improvements in control over the orientation of fabricated layers , BP may find large utility in sensing applications.[353] However, the biggest challenge in the application of BP for sensing technologies lies in its limited stability to light and oxygen and the possibility of formation of phosphoric acid species in the presence of moisture.[159, 365] Known strategies to improve stability of BP to degradation under ambient conditions rely on the incorporation of protective coatings,[365] nanomaterials [366] or ionic liquids.[367]

3.3. Transition Metal Dichalcogenides

Transition metal dichalcogenides (TMDC) are a family of inorganic materials with a chemical formula of MX_2, where M is a hexavalent transition metal ion, and X is a divalent chalcogen (S, Se, Te).[84, 368] A subset of TMDCs (mainly those based on group 4–7 transition metals) crystallize as layered structures, in which the monolayers stack together through the van der Waals forces. In MoS_2, each monolayer contains three rows of atoms, a layer of metal atoms sandwiched between the top layer and bottom layer of the chalcogenide atoms. Each layer has a covalently bound X–M–X unit with 6–coordinate metal sites adapting either trigonal prismatic (D_{3h}) symmetry or trigonal antiprismatic (D_{3d}) symmetry (**Figure 15a–b**).[84] The monolayer of TMDC was first isolated by Joensen et al. in 1986 with the characterization of atomically thin MoS_2.[369-370] In contrast to graphene, TMDCs can display a wide range of polymorphs and polytypes.[371-372] For example, MoS_2 has four different crystal structures, 2H, 1T, 1T', and 3R, depending on the coordination modes between the Mo and S atoms and/or stacking orders between layers.[373] Conductivity of bulk TMDCs ranges from insulators (HfS_2), to semiconductors (MoS_2, WS_2), semimetals (WTe_2, $TiSe_2$), and metals (NbS_2, TaS_2).[374] The electronic properties of TMDC layered structures differ significantly from the bulk properties due to confinement effects, as well as the scission of interlayer coupling.[368, 375-376] Exfoliation of bulk TMDC disrupts the s–p_z orbital interactions between adjacent layers and causes the band gap to widen.

Synthesis of single and few layer TMDCs can be accomplished through top–down methods including mechanical or liquid–phase exfoliation of bulk layered crystals,[377-380] or through bottom–up methods such as CVD.[381-383] Currently, mechanical exfoliation provides the highest quality monolayer samples at the cost of low synthetic yield. However, inherent atomic scale defects are still found in MoS_2 single layers made by mechanical exfoliation (**Figure 15c–d**).[384-385] CVD methods are more suitable for large–scale manufacturing of TMDCs than exfoliation techniques. The uniform growth of single–layer TMDCs remains a challenge.[84]

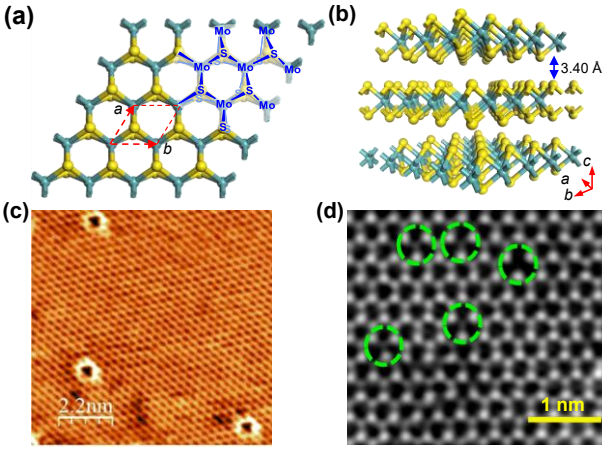

Figure 15. (a) Schematic diagram of single layer of MoS_2. (b) Three–dimensional representation of the structure of MoS_2. (c) STM images of single–layer MoS_2 with triangular and circular shaped point defects.[384] Reproduced with permission from Ref. [384] Copyright 2016 Nature Publishing Group. (d) Atomic resolved STEM–ADF images to reveal the distribution of different point defects.[385] Reproduced with permission from Ref. [385] Copyright 2015 Nature Publishing Group.

When TMDC is exfoliated into 2D thin sheet, both the basal planes and the prismatic edges are exposed, presenting distinct structural and electrical features.[73] The surface chemistry of the basal plane of TMDCs is dominated by chalcogenide lone pairs, which are projected perpendicularly to the TMDC basal surface;[73, 138, 386] on the prismatic edges, either metal or chalcogenide atoms can be present,

depending on the growth environment.[321] Once the lateral size is decreased, the presence of low–coordination step–edges, kinks and corner atoms dominate the overall observed chemistry of the TMDC materials.[387] For example, the location and amount of S vacancies at the edges of MoS_2 nanosheets can critically influence their stability and catalytic activity.[388] Theoretical calculations show that MoS_2 with S vacancies exhibits excellent adsorption ability for several nonpolar gases, while perfect MoS_2 sheets showed little or no adsorption.[303] S vacancies in MoS_2 are most favorably formed either at the edge or the corners of the nanosheet layer, whose specific location/distribution is further dictated by the size of the 2D sheet. Therefore, it is important to control the specific shape (e.g., hexagonal platelets, plate–like crystallites, and trigonal sheets) of TMDC nanosheets both in the context of their morphology and dimensionallity.[389-390] For small–sized MoS_2 nanosheets, the shape of the material can be engineered by the edge–plane functionalization, as the equilibrium shape geometry is highly sensitive to the energetics of the edge atoms. Both metal–terminated and sulfur–terminated examples of TMDCs fabricated using this experimental approach have been demonstrated. This level of molecular control allows great tunability in the reactivity and electronic properties of 2D TMDC nanosheets for applications in sensing technologies. Post–transition metal dichalcogenides (pTMDC) materials, like SnS_2, exhibit many of the similar properties with TMDC due to their isostructural nature.[391-393]

Metal dichalcogenides (MDC) encompass diverse morphological and compositional structures.[386] Numerous metals and chalcogens have been used as components in 2D sheets from bottom-up synthetic methods.[73] MDCs can be found as insulators, semiconductors, or metallic conductors[368, 386], allowing them to be incorporated into a broad range of analytical devices in which charge transport can be easily modulated by surface adsorbents. Despite compositional control over physical parameters such as conductivity, a wide range of synthetic options for producing MDCs must be optimized.[387] There is als a significant challenge in obtaining MDCs with specific layer multiplicity and tailored edge functionality.[387] Both aspects play a large role in the sensitivity towards various analytes.[394] Yet, the numerous benefits of MDCs such as high thermal and chemical stability coupled with large abundance of metal host-guest sites render these materials as promising candidates for gas detectors and future gas sensing applications.

3.4. Metal Oxides

Metal oxides are compounds formed from metal and oxygen in the form of oxide ion, which constitute one of the most diverse classes of solids, exhibiting a variety of structures and properties.[86, 395-396] 2D metal oxides can be divided into two groups—2D layered metal oxides, e.g., MoO_3, TaO_3, and WO_3, and 2D non–layered metal oxides (e.g., ZnO, CuO, and SnO_2 in their nanosheet or nanofilm forms) — depending on the presence/absence of van der Waals layered structure in the bulk.[86, 102, 121] As shown in **Figure 16a–b**, orthorhombic MoO_3 (space group *Pcmn*, a = 3.963 Å, b = 3.696 Å, c = 13.855 Å) possesses layered crystal phase of molybdenum trioxide, in which dual layer planar crystals of distorted MoO_6 octahedra are held together in the vertical direction by weak van der Waals forces.[87] These weak interactions between layers are favorable for exfoliation by either liquid or gas phase techniques to obtain nanosheets.[397-398] The basal surfaces of layered metal oxides are terminated by oxygen atoms leading to high chemical stability under air and water. 2D metal oxides without the intrinsically layered structures, like nanosheet of ZnO as shown in **Figure 16c**, are not readily synthesized by top–down approaches because such materials contain strong chemical bonds between different crystal layers. Instead, ultrathin sheets with atomic thickness (**Figure 16d**) can be obtained via morphological transformations,[399] self–assembly from its corresponding oligomers with the assistance of surfactants,[399] and salt–template methods.[400] Different metal oxides give rise to distinct electronic properties, and their conductivity can range from metallic to wide–gap insulating.[395] Additionally, the conductivity of specific metal oxides can be further tuned by varying the crystal size, morphology, dopant, contact geometry and operation temperature.[73, 401]

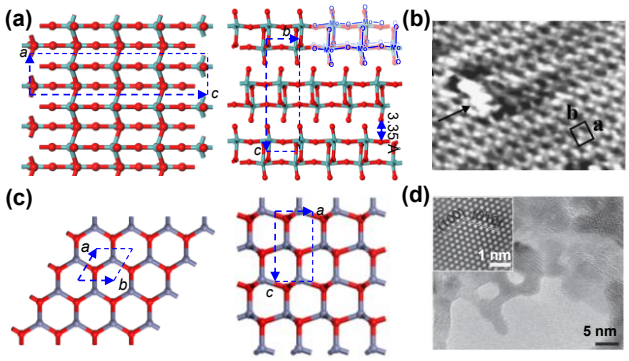

Figure 16. (a) Layered crystal structure of MoO_3. (b) High resolution STM image showing a rectangular unit cell with a = 0.50 nm and b=0.57 nm ± 10%, obtained at 300 K. Defects are indicated by arrows.[402] Reproduced with permission from Ref. [402] Copyright 2004 AIP Publishing. (c) Structure of ZnO which is intrinsically nonlayered. (d) TEM images of ultrathin 2D ZnO nanosheets. The inset is high resolution TEM images of the crystal lattice structure of the nanosheets.[399] Reproduced with permission from Ref. [399] Copyright 2014 Nature Publishing Group.

The oxygen ions and the ionic character of metal–oxygen bond are the two key factors that determine the surface properties of the metal oxides.[403] The unique character of the oxygen ion dominates the surface properties of 2D metal oxides in the context of chemical sensing including molecular adsorption, charge transfer, and catalytic performance.[404-406] The high polarizability of O^{2-} enables 2D metal oxides to exhibit large, nonlinear, and non–uniform distributions of charges within their lattices, leading to electrostatic screening zone (1–100 nm in thickness) that generates exceptional local surface and interfacial properties.[403] For this reason, the specific energy states near or on the surface of 2D metal oxides can induce significant Columbic interactions with adjacent ions. Therefore, if surfaces of two

metal oxides are brought in contact with one another, a build–in interface potential will arise, shifting the Fermi levels of the surface planes.[407] Due to strongly ionic character of transition metal oxides, the surfaces of 2D metal oxides can become electronically activated.[408] The surface of a metal oxide can be treated as ordered arrays of Lewis acid–base centers, which enable adsorption of various small molecules on its surface. For example, oxygen is usually chemisorbed on the surface of 2D metal oxide, at room temperature, in the form of negatively charged species.[409]

Metal oxides have been widely used in chemical sensors due to their semiconductive properties.[86] These materials become more conductive at elevated temperatures (T> 250 °C) as atmospheric oxygen increases hole-carrier concentration by binding to oxygen vacancies on the metal oxide surface.[110, 127] Synthetically, metal oxides are one of the least expensive, most readily produced materials that can exist on a 2D scale.[114, 410-411] They are robust to oxidizing and reducing conditions, elevated temperatures, and humid analyte mixtures.[128] However, the application of metal oxides towards mobile and miniaturized sensing platforms requires elevated operating temperatures, which consume large amounts of power, relative to sensors that can be operated at room temperatures.[412-413] The 2D subfamily of metal oxides have recently shown great promise in overcoming the drawbacks of high temperature operation, enabling room temperature sensing of gaseous analytes.[114, 127]

3.5. Metal–Organic Frameworks

First developed in the 1990s by Yaghi and co–workers, metal–organic frameworks (MOFs) are crystalline and porous hybrid materials formed via molecular self–assembly of inorganic metallic nodes with ditopic or polytopic organic ligands (e.g., carboxylate, hydroxyl, thiol, amino) to form bulk crystals.[414] MOFs can adapt various forms of crystal structures in different space groups depending on the type of metals and linkers used for their synthesis, resulting in 1D, 3D as well as in 2D layered structures.[415] Two experimental approaches have been developed for the fabrication of 2D sheets of MOFs — the top–down and bottom–up methods. Top–down techniques rely on the exfoliation (e.g., through sonication) of layered bulk MOFs, which is sufficient to break down the weak interactions between adjacent stacks (van der Walls forces or hydrogen bonding).[115] In the case of solvothermal bottom–up synthesis, the growth of 2D MOF proceeds parallel to the basal plane, while vertical growth is restricted. Although, MOFs serving as molecular–scale cages/scaffolds for the integration/immobilization of electrical components have been widely reported, [115, 416-417] the limited electrical conductivity of the vast majority of MOFs renders them often unusable for the development of electrically–transduced sensors. Section 4 thus focuses on 2D inherently conductive MOFs and their application in electronic devices for chemical sensing.

Conductive 2D MOFs have been synthesized from redox-active planar aromatic ligands with ortho–disubstituted hetero–donor atoms (O, S or NH) coordinated to late transition metal ions that display square planar coordination environment. Taking Ni_3HITP_2 as an example, its hexagonal pores with a diameter of approximately 2 nm are formed through the coordination between the hexaaminotriphenylene ligand and Ni^{2+} node in a 2D extended sheet, which are further held together by non–covalent interactions with a interlayer distance of ~3.3 Å (**Figure 17a, 17c**).[418] The charge neutrality of the framework can be preserved by the organic linker, which can adopt multiple oxidation states to ensure the charge balance with the metal centers.[88, 419] For instance, in the structure of Ni_3HITP_2 the ligand adopts a tris–semiquinone form that leaves an unpaired radical on the ligand (**Figure 17b**).[418] Depending on the metal ion or linker, 2D MOFs can display different packing modes, including slipped parallel, eclipsed stacking, and staggered modes.[419] Although, the lateral intra–sheet electrical transport is likely to dominate the electrical properties of 2D MOFs, the mode of stacking may potentially influence charge mobility across the 2D stacks.[88] The band gap of 2D conductive MOFs can be strategically engineered by careful selection of structural motifs (metal centers and organic ligands) which dictate the efficiency of through–bond or through–space charge transport in the MOF.[420-421 88, 419] This structural tunability allowed the development of 2D MOFs with electrical conductivity ranging from 10^{-6} to 2500 S cm^{-1} at room temperature.[88, 419-421]

Besides their porous scaffolds, ordered structure and tunable conductivity, 2D conductive MOFs have versatile and unique surface chemistry[176] The metal centers on their 2D surface can adapt either octahedral or square planar coordination, featuring equatorial coordination with the organic likers and two axial ligands.[88, 422] The axial ligand can be absent in the pristine MOFs or be removed through activation procedures, which will result in the presence of open coordination sites on the MOF surface, available for molecular interaction.[423] Theoretical and experimental calculations showed that gas molecules, e.g., CO, NO, NH_3, can be chemically adsorbed on the surface of the 2D MOF nanosheet through binding at the open metal centers.[173, 424] Experimental results based on MOFs containing ligand centered radicals further reinforced these observations and demonstrated that molecular adsorption of analytes onto the MOFs can proceed through the ligand–adsorbent radical recombination.[425-426] The existence of potential defects, edges (**Figure 17d**), and the permanently trapped adsorbents, however, can complicate the chemical environment of the MOF surface. Development of a more complete understanding of the surface chemistry of conductive MOFs is critically important to the continued improvement of this class of materials in chemicial sensing.

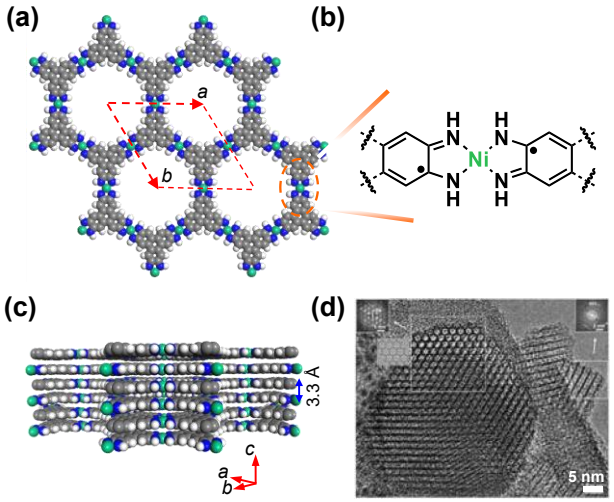

Figure 17. (a) Schematic diagram of single layer of MOF Ni_3HITP_2. (b) Chemical details of the metal complex that constitute the hexagonal pore. (c) Side view of the MOF layers.[427] (d) High–magnification TEM image of MOF Ni–HHTP, the inset images are the fast Fourier transform (FFT) analysis of the corresponding areas indicated by arrows.[422] Reproduced from Ref. [422] Copyright 2012 American Chemical Society.

The majority of reported MOFs are topological insulators.[428-429] Introducing planar and fully conjugated ligands have given rise to MOFs that are semiconductive or conductive in nature.[88] These MOFs combine typical MOF multifunctionality, such as porosity, high surface area, and tunability, with non-traditional MOF characteristics of conductivity and charge transport.[88, 419] The coalescence of these properties may provide enahnced responses in chemicals sensing.[421]

3.6. Other 2D Materials

With the rapid development of 2D materials for sensing applications, other 2D materials, including Xenes, 2D metals, carbon nitride, boron nitride, MXenes, and layered Group III–IV semiconductors, also show great potential in electrically–transduced sensing.[94, 113-114, 146, 229]

Xenes refer to a mono–elemental class of 2D crystals of group IVA elements, including silicene, germanene, and stanene.[430-432] In their most stable form, 2D–Xenes based on Si, Ge or Sn atoms, adopt a buckled hexagonal honeycomb structure (**Figure 18a–b**), unlike graphene, which is ideally flat. The bond length in silicene (~2.28 Å) is much longer than in graphene (~1.42 Å) preventing the Si atoms from forming strong π bond. The buckling of the Si atoms brings them closer together to enable a stronger overlap of their p_z orbitals, resulting in a mixed sp^2–sp^3 hybridization, which further stabilizes their hexagonal arrangement. Xenes have higher reactivity compared to graphene, which can be beneficial in terms of functionalization, but it causes fast degradation and oxidation under ambient atmosphere, complicating the establishment of scalable routes for device integration.[432] Their electronic structure ranges from insulators, through semiconductors with tunable gaps, to semi–metallic, depending on the substrate, chemical functionalization and strain. Theoretical calculations show that the band gaps of Xene monolayers can be tuned effectively by the adsorbed molecules.[162-163, 433-434] Depending on different type of molecules, the material–analyte interactions can be varied from weak van der Waals to strong charge transfer interactions. Vacancy defects and doping pristine silicene with either B or N atoms, can lead to enhanced binding energy as well as charge transfer, and subsequently significant improvements in sensitivity.[161, 163]

Metals are a class of materials that play important role in the fundamental studies of sensing and industrial applications.[435-436] In the crystal lattice of a metal, atoms are closely positioned to neighboring ones (for example, Pd shown in **Figure 18c**) in one of three most common arrangements, including body–centered cubic, face–centered cubic, and hexagonal close–packed.[437-440] Ultrathin 2D metal nanostructures normally exhibit the same crystal structures as their corresponding bulk materials.[437-440] However, as the thickness of the metal layer decreases, the contribution of the electrons close to the surface to the total conductivity of the material increases, and the charge mobility and scattering then depends on the surface interactions. Similar to graphene and its inorganic analogues, metal nanoplates and nanosheets have also shown some unique sensing properties compared to nanostructures with other shapes, such as nanoparticles, nanorods, and nanowires.[438, 440-441] Thin metal sheets (**Figure 18d**) can be prepared via bottom–up methods from metal salts or small metal nanoparticles. Top–down approaches, such as electron beam nanolithography, nanoimprint lithography and hole–mask colloidal lithography, have also been developed.[436] On the surface of some metals (e.g., iron, zinc, and copper), a layer of metal oxides can be formed due to the presence of atmospheric oxygen.[165] Other metals, like palladium, platinum and gold, though do not react with oxygen, they can have special reactivity towards some molecules. For example, palladium and platinum can catalytically dissociate hydrogen,[442] while gold has strong affinity toward thiol compound through the formation of Au–S bond.[443] Due to the close packing of metal atoms, ultrathin metallic structures with a plethora of unsaturated atoms, are difficult to stabilize and their synthesis remains challenging.[444-446]

Hexagonal boron nitride (*h*–BN), commonly known as "white graphene", has a similar periodic structure in plane to graphene but exhibits different stacking order, in which equal numbers of B and N atoms are arranged into a honeycomb structure (**Figure 18e–f**).[447] The adjacent layers, with a distance at 3.30 to 3.33 Å, are held together by van der Waals force to form a bulk crystal. *h*–BN is an electrical insulator with a band gap of 5.2 eV and high thermal conductivity (~2000 W m^{-1} K^{-1} obtained by theoretical calculations and 380 W m^{-1} K^{-1} experimentally determined), excellent dielectric property, and high–temperature antioxidation resistance.[63, 447-449] *h*–BN nanosheets exhibit lower surface areas than their other 2D counterparts,[448] but the doped or defective *h*–BN nanosheet showed response to

several gaseous molecules as suggested by theoretical calculation.[447]

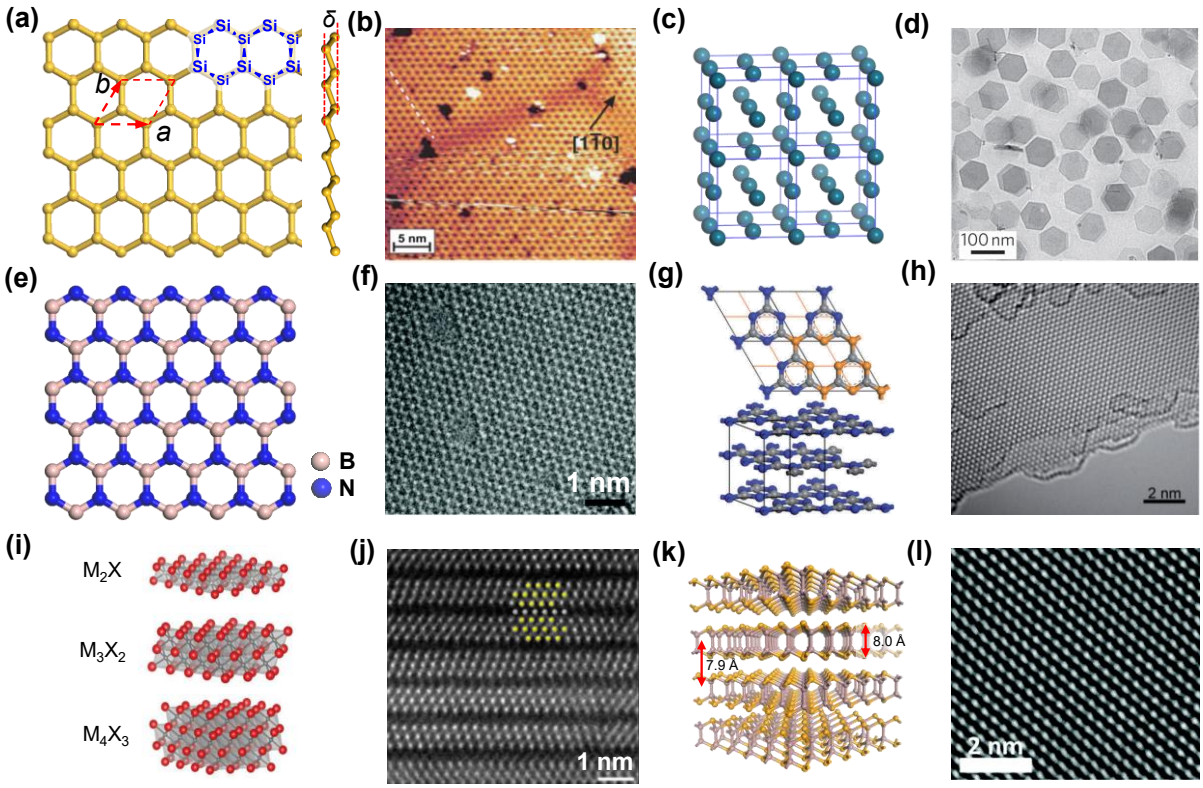

Figure 18. (a) Front and side view of Schematic diagram of single layer of silicene. (b) Filled–states STM image of the 2D Si layer on Ag (111) showing the honeycomb–like structure.[431, 450] Reproduced with permission from Ref. [411] Copyright 2012 American Physical Society. (c) Crystal structure of palladium. (d) TEM images of palladium nanosheets.[438] Reproduced with permission from Ref. [438] Copyright 2011 Nature Publishing Group. (e) Flat structure diagram of *h*–BN. (f) TEM image of *h*–BN showing triangular holes defects.[357, 451 452] Reproduced with permission from Ref. [452] Copyright 2015 The Royal Society of Chemistry. (g) Crystallographic unit cell and AB stacking arrangement of triazine–based graphitic carbon nitride (TGCN) layers. Carbon and nitrogen atoms are represented as gray and blue spheres, respectively. A hexagonal grid of half–cell size with nitrogen atoms at its nodes has been overlaid as guide for the eye in orange. (h) High–resolution TEM image of mechanically cleaved layers of TGCN. [453-454] Reproduced with permission from Ref. [454] Copyright 2014 Wiley-VCH Verlag GmbH & Co. KGaA, Weinheim. (i) MXene sheets consist of 3, 5 or 7 atomic layers for M_2X, M_3X_2, and M_4X_3, respectively. [157] (j) HR STEM image of $Mo_2TiC_2T_x$.[455] Reproduced from Ref. [455] Copyright 2015 American Chemical Society. (k) Crystal structure and (l) high resolution TEM images of few–layer GaSe.[456] Reproduced with permission from Ref. [456] Copyright 2016 The Royal Society of Chemistry.

Graphitic carbon nitride (g–C_3N_4) is another analogue of graphite with a layered van der Waals structure, where each layer is formed through the sp^2 hybridization of carbon and nitrogen atoms.[457] There are two different structural models that account for the geometry and stoichiometry of g–C_3N_4, which are based on triazine [454] and heptazine units, respectively (**Figrue 18g–h**).[458] The semiconducting bandgaps of g–C_3N_4 are around 2.5–2.8 eV, which lead to poor electronic conductivity. Due to the incomplete condensation during the synthesis, g–C_3N_4 contains a small amount of hydrogen in the form of primary and/or secondary amine groups on the terminating edges. The presence of terminal hydrogen together with high electron affinity of nitrogen to many analytes results in rich surface properties of g–C_3N_4, including basic surface functionalities, electron–rich properties, and H–bonding motifs.[459] The structural features of g–C_3N_4 nanosheets such the homogeneous dispersion of carbon and nitrogen elements in each nanosheet, thermal stability, and tunable bandgap may lead to enhanced performance in chemical sensing applications.

MXenes is a class of 2D transition metal carbide (**Figure 18i–j**) generated by selectively etching a certain element from $M_{n+1}AX_n$ phases where M represents an early transition metal, A is related to a main group (mostly group III A and IV A) element, X is C and/or N, and n = 1, 2, or 3.[460] O, F, and OH functional groups are generally found on the surfaces of exfoliated MXenes, which are introduced during the chemical etching process.[177-178] The choice of synthetic method has a great influence on the ratio of these groups on the surface of synthesized MXene. Mono layers of MXene are predicted to be metallic, with a high electron density near

the Fermi level.[178, 461-462] Density functional theory (DFT) calculations showed that the type and concentration of these surface terminations largely affect the properties of MXenes, through which analytical performance of MXenes can be tailored in compliance with various applications.[462-464] The metallic and tunable conductivity, as well as the high abundance of functional groups on the outer surface makes MXene a new generation of promising materials for sensing applications.

The III–VI layered semiconductors are a class of metal chalcogenides with a general formula of MX (M = Ga, In; X = S, Se, Te).[465-466] In the bulk material, each of the layers can be recognized as a double Ga or In layer intercalated in two layers of chalcogen to form the structure X–M–M–X as shown in **Figure 18k–l**. Different layers are held together by van der Waals interactions at an interlayer distance of ~8 Å. The atomically thin films of III–VI layered semiconductors have limited stability under ambient atmosphere, and the chalcogen atoms on its surface can react with oxygen and water in the air.[467-470] Theoretical calculations have revealed that the lone pair states of Se were located at the top of the valence band of InSe, close to the Fermi energy level, which indicates the ability of InSe to interact with external molecules.[471] The lone–pair on the chalcogen atom could be harnessed for surface functionalization via Lewis acid–base chemistry, which could improve their versatility and widen their applicability in electronics and sensing.[472]

2D materials share a general morphological structure that exhibits strong in-plane bonding to form 2D sheets, and weak interlayer van der Waals forces that lead to stacked layers of 2D sheets.[70, 73, 321] The difference in bonding strength between the two modes of bonding allows isolation of robust atomically thin sheets by exfoliation of stacked layers.[473] The trend of strong bonding in-plane often gives rise to the anisotropic charge transport of 2D materials that favors in-plane rather than through-stack transport.[474] In systems with isolated 2D atomically thin materials, this confines charge transport to directions parallel to the free surface.[474] This free surface is the location of host sites that allows host-guest interactions with the surrounding environment.[94] The proximity of charge transport to the host-guest sites, forced by the 2D nature of the material, can lead to large changes in electronic properties instigated by small changes in the chemical environment.[53] These morphological similarities across many classes of 2D materials are beneficial to their funtion in chemical sensing. In addition to a beneficial morphological trend, broad chemical diversity has been achieved in 2D systems, stemming from diverse element utilization and expanssion of synthetic methods.[73] Such diversity has provided a great deal of tunability of exposed host-guest sites that can be adjusted to favor or discriminate against specific analyte-material interactions.[114, 146] The future role of sensing with these 2D materials will be concerned with controlling both the morphology and surface chemistry of 2D materials.

4. Sensing Applications

Many families of 2D materials have been applied to sensing across a wide range of analytes.[73, 138, 321, 475] This review classified analytes as four main categories: gases, volatile compounds, aqueous ions, and aqueous biomolecules are targets of interest. Because each category offers unique challenges and requires unique strategies to resolve them, these four categories are addressed separately. To provide the most suitable comparisons, each family of sensing material is reviewed separately under each category of analyte. We have demarcated 2D material into six sub-families, namely graphene and graphene oxides, black phosphorus, transition metal and post-transition metal dichalcogenides, metal oxides, metal-organic frameworks, and other 2D materials (e.g., MXenes, hexagonal boron nitride, metals, graphitic carbon nitride).

4.1. Detection of Gases

Carbonous (CO, CO_2), sulfurous (H_2S and SO_x) and nitrogenous (NH_3, NO, N_2O, N_2O_4, etc.) gases originate from a wide range of anthropogenic and natural sources. All of these chemicals are gases at standard temperature and pressure and are targets for chemical sensing as their local concentrations carry implications for human health and safety, industrial process monitoring, as well as emissions control and air quality management.[56, 476-477] Many of these gases are byproducts of industrial processes, others are important feedstocks for world economies, and some play a vital role in physiological signaling. For example, suboptimal combustion of fossil fuels can lead to exhaust gases that carry hazardous compounds in addition to CO_2. A few examples of these are CO, which is produced from hypothermic combustion,[478] NO, and NO_x which are produced during hyperthermic combustion,[479] and H_2S and SO_x compounds, which are byproducts of combustion of sulfur containing fuels.[480] Other gases are important precursors for commodity, fine, or specialty chemicals. For example, NH_3 mostly produced by the reduction of N_2 by H_2, the nitrogen–fixing Haber–Bosch process, is an important feedstock for fertilizers and is the backbone of the world's agricultural infrastructure.[481] Monitoring NH_3 production as well as downstream utilization requires solutions that allow ubiquitous monitoring such as robust, inexpensive, miniaturized sensors with strong analytical characteristics.[481]

Beyond their well–known role in industrial chemistry and hazardous presence in other aspects of life, CO, H_2S, and NO—so–called gasotransmitters, are known to have biological importance as endogenously produced signaling molecules that are important modulators of various cellular processes.[482] Furthermore, these biologically produced species have recently been explored as therapeutic vectors to treat ischemia related reperfusion injury, carcinomas, and neurodegenerative diseases, yet are highly toxic at elevated concentrations from external sources. Monitoring these gases for biomedical purposes requires a unique set of sensor design criteria, where cost, size, and reusability are still determinants of a successful sensing platform. Sensors that can monitor *in vivo* processes are of great interest as well.[483]

Detection of gaseous compounds such as small reactive gases (SRG) is the most straightforward subsect of chemical sensing. The concentration of analyte streams can be accurately dialed from sub–ppb to 100 % concentrations using mass–flow controllers and inert gas streams. Additionally, powerful reducing gases such as NH_3, or oxidizing gases such as NO_2, circumscribe the family of SRGs that easily induce observable electronic changes in many conductive materials. However, less reactive species such as H_2, CO_2, and C_2H_4 gases require more specialized materials or material hybrids to provide robust detection. As such, many fundamental studies of chemical sensing using novel materials are demonstrated by the detection of SRGs. This testing ground for potential materials offered the first demonstration of the gas–sensing capabilities of graphene, BP, MOFs, TMDCs, and more.

As the need for industrial, environmental, and human health and safety related sensors increases, the demand for easily produced, robust, inexpensive, and highly integrable devices and design strategies will foster continued research in the field of gas sensing using 2D materials.[484-485] The following section highlights state–of–the–art theory and practice of gas sensing in the regime of electronic transduction using 2D materials.

4.1.1. Graphene and Graphene Oxides

NH_3 and N_xO_y. Novoselov and co–workers demonstrated the first application of atomically thin graphene in sensing of gaseous analytes.[157] Graphene monolayers (area ~10 μm^2) were prepared by micromechanical cleavage of HOPG. The isolated graphene sheets were transferred to the surface of SiO_2 and e–beam lithography was then used to fabricate a Hall–bar device with evaporated Au as electrodes (**Figure 19a**). This device allowed the authors to investigate the electronic properties of graphene as it was perturbed by the adsorption of NH_3, NO_2, I_2, H_2O, and CO gases. The charge carrier concentration in graphene increased linearly with increasing concentration of NO_2 gas. This device was able to detect 1 ppm of NH_3 and NO_2 in an inert atmosphere, which was comparable with the most sensitive gas sensors. The authors also observed reverse electronic responses upon to exposure to electron donating (e.g., NH_3) vs electron withdrawing gases (e.g., NO_2) (**Figure 19b**). Annealing the device at 150 °C removed the doping effects of the gases. When a high driving current was used to suppress the Johnson noise, step–like changes in resistivity were observed during the long–term exposure to dilute NO_2 gas (1 ppm), originating from single–molecule adsorption/desorption events and subsequent charge transfer between the gas and graphene (**Figure 19c–d**), indicating that the Gr–based sensor could detect even single NO_2 molecules. Four characteristics of graphene help explain its excellent sensing performance.[157] *First*, graphene is strictly two–dimensional with its whole volume exposed to surface adsorbates, which maximizes the possibility of their interaction with the 2D material. *Second*, graphene possess metallic conductivity, thus has very low Johnson noise. *Third*, graphene exhibits low levels of excess (1/f) noise due to its high crystallinity. *Fourth*, graphene can be integrated into diverse device architectures with ohmic contact that have low resistance.

Since the first application of graphene in sensing, graphene–based materials have become extensively utilized in the development of gas sensors, prompting both theoretical and experimental investigation into the working principles of graphene–based devices. Wehling et al. used calculations based on local density approximation (LDA) and gradient–corrected exchange correlation (GGA) method to show that open shell NO_2 is a more effective electron acceptor than the closed–shell N_2O_4 system.[486] Additional first–principles studies conducted by Leenaerts et al. examined the interaction of NO_2 and NH_3 with pristine graphene surfaces.[487] Two primary mechanisms for charge transfer between small molecules and the graphene surfaces were proposed based on their work. The first mechanism, applicable to all molecules, operates through orbital hybridization and results in a small charge transfer, as in the case of physisorption. The second mechanism depends on the position of the HOMO and LUMO of the molecule with respect to the Dirac point of graphene, and is only applicable to open shell molecules leading to large charge transfer between adsorbed molecules and graphene.[487]

Sensing ultra-low concentration of analyte is important in environmental monitoring, control of chemical and agricultural processes, space missions, and medical applications.[488-489] Chen and coworkers demonstrated that pristine graphene can detect gas molecules at extremely low concentrations with detection limits for NO estimated to be as low as 158 parts–per–quadrillion (ppq) at room temperature.[490] This response was approximately 300% better than the sensitivity of CNT-based gas sensors tested under the same experimental conditions. This unprecedented sensitivity was achieved by continuous in situ cleaning of the sensing material with ultraviolet light, which probably involved a photo induced molecular desorption mechanism.[491] The ultra–sensitivity of pristine graphene was further confirmed by the ppt to ppb level detection of other common gas species, including NO_2, NH_3 N_2O, O_2, SO_2, CO_2, and H_2O (**Figure 19e–g**).[490]

Koley and co–workers fabricated reverse–biased graphene/Si heterojunction capable of detecting NO_2 and NH_3 at 200 ppb and 10 ppm concentrations, respectively.[492] The alteration of Schottky-barrier height due to molecular adsorption of gaseous analytes on graphene surface led to the exponential change in the junction current, thus resulting in ultra-high sensitivity. The developed sensing devices at ambient conditions were approximately 13 times and 3 times more sensitive to NO_2 and NH_3 gases than analogous graphene based amperometric devices. The reverse bias operation also led to significant reduction in the operating power of the sensor (~500 times) for the same magnitude of applied voltage. In addition, the reverse bias operation permited modulation of the work function of graphene, and consequently Schottky-barrier height, enabling wide tunability of the sensor performance characteristics (sensitivity and response time).[492]

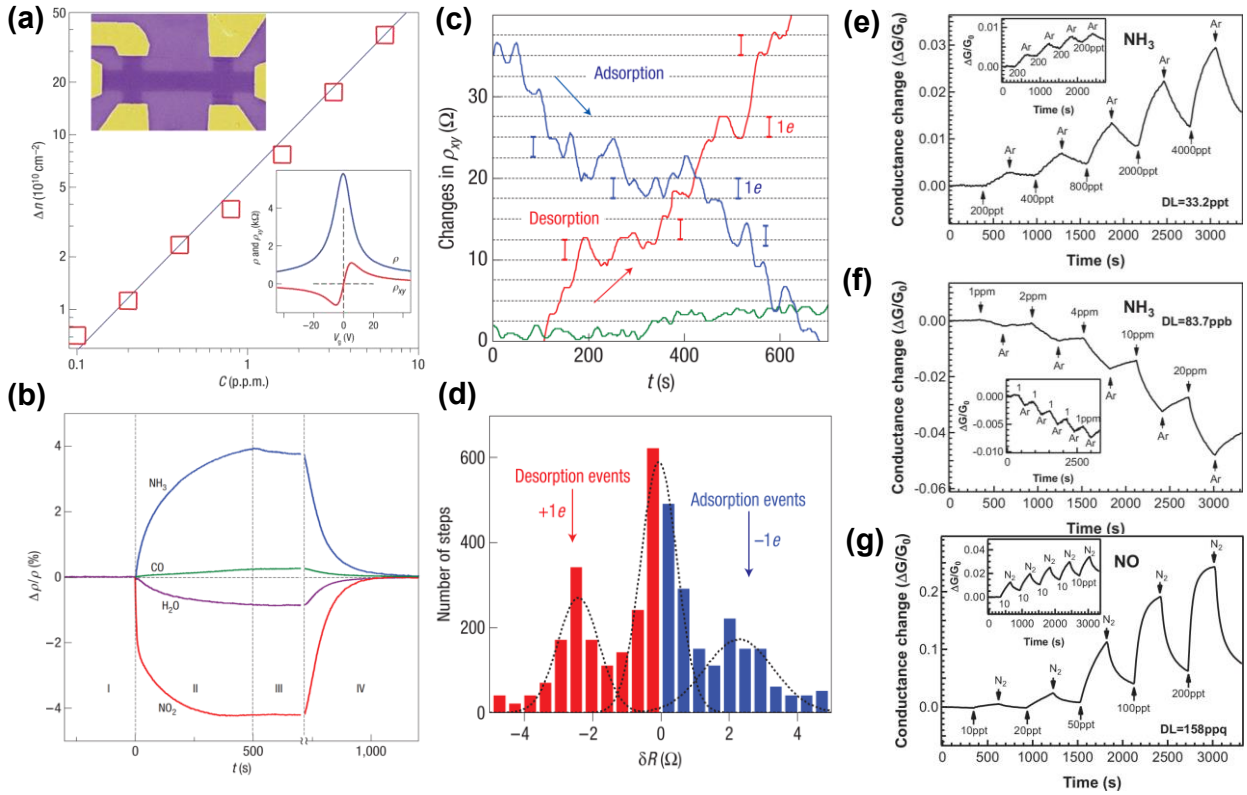

Figure 19. (a) Concentration, Δ*n*, of chemically induced charge carriers in single–layer graphene exposed to different concentrations, *C*, of NO_2. Upper inset: Scanning electron micrograph of this device (in false colors matching those seen in visible optics). The scale of the micrograph is given by the width of the Hall bar, which is 1 μm. Lower inset: Characterization of the graphene device by using the electric–field effect. (b) Changes in resistivity, *ρ*, at zero *B* caused by graphene's exposure to various gases diluted in concentration to 1 ppm. The positive (negative) sign of changes is chosen here to indicate electron (hole) doping. Region I: the device is in vacuum before its exposure; II: exposure to a 5 l volume of a diluted chemical; III: evacuation of the experimental set–up; and IV: annealing at 150 °C.[157] (c) Examples of changes in Hall resistivity observed near the neutrality point ($|n| < 10^{11}$ cm^{-2}) during adsorption of strongly diluted NO_2 (blue curve) and its desorption in vacuum at 50 °C (red curve). (d) Changes in ρ_{xy} larger than 0.5 Ω and quicker than 10 s were recorded as individual steps.[157] Reproduced with permission from Ref. [157] Copyright 2001 Springer Nature. (e) Response to NH_3 under *in situ* UV light illumination. The inset shows the reproducibility of sensor response at 200 ppt of NH_3 exposure. The detection limit is estimated at 33.2 ppt. (f) Response to NH_3 without UV light illumination, where the detection limit is estimated to be 83.7 ppb. (g) Relative change of conductance ($\Delta G/G_0$) versus time recorded with NO exposures ranging from 10 to 200 ppt. The inset shows the reproducibility of sensor response at 10 ppt of NO exposure. The detection limit is estimated at 158 ppq. [490] Reproduced from [490], with the permission of AIP Publishing.

The presence of defects and intentional doping can significantly influence the properties and gas sensitivity of intrinsic graphene. Using first–principles calculations, Zheng et al. explored the role of dopants (B, P) and defects in graphene on the interaction of the material with NH_3, NO, NO_2, and CO gases.[336] The authors demonstrated that the interactions of gaseous molecules with pristine graphene are substantially weaker than of the defective or doped graphene. These findings further suggested that the sensing performance of pristine graphene could be improved either by doping or by the incorporation of defects. Defective graphene was able to enhance interactions with NO, and NO_2 gases, but did not alter the response of the device to NH_3. Furthermore, the degree of doping by a specific analyte was not affected by the location of binding to the graphene surface, but instead was highly dependent on the geometry and orientation of the host–guest interaction.[336] This computational study also suggested that the doping ability of NH_3 towards pristine graphene was very limited, which was inconsistent with the high sensitivity of graphene to NH_3 demonstrated by Novoselov and co–workers.[157]

To examine the impact of the defects of graphene made from conventional nanolithography procedure on the sensor characteristics, Johnson and co–workers experimentally compared the sensing performance of FET devices fabricated through mechanically exfoliated graphene followed by a standard electron beam lithography (EBL) procedure before or after undergoing a high temperature cleaning process.[493] The authors showed that standard EBL processing leads to a formation of ~1 nm thick layer on the surface of graphene, which can affect the charge transport properties of this 2D material. The thermally cleaned devices contained roughly 1/3 of the concentration of doped carriers

and exhibited four–times higher carrier mobility. However, the cleaned devices produced a much weaker electrical response to gases such as NH_3. It was found that the contaminant layer enhanced carrier scattering, and acted as an absorbent for preconcentration of analyte molecules at the graphene surface, thereby enhancing the sensor response.[493]

Before 2009, the development of graphene–based sensors was limited by laborious preparation of single-layer graphene through either mechanical exfoliation or EBL processes, which are typically low yielding and time consuming. These issues were gradually resolved between 2007–2009 when novel methods for the preparation of reduced graphene oxide (rGO) were developed. The chemical reduction of GO, for example using Hummer's method, proved to be most suitable for nanoelectronics fabrication at low–cost with increased yield.[494-497] However, the use of harsh chemical treatment (e.g., strong acids) may result in the formation of structural and compositional defects, in the final structure of the material, which may influence the gas sensing properties of the resulting device. Recently, GO and rGO have been demonstrated as promising materials for gas sensing applications due to their versatile chemical, physical, and electronic properties, such as large surface–to–volume ratio, the presence of oxygen functional groups or defects, and high feasibility for surface functionalization.[498-500]

Fowler et al. reported on the development of chemical sensors based on rGO synthesized via Hummer's method.[498] The dispersions of rGO were spin–coated onto interdigitated electrode arrays to create single–layer films for detection of NO_2 and NH_3. Furthermore, a micro hot plate sensor substrate was employed to increase the recovery speed of the device, however at the expense of diminished sensitivity to NO_2.[498] Guha and co–workers used chemically reduced GO to sense ammonia at room temperature.[501] The sensing layer was synthesized directly onto a ceramic substrate with pre–patterned platinum electrodes. The resulting sensors exhibited 5.5% change in response to NH_3 at 200 ppm and 23% change at 2800 ppm of NH_3, as well as good recovery time without the application of heat. In addition, the sensor was exposed to different vapors and found to be selective toward NH_3.[501] Manohar and coworkers developed a flexible sensor based on rGO, chemically reduced by vitamin C, for reversible detection of NO_2 and Cl_2 gases at room temperature, with ppb sensitivity.[502] Chen and co–worker utilized porous rGO, synthesized from one–pot hydrothermal treatment, for room temperature sensing of NO_2.[503] High porosity of rGO provided not only sufficient active sites for gas adsorption, but also supplied channels for gas diffusion. The resulting sensor exhibited an enhanced performance to NO_2 gas with ppb detection limits. These results demonstrated that the structural modification of rGO by perforation was a promising approach for improving the sensing performance of graphene–based devices.

Recently, laser irradiation has attracted increasing attention as an alternative approach for the direct reduction and pattering of GO films due to its rapid material processing speed, large scan area, nanometer spatial resolution and single–step capability.[504-505] Kaner et al. reported on the development of gas sensors fabricated directly through laser induced reduction and patterning of rGO, on various flexible substrates.[506] By varying laser intensity, the conductivity of the synthesized rGO could be precisely tuned over 5 orders of magnitude, which has proven difficult to achieve through chemical reduction methods.[495-497] The resulting rGO–based sensors exhibited high sensitivity and reversible response to NO_2, demonstrating the feasibility of this fabrication approach for gas sensor development.

Through chemical modifications of rGO, functional groups or atoms can be introduced into the material to further tailor the surface properties of rGO, which may lead to enhancements in sensing performances of fabricated gas sensors. For example, Shi and co–workers fabricated a chemiresistive gas sensors based on chemically modified graphene materials including sulfonated rGO (rGO–S) or ethylenediamine–modified rGO (rGO–EDA).[507] The resulting devices exhibited high sensitivity to NO_2 with low detection limits of 0.07 ppm and 3.6 ppm for rGO–S and rGO–EDA based sensors, respectively.[507] The rGO–S and rGO–EDA sensing devices also showed 4–16 times stronger responses to NO_2 than the non–functionalized rGO–based gas sensors. In addition, the complete sensor recovery was observed upon the delivery of N_2 gas to the device without the need for UV or IR irradiation or thermal assistance. These results indicated that chemical modification of rGO is an effective approach for improving its gas–sensing performance through the incorporation of the high–energy adsorption sites for analyte interactions. However, chemical modifications can alter the electronic properties of the 2D material, which may permanently increase the resistivity and noise of graphene oxide–based devices, thus diminishing the sensitivity of the fabricated sensors.[508] Therefore, the structure–property relationship should be comprehensively balanced in the material design step.

Functionalization of graphene–based materials with metal nanoparticles, metal oxides, and polymers has led to the formation of unique hybrid nanostructures with exciting properties arising from synergistic effect between the incorporated components. Liu et al. developed highly sensitive NO sensors by decorating reduced graphene oxide with Pd nanosheets and incorporating the hybrid material (rGO–Pd) into a FET device.[509] The FET sensors responded to NO gas in the concentration range of 2 to 420 ppb at room temperature. CVD–grown graphene contacts of rGO–Pd improved the stability and sensitivity of the devices due to the work function matching between graphene and rGO. Improved gas–sensing performance can be further realized by combining chemical modification approaches with metal nanoparticle decoration.[510] Huang et al. reported on a flexible NO_2 sensor composed of the sulfonated rGO (rGO–S) decorated with Ag nanoparticles (rGO–S–Ag), which was printed onto a polyimide (PI) substrate by a gravure printing technique. Surface functionalization of rGO with $-SO_3H$ groups and Ag NPs, resulted in high sensitivity of the fabricated chemiresistive device to NO_2 (74.6% for 50 ppm), at room temperature.[510] In addition, the sensor demonstrated

fast response and recovery times of 12 s and 20 s, respectively.[510]

Surface functionalization of graphene or rGO with metal oxides has proven to be another effective method for achieving high–performance detection of gases. Sow and co–workers immobilized Cu_2O nanowires on rGO sheets, and investigated their ability to detect NO_2.[511] The response of rGO–Cu_2O hybrid material was 67.8% for 2 ppm NO_2, much higher than that of rGO (22.5%) or Cu_2O nanowires (44.5%) alone. The LOD recorded for the composite material was 64 ppb compared with 81 ppb and 82 ppm for unmodified rGO or Cu_2O, respectively. The composite material displayed a significantly enhanced sensing performance to NO_2 at concentrations higher than 1.2 ppm. Blending of Cu_2O with rGO can eliminate the need for an oxygen activation layer, which is usually required in metal–oxide based sensing.[152] Recently, Feng et al. reported on the synthesis of In_2O_3 cubes uniformly embedded into rGO networks for detection of NO_2.[512] The gas sensors based on In_2O_3–rGO composite exhibited a significant response to NO_2 at room temperature with a LOD of < 1 ppm, and excellent selectivity against interfering gases. The effective electronic interaction between n-type In_2O_3 cubes and p-type rGO facilitates the gas molecule detection via the resistance change of the hybrid architectures.[512] Meanwhile, the existence of Gr sheets in the hybrid composite improves the electrical conductivity and provide high surface areas of In_2O_3 at room temperature.[512] This synergistic effect enhanced sensing performance of the nanocomposite comprising uniformly distributed In_2O_3 cubes and rGO sheets. Similar strategy towards the improvements in the sensitivity for the detection of NH_3 and NO_2 have also been demonstrated by integrating WO_3[513], Fe_2O_3[514], SnO[515-518], and ZnO[519] graphene–based composites into functional sensing devices.

Composite systems formed by coating graphene materials with polymers, including PANI, polypyrrole (PPy), and poly(3,4–ethylenedioxythiophene) (PEDOT) have also been shown as effective strategies to further enhance the sensing performance of graphene based sensors.[520-523 524-525] For example, conjugation polymer PANI demonstrates sensitivity towards many analytes due to possible transformations between different forms of PANI, however, it has limited chemical stability.[526] PANI can interact with rGO sheets through π–π interaction,[527] which are helpful to improve the stability of the PANI. In addition, the electron transfer may occur between PANI and rGO sheets, and consequently improve the sensing performance (e.g. sensitivity, reversibility) of the resultant material.[528] Hybrid devices utilizing rGO–PANI exhibited much better response to NH_3 than the devices constructed from individual PANI nanofibers or rGO material (3.4 and 10.4 times, respectively at 50 ppm of NH_3).[520]

H_2. Hydrogen gas sensors are of increasing relevance, in connection with the development and more extensive use of hydrogen gas as a fuel gas or chemical reactant in energy applications, automotive industries or aerospace.[529] Since hydrogen gas is odorless, colorless, and highly flammable, the development of early warning systems for H_2 monitoring together with the implementation of appropriate safety protocols is essential. The low adsorption energy of H_2 is reflected by a weak interaction between this gas molecule and graphene resulting in its challenging detections even under high concentrations.[530] The incorporation of defects and dopants is an effective strategy to enhance the ability of graphene to interact with H_2. Ural and coworkers reported on the H_2 detection with a functionalized graphene substrate.[531] The sensing material was a hybrid of multilayer graphene nanoribbons and Pd nanoparticles (**Figure 20a**). mounted on a micromachined porous substrate. A response of–55% was reported for H_2 at 40 ppm. The improvement in sensitivity to H_2 was attributed to the presence of metallic NP that can form metal–hydride bonds, as in the case of Pd and Pt. (**Figure 20b**).[532] A similar experimental approach was utilized by Jang and coworkers, who integrated Pd–decorated graphene into the chemiresistive device architecture for the detection of H_2. The fabricated sensor could detect H_2 gas at concentrations as low as 0.1 ppm. Hydrogen molecules could react with Pd to produce PdH_x, which decreased the work function of the hybrid material, and consequently resulted in the decrease of the resistance (**Figure 20c**). Lee et al. also fabricated a highly sensitive H_2 sensor using a polymer–coated Pd nanoparticle–Gr hybrid. The resulting device exhibited high selectivity to H_2 over CH_4, CO, and NO_2 gases.[533]

Based on these developments, Jang and co–workers fabricated wireless H_2 sensors by using rGO–Pt composite materials.[534] The radio frequency identification (RFID)–based wireless smart–sensor system is composed of an RFID–reader antenna–connected network analyzer and rGO–Pt sensing material immobilized RFID sensor tag that included the dipole tag antenna, sensing area, and IC chip. The network analyzer emitted an interrogation signal at a power threshold of P1 to activate the sensor tag, which was then reflected back to the RFID–reader antenna at a power level of P2 based on its radar cross section. The rGO–Pt based RFID sensor tag exhibited a high sensitivity to hydrogen gas at unprecedentedly low concentration of 1 ppm.[534] The increasing resistance of tag antenna upon exposed to H_2 leads to impedance mismatching between antenna and IC chip compared to without hydrogen exposure and then, the RFID sensor tag decreases radar cross section resulting in a diminish reflection (**Figure 20e**).

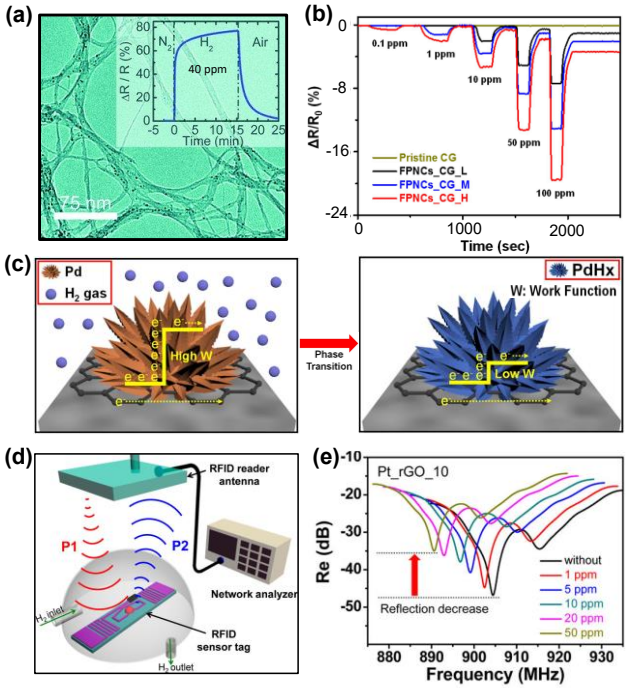

Figure 20. (a) Pd-functionalized multi-layer graphene and its response to 40 ppm of H_2.[531] Reproduced with permission from Ref.[531] Copyright 2010, John Wiley and Sons. (b) Normalized resistance changes of palladium decorated graphene at room temperature upon sequential exposure to H_2 gas of increasing concentrations (0.1 to 100 ppm). (c) Scheme of hydrogen gas sensing mechanism of palladium decorated graphene.[532] Reproduced with permission from Ref.[532] Copyright 2018 Springer Nature. (d) Schematic diagram of the ultrahigh frequency–RFID wireless sensor system for H_2 sensing which is composed of a RFID sensor tag and RFID–antenna–connected network analyzer. (e) Change in the reflectance of rGO–Pt–based wireless sensors as a function of the hydrogen gas concentration for a 2 min exposure.[534] Reproduced from Ref.[534] Copyright 2015 American Chemical Society.

Besides doping with metal NP,[535] surface functionalization of graphene materials with metal oxides and polymers that are able response to H_2 but with low surface-to-volume ratio and poor electrical conductivity, has also proved effective in improving the sensitivity of graphene to H_2. This strategy of detecting H_2 gas has been reported with metal oxides including SnO_2[536] and ZnO[537] decorated on graphene. For example, Al–Mashat et al. using Gr–PANI nanocomposite for H_2 sensing, demonstrated a sensitivity of 16.57% toward 1% of H_2, which was considerably larger than of the sensors based on either graphene sheets or PANI nanofibers alone.[538] Maeng and co–workers demonstrated that fully organic PEDOT-PSS heterojunctions, modified with graphene, could be used to detect H_2 at 100 ppm.[539]

CO and CO_2. CO is a colorless, odorless and tasteless gas with high toxicity to humans and animals. Therefore, it is important to develop reliable sensing platforms that would enable continuous monitoring of CO in both industrial and home–based applications. The initial report by Novoselov and co–workers showed that graphene produced a significantly weaker response to CO than to more reactive gases such as NH_3 or NO_2.[157] First–principles calculation performed by Ao et al. demonstrated that the incorporation of defects and dopants can enhance the reactivity of graphene towards CO.[183] Majumdar and co–workers synthesized rGO and used it for chemiresistive detection of CO.[540] The resulting sensor produced a 33% $\Delta R/R_0$ change in response to 10 ppm of CO at room temperature with minimal response to interferents such as CH_4, H_2, or NH_3. CO detection by a three–component hybrid system was also achieved by Kim and coworkers.[541] The application of rGO/SnO_2/Au hybrid materials enabled the detection of CO at 2 ppm levels with 20.3 % change in response. A sub–ppm–level CO gas sensor with a wide detection range of 0.25 ppm to 1000 ppm, based on CuO–decorated graphene hybrid nanocomposite, was recently reported by Zhang et al.[542] The superior sensing performance for the presented sensor was ascribed to the hierarchical porous nanostructure and the heterojunction formed at the CuO–graphene interfaces

One of the earliest reports of CO_2 sensing with pristine graphene was demonstrated by Cheng and co–workers in 2011, who were able to detect CO_2 at concentrations as low as 10 ppm. The resulting graphene sensor showed significant change in conductance when exposed to 10–100 ppm of CO_2 in air with a response time of less than 10 sec. Due to the weak nature of interactions between CO_2 and graphene, the device response was rapid and reproducible. Nemade and Waghuley using few layered graphene–based chemiresistive device could detect CO_2 at 3 ppm concentrations, with the response time of 11 sec. The improved sensitivity to CO_2 was attributed to the presence of defect sites in graphene materials that could interact with CO_2 gas molecules.[543] The highest sensitivity to CO_2 was achieved by Cheng et al. through a in situ cleaning of graphene using UV light. The resulting sensor could detect CO_2 at concentrations as low as 136 ppt.[490] Composites including Gr–Y_2O_3 quantum dots (QDs), Gr–Sb_2O_3 and Gr–Al_2O_3, were also successfully used for CO_2 sensing at room temperature.[543, 544-545]

H_2S and SO_2. Hydrogen sulfide (H_2S) and sulfur dioxide (SO_2) are atmospheric pollutants, and the main contributors to acid rain. Both gases are toxic to humans and ecosystems. Detection of H_2S and SO_2 with graphene materials has been widely explored by first–principles methods.[546-551] These investigations showed that SO_2 and H_2S adsorb only weakly on pristine graphene, yet various modifications, including doping with defects and additives, can improve sensitivity to these gases. In recent years, several sensors based on graphene materials have been developed for the detection of H_2S and SO_2. Jin et al. fabricated a FET sensor using chemically edge–tailored GO nanosheet–based materials which could selectively detect SO_2 gas at room temperature in ambient air.[552] The fabricated GO sensor showed good sensing performance including a wide range of sensitivities, fast response and recovery times. The high sensitivity to SO_2 was attributed to the presence of holes induced by the protonation and isomerization of edge–

tailored GO nanosheets upon exposure to the acidic sulfurous gases. In addition, the GO–based sensing devices exhibited limited response to a series of organic vapors (e.g., tetrahydrofuran, formaldehyde or benzene) confirming its high selectivity for SO_2 gas. Ruoff and co–workers found that increasing the temperature can not only speed up the response and recovery of the graphene based FET sensor for SO_2, but can also improve its sensitivity.[553] Zhang et al. fabricated layer–by–layer self–assembled TiO_2/graphene film device and used it for the detection of SO_2 gas at room temperature. The resulting sensor exhibited ppb–level detection, rapid response and recovery (71 s–73 s and 95s–128s, respectively), good reversibility, selectivity and repeatability for SO_2 gas sensing (**Figure 20d**).

Sensing of H_2S has mainly been realized by using composite materials where graphene or graphene oxide was modified with metal oxides in the form of nanorods/nanocrystals,[554-556] nanofibers, nanosheets,[343-344, 557-558] or polymers,[559-560] because metal oxides usually show strong chemisorption of toxic H_2S gas at room temperature[561-562] For example, Zhou et al. fabricated a rGO/Cu_2O nanocomposite–based sensor, which demonstrated the detection limit of 5 ppb at room temperature. The observed high sensitivity to H_2S was due to the high surface activity for adsorption of H_2S gas molecules onto the surface of Cu_2O and the high electron transfer efficiency in the conducting network.[554] Jiang and co–workers reported on the ultrafast responses to H_2S of 500 µs, as well as a fast recovery time of less than 30 s.[557] The authors used magnetic fields with different orientations to control the fabrication progress of the Gr–Fe_2O_3 nanosheets. The experimental results illustrated that structural orientation of nanosheets played an essential role in maximizing efficiency of the device. Another strategy to fabricate sensitive H_2S sensor was demonstrated by Fattah and Kathami who used mechanically exfoliated graphene as a sensing layer in the Schottky heterojunction device configuration (Gr/n-Si).[563] The authors observed increase in sensitivity from 71% to 435% as the concentration of H_2S was varied from 10 ppm to 1000 ppm with the response time of approximately 20 seconds at 100 °C.

O_2. Oxygen is a reactive species that composes more than 20 % of air. It is an important analytical target in a variety of areas including industrial safety, combustion process monitoring, as well as environmental and biomedical fields.[564] Detection of oxygen by monolayer graphene in gas flow has been achieved by Hung and co–workers in 2011.[565] The CVD–grown monolayer graphene device, exhibited a p–type doping behavior to O_2 at 1.25 vol% concentrations. The authors observed that the sensitivity of fabricated sensors to O_2 could be further improved (LOD of 134 ppm) by illumination with UV light.[566] These results are comparable with earlier reports of a Gr–TiO_2 hybrid O_2 senor by Wang et al.[567] A carbon nitride/rGO hybrid system developed by Star and co–workers was capable of detecting oxygen in the 300–100000 ppm concentration range.[568]

A wide variety of graphene and graphene–oxide sheets have been constructed that had increased functionality imbued by metal nanoparticles and metal–oxide nanoparticles. The growing set of methodologies for modifying graphene to provide more selective and sensitive hybrid materials will promote the fabrication of novel sensing technologies. The reports of flexible sensors based on graphene materials integrated onto the cotton or paper substrates opened the doors for low cost sensing and the development of wearable, wireless sensors.[124] Future work in the field of graphene–based sensors will continue to look towards new methods of integrating graphene and graphene hybrid materials in ways that allow for intimate integration into specific applications.[125, 324]

4.1.2. Black Phosphorous

Black phosphorus was initially predicted to be a superior gas sensing material over graphene and MoS_2 by a first–principles study carried out by Chen's group in 2014.[98] Their work predicted optimal adsorption positions of gas molecules on a monolayer of phosphorene. They also showed that high charge transfer is the driving mechanism behind strong adsorption of analytes on the surface of BP. The first experimental reports utilizing BP as active element in gas sensing were demonstrated in two independent publications in 2015. Zhou and co–workers integrated chemically synthesized BP into FET devices to detect NO_2 down to 5 ppb in an argon environment (**Figure 21a–b**).[159] The authors observed a systematic increase in conductance with changing concentrations of NO_2, which was indicative of hole doping charge transfer, and was consistent with the p–type semiconductor electronic structure of BP (**Figure 21c–d**).[159] The change in conductance fitted well within the Langmuir isotherm further confirming that molecular adsorption of NO_2 through active site binding, and the charge transfer was the principle sensing mechanisms governing the response of the fabricated sensing devices.[159]

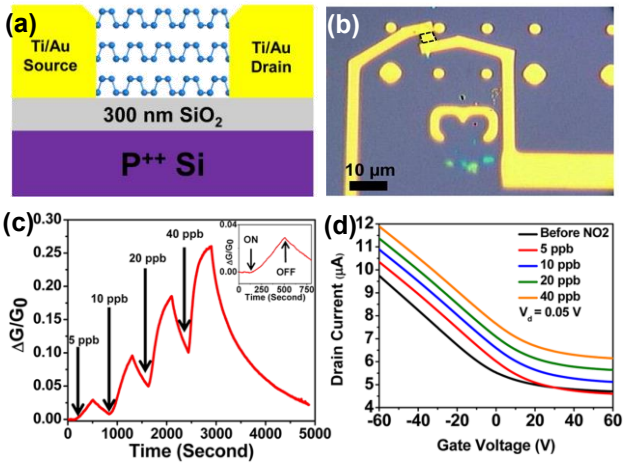

Figure 21. (a) Scheme of a multilayer BP FET. (b) An optical image of the multilayer BP flake between two Ti/Au electrodes used in this study. The BP flake is bordered by a dashed black line to guide the eye. (c) Relative conductance change ($\Delta G/G_0$) vs time (seconds) for a multilayer BP sensor showing a sensitivity to NO_2 concentrations (5–40 ppb). Inset shows a zoomed in image of a 5 ppb NO_2 exposure response with identification of points in time where the NO_2 gas is switched on and off. (d) I_d–V_g curves of multilayer BP FET under different concentrations of NO_2 showing a clear

upshift in the curves as the concentrations increase.[159] Reproduced from Ref [159] Copyright 2015 American Chemical Society.

In the same year, Cui et al. incorporated 2D layers of BP into the FET devices by using the 'Scotch tape' mechanical exfoliation method (**Figure 22a–b**) and utilized the resulting device for the sensitive detection of NO_2 at a wide concentration range of 20–1000 ppb (**Figure 22c**).[158] They reported on the thickness dependent sensitivity of BP layers to targeted analyte, with an optimal thickness of 4.8 nm (**Figure 22d**).[158] DFT calculations showed that the change in sensitivity with respect to thickness was dictated by the band gap for thinner sheets (<10 nm) and by the effective thickness on gas adsorption for thicker sheets (>10 nm). The authors also demonstrated that BP exhibited a significantly higher response to NO_2 over analytes such as CO, H_2, and H_2S suggesting that layered BP could be potentially used for the fabrication of selective gas sensors. Donarelli et al. expanded on device integration technology by fabricating chemiresistive devices through drop–casting chemically exfoliated BP sheets onto a Si_3N_4 substrate, pre–patterned with Pt comb–type interdigitated electrodes. The resulting analytical devices displayed a p–type response to NO_2 and NH_3, with LODs of 7 ppb and 1 ppm at room temperature, respectively with minimal interference from CO or CO_2. The authors suggested that the high edge–plane content as a function of BP morphology enhanced the sensitivity of this 2D material to targeted gaseous molecules.[158]

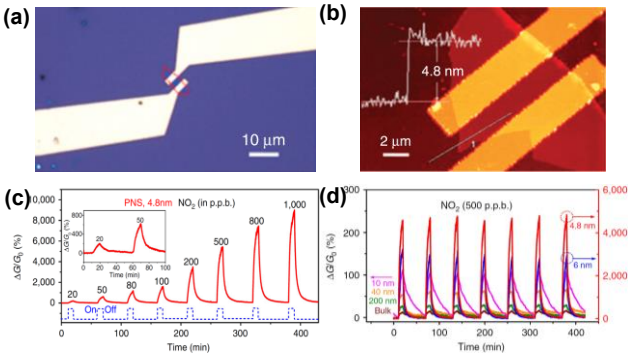

Figure 22. (a) Optical microscopy and (b) AFM images of the BP sensor device showing that the BP nanosheet electrically bridges the gold electrodes. (c) Dynamic response curves of relative conductance change versus time for NO_2 concentrations ranging from 20 to 1000 ppb (balanced in dry air) for BP nanosheet (thickness 4.8 nm). A drain–source voltage of 0.6 V was applied to the device. The dashed line demonstrates the 'on/off' of NO_2 gas. The sensitivity here is defined as the differential response between $D_G/G_0 = 0$ in the air environment at the first cycle and the D_G/G_0 at the end of gas 'off' for each concentration. (b) Thickness–dependent multi–cycle responses of the BP nanosheet sensor to 500 ppb. NO_2.[158] Reproduced from Ref.[158] Copyright 2015 American Chemical Society.

Further improvements in sensing properties of BP to gaseous analytes were realized by means of surface functionalization through the incorporation of metal nanoparticles on the surface of BP. For example, Jung and co–workers enabled chemiresistive sensing of H_2, which typically cannot be achieved using pristine BP, by incorporating either Au or Pt nanoparticles directly onto the surface of BP.[569] The fabricated devices based on BP–Pt NP could sense H_2 at concentration as low as 5 ppm at room temperature without significant degradation in the response characteristics over the 30 day testing period. The enhanced stability of BP to ambient conditions (oxygen and humidity) was attributed to the increase in effective blockage of the lone pair of electrons on the surface of BP by the NPs. Interestingly, the authors also observed that through the incorporation of Au NP onto the 2D BP, the work function of this 2D material can be further modulated by the transfer of electrons from the Au, thus causing a change in response from p–type to n–type in the presence of oxidizing gases. This demonstrated a great potential for developing tunable BP–based gas sensors. Using first-principles calculations, Ying et al. also explored the effect of metal doping on the sensitivity of BP to CO.[570] The authors reported that the presence of incorporated Li, Na, K, Ca, Sr, Ba, and La–metals improved the adsorption energy of CO on the surface of BP which was attributed to enhanced coupling between carbon monoxide and tested metals, indicating that these systems can be potentially employed in electrically–transduced gas sensing of CO.

BP–based materials have been increasingly used in the development of gas sensing technologies due to its intriguing electrical properties such as tunable band gap, large electronic anisotropy, and high surface area. Although, BP possess many attractive features for sensor development, its limited stability to oxygen and water remains the biggest challenge for practical applications. This issue can be partially addressed through the incorporation of nanoparticles, or by using protective coatings that would inhibit outside environmental influence.[367, 571] In addition, novel scalable, and cost–effective chemical strategies that allow fabrication of BP with precisely controlled structure and composition need to be developed for further progress towards practical applications in gas sensing.[572-574]

4.1.3. Transition Metal Dichalcogenides

2D transition metal dichalcogenides have attracted attention in chemical gas sensing application for its outstanding properties, including tunable band gap,[575-576] large surface–to–volume ratio and possibility of operating at room temperature, following the popularity of graphene and other carbon–based materials.[577]

NH_3 and N_xO_y. Zhang and co–workers demonstrated the first application of MoS_2 in gas sensing by integrating thin layers of mechanically exfoliated MoS_2 into a FET device.[578] The resulting devices exhibited n–type doping behavior upon the exposure to NO with a detection limit of 0.8 ppm (**Figure 23a–b**). The authors also observed that single–layered MoS_2 produced a faster response (5 s) to NO than multilayer (2-4 layers) MoS_2; however, its analytical signal was largely unstable. Interestingly, the signal stability of the fabricated FET devices was improved by increasing the number of MoS_2 layers. Thickness–dependency of

MoS_2 layers on the sensitivity to NO_2 was further investigated by Late et al.[101] They demonstrated that 5–layer MoS_2 exhibited improved gas–sensing performances as compared to 2–layer MoS_2 for detection of NO_2 (100 ppm) and NH_3 (100 ppm) (**Figure 23c–d**). First–principles calculations showed that the charge transfer mechanism and contact resistance between the MoS_2 layer and electrodes dictates the response of MoS_2–based FET devices. A very slight increase in the adsorption with the increase in the number of MoS_2 layers was also found, which may explain the very small increase in sensitivity for five layers as compared to two layers.

Duesburg and co–workers employed chemical vapor deposition to synthesize MoS_2 layers directly onto interdigitated gold electrodes and used it for the detection of ammonia gas. The resulting device displayed high sensitivity to NH_3 at 300 ppb concentration with a theoretical LOD of 51 ppb. MoS_2 was also demonstrated to exhibit excellent sensing characteristics for O_2 detection.[579] Kim et al. reported a chemiresistive device with a broad linear response range to O_2 concentrations (1–100%) at 300°C using liquid–exfoliated MoS_2 with a high abundance of edge sites.[579] First-principles calculations showed that the density of states in liquid–exfoliated MoS_2 was localized along the edges of the material resulting in the large presence of active sites for O_2 adsorption, thus being responsible for high sensitivity of the MoS_2–base device.

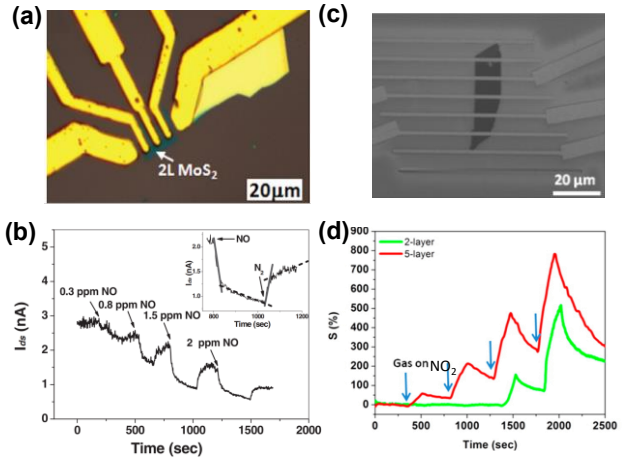

Figure 23. (a) Optical microscope image of an FET device based on the 2–layer (2L) MoS_2 film. (b) Real–time current response after exposure of the 2L MoS_2 FET to NO with increasing concentrations. Inset: A typical adsorption and desorption process of NO on the 2L MoS_2 FET.[578] Reproduced with permission from Ref.[578] Copyright 2011 John Wiley and Sons. (c) SEM image of two–layer MoS_2 transistor device (d) Comparative two–and five–layer MoS_2 cyclic sensing performances with NO_2 (for 100, 200, 500, 1000 ppm).[101] Reproduced from Ref.[101] Copyright 2013 American Chemical Society.

Numerous other chalcogenides including $MoSe_2$, $MoTe_2$, WS_2, and SnS_2 have demonstrated great potential in the development of functional devices for gas sensing applications. Bougouma and co–workers integrated a single layer of $MoSe_2$, obtained through mechanical exfoliation from bulk crystal, into a FET device for sensing of gaseous NH_3.[580] The authors reported on detection limits of 50 ppm for NH_3 with the response time of 2.5 min and recovery time of 9 min.[580] The sensing mechanism of the $MoSe_2$–based FET was proposed to occur through charge transfer between the adsorbed gas molecules and the 2D nanomaterial. Tuning the electrical properties of TMDCs through doping has been shown as effective strategy to increase sensitivity to gaseous analytes.[581] Recently, Choi et al. investigated the effect of Nb doping of $MoSe_2$ on its gas sensing performance,[582] in which Nb concentration could be precisely controlled by varying the number of Nb_2O_5 deposition cycles in the plasma enhanced atomic layer deposition process (**Figure 24a**). Addition of Nb along the grain boundaries can meditate a large number of dangling bonds and vacancies which are more vulnerable to the oxidation. Thus, by doping 2D layered $MoSe_2$ with Nb, a stable gas response as well as a long-term stability can be achieved.[583] However, high Nb doping concentration deteriorated the response to NO_2 which might be attributed to a considerable increase in the number of metallic $NbSe_2$ regions that didn't respond to gas molecules (**Figure 24b–c**).[584] At relatively low Nb dopant concentrations, $MoSe_2$ showed enhanced device durability as well as improved response to NO_2, attributed to both its small grains and stabilized grain boundaries.[582] Higher molecular weight $MoTe_2$ materials have been also shown to exhibit high sensitivity to gaseous analytes. Zhang and co–workers fabricated FET devices by using $MoTe_2$ (**Figure 24d**). The device could detect NO_2 and NH_3 at concentration of 100–1000 ppb and 2–ppm, respectively (**Figure 24e–f**).[585] They found that the recovery kinetics after each sensing cycle can be effectively modulated by biasing the sensor at different gate voltages and can achieve more than 90% recovery within 10 min at room temperature under the optimum biasing potential.[585]

O'Brien et al. utilized plasma assisted synthesis to deposit nanolayers of WS_2 onto interdigitated electrodes for the detection of NH_3.[586] They observed high sensitivity to NH_3 with the LOD of 1.4 ppm in N_2 at room temperature. Zhang and co–workers further explored the gas sensing properties of WS_2 to NH_3 using a chemiresistive electrode configuration.[470] The resulting device displayed a p–type response to ammonia in the concentration range of 1–10 ppm with minimal interference from ethanol, methanol, formaldehyde, benzene, and acetone. This sensor also showed increased response at higher humidity levels due to sulfide ion–assisted hydroxylation process of adsorbed water molecules, and the oxidation of the solvated ammonia with adsorbed oxygen ions at the surface of the 2D WS_2. Kim et al. explored the utility of WS_2 in chemiresistive sensing of NO_2 and acetone.[587] The pristine WS_2–based device exhibited high sensitivity to acetone, while minimal analytical response coupled with partial recovery was observed for 500 ppm of NO_2. Interestingly, incorporation of Ag NWs onto the surface of WS_2 resulted in a 12–fold improvement in sensitivity (667%) and recovery (> 90%) to NO_2 due to the catalytic and n–type doping effect of Ag NWs.[587]

TMDCs, like MoS_2 and $MoSe_2$, showed good selectivity to NO_2, however, they don't have sufficiently fast recovery kinetics [101]. Compared to TMDs, SnS_2 has a larger

electronegativity, potentially enhancing gas adsorption sites.[588] Moreover, the electronic band structure of SnS_2 has relatively stronger temperature dependency. This feature can possibly enable the optimization of sensing response and be used for enhancing recovery kinetics at moderately elevated temperatures. [589] Ou et al. explored the sensing of NO_2 by incorporating 2D SnS_2 nanoflakes into chemiresistive device.[391] The planar 2D SnS_2 flake, synthesized via a facile wet chemical route (**Figure 24g**), both provided large active surface area and also facilitated gas accommodation into the van der Waals spacing due to small SnS_2 interlayer binding energy. The hybrid sensor displayed good sensitivity to NO_2 at concentrations ranging from 0.6 to 10 ppm at 120 °C with a LOD of 30 ppb (**Figure 24h**). An excellent NO_2 selectivity was observed with respect to H_2, CH_4, CO_2, and H_2S (**Figure 24i**), which is uncommon for NO_2 gas sensors operating based on the charge–transfer mechanism. This unique selectivity was ascribed to the strong physical affinity of paramagnetic NO_2 gas molecules toward SnS_2 surfaces as well as the relatively favorable position between the Fermi level of SnS_2 and NO_2 partially occupied molecular orbitals. In addition, this gas sensor was also showed excellent recovery to the baseline in contrast to other 2D TMDs, such as 2D MoS_2.[578, 101]

Although excellent sensing properties using 2D TMDCs in the context of chemical gas sensing have been realized, there are still numerous challenges that need to be addressed prior to their practical implementation in sensing technologies. *First,* novel synthetic approaches need to be developed to allow for controlled large-scale production of TMDCs.[577] *Second,* the long–term stability of these 2D materials is often compromised by surface oxidation and moisture absorption.[590] This issue may be addressed by forming hybrid composite materials e.g., through the incorporation of nanoparticles, or by using protective coatings that block the 2D material from ambient conditions.[575] *Third*, the partial recovery of 2D TMDC–based gas sensors after exposure to certain analytes may pose challenges for practical applications. Thermally induced recovery may assist with answering this problem, but this process would compromise one of the biggest advantages of TDMC–based gas sensors, the ability to operate at room temperature. Therefore, new strategies that would ensure full system recovery during the analytical measurements are required to harness the full potential of 2D metal chalcogenides in sensing applications.

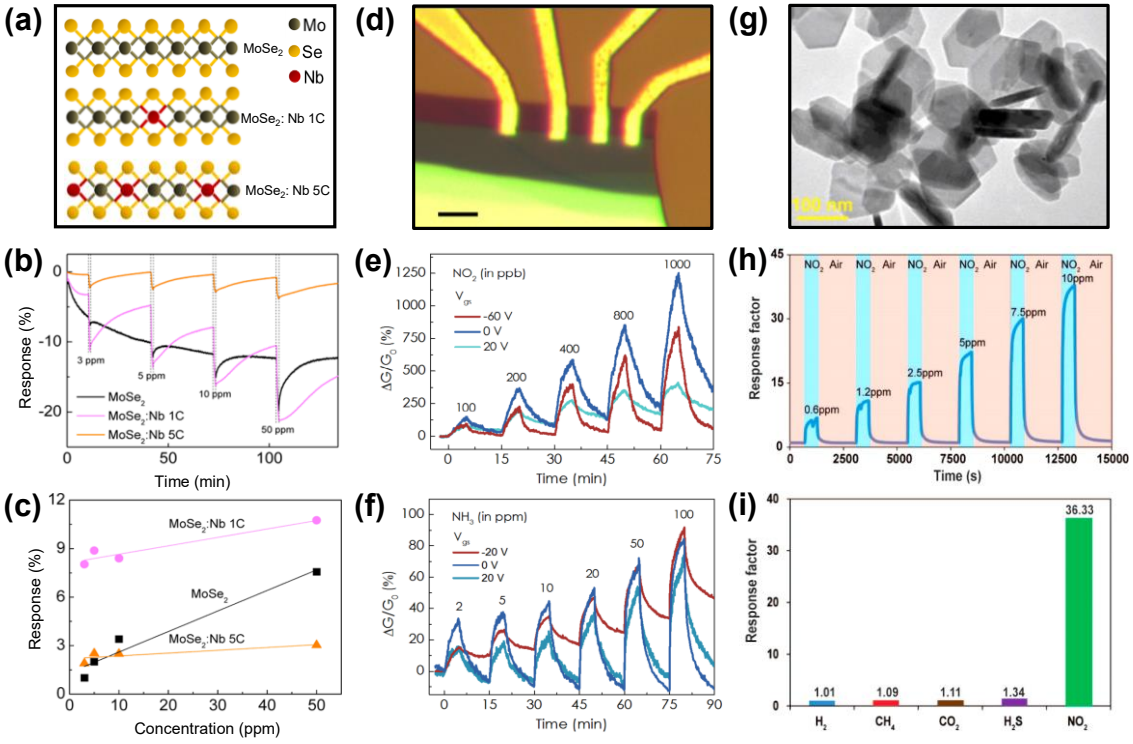

Figure 24. (a) Schematic atomic structures of $MoSe_2$ (top), $MoSe_2$:Nb 1C (middle), and $MoSe_2$:Nb 5C (bottom). (b) Transient gas response of the $MoSe_2$, $MoSe_2$:Nb 1c, and $MoSe_2$:Nb 5c devices at NO_2 concentrations ranging from 3 to 50 ppm. (c) Comparison of gas responses of the three devices as a function of the NO_2 gas concentration.[582] Reproduced from Ref.[582] Copyright 2017 American Chemical Society. (d) Optical microscope image of the $MoTe_2$ FET on top of SiO_2/Si substrate with Ti/Au electrodes. Scale bar is 5 μm. (e) Real–time conductance change of p–type $MoTe_2$ FET sensor upon exposure to different concentrations of NO_2 under different gate biases. (f) Real–time conductance change of n–type $MoTe_2$ FET sensor to different concentrations of NH_3 under different gate biases.[585] Reproduced with permission from Ref. [585] Copyright 2016 IOP Publishing Ltd. (g) TEM image of 2D SnS_2 flakes. (h) Dynamic sensing performance of 2D SnS_2 flakes toward NO_2 gas at concentrations ranging from 0.6 to 10 ppm under the operation temperature of 120 °C. (i) Measured cross–talk of 2D SnS_2 flakes toward H_2 (1%), CH_4 (10%), CO_2 (10%), H_2S (56 ppm), and NO_2 (10 ppm).[391] Reproduced from Ref.[391] Copyright 2015 American Chemical Society.

4.1.4. Metal Oxides

Metal oxide (MO) gas sensors constitute a well–established class of analytical devices that has revolutionized gas sensing applications since the 1960s.[218] Traditional materials such as thick films or particles of SnO_2, ZnO, TiO_2, WO_2, In_2O_3, Fe_2O_3, or MoO_3 have shown excellent sensitivity for gas sensing at elevated temperatures.[218] Many commercial systems rely on MOs technologies to provide inexpensive reliable sensing of gaseous compounds.[591] MOs materials operate at high temperatures because of the high activation energy required for the reaction between the surface–adsorbed oxygen and analyte.[152] Room temperature sensing can be achieved through the strategic control over the structure and surface chemistry of MOs at the nanoscale.[413] Surface functionalization approaches with nanowires, nanotubes, and nanoparticles are effective methods for improving the sensing performance of MOs, not only with respect to working temperature, but also to enhance sensitivity and response time.[127]

NO_2. The sensing of NO_2 has been realized by using various 2D MOs, including ZnO, NiO, WO_3. Among these, ZnO—in the form of either nanosheet, nanowall, or nanoflake—has been mostly applied for gas detection due to its high sensitivity, stability, and low cost.[592] In 2011, Chen et al. reported NO_2 detection using ZnO polygonal nanoflakes (thickness of 40–80 nm) synthesized by microwave hydrothermal method.[593] The resulting ZnO sensor, with an optimal operating temperature of 175 °C, exhibited excellent selectivity to NO_2 at 0.5 ppm concentrations over other nine gaseous interferants fixed at 80 ppm. Because intrinsic defects of ZnO, including oxygen vacancy and zinc interstitial, are involved in the mechanism of gas sensing, the gas sensing properties of ZnO nanoflakes were found to be independent of particle size, but greatly relied on the crystal defect structure in the material. In situ diffuse reflectance infrared Fourier transform spectroscopy technique indicated that nitrate ions, and nitrite anions were the main adsorbed species on the surface of ZnO.

The application of ZnO in the form of nanosheet or nanowall with smaller thickness than that of nanoflake can usually exhibit superior sensing performance, e.g., higher sensitivity, faster response/recovery and lower operation temperature. Yu et al. showed the ability of ZnO nanowalls, deposited on an ITO glass substrate, to sense NO_2 in the concentration range of 1–50 ppm. The ZnO nanowalls with average thickness of ~20 nm exhibited good response toward 50 ppm NO_2 (S=30) at the operating temperature of 220 °C, together with fast response and recovery times of 30 s and 48 s, respectively.[594] Further study showed that ZnO annealing can significantly improve its sensing performance.[595] The ZnO nanowalls annealed at 450 °C could be used for room–temperature detection of NO_2 with fast response and recovery time (23 s and 11 s, respectively), which enhanced performance may be due to the presence of significant porosity and oxygen vacancies introduced into the nanowalls during annealing. Xiao et al. synthesized ZnO nanosheets with an average thickness of 20 nm and (100) exposed facets.[596] The ZnO nanosheets could detect NO_2 in a range of 1–4 00 ppm at 180 °C. This ZnO nanosheet–based sensor showed faster response/recovery times (3 s and 12 s to 10 ppm NO_2, respectively) and excellent selectivity over 8 other interfering gases. The abundant oxygen vacancies on the (100) exposed surfaces were considered as the active sites for NO_2 adsorption, which were responsible for the high response. Au–decorated ZnO nanosheets[597-598] and ZnO–polymer composites were also used for NO_2 sensing often giving rise to enhanced sensitivity compared to non–modified ZnO.

The aggregation of conventional nanosheet can lead to a lower specific surface area and fewer number of activation sites. [599]. The utilization of mesoporous metal oxide nanosheets not only reduces the synthesis expense, but also expands their potential applications in gas sensing. Hoa et al. reported on a facile synthesis of NiO sheets with large degree of mesoporosity from the hydrothermal treatment of $NiCl_2$ with NH_4OH followed by calcination at 300 °C (**Figure 25a**).[600] Sensors using the calcinated NiO materials were able to detect NO_2 at 1 ppm with a response change of 13% (**Figure 25b–c**). The fabricated sensor was selective to NO_2 over CO (0% response to 20 ppm CO). The sensing mechanism was hypothesized to arise from the injection of holes into the p–type semiconductive NiO material as electronegative NO_2 reacts with the surface conduction band. The exposure to NO_2 reduced the resistance of the material, which is consistent with the proposed mechanism of sensing and material properties. In this study, gas sensing was performed at 250 °C, which temperature is lower than typical MOs operating temperatures but is still far from room temperature. The operating temperature of NiO based NO_2 sensors was lowered by the construction of NiO/WO_3 heterogeneous nanoparticles. NiO is a p–type semiconductor, while WO_3 is a n–type semiconductor. Bao et al. combined the p–and n–type character of the NiO and WO_3, respectively, by synthesizing sheet–like heterogeneous nanoparticles from the thermal annealing of $Ni(OH)_2$ sheets and H_2WO_3 sheets (**Figure 25d**).[601] The resulting materials showed an enhanced sensing response to NO_2 over WO_3 or NiO in their pristine states (**Figure 25e–f**). The materials were able to sense a range of toxic gaseous analytes at 30 ppm at room temperature. The authors observed that the fabricated device produced the greatest response to NO_2 amongst other analyte, suggesting that this composite material could be used for a selective detection of NO_2. Overall the device exhibited p–type sensing behavior, probably due to the high molar ratio of NiO:WO_3 (2.7 : 1).[601]

NH_3. Liu and co–workers demonstrated that porous ZnO, prepared by annealing ZnS(ethylenediamine)$_{0.5}$ precursor, can be used for indoor detection of NH_3.[602] The authors reported on high sensitivity to the targeted gas in the concentration range of 50–500 ppm, at 250 °C and 30% RH with excellent retention of sensitivity after 3 months of operation.[602] Nguyen et al. integrated ZnO–WO_3 nanocomposite, synthesized from hydrothermal treatment, into gas sensing devices for the detection of NH_3.[603] The fabricated device exhibited n–type response to varying concentrations

of NH_3 in the 25 ppm to 300 ppm range at operating temperature of 300 °C with good selectivity over ethanol and liquid petroleum gas. The high sensitivity to NH_3 gas was attributed to the large exposed surface area of ZnO–WO_3 material and the existence of the hetero–junctions between the WO_3 and ZnO in the composite.

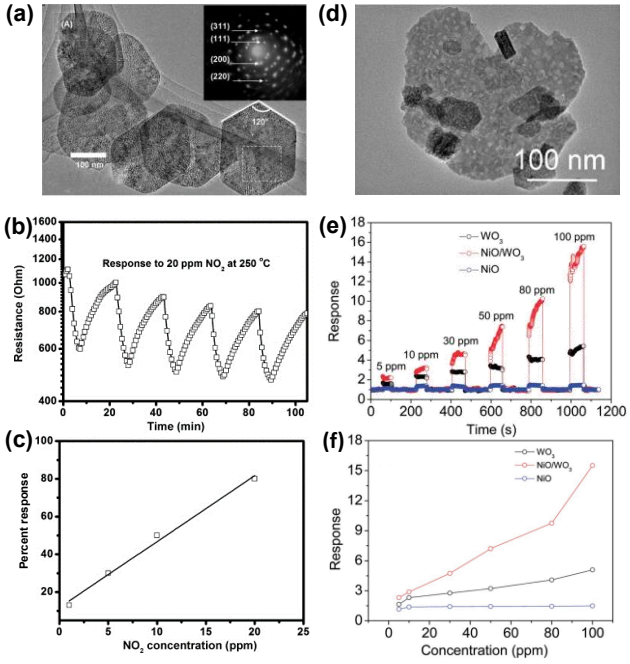

Figure 25. (a) TEM image of mesoporous NiO nanosheets that have irregular hexagonal shapes with average sizes of 250 nm. (b) The change in sensor resistance upon five-cycle exposure to 20 ppm of NO_2. (c) Sensor response as a function of NO_2 concentration.[600] Reproduced with permission from Ref.[600] Copyright 2011 John Wiley and Sons. (d) TEM image of NiO/WO_3 composites. (e) Sensing response of hybrid material NiO/WO_3 (red trace), and starting materials WO_3 (black trace), and NiO (blue trace) to NO_2 from 5–100 ppm. (f) Sensor response for all three materials as a function of concentration.[601] Reproduced with permission from Ref.[601] Copyright 2014 Royal Society of Chemistry.

Yang and co–workers further enhanced sensitivity to NH_3 by incorporating ZnO–PPy hybrid material into chemiresistor device architecture.[604] This nanocomposite showed high sensitivity to NH_3 with relative resistance change of ~20% towards 0.5 ppm of the gas analyte wide response range of 0.5–200 ppm and high selectivity over 9 others gaseous interferants (e.g., methanol, acetone, ether, hexane, tetrahydrofuran, ethanol, propylamine, butylamine and diethylamine). The formation of p/n junction between p–type PPy and n–type ZnO was suggested to be responsible for the improved sensing performance to NH_3 of the fabricated device.[604] Sensitive detection of NH_3 could be also achieved by using NiO based materials. For example, Wang et al. used hydrothermal synthesis coupled with high temperature oxidation method to fabricate porous NiO films composed of small particle with diameters ranging from 8 to 30 nm.[605] The resulting gas sensor exhibited 18% conductance change to 30 ppm of NH_3 with response time of 27 s and high selectivity towards ammonia over other organic gases such as chloroform, dichloromethane, ethylacetate, formaldehyde, heptane, iso–propanol, and toluene at room temperature. Zhang and co–workers integrated NiO–TiO_2 composite into a chemiresistive gas sensing device, which could detect ammonia in 10 to 100 ppm concentration range at room temperature under UV illumination. .[606] The prepared sensor also showed minimal response to VOCs including ethanol, methanol, formaldehyde and acetone. High selectivity to ammonia was attributed to the formation of the p–n heterojunction, which led to the cancelation of the opposite responses of n–type TiO_2 and p–type NiO materials to tested reducing gases.

H_2S. Detection of H_2S has been accomplished with a number of MOs systems and traditional thick–films of bulk materials. Recent advancements using nanoscale materials, have led to significant improvement in sensing performance of gas sensors for H_2S detection. In 2010, Zhang and co–workers used CuO nanosheets to detect H_2S in the concentration range of 2 ppb–1.2 ppm.[607] The nanosheets were synthesized via a facile surfactant free method. The response and recovery times were 6 s and 9 s, respectively at an operating temperature of 240 °C.[607] Li and co–workers also integrated sheets of CuO with thickness of 62.5 nm, prepared using a facile hydrothermal synthesis, into H_2S gas sensing devices.[608] The resulting sensor responded to H_2S in the concentration range of 10 ppb–60 ppm at room temperature, and demonstrated high selectivity to targeted analyte at 0.2 ppm over SO_2, NO, NO_2, H_2, CO, ethanol, and NH_3 gases at 40 ppm.[608] In addition, CuO nanosheets exhibited good long–term stability with only <5% deviation in response after testing the sensor performance for 1 month at 200 ppb of H_2S. The high sensitivity of CuO–based sensor to H_2S was attribute to the large abundance of nanopores in the nanosheet of the 2D material, which favors adsorption and desorption of the gas on its surface. Huo and co–workers further improved the sensitivity to H_2S by using hierarchically structured, porous nanowall NiO arrays grown by hydrothermal reaction and subsequent calcination onto ceramic tubes with pre–patterned Au electrodes.[609] The authors could detect H_2S in the range of 1 ppb–100 ppm at 92 °C with high selectivity over triethylamine, formaldehyde, chlorobenzene, acetone, ethanol, carbon monoxide, and ammonia. The excellent sensing performance of the fabricated gas sensor was attributed to the porous structure of the NiO material with a large specific exposed surface area, which promotes adsorption/desorption of H_2S gas molecules onto/from its surface as well as improves electron transfer.

WO_3 in the form of nanosheets, formed by solvothermal synthesis, was recently utilized for the detection of H_2S by Gardner and co–workers.[610] The response of the fabricated device to H_2S was measured from 100 ppb to 5 ppm with normalized responses of 1.4% and 3.9%, respectively. The same sensor also displayed high cross reactivity with humidity (25% RH) at 350 °C.[610] MoO_3 nanobelts were used to sense H_2S by depositing a mat of fibers described as "nanopaper" across interdigitated electrodes (**Figure 26a**). The resulting device was used to detect 250 ppb H_2S at an

operating temperature of 250 °C (**Figure 26b**).[611] Hu et al. reported on ultra–fast detection time at sub–ppm concentrations of H_2S by integrating MO_3–WO_3 composite, synthesized by stirring WO_3 nanosheets with definite amounts of ammonium heptamolybdate tetrahydrate in H_2O followed by calcination at 500 °C, into a gas sensor. The resulting chemiresistor was capable of detecting 20 ppb H_2S with a response time of 2 s and a recovery time of 5 s at 250 °C.[612] The excellent gas sensing performance of the MO_3–WO_3 samples might be ascribed to the heterojunction structure in which a thicker electron depletion layer forms at the interface between MoO_3 and WO_3, resulting in larger resistance change compared to the pure WO_3.

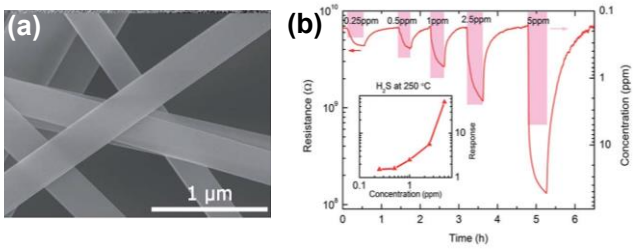

Figure 26. (a) SEM images of the MoO_3–nanopaper. (b) Response–recovery curves of the MoO_3–nanopaper sensor to different H_2S concentrations at 250 °C. The insets show the response of the sensor to various gas concentrations.[611] Reproduced with permission from Ref.[611] Copyright 2017 Royal Society of Chemistry.

Other gases. 2D metal oxides have also been applied in the sensing of other gaseous analytes, such as CO, H_2, CH_4 and more, most of which are reducing gases. Lee and co–workers reported on the highly sensitive and fast responding CO sensor fabricated from a sheet–like SnO_2.[613] The response of 2D SnO_2 nanosheets to 10 ppm CO was 2.34, with response time of 6 s, which is significantly improved than observed for the SnO_2 bulk powder (1.57 s and 88 s, respectively), respectively. The realization of both high sensitivity and fast response was explained in terms of rapid gas diffusion over the entire sensing surface, and the very thin structure of SnO_2 nanosheets. Jones and Maffeïs experimentally tested a mathematical model of the reactions on the surface of a ZnO nanosheet–based CO sensor.[614] The sheets, with a thickness of 20–100 nm, were exploited to investigate the response to different CO concentrations ranging from 50 ppm to 200 ppm at different operating temperatures (393 °C to 484 °C). The measured responses of this system were well described by the theoretical model, where the CO reacts only with the surface oxygen species via an Eley–Rideal mechanism.[614] Nanostructures with the high surface area and surface accessibility can improve the gas-sensing properties. Zeng et al. prepared a sensor based on hierarchically porous ZnO nanosheet thin films, vertically grown on a silicon substrate, which could sense CO in the range of 5 ppm to 500 ppm with excellent sensitivity (S = 11.2 at 100 ppm CO) and short response/recovery times (25 s and 36 s, respectively) at 300 °C.[615] The same device also exhibited good selectivity against typical interfering gases such as SO_2, NO_2, NH_3, H_2, and VOCs.[615] The less agglomerated and porous network of the ZnO structure, in addition to providing a high surface area, favored rapid access to the surface and effective diffusion of CO molecules.[615] Chang et al. investigated the CO sensing performance of ZnO nanowalls with (001) exposed crystal planes, vertically grown on a glass substrate, which could detect CO in a range 100 to 5000 ppm with a response of 0.3 s to 100 ppm CO at 300 °C.[616]

Chen et al. investigated the H_2 and CH_4 sensing performance of ZnO–based gas sensor consisting of interconnected ZnO nanowalls of 1.3 μm in length and approximately 60 nm in thickness, grown along the c–axis.[617-618] The resulting sensor showed good response to 100–3000 ppm of both gases at 300 °C, but higher sensitivity was observed for methane. The good sensitivity and short response/recovery times were attributed to the presence of ZnO nanowalls with large surface to volume ratio that favors the effective and fast adsorption/desorption of gas molecule. H_2 sensing was also realized by 2D layered MoO_3 by Alsaif et al. [619] and Gu and co–workers.[620] Especially, [001]–oriented α–MoO_3 nanoribbons exhibited a room–temperature response to H_2 with high sensitivity to H_2 at concentrations as low as 500 ppb and good selectivity against CO, ethanol, and acetone. The impressive analytical performance of these devices was attributed to the 2D flake–like structure of MoO_3. [619-620]

The development of thin MOs materials and MOs materials that can approximate similar behaviors allows the fabrication of sensors capable of detecting of a range of toxic gaseous compounds. Although somewhat limited by the necessity of operating at high temperatures, MOs sensors display excellent response/recovery times, robustness over time in terms of sensor reversibility, and the ease of synthesis. Further advancements in the field of MOs sensors will be focused on: the development of materials with low operating temperature, diversifying the range of applicable analytes, the exploration of the properties imbued by nanostructured confinement and the ability of those properties to enhance sensor–type behaviors of these materials.

4.1.5. Metal–Organic Frameworks

Benefiting from a unique atomic structure, 2D conductive MOFs demonstrate unique features in gas sensing applications, such as large surface–to–volume ratio, synthetic accessibility through bottom–up strategies, tunable band gap and large structural modularity that enables integration of highly tailored host–guest interactions into the porous scaffold.[88, 421] The first demonstration of chemical gas detection using 2D conductive MOF was reported by Dincă and co–workers in 2015.[418] The authors used drop–casting method to integrate the Cu_3HITP_2 MOF within a chemiresistive device architecture to achieve the detection of NH_3 gas at sub–ppm concentrations (0.5 ppm) at room temperature (**Figure 27a–b**). Sensing performance of the resulting devices was also unaltered in the presence of high levels of humidity (<60%) (**Figure 27c**). Interestingly, under the same experimental conditions, the isostructural Ni_3HITP_2 MOF did not produce a measurable response during the exposure to NH_3 indicating metal–induced selectivity in chemiresistive sensing with MOF–based devices.[418]

Our group developed a unique approach that merged synthesis and device integration of MOFs into a one-step process.[621] Using solvothermal synthesis, we integrated 2D conductive M_3HHTP_2 MOFs (M = Ni and Cu) into polymeric device platforms with pre–patterned graphitic electrodes (**Figure 28a**).[621] The fabricated devices were capable of detecting and discriminating between NH_3, NO, and H_2S gases at ppm concentrations (10–80 ppm) (**Figure 28b**). Our group also fabricated flexible NO and H_2S gas sensors through the direct solution self–assembly of Ni_3HHTP_2 and Ni_3HITP_2 MOFs on cotton–based substrates (**Figure 28c**).[622] The resulting sensors were simultaneously capable of detecting, and filtering NO and H_2S with sub–ppm limits of detection (NO = 0.16 ppm and for H_2S = 0.23 ppm) (**Figure 28d**). The chemiresistive response was largely unaltered by the presence of humidity (18% RH) and was fully recoverable by washing the devices in water. Another contribution by our group has also involved the fabrication of chemiresistive sensing arrays comprising of M_3HHTP_2 MOFs/graphite blends (M = Fe, Co, Cu, Ni) by mechanical abrasion using a compressed MOF powder.[176] The formation of graphite/MOF composites was required to establish good electrical contact within the fabricated chemiresistive devices and to enable direct integration of only moderately conductive MOFs that otherwise would not be suitable for electrically–transduced sensors. The fabricated gas sensing devices could detect and differentiate between NH_3, NO, and H_2S at 80 ppm.

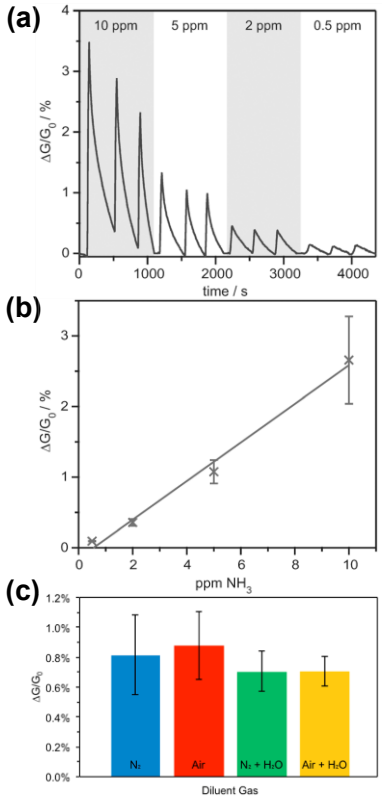

Figure 27. (a) Relative responses of a Cu_3HITP_2 device to 0.5, 2, 5, and 10 ppm ammonia diluted with nitrogen gas. (b) Device response as a function of ammonia concentration. (c) Comparison of responses of Cu_3HITP_2 devices to a 5 ppm ammonia under various oxygen and relative humidity levels.[418] Reproduced with permission from Ref.[418] Copyright 2015 John Wiley and Sons.

A significant advancement in gas sensing using 2D conductive MOFs was recently demonstrated by Xu and co–workers.[173] The authors utilized layer–by–layer liquid–phase epitaxial growth method to install epitaxially–oriented thin–films of Cu_3HHTP_2 MOF into the chemiresistive devices.[173] The resulting sensors exhibited detection limits of 0.5 ppm to NH_3 gas and minimal interference from 10 other reducing gases (benzene, H_2, toluene, acetone, ethanol, methanol, methane, n–hexane, CO, and ethylbenzene), indicating great potential for constructing selective gas sensors. In addition, the response and recovery time was up to 54% faster than observed for bulk powder counterparts.[173] This observation was attributed to enhanced contact of gaseous analytes with the active sites in the MOF with minimal diffusion barriers.[173]

Recently, Rubio-Giménez et al. through combining experimental data with computational modelling, described a possible origin for the underlying mechanism of chemresistive response for NH_3 in ultrathin films (~30 nm) of Cu_3HHTP_2.[175] The results indicate that the chemiresistive response of this family of conductive MOFs is linked to the direct interaction of gas molecules with the Cu(II) inorganic linker. This interaction resulted in slight distortions of the internal structure of the layer or changes in the coordination geometry of the metal node, subsequently leading the modifications of the band gap of the material. These demonstration are consistent with previous reports,[173-174, 418] which suggest a possible relationship between the nature of the metal nodes and the coordination ability of the analytes with the intensity and selectivity of the "turn-on" response.

Despite many improvements and great promise in the applications of 2D conductive MOFs in gas sensing technologies, many challenges need to be addressed prior to their pracital implementation in sensing. *First*, the host–guest interactions between 2D MOFs and targeted analytes are not yet well understood,[175] and require more rigourous computational modelling and experimental investigation. *Second*, the preparation of ultrathin 2D MOF nanostructuress with desired structural characteristics in a highly controllable manner remains a key challenge. *Third*, the influence of structural and compositional defects on electronic properties of MOF must studied to fully understand the nature of host–guest interactions that dictate the sensing performance of MOF–based devices. *Fourth,* the stability of 2D conductive MOFs in ambient conditions have not been yet fully investigated, and remains a critical issue for the practical use in sensing applications. Improvements in stability and robustness of 2D MOF may be realized through strategic modifications of the bond strength of metal–ligand structural units. Nonetheless, the potential of 2D conductive MOFs lies in the vast modularity of the building blocks that enables incorporation of host–guest interactions for the gas sensing applications.

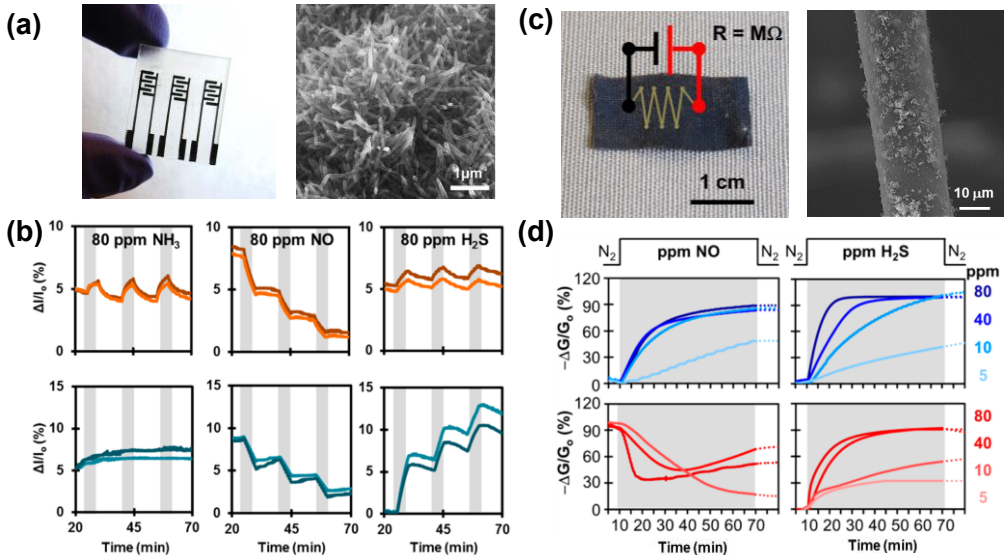

Figure 28. (a) Photograph showing the process of drawing electrodes on a shrinkable polymeric film with a commercial HB pencil (left). SEM images of MOF films incorporated into devices (right). (b) Representative sensing traces (3×80 ppm) for Cu_3HHTP_2 (upper row) and Ni_3HTTP_2 (lower row).[621] Reproduced from Ref.[621] Copyright 2016 American Chemical Society. (c) Conductive SOFT devices: textiles coated with nanoporous MOF (Left). SEM image of MOF coating on fibers (right). (d) Representative response for Ni_3HITP_2 (blue) and Ni_3HHTP_2 (red) SOFT–sensors when exposed to (from left to right) NO or H_2S.[622] Reproduced from Ref.[622] Copyright 2017 American Chemical Society.

4.1.6. Other 2D Materials

MXenes have only recently been explored as a novel class of 2D materials with remarkable possibilities for composition variations and property tuning in the development of gas sensing technologies. Lee et al. integrated the 2D $Ti_3C_2T_x$ sheets synthesized through the removal of Al atoms from Ti_3AlC_2 onto flexible polyimide platforms to fabricate gas sensing devices.[203] The $Ti_3C_2T_x$–based sensor, operating at room temperature, exhibited a p–type sensing behavior to gaseous analytes (ammonia, ethanol, methanol, and acetone) with the highest sensitivity observed for NH_3 at 100 ppm concentrations. The high sensing performance of the fabricated device was attributed to the effective adsorption of NH_3 onto the surface of the $Ti_3C_2T_x$ facilitated by the analyte interactions with surface functional groups and defects.[203] Jung and co–workers through chemiresistive gas sensing measurements further confirmed high sensitivity of $Ti_3C_2T_x$ MXene to NH_3.[623] The authors reported on the high selectivity of the fabricated sensor to hydrogen bonding gases such as NH_3, ethanol or acetone with minimal interference from acidic gases (e.g., SO_2, NO_2, or CO_2). The same sensor could detect NH_3 in a wide range of concentrations from 50 ppb to 1000 ppb with the LOD of 0.13 ppb at room temperature. Noise power spectral density measurements and density functional calculations showed that the metallic conductivity of the core channels in the $Ti_3C_2T_x$ together with the strong adsorption energy of the surface functional groups/defects are responsible for the good sensing properties of the fabricated sensors. Recently, plane wave–based DFT calculations explored the selectivity and reactivity of M_2C MXenes (M = Ti, V, Nb, Mo) and their oxygen–functionalized counterparts (M_2CO_2) to 11 gaseous analytes including H_2, H_2O, H_2S, NH_3, CO, CO_2, SO_2, NO, NO_2, NH_3, and N_2.[333] The authors observed that the selectivity of MXenes to gases such as NO or NH_3 was improved upon oxygen surface functionalization.

An ever–expanding range of 2D conductive materials continue to be explored by ab initio calculations for their ability to selectively interact with gaseous analytes in sensing applications. Prominent examples include 2D borophene,[624] GaN,[625] and C_2N.[626] Experimental demonstration of C–rich nitrides as gas sensors were first reported in 2014 by Wang et al.[627] The *g*–C_3N_4 prepared by a two–step thermal treatment of glucose and urea exhibited porous structure and high abundance of pyridine N atoms with good binding affinity for NO_2. The fabricated *g*–C_3N_4 chemiresistive sensor was able to sense NO_2 at 140 ppb under ambient conditions (65% RH). The sensitivity of *g*–C_3N_4 to NO_2 was further enhanced (LOD of 60 ppb) by the surface functionalization with Au nanoparticles.[628] The improvement in sensing performance after doping with AuNP was attributed to the increased interface area for gas absorption, as well as the formation of Schottky–type junctions, whose potential barrier may be modulated by analyte–material interactions. The synthesis of *g*–C_3N_4 composites is another strategy to enhance sensing performance of gas sensing devices.[629] For example, Long and co–workers fabricated an impedance semiconductor gas sensor based on Pt–ZnO–*g*–C_3N_4 hybrid materials for detection of NO_2 with sub–ppm sensitivity (LOD of 0.072 ppm).[630] This good sensing behavior to NO_2 was attributed to the synergistic effect between the 2D materials, ZnO and Pt, which together improved the separation of electron–hole pairs in the material leading to enhanced charge carriers transport properties.

Raghu et al. through surface functionalization of *g*–C_3N_4 with Pd NPs was able to detect H_2 at 4% levels (99.8% sensitivity) with the response time of 88 seconds at 30 °C.[631] *h*–BN based materials has been also recently utilized in

electrically–transduced detection of gaseous analytes including CH_4, NH_3 and NO_2.[632] For example, Sajjad and Feng demonstrated that atomically thin nanosheets of *h*–BN synthesized using CO_2–pulsed laser deposition methods, were capable of reversible detection of CH_4 gas at operating temperature of 175 °C.[632] Wang and coworkers tested the gas–sensing properties of the ultra–thin *h*–BN nanosheets towards NH_3, and found that the fabricated gas sensors showed a fast response and excellent repeatability to ethanol at optimal operating temperature of 300 °C.[633]

Ayari et al. fabricated AlGaN/GaN gas sensors on the 2D nanolayer of *h*–BN. The existence of *h*-BN layer allowed the transfer of the devices to a flexible and heat insulating acrylic tape[634] which results in a modification of relevant device properties, leading to a doubling of the sensitivity to 100 ppm NO_2 gas at 30 °C and an average response time of 5 min—6 times faster than before transfer. Besides using a single 2D materials, different type of 2D materials can be stacked together and held by van der Waals forces, creating an artificial van der Waals hetero–structure despite lattice mismatches. The van der Waals hetero–structures have an abrupt transition between the two materials and a sharp gradient of carrier concentration across the interface. Furthermore, owing to their nanoscale thickness, the carrier concentration and band alignment inside the hetero–structure can be very effectively modulated by electrical means, which provides possibilities for a large array of novel devices and applications.[635-636]

Jiao and coworkers synthesized a fiber–like rGO–MoS_2 composite, where graphene provides a substrate for nucleation of MoS_2.[637] Compared to traditional film or sheet-type devices, the fiber form of devices is more advantageous for their lower weight, flexibility and compactness in practical applications.[638] In the composite, MoS_2 nanosheets can be anchored onto the surface of graphene through both physical adsorption and electron transfer by hydrothermal method. The gas sensing properties were evaluated in an intelligent gas sensing analysis system. The obtained composite fiber devices showed an excellent sensitivity and selectivity to NO_2 and NH_3 than the individual components under different light illumination. The LOD of rGO–MoS_2 (3:1) to NO_2 was 53 ppb, which was comparable with or lower than the high–performance NO_2 sensors based on the rGO–Cu_2O NWs conjugates (64 ppb).[507] Recently, Zhou et al. prepared a rGO/MoS_2 composite films for NO_2 sensing at low temperature with a LOD as low as 5.6 ppb.[639] The experimental results revealed a significant response improvement (~200% enhancement) for rGO/MoS_2 composite film as compared to pure rGO, together with a high selectivity over NH_3, H_2S, CO and HCHO.

The similarity in 2D structures as well as the complementary properties between *g*-C_3N_4 and graphene can result a synergetic effect in sensing performance when the two components are composited as a gas sensor material. A *g*–C_3N_4–Gr nanocomposite prepared by Zheng et al. was demonstrated to be a promising sensing material for detecting NO_2 gas at room temperature, which exhibited better recovery as well as two–times faster response compared to pure graphene sensor.[629]

Zhang and coworkers demonstrated a BP/$MoSe_2$ van der Waals hetero–junction chemical sensor with excellent sensing performance for NO_2 detection.[640] The hetero–junction was created by stacking multi–layered BP on top of the $MoSe_2$ flake (**Figure 29a–b**). The response of the hetero–junction for NO_2 was 4.4 and 46 times higher than those of the $MoSe_2$ and BP FETs at 200 ppb concentration, respectively. The device also exhibited ultra–low detection limit of 10 ppb for NO_2, which was 6 times and 20 times lower than the $MoSe_2$ and BP FET sensors built on the same chip, respectively (**Figure 29c–f**). The modulation of barrier height in $MoSe_2$, which is induced by the modulation of both the total built–in potential and the ratio between majority carrier concentrations of both materials, was believed to be responsible for the enhanced sensitivity. This new configuration provides a new platform for a variety of sensing applications.

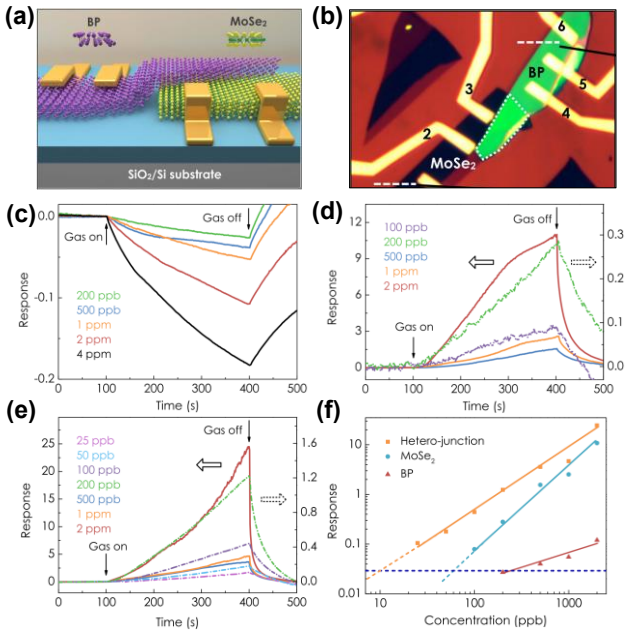

Figure 29. (a) Schematic illustration of the BP/$MoSe_2$ hetero–junction device. (b) Optical microscope image of the device. Real–time response of BP FET (c), $MoSe_2$ FET (d) and hetero–junction (e) sensors to different concentrations of NO_2. (f) Response of all three sensors as a function of gas concentration in logarithm scale.[640] Reproduced with permission from Ref. [640] Copyright 2016 IOP Publishing Ltd.

Despite the rapid progress, the sensing application of MXenes, *g*–C_3N_4 or *h*–BN nanostructures is only at the beginning and faces ample challenges. The fabrication of uniform 2D film with controlled structure and composition, at industrially relevant scale, remains a big challenge.[114] Novel synthetic approaches, that are ideally compatible with current sensor manufacturing technologies are needed to fully harness the potential of these 2D materials in gas sensing

applications.[117] The gas sensing performance of MXenes, *g*–C_3N_4 or *h*–BN–based materials was also demonstrated to be strongly dependent on their surface chemistry (e.g., presence of compositional and structural defects). Therefore, the role of defects on the sensing parameters of these 2D materials need to be further investigated, which will ideally lead to improvements in sensitivity and selectivity through careful ligand functionalization or defect engineering. In addition, the landscape for creating nanocomposite materials is rich in potential, with numerous possibilities to benefit from the unique chemical, electrical, and physical properties of each component, and yet to be explored for gas sensing applications. Most of the reported gas sensors based on MXenes, *g*–C_3N_4 or *h*–BN have been investigated in proof–of–concept studies, and only few sensors has been utilized for real sample detection. It is, therefore, critical to construct robust sensing interfaces with low nonspecific absorption to satisfy the requirements for sensitive and selective determination of analytes in practical applications.

Table 3. Summary of Sensing Performances for Volatile Compounds by 2D Materials.

Analyte	Material	Architecture	LOD	Experimental range	Sensing environment	Ref.
Cl_2	rGO	chemiresistor: Au/rGO/Au	N/A	6–75 ppm	Air, r.t.	502
Cl_2	rGO–PET	chemiresistor: rGO/rGO–PET/rGO	6 ppm	6–75 ppm	Air, r.t.	502
CO	Gr	chemiresistor: Au–Ti/Gr/Au–Ti	N/A	1 ppm	He	157
CO	rGO	chemiresistor: Au/rGO/Au	10 ppm	10–30 ppm	r.t.	540
CO	rGO–SnO_2–Au	N/A	2 ppm	2–5 ppm	400 °C	541
CO_2	Gr	chemiresistor: Au–Ti/Gr/Au–Ti	136 ppt	200 ppt	N_2, r.t.	490
CO_2	Gr	chemiresistor: Ag/Gr/Ag	3 ppm	3–50 ppm	Air, 320 to 470 K	641
CO_2	Gr	chemiresistor: Cr/Gr/Au	10 ppm	10–100 ppm	Air	642
H_2	BP–Pt NPs	Microelectrode/BP–Pt NPs	10 ppm	10–10000 ppm	N_2, r.t.	569
H_2	Gr–Pd NPs	chemiresistor: Ti/Gr/Pd NPs/Au	40 ppm	40–8000 ppm	N_2, r.t.	531
H_2	Gr–Pd NPs	chemiresistor: Ag/Gr/Pd NPs/Ag	20 ppm	20–1000 ppm	N_2, r.t.	643
H_2	Gr–Pd NPs	chemiresistor: Au/Gr/Pd NPs/Au	0.1 ppm	0.1–100 ppm	Air_D	532
H_2	Gr–Pd NTs	chemiresistor: Au/Gr–Pd NTs /Au	10 ppm	10–10000 ppm	Air, r.t.	644
H_2	Gr–p–H_2O_3P–calix[8]arene–Pt NPs	chemiresistor: IDE/Gr–p–H_2O_3P–calix[8]arene–Pt NPs/IDE	0.2 vol%	0.1 vol%–10 vol%	N_2, r.t.	645
H_2	Gr–PMMA–Pd NPs	chemiresistor: Ti–Au/Gr–PMMA–Pd NPS/Ti–Au	250 ppm	0.025 vol%–2 vol%	N_2, r.t.	533
H_2	Gr–Pt NPs–MWCNT	chemiresistor: Cu/Gr–Pt NPs–MWCNT/Cu	4 vol%	4 vol%	Air, r.t.	646
H_2	Gr–Pt–SiC	chemiresistor: Ti–Au/ Gr–Pt–SiC/Ti–Au	50 ppm	50 ppm–20 vol%	N_2, r.t.	647
H_2	Gr–Pt–SiC	chemiresistor: Ti–Au/Gr–Pt–SiC/Ti–Au	1 vol%	1 vol%	N_2, 27–175 °C	341
H_2	Gr–SnO_2 NPs	FET: Si/SiO_2/Gr–SnO_2 NPs/Cr/Au	1 ppm	1–100 ppm	50 °C	648
H_2	MoS_2–M (M=Ag, Pd, Pt, Sc, Y)	FET: Si/SiO_2/MoS_2–M/Ni–Au/Ni–Au	<3 ppm	N/A	Air, r.t.	581
H_2	rGO–PEDOT–PSS	chemiresistor: W/GO–PEDOT–PSS/W	100 ppm	30–180 ppm	100 °C	539
H_2S	Cu_3HHTP_2, Ni_3HHTP_2	chemiresistor: Gr/Cu_3HHTP_2(Ni_3HHTP_2)/Gr	40 ppm	2.5–80 ppm	N_2, r.t.	621
H_2S	CuO	chemiresistor: Al_2O_3/Au/CuO/Au	2 ppb	2 ppb–1.2 ppm	Dry air, 240 °C	607
H_2S	Gr–PSS–PANI	chemiresistor	1 ppm	1 to 50 ppm	Air_d, r.t.	559
H_2S	M_3HHTP_2–Gr (M = Fe, Co, Ni, or Cu)	chemiresistor: Ag/M_3HHTP_2–Gr/Ag	35 ppm	5–80 ppm	N_2, r.t.	176
H_2S	MoO_3	FET: Si/SiO_2/Pt/MoO_3/Pt	250 ppb	0.25–5 ppm	Air, 250 °C	611
H_2S	Ni_3HITP_2, Ni_3HHTP_2	chemiresistor: Au/Ni_3HITP_2(Ni_3HHTP_2) on cotton/Au	0.52 ppm	5 – 80 ppm	N_2 and 18% RH, r.t.	622
H_2S	rGO–Cu_2O	chemiresistor: Au/rGO–Cu_2O/Au	5 ppb	5–100 ppb	N_2, r.t.	554
H_2S	rGO–SnO_2 NW	chemiresistor: Au/ rGO–SnO_2 NW/Al_2O_3/Au	1 ppm	1–5 ppm	95% RH, 200 °C.	558
H_2S	WO_3	chemiresistor: Au/WO_3/Au	0.1 ppm	0.1–5 ppm	Air, 350 °C	610
H_2S	WO_3–MoO_3	chemiresistor: Ni–Cr/WO_3–MoO_3/ Ni–Cr	20 ppb	50 ppb–10 ppm	Air, 250 °C	612
N_2O	Gr	chemiresistor: Au–Ti/Gr/Au–Ti	103 ppt	200 ppt	N_2, r.t.	490
NH_3	BP	chemiresistor: Pt/BP/Pt	10 ppm	10–300 ppm	N_2, r.t.	136
NH_3	Cu_3HHTP_2	chemiresistor: Au/Cu_3HHTP_2/Au	0.5 ppm	1–100 ppm	Air_d, r.t.	173
NH_3	Cu_3HHTP_2 and Ni_3HHTP_2	chemiresistive: Gr/Cu_3HHTP_2(Ni_3HHTP_2)/Gr	10 ppm	2.5–80 ppm	N_2, r.t.	621
NH_3	Cu_3HIIP_2	chemiresistor: Au/Cu_3HITP_2/Au	0.5 ppm	0.5 to 10 ppm	N_2 and air 60% RH, r.t.	418
NH_3	Gr	chemiresistor: Au–Ti/Gr/Au–Ti	N/A	1 ppm	He	157

Analyte	Material	Architecture	LOD	Experimental range	Sensing environment	Ref.
NH_3	Gr	chemiresistor: Au–Ti/Gr/Au–Ti	33.2 ppt	200 ppt	N_2, r.t.	490
NH_3	Gr	chemiresistor: Au–Cr/Gr/Au–Cr	1000 ppm	1000 ppm	N_2, r.t.	493
NH_3	Gr	FET: Si/SiO_2/Gr/Ti–Au/Ti–Au	160 ppb	5 ppm–100 ppm	Air_D, r.t.	649
NH_3	Gr	FET: Si/SiO_2/Mica/Gr/Au–Ti/Au–Ti	N/A	10–500ppm	Air, r.t.	650
NH_3	Gr–MoS2	chemiresistor: Au–Ti/Gr–MoS_2/Au–Ti	N/A	5–100 ppm	N_2, 100 °C	651
NH_3	M_3HHTP_2–Gr (M = Fe, Co, Ni, or Cu)	chemiresistor: Ag/M_3HHTP_2–Gr/Ag	19 ppm	5–1200	N_2, r.t.	176
NH_3	MoS_2	FET: Si/SiO_2/Ni–Au/MoS_2/Ni–Au	0.3 ppm	0.3–30 ppm	N_2, r.t.	652
NH_3	MoS_2	FET: Si/SiO_2/MoS_2/Ti–Au/Ti–Au	1 ppm	1500 ppm	Air, r.t.	191
NH_3	MoS_2	FET: Si/SiO_2/MoS_2/Ti–Au/Ti–Au	N/A	100–1000 ppm	N_2, r.t.	101
NH_3	$MoSe_2$	chemiresistor: Ti–Au/$MoSe_2$/Au	50 ppm	50–1000 ppm	Ar, r.t.	580
NH_3	$MoTe_2$	FET: Si/Si–O_2/Ti–Au/$MoTe_2$/Ti–Au	1 ppm	2–100 ppm	N_2, r.t.	585
NH_3	rGO	chemiresistor: Au/rGO/Au	5 ppm	5 ppm	N_2, r.t. 21–149 °C	498
NH_3	rGO	chemiresistor: Cr–Au/rGO–PANi/Cr–Au	20 ppm	20–50 ppm	Air, 25 °C	653
NH_3	rGO	chemiresistor: Cr–Au/rGO/Cr–Au	1 ppb	1 ppb–50 ppm	Air, r.t.	654
NH_3	rGO–Cu_2O	chemiresistor: Au/rGO–Cu_2O/Au	100 ppm	100–500 ppm	Air, r.t.	655
NH_3	rGO–P3HT	FET: Si/SiO_2/rGO–P3HT/Ti–Au/Ti–Au	N/A	10–50 ppm	Air, r.t.	656
NH_3	rGO–Py	chemiresistor: Au/rGO–Py/Au	5 ppb	5 ppb–100 ppm	Air, r.t.	657
NH_3	SnS_2–SnO_2	chemiresistor: Au/ SnS_2–SnO_2/Au	10 ppm	10–500 ppm	Air_D, r.t.	658
NH_3	$Ti_3C_2T_x$	chemiresistor: Au/$Ti_3C_2T_x$/Au	0.13 ppb	100–1000 ppb	N_2, r.t.	623
NH_3	WS_2	chemiresistor: Au/WS_2/Au	1 ppm	1–10 ppm	Air, r.t.	470
NO	Cu_3HHTP_2 and Ni_3HHTP_3	chemiresistor: Gr/Cu_3HHTP_2(Ni_3HHTP_2)/Gr	40 ppm	2.5–80 ppm	N_2, r.t.	621
NO	Gr	chemiresistor: Au–Ti/Gr/Au–Ti	158 ppq	10 ppt	N_2, r.t.	490
NO	M_3HHTP_2–Gr (M = Fe, Co, Ni, or Cu)	chemiresistor: Ag/M_3HHTP_2–Gr/Ag	17 ppm	5–80 ppm	N_2, r.t.	176
NO	MoS_2	FET: Si/SiO_2/MoS_2/Ti–Au/Ti–Au	0.8 ppm	0.3 to 2 ppm	N_2, 25 °C	578
NO	Ni_3HITP_2 and Ni_3HHTP_2	chemiresistor: Au/Ni_3HITP_2(Ni_3HHTP_2) on fabrics/Au	0.16, 1.4 ppm	5–80 ppm	N_2 and 18% RH, r.t.	622
NO_2	BP	FET: Si/SiO_2/BP/Au/Au	20 ppb	20–1000 ppb	Air, r.t.	158
NO_2	BP	FET: Si/SiO_2/Ti–Au/BP/Ti–Au	5 ppb	5–40 ppb	Ar, r.t.	159
NO_2	BP	chemiresistor: Pt/BP/Pt	20 ppb	20–1000 ppb	N_2, r.t.	136
NO_2	BP–$MoSe_2$	PN Diode: Ti–Au/BP–$MoSe_2$/Ti–Au	10 ppb	25 ppb–2 ppm	r.t.	640
NO_2	BP–Pt NPs	FET: Au–Ti/BP–Pt NPs/ Au–Ti	1 ppm	1–50 ppm	N_2, r.t.	569
NO_2	g–C_3N_4	chemiresistor: Ti–Au/g–C_3N_4/Ti–Au	140 ppb	1–40 ppm	Air 25% RH, r.t.	627
NO_2	GO	chemiresistor: Au/GO/Au	1.3 ppb	0.2–200 ppm	r.t.	659
NO_2	Gr	chemiresistor: Au–Ti/Gr/Au–Ti	N/A	1 ppm	He	157
NO_2	Gr	chemiresistor: Au–Ti/Gr/Au–Ti	2.06 ppt	40 ppt	N_2, r.t.	490
NO_2	Gr	FET: Si/SiO_2/Gr/Ti–Au/Ti–Au	15 ppb	1 ppm–10 ppm	Air_D, r.t.	649
NO_2	Gr–MoS_2	chemiresistor: Au–Ti/Gr–MoS_2/Au–Ti	1.2 ppm	5–100 ppm	N_2, 100 °C	651
NO_2	Gr–NiO	chemiresistor: Ni–Au/Gr–NiO/Ni–Au	N/A	1–15 ppm	N/A	660
NO_2	Gr–PETP	chemiresistor: Au/Gr–PETP/Au	200 ppm	N/A	Air	661
NO_2	Gr–WO_3	chemiresistor	1 ppm	1–20 ppm	Air, r.t. and 200 °C–300 °C	662
NO_2	MoS_2	FET: Si/SiO_2/MoS_2/Ti–Au/Ti–Au	20 ppb	20–400 ppb	Air, r.t.	191
NO_2	MoS_2	FET: Si/SiO_2/MoS_2/Ti–Au/Ti–Au	100 ppm	100–1000 ppm	N_2, r.t.	101
NO_2	MoS_2–Pt NPs	FET: Si/SiO_2/MoS_2–Pt/rGO/rGO	2 ppb	0.5–5 ppm	N_2	663
NO_2	MoS_2–rGO	FET: Si/SiO_2/ MoS_2–rGO/Ti–Au/Ti–Au	5.7 ppb	0.12–8 ppm	Air, 60 °C	639
NO_2	MoS_2-SnO_2	chemiresistor: Si/SiO_2/MoS_2–SnO_2/Au/Au	0.5 ppm	05 to 10 ppm	Air, r.t.	664
NO_2	$MoSe_2$–Nb	chemiresistor: Cr–Au/MoSe–Nb/Cr–Au	3 ppm	3–50 ppm	150 °C	582
NO_2	$MoTe_2$	FET: Si/SiO_2/Ti–Au/$MoTe_2$/Ti–Au	12 ppb	100–1000 ppb	N_2, r.t.	585
NO_2	NiO	chemiresistor: Ni–Au/NiO/Ni–Au	1 ppm	1–20 ppm	Air, 250 °C	660
NO_2	NiO–WO_3	chemiresistor: Au/NiO–WO_3/Au	5 ppm	5–100 ppm	Air, r.t.	601
NO_2	rGO	chemiresistor: Cr–Au/rGO/Cr–Au	1 ppm	1–20 ppm	53 ± 3% RH, 23.0 ± 1.5 °C	665

Analyte	Material	Architecture	LOD	Experimental range	Sensing environment	Ref.
NO_2	rGO–Fe_2O_3	chemiresistor: Au/rGO–Fe_2O_3/Au	0.18 ppm	0.18–90 ppm	Air, r.t.	666
NO_2	rGO–In_2O_3	chemiresistor: Pt/rGO–In_2O_3/Pt	5 ppm	5–100 ppm	Air, r.t., 30% RH	490
NO_2	rGO–PET	chemiresistor: rGO/rGO–PET/rGO	0.5 ppm	0.5–10 ppm	Air, r.t.	502
NO_2	rGO–S–Ag	chemiresistor: Ag/rGO–S–Ag/Ag	0.5 ppm	0.5 to 50 ppm	Air, 30%RH, 25 °C	667
NO_2	rGO–ZnO	chemiresistor: Au/rGO–ZnO/Au	5 ppm	1–25 ppm	Air, 25% RH, r.t.	519
NO_2	SnS_2	chemiresistor: Pt/SnS_2/Pt	0.6 ppm	0.6 to 10 ppm	120 °C	391
NO_2	WS_2–Ag NW	chemiresistor: Cr–Au/WS_2–Ag NW/Cr–Au	1 ppm	25–500 ppm	Air, 100 °C	587
NO_2	ZnO	chemiresistor: Au/ZnO/Au	50 ppb	0.05–10 ppm	Air, 180 °C	593
O_2	Gr	chemiresistor: Au–Ti/Gr/Au–Ti	38.8 ppt	200 ppt	N_2, r.t.	490
O_2	Gr	chemiresistor	1.25 %	1.25–4.7 vol%	N_2, r.t.	565
O_2	Gr–*g*–C_3N_4	chemiresistor: Au/Gr–*g*–C_3N_4/Au	300 ppm	300–100000 ppm	N_2, r.t.	568
O_2	Gr–TiO_2	chemiresistor: Au/Gr–TiO_2/Au	134 ppm	134 ppm–100 vol%	N_2, r.t.	566
O_2	MoS_2	chemiresistor: Ti–Pt/MoS_2/Ti–Pt	1 vol%	1–100 vol%	N_2, 300 °C	579
SO_2	GO	chemiresistor: Au/GO/Au	5 ppm	5–1100ppm	Air, r.t.	552
SO_2	Gr	chemiresistor: Au–Ti/Gr/Au–Ti	67.4 ppt	200 ppt	N_2, r.t.	490
SO_2	Gr	FET: Si/SiO_2/GO/Au/Au	50 ppm	50 ppm	40–100 °C	553

Note: chemiresistor is described in a way of electrode/conductive material/electrode. FET is described in a way of gate electrode/insulator/channel material/source electrode/drain electrode. Diode is described in a way of electrode/semiconductor/electrode. N/A, not available. Air_D, dry air and r.t., room temperature.

4.2. Detection of Volatile Compounds

Volatile compounds include organic and inorganic compounds that are easily vaporized but exist as solids or liquids under standard temperature and pressure. Volatile inorganic compounds mainly include water, volatile acids, halogen streams and mercury streams. Among these, humidity sensing is especially important. Because humidity has a great influence on people's lives including physiological activities, climate, building constructions, storage facilities for medicines and foods, electronic devices, chemical refineries, corrosion and degradation of instruments.[668] Humidity sensor with high sensitivity, selectivity, repeatability, long–term stability under ambient conditions, corrosion resistance to pollutants, and low cost of manufacturing, are in great demand.

Detection and monitoring the concentration of volatile organic compounds (VOCs) is important in environmental protection, chemical process control, and personal safety.[669] VOCs are composed of a variety of chemicals, examples including gasoline, alcohols, formaldehyde, aromatic solvents such as benzene, toluene and xylene, styrene, and perchloroethylene. Long–term exposure to VOCs can cause damage to the liver, kidneys, and central nervous system.[670] Short–term exposure can cause eye and respiratory tract irritation, headaches, dizziness, visual disorders, fatigue, loss of coordination, allergic skin reactions, nausea, and memory impairment.[670] VOCs also constitute an important fraction of gaseous pollutants over urbanized areas, which originate from exhaust gases, evaporation of petroleum products and utilization of organic solvents. The World Health Organization (WHO) recognized VOCs as the most important pollutants of indoor air.[671] For these reasons, the concentrations of VOCs both indoors and outdoors are strictly regulated. Taking formaldehyde as an example, which is one of the VOCs widely used in household materials, the WHO has set a 30 min exposure limit of 0.08 ppm, and the US National Institute for Occupational Safety and Health (NIOSH) has established a maximum long–term exposure limit of 0.016 ppm (TWA).[672] This section highlights the sensing of volatile compounds using different type of sensory material.

4.2.1. Graphene and Graphene Oxides

Humidity. At relatively low concentration, the adsorption of water molecules can break the sublattice and symmetry of the graphene, and successively widen its band gap.[673] Functional group on graphene and graphene oxide, like defects, hydroxyl, and carbonyl groups, can interact with water, causing a conductance change.[674-675] These water molecules usually act as electron donor, leading to an increase in the resistance of p–type graphene material. Water molecules can also induce the ionization of the oxygen–containing groups (for example, –OH and –COOH) in GO bulk material to generate a concentration gradient of protons. This gradient facilitates the diffusion of protons through the material to deliver a voltage and current in the external circuit.[676] In addition, graphene oxide has super–permeability to water molecules, which can lead to sensing devices with fast response time.[677] Together with their flexibility and suitability for large–scale manufacturing, graphene–based materials have emerged as key elements for fabricating humidity sensors.

Borini et al. developed a chemiresistive humidity sensor by using GO as the active material.[678] Ultra–thin (15 to 25 nm) GO films were deposited by either drop–casting or spray coating on silver screen–printed interdigitated electrodes on a polyethylene naphthalate (PEN) substrate (**Figure 30a**). The effect of water molecules on the electrical properties of GO films was investigated by impedance measurements. The response and recovery times were less than 100 ms (**Figure 30b**). The sensing performance of the GO sensor were comparable to the commercial sensors (**Figure 30c**) and allowed to observe the change of moisture content in breath (**Figure 30d**).

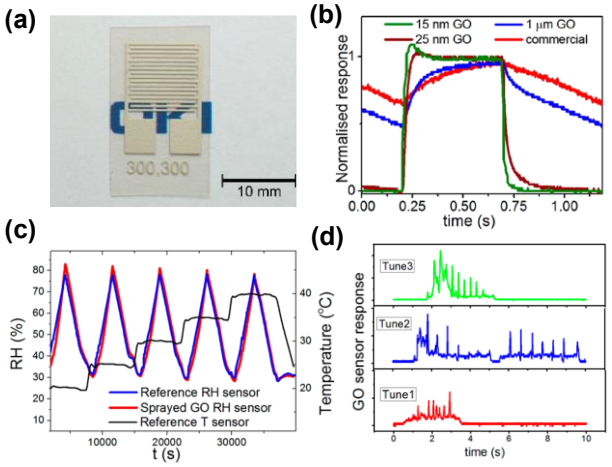

Figure 30. (a) Photograph of a sprayed GO sensing element. Due to the transparency of the ultrathin GO film, only the printed Ag electrodes on top of the PEN substrate are visible. (b) Normalized response of a 15 nm thick GO sensor to a modulated humid air flow at 10 Hz. (c) Sensing performance of a 15 nm thick GO sensor (red line) compared to the response of a commercial high precision RH sensor (blue line). (d) Responses of an ultrathin GO sensor to 3 different tunes whistled by three different users.[678] Reproduced from Ref.[678] Copyright 2013 American Chemical Society.

Sun and co–workers fabricated a microscale capacitive humidity sensor by using graphene oxide films as humidity sensitive material.[679] Compared with conventional capacitive humidity sensors with sensitivities ranging from 43% to 2900%,[680-684], this GO based sensor exhibited sensitivity of up to 37800%, which was more than 10 times higher than that of the best sensor among conventional sensing devices at 15%–95% relative humidity. This humidity sensor also showed a faster response time and recovery time (10.5 s and 41.0 s, respectively), which are less than 25% and 50% of those observed for conventional devices. To overcome mechanical stability issues of the fabricated sensors, including swelling of the material upon exposure to humidity, the graphene oxide layer was covalently anchored to the substrate, which improved the long–term stability of the device.[685] To fabricate flexible humidity sensor, Zhang et al. deposited rGO on polyimide substrate and poly(diallylimethyammonium chloride) (PDDA) nanocomposite (**Figure 31a**).[686] The sensor worked within 11–97% RH range at room temperature, and showed good repeatability when used for five exposure/recovery cycles at 43%, 75%, and 97% RH (**Figure 31b–c**). The authors also reported on a response time of 108–147 s and recovery time of 94–133 s during analytical measurements. Two–beam–laser interference was used for the simultaneous reduction, patterning and nanostructuring of graphene oxide on flexible polyethylene terephthalate substrates for the development of high performance humidity sensing devices.[687] Ma and Tsukruk demonstrated a flexible GO–silk–based chemiresistive sensor, which showed a fast response time of 3 s, high sensitivity to humidity in the 20–97% RH range, and good stability to thousands of folding–unfolding cycles and chemical solvents.[688] Knopf et al. printed graphene interdigitated capacitive (IDC) sensors on the flexible polyimide substrates. As the total capacitance of the IDC sensor is determined by multiplying each unit cell capacitance, interdigitated configuration can increase the effective capacitance of the structure and the effective active area of the sensor. The printed sensors were used to measure water content of ethanol solution, which demonstrated the fabrication methodology for creating chemical sensors on thin membranes by using conductive aqueous graphene ink.[689] Layer–by–layer inkjet printing technique was also used to print the polymer particles and graphene oxide to fabricate humidity sensors.[690] Deen et al. recently demonstrated a wireless humidity sensor based on the quantum capacitance effect in graphene.[691] The sensor consisted of a metal oxide/graphene variable capacitor (varactor) coupled to an inductor, to create a resonant oscillator circuit. The resonant frequency was found to shift in proportion to water vapor concentration for relative humidity (RH) values ranging from 1% to 97% with a linear frequency shift of 5.7 kHz/%RH ± 0.3 kHz/%RH.

Understanding the interactions of ambient molecules with graphene and adjacent dielectrics is of fundamental importance for a range of graphene–based sensors, particularly for sensors where such interactions could influence the analytical operation of the device.[692-694] Koester and co–workers using a metal–oxide/graphene varactor structure showed that graphene can be used to capacitively sense the intercalation of water between graphene and HfO_2, and that this process was reversible on a timescale of minutes.[695] Molecular dynamics simulations indicated that a likely mechanism for the intercalation involved adsorption and lateral diffusion of water molecules beneath the graphene. Shehzad et al. designed multimode environment sensors by fabricating a graphene based metal–semiconductor field–effect transistor.[696] This FET device was composed of graphene as the channel material in the horizontal direction, and the graphene contact with silicon in the vertical direction to form a graphene/silicon Schottky junction (**Figure 31d**).[696] The device was sensitive toward humidity under both forward and reverse biases and operated in resistive as well as capacitive modes (**Figure 31e–f**). Sensitivity of these devices reached to 17%, 45%, 26%, and 32% per relative humidity (%RH) for reverse biased, forward biased, resistive, and capacitive modes, respectively. Lemme and co–workers performed humidity sensing using a change in the electrical resistance of single–layer graphene, deposited on top of a SiO_2 layer on a Si wafer through chemical vapor deposition.[697] The measured response and recovery times of the graphene humidity sensors were on the order of several hundred milliseconds from 1% to 96% RH. Density functional theory simulations showed that the interactions between the electrostatic dipole moment of the water and the impurity bands in the SiO_2 substrate led to electrostatic doping of the graphene layer.

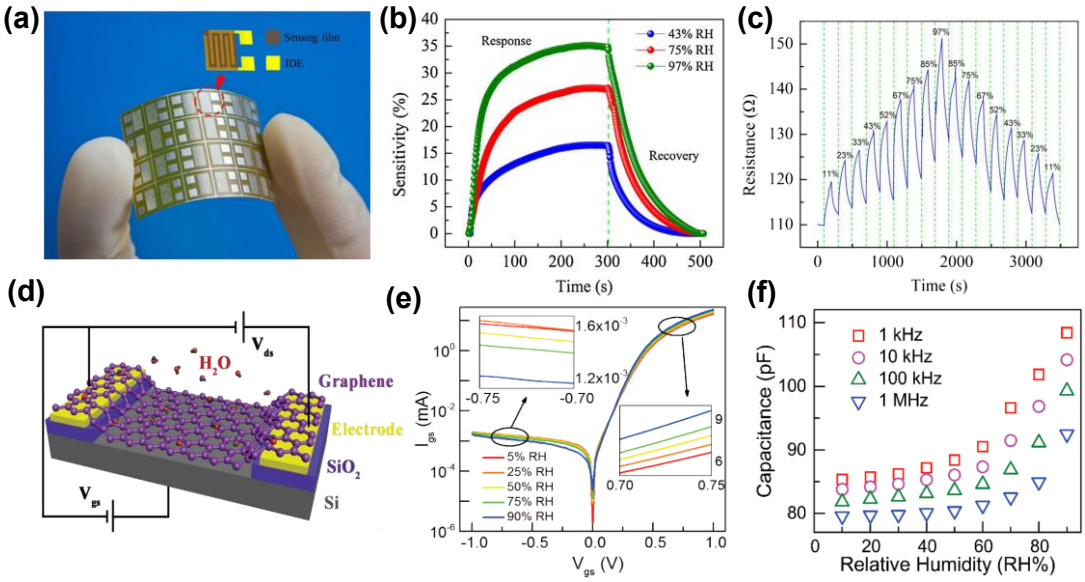

Figure 31. (a) Optical image of 4×6 sensors array on a flexible PI substrate. (b) response and recovery curves of the PDDA/RGO film sensor to a relative humidity pulse at 0% 43%, and 97% RH, respectively. (c) Resistance measurement of the PDDA/RGO film sensor under switching RH.[686] Reproduced with permission from Ref.[686] Copyright 2014 Elsevier B.V. (d) Schematic of the multimode humidity sensor with source–drain voltage V_{ds} and gate voltage V_{gs} control. (e) *I*–*V* curves under various humidity conditions. (f) Capacitance change under different humidity.[696] Reproduced with permission from Ref. [696] Copyright John Wiley and Sons.

Besides unmodified graphene–based sensor, humidity sensors based on functionalized graphene and graphene oxides are also routinely utilized, which usually exhibit improved performance over the non–functionalized graphene sensors. Aziza et al. showed that the sensing performance of graphene–based FET humidity sensor could be largely improved through polymer functionalization (**Figure 32a**).[364] After the chemically vapor deposited graphene was functionalized with amine rich polymer, the electron transfer from amine groups in the polymer to graphene was enhanced. The functionalized sensor showed 4% resistance change for a variation of RH from 10% to 40%, which is about 10 times higher than the non-functionalized graphene (**Figure 32b**). Kang and co–workers reported on a self–powered humidity sensor based on graphene oxide (GO) and poly(styrenesulfonate) (PSS)–intercalated composite films, which were used as humidity–responsive dielectrics (**Figure 32c**).[698] The fabricated sensors were equipped with the charge pumping system to produce a voltage output in a response to humidity. The GO–PSS sensor showed enhanced sensing responses compared to the GO sensor, providing ~5.6 times higher voltage output and three times faster responses in humidity sensing (**Figure 32d**).

Polypyrrole is a conducting polymer with good environmental stability, but itself has limited sensitivity for humidity.[275] Wu et al. showed that a graphene–polypyrrole composite containing only 10% graphene could sense humidity within a range between 12% and 90% with high sensitivity (S = 138) The response and recovery times were approximately 15 s and 20 s, respectively.[699] Gr-PPy composites showed better humidity sensing properties than either pure graphene or PPy because of the formation of the entrained coverage of PPy by graphene that could result different conduction mechanism under low or high humidity.[699] Su et al. developed flexible impedance–type humidity sensors using GO and AuNPs by self–assembly and the sol–gel technique. The AuNPs–GO–hydrolyzed 3–mercaptopropyltrimethoxysilane (MPTMOS) sol–gel film with 9.0 wt% added GO exhibited optimal flexibility, sensitivity, linearity, and long–term stability.[609] Su et al. also developed impedance–type humidity sensors from diamine–functionalized GO films coated on alumina or plastic substrates.[700]

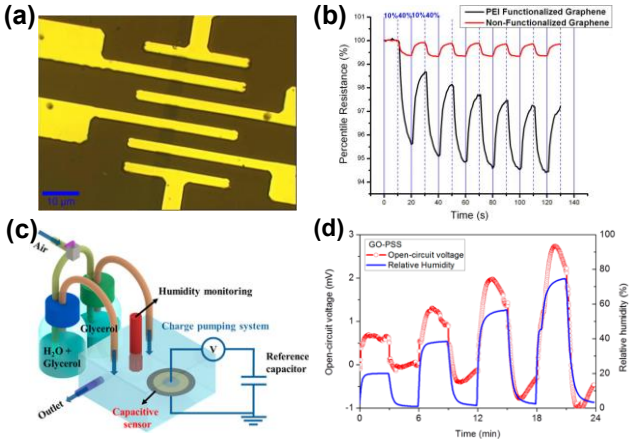

Figure 32. (a) Optical image of FET fabricated on silicon oxide/p⁺–doped silicon substrate; the channel width and length are both equal to 4 μm. (b) Humidity responses (RH: 10%–40%) at room temperature for non–functionalized

(red) and functionalized (black) graphene.[364] Reproduced with permission from Ref. [364] Copyright John Wiley and Sons. (c) Schematic diagram of the RH controlled–environment chamber and charge pumping system. (d) Performance evaluation of the self–powered humidity sensor. Voltage outputs of GO–PSS sensors were investigated over the RH range, 0–80%.[698] Reproduced from Ref. [698] Copyright 2014 American Chemical Society.

Hydrogen cyanide. Hydrogen cyanide (HCN) is widely used in various manufacturing processes including electroplating or precious metal extraction, however it is highly toxic to humans. Therefore, it is necessary to develop portable sensing devices capable of detecting trace amounts of HCN in the surrounding environment.[701] Robinson fabricated molecular sensors based on rGO thin film networks. These devices were capable of detecting 10 s exposure to HCN at the concentration of 70 ppb.[702] Graphene quantum dots (GQDs) are atomically thick, conductive nanosheets of sp^2 hybridized carbons, and can be considered as the nanometer-sized fragments of graphene with abundant edge groups (e.g., carboxyl and hydroxyl group).[703-704] Alizadeh et al. developed a chemiresistor HCN sensor by using GODs with average lateral size of 18nm.[705] The detection limit of the sensor was estimated at 0.6 ppm (S/N) with the response range of 1 to 100 ppm. The sensing was reversible with a response time of 1.5 min, which was faster than the response of many metal oxide and polymeric film–based sensors.[706-709]

Alcohols. Alcohols, including methanol and ethanol, are within the mostly used raw materials in chemical industry as solvents, and they are extensively used in fuels and medicine synthesis.[710] Monitoring the concentration of alcohols is also important for air quality inspection, diseases diagnosis and alcohol consumption detection.[711-712] Manohar and co–workers described a flexible and lightweight chemiresistor made of a thin film of overlapped and reduced graphene oxide.[502] Inkjet techniques were used to print the surfactant–supported dispersions of rGO powder onto flexible plastic surfaces. The sensor could not only reversibly and selectively detect chemically reactive vapors such as NO_2, Cl_2, but also showed good response to alcohols (CH_3OH, C_2H_5OH). Chen et al. investigated the fabrication of back–gated graphene FET arrays on microchannels.[713] The I_{DS} of the FET immediately changed by 17% upon the exposure to ethanol vapor, and the device showed full recovery immediately after the ethanol was pumped out. This work provided a convenient way of constructing back–gated graphene FETs for sensing applications.

Park and co–workers reported on the fabrication of an ethanol gas sensor with an oleylamine–modified graphene oxide (OA–GO)–poly(9–90–dioctyl–fluorene–co–bithiophene) (F8T2) composite as an active layer.[714] This sensor showed 6 time better sensitivity than that of a comparable device with the F8T2–only active layer due to the presence of polar functional groups of OA–GO that could undergo stronger interactions with gas analytes. Zhu et al. developed the strategy for anchoring α–Fe_2O_3–nanoparticles on graphene and used it as ethanol sensor material.[715] The α–Fe_2O_3–graphene composite exhibited better sensing performance in comparison with pure α–Fe_2O_3 counterpart, which was due to the enhancement in the specific surface area, with the addition of only 2% of graphene. Liu et al. reported on the technique to selectively sense H_2O and methanol, using a single graphene FET device by measuring real–time conductance as a function of gate voltage.[716] By analyzing the conductance versus gate voltage of the graphene–based device, the long–range scattering limited carrier mobility and the Dirac Point voltage could be derived, and then utilized for selective gas sensing in real time.

Formaldehyde. Formaldehyde (HCHO) is one of the most harmful gases among indoor air pollutants. It has been proven to be a human carcinogen and an allergen, and can cause dermatitis, respiratory irritation, asthma, and pulmonary edema.[672, 717] Alizadeh and Soltani used graphene/poly(methylmethacrylate) blends as a sensitive and selective materials for the detection of formaldehyde vapor.[718] The use of the polymer–graphene composite led to an enhanced physical durability of the sensor, and decreased the interfering effect of humidity on the sensor performance. The graphene/polymer ratio was found to be an important parameter in defining the dominant sensing mechanism and sensor performance. The response of the optimized sensor showed a good linear relationship within 0.05 to 5.0 ppm concentration range with the LODs of 10 ppb. Lee developed a new class of chemical sensors for formaldehyde determination at ppb levels.[719] This diode–based sensor consisted of a composite layer of reduced graphene oxide with epitaxially oriented zinc oxide nanorods together with a Schottky contact material of $Al_{0.27}GaN_{0.73}$(~25 nm)/GaN. The Schottky diode exhibited high sensitivity (0.875 ppm) with the LOD down to 120 ppb, and fast response time (~2 min) at room temperature.

Acetone. Acetone is known as a biomarker for diabetes, and exhaled breath of diabetes patients contains more than 1.8 ppm of acetone.[704] Selective real-time detection of acetoneat sub–ppm concentration thus can be a promising non–invasive diagnostic tool to identify at-risk populations.[720-722] Kim and co–workers reported on acetone sensor fabricated by sensitizing electrospun SnO_2 nanofibers with reduced graphene oxide (rGO) nanosheets [558] The LODs of this sensor were as low as 100 ppb for acetone with good selectivity over other gases (**Figure 33a–b**), e.g., ethanol, toluene, CO, and NH_3. However, a high operating temperature of 350 °C was needed. Further GO/Co_3O_4 sensors could achieve a detection limit of 120 ppb at 300 °C in a highly humid atmosphere (90% RH) similar with the humidity in human breath.[723] To decrease the working temperature, Liu et al. investigated the gas–sensing properties of graphene–$ZnFe_2O_4$ composite, graphene–mixed $ZnFe_2O_4$ for acetone vapor detection.[724] Experimental results revealed that the mixing of graphene with $ZnFe_2O_4$ could lower the operating temperature to 275°C. Staii and co–workers quantitatively analyzed the chemical gating effects in rGO–based chemical sensors.[725] The authors combined the electronic transport/Kelvin probe microscopy measurements, to directly image the surface potential and local charge distribution of rGO before and after chemical doping.

This approach enable quantification of the amount of charge transferred to rGO during the exposure to electron–acceptor (acetone) and electron–donor (ammonia) analytes.[725] This method can be potentially applied to explore other two–dimensional chemical sensors where the sensing mechanism is based on the charge transfer between the analyte and the sensory materials.

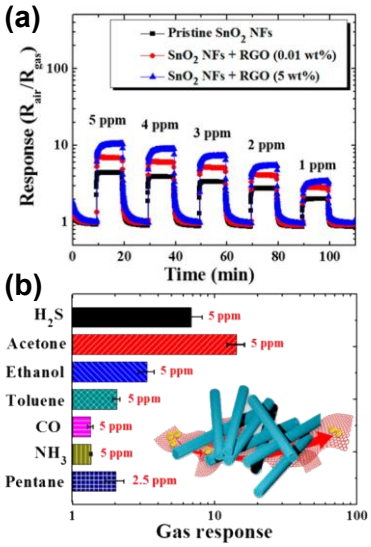

Figure 33. (a) Response of pristine SnO_2 NFs and rGO NS–SnO_2 NF composite sensors upon cyclic exposure to residual acetone concentrations between 1 and 5 ppm in humid air at an operation temperature of 350 °C. (b) rGO NS (5 wt %)–SnO_2 NF toward acetone at 350 °C with respect to the interfering gases of ethanol, toluene, carbon monoxide, ammonia, and pentane.[558] Reproduced from Ref. [558] Copyright 2014 American Chemical Society.

Aromatics. Graphene–based sensors have proven to be highly sensitive to gaseous analytes, however their limited ability to distinguish between different molecular species remains a major problem for practical applications. Detection of weakly interacting organic molecules is still challenging. To understand the influence of weak non–covalent molecular interactions on the electronic structure of graphene and the charge transfer mechanism, Cervenka et al. used a CVD method to grow a single layer of graphene in the bottom–gated FET device (**Figure 34a**).[230] The gate dependence of I_{SD} showed a clear change upon adsorption of the melamine molecules onto the graphene FET, with the Dirac point shifting to the higher gate voltage with deposition of melamine, corresponding to electron removal (p–type doping) (**Figure 34b**). Deposition of triazine on graphene–based FETs have resulted in a similar behavior as observed during the exposure to melamine. These results also showed that adsorbed molecules containing polar functional groups on graphene exhibited different coverage behavior to nonpolar molecules, indicating that molecular depolarization plays a significant role in charge transfer mechanisms even at submonolayer coverage (**Figure 34c**), particularly for molecules which possess strong dipoles.[230]

Myers et al. report on the detection of a series of aromatic VOCs, including benzene, toluene, ethylbenzene and xylenes, in water at low ppm concentration levels, by using functionalized graphene incorporated into a microelectrode chemiresistor platform.[726] The use of microelectrodes resulted in a small double layer capacitance that impeded the charge transfer through the solution and allowed the resistance of the graphene film to be measured preferentially. Because both the non–aromatic molecule (cyclohexane) and aromatic compounds (e.g., toluene) had very distinct charge transfer ability, they showed comparable analytical response. The occurrence of response was due to film swelling rather than doping through the direct interaction of the gaseous molecule with the graphene basal plane.[726]

Duesberg and co–workers developed graphene diode sensors composed of monolayer graphene laterally in contact with the n– and p–type silicon substrates, consequently allowing exposure to liquids and gases from above (**Figure 34d**).[226] The resulting sensor displayed good sensitivity towards aromatic electron donor and acceptor substances, such as anisole, benzene, chlorobenzene, and nitrobenzene. Pristine graphene in ambient conditions displayed a p–type behavior upon the exposure to aromatic molecules, due to the presence of adsorbed moisture or oxygen, resulting in an increase in the resistance of the material for the electron donor gases and the decrease for electron acceptors, independently of the substrate type (**Figure 34e**). This resistance change can be used to determine the concentration of electron donor or acceptor in neutral solvent (**Figure 34f**).[226] The resistance also increased linearly with increasing anisole concentration. The recorded data fitted into an equivalent circuit model showed that the adsorption of various analytes caused a variation of the Schottky barrier height, and consequently in the conductivity of graphene.[727]

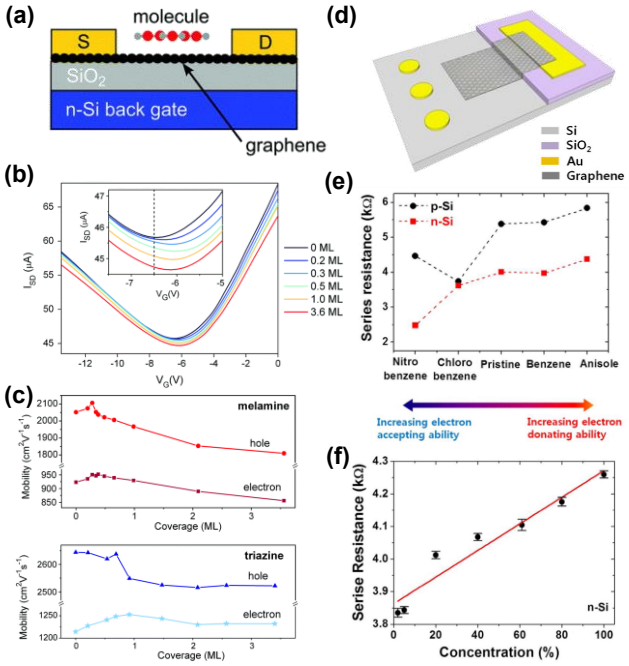

Figure 34. (a) Schematic illustration of the cross–section through a graphene FET with adsorbed molecules on the surface. (b) Gate voltage dependent source–drain current (I_{SD}) spectra of a graphene FET at a constant source voltage (V_{SD} = 50 mV) as a function of increasing melamine coverage. The inset shows a positive shift of the conductivity minimum (the Dirac point) upon adsorption of melamine, corresponding to p–type doping. (c) Graphene charge carrier mobility as a function of increasing melamine (top) and triazine (bottom) coverage.[230] Reproduced with permission from Ref. [230] Copyright 2015 The Royal Society of Chemistry. (d) Graphical presentation of a graphene diode sensor. (e) Variation of the series resistance for n–Si and p–Si GDS's upon exposure to liquid aromatic molecules. (f) Rs of the n–Si GDS as a function of the concentration of anisole in benzene.[226] Reproduced from Ref. [226] Copyright 2013 American Chemical Society.

DMMP. Dimethyl methylphosphonate (DMMP) is a simulant of the nerve agent sarin (2–(fluoro–methyl–phosphoryl)oxypropane), which is one of the most toxic warfare agents.[728] Alizadeh and Soltani designed a sensor array for the discrimination of DMMP vapor from triethylamine, tetrahydrofuran, acetonitrile and alcohols rGO,[729] obtained by the reduction of graphene oxide with hydrazine hydrate or sodium borohydride. This sensor was capable of interacting with DMMP vapor in the chemiresistor configuration. The reducing agents had a significant effect on the DMMP sensitivity, in which rGOs prepared by hydrazine hydrate and sodium borohydride showed best ability to efficiently discriminate between DMMP and its interferents. Wang et al. also used rGO, prepared through the reduction of GO from p–phenylenediamine (PPD) for DMMP sensing. PPD reduced rGO exhibited much better (5.7 times with the concentration of DMMP at 30 ppm) response to DMMP than that of rGO reduced with hydrazine.[730] Kyungmin et al. developed a wireless sensing system for DMMP detection by using the integrated arrays of field–effect transistors and sensors comprising of graphene channels, and silver nanowire electrodes interconnected with a wireless communication antenna.[731] These devices were highly flexible and could be readily transferred onto both planar and non–planar substrates, including paper, clothes, fingernails, and human skin. The printed wireless sensing antenna responded to the gases by detecting the change in sensor resistance.

Defects in graphene, like grain boundaries, ripples, wrinkles, and point defects, are important factors that dictate the sensing characteristics of the device. [493, 732] Sensing with a defect free graphene may thus provide better understanding of the mechanistic nature of interactions between the targeted gas analytes and the 2D materials as well as deepen the understanding on the role of defects on sensing characteristics. Salehi-Khojin and co–workers explored the mechanisms of gas detection (DMMP and 1,2–dichlorobenzene) in pristine graphene–based chemical FETs, and showed that only small change in the conductivity of the fabricated pristine graphene–based chemFETs is observed upon the exposure to gaseous analytes, indicating that graphene was not intrinsically sensitive to the adsorbed gas molecules.[692] The sensitivity of pristine graphene chemFETs was enhanced by the presence of external defects in the insulating substrate, which could modulate the electronic properties of graphene.[692]

Other VOCs. Nagareddy et al. studied chemiresistive sensing of graphene oxide synthesized by plasma processing for polar organic analyte vapors, including ethylene glycol, hydrogen peroxide, dimethyl acetamide, *N*–methyl–2–pyrrolidone, and acetic anhydride. The mechanism of chemical sensing in GO sensor is dictated by electron transfer between the analyte and graphene that changes the local charge carrier concentration and leads to the observed change in resistance of graphene. The nature of charge transfer and the magnitude of carrier injection further depend on the electronic nature of the active graphene surface and the chemical nature of the analyte being used. Compared with the non–functionalized graphene, this GO sensor showed a significant increase in response rate and an order of magnitude improvement in the recovery rate.[733] This example illustrated the role of oxygen functionalization on the sensor response, whose presence not only improved the selectivity of the sensor but also greatly reduced the response and recovery times.[702, 734] The analytical performance showed a strong dependence on the analyte properties, in which the sensor resistance increased upon the exposure to polar protic analytes and decreased in the presence of polar aprotic vapors. The molecular dipole moment of analytes, arising from the presence of attached functional groups and their asymmetrical molecular arrangement, determines the adsorption ability of analyte on the surface of materials.[735] The magnitude of the change in the sensor response was found to be linearly proportional to the dipole moment of an analyte.[735]

Li and co–workers fabricated chemical vapor sensors based on an unmodified graphene, and characterized their sensing properties through the exposure to headspace vapors containing a variety of solvents and related compounds (**Figure 35a**).[736] The resulting sensor exhibited excellent discrimination power towards a variety of chemical compounds including cylohexanone, diether ether, and dimethyl sulfoxide. Principle component analysis (PCA) was performed to explore the extent of grouping, and separation between compounds and chemical classes. The combination of PCA and prediction accuracies further confirmed the discrimination capability of an unmodified graphene chemical vapor sensor (**Figure 35b**). These sensors exhibited desirable characteristics for practical applications, such as room temperature operation, rapid response and recovery, reversibility, reproducibility, however, the magnitude of response for most of the gases was rather low due to lack of available binding sites in the unmodified graphene.

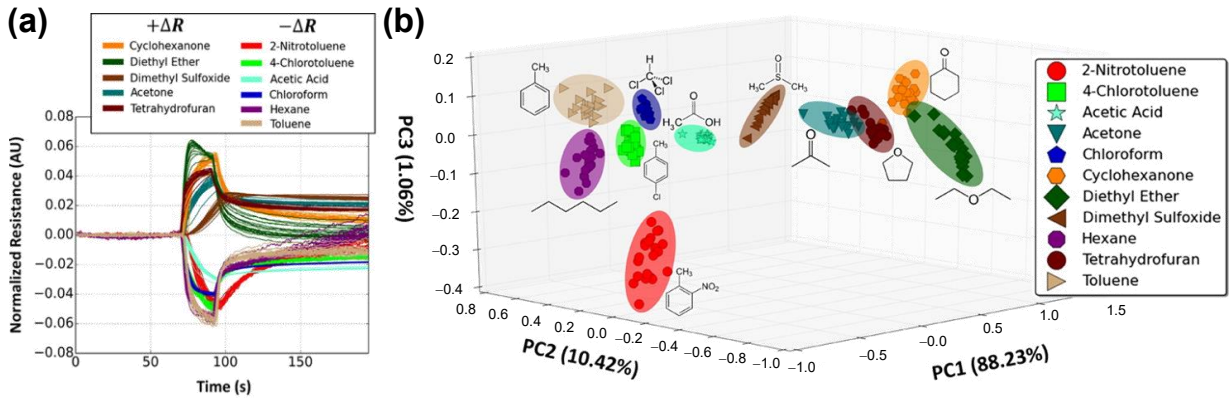

Figure 35. (a) Normalized sensor response to a chemically diverse set of compounds and (b) corresponding PCA transform.[736] Reproduced from Ref. [736] Copyright 2016 American Chemical Society.

Fattah et al. fabricated a graphene/silicon heterojunction Schottky diode sensor for detection of different chemical vapors, including chloroform, phenol, methanol, using EIS.[737] The adsorbed molecules change the local carrier concentration in graphene, which led to the changes in impedance response. Highly sensitive and selective impedance responses when graphene layer was in contact with different vapors were observed. The impedance responses to vapors formed by using phenol solutions of different concentrations were observed. The resulting device exhibited linear response for phenol within the range of 0.001 to 1 M with a high reproducibility (RSD 4.4%). Taromi and co–workers demonstrated a highly efficient chemiresistive sensor based on the nanocomposite fabricated from PEDOT–PSS and ultra–large graphene oxide.[738] This sensor was able to sense several VOCs, including methanol, ethanol, acetone, toluene, water, chlorobenzene, and propanol at room temperature. The incorporation of GO in PEDOT–PSS led to considerable enhancement of sensing performance for VOCs, due to the improvements in the direct charge transfer, increase of the specific surface area, and π–π interaction in the sensing film. The sensitivity, response and recovery times of the gas sensor with 0.04 wt% of GO were 11.3 %, 3.2 s, and 16 s, respectively, at methanol vapor concentrations as low as 35 ppm. Teradal et al. developed a capacitive vapor sensor based on phenyl group functionalized porous graphene oxide, with large open pores and high surface area, to enhance molecular interactions with the targeted vapor analyte.[739] The data indicated that porous GO was responsible for the extraordinary sensing properties of this capacitive detector including low detection thresholds, recyclability, short response and recovery times, and applicability for the detection of diverse target molecules, including humidity, ethanol, phenol, toluene, and cyclohexane.

Kulkarn et al. reported on a fundamentally different sensing mechanism, based on molecular dipole detection, enabled by a pioneering graphene nanoelectronic heterodyne sensor.[740] The device, different with other nanoelectronic–sensing technologies, used graphene FET as a high–frequency (>100 kHz) mixer with surface–adsorbed molecules as an oscillating gate. The oscillating molecular dipole (excited by AC–driving voltage) induced a conductance modulation on the graphene channel; this conductance fluctuation was frequency–mixed with the AC excitation, thus generating a heterodyne mixing current **(Figure 36a–b)**. Importantly, by using higher frequencies, the slow sensing response, which usually hinders conventional nanoelectronic sensors, could be overcome when the AC field switching outpaces the slow dynamics of interface states. This prototype graphene sensor could achieve simultaneous rapid (down to 0.1 s) and sensitive (down to 1 ppb) detection of a wide range of VOCs **(Figure 36c–d)**, demonstrating orders of magnitude improvement in both response time and sensitivity over state–of–the–art nanoelectronic sensors.[740]

Johnson and co–workers fabricated chemical vapor sensor based on graphene field effect transistors functionalized with single–stranded DNA.[741] Single–stranded DNA was chosen as the functionalization layer due to its affinity to a wide range of target molecules while π–π stacking interaction with graphene ensured minimal degradation of device performance. DNA–decorated graphene sensor arrays showed analyte–and DNA sequence–dependent responses down to ppb concentrations. DNA/GFET sensors were able to differentiate among chemically similar analytes, including a series of carboxylic acids, and structural isomers of carboxylic acids and pinene.[741]

Gautam and Jayatissa used CVD to grow graphene surface as a sensing channel for the detection of organic vapors (ethanol, acetic acid, and acetone) at concentrations lower than 200 ppm, at room temperature.[742] They showed that the response of the sensor could be further enhanced by functionalizing its surface with catalytic metals such as platinum (Pt), palladium (Pd), aluminum (Al), and Gold (Au). Waghuley et al. investigated chemiresistive sensing of liquid petroleum gas (LPG), at room temperature, by using few-layer graphene.[641]The chemiresistor exhibited good sensing response (0.92 for 100 pm), short response and recovery time (5 s and 18 s, respectively), LOD of 4 ppm and excellent stability for LPG at room temperature. Further study showed that the composite of comprising graphene and 20% wt CeO_2 quantum dots can improve the sensing response for 100 ppm LPG to 1.3.[743] The enhanced response

of graphene-CeO2 quantum dots may due to the catalytic oxidation reaction of the LPG happened at the surface of CeO_2.[744] Sevilla and co–workers prepared graphene–nylon–6 nanocomposite which could be used in chemiresistor architecture for gas sensing of trimethylamine vapor.[745-746] The detection limit is as low as 0.39 mg L^{-1} within a working concentration range of 23–230 mg L^{-1}.[729]

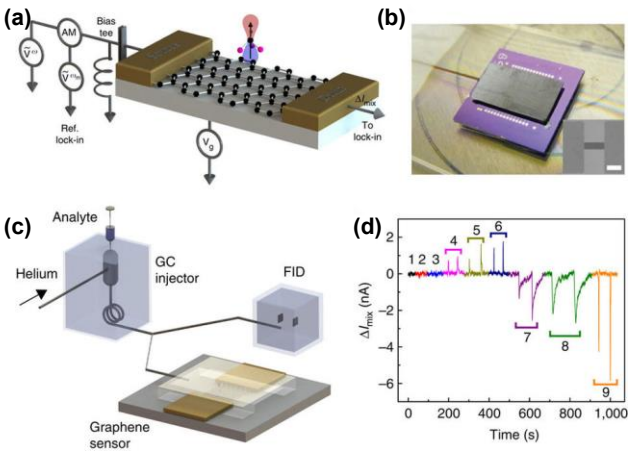

Figure 36. Rapid and high–sensitivity graphene nanoelectronic heterodyne sensor. (a) Schematic showing a graphene transistor configured as a high–frequency mixer for heterodyne vapor sensing; and an illustration of a chloroform molecule on top of a graphene channel**.** (b) Optical image of the graphene sensor capped with a silicon flow channel and a GC guard column inserted at one end. (c) Experimental setup showing a GC injector connected to the graphene sensor and a FID through a GC separation column and a Y–split. (d) Mixing current response of a graphene heterodyne sensor to injections of various masses of (1) pentane, (2) hexane, (3) benzene, (4) chlorobenzene, (5) dichloromethane, (6) chloroform, (7) DMF, (8) DMMP and (9) acetone.[740] Reproduced with permission from Ref. [740] Copyright 2014 Springer Nature.

Graphene–based vapor sensors have attracted much attention due to their variety of structures, unique sensing performances, room–temperature working conditions, and tremendous application prospects. There are still several challenges associated with Gr–based vapor sensors need to be addressed before their broader and more practical application. Firstly, to improve the selectivity, more functionalization methods need to be explored to provide graphene materials with specific analyte–binding property and long–term stability.[347, 475] Secondly, although drop casting, spin coating and inkjet printing have been employed to deposit sensing materials on electrodes, it is required to develop technologies to fabricate sensors massively in large scale on to produce reliable and low–cost devices.[125] Thirdly, standardized integration methods need to be explored to develop sensor with wearable and wireless features which would be especially needed in healthcare, robotics, artificial intelligence, military, remote explorations.[124]

4.2.2. Black Phosphorous

Humidity. Black phosphorous can absorb ambient moisture and form a layer of liquid as a result of its hydrophilicity.[571, 747] Due to the autoionization process of water molecules (formation of mobile H^+ ions), the absorbed moisture layer on the surface of BP can be ionically conductive. Additionally, previous studies have demonstrated that the BP can be oxidized to phosphorus oxides or phosphoric acid on exposure to water molecules and oxygen,[748] which will further ionically dissolve in the moist media, thus enhancing the concentration of H^+ ions on the surface. Both autoionization of water and ionic solvation of the phosphorus oxoacids, in the absorbed moist layer, provide substantial number of mobile ions for the electric transport through BP.[574] Although black phosphorus atomic layers undergo chemical degradation in humid air, in more robust configurations, such as films, composites and embedded structures, BP can be potentially used as sensory materials for humidity. Salehi–Khojin and co–workers found that the films of BP NFs exhibited excellent sensitivity and selectivity for humidity detection with quick recovery characteristics (**Figure 37a**).[749] The drain current of the BP FET sensor increased by ~4 orders of magnitude as the relative humidity (RH) was varied from 10% to 85%. The impedance spectroscopy and electrical characterizations suggested that the sensing mechanism of the BP film sensors was based on modulation in the leakage ionic current (**Figure 37b**).[749] Despite the ambient instability of atomically thin BP flakes, the BP films in this study revealed highly stable sensing characteristics after prolonged (months) exposure to humid environments (**Figure 37c–d**).[749]

Erande et al. synthesized few atomic layer thick nanosheets of black phosphorus using an electrochemical exfoliation method. The BP nanosheet thick film was integrated into a FET devices, and used for the detection of humidity levels.[750] The authors showed that the few layer (3-15 layer) thick film of BP nanosheets exhibited creditable sensitivity (S=521%) and fast recovery time of 26 s during exposure to humidity. Compared with bulk black phosphorus sample, whose resistance is on the order of a few hundred ohms, the resistance of nanosheets film under humid environments (11%-97% RH) is 13-81 kΩ attributed to the randomly stacked nanosheets. The large channel resistance is an advantage for the sensing of humidity, because the ionic conduction through the absorbed water layer can be measurable; while it is not the case in bulk black phosphorus crystal because of the high conductance and instability at high current.[749] They also investigated the sensing properties of the FET devices fabricated from liquid exfoliated black phosphorus nanosheets. These devices showed an improved response and recovery time (255 s and 10 s, respectively).[751]

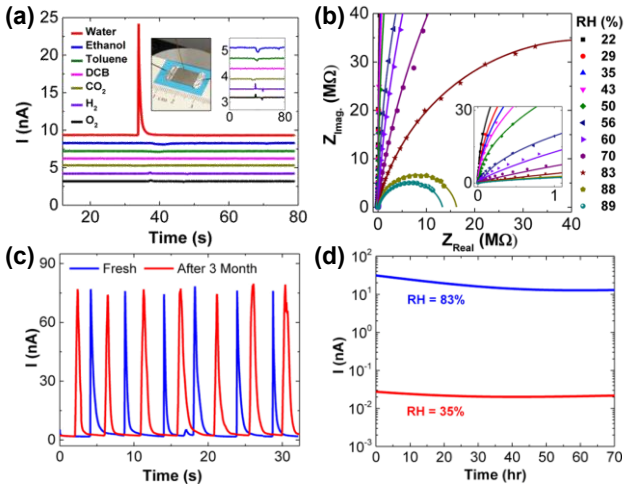

Figure 37 (a) Response of the stacked BP NFs to different analytes. The inset (right) magnifies the same curves. (b) The results obtained from a typical BP film sensor at different RH at 25 °C in a frequency range from ~300 Hz to 10 MHz. (c) Sensing response of the liquid exfoliated sensor upon exposure to multiple injections of water vapor immediately after preparation (blue) and after 3 months exposure to ambient conditions (red), without any noticeable change in its sensitivity. The responses are drawn with offset for clarity. (d) Drift of the sensor in prolonged exposure to 35% and 83% RH at 25 °C.[749] Reproduced from Ref. [749] Copyright 2015 American Chemical Society.

The lack of ambient stability makes incorporation of BP into practical devices very challenging as it demands for an inert operating environment. To produce air–stable BP sensors, Wang et al. explored the humidity sensing properties of BP field–effect transistors fully encapsulated by a 6 nm–thick Al_2O_3 encapsulation layer deposited by atomic layer deposition.[752] The encapsulated BP sensors exhibited superior ambient stability with no noticeable degradation in sensing response after being stored in air for more than a week. Compared with the bare BP devices, the encapsulated sensors offered enhanced long–term stability, however, with a trade–off in reduced (~50%) sensitivity.[752]

In order to analyze the deterioration of BP under ambient conditions, Walia et al. studied the individual effects of key environmental factors, such as temperature, light, and humidity on the performance of BP–based sensors.[753] Few–layer BP was employed as a recoverable humidity sensor with detection levels down to 10% RH within a broad dynamic range of 10%–90% RH at 30 °C. The detection range could be further extended with both more optimal device design and improved BP deposition techniques to achieve a sensitive layer with full coverage. It was shown that humidity itself does not lead to material degradation. Hence, by isolating BP from light, its lifetime can be prolonged even in the presence of O_2.

Methanol. The detection of methanol is of very high importance because of its human toxicity. In industrial settings, the inhalation of high concentrations of methanol vapor and the absorption of methanol through the skin are as effective as oral uptake in causing toxic effects.[754] Pumera and co–workers developed a methanol sensing device based on an interdigitated gold electrode modified with layered black phosphorous using electrochemical impedance spectroscopy as the transduction method.[755] The resulting device was highly sensitive and selective to methanol over toluene, acetone, chloroform, dichloromethane, ethanol, and more, which is due to the higher dielectric constant of methanol over than other small molecules tested The impedance phase depended linearly on the methanol concentration between 380 and 1900 ppm. The detection limit was 28 ppm, which is below the approved exposure limit of 200 ppm.

Although these studies have revealed the great potential of using BP as the vapor sensor to realize selective and sensitive detection, most of the applications are limited to the sensing of humidity and alcohols, probably because of the special reactivity of BP with this type of analyte. It would be worthwhile to explore the utilization of BP for sensing of other volatiles, as the adsorption abilities of BP for a wide range of gaseous molecules have been theoretically and experimentally identified. More work, regarding to the control of the directional alignment of nanosheets on the substrate, overcoming the environmental instability, as well as the control the chemical functionalization of the BP surface, needs to be addressed in the future.

4.2.3. Transition Metal Dichalchogenides

Humidity. Wu and co–workers used vanadium disulfide (VS_2) nanosheets with quasi–two–dimensional electronic structure as the moisture responsive material.[756] The electric conductivity of this oriented film was highly sensitive to environmental humidity, which showed a resistance change of almost two orders of magnitude in the range of 0% to 100% of RH (**Figure 38a–b**). Based on these results, flexible, and touchless positioning interface that could map the spatial distribution of moisture was developed (**Figure 38c–e**). This concept utilized VS_2 ultrathin nanosheets as the sole functional material, through which not only the 2D position of an applied humid pointer, like finger tips, could be localized, but also the relative height information could be detected as the third dimensionality (**Figure 38f–g**). The moisture sensing based positioning interface provided new avenues for real–time humidity mapping matrix or non–contact control interfaces for advanced man machine interactive systems.

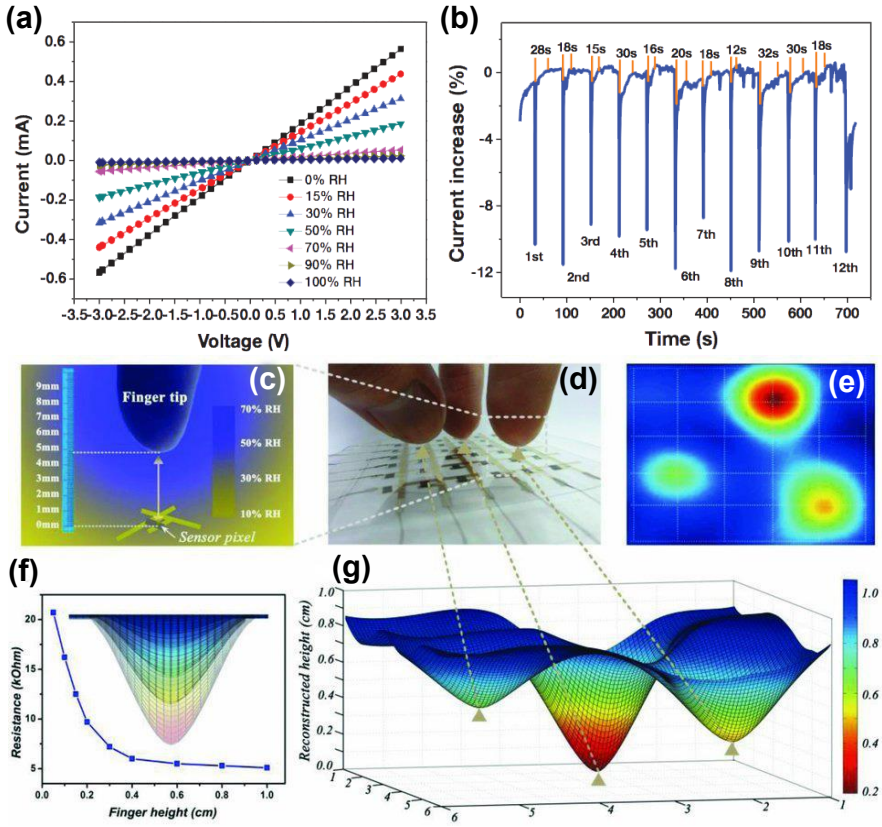

Figure 38. (a) *I–V* behaviors measured under different RH values, showing an obvious slope decreasing with the increasing of RH. (b) The cycling behavior and recovery time under fast pulse moisture stimuli by rapidly turning on/off the fast–flowing humid gas (10% RH), revealing the high–speed responsiveness of the as–fabricated moisture detector**.** (c) The schematics of RH distribution on the near surface of a fingertip. (d) The digital photograph of the relative positions of three fingertips above the 6×6 matrix. (e) Top–viewed 2D signal intensity distribution measured from the sensor matrix by an electronic analyzer. (f) Height–resolved resistance diagram on the near surface of a fingertip measured by the as–established humidity sensor. Inset is the colored illustration of the surface humidity gradient of the finger. (g) Side–viewed 3D mapping of the relative positions of the applied three fingertips, showing successful 3D positioning function.[756] Reproduced with permission from Ref. [756] Copyright 2012 John Wiley and Sons.

Yang and co–workers reported on the fabrication of humidity sensor by using few–layer molybdenum disulfide (MoS_2), synthesized by ultrasound–assisted liquid method.[757] The thin film sensors were exposed to moisture gases with relative humidity ranging from 0 to 60%. The sensors showed excellent sensitivity with very quick response (~9 s) and recovery (~17 s) speed to humidity gas, which was partially attributed to the intrinsic hydrophobic property of MoS_2 that accelerated the desorption process of water molecules from the surface.[758] The sensors showed a size–dependent performance, where the nanosheets with smaller size exhibited a better response towards humidity due to the increased surface area and larger abundance of exposed edge sites. Late and co–workers reported on a one–step synthesis method of a wafer–scale, highly crystalline tungsten disulfide (WS_2) nanoparticle thin film by using a modified hot wire chemical vapor deposition (HW–CVD) technique.[759] The WS_2 nanoparticle thin film based device showed good response to humidity with excellent long–term stability.[759] It was found that the resistance of the films decreased with the increasing RH. The maximum sensitivity of 469% along with the response time of ~12 s and recovery time of ~13 s was observed for this WS_2 thin film humidity sensor device.

Guo et al. fabricated a large–area WS_2 film through sulfurization of a tungsten film and assessed its humidity sensing performance in both the natural flat and high mechanically flexible states (bending curvature down to 5 mm).[760] The conductivity of as–synthesized WS_2 increased over a wide relative humidity range (0% to 90%) with fast response and recovery times (5–6 s). A transparent, flexible, and stretchable resistive type humidity sensor was subsequently fabricated by using graphene as electrodes and thin polydimethylsiloxane (PDMS) as a substrate (**Figure 39a**). The resulting device, even when laminated onto the skin, retained stable water moisture sensing behavior in the undeformed relaxed state as well as under compressive and tensile loadings (**Figure 39b–c**). Its high sensing performance enabled real–time monitoring of human breath.

Hg vapor. Mercury is extremely toxic to aquatic life and humans due to its persistent and bio-accumulative properties. Elemental Hg, as one of the main forms of Hg, has a long lifetime, high migration ability and it is indistinguishable because of its low melting point, high equilibrium vapor pressure, raising more concerns.[761] The permissible exposure limit of mercury vapor for an 8-hour time-weighted average in workplace set by Occupational Safety and Health Administration of USA is 0.1 mg/m^3.[762] Wang et al. demonstrated a new room temperature elemental mercury sensor based on MoS_2–polyanline nanocomposite.[763] The sensor exhibited fast response and recovery time, good selectivity, and long–term stability to a wide range of Hg vapor concentrations, spanning from 0.55 to 452.51 mg m^{-3}.

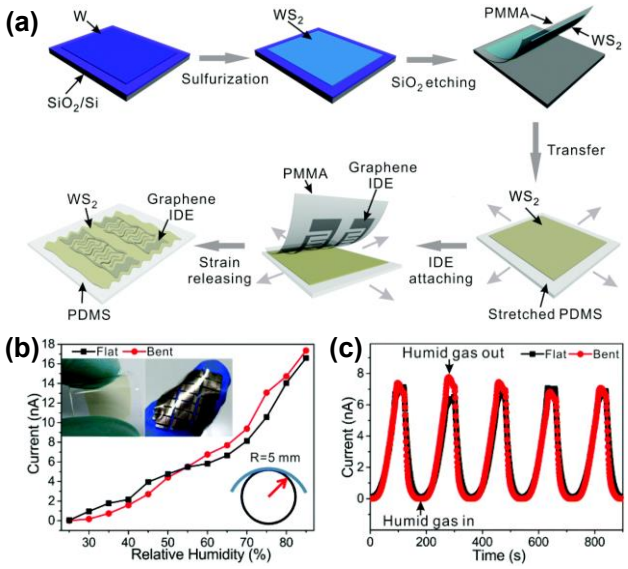

Figure 39. (a) Schematic of the device fabrication process. (b) Current response of the flexible sensor working in flat and bent states, respectively. (c) Dynamic response of the flexible humidity sensor in flat and bent states with the RH level periodically increasing and decreasing.[760] Reproduced with permission from Ref. [760] Copyright 2017 The Royal Society of Chemistry.

Trimethylamine. Perkins and co–workers fabricated resistor device by depositing single monolayer MoS_2 on SiO_2/Si wafer for the sensing of chemical vapors (**Figure 40a**).[166] As shown in **Figure 40b**, electrical contacts were deposited on the MoS_2 flake by using electron beam lithography followed by electron beam evaporation of Au and Ti/Au. The device provided sensitive transduction of transient surface physisorption events to the conductance of the monolayer MoS_2, and exhibited highly selective reactivity to a range of analytes. Its conductance increased rapidly upon the exposure to trimethylamine (**Figure 40c**) and was unaffected by the exposure to many other analytes or gases, including dichlorobenzene, dichloropentane, nitromethane, nitrotoluene, and water vapor. The sensor showed selective response to electron donors, and limited response to electron acceptors (**Figure 40d**), which was consistent with the weak n–type character of MoS_2. The monolayer MoS_2–based sensing device also exhibited a much higher selectivity to trimethylamine than carbon nanotubes–based sensors, which showed crossed sensitivity with acetonitrile, methanol, and nitrobenzene vapors.

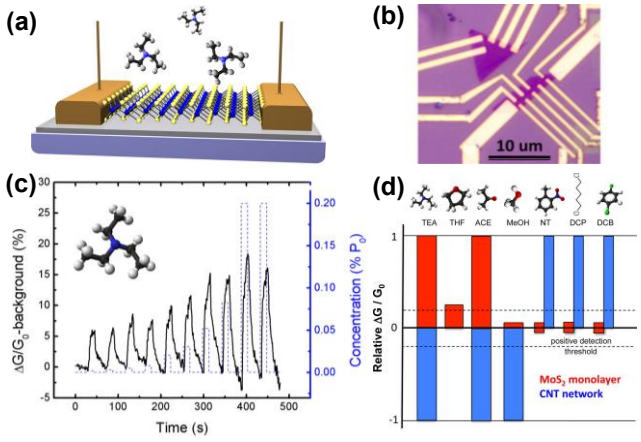

Figure 40. (a) Schematic and image of the MoS_2 monolayer sensor. A single monolayer of MoS2 is supported on an SiO_2/Si substrate and contacted with Au contact pads. (b) An optical image of the processed devices showing the monolayer MoS_2 flakes electrically contacted by multiple Au leads. (c) Change in conductivity of the monolayer MoS_2 sensor channel upon exposure to TEA. (d) Histogram of MoS_2 and CNT–network sensor responses to various analytes.[166] Reproduced from Ref. [166] Copyright 2013 American Chemical Society.

Friedman et al. fabricated MoS_2 FET sensors on SiO_2 substrate and measured their responses to a variety of gaseous analytes.[764] They found that the resulting sensing device produced the largest response to trimethylamine, while the exposure to electron acceptors produced no change in the analytical signal.[764] Mo $3d_{yz}$ orbitals and S 2p orbitals were identified as sites that were potentially free to interact with the environment on the surface of MoS_2.[765] After MoS_2 layer was deposited onto thermally grown SiO_2 substrate, the charge on Mo $3d_{yz}$ orbital was compensated by the negative charge on SiO_2. This left the positively charged S 2p orbital as the only active sites available for gas/surface interactions.[766] Thus, the MoS_2 sheet tends to interact strongly with donor–like analytes. The MoS_2 sensors provided comparable sensitivity and much higher selectivity than other low–dimensional sensors such as carbon nanotube and graphene chemical sensors.

Ethanol. Wang and co–workers prepared composite electrodes consisting of SnO_2 nanoparticles dispersed on the surface of MoS_2 nanosheets by low temperature hydrothermal method.[767] The combination of large surface area of MoS_2 nanosheets and the superior gas–sensing performance provided by ultra–small SnO_2 nanoparticles, resulted in high response and good selectivity to ethanol gas by the SnO_2–MoS_2 composite sensor.[767] Li and co–workers studied the sensing performance of FET sensors fabricated from the multilayer WS_2 nanoflakes to physically–adsorbed ethanol.[768] The study showed that the charge transfer

occurred between the multilayer WS_2 and adsorbed gas molecules, which influenced the photoelectrical properties of the devices. Ethanol molecules acted as "n–dopants" thus significantly enhancing the photo–responsivity, and external quantum efficiency, demonstrating that the multilayer WS_2 has great potential for applications in gas sensors.

Dwivedi et al. reported on a highly selective ethanol sensor based on MoS_2–functionalized porous silicon (PSi).[769] Interdigitated electrodes (IDEs) were used to record resistive measurements from MoS_2/PSi sensors in the presence of VOCs, and moisture at room temperature. Due to formation of *p-n* junction between MoS_2 and PSi , a substantial enhancement in sensitivity and selectivity for ethanol vapor was observed, with the LOD of 1 ppm.[769] Compared with the single–layer MoS_2 on crystalline silicon, the ethanol sensitivity was found to increase by a factor of 5 when MoS_2/Psi was used as a sensing material. As the devices composed of a MoS_2 thin film or PSi alone were not very sensitive to ethanol, the formation of the p–n heterojunction by PSi and MoS_2 may explain the higher sensitivity of MoS_2/PSi. The modulation of the resistance from interfaces played a more dominant role than that of the bulk MoS_2.

Acetone. Ko et al. demonstrated that large–area WS_2 nanosheets (1, 2 and 4 layers, **Figure 41a**) exhibited a significant response to acetone.[587] The schematic images in **Figure 41c** summarize the gas–sensing mechanism. When the pristine WS_2 gas sensor was exposed to acetone gas, volatile molecules (CO_2, H_2O) were formed via reaction between acetone and oxygen species adsorbed on the WS_2 surface. The oxygen species, such as O^{2-} and O^-, were adsorbed during the air–purging step with dry air. Then, the captured electrons were released to the WS_2, resulting in the electron–hole compensation or recombination, and eventually diminishment in the hole concentration, which predominantly affected the current flow on the WS_2 surface. This reduced hole concentration caused a decrease in the current, as shown in **Figure 41b**.

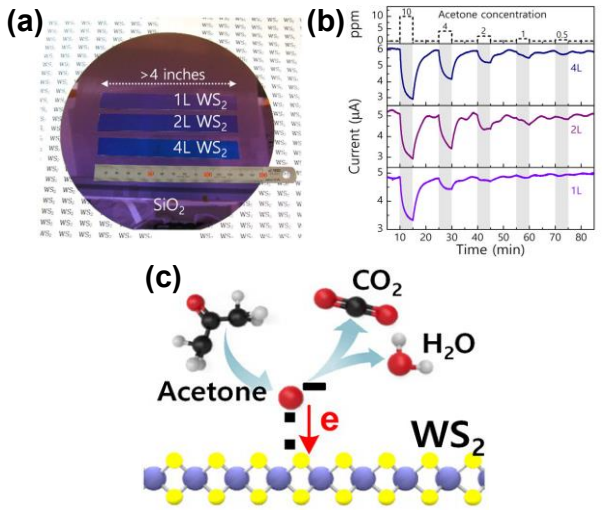

Figure 41. (a) Photograph of the synthesized large–area 1L, 2L, and 4L WS_2 nanosheets on an 8 in. SiO_2 wafer. The WS_2 nanosheets are uniform over a 4 inches length. (b) Gas–sensing results for the pristine WS_2 gas sensors consisting of 1L, 2L, and 4L WS_2 nanosheets upon acetone exposure (0.5, 1, 2, 4, and 10 ppm). (c) Schematic illustration of the gas–sensing mechanism. Upon acetone gas exposure, the adsorbed oxygen species interact with the acetone molecules, and volatile species such as CO_2 and H_2O are generated. The electrons are returned to WS_2.[587] Reproduced from Ref. [587] Copyright 2016 American Chemical Society.

Other VOCs. Balandin and co–workers demonstrated the selective gas sensing using MoS_2 bilayer FET devices. The FETs were fabricated through the exfoliation from bulk MoS_2 crystals, and its deposition onto Si/SiO_2 substrates.[770] During the exposure to ethanol, acetonitrile, toluene, chloroform, and methanol vapors, the FET showed higher and quicker response to methanol and ethanol than to other probed analytes. The magnitude of the change for the source–drain current was strongly dependent on the polarity of the analyte.[771]

Jung and co–workers reported on a high–performance chemiresistor with a tunable sensor response and high sensitivity for representative VOC groups by using thiolated ligand mercaptoundecanoic acid (MUA) functionalized molybdenum disulfide (MoS_2).[772] Primitive and MUA–conjugated MoS_2 sensing channels exhibited distinctly different responses toward VOCs. These MoS_2 sensors showed high sensitivity to representative VOCs, down to the concentrations of 1 ppm. This approach to fabricate a tunable and sensitive VOC sensor may become a valuable tool in real–world application for lung cancer diagnosis. Incorporation of noble metals, such as Au, Pt, or Pd, can be another effective way of doping 2D materials, as these elements have a high resistance to environmental corrosion and oxidation, which can further improve the stability of the doped semiconducting 2D materials under ambient conditions.[581, 773] Additionally, highly catalytic properties of these metals can be further exploited to realize chemical and electrical sensitization of the semiconducting materials.[773-775] TMDCs are known to non–specifically adsorb diverse range of VOCs such as hydrocarbons, ketones, and alcohols, showing only a single response behavior upon adsorption of the target gases.[772] Jung and co–workers found that the gas–sensing performance could be significantly enhanced and tuned (from "turn on" to "turn off" type response, or inversely) by the functionalization of MoS_2 with Au nanoparticle.[774] Au nanoparticles caused a n–doping effect and facilitated electron transfer from Au to MoS_2. Controlling the n–doping effect enabled the tuning of the response of hydrocarbon–based volatile organic compounds (VOCs) and oxygen–functionalized compounds by MoS_2. This controllable tuning of the VOC–sensing performance by MoS_2 can be used in early detection technologies, using multichannel sensing systems, that have different responses and recognition patterns for target analytes. Umar et al. demonstrated the use of SnS_2 nanoflakes as efficient electron mediators for the fabrication of nitroaniline chemiresistive sensor.[776] High–sensitivity of ~505.8 ± 0.02 mA cm^{-2} mol L^{-1} and experimental detection limit of ~15×10^{-6} mol L^{-1} in a response time of ~10.0

s with LDR in the range of 15.6×10^{-6}–0.5×10^{-3} mol L^{-1} were observed.

TMDCs are very promising candidates for the fabrication of high-performance vapor sensors operated in diverse environments, considering the wide diversity of the TMDCs family and their versatile and tunable properties. There have been extensive applications of TMDCs, especially in gas and vapor sensing. However, there is still significant room for improving the performance of sensing devices with respect to their selectivity, recovery characteristic and large–scale fabrication. It would be beneficial to understand the details of the specific properties of nanostructured TMDCs and the change of the electronic properties upon the interaction with analytes, as the sensing mechanisms of devices based on TMDCs have not been yet completely explained. Theoretical calculations can be used to identify the appropriate modification of these materials, which would shed insights into material design and enable screening across TMDC materials for the fabrication of gas/vapor sensors with optimized performance. The density of active sites in TMDCs can also be improved for selective and effective analyte binding, which can be hopefully realized through the morphology control and post–synthetic modification. The vast number of possibilities in terms of designing and fabricating different members of TMDCs and integrating them in functional device to achieve tailored properties for specific applications, will still require substantial experimental and theoretical efforts.

4.2.4. Metal Oxides

As demonstrated in previous sections, oxygen molecules can be chemically adsorbed on the surface of metal oxides in air to form O^{2-}, O^{-}, and O^{2-}, which withdraw electronic density from the metal oxide surface. When the sensor is exposed to a reducing gas, e.g., ethanol, a reaction occurs between adsorbed oxygen species and the reducing molecules, resulting in a change in the conductance of the sensor.[151-152]

Alcohols. Jing and Zhan fabricated a chemresistor–based gas sensor by using porous ZnO nanoplates synthesized through a simple microwave process after annealing the plate–like precursor hydrozincite at 400 °C.[777] The sensor exhibited strong response to ethanol at relatively high operating temperatures from 250 to 450 °C. The response and recovery times were 32 and 17 s for 100 ppm ethanol, respectively. The results suggested that porous ZnO nanoplates possessed multifunctional properties, and thus showed promise in in ethanol detection applications.

Zhang et al. investigated ethanol sensing using Au–functionalized ZnO nanoplates.[778] They demonstrated that the Au/ZnO nanoplate sensors had faster response and recovery as well as enhanced response compared to the pristine ZnO sensor. At 300 °C, the response time of Au/ZnO to 5 ppm ethanol was 13 s, while the response time of ZnO was 135 s. The improved sensor performance was attributed to the unique chemical properties of Au nanoparticles and the electronic metal–support interactions. Zhu and co–workers also built a gas sensors based on the ZnO nanosheets, which exhibited high sensitivity, fast response and recovery time (7 s and 19 s at 200 ppm), good selectivity over a series of alkanes, haloalkane and benzene, and appreciable long–term stability (up to 2 months) to 0.01–1000 ppm ethanol at 400 °C (**Figure 42a**, **42e**).[779] Extremely low concentrations of ethanol (down to 10 ppb) could be readily detected using the same sensor configuration ($S = 3.05 \pm 0.21$). The excellent ethanol–sensing performance of ZnO was mainly attributed to its hierarchical structure with a large specific surface area, abundant mesopores, high crystallinity, the plane–contact between sheets, three–dimensional network architecture, and characteristically small thickness. These hierarchical structures made of sheets, at nanometer thicknesses, allowed quick gas diffusion, which could consequently give faster sensing response. Besides higher response, chemresistive sensor made from the flower–like hierarchical structures of ZnO nanosheet al.so showed shorter response and recovery times than those made with ZnO powder.[780]

Chen and co–workers synthesized multi–layer SnO_2 nanoplates by annealing single–layer SnO nanoplates under O_2 at 700 °C. The resulting thicknesses of the multi–layer SnO_2 were ranging from 35 nm to 80 nm for 3 to 4 layers. They used the multi–layer SnO_2 nanoplates to fabricate a chemiresistive device capable of detecting 50 ppm of ethanol at 350 °C. The observed sensitivity was more than double that of a single–layer SnO_2 nanoplates.[781] The higher sensitivity of the multi–layer nanoplates was attributed to their larger surface/volume ratio. Sun used SnO_2 nanosheets synthesized by hydrothermal process, with a thickness of 10 nm, for ethanol sensing (**Figure 42b**).[782] At the operating temperature of 250 °C, the sensor showed higher response to ethanol than to other seven tested VOCs at a concentration of 100 ppm (**Figure 42f**), and exhibited good linear concentration dependence in the range of 20 to 90 ppm. Zhang and coworkers fabricated an ethanol sensor, using SnO_2 nanosheets synthesized via a hydrothermal method, capable of operating at low temperature of 165 °C within a wide concentration range of 1–1000 ppm.[783] Porous SnO_2 hierarchical nanosheets, after annealing, were also used, which exhibited better ethanol sensing properties compared with the sensor based on conventionally prepared SnO_2 nanoparticles (**Figure 42c, 42g**).[784] Zhang's group also confirmed the high sensitivity of SnO_2 nanosheets to 100 ppm ethanol (S=39.6 at 300 °C), which was approximately 3.6 and 6.1 times higher than that of the nanospheres–like and the nanoparticles, respectively.[785] The findings from other reports utilizing hierarchical structure consisting of SnO_2 nanosheets indicated that enhanced gas sensing performance for the hierarchical SnO_2 nanosheets towards ethanol may be mainly attributed to the confined effect provided by numerous nano–or micro–reaction regions that provided adequate room for gas–sensing reactions.[786-789]

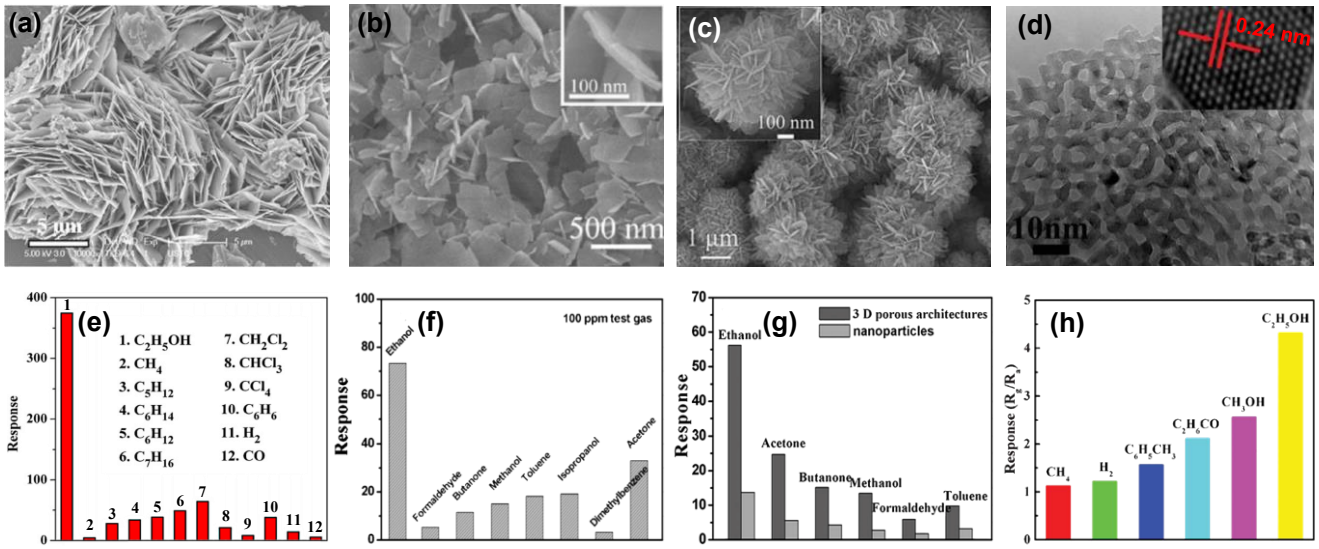

Figure 42. SEM image of (a) the ZnO nanosheet,[779] (b) SnO_2 nanosheet,[782] (c) porous hierarchical nanosheets of SnO_2[784]and (d) TEM image of NiO nanosheets showing the porous nature.[790] (e) The cross–response of the sensor to ethanol and other 11 interfering gases at 400 °C.[779] Reproduced with permission from Ref. [779] Copyright 2012 Elsevier B.V. (f) Responses of the sensor using SnO_2 nanosheets to 100 ppm various test gases at 250 °C.[782] Reproduced with permission from Ref. [782] Copyright 2011 Elsevier B.V. (g) Responses of sensors based on porous SnO_2 architectures to various gases.[784] Reproduced with permission from Ref. [784] Copyright 2011 The Royal Society of Chemistry. (h) The cross–response of the sensor to ethanol, methanol, acetone, toluene, hydrogen and methane at a concentration of 500 ppm.[790] Reproduced with permission from Ref. [790] Copyright 2013 The Royal Society of Chemistry.

Porous NiO nanosheets synthesized by a chemical bath deposition method showed a response to ethanol in a range of 5–500 ppm at low temperature of 200 °C (**Figure 42d, 42h**).[790] The enhanced gas–sensing performance towards ethanol could be explained in association with the ultrathin nanosheets that are close to Debye length scale.[790-791] Jia et al. used CuO nanosheets made by mild hydrothermal synthesis for ethanol sensing. The authors demonstrated that the CuO nanosheets, with a thickness of 20~25 nm, had a stable response to ethanol.[792] Microspheres composed of the nanosheets responded to 100 ppm of ethanol in 13.7 s at a working temperature of 150 °C.[699]

2D nanosheets assembled from Co_3O_4 microspheres had been used as ethanol sensor, demonstrating a strong response of 8.3 and the response time of 16 s toward 100 ppm ethanol gas at 180 °C.[793] Chen and coworkers used two–dimensional WO_3 nanoplates as an active element to fabricate chemiresistive device for alcohols sensing.[794] They showed that WO_3 nanoplate–based sensors were highly sensitive to alcohols (e.g., methanol, ethanol, isopropanol, and butanol) at moderate operating temperatures (260–360 °C). A response of 70 was realized for ethanol at 200 ppm. The response and recovery times of the WO_3 nanoplate sensors were less than 15 s for all tested alcohols. Liu and co–workers compared the ethanol sensing performance between bulk and 2D nanosheets of MoO_3 using chemiresistive device architecture.[795] 2D–MoO_3 nanosheets provided a significantly enhanced chemical sensor performance compared with bulk MoO_3, including the increased response from 7 to 33 by using 2D–MoO_3 nanosheet. This superior performance was attributed to the 2D–structure with increased surface area and high abundance of reactive sites. TiO_2 nanosheets with exposed [001] high–energy facets were also developed as gas sensing materials.[796] The sensor displayed a regular n–type response to alcohols with high sensitivity at temperatures above 250 °C, but exhibited an abnormal p–type sensing behavior over a wide temperature range spanning from room temperature to 120 °C. The unusual p–type sensing response, unprecedented for the *n*–type TiO_2 nanomaterials, was attributed to the proton transfer between alcohol molecules and adsorbed water molecules on the surface of TiO_2 nanosheets

Formaldehyde. Liu et al. fabricated novel single–crystalline ZnO nanosheets with porous structure by annealing $ZnS(en)_{0.5}$ (en = ethylenediamine) complex precursor.[602] The as–prepared ZnO nanosheets were used for the fabrication of gas sensors for indoor air contaminant monitoring. It was found that the as–fabricated sensors not only exhibited highly sensitive performance, but also possessed significant long–term stability in sensing formaldehyde. It is indicated that these ZnO nanostructures could be promising for applications in electronic devices for environmental testing.

Guo et al. synthesized ultra–thin hexagonal ZnO nanosheets with a thickness of 17 nm by simple hydrothermal method.[797] The ultrathin nanosheets exhibited excellent gas sensing properties to formaldehyde gas at optimal temperature of 350 °C at the concentration of 50 ppm. Zhang and co–workers used porous NiO sheets, obtained from β–$Ni(OH)_2$ ultrathin nanosheets, for formaldehyde sensing.[798] The chemiresistive sensors, operating at 240 °C,

showed good selectivity towards formaldehyde over other interferents including alkanes, humidity, and hydrogen, as well as it demonstrated a large detection range of 1–1000 ppm. The sensor fabricated from ultrathin SnO_2 nanosheets showed very fast response and recovery (1 s and 6 s, respectively) towards 100 ppm of formaldehyde, good repeatability and selectivity at a relatively low working temperature. The high sensitivity of this device was related to the ultrathin nanosheet morphology of SnO_2 that provided a large specific surface areas and direct conduction pathways for analyte interactions.

Acetone. Ultrathin porous Co_3O_4 nanosheets have been also used for acetone sensing.[799] The sensor showed a superior acetone gas–sensing performance at low operating temperature of 150 °C. The response to 100 ppm acetone reached 11.4 with good reproducibility. The detection limit of the Co_3O_4 nanosheet sensor was lower than 1.8 ppm, which is the diagnostic criteria for diabetes

Others. Su and co–workers reported on the detection of volatile and toxic gases including ethanol, ethyl–acetate, acetone, xylene, and toluene, using 2D sheet–like CuO nanostructures obtained from the microwave–assisted synthesis.[800] Porous ZnO nanoplates based sensors exhibited high response to chlorobenzene at relatively low operating temperatures, from 150 to 250 °C.[777] 2D SnO_2 nanosheets showed high sensitivity to 200 ppm of ethylene glycol with fast response/recovery (65 s/72 s) and a wide linear dynamic range from 5 to 1000 ppm.[801]

Although metal oxides have been widely used in gas sensing because of their advantages, including low cost, easy production, compact size and simple measuring electronics.[410-411] The challenge for developing high performance metal oxides sensor still remains. *Firstly*, many metal oxide sensors demonstrated high signal and low noise levels only at high temperatures due to the high activation energy of the adsorbed oxygen mediated reaction, which is a critical limitation for the development of portable devices. *Secondly*, although much of current research aimed at the investigations of the effects of morphology and crystal size on the sensing behavior, exploration of the crystal plane–dependent properties may be valuable,[802] because high energy crystal facets easily absorb oxygen species, which are primarily involved in the sensing mechanism of metal oxides towards different gases.[592, 596]

4.2.5. Metal–Organic Frameworks

Dincă and co–workers developed a cross–reactive sensor array through the use of 2D MOFs capable of discriminating several classes of volatile organic compounds (VOCs) containing different functional group, including alcohols, ketones, ethers, aromatics, amines and aliphatics.[174] Three structurally related MOFs, Ni_3HITP_2, Cu_3HITP_2, and Cu_3HHTP_2 were used to fabricate chemiresistive sensors by drop–casting the dispersion of each MOF onto interdigitated gold electrodes. The chemiresistive responses of the devices towards various VOC vapors at 200 ppm concentration levels are shown in **Figure 43a**. Polar VOCs produced higher response, while the exposure to aliphatic hydrocarbons showed no appreciable signal. These observations may be related to the reductive or oxidative nature of tested analytes and their varied affinities for the interactions with 2D conductive MOFs.[418, 427, 621, 803] Both "turn–on" and "turn–off" type responses were observed for a single analyte when a different MOF was used, which was proposed to be related to the different semiconductor characteristic of the material.[174] Using statistical analysis method, PCA, it was shown that the MOFs chemiresistive responses could be used to distinguish between five categories of VOCs with >90% accuracy (**Figure 43b**). Recently, Hoppe and coworkers prepared thin and homogenous films by spray-coating water-based dispersions of Cu_3HHTP_2 MOF on glass and on polymer substrates.[804] In the films, the nanoplatelets of the MOF were oriented parallel to the substrate with intimate contact. This frabrication method led to a high electrical conductivity combined with an easily accessible pore system. The coatings deposited with Cu_3HHTP_2 plates showed very responses to methanol in the gas phase.[804]

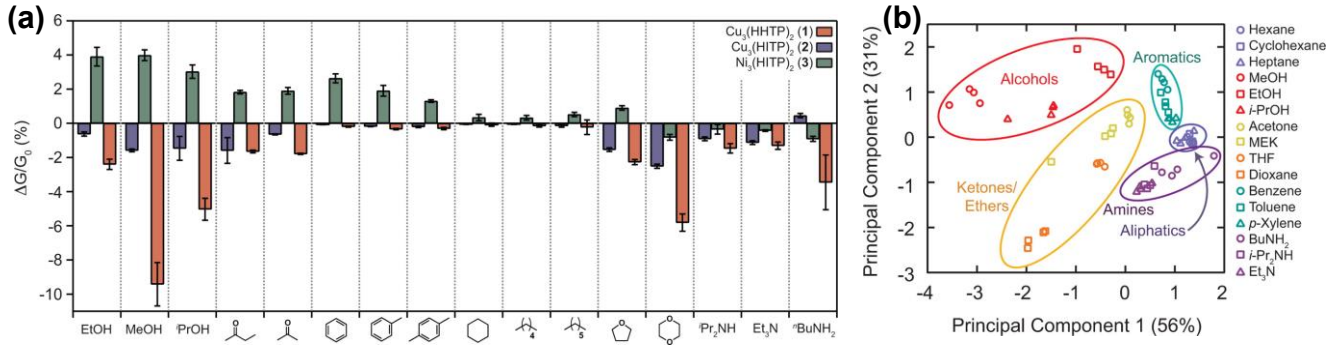

Figure 43 (a) Sensing responses of the MOF array to representative examples from different categories of VOCs, where $\Delta G/G_0$ is the relative response (change in conductance) upon a 30 s exposure to 200 ppm of the VOC vapor. (b) Principal component analysis of the MOF sensor array's responses to VOCs.[174] Reproduced from Ref. [174] Copyright 2015 American Chemical Society.

The mechanisms of VOCs sensing with 2D MOFs are still under investigation, but the preliminary results, [174, 418, 427, 621, 803] reported to date, suggest that MOF–based chemiresistors are promising platforms in the field of sensing.[421] Rational tuning of chemical and electronic structure of the MOF may lead to the development of improved sensor

materials with excellent sensitivity and selectivity. Conductive MOFs hold the possibility for engineering both its surface chemistry and electronic property through bottom–up strategy, and thus provide an exciting and powerful platform for the development of new sensing technologies.[89, 416, 421]

4.2.6. Other 2D Materials

g–C_3N_4 planes consist of highly ordered triazine units linked through planar tertiary amino groups, which contain many coordination sites called "nitrogen pots" where the nitrogen lone–pair electrons can interact with the metal ions. The weak van der Waals layered structure of *g*–C_3N_4 is beneficial for the formation of an intercalation compound with improved physicochemical properties. These properties of *g*–C_3N_4 would create new opportunities for the development of intercalated *g*–C_3N_4 nanosheets in sensing devices. Mesoporous *g*–C_3N_4 decorated with Ag NPs was incorporated into impedance–based gas sensor by Tomer et al. for sensitive detection of humidity in the 11–98% RH range with the response time of 3 s and recovery time of 1.4 s at room temperature.[805] The presence of Ag NPs improved the sensing response by 4 time compared with nonfunctionalized mesoporous *g*–C_3N_4 These impressive features originate from not only the planar morphology of *g-CN,* but also unique physical affinity and favorable electronic band positions of Ag that facilitate water adsorption and charge transportation.[806] Using a similar strategy, Dong and co–workers fabricated a humidity sensor composed of *g*–C_3N_4 with intercalated LiCl guest molecules.[807] The resulting devices exhibited ultra–fast response and recovery time of 0.9s and 1.4 s, respectively, to changing concentrations of humidity (11–95% RH). The improved sensing response was ascribed to an increase in the concentration of protons in 2D *g*–C_3N_4 as a function of enhanced H_2O adsorption onto the surface of LiCl decorated 2D nanostructure. Choi and co–workers explored the potential of a *h*–BN and polyethylene oxide composite in humidity monitoring through impedance–based sensing. The resulting device produced response to humidity in the 0% to 90% RH range with response time of 2.7 s and minimal interference from O_2, N_2, and CH_4.[808]

Gas detection devices are usually fabricated on solid substrates such as silicon wafers and indium tin oxide–coated glass, and thus cannot be often readily integrated into wearable electronics. The commercially available metal oxide sensors usually operate at relatively high temperature (over 100 °C), which significantly limits their application in wearable techonologies.[809-810] It is thus essential to explore new materials capable of operating at room temperature and that can be integrated onto flexible substrates. To obtain high sensitivity in resistive sensor mode, the sensory materials should be able to provide low electrical noise and strong analytical signal. MXenes, such as $Ti_3C_2(OH)_2$, not only possess metallic conductivity,[462] but also have abundant functional groups at the outer surface (**Figure 44a**).[811] This combination renders them highly attractive for gas sensors development with a high signal–to–noise ratio, as the high coverage of functional groups allows effective and strong interactions with targeted analytes; meanwhile the high metallic conductivity intrinsically leads to a low signal noise. Kim and co–workers demonstrated, for the first time, the room temperature gas sensing of ethanol, methanol, acetone, and ammonia using $Ti_3C_2T_x$ devices.[203] The $Ti_3C_2T_x$ sensors could successfully detect ethanol, methanol and acetone vapors at room temperature showing a p–type sensing behavior (**Figure 44b–c**). The theoretical limit of detection for acetone was calculated at 9.27 ppm, demonstrating better performance compared to other sensors based on 2D materials, including graphene and MoS_2.[166, 812] The proposed sensing mechanism involved the interactions between the majority charge carriers of $Ti_3C_2T_x$ and gas species. This study opened new directions for the potential applications of this $Ti_3C_2T_x$ for gas–sensing applications.

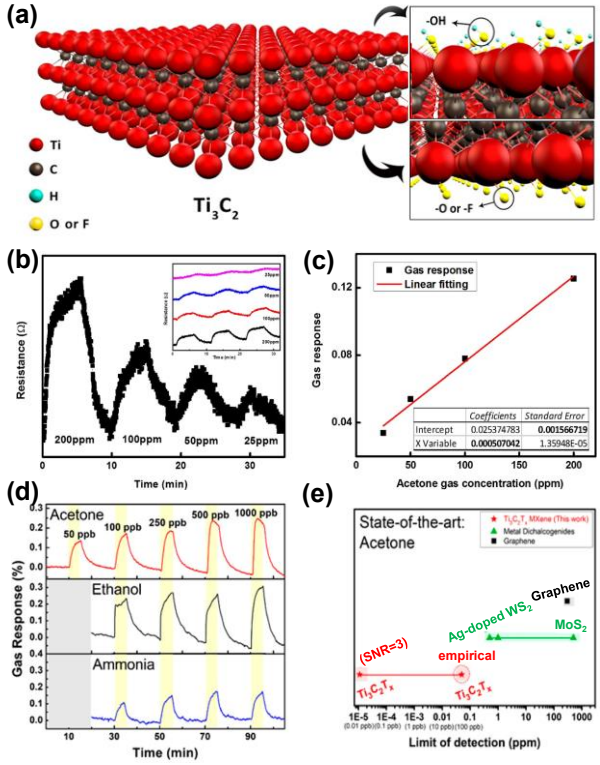

Figure 44. (a) Schematic representation of $Ti_3C_2T_x$ structure and different functional groups on the surface of $Ti_3C_2T_x$ nanosheets. (b) Combined resistance profile of a $Ti_3C_2T_x$ sensor as a function of the acetone concentration. (c) Relationship between gas response and acetone concentration.[203] Reproduced from Ref. [203]Copyright 2017 American Chemical Society. (d) Resistance variation versus time upon exposure to acetone (top), ethanol (middle), and ammonia (bottom) in 50–1000 ppb. (e) State–of–the–art diagram of the LOD for room temperature sensors based on 2D materials to detect acetone, showing $Ti_3C_2T_x$ MXene has the smallest LOD.[623] Reproduced from Ref. [623] Copyright 2018 American Chemical Society.

The detection of VOCs at the ppb level is critical for the early diagnosis of diseases.[813-814] Kim et al. further experimentally demonstrate that MXenes could act as metallic channels in chemiresistive devices with ultrahigh

sensitivity for acetone, ethanol and ammonia (**Figure 44d**).[623] $Ti_3C_2T_x$ MXene sensors exhibited a very low limit of detection of 50 ppb for acetone with SNR of 25.6 at room temperature (**Figure 44e**). Also, the low magnitude of noise resulted in a signal–to–noise ratio of two orders of magnitude higher than that of other 2D materials. DFT calculations showed that $Ti_3C_2(OH)_2$ displayed the strongest binding energy strengths, which were more than twice that of other 2D materials, like MoS_2, graphene, and BP. This superior gas adsorption properties on the hydroxyl groups of $Ti_3C_2T_x$ may largely contribute to its high sensitivity, observed in experimental data. This result provided insight into utilizing highly functionalized metallic sensing channels for the development of sensing technologies.

Although the use of MXenes for volatile sensing is at a very early stage, MXenes are exhibiting its great potential in this area with more unique chemical and physical properties being recently realized.[177, 811] As the surface of MXenes is covered with functional groups, selectivity towards certain gases may be further controlled by surface functionalization or defect engineering. It is noteworthy that only one type of MXenes is currently studied for volatile sensing,[623] and a large family of other MXenes can be potentially employed as highly sensitive sensors. Nevertheless, the elegant combination of the abundant surface chemistry and their metallic conductivity, which are critically needed in the electrically–transduced devices, will ideally result in more applications of MXenes in sensing of volatile molecules in the future.[203, 623]

Table 4. Summary of Sensing Performances for Volatile Compounds by 2D Materials.

Analyte	Material	Architecture	LOD	Experimental range	Sensing environment	Ref
2–butanone	M_3HXTP_2 (Cu_3HHTP_2, Cu_3HITP_2, Ni_3HITP_2)	chemiresistor: Au/M_3HXTP_2/Au	N/A	200 ppm	N_2, r.t.	174
acetaldehyde	MoS_2–Au	chemiresistor: Au/ MoS_2–Au/Au	N/A	1000 ppm	N_2	774
acetic acid	Gr–Au NPs or Pt NPs	chemiresistor: Au/G–AuNPs or Pt NPs/Au	50 ppm	50–200 ppm	Air_D, r.t.	742
acetone	Co_3O_4	chemiresistor: Ag–Pd /Co_3O_4/Ag–Pd	1.8 ppm	1–100 ppm	Air, 150 °C	799
acetone	GO–Co_3O_4 NFs–Ir NPs	chemiresistor: Au/GO–Co_3O_4 NFs–Ir NPs/Al/Au	120 ppb	1–5 ppm	Air, 90 % RH, 300 °C	723
acetone	Gr	FET: Si/ thermal oxide /Gr/Ti–Au/Ti–Au	N/A	N/A	Air, r.t.	740
acetone	Gr–$ZnFe_2O_4$	chemiresistor	N/A	1–1000 ppm	180 °C	724
acetone	M_3HXTP_2 (Cu_3HHTP_2, Cu_3HITP_2, Ni_3HITP_2)	chemiresistor: Au/M_3HXTP_2/Au	N/A	200 ppm	N_2, r.t.	174
acetone	MoS_2	chemiresistor: Ti–Au/MoS_2/Ti–Au	500 ppm	50–5000 ppm	N_2, r.t.	166
acetone	MoS_2–mercaptoundecanoic acid	chemiresistor: Au–Cr/MoS_2–mercaptoundecanoic acid/Au–Cr	<1 ppm	1–1000 ppm	N_2, 25 °C	772
acetone	MoS_2–Au	chemiresistor: Au/ MoS_2–Au/Au	N/A	1000 ppm	N_2	774
acetone	rGO	FET: Si/SiO_2/rGO/Au/Au	N/A	200 ppm	Air, r.t.	725
acetone	rGO–SnO_2	chemiresistor: Au/rGO–SnO_2/Au	100 ppb	1–5 ppm	Air, 85–95% RH, 350 °C	558
acetone	SnO_2–Eu	chemiresistor: Au–Ti/SnO_2–Eu/Au–Ti	131 ppb	5–100 ppm	30 to 70 RH%, 210 °C	815
acetone	$Ti_3C_2T_x$	chemiresistor:Pt/$Ti_3C_2T_x$ /Pt	9.27 ppm	25–200 ppm	Air, r.t.	203
acetone	$Ti_3C_2T_x$	chemiresistor: Au/$Ti_3C_2T_x$ /Au	0.011 ppb	50–1000 ppb	N_2, 25 °C	623
acetone	WS_2–Ag	chemiresistor: Cr–Au/WS_2–Ag/Cr–Au	25 ppm	0.5–10 ppm	Air_d, 100 °C	587
acetonitrile	MoS_2	FET: Si/SiO_2/MoS_2/Au/Au	N/A	N/A	N/A	771
benzene	Gr–ODA	chemiresistor: Au/Gr–ODA/Au	10 ppm	5–100 ppm	1 vol.% ethanol	726
benzene	M_3HXTP_2 (Cu_3HHTP_2, Cu_3HITP_2, Ni_3HITP_2)	chemiresistor: Au/M_3HXTP_2/Au	N/A	200 ppm	N_2, r.t.	174
chlorobenzene	Gr	FET: Si/thermal oxide/Gr/Ti–Au/Ti–Au	N/A	N/A	Air, r.t.	740
chlorobenzene	ZnO	chemiresistor: Pt/ZnO/Pt	N/A	100–250 ppm	Air, 200 °C	777
chloroform	GO–PPr	chemiresistor: Pt/GO–PPr/Pt	400 ppm	400–1000 ppm	N_2, r.t.	816
chloroform	Gr	PN diode: Au–Cr/Gr–Si/Au–Cr	N/A	N/A	r.t.	737
chloroform	MoS_2	FET: Si/SiO_2/MoS_2/Au/Au	N/A	N/A	N/A	771
chloroform,	Gr	FET: Si/thermal oxide/Gr/Ti–Au/Ti–Au	N/A	N/A	Air, r.t.	740
cyclohexane	Gr–ODA	chemiresistor: Au/Gr–ODA/Au	5 ppm	5–100 ppm	1 vol.% ethanol	726
dichloromethane	Gr	FET: Si/thermal oxide/Gr/Ti–Au/Ti–Au	N/A	N/A	Air, r.t.	740
DMA	GO	chemiresistor: Ti–Au/Gr/Ti–Au	N/A	N/A	N/A	733

Analyte	Material	Architecture	LOD	Experimental range	Sensing environment	Ref
DNT	rGO	chemiresistor: Ti–Au/rGO/Ti–Au	0.1 ppb	N/A	N_2	702
DMMP	Gr	chemiresistor: Ag/Gr/Ag	N/A	5–15 ppm	N/A	731
DMMP	Gr	FET: Si/SiO_2/Gr/Au/Au	N/A	N/A	N/A	541
DMMP	Gr	FET: Si/thermal oxide/Gr/Ti–Au/Ti–Au	0.64 ppb	N/A	Air, r.t.	740
DMMP	rGO	chemiresistor: Pt/rGO/Pt	N/A	10–60 ppm	N_2, 25 °C	729
DMMP	rGO	chemiresistor: Cr–Au/rGO/Cr–Au	N/A	5–80 ppm	Air_D, 25 °C	730
DMMP	rGO	chemiresistor: Ti–Au/rGO/Ti–Au	5 ppb	N/A	N_2	702
ethanol	Co_3O_4	chemiresistor: Pt/Co_3O_4/Pt	N/A	5–500 ppm	Air, 180 °C	793
ethanol	CuO	chemiresistor	N/A	1–100 ppm	Air, 150 °C	699
ethanol	CuO	chemiresistor: Au/CuO/Au	N/A	10–1000 ppm	Air, 260 °C	800
ethanol	Gr–AuNPs or Pt NPs	chemiresistor: Au/G–Au NPs or Pt NPs/Au	50 ppm	50–200 ppm	Air_D, r.t.	742
ethanol	GO–OA–F8T2	FET: Si/SiO_2/GO–OA–F8T2/Au/Au	N/A	N/A	r.t.	714
ethanol	GO–phenyl	capacitor: Au/GO–phenyl/Au	N/A	70–1000 ppm	r.t.	739
ethanol	Gr	FET: Si/SiO_2/Gr/Pt/Pt	N/A	N/A	N/A	713
ethanol	Gr–Fe_2O_3	chemiresistor: Pt/Gr–Fe_2O_3/Pt	N/A	1–1000 ppm	280 °C	715
ethanol	M_3HXTP_2 (Cu_3HHTP_2, Cu_3HITP_2, Ni_3HITP_2)	chemiresistor: Au/M_3HXTP_2/Au	N/A	200 ppm	N_2, r.t.	174
ethanol	MoO_3	chemiresistor: Ag–Pd/MoO_3/Ag–Pd	N/A	10–500 ppm	Air, 300 °C	795
ethanol	MoS_2	FET: Si–SiO_2/Oxide/MoS_2/Au/Au	N/A	N/A	N/A	771
ethanol	MoS_2	chemiresistor: Cr–Au/MoS_2–SnO_2/Cr–Au	1 ppm	5–40 ppm	r.t.	769
ethanol	MoS_2	FET: Si/SiO_2/MoS_2/metal/matal	N/A	N/A	r.t.	770
ethanol	MoS_2–mercaptoundecanoic acid	chemiresistor: Au–Cr/MoS_2–mercaptoundecanoic acid/Au–Cr	<10 ppm	1–1000 ppm	N_2, 25 °C	772
ethanol	MoS_2–SnO_2	chemiresistor: Au/ MoS_2–SnO_2/Au	N/A	50–1000 ppm	Air, 280 °C	767
ethanol	NiO	chemiresistor	N/A	5–500 ppm	Air, 200 °C	790
ethanol	NiO	chemiresistor: Au/NiO/Au	N/A	100–700 ppm	Air, 300 °C	791
ethanol	rGO	FET: Si/SiO_2/rGO/Ti–Pt/Ti–Pt	N/A	N/A	N/A	713
ethanol	SnO_2	chemiresistor: Au/SnO_2/Au	N/A	1.5–50 ppm	Air, 350 °C	781
ethanol	SnO_2	chemiresistor: Au/SnO_2/Au	N/A	20–90 ppm	Air, 250 °C	782
ethanol	SnO_2	chemiresistor: Au/SnO_2/Au	N/A	1–1000 ppm	Air, 165 °C	783
ethanol	SnO_2	chemiresistor: Au/SnO_2/Au	N/A	100 ppm	Air, 300 °C	784
ethanol	SnO_2	chemiresistor: Au/SnO_2/Au	N/A	5–200 ppm	Air, 300 °C	786
ethanol	SnO_2	chemiresistor	N/A	10–100 ppm	Air, 250 °C	787
ethanol	SnO_2	chemiresistor: Au/SnO_2/Au	1.37 ppm	50–300 ppm	Air, 250 °C	788
ethanol	SnO_2	chemiresistor: Au/SnO_2/Au	<5 ppm	5–500 ppm	N/A	789
ethanol	SnS_2	chemiresistor: Cu/SnS_2/Cu	N/A	N/A	r.t.	393
ethanol	$Ti_3C_2T_x$	chemiresistor:Pt/$Ti_3C_2T_x$/Pt	N/A	100 ppm	Air, r.t.	203
ethanol	$Ti_3C_2T_x$	chemiresistor: Au/$Ti_3C_2T_x$/Au	<1 ppb	100–100 ppb	N_2, 25 °C	623
ethanol	TiO_2	chemiresistor: Ag–Pd/TiO_2/Ag–Pd	N/A	200–6000 ppm	Air, r.t./310 °C	796
ethanol	WO_3	chemiresistor: Pt/WO_3/Pt	N/A	10–300 ppm	air, 300 °C	794
ethanol	WS_2	FET: Si/SiO_2/ WS_2/Au/Au	N/A	N/A	r.t.	768
ethanol	ZnO	chemiresistor: Pt/ZnO/Pt	N/A	100–250 ppm	Air, 380 °C	777
ethanol	ZnO	chemiresistor	10 ppb	0.01–1000 ppm	Air, 400 °C	779
ethanol	ZnO–Au	chemiresistor: Pt/ZnO–Au/Pt	N/A	50–800 ppm	Air, 300 °C	778
ethyl acetate	CuO	chemiresistor: Au/CuO/Au	N/A	10–1000 ppm	Air, 260 °C	800
ethylbenzene	Gr–ODA	chemiresistor: Au/Gr–ODA/Au	3 ppm	5–100 ppm	1 vol.% ethanol	726
ethylene glycol	SnO_2	chemiresistor: Au/SnO_2/Au	1.3758ppm	5–1000 ppm	Air_D, 220 °C	801
formaldehyde	Gr-PMMA	chemiresistor: Pt/Gr–PMMA/Pt	10 ppb	0.05–5.0 ppm	N_2, r.t.	718
formaldehyde	NiO	chemiresistor: Au/ NiO/Au	100 ppb	1–1000 ppm	Air, 240 °C	798
formaldehyde	rGO–ZnO	Diode: Au–Ti/ rGO–ZnO/Au–Ti	0.875 ppm	120 ppb to 1 ppm	Air_D, r.t.	719
formaldehyde	ZnO	chemiresistor: Au/ ZnO/Au	N/A	50–500 ppm	Air_D, 250 °C	602

Analyte	Material	Architecture	LOD	Experimental range	Sensing environment	Ref
formalde-hyde	ZnO	chemiresistor: Au/ ZnO/Au	N/A	50 ppm	Air, 350 °C	797
H_2O	BP	FET: Si/SiO_2/BP/Au/Au	21% RH	21–83% RH	Ar	752
H_2O	BP	chemiresistor: Au/BP/Au	N/A	10%–85% RH	Air, 25 °C	749
H2O	BP	FET: Si/ SiO_2 /Gr–DNA/Ti–Au/Ti–Au	N/A	11%–97%	25 °C	750
H_2O	BP	FET: glass/ITO/ BP/Ti–Au/Ti–Au	N/A	11%–97%	r.t.	751
H_2O	BP QDs	chemiresistor: Al/BP/Al	N/A	15%–90% RH	Air, 21 °C	817
H_2O	GO	chemiresistor: Ag/GO/Ag	30% RH	30–80% RH	Air, 10–40 °C	818
H_2O	GO	capacitor: elec-trode/GO/electrode	N/A	15%–95% RH	25 °C	679
H_2O	GO	chemiresistor: Au/GO/Au	N/A	30%–90% RH	Air, 25 °C	685
H_2O	GO	chemiresistor: Au/GO/Au	N/A	11%–95%RH	r.t.	687
H_2O	GO–PSS	capacitor: Ag/GO–PSS/Ag	N/A	0%–80%RH	Air	698
H_2O	GO–EA or HA	chemiresistor: Au/GO–EA/Au	N/A	20%–90%	Air, r.t.	700
H_2O	GO–phenyl	capacitor: Au/GO–phenyl/Au	<6%	6%–97% RH	r.t.	739
H_2O	Gr	capacitor: Gr/Analyte/Gr	N/A	0–25 w/w% in ethanol	ethanol	689
H_2O	Gr	varactor: Si/SiO_2/Gr/Ti–Pd–Au/Ti–Pd–Au	N/A	1%–97% RH	Air, 23 °C	691
H_2O	Gr	varactor: Si/SiO_2/Gr/metal/metal	N/A	20%–90%RH	Air, r.t.	695
H_2O	Gr	FET: Si/SiO_2/Gr/metal/metal	N/A	5%–90% RH	r.t.	696
H_2O	Gr	chemiresistor: Ti–Au/Gr/Ti–Au	N/A	1%–96%RH	Air, r.t.	697
H_2O	Gr–PEI	FET: Si/SiO_2/Gr–PEI/Au–Ti/Au–Ti	N/A	10%–60%RH	r.t.	364
H_2O	GO–Au NPs–MPTMOS	chemiresistor: Au/ GO–AuNPs–MPTMOS/Au	N/A	20%–90% RH	Air, r.t.	609
H_2O	Gr–PPy	chemiresistor: Au/Gr–PPy/Au	N/A	12%–90% RH	Air, r.t.	699
H_2O	MoS_2	chemiresistor: Pt/ MoS_2/Pt	N/A	0%–60%RH	N/A	757
H_2O	rGO	chemiresistor: Au/rGO/Au	N/A	20%–97%RH	25 °C	
H_2O	rGO–PEDOT	chemiresistor	N/A	0%–98% RH	Air, r.t.	690
H_2O	rGO–PDDA	chemiresistor: Cu–Ni/rGO–PDDA/Cu–Ni	N/A	11%–97%RH	Air, r.t.,	686
H_2O	SnS_2	chemiresistor: Cu/SnS_2/Cu	N/A	11–97% RH	r.t.	393
H_2O	VS_2	chemiresistor: Au/ VS_2/Au	N/A	0%–100% RH	25 °C	756
H_2O	WS_2	FET: Si/SiO_2/ WS_2/Ag/Ag	N/A	11.3%–97%RH	r.t.	759
H_2O	WS_2	chemiresistor: Gr/WS_2/Gr	N/A	0%–90%RH	N_2, r.t.	760
HCN	Gr QDs	chemiresistor: Pt/Gr QDs/Pt	0.6 ppm	1–100 ppm	Air, 25 °C	705
HCN	rGO	chemiresistor: Ti–Au/rGO/Ti–Au	70 ppb	N/A	N_2	702
hexane	GO–PPr	chemiresistor: Pt/GO–PPr/Pt	<200 ppm	200–900 ppm	N_2, RT	816
hexanoic acid	Gr–DNA	FET: Si/ SiO_2/Gr–DNA/Au–Ti–Pd /Au–Ti–Pd	N/A	3–63 ppm	Air, 33% RH	741
Hg	MoS_2–PANI	chemiresistor: Pt/MoS_2–PANI/Pt	N/A	0.55–452.51 mg m^{-3}	r.t.	763
humidity	MoS_2	FET: Si/SiO_2/MoS_2/Ti–Au/Ti–Au	N/A	4%–84%RH	N_2, r.t.	101
isopropanol	M_3HXTP_2 (Cu_3HHTP_2, Cu_3HITP_2, Ni_3HITP_2)	chemiresistor: Au/M_3HXTP_2/Au	N/A	200 ppm	N_2, r.t.	174
isopropyl al-cohol	SnS_2	chemiresistor: Cu/SnS_2/Cu	N/A	N/A	r.t.	393
liquid petro-leum gas	Gr	chemiresistor: Ag/Gr/Ag	4 ppm	N/A	Air, r.t.	641
melamine	Gr	FET: Si/SiO_2/rGO/Au/Au	N/A	N/A	175 °C	230
methanol	BP	chemiresistor: Au/BP/Au	28 ppm	380–1900 ppm	r.t.	755
methanol	GO–PEDOT–PSS	chemiresistor: Au/GO–PEDOT–PSS/Au	N/A	35–1000 ppm	r.t.	738
methanol	Gr	FET: Si/SiO_2/Gr/Cr–Au/Cr–Au	N/A	N/A	r.t.	716
methanol	Gr	PN diode: Au–Cr/Gr–Si/Au–Cr	N/A	N/A	r.t.	737
methanol	M_3HXTP_2 (Cu_3HHTP_2, Cu_3HITP_2, Ni_3HITP_2)	chemiresistor: Au/M_3HXTP_2/Au	N/A	200 ppm	N_2, r.t.	174
methanol	MoS_2	FET: Si/SiO_2/MoS_2/Au/Au	N/A	N/A	N/A	771
methanol	SnS2	chemiresistor: Cu/SnS_2/Cu	N/A	N/A	r.t.	393
methanol	$Ti_3C_2T_x$	chemiresistor: Pt $Ti_3C_2T_x$ /Pt	N/A	100 ppm	Air, r.t.	203
m–xylene	Gr–ODA	chemiresistor: Au/ Gr–ODA/Au	3 ppm	5–100 ppm	1 vol.% ethanol	726
DMF	Gr	FET: Si/thermal oxide/Gr/Ti–Au/Ti–Au	N/A	N/A	Air, r.t.	740

Analyte	Material	Architecture	LOD	Experimental range	Sensing environment	Ref
n–butylamine	M_3HXTP_2 (Cu_3HHTP_2, Cu_3HITP_2, Ni_3HITP_2)	chemiresistor: Au/M_3HXTP_2/Au	N/A	200 ppm	N_2, r.t.	174
n–hexane	MoS_2–mercaptoundecanoic acid	chemiresistor: Au–Cr/MoS_2–mercaptoundecanoic acid/Au–Cr	<1 ppm	1–1000 ppm	N_2, 25 °C	772
nitroaniline	SnS_2	LSV: SnS_2/GCE	15×10^{-6} mol/L	15.6×10^{-6}–0.5×10^{-3} mol/L	N/A	776
NMP	GO	chemiresistor: Ti–Au/Gr/Ti–Au	N/A	N/A	N/A	733
octanoic aicd	Gr–DNA	FET: Si/SiO_2/Gr–DNA/Au–Ti–Pd/Au–Ti–Pd	1 ppm	N/A	Air, 33% RH	741
o–xylene	Gr–ODA	chemiresistor: Au/Gr–ODA/Au	3 ppm	5–100 ppm	1 vol.% ethanol	726
phenol	GO–phenyl	capacitor: Au/GO–phenyl/Au	N/A	70–1000 ppm	r.t.	739
phenol	Gr	PN diode: Au–Cr/Gr–Si/Au–Cr	N/A	1 mM–1 M	r.t.	737
propanal	MoS_2–mercaptoundecanoic acid	chemiresistor: Au–Cr/MoS_2–mercaptoundecanoic acid/Au–Cr	1 ppm	1–1000 ppm	N_2, 25 °C	772
propanal	$Ti_3C_2T_x$	chemiresistor: Au/$Ti_3C_2T_x$/Au	<1 ppb	N/A	N_2, 25 °C	623
propionic acid	Gr–DNA	FET: Si/ SiO_2/Gr–DNA/Au–Ti–Pd/Au–Ti–Pd	N/A	50–1000 ppm	Air, 33%RH	741
p–xylene	Gr–ODA	chemiresistor: Au/ Gr–ODA/Au	3 ppm	5–100 ppm	1 vol.% ethanol	726
p–xylene	M_3HXTP_2 (Cu_3HHTP_2, Cu_3HITP_2, Ni_3HITP_2)	chemiresistor: Au/M_3HXTP_2/Au	N/A	200 ppm	N_2, r.t.	174
tetrahydrofuran	M_3HXTP_2 (Cu_3HHTP_2, Cu_3HITP_2, Ni_3HITP_2)	chemiresistor: Au/M_3HXTP_2/Au	N/A	200 ppm	N_2, r.t.	174
tetrahydrofuran	M_3HXTP_2 (Cu_3HHTP_2, Cu_3HITP_2, Ni_3HITP_2)	chemiresistor: Au/M_3HXTP_2/Au	N/A	200 ppm	N_2, r.t.	174
toluene	GO–PPr	chemiresistor: Pt/GO–PPr/Pt	24 ppm	24–500 ppm	N_2, r.t.	816
toluene	Gr–ODA	chemiresistor: Au/Gr–ODA/Au	5 ppm	5–100 ppm	1 vol.% ethanol	726
toluene	M_3HXTP_2 (Cu_3HHTP_2, Cu_3HITP_2, Ni_3HITP_2)	chemiresistor: Au/M_3HXTP_2/Au	N/A	200 ppm	N_2, r.t.	174
toluene	MoS_2	FET: Si–SiO_2/Oxide/MoS_2/Au/Au	N/A	N/A	N/A	771
toluene	MoS_2–mercaptoundecanoic acid	chemiresistor: Au–Cr/MoS_2–mercaptoundecanoic acid/Au–Cr	<10 ppm	1–1000 ppm	N_2, 25 °C	772
triazine	Gr	FET: Si/SiO_2/rGO/Ti–Au/Ti–Au	N/A	N/A	140 °C	230
triethylamine	MoS_2	chemiresistor: Ti–Au/MoS_2/Ti–Au	10 ppb	50–5000 ppm	N_2, r.t.	166
triethylamine	MoS_2	chemiresistor: Ti–Au/MoS_2/Ti–Au	10 ppb	1–100 ppm	N_2, r.t.	166
trimethylamine	MoS_2	FET: Si/SiO_2/ MoS_2/Ag/Ag	N/A	N/A	r.t.	764
trimethylamine	rGO–nylon–6	chemiresistor: Au/rGO–nylon–6/Au	0.39 mg/L	23–230 mg/L	50% RH, r.t.	745

Note: chemiresistor configuration is described by: electrode/conductive material/electrode. FET is described as: gate electrode/insulator/channel material/source electrode/drain electrode. Diode is described in a way of electrode/semiconductor/electrode. N/A, not available. Air_D, dry air and r.t., room temperature.

4.3. Detection of Ions

In recent years, there has been an increasing ecological and public health concern associated with environmental contamination of global natural resources. In particular, the discharge of metallic contaminants from industrial processes, most typically in the form of heavy metal ions, led to extensive contamination of drinking water and agricultural products.[819] Therefore, there is a big commercial demand to manufacture rapid, sensitive, and simple analytical platforms for the detection and monitoring of metallic contaminants in water, and soil.[820] In addition, ionic electrolytes are essential for various bodily functions such as cell functioning and cell signaling. Their imbalance can result in the number of life threatening conditions including cardiac arrest, neurological disorders or kidney failure. It is thus important to develop portable point–of–care diagnostic devices that can provide real–time information about electrolyte concentrations in biological samples.[821] 2D materials have been identified as a new class of materials that can be used to construct sensitive detection platforms for sensing ionic analytes based on either voltammetric or potentiometric techniques.[821]

4.3.1. Graphene and Graphene Oxides

Heavy metals. Graphene and graphene oxide electrodes are capable of providing more sensitive electrode interfaces due to the large surface area, and fast electron transfer and mass transport rates.[821-822] Recently proposed graphene–based electrochemical sensors, for the analysis of heavy metals, achieved extremely good analytical performances, surpassing even those obtained either by using carbon nanotubes or metal nanoparticles.[823-825]

A serial graphene nanocomposite modified electrodes have been used for Pb^{2+} and Cd^{2+} detection. Zhu et al.

reported on the simultaneous detection of Pb^{2+} and Cd^{2+} ions in spring water samples using square wave anodic stripping voltammetry (SWASV) at a gold nanoparticle–cysteine graphene functionalized bismuth film electrode.[826] They observed linear concentration dependence in the range between 0.50 to 40 $\mu g L^{-1}$ with the LODs of 0.10 $\mu g\ L^{-1}$ for Cd^{2+} and 0.05 $\mu g\ L^{-1}$ for Pb^{2+} ions and high selectivity to target analytes against 8 other cationic species. The improvement in stripping peaks of Pb^{2+} and Cd^{2+} resulted from the enlarged activated surface area and good electrical conductivity of the Au–Gr scaffold together with high affinity of cysteine to metal cations. A liquid-gated field-effect transistor chemical vapor grown graphene film as the conducting channel could detect Pb^{2+} at concentrations as low as 0.1 pM.[827]To induce high sensitivity and selectivity to Pb^{2+} ions, the surface of graphene was decorated with AuNP which served as the anchoring sites for covalent attachment of thiolated DNAzyme molecules. The fabricated devices responded to changing concentration of Pb^{2+} in a dose-dependent manner, where the Dirac point shifted to a more positive voltages at higher concentrations of Pb^{2+} ions.[827] Park and co–workers further improved sensitivity to Pb^{2+} and Cd^{2+} ions by micropatterning rGO onto Si/SiO_2 wafers using lithography followed by electrodeposition of bismuth to form rGO–Bi nanocomposite electrodes.[828] The fabricated micro–sensor, using SWASV, responded linearly from 1.0 $\mu g\ L^{-1}$ to 120.0 $\mu g\ L^{-1}$ for both metal, with LODs of 0.4 $\mu g\ L^{-1}$ and 1.0 $\mu g\ L^{-1}$ for Pb^{2+} and Cd^{2+}, respectively. The improved performance was due to the efficient electrocatalytic activity of GO, which facilitated the electron transfer kinetics at the electrode surface. Li et al. fabricated Nafion–graphene electrodes for the detection of Pb^{2+} and Cd^{2+} using differential pulse anodic stripping voltammetry (DPASV).[829] The LODs for both analytes were estimated to be at 0.02 $\mu g\ L^{-1}$. The practical application of this sensing platform was further verified in the water sample determination. The authors indicated that the strong adsorptive capability and high specific surface area of graphene together with cationic exchange capacity of Nafion is responsible for the enhanced selectivity to metal detection.

Willemse et al. also used a graphene–Nafion modified glassy carbon electrode (GCE) with an in situ plated mercury film on the surface as electrochemical sensing platform for Zn^{2+}, Cd^{2+}, Pb^{2+}, and Cu^{2+}.[830] SWASV could selectively differentiate between Zn^{2+}, Cd^{2+}, and Pb^{2+}, ions at their sub–micromolar concentrations–0.07 $\mu g\ L^{-1}$, 0.13 $\mu g\ L^{-1}$, and 0.14 $\mu g\ L^{-1}$, respectively. However, Cu^{2+} analysis was performed independently due to intermetallic interference that exists between Cu^{2+} and Zn^{2+}. Another multi–ion sensor was developed by Gode et al., who functionalized reduced graphene oxide with 1-ethyl-3-(3-dimethylaminopropyl)carbodiimide (EDC) calixarene and used it for simultaneous determination of Fe^{3+}, Cd^{2+}, and Pb^{2+}. SWV showed linear concentration dependence to all tested analytes in the 1.0×10^{-10}–1.0×10^{-8} M range using the CA–rGO/GCE electrodes. The LODs for the metal ions determination were found to be at 2.0×10^{-11} M, and were attributed to good selectivity of calixarene ionophore to target metals. The same sensors also demonstrated good analyte recovery for practical analysis of pharmaceutical formulations. Pyrene modified gold electrodes were also used as anchors for immobilization of free rGO sheets through π–π stacking interactions.[831] The resulting sensing devices were capable of detecting Cu^{2+} at concentrations as low as 1.5 nM and Pb^{2+} at 0.4 nM levels with good reusability and repeatability. Using similar strategy, Teoh and co–workers covalently attached rGO sheets onto the surface of L–cysteine modified gold electrodes.[832] The attached rGO sheets provided the extended heterogeneous sites for the adsorption of metal ions, through the oxygenated sites, allowing detection of Pb^{2+} at 25 ppb levels. Alternatively, gold electrodes modified with 4-aminophenyl or aryl diazonium moieties as scaffolds for the attachment to GO demonstrated 1–2 orders improvements in detection limits for Pb^{2+} ions.[833]

Despite high sensitivity of Gr–Nafion modified electrodes to heavy metal ions, the typically employed preparation methods of the nanocomposite films, through mixing of reagents, were recently criticized.[834-835] Drop–casting of Gr–Nafion films may lead to the formation of graphene aggregates, and consequently restacking of graphene sheets to form graphite due to van der Waals and π–π stacking interactions between individual sheets of graphene. The proposed strategies to minimize the extent of aggregation of graphene were focused on the incorporation of metallic nanoparticles onto the surface of graphene. For example, Zhang and co–workers developed a nanocomposite electrode consisting of rGO functionalized with poly(vinylpyrrolidone), chitosan, and gold nanoparticles for the Hg^{2+} detection in river waters.[836] The resulting sensor could detect Hg^{2+} at 0.6 ppt with 5 min accumulation time using SWASV. Selectivity studies confirmed the insensitivity to 6 ionic interferants. Wei et al. fabricated SnO_2/reduced GO nanocomposite modified GCE, for simultaneous determination of Cd^{2+}, Pb^{2+}, Cu^{2+}, and Hg^{2+} ions in drinking waters.[837] The LODs of this sensing platforms, determined through SWASV, were 1.0×10^{-10} M, 1.8×10^{-10} M, 2.3×10^{-10} M, and 2.8×10^{-10} M for Cd^{2+}, Pb^{2+}, Cu^{2+}, and Hg^{2+}, respectively. The analytes responded linearly within 0.3 to 1.2 μM concentration range (**Figure 45**). Further improvements in sensitivity to Hg^{2+} could be realized through the incorporation of rGO–polyfuran (PF) nanohybrids into FET devices.[838] The resulting sensor demonstrated rapid response (<1 s), high sensitivity (10 pM) Hg^{2+} sensor and excellent selectivity against Zn^{2+}, Ce^{2+}, Na^{+}, Ni^{2+}, Pb^{2+}, Cu^{2+}, Co^{2+}, and Li^{+} ions. The high inherent sensitivity and selectivity to Hg^{2+} was attributed to the enhanced surface area provided by the rGO-PF nanohybrid and the presence of PF nanotubes that could act as molecular probes for the detection of Hg^{2+}.[838]

More recently, Zhang and co–workers developed a sensitive platform for Hg^{2+} detection based on the thymine–mercury(II)–thymine (T–Hg^{2+}–T) interactions with chemically reduced GO employed as a transducer.[839] They observed that the redox current of ferrocene labelled nucleic acid immobilized on the surface of graphene (ssDNA) was significantly amplified by the presence of graphene during DPV measurements. Upon the addition of Hg^{2+}, the ferrocene–labeled thymine–rich DNA probe hybridized with target probe to form double stranded DNA (ds–DNA) via the

Hg^{2+} mediated coordination of T–Hg^{2+}–T base pairs. Because of the weak affinity of graphene to ds–DNA, the ferrocene complex was drawn away from the electrode surface consequently reducing the magnitude of recorded current. This sensor, under optimal experimental conditions, could sense Hg^{2+} ions at 5 pM with high specificity.

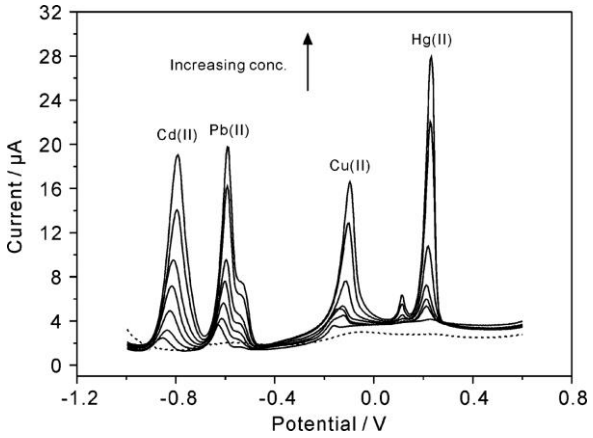

Figure 45. SWASV response of the SnO_2/reduced graphene oxide nanocomposite modified GCE for the simultaneous analysis of Cd^{2+}, Pb^{2+}, Cu^{2+}, and Hg^{2+} over a concentration range of 0 to 1.2 µM for each metal ions. From bottom to top, 0, 0.3, 0.4, 0.5, 0.6, 0.7, 0.9, and 1.2 µM.[837] Reproduced from Ref. [837] Copyright 2011 American Chemical Society.

Non-covalent modification of an electrochemically reduced GO (ERGO)-based diode with *N*-[(1-pyrenyl-sulfonamido)-heptyl]-gluconamide (PG) used as the modifier allowed ultra-sensitive detection of Hg^{2+} ions at 0.1 nM concentrations.[840] The resulting sensor also demonstrated high selectivity to mercury over other ionic interferants including K^+, Na^+, Cu^{2+}, Zn^{2+}, Fe^{3+} and Cd^{2+}. Sensitive detection of Hg^{2+} could be also realized using monolayer GO sheets functionalized with a single-stranded DNA aptamer assembled onto interdigitated electrodes in chemiresistor configuration.[841] High binding affinity of the DNA aptamer to mercury ions permitted detection of Hg^{2+} at 0.5 nM concentrations with high selectivity against Na^+, K^+, Li^+, Cd^{2+}, Ni^{2+}, Zn^{2+}, Co^{2+}, Mg^{2+}, Cu^{2+}, Pb^{2+}, Ag^+, Ca^{2+} and Fe^{3+} ionic interferents. Another strategy to detect Hg^{2+} was demonstrated by Zhang et al. who functionalized surface of exfoliated graphene with a self-assembled monolayer of 1-octadecanethiol in FET device architecture.[842] The resulting sensor could successfully detect Hg^{2+} ions at 10 ppm concentrations. The high sensitivity to mercury was attributed to the presence of thiol groups in 1-octadecanethiol monolayer. Baykara and co–workers further demonstrated that chemically vapor grown graphene functionalized with 1–octadecanethiol could detect both mercury and lead ions at 10 ppm concentrations.[843] The authors proposed that the electrostatic gating effect was responsible for the sensing behavior of the fabricated sensing devices. Interestingly, the same devices modified with a self–assembled monolayer of 1–dodecanethiol instead of 1–octadecanethiol demonstrated p-type character, before and/or after exposure to heavy Hg^{2+}, and Pb^{2+}. This effect was attributed to the high degree of p–doping in the 1–dodecanethiol/Gr based FET, which caused the Dirac point to be located beyond the applicable gate voltage range.[843]

Graphene and graphene oxide based sensors have also been employed for the detection of noble metals, toxic elements and nuclear waste.[264, 821] For instance, Wang and co–workers reported on the rGO–cysteic acid composite films for the detection of Ag^+ in natural waters with nanomolar detection limits (1 nM).[844] In addition, electrodes modified with graphene bismuth, mercury or AlOOH nanocomposites have been demonstrated as promising platforms for heavy metal determination due to their strong complexing affinity for metals.[845-847] Silwana et al., through the incorporation of Sb nanoparticles onto the surface of rGO, and by using dimethylglyoxime as a chelating agent, were able to simultaneously sense Pd^{2+}, Pt^{2+}, and Rh^{3+} cations.[848] Under optimal conditions differential pulse cathodic stripping voltammetry could detect Pd^{2+}, Pt^{2+}, and Rh^{3+} at 0.45 pg L^{-1}, 0.49 pg L^{-1}, and 0.49 pg L^{-1} concentrations, respectively. The developed electrochemical sensor also exhibited good precision with a relative standard deviation of 4.2%, 2.55% and 2.67% with 92–117% recoveries for environmental samples containing Pd(II), Pt(II) and Rh(III), respectively.

Another notable example was demonstrated by Ziolkowski and co–workers, who employed carboxylated graphene to sense uranyl ions in aqueous solutions using SWV.[849] The enhanced selectivity to uranyl anions was ascribed to the high affinity of COO^- for UO_2^{2+} species through hydrogen bonding. These findings are consistent with the results of DFT calculations performed by Qun–Yan Wu et al.[850] The fabricated sensor platform showed linear response within the range of 5.0×10^{-8} to 5.0×10^{-6} mol L^{-1} and significant selectivity towards UO_2^{2+} ions over seven other ionic interferents. Kumar et al. reported on the functionalization of GO with L–leucine and Nafion for selective detection of arsenic.[851] The GO–Au–Leucine–Nafion modified electrodes could detect arsenic at 0.5 ppm levels in drinking waters with minimal interference from common ionic contaminants such as Zn^{2+}, Pb^{2+}, and Hg^{2+}. High selectivity of the resulting sensors was provided by the biorecognition element–L–leucine, while GO ensured good carrier mobility and increased electron transfer rates.

Electrolytes. Graphene based electrodes were also used as solid ion–to–electron transducers in ion–selective electrodes (ISEs). Ying et al. and Niu et al. reported on the first application of graphene and graphene oxide as transducer layer in ISEs.[261, 852] The authors formed K^+–ISEs through drop–casting graphene/GO onto GCE and covering the electrodes with K^+–selective membrane (**Figure 46a–b**). The fabricated sensors exhibited high interfacial double layer capacitance of approximately 80 µF and potential drift as low as 12.6 ± 1.1 µV h^{-1}.In addition, the drop–cast layer of graphene/GO suppressed the formation of water layer at the electrode/ion–selective membrane interface, thus further minimizing potential drifts (**Figure 46c**). The same electrodes were also relatively insensitive to O_2, light and redox interferences, confirming the inherent advantages of

2D carbons over conductive polymers in ISEs (**Figure 46d**).[247] Rius and co–workers found that 1500 nm layer of rGO drop–cast on GCE improved signal–to–noise ratio of fabricated Ca^{2+}–ISEs, with potential drift of only 10 μV/h recorded during potentiometric measurements.[263] They also demonstrated that mechanism of ion–to–electron transduction proceeds through the formation of double layer in which one side carries charge in the form of ions (ion selective membrane), while the other side is formed by electrical charge, e.g., electrons or holes in the 2D material. He et al. recently demonstrated an in–situ fabrication of K^+–ISEs, on a Si/SiO_2 wafer, which used inkjet printing technique for efficient integration of graphene as transducer and electronic conductor in potentiometric sensors.[262]

Another approach to achieve high sensitivity to electrolytes can be realized through the development of ion-sensitive field effect transistors (ISFET).[853-854] However, the practical utility of Si-based ISFET is often limited by the migration of ions (e.g., H^+, OH^-) into the oxide and their accumulation at the SiO_2/Si interface. This effects cause alteration in the threshold voltage of the FET devices leading to the degradation of the device with repeated usage. Graphene's impermeability to ions opens a wide range of exciting opportunities in the development of ISFETs. [854-858] Chemical vapor deposited graphene sandwiched with valinomycin based membrane coating in ISFET configuration was capable of detecting K^+ ions at 1 μM concentrations in the 1 μM – 20 mM range.[859] The same sensor demonstrated high selectivity to K^+ with respect to common biological interferants Na^+ and Ca^{2+} with retention of performance over two-months testing period.

Mao et al. fabricated a FET device using rGO nanosheets as the sensing channel, and ferritin as the specific detection probe for orthophosphate ions.[860] This sensor could detect orthophosphate ions with detection limit of 26 nM, and good selectivity in the presence of Cl^-, SO_4^{2-} and CO_3^{2-}. Chen and co-workers showed that the FET devices composed of rGO functionalized with calmodulin (Ca^{2+} binding protein) can detect calcium at 0.1 – 1 μM levels.[861] The binding of Ca^{2+} onto rGO, can be attributed to the field-effect modulation of rGO-FETs introduced by the positively charged ions. The same device demonstrated good selectivity to Ca^{2+} against other interfering ions including Na^+ and K^+. Sensitive detection of Na^+ was realized through integrating mechanically exfoliated graphene into the FET device configuration. [862] The fabricated device was capable of detecting Na^+ ions in solutions over a wide range of concentrations ranging from 1.0 nM to 1.0 mM. Exposure to Na^+ modulates electrical potential of graphene channels, leading to shifts toward a negative direction of the transfer curves of the device with increasing Na^+ concentration. This effect was attributed to the accumulation of Na^+ on the graphene channel.[862] Recently, Hall–effect ion sensor based on guanine-rich DNA immobilized on the surface of graphene was used for sensitive detection of K^+.[863] The resulting devices responded linearly in the 1 nM – 10 μM concentration range with high selectivity against other alkali cations including Na^+, Mg^{2+}, Ca^{2+}, Fe^{3+}, Zn^{2+}, NH_4^+, and Mn^{2+} ions. High affinity of the developed sensor to K^+ was attributed to the presence the guanine-rich DNA.

Despite many improvements and large promise in the application of graphene–based materials as either a transducer, molecular scaffold or recognition element in electrochemical sensing of ions, there are several challenges that require to be addressed. *First*, the impact of the structural and compositional defects and chemical functionalization of graphene on the electrical properties and the sensing performances of the fabricated analytical devices renders further investigation. Therefore, novel chemical strategies are required to tailor the physio–chemical properties of graphene, and consequently to induce the desired sensing characteristics for targeted applications. *Second*, interfacing graphene–based materials with other components (e.g., electrodes, substrates) within functional sensing devices will remain an important aspect to achieve flexible, miniaturized, and fully integrated electrochemical ion sensors. *Third*, scalable and cost–effective manufacturing strategies with high degree of control over the structure and properties of graphene–based materials need to be developed if such systems were employed for practical sensing applications. Regardless of these challenges, graphene holds a great promise as active component for applications in sensing industry.

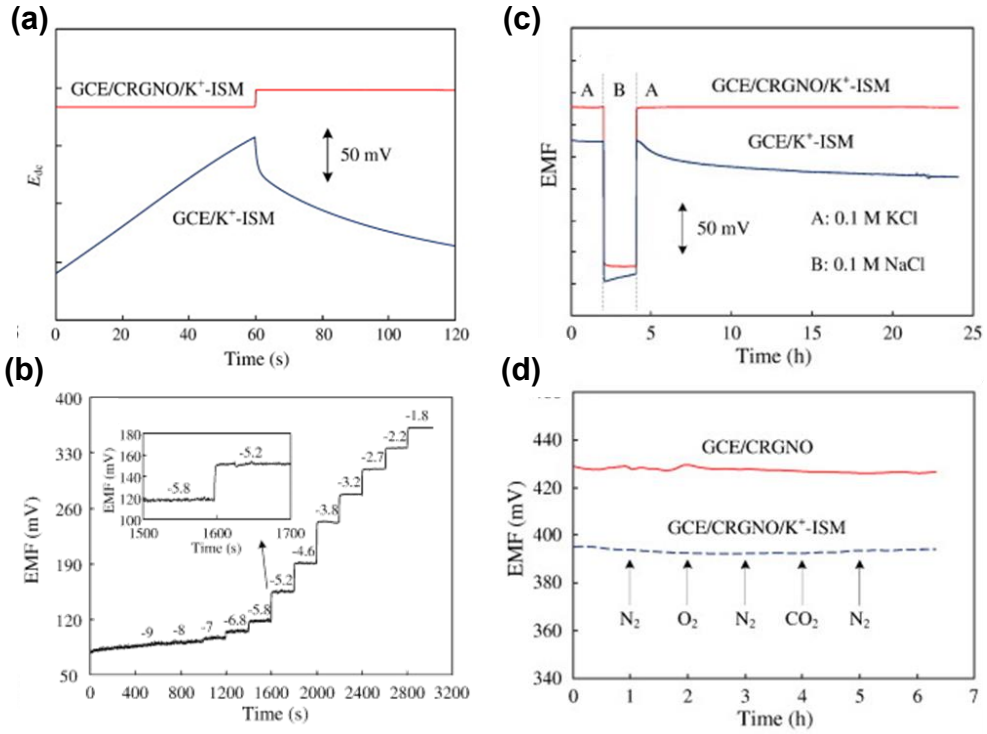

Figure 46. (a) Chronopotentiograms for GCE/K^+–ISM and GCE/rGO/K^+–ISM recorded in 0.1 M KCl solution. The applied current is + 1 nA for 60 s and –1 nA for 60 s. (b) EMF measurements recorded for increasing the concentration of K^+ in the solution, *inset*: expansion of the selected range. (c) Water layer test for the GCE/K^+–ISM and GCE/rGO/K^+–ISM, the measurements were switched between 0.1 M KCl and 0.1 M NaCl. (d) Sensitivity to O_2 and CO_2 in 0.1 M KCl solution for the GCE/rGO (solid line) and GCE/rGO/K^+–ISM (dashed line).[261, 852]Reproduced with permission from Ref. [261, 852] Copyright 2011 Elsevier B.V.

4.3.2. Black Phosphorous

Layered BP exhibits high carrier mobility[864-865], (1,000 $cm^2\ V^{-1}\ s^{-1}$) and larger current on/off ratio in field–effect transistors [866-867] (1×10^3 to 1×10^5) and comparable or even stronger molecule adsorption abilities than those of graphene and MoS_2.[98] These properties, together with its extremely large surface–to–volume ratio, make BP a promising nanomaterial for chemical ion sensing. Cao and co–workers integrated BP into FET device through mechanical exfoliation by scotch tape–based method.[198] The resulting device was used for label–free trace detection of Hg^{2+} with LODs of 0.01 ppb and response time under 3 s. The sensing mechanism of BP was attributed to the carrier density variation due to surface charge gating effect. Zhang et al. also fabricated a FET device in which mechanically exfoliated BP was integrated between two Ti/Pd electrodes (**Figure 47a**) and subsequently covered with ion–selective membranes.[868] The BP sensors were then employed for multiplex detection of environmental pollutants, including As^{3+}, Pb^{2+}, Cd^{2+}, and Hg^{2+} with sub–ppm sensitivity to Pb^{2+} ions (**Figure 47b**). In each situation, the ion selective membrane was used as selective barrier that allowed diffusion of only targeted species towards the surface of BP, and thus modulated the hole density and conductance of BP. Recently, a few layer BP film has been used as ion–to–electron transducer in ISEs. The authors observed that the presence of BP diminished the charge transfer resistance across the ion–selective membrane/BP/solid contact interfaces, and lead to increased signal stability of Ca^{2+}–ISEs.[869] Recently, BP functionalized with ionophore was used to develop flexible sensor array for multiplex detection of Hg^{2+}, Cd^{2+}, Pb^{2+}, and Na^+.[870] The resulting device demonstrated high sensitivity to Hg^{2+} with LODs estimated at 1 μg/L, and short response time. demonstrated excellent mechanical flexibility (strain limits of 1%) and stability (bending 500 times). Small strain variation from 0.33% to 0.16% led to 175% improvement in sensitivity due to Schottky barrier modulation. The authors also demonstrated the capability of detecting Cd^{2+} ions in tap water samples and Na^+ in human sweat.

As shown above, BP–based materials represent a conceptually new class of 2D nanostructures with great potential utility in the development of ion sensing technologies. Without a doubt, the full potential of BP based ion sensors is far from being reached. Currently, the exploration of BP–based ion sensing devices is largely hindered by limited stability of BP to aerobic and aqueous environment that ultimately lead to material degradation. Therefore, considerable efforts must be devoted to improving stability of BP either through the use of protective coatings/inert masks that directly reduce the impact of outside environment or by altering its surface chemistry using novel synthetic approaches. Because of its tunable bandgap and anisotropic electronic properties, many challenges remain in finding

new synthetic routes that offer good degree of control over the size, composition, thickness, and number of incorporated defects. And finally, further experimental and computational mechanistic investigation of structure–property relationship of BP is required to gain more understanding about the role of this material in ion sensing, which ideally will guide the design of future sensing technologies.

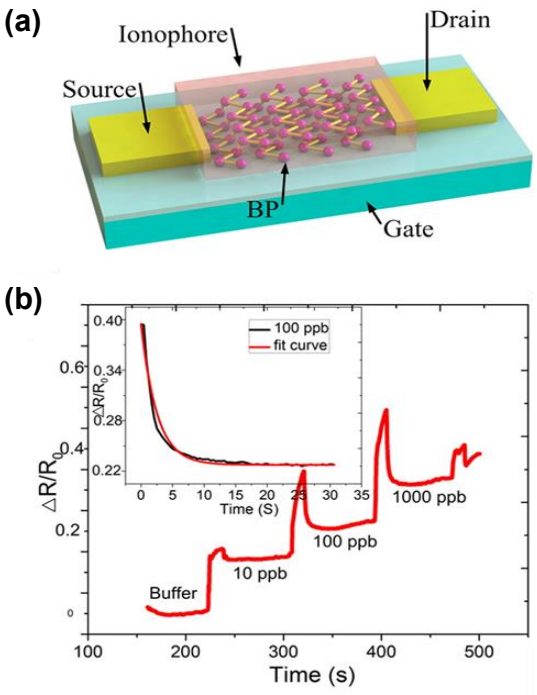

Figure 47. (a) Schematic view of a BP sensor in which the BP flake is covered with ionophore film. (b) Relative resistance change ($\Delta R/R_0$) of BP versus time (V_{GS} = 0 V) under the different concentrations of Pb^{2+}. The curve fit in the inset demonstrates the time constant, τ, is 5 s.[868] Reproduced from Ref. [868] Copyright 2015 American Chemical Society.

4.3.3. Transition Metal Dichalcogenides

Inspired by the use of graphene as recognition elements and transducers in electrochemical sensors,[321, 821] 2D TMDs have been more extensively employed in the development of sensing devices due to their good conductivity, large surface area, fast electron transfer kinetics, high signal/noise ratio, and more importantly, their feasibility for forming composites.[871] Zhou et al. fabricated MoS_2–Au nanoparticle–DNA functionalized on the surface of Si/SiO_2 FET device for determination of Hg^{2+} (**Figure 48a**).[872] In this configuration, the MoS_2 TMD film served as the conducting channel with the dispersed Au nanoparticles acting as molecular anchors for the immobilization of Hg^{2+} specific DNA probes. The analytical measurements were enabled by monitoring the change of the source–drain current as a function of Hg^{2+} concentration in the p–type MoS_2 channel (**Figure 48b**). The developed biosensor displayed LODs of 0.1 nM and good selectivity to other ionic interferants. Jiang and co–workers integrated thin layers of MoS_2 into the FET device and used it as an electrochemical sensor for the determination of Hg^{2+} ions in solutions (**Figure 48c–d**).[873] They observed that Hg^{2+} can readily coordinate with the sulfur sites on the surface of MoS_2, producing a p–type doping effect, and consequently modulating the electron transport in the 2D layer. The resulting sensors exhibited low detection limits (30 pM) and good specificity to Hg^{2+} in the presence of 15 ionic interferants demonstrating potential utility of the sensors for mercury determination **(Figure 48e)**. Silver/halloysite nanotube/molybdenum disulfide modified carbon paste electrodes were recently realized as amperometric sensors for nitrite detection.[874] The resulting devices could detect NO_2^- in the 2 μM to 425 μM concentration range with detection limits of 0.7 μM and high selectivity against NaCl, $CuSO_4$, $KClO_4$, K_2CO_3, $Al(NO_3)_3$, CH_3COONa, KIO_3, urea, ascorbic acid and glucose. The same ion–sensor retained 95.5% of its initial current response after the three weeks testing period with 96.5–99.6% recoveries in nitrite determination in tap water samples.

The application of TMDCs materials in the electrochemical sensing of ions have recently gained rapid momentum, due to their intriguing physical, chemical and electronic properties. Nonetheless, this application area is still within its early stages, and therefore it faces many challenges before their practical implementation in sensing devices. From the materials standpoint, scalable and controlled synthesis of 2D TMDCs with predictable and desired structures remains difficult to achieve using available synthetic methods. Therefore, novel synthetic approaches are needed to fabricate uniform 2D TMDCs materials with consistent properties. In addition, further research focused on the chemical functionalization of TMDCs structure to induce selectivity towards targeted analytes should be pursued, thus potentially opening the wide window for further implementation of these materials in ion sensing applications.

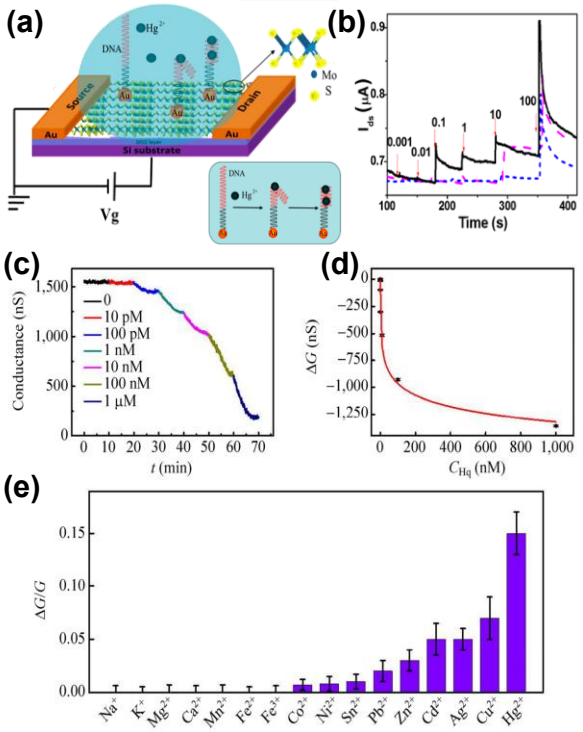

Figure 48. (a) FET sensor platform was based on the hybrid structure. The formation of T–(Hg^{2+})–T chelates, through reactions between Hg^{2+} and the thymidine of the DNA molecules on the Au NPs, leading to (b) the change in the MoS_2 electrical conductivity as a sensor signal.[872] Reproduced from Ref. [872] Copyright 2016 American Chemical Society. (c) Real–time electrical readout of Hg^{2+} ion signal by MoS_2 sensor. Real–time electrical measurement at different concentrations of Hg^{2+} ions. (d) Calibration curve: conductance change versus Hg^{2+} ion concentration. (e) The red line is the fitted curve on a natural log scale. Selectivity of the MoS_2 mercury (II) sensor.[873] Reproduced with permission from Ref. [873] Copyright 2015 Springer Nature.

4.3.4. Other 2D Materials

The promising properties of 2D metal oxide nanostructures such as high electrochemical stability and large adsorption capacity to ions have shown a great promise in the development of electrochemical sensing platforms.[875] For example, glassy carbon electrodes modified with porous Co_3O_4 microsheet/Nafion composite were capable of sensing Pb^{2+} in the 0.05–0.275 μM concentrations with sensitivity of 71.57 μA μM^{-1} and detection limit of 0.018 μM.[876] High sensitivity of the fabricated sensor was attributed to presence of nanochannel in the structure of Co_3O_4 that are readily accessible for the diffusion of Pb^{2+} ions providing large available surface area for metal crystal growth. In a recent study, further improvements in analytical performance for the determination of Pb^{2+} ions in real water were achieved through electrodeposition of Co_3O_4 nanosheets directly onto the indium tin oxide (ITO) electrodes.[877] The resulting electrodes, using DPASV, were capable of detecting Pb^{+2} in 1 – 100 μg L^{-1} concentration range with the LOD of 0.52 μg L^{-1} and high selectivity against Ca^{2+}, Mg^{2+}, Fe^{2+}, Zn^{2+} Mn^{2+} ionic interferents. Whereas, Lin and coworkers used ultrathin two-dimensional TiO_2 nanosheets doped with fluorine, in layered electrode architecture (TiO_2/GCE) for the detection of Pb^{2+} ions.[878] The fabricated electrodes exhibited 53.63 μA/μM sensitivity towards Pb^{2+} ions in the concentration range of 0.2 – 1.4 μM, the LOD of 7 nM, and high selectivity over Al^{3+}, Mg^{2+}, Na^{+}, NH^{4+}, K^{+}, Ca^{2+}, Cl^{-}, PO_4^{3-}, SO_4^{2-}, and NO^{3-} interferents. Theoretical calculations revealed that fluorine doping could enhance the adsorption energy of Pb^{2+} on the TiO_2 nanosheets, and increase the ion loading capacity. In addition, the authors observed that F doping further facilitated the electron transfer to the electrode, which led to improvements in sensitivity for Pb^{2+} determination.[878]

Metal–organic frameworks have emerged as a unique class of multifunctional materials in electrochemical sensors due to their large surface area, tunable bandgap, and compositional and structural diversity accessible through bottom-up self-assembly. Conductive 2D MOFs (Ni_3HHTP_2, Cu_3HHTP_2, and Co_3HHTP_2) drop–cast onto the GCE and covered with a layer of polymeric ion-selective membranes were successfully utilized as ion-to-electron transducers in potentiometric detection of K^+ and NO_3^- ions (**Figure 49**).[879] The resulting devices demonstrated excellent signal stability of 14.6 μV s^{-1} under polarizing conditions of 1 nA, low long-term drift (11.1 μV s^{-1}), and high sensitivity to K^+ and NO_3^- with the detection limit of $6.31 \pm 0.01 \times 10^{-7}$ M and $5.01 \pm 0.01 \times 10^{-7}$ M, respectively. The excellent analytical performance of fabricated sensors was attributed to large double-layer capacitance (204.1 μF) in MOF-coated electrodes. The authors proposed that ion-to-electron transduction proceeds through the formation of electrical double layer in the case of Ni_3HHTP_2 and Co_3HHTP_2 MOFs with an additional contribution from redox doping/un–doping in Cu_3HHTP_2 MOFs.

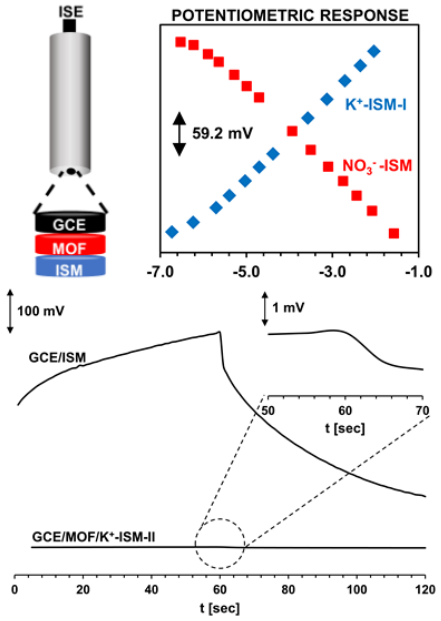

Figure 49. Schematic representation of layered electrode architecture used for potentiometric measurements.[879] In this configuration, a thin film of 2D MOF was drop-casted directly on the top of a glassy carbon electrode (GCE), and then covered with an ion-selective membrane (ISM) to enable potentiometric ion sensing. Potentiometric response of GCE/Ni_3HHTP_2 MOF/ISM devices to K^+ (blue diamonds) and NO_3^- (red squares) ions. Chronopotentiograms obtained during the analysis of K^+–ISM–II based ISEs under polarizing conditions. (top) K^+–ISM–II applied directly onto a GCE contact without the MOF as undelaying conductive layer; (bottom) GCE/Ni_3HHTP_2MOF/K^+–ISM–II electrode. Inset demonstrates a close-up of response obtained for the GCE/Ni_3HHTP_2 MOF/K^+–ISM-II. Experimental conditions: applied current +1 nA for 60 seconds followed by −1 nA for 60 seconds in 0.1 M KCl.[879] Reproduced from Ref. [879] Copyright 2018 American Chemical Society.

The emerging properties of 2D nanomaterials such as large surface area, tunable conductivity, low-dimensionality or synthetic accessibility carry great promise in the development of the next generation of electrochemical sensing devices for ion determination.[73, 321] In particular, high degree of synthetic modularity in MOF enables incorporation of functional groups or ion chelators that can impart high selectivity towards targeted ionic species.[89] Interfacing these materials with polymeric membranes, ion–receptors, electrodes and flexible substrates will become crucial to

fabricate portable, miniaturized, robust, and selective electrochemical ion sensors. To this date, only a handful of metal oxides and 2D conductive MOFs have been explored in ion sensing applications indicating large potential for their applications as active components in ion sensing devices. The unique combination of structural tunability together with high electrical conductance, which are critically needed in the electrically–transduced devices, will ideally lead to more applications of these materials in sensing of ionic species in the future.

Table 5. Summary of Sensing Performances for Ions by 2D Materials.

Specific Analyte	Material	Architecture	Readout/ Method	LOD	Experimental range	Sensing environment	Notes	Ref
Ag^{+}	rGO–CsA	rGO–CsA/GCE	DPASV	1.0×10^{-9}	1.0×10^{-8}–2.0×10^{-4} M	HNO_3 (0.01 M)	Cd^{2+}, Cu^{2+}, Zn^{3+}, Ni^{2+}, Cr^{6+}, Pb^{2+}, Hg^{2+}, Fe^{3+}	844
As^{3+}	GO–LEU–Nafion	GO–LEU–Nafion/Au	CV	6.7×10^{-6} M	6.7×10^{-5}–6.7×10^{-4} M	CB (0.1 M, pH = 5.0)/River water	Zn^{2+}, Pb^{2+}, Hg^{2+}, Cd^{2+}	851
Ca^{2+}	BP	BP/Ca^{2+}–ISM/GCE	E	4.0×10^{-7} M	1.0×10^{-1}–1.0×10^{-6} M	DI/Wine samples	H^{+}, Na^{+}, K^{+}, Mg^{2+}	869
Ca^{2+}	rGO-calmodulin	FET: H_2O/SiO_2/rGO-calmodulin/Ag/Ag	I	1 nM	1–28 nM	Lake water, DI water	Mg^{2+}	861
Ca^{2+}	rGO/Ca^{2+}–ISM	rGO/Ca^{2+}–ISM/GCE	E	6.3×10^{-7} M	3.2×10^{-3}–1.0×10^{-5} M	DI	Ba^{2+}, Na^{+}, Li^{+}, Mg^{2+}, K^{+}	263
Cd^{2+}	Gr–Bi	Gr–Bi/CPE	SWASV	0.07 μg L^{-1}	0.10–50.0 μg L^{-1}	HCl (0.05 M)/Tap and sea water	Pb^{2+}	845
Cd^{2+}	Gr–Cys–AuNP	Gr–Cys–AuNP/GCE	SWASV	0.10 μg L^{-1}	0.50 μg L^{-1}–40 μg L^{-1}	ABS (0.1 M, pH = 4.5, Bi^{3+})/River water	Co^{2+}, Fe^{3+}, Ni^{2+}, Cr^{3+}, Zn^{2+}, Cu^{2+}, In^{3+}, Sn^{2+}	826
Cd^{2+}	Gr–Nafion	Gr–Nafion/Hg	SWASV	0.08 μg L^{-1}	1.0 μg L^{-1}–7.0 μg L^{-1}	ABS (0.1 M, pH = 4.5)/Wetland water	Pb^{2+}, Cu^{2+}, Zn^{2+}	830
Cd^{2+}	Gr–Nafion–Bi	Gr–Nafion–Bi/GCE	DPASV	30 μg L^{-1}	0.5 μg L^{-1}-50 μg L^{-1}	ABS (0.1 M, pH = 4.5)/Lake water	Triton X, SDS, CTAB	829
Cd^{2+}	rGO–AlOOH	rGO–AlOOH/GCE	SWASV	3.52×10^{-11} M	0.2–0.8 μM	ABS (0.1 M, pH = 6.0)/Real water	K^{+}, Ca^{2+}, Na^{+}, Mg^{2+}, Al^{3+}, Cu^{2+}, Hg^{2+}, Zn^{2+}, Cl^{-}, NO_3^{-}, SO_4^{2-}, PO_4^{3-}	847
Cd^{2+}	rGO–Bi	rGO–Bi/Au	SWASV	1.0 μg L^{-1}	1.0 μg L^{-1}–120.0 μg L^{-1}	ABS (0.1 M, pH = 4.5)/Drinking water	Pb^{2+}	828
Cd^{2+}	rGO–SnO_2	rGO–SnO_2/GCE	SWASV	1.0×10^{-10} M	0.3–1.2 μM	ABS (0.1 M, pH = 5.0)	Pb^{2+}, Cu^{2+}, Hg^{2+}	837
Cu^{2+}	GO-L-cystene	GO-L-cystene/Au	SWASV	1.2 ppb	1.2–200 pbb	ABS (pH = 7)	N/A	832
Cu^{2+}	GO-Ph	GO-Ph/Au	OSWV	1.7×10^{-9} M	$1.7\text{-}100\times10^{-9}$ M	ABS (pH= 7)	Zn^{2+}, Fe^{3+}, Cd^{2+}, Cr^{6+}, Cu^{2+}, Hg^{2+}	810
Cu^{2+}	Gr–Nafion	Gr–Nafion/Hg	SWASV	0.13 μg L^{-1}	20.0 μg L^{-1}–190.0 μg L^{-1}	ABS (0.1 M, pH = 4.5)/Wetland water	Pb^{2+}, Cd^{2+}, Zn^{2+}	830
Cu^{2+}	rGO-pyrene	rGO-pyrene/Au	OSWV	1.5×10^{-9} M	1.5–20 $\times10^{-9}$ M	ABS (pH = 7)	Cd^{2+}, Co^{2+}, Ni^{-2+}, Zn^{2+}, Ca^{2+}, Mg^{2+}	831
Cu^{2+}	rGO–SnO_2	rGO–SnO_2/GCE	SWASV	2.3×10^{-10} M	0.3–1.2 μM	ABS (0.1 M, pH = 5.0)	Pb^{2+}, Hg^{2+}, Cd^{2+}	837
Hg^{2+}	BP	FET: HfO_2/PET/BP-ISM/Ti-Au/Ti-Au	I	1 μg/L	0.03–100 mg/L	Tap water	Cd^{2+}, Pb^{2+}, Na^{+}, K^{+} (array)	870
Hg^{2+}	Gr-SAM	FET: Si/SiO_2/G-SAM/Au-Cr/Au-Cr	I	10 ppm	N.R.	N.R.	N.R.	842
Hg^{2+}	Gr-SAM	FET: Si/SiO_2/Gr-SAM/Au-Cr/Au-Cr	I	10 ppm	N.R.	DI water.	Pb^{2+}	843
Hg^{2+}	Gr–AuNP–CT	Gr–AuNP–CT/GCE	SWASV	8.0×10^{-12} M	4.0×10^{-11} M – 2.5×10^{-10} M; 5.0×10^{-10} M –3.0×10^{-7} M	HCl (1 M)/River water	Cd^{2+}, Cu^{2+}, Zn^{3+}, Co^{2+}, Fe^{3+}, I^{-}	836
Hg^{2+}	Gr–DNA	Gr–DNA/GCE	DPV	5 pM	25 pM–10 μM	Tris–HCl (0.05 M, pH = 7.4)/River water	Na^{+}, K^{+}, Ba^{2+}, Mg^{2+}, Zn^{2+}, Pb^{2+}, Mn^{2+}, Co^{2+}, Ni^{2+},	839

Specific Analyte	Material	Architecture	Readout/ Method	LOD	Experimental range	Sensing environment	Notes	Ref
Hg^{2+}	MoS_2	FET: $Si/SiO_2/MoS_2/Ni–Au/Ni–Au$	I	30 pM	0.0–1.0 μM	DI	Fe^{2+}, Fe^{3+}, Al^{3+}, Mo, Mn, As, Cr, Cd, Cu, V, Ag K^+, Ca^{2+}, Na^+, Mg^{2+}, Mn^{2+}, Cu^{2+}, Hg^{2+}, Ag^+, Cd^{2+}, Zn^{2+}, Pb^{2+}, Sn^{2+}, Fe^{2+}, Fe^{3+}, Ni^{2+}, Co^{2+},	873
Hg^{2+}	MoS_2–DNA–AuNP	FET: $Si/SiO_2/MoS_2$–DNA–AuNP/Au/Au	I	0.1 nM	0.1–10 nM	DI	As^{5+}, Ca^{2+}, Cd^{2+}, Cu^{2+}, Fe^{3+}, Mg^{2+}, Na^+, Pb^{2+}, Zn^{2+}	872
Hg^{2+}	rGO–SnO_2	rGO–SnO_2/GCE	SWASV	2.8×10^{-10} M	0.3–1.2 μM	ABS (0.1 M, pH = 5.0)	Pb^{2+}, Cu^{2+}, Cd^{2+}	837
Hg^{2+}	rGO-metal-lothionein	FET: H_2O/SiO_2/rGO–metallothionein /Ag/Ag	I	1 nM	1–28 nM	Lake water, DI water	Cd^{2+}	861
Hg^{2+}	rGO-DNA	Au/rGO-DNA/Au	I	5×10^{-9}	5×10^{-9} M–1.02×10^{-6} M	River water/ DI water	Na^+, K^+, Li^+, Cd^{2+}, Zn^{2+}, Co^{2+}, Mg^{2+}, Cu^{2+}, Pb^{2+}, Ag^+, Ca^{2+}, Mn^{2+}, Fe^{3+}	841
Hg^{2+}	rGO-PF	FET: PBS/SiO_2/rGO-PF/Au-Cr/Au-Cr	I	1×10^{-13} M	1×10^{-13} M–1×10^{-9} M	PBS (pH = 7.4)	Zn^{2+}, Ce^{2+}, Na^+, Ni^{2+}, Pb^{2+}, Cu^{2+}, Co^{2+}, li^+	815
Hg^{2+}	rGO-py-rene-glu-cose	Au/rGO-pyene-glucose/Au	I	1×10^{-10}	$1–40\times10^{-10}$	DI water	Cd^{2+}, Zn^{2+}, K^+, Na^+, Cu^{2+}, Fe^{3+}	840
Hg^{2+}	GO-Ph	GO-Ph/Au	OSWV	1.7×10^{-9} M	$1.7–150\times10^{-9}$ M	ABS (Ph = 7)	Zn^{2+}, Fe^{3+}, Cd^{2+}, Cr^{6+}, Cu^{2+}, Hg^{2+}	833
Hg^{2+}	GO-L-cystene	GO-L-cystene/Au	SWASV	0.8 ppb	0.8–10 ppb	ABS (pH = 7)	N/A	832
K^+	Gr	FET: Si/SiO_2/Gr-K^+-ISM/Ti-Ni/Ti-Ni	I	1 μM	1 μM–20 mM	Tris-HCl (pH = 7.4)	Na^+, Ca^{2+}	859
K^+	Gr	Gr/K^+–ISM/GCE	E	1.0×10^{-5} M	1.0×10^{-1}–3.2×10^{-5} M	DI	Ca^{2+}, Na^+, Li^+, Mg^{2+}, NH_4^+	852
K^+	Gr	Gr/K^+–ISM/Gr	E	7.0×10^{-6} M	1.0×10^{-1}–1.0×10^{-5} M	DI	Ca^{2+}, Na^+, Mg^{2+}	262
K^+	Gr-DNA	Hall-device: Si/SiO_2/G-DNA/ rGO/K^+–ISM/GCE	Hall-effect	1 nM	1 nM–10 μM	TE buffer (pH = 8)	Na^+	863
K^+	rGO		E	6.3×10^{-7} M	1.0×10^{-1}–1.6×10^{-6} M	DI	Ca^{2+}, Na^+, Li^+, Mg^{2+}	261
K^+	Ni_3HHTP_2	ISM/Ni_3HHTP_2/GCE	E	$6.76 \pm 0.03 \times 10^{-6}$ M	10^{-7}–5×10^{-1} M	DI	Na^+, NH^{4+}, Ca^{2+}	879
HPO_4^{2-}	rGO-ferri-tin	FET: Si/SiO_2/rGO-ferritin/Au/Au	I	5 nM	5 nM–10 μM	DI water (pH = 7.5–8.9)	Cl^-, SO_4^{2-}, CO_3^{2-}	860
Na^+	Gr	FET: Si/SiO_2/G/Ni-Au/Ni-Au	I	1 nM	1 nM–1 mM	Tris-HCl	N.R.	862
Pb^{2+}	BP	FET: Si/SiO_2/BP–Hg^{2+}–ISM/Ti–Pd/Ti–Pd	I	0.48×10^{-8} M	4.8×10^{-8}–4.8×10^{-4} M	ABS (0.1 M, pH = 4.6)	Hg^{2+}, Cd^{2+}, AsO_2^-	868
Pb^{2+}	BP	FET: Si/SiO_2/BP–Hg^{2+}–ISM/Ti–Pd/Ti–Pd	I	0.48×10^{-8} M	4.8×10^{-8}–4.8×10^{-4} M	ABS (0.1 M, pH = 4.6)	Hg^{2+}, Cd^{2+}, AsO_2^-	868
Pb^{2+}	GO-L-cystene	GO-L-cystene/Au	SWASV	0.4 ppb	0.4–20 ppb	ABS (pH = 7)	Zn^{2+}, Fe^{3+}, Cd^{2+}, Cr^{6+}, Cu^{2+}, Hg^{2+}	832
Pb^{2+}	GO-Ph	GO-Ph/Au	OSWV	3×10^{-10} M	$3–500\times10^{-10}$ M	ABS (Ph = 7)	Zn^{2+}, Fe^{3+}, Cd^{2+}, Cr^{6+}, Cu^{2+}, Hg^{2+}	833
Pb^{2+}	Gr–Bi	Gr–Bi/CPE	SWASV	0.04 μg L^{-1}	0.10–50.0 μg L^{-1}	HCl (0.05 M)/Tap and sea water	Cd^{2+}	845
Pb^{2+}	Gr–Cys–AuNP	Gr–Cys–AuNP/GCE	SWASV	0.05 μg L^{-1}	0.50 μg L^{-1}–40 μg L^{-1}	ABS (0.1 M, pH = 4.5, Bi^{3+})/River water	Co^{2+}, Fe^{3+}, Ni^{2+}, Cr^{3+}, Zn^{2+}, Cu^{2+}, In^{3+}, Sn^{2+}	826
Pb^{2+}	Gr-DNA-AuNP	FET: HEPEs/SiO_2/Gr-	I	2×10^{-11}	1×10^{-7}	HEPEs buffer	Cu^{2+}, Ca^{2+}, Cd^{2+}, Mg^{2+}, Ni^{2+}, Zn^{2+}	827

Specific Analyte	Material	Architecture	Readout/ Method	LOD	Experimental range	Sensing environment	Notes	Ref
Pb^{2+}	Gr–Nafion	DNA-AuNP/Ag/Ag Gr–Nafion/Hg	SWASV	0.07 μg L^{-1}	1.0 μg L^{-1}–7.0 μg L^{-1}	ABS (0.1 M, pH = 4.5)/Wetland water	Cd^{2+}, Cu^{2+}, Zn^{2+}	830
Pb^{2+}	Gr–Nafion–Bi	Gr–Nafion–Bi/GCE	DPASV	1.5 μg L^{-1}	0.5 μg L^{-1}–50 μg L^{-1}	ABS (0.1 M, pH = 4.5)/Lake water	Triton X, SDS, CTAB	829
Pb^{2+}	Gr-SAM	FET: Si/SiO_2/Gr-SAM/Au-Cr/Au-Cr	I	10 ppm	N.R.	DI water.	Hg^{2+}	843
Pb^{2+}	rGO-pyrene	rGO-pyrene/Au	OSWV	1.5×10^{-9}	1.5–20 $\times10^{-9}$	ABS (pH = 7)	Cd^{2+}, Co^{2+}, Ni^{-2+}, Zn^{2+}, Ca^{2+}, Mg^{2+} K^{+}, Ca^{2+}, Na^{+},	831
Pb^{2+}	rGO–AlOOH	rGO–AlOOH/GCE	SWASV	9.32×10^{-11} M	0.2–0.8 μM	ABS (0.1 M, pH = 6.0)/Real water	Mg^{2+}, Al^{3+}, Cu^{2+}, Hg^{2+}, Zn^{2+}, Cl^{-}, NO_3^{-}, SO_4^{2-}, PO_4^{3-}	847
Pb^{2+}	rGO–Bi	rGO–Bi/Au	SWASV	0.4 μg L^{-1}	1.0 μg L^{-1}–120.0 μg L^{-1}	ABS (0.1 M, pH = 4.5)/Drinking water	Cd^{2+}	828
Pb^{2+}	rGO–PPy	rGO–PPy/GCE	SWASV	4 pM	5 nM–60 nM	HCl/KCl (0.1 M, Hg^{2+}, 1 μM)	Cu^{2+}, Mg^{2+}, Cd^{2+}, Zn^{2+}, As^{3+}	846
Pb^{2+}	rGO–SnO_2	rGO/SnO_2/GCE	SWASV	1.8×10^{-10} M	0.3–1.2 μM	ABS (0.1 M, pH = 5.0)	Cu^{2+}, Hg^{2+}, Cd^{2+}	837
Pd^{2+}	rGO–SbNP	rGO–SbNP/GCE	DPCSV	0.45 pg L^{-1}	40–400 pg L^{-1}	ABS (0.2 M, pH = 5.2)/Dust samples	Fe^{2+}, Ni^{2+}, Co^{2+}, Na^{+}, Cu^{2+}, SO_4^{2-}, PO_4^{3-}	848
Pd^{2+}	Co_3O_4	Co_3O_4-nafion/GCE	SWASV	0.018 μM	0.05–0.275 μM	0.1 M acetate buffer (NaAc–HAc, pH 5.0)	N/A	853
Pd^{2+}	Co_3O_4	Co_3O_4/ITO	DPASV	0.52 μg L^{-1}	1–100 μg L^{-1}	0.1 M NaAc–HAc buffer, 400 μg L^{-1} bismuth, pH 5.0	Ca^{2+}, Mg^{2+}, Fe^{2+}, Zn^{2+} Mn^{2+}	877
Pd^{2+}	TiO_2	TiO_2/GCE	SWASV	7nM	0.2–1.4 μM	0.1 M NaAc-HAc solution, pH 5.0	Al^{3+}, Mg^{2+}, Na^{+}, NH^{4+}, K^{+}, Ca^{2+}, Cl^{-}, PO_4^{3-}, SO_4^{2-}, and NO^{3-}	878
Pt^{2+}	rGO–SbNP	rGO–SbNP/GCE	DPCSV	0.49 pg L^{-1}	0–260 pg L^{-1}	ABS (0.2 M, pH = 5.2)/Dust samples	Fe^{2+}, Ni^{2+}, Co^{2+}, Na^{+}, Cu^{2+}, SO_4^{2-}, PO_4^{3-}	848
Rh^{3+}	rGO–SbNP	rGO–SbNP/GCE	DPCSV	0.49 pg L^{-1}	40–400 pg L^{-1}	ABS (0.2 M, pH = 5.2)/Dust samples	Fe^{2+}, Ni^{2+}, Co^{2+}, Na^{+}, Cu^{2+}, SO_4^{2-}, PO_4^{3-}	848
UO_2^{2+}	Gr–COOH	Gr–COOH/GCE	SQW	5.0×10^{-8} M	5.0×10^{-8}–5.0×10^{-6} M	Tris–HCl (0.05 M, pH = 5.0)	Cd^{2+}, Ca^{2+}, Sr^{2+}, Co^{2+}, Mg^{2+}, Pb^{2+}, Fe^{3+}	849
Zn^{2+}	Gr–Nafion	Gr–Nafion/Hg	SWASV	0.07 μg L^{-1}	1.0 μg L^{-1}–7.0 μg L^{-1}	ABS (0.1 M, pH = 4.5)/Wetland water	Pb^{2+}, Cu^{2+}, Cd^{2+}	830
NO_2^{-}	MoS_2-halloysite-NT-Ag	Pt/CPE/MoS_2-halloysite-NT-Ag	I	0.7 μM	2 μM–425 μM	0.1 M PBS (pH = 4)	Cl^{-}, SO_4^{2-}, ClO_4^{-}, CO_3^{2-}, NO_3^{-}, IO_3^{-}, urea, AA, glucose	874
NO_3^{-}	Ni_3HHTP_2	ISM/Ni_3HHTP_2/GCE	E	$5.01 \pm 0.01 \times 10^{-7}$ M	10^{-7}–5×10^{-1} M	DI	N/A	879

Note: FET components are described in the following order: gate electrode/insulator/channel material/source electrode/drain electrod.

4.4. Detection of Biomolecules

The use of 2D materials in the context of electrochemical sensors has been widely reported due to their inherent properties, which include enhanced mass transport, large accessible surface area, high sensitivity and improved signal to noise ratio.[321] 2D nanomaterials can be used either as molecular carriers for loading signal labels or directly as recognition elements for sensitive and selective detection of biologically relevant molecules including vitamins, metabolites, neurotransmitter, biomarkers, and others.[7, 73, 121, 282, 321, 880-882] The application of 2D nanostructures can also improve heterogenous electron transfer rates if integrated as functional materials on electrode surfaces. More recently, 2D nanomaterials are being utilized to increase the sensitivity of the electrochemical sensors to target molecules. The following subsections describes the analytical strategies employed to form an electrochemical sensing platform according to their detection mode and 2D material

used for their preparation. Their analytical performance was assessed through various analytical parameters such us sensitivity (detection limits), dynamic range of response, selectivity to interferants and reproducibility, which are commonly used for validation of novel sensing platforms.

4.4.1. Graphene and Graphene Oxides

Great body of literature has been already dedicated to the application of graphene and graphene oxide in the development of electrochemical sensors for the analysis of biologically relevant molecules due to its unique properties such as high surface area, high electrical conductivity, excellent electrochemical stability in aqueous media, and strong mechanical strength.[80, 126, 272, 282-283, 321, 821, 883] Graphene can interact with targeted analytes through π–π stacking, non–covalent interactions and high electrostatic force. The electrochemical properties of graphene, in sensing applications, however are strongly dependent on the ratio of its basal and edge plane content. Typically, graphene containing a low proportion of edge plane sites exhibits slow heterogenous electron transfer rates, and consequently poor electrochemical responses towards various analytes.[821] Graphene can also serve as a molecular scaffold for immobilizing the desired functional groups to target biomolecular analytes, consequently leading to enhancements in the selectivity of a biosensor (**Figure 50**). These sensors are most commonly used for clinical determination of glucose, cholesterol, H_2O_2, dopamine (DA), ascorbic acid (AA), uric acid (UA), β–nicotinamide adenine dinucleotide (NAD^+/NADH), carcinoembryonic antigen (CEA), α–fetoprotein, thrombin, and prostate specific antigen (PSA).[881]

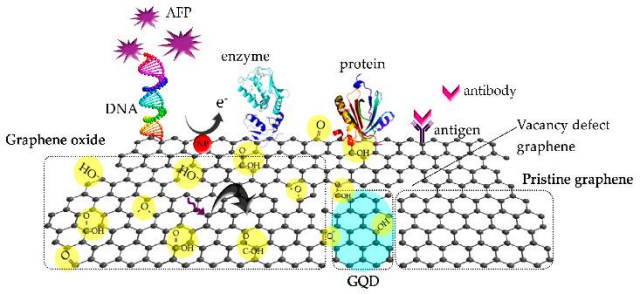

Figure 50. Schematic illustration of the graphene–based materials that can be immobilized with biomolecules as the receptor.[282] Reproduced with permission from Ref. [282] Copyright 2017 MDPI(Basel, Switzerland).

Glucose. Owing to the increasing number of people diagnosed with diabetes every year, the demand for constructing point–of–care portable glucose sensing platforms have also risen.[273] Glucose–selective electrochemical biosensors are most often formed by the immobilization of glucose–specific enzymes such as glucose oxidase (GOD), which can function as either a mediator or recognition element during the sensing process.[273] The two redox–active centers in GOD are wrapped by the protein layer which inhibits the electron transfer between each redox center and the electrode surface. In this situation, Gr can be employed as electrical conductor, which promotes enzyme activity and facilitates electron transfer between the electrode substrate and GOD redox–active centers, thus allowing detection of glucose. Kang and co–workers employed this experimental approach to fabricate rGO–chitosan–GOD modified GCE for sensitive detection of glucose.[884] The resulting biosensors responded linearly in the 0.08 mM–12 mM concentration range with the detection limit of 0.02 mM and an electron transfer rate constant of 2.83 ± 0.18 s^{-1}. The enhanced performance of fabricated biosensor was ascribed to large surface–to–volume ratio and high conductivity of graphene, together with good biocompatibility of chitosan, which enhanced the enzyme absorption, and promoted direct electron transfer between redox enzymes and the surface of electrodes.

Wang and co–workers used nitrogen–doped rGO–Chitosan–GOD/GCE hybrid electrode for glucose biosensing with concentrations as low as 0.01 mM, in the presence of UA and AA interferants.[885] Cai et al. by directly immobilizing GOD onto the surface of GO could detect glucose at concentrations as low as 0.01 mM through bio–electrocatalytic reduction of oxygen.[884] They observed that the native structure and bioactivity of GOD was retained after the successive immobilization on GO. This biosensor also underwent effective direct electron transfer reaction with an apparent rate constant of 2.68 s^{-1}. A Gr–polypyrrole (PPy)–GOD composite was used by Li and coworkers for glucose determination (LOD of 3 μM).[886] The PPy conductive polymer provided excellent conductivity, biocompatibility and enhanced surface–to–volume ratio for Gr–GOD immobilization. Another glucose sensitive polymer–graphene composite was prepared by Zeng et al. through layer–by–layer deposition of alternating layers of Gr sheets modified with pyrene–grafted poly(acrylic acid) (PAA) and poly(ethyleneimine) (PEI).[887] The modified electrodes were then used for selective detection of glucose and maltose through the immobilization of multienzyme system (GOD and glucoamylase) on the surface of Gr nanocomposite. Both sensors exhibited good sensitivity to maltose and glucose with LOD of 1.37 mM and 0.168 mM, respectively. Expanding on this approach, Shan et al. immobilized polyvinylpyrrolidone (PVP)–protected graphene–polyethylenimine–functionalized ionic liquid nanocomposites onto GCE for glucose determination.[888] This biosensor responded linearly to glucose in the range of 2 to 14 mM.

Further improvements in sensitivity to glucose were focused on the enhancements of the electron transfer rates through incorporation of nanomaterials such as Au,[889-890] Pd,[891] Ag,[892] and Pt.[893] For example, Chen et al. used GOD–Au–Gr biosensor to determine blood sugar concentrations in human serum.[889] The detection limit for glucose was found at 8.9 μM, and the linear range of blood sugar concentration was found at 43.6 μM–261.6 μM. Wu et al. lowered the detection limits of glucose down to 0.6 μM through electrochemical deposition of Pt nanoparticles onto rGO.[893] Recently, Park and co–workers integrated a wireless FET device consisting of graphene–Ag NW composite as source and drain electrodes (**Figure 51a–b**), graphene with immobilized GOD as an active sensing channel layer, Cr/Au as interconnect and SU8 as a passivation layer, onto a soft contact lenses, and used it for the in vivo detection of glucose in tears (**Figure 51c**).[894] The resulting sensing device could

selectively respond to glucose in the presence of 50 μM of AA, 10 mM of lactate and 10 mM of UA with the detection limit of 1 μM (**Figure 51d–f**). This wireless contact lenses–FET sensors also allowed glucose monitoring in the rabbit tear fluid (**Figure 51g–i)**, exhibiting good stability to repeated eye–blinking, and demonstrating its potential for the design of new generation technologies for personalized medicine.[894]

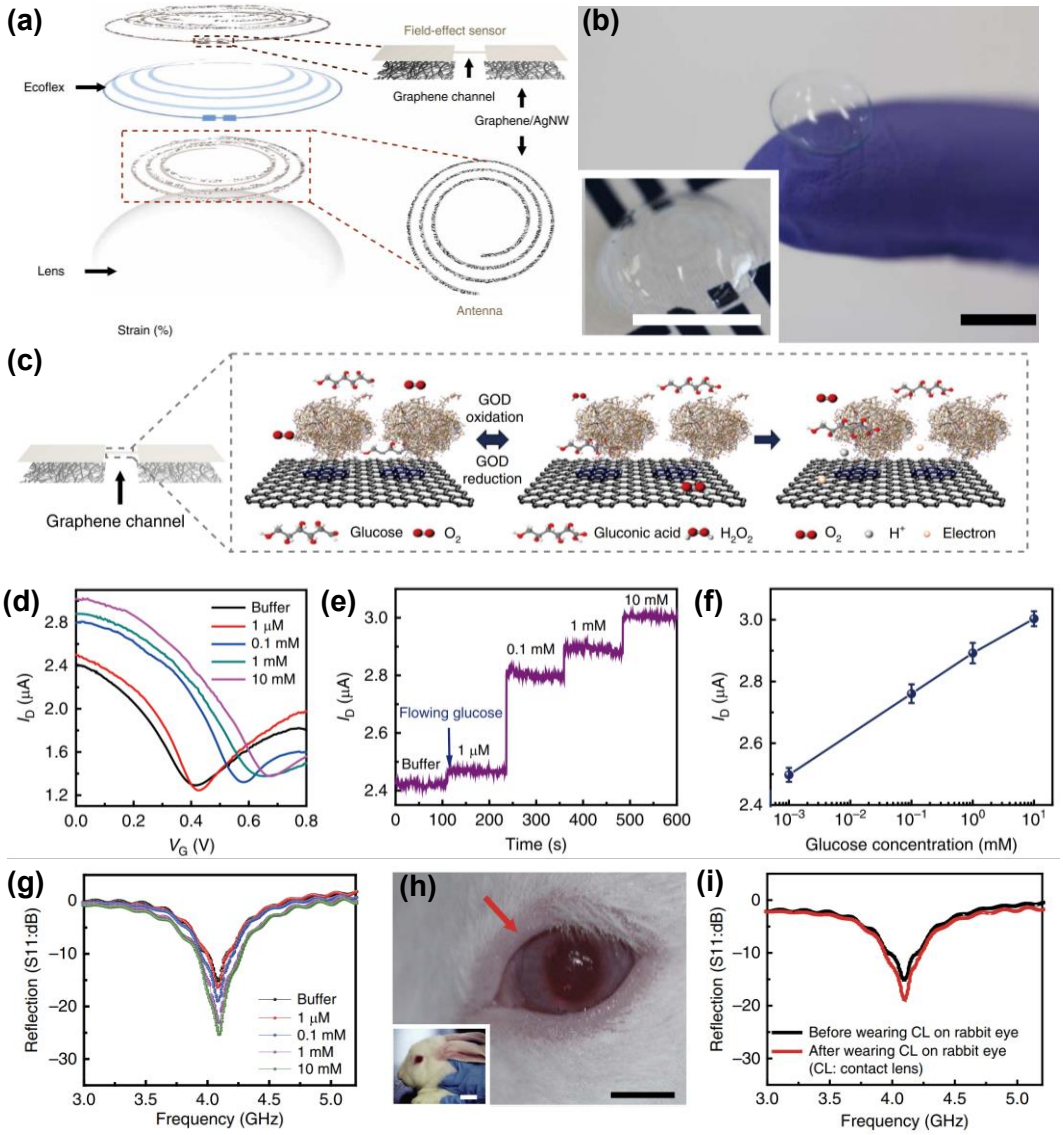

Figure 51. (a) Schematic of the wearable contact lens sensor, integrating the glucose sensor and intraocular pressure sensor. (b) A photograph of the contact lens sensor. Scale bar, 1 cm. (Inset: close–up image of the antenna on the contact lens. Scale bar, 1 cm.). (c) Schematic illustration and principle of glucose detection with the GOD–pyrene functionalized graphene. (d) Transfer (I_D–V_G) characteristics of the sensor at varied concentrations of glucose (V_D = 0.1 V). (e) Real–time continuous monitoring of glucose concentrations (V_G= 0 V). (f) The calibration curve generated by averaging current values and the glucose concentration from 1 mM to 10 mM. Each data point indicates the mean value for 10 samples, and error bars represent standard deviation. (g) Wireless monitoring of glucose concentrations from 1 mM to 10 mM. (h) Photographs of wireless sensor integrated onto the eyes of a live rabbit. Black and white scale bars, 1 cm and 5 cm, respectively. (i) Wireless sensing curves of glucose concentration before and after wearing contact lens on an eye of live rabbit. [894] Reproduced with permission from Ref. [894] Copyright 2017 Springer Nature.

Despite high selectivity and sensitivity of enzyme–based biosensors their practical application is often limited by the lack of long–time stability originating from the intrinsic nature of enzymes.[895] A possible solution to this problem is through the development of non–enzymatic glucose sensors that can directly oxidize glucose in the measured sample. Majority of non–enzymatic glucose biosensor relies on the presence of metal catalyst (metal hybrids, alloys, metal oxides and metal complexes) that can facilitate the electron transfer between glucose and electron surface.[273]

However, these nanocomposites are often not suitable for direct glucose detection due to their poor electrical conductivity and limited mechanical and chemical stability. The presence of graphene in non–enzymatic glucose sensors improves electrical conductance, and surface–volume ratio for the incorporation of guest molecules thus improving electrocatalytic effect for glucose oxidation.[821] Graphene based sensors doped with transition metals such us CuO and CuS,[896-898] PtNi,[899] NiO,[900] Co_3O_4[901] and noble metals,[902-903] were successfully employed for the enzyme–free detection of glucose. For instance, Yang et al. used rGO/CuS nanocomposites modified GCE to detect glucose and human urine and blood serum samples.[898] The prepared non–enzymatic platform exhibited good catalytic activity towards glucose oxidation over a wide linear range (1–2000 μM), with LOD of 0.19 μM. Dong and co–workers integrated cobalt oxide (Co_3O_4) nanowires onto the graphene foam via the hydrothermal procedure.[901] The resulting bio–platform could sense glucose amperometrically at concentrations as low as 25 nM**.** Recently, palladium nanoflower decorated CVD graphene/Nafion/glucose oxidase nanocomposite in FET device was shown to detect glucose at 1 nM concentrations with excellent selectivity against uric and ascorbic acid.[904] The high sensitivity to glucose was ascribed to the pointed morphology of Pd nanoflowers, which provided more active sites for analyte interactions.

Dopamine, ascorbic acid and uric acid. Dopamine (DA) is an important neurotransmitter, which plays a vital role in proper functioning of central nervous system (CNS), cardiovascular and hormonal systems.[905] Its abnormal levels are often associated with schizophrenia, attention deficit hyperactivity disorder, restless legs syndrome (RLS) and Parkinson's disease.[905] DA detection is typically challenged by its very low physiological concentration ranging from 0.01 μM–1 μM and interference from much more abundant biomolecules such as ascorbic acid (AA) and uric acid (UA).[906] In addition, the redox oxidation potentials of DA, UA, and AA are often not distinguishable, therefore novel electrocatalytic systems are needed to separate signals from each other. High density of edge sites in graphene together with its excellent electronic conductivity led to the development of numerous graphene–based sensors for the detection of these molecules.[907] To demonstrate this approach, Shang et al. integrated multilayer graphene nanoflakes films (**Figure 52a–b**) onto the Si substrate through microwave plasma enhanced chemical vapor deposition for simultaneous determination of AA, DA, and UA.[908] The edge plane defects in graphene facilitated the electrochemical transfer rates for oxidation of the three biomolecules allowing sensitive detection of DA with LODs of 0.17 μM in the presence of 1 mM AA and 0.1 mM UA (**Figure 52c–d**). Another example of incorporating graphene to sense DA was showed by Wang and co–workers.[909] The authors fabricated rGO–chitosan nanocomposite electrodes which responded selectively to DA over linear response range of 5–200 μM in the large excess of AA and UA (500 μM). The high inherent selectivity of graphene to DA over AA was attributed to π–π interactions between phenyl rings of DA and two–dimensional planar hexagonal carbon structure of graphene.

Hou et al. fabricated a sensitive bio–platform made of Nafion and *N*–(trimethoxysilylpropyl) ethylenediamine triacetic acid (EDTA) incorporated into rGO to detect dopamine with a LODs of 0.01 μM. The EDTA groups, combined with ionic sulfuric groups of Nafion, could preconcentrate the DA from solution, while the EDTA–rGO promoted electron transfer between dopamine and electrode. The oxygen rich rGO further inhibited the diffusion of AA, and thus provided enhanced selectivity and sensitivity.[910] To further lowered the LODs of DA, Zhang et al. employed modified graphene sheets with β–cyclodextrin drop–cast on GCE. The adsorbed β–CD prevented the formation of graphene aggregates and ensured good accessibility of active sites in graphene for electron transfer.[911] One of the most sensitive electrochemical sensors for DA detection was developed by Liu et al. through using a rGO–polyvinylpyrrolidone (PVP) polymer nanocomposite as a sensing layer. This biosensor displayed a wide linear response range of 5×10^{-10}–1.13×10^{-3} M to DA with a detection limit of 0.2 nM in 1 mM AA.[912] Numerous other examples of electrodes modified with graphene and sulfonyl groups,[913] Fe_3O_4,[914] Pd nanoparticles[915] or Al/Zn hydroxides[916] were reported for selective determination of dopamine. Interestingly, electrodes constructed of polydopamine (PDA)–rGO–SnO_2 layer coated on Au were able to detect dopamine at 5 nM concentrations.[917] The outstanding sensitivity of this bio–platform was ascribed to i) superior electronic conductivity of graphene sheets; ii) Au and PDA prevented aggregation of graphene sheets, and thus enhanced conductivity of the composite; iii) SnO_2 improved ability of analytes to be adsorbed and transferred to the electrode surface. Aptamer functionalized rGO/nile blue/AuNP complex-modified glassy carbon electrode was capable of detecting DA in 10 nM to 0.2 mM with the LOD of 1 nM.[918] The resulting sensor also demonstrated good selectivity for DA in the presence AA, UA, epinephrine, norepinephrine and glucose. In real biological samples, the nanocomposite modified electrode could detect DA, with high detection recoveries of 97.0–104.0%.

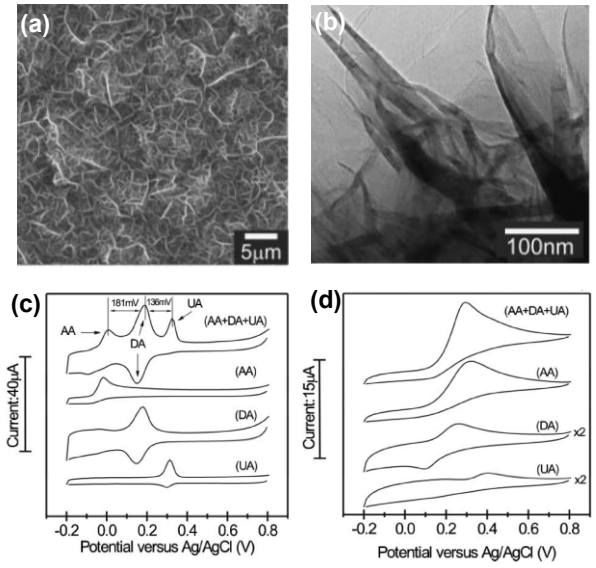

Figure 52. (a) SEM and (b)TEM images of MGNFs. (a) and (b) CV profiles of the MGNF and bare GCE electrodes, respectively, in the solution of 50 mM, pH 7.0 PBS with 1 mM AA, 0.1 mM DA, and 0.1 mM UA.[908] Reproduced with permission from Ref. [908] Copyright 2008 John Wiley and Sons.

Although AA and UA are widely recognized as bio–interferants during electrochemical sensing of dopamine, there is an on–going demand to develop reliable sensing bio–platforms for their determination due to large biological importance of AA and UA.[919] Brownson et al. demonstrated that with increasing basal plane contribution in graphene modified electrodes, the heterogenous electron transfer rate is significantly diminished resulting in poor kinetics for oxidation of biomolecules such as AA.[920] Correspondingly, fast heterogeneous electron transfer can be achieved in the electrodes with an increased edge plane content. Keeley et al. used liquid phase exfoliation to fabricate a sensing platform for AA detection using graphene nanosheets immobilized on pyrolyzed photoresist film (PPF) electrodes. Effective response to AA was found in the range 0.4 to 6.0 mM with a 0.12 mM detection limit.[921] Shi and co–workers used graphene functionalized with positively charge gold nanoparticles to sense UA in the range of 2.0×10^{-6}–6.2×10^{-5} mol L^{-1} with the LODs of 2×10^{-7} mol L^{-1} using.[922]

Cholesterol. Cholesterol and its esters are essential membrane constituents widely found in biological systems, which serve a unique purpose of modulating membrane fluidity, elasticity, and permeability. The undesired accumulation of cholesterol and its esters may lead to critical health problems including heart diseases, cerebral thrombosis or artherosclerosis.[923] Therefore, there is a continuous need for new point–of–care diagnostics to measure lipid panels, including total cholesterol. De and co–workers utilized β–CD modified Gr as a non–enzymatic platform for the electrochemical detection of cholesterol using methylene blue (MB) as redox indicator.[924] They observed that MB can form inclusion complexes with β–CD–Gr, which in the presence of cholesterol, undergo displacement reaction releasing MB back into the solution. This process can be directly monitored with DPV permitting cholesterol detection at concentrations as low as s 1 μM. Yuan et al. used TiO_2–Gr–Pt–Pd nanocomposite modified electrodes to improve surface/volume ratio for immobilization of cholesterol oxidase (ChOx).[925] The developed bio–platforms exhibited wide linear range of responses to cholesterol in the concentrations spanning from 5.0×10^{-8} to 5.9×10^{-4} M, with the LODs of 0.017 μM, and response time under 7 seconds. The authors also demonstrated that cholesterol can be detected in real food products such as egg, meat, margarine and fish oil. More recently, Galdino et al. prepared ionic liquid (1–(3–aminopropyl)–1H–imidazol–3–ium bromide) GO–Au–ChOx composite modified electrodes for cholesterol sensing.[925] Raj et al. successfully loaded cholesterol esterase and ChOx enzymes on the rGO–Pt modified electrodes.[926] Pt nanoparticles catalyzed the electrochemical oxidation of hydrogen peroxide and the enzymes enhanced hydrolysis of cholesterol. They used then amperometry for the detection of cholesterol and its esters with a LOD of 0.2 μM.

NADH. The detection of dihydronicotinamide adenine dinucleotide (NADH) has received considerable attention, owing to its very important role as a cofactor in many naturally occurring enzymatic reactions, including the conversion of important substrates such as alcohol, lactate, and glucose.[927] Govindhan et al. reported on non–enzymatic β–NADH biosensor based on rGO decorated with Au nanoparticles on GCE. The fabricated sensor exhibited a high sensitivity of 0.916 μA/μM cm^2, wide linear range of 50 nM to 500 μM with detection limits of 1.13 nM.[928] The interferences from the common interferants such as glutathione, glucose, ascorbic acid, and quanine were negligible. The improved electrocatalytic activity to NADH oxidation of the rGO–Au/GCE nanocomposite was facilitated by the highly dispersed Au nanoparticles on the surface of rGO through the formation of a 3D electronic conductive network. This sensor could also detect NADH in human urine. Tabrizi and Zand prepared rGO through a hydrothermal process using NADH as a reducing agent.[929] Amperometric measurements indicated that the rGO modified GCE electrode exhibited good electrocatalytic activity towards the oxidation of NADH at the potential of + 0.35 V yielding LOD of 0.6 μM. Li and co–workers utilized cycling voltammetry to electrodeposit ERGO–polythiophene (PTH) composite layer directly onto GCE, and used it for the fabrication of NADH amperometric biosensor. The ERGO–PTH modified electrodes displayed LODs of 0.1 μM over 0.01–3.9 mM concentration range.[930] Sensitivity to NADH was further increased by Li et al., who used gold disk electrode coated with Gr–Au NPs–DNA tetrahedron, as scaffold for graphene immobilization, to form an amperometric biosensor. DNA–Au scaffold kept Gr fragments in a more vertical position instead of lying down on the surface of electrode, which offered more opportunities for graphene fragments to adsorb and react with NADH molecules due to larger density of edge–plane sites. The resulting platform could detect NADH at concentrations as low as 1 fM.[931]

Hydrogen peroxide. Hydrogen peroxide aside from being an enzymatic end–product of many biological processes, is also an essential mediator in food, pharmaceutical, clinical, industrial, and environmental analysis.[932] Xu and co–workers fabricated a H_2O_2 sensor using rGO–chitosan nanocomposites as scaffolds for the immobilization of hemoglobin (Hb) molecules.[933] The resulting bio–platform showed LODs of 0.51 μM. The enhanced electrocatalytic effect was attributed to the large available surface area of the rGO–chitosan matrix for Hb loading, allowing this enzyme to retain its native structure during electrochemical transformations. The electron transfer between the composite film and the electroactive center of Hb was further facilitated by the presence of rGO. The percolating 3D network of rGOs also provided multiplexed paths to rapidly conduct away the charges.

The integration of enzyme can improve the sensing performance. Lu et al. improved sensitivity to H_2O_2 through immobilization of horseradish peroxidase (HRP), a heme enzyme, onto the surface of graphene.[934] Graphene sheets, prepared through exfoliation by the tetrasodium 1,3,6,8–pyrenetetrasulfonic acid, enhanced the capacity to effectively anchor the HRP enzymes and to mediate the charge transfer. The resulting biosensors could sense H_2O_2 at lowest concentrations of 0.106 μM in the range of 0.63 μM to 16.8 μM. Different approach to immobilize HRP onto the surface of electrode was demonstrated by Zeng and co–workers. The authors reported on a hierarchical nanostructure formed by layer–by–layer assembly of HRP enzyme together with the sodium dodecyl benzene sulfonate (SDBS) surfactant functionalized rGO as sensitive platform for the detection of H_2O_2. Large capacity of rGO film for enzyme incorporation resulted in LODs of 0.1 μM for H_2O_2 catalysis.[935] Zhou et al. decorated rGO with Au nanoparticles and microperoxidase–11 enzyme for the amperometric detection of H_2O_2 with a linear range from 2.5 to 135 μM.[936] Wang et al. extended the linear response range (1 μM to 500 Mm) and lowered LODs to 80 nM by using one–step microwave–assisted thermal reduction to fabricate Pt nanoparticle–rGO composite electrodes.[937] The high performance of the fabricated bio–platform was ascribed to the high–density of uniformly distributed Pt nanoparticles on the rGO surface, which resulted in rapid charge transfer between metal nanoparticles and rGO.[937]

Using Prussian blue immobilized on the surface of rGO, Cao et al. improved the LODs for H_2O_2 detection to 45 nM.[938] One of the most sensitive biosensor to H_2O_2 was developed by Sun and co–workers. They assembled atomically thick Pt–Ni nanowires on the surface of rGO through ultrasonic self–assembly method to improve the electrocatalytic effect to H_2O_2 catalysis.[939] This enzyme–free biosensor exhibited wide linear range of response to H_2O_2 spanning from 1 nM to 5.3 mM with the detection limits as low as 0.3 nM. Such electrode modifications enabled the detection of traced amounts of H_2O_2 released from Raw 264.7 cells.[939] Through using rGO doped with manganese ferrite ($MnFe_2O_4$) nanoparticles, Rani et al. developed a non–enzymatic amperometric sensor for H_2O_2 determination. They reported on LODs of 0.35 μm, and sensitivity of 1180 μA mM^{-1} cm^{-2} for H_2O_2 oxidation.[940]

Other small–molecule bioanalytes. Other notable examples of graphene modified electrodes for biosensing of small molecules also include the detection of food additives, psychoactive substances or pesticides. For instance, Long and co–workers used graphene nanosheets decorated with cobalt–nickel bimetallic nanoparticles for the detection of octylphenol. The resulting platform was used to quantify the amount of target analyte in plastic bottles, metal bottles and food packaging bags at picomolar concentrations.[941] Oliveira et al. developed a bi–enzymatic biosensor based on graphene and gold nanoparticles for the detection of common pesticides–carbamates. This sensor could sense carbamates in citrus fruit samples (orange, lemon, and tangerine), without significant interferences from ascorbic acid, citric acid, and glucose.[942] For a comparative investigation on the determination of caffeine in coffee, energy drinks and tea, the research group lead by Khoo and co–workers utilized several chemically modified graphene based bio–platforms including graphite oxide (GPO), GO and electrochemically reduced graphene oxide (ERGO). They concluded that ERGO exhibited the best response characteristics based on sensitivity, linearity, and reproducibility of the response because of the lowest content of oxygen functionalities.[943]

Nucleic acid. Sequencing of the human genome is now approaching its final stage. Gene sequence data alone may be of limited clinical use unless it is directly correlated to sickness relevance. In order to screen significant populations for specific nucleotide sequences in of their genomes as well as to monitor gene expression, novel technologies are required.[944]

Two experimental approaches are typically employed for the electrochemical (voltammetric, amperometric) detection of nucleic acids: (i) direct detection of DNA bases and polynucleotides or (ii) via introducing DNA specific electroactive labels. Huang et al. electrochemically differentiated between adenine and guanine nucleobases at concentrations as low as 50 nM and 25 nM using GCE electrodes modified with Gr–COOH.[945] The observed sensitivity was attributed to the presence of negatively charged graphene–COOH composite that facilitated adsorption of positively charged guanine and adenine onto the electrode surface, and consequently enhanced the magnitude of measured signal. Dong et al. employed GO modified GCE for simultaneous detection of all four DNA bases in both ssDNA and dsDNA without the need of a pre–hydrolysis step.[331] GO nanosheets immobilized on disposable graphite electrodes were used by Muti and co–workers as label free bio–platform for nucleic acid determination in Hepatitis Virus B sequence.[946] The modifications of electrode with a GO layer increased surface coverage by providing enhanced adsorption of nucleic acids onto electrode, giving rise to higher sensitivity. Different experimental approach was demonstrated by Yin and co–workers in which rGO–chitosan electrodes were doped with Fe_3O_4 particles for sensitive determination of guanosine.[947] The oxidation peak current,

measured with DPV, was proportional to guanosine concentration in the range of 2.0×10^{-6} to 3.5×10^{-4} M with a LOD of 7.5×10^{-7} M. The authors indicated that the presence of metal–oxide nanoparticles diminished the electron transfer resistance. Du and co–workers constructed a DNA sensor based on ERGO decorated with Au nanoparticles through direct electrochemical deposition methods.[948] They observed that the presence of gold nanoparticles was essential to differentiate the DPV signals of T from that of A within a single–base alteration. Xu et al. utilized composite films of PPy/Gr for the quantitative detection of adenine and guanine. PPy/GR electrodes enhanced the adsorption of the electropositive adenine and guanine through strong π–π interactions and electrostatic adsorption on negatively charged surface of the electrode. This biosensor demonstrated linear response in the 0.06–100 μM and 0.04–100 μM ranges, and LODs of 0.02 μM and 0.01 μM, for adenine and guanine, respectively.[949]

Taking the advantage of its abundant electrochemically-active edge planes, Ambrosi and Pumera fabricated GCE deposited with stacked graphene nanofibers, which is able distinguish four nucleobases with a sensitivity up to four folds larger than reported for CNTs electrodes.[950] They employed this bio–platform for direct label–free detection of A(H1N1) human influenza strands. High sensitivity of stacked graphene nanofibers over CNTs could be due to large density of edge planes of individual graphene sheets in comparison to large basal plane contribution in CNTs. Lim et al. utilized anodized epitaxial graphene modified electrodes to separate anodic peaks of all four nucleic acid bases with great selectivity in double stranded and single stranded nucleic acids (**Figure 53a–d**).[951] Impressive results were demonstrated by Akhavan et al., who used electrophoretic deposition to fabricate graphene oxide nanowalls, with a preferred vertical orientation, deposited on a graphite electrode for ultra–sensitive determination of DNA nucleotides (A, G, C, and T).[952] The resulting bio–sensors could successfully detect dsDNA oligonucleotides at concentrations as low as 9.4 zM. This extremely high sensitivity was ascribed to the high density of active edge sites in the 2D material.

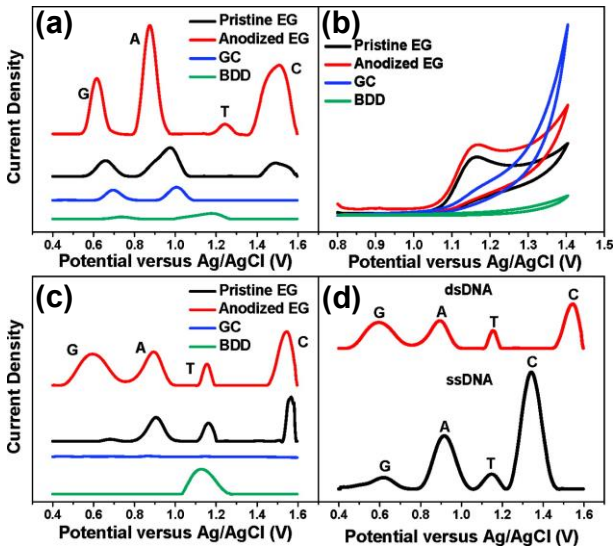

Figure 53. DPV profiles for pristine EG, anodized EG, GC, and BDD electrodes in (a) 30 μM equimolar mixture of G, A, T, and C, (b) 1.0 mM thymine, (c) 30 μg mL^{-1} dsDNA, (c) anodized EG in 30 μg mL^{-1} dsDNA and 30 μg mL^{-1} ssDNA. Supporting electrolyte: 10 mM KCl/10 mM PBS solution at pH 7.[951] Reproduced from Ref. [951] Copyright 2010 American Chemical Society.

In the second strategy, a single–stranded probe sequence is often immobilized onto the electrode surface (recognition layer), where the base–pairing interactions ensure high affinity of the probe for target DNA sequences. To demonstrate the feasibility of this approach, Cai et al. formed a graphene–MoS_2 composite with immobilized DNA and used it as a label–free DNA sensing platform.[953] This bio–platform could detect DNA at concentrations reaching 1.0×10^{-17} M within the 1.0×10^{-16} M to 1.0×10^{-13} M range.[953] Pham and co–workers developed an immunosensor for microRNA (miR–141 and miR–29b–1, which are known as prostate and lung cancer biomarker, respectively) determination based on screen printed electrodes modified with rGO and CNTs. This sensor could detect miRNA with a limit of detection as low as 10 fM.[954] Xu et al. fabricated a label–free electrochemical sensor for the determination of miRNAs using a GO conducting polymer modified electrode. This platform demonstrated high selectivity, with current increases upon hybridization from 1 fM to 1 nM of target miRNA, with LODs of 8 fM.[955] Liu et al. used graphene–gold nanoparticles composite as a scaffold for the immobilization of the DNA probes. They employed a sandwich–type detection strategy to bind target DNA strands and secondary HRP–labeled oligonucleotides.[956] Through amperometric and CV measurements, the authors observed good linear relationship between the current signal and the logarithmic function of complementary DNA concentration in a range of 50–5000 fM with the LOD of 3.4 fM.

Lin et al. fabricated a DNA sensor based on the Gr–Au composite with 1,10–phenanthroline cobalt ($[Co(phen)_2(Cl)(H_2O)]^+$) complex used as an electroactive indicator.[957] The resulting sensor could detect target DNA

from *Escherichia coli* (*E. coil*), in a linear range from 2.50×10^{-11} to 1.25×10^{-9} M and LODs of 8.33×10^{-12} M. Bonnani and co–workers used GO nanoplatelets as an electroactive label for the discrimination of the single–base mutation in the DNA sequence related to Alzheimer's disease.[958] They observed that the GO nanoplatelets exhibited different affinity for binding single–and double–stranded DNA, thus allowing selective differentiation among complementary, noncomplementary, and one–mismatch DNA sequences. In a recent study, Ping and co–workers developed a sensitive DNA FET biosensor with high yield transport properties (> 90%).[959] They used CVD–grown graphene monolayers (on the Si substrate), as scaffold for the immobilization of probe molecules such as ssDNA to impart selectivity to target DNA strands. The resulting sensing bio–platform exhibited LODs of 1 fM for 60–mer DNA oligonucleotides in aqueous solutions. Dong et al. also fabricated a DNA selective sensor by incorporating probe labeled gold nanoparticles (ssDNA–AuNP) onto electrochemically reduced graphene oxide modified electrodes with thiol group tagged (GT) DNA strand ($d(GT)_{29}SH$) coupled with horseradish peroxidase (HRP) functionalized carbon sphere (CNS) used as tracer molecules.[960] The authors observed high sensitivity to DNA with the LODs down to 5 aM and a linear response range spanning over 5 orders of magnitude (from 1.0×10^{-17} M to 1.0×10^{-13} M). This biosensor exhibited high selectivity to differentiate single–base mismatched and three–base mismatched sequences of DNA. A DNA label–free electrochemical biosensor has been developed by Benvidi et al. for BRCA1 mutation detection based on Au nanoparticles–rGO/GCE functionalized with ssDNA BRCA1 5382 insC probe.[961] The rGO–Au nanocomposite enhanced the sensitivity of this sensor through increasing the number of immobilized active sites. This label–free electrochemical biosensor showed LODs of 1.0×10^{-20} M for target DNA and two linear response ranges spanning over 13 orders of magnitude in concentration and could effectively distinguish between the complementary and non–complementary sequences.[961]

Proteins. Electrochemical protein biosensors rely on the presence of specific analyte recognition centers that are immobilized on the surface of electrode: (1) antibodies, which can selectively recognize and bind specific target antigens, and (2) aptamers, which are small peptides or oligonucleotides that exhibit conformations and structures suitable for binding target biomolecules.[265] Roy and co–workers used GO as scaffold for anti–IgG immobilization to detect Rabbit IgG antibodies over the concentration range of 3.3 nM–683 nM with the LODs of 0.67 nM. The developed impedimetric sensor exhibited high selectivity towards Rabbit IgG antibody as compared to the non–complementary myoglobin.[883] Zhang et al. developed a sandwich–type double–signal immunosensor for the detection of human IgG based on PDA–rGO–AuNPs and Ag/C nanocomposite acting as a signal label (**Figure 54a–b**).[962] The fabricated immunosensor responded to human IgG within the concentration ranges of 0.1 to 100 ng mL^{-1} and 0.01–100 ng mL^{-1} with the LODs of 0.001 ng mL^{-1} in the absence and presence of H_2O_2 and hydroquinone.

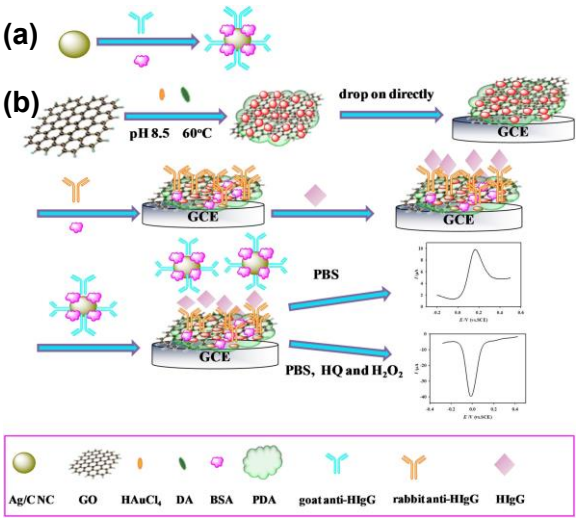

Figure 54. The fabrication processes for the electrochemical immunosensor.[962] (a) preparation of the Ag/C NC by functionalization with bovine serum albumin (BSA) and goat anti-HLgG. (b) preparation of GO-based sensing composite mounted on a GCE.[962] Reproduced with permission from Ref. [962] Copyright 2015 Elsevier B.V.

Su et al. developed a sensitive immunosensor for the determination of alpha–fetoprotein (AFP) by means of immobilization of horseradish peroxidase–anti–AFP conjugates onto the Au functionalized graphene.[963] The AFP antibody–antigen partially inhibited the active center of HRP, and thus decreased the catalytic reduction of H_2O_2 by HRP. Meanwhile the redox–active TH 55 together with HRP mediated the electron transfer from H_2O_2 to the electrode surface. This experimental approach allowed determination of AFP at concentrations as low as 0.7 ng mL^{-1}. The same immunoassay was also evaluated in clinical human serum samples analysis correctly identifying samples containing AFP in accordance with the results from commercial clinical devices. Yang and co–workers used rGO–Au NP–PEDOT–PB composite film as label–free AFP selective electrochemical immunosensor.[964] Electrochemical measurements revealed good stability to prolonged voltammetric cycling with performance retention up to 89.45% after 100 consecutive measurements. The composite electrode demonstrated high specific capacity for capture of the AFP antibody lowering detection limits down to 3.3 pg mL^{-1} concentrations. In addition, this biosensor was successfully employed for the determination of AFP in serum samples. Wei et al. further enhanced the sensitivity to AFP by incorporating anti–AFP on Gr and thionine (Thi) modified GCE through π–π interaction followed by covalent crosslinking of AFP antibodies with Thi.[965] Similarly, the AFP interactions with the electrode diminished electron–transfer and mass–transfer of TH resulting in reduced read–out. This immunosensor detected AFP at levels down to 5.77 pg mL^{-1}. In recent studies, the immobilization of anti–carcinoembryonic antigen (CEA) on the surface of graphene in the FET device architecture enabled label–free detection of this cancer biomarker (CEA) at 0.5 pM concentrations, far exceeding that of the clinical

diagnostics cut-off value.[966] The fabricated device demonstrated excellent selectivity against neuron specific enolase (NSE) and cytokeratin-19-fragment (CYFRA21-1) interferants. The authors confirmed that the immobilized antibody (anit–CEA) exhibited high binding affinity to CEA (dissociation constant of 6.35×10^{-11} M), thus allowing selective detection of the targeted protein.[966]

A sandwich–type immunoassay system using horseradish peroxidase modified GO nanosheets was developed by Tang et al. who used it for the impedimetric detection of carcinoembryonic antigens.[967] The dynamic concentration range of this biosensors ranged from 1.0 pg mL^{-1} to 80 ng mL^{-1} with LOD of 0.64 pg mL^{-1}.[967] Yang et al. utilized nitrogen–doped graphene functionalized with Au nanoparticles as immunosensor for matrixmetalloproteinase–2 (MMP–2) determination.[968] Notably, the design of the immunosensor also involved a polydopamine–functionalized graphene oxide hybrid conjugated to the horseradish peroxidase–secondary antibodies by covalent bonds as a multi–labeled and biocompatible probe to amplify the electrochemical response. This resulting biosensor successfully detected MMP–2 in human serum with LODs as low as 0.11 pg mL^{-1}. Chen and co–workers detected cell apoptosis through monitoring the caspase–3 triggered signal–on strategy with GO–assisted amplification. As the target protein, caspase–3 can be detected in a range of 0.1–100 pg mL^{-1}. A low detection limit of 0.06 pg mL^{-1} was obtained which is 103–105 times more sensitive compared to other reports.[969] Antiapolipoprotein B 100 functionalized electrodes consisting of a mesoporous few layer rGO and NiO nanocomposite were used by Ali et al. for highly sensitive detection of low density lipoprotein molecules (LOD: 0.07 mg dL^{-1}).[970] Recently, Ates et al. functionalized glassy carbon electrode with rGO–Pt NPs–Nafion nanocomposite to detect renin inhibitor–alistiren in human blood plasma at nanomolar concentrations (LODs of 8.2 nM).[971] Er and co–workers using the same device architecture quantified the content of α_1–AR antagonist silodosin in blood plasma.[972] The resulting bio–platform exhibited linear calibration curve in the range of 1.8–290.0 nM with the LODs of 0.55 nM. Group led by Pumera developed a selective thrombin biosensor through the modification of a disposable electrical printed carbon electrodes with the thrombin aptamer utilizing GO as the molecular label.[973] The binding event between thrombin and the immobilized aptamer facilitate its partial release from the surface of the electrode, resulting in uncovered underlying surfaces available for charge transfer between GO and the electrode. The measured signal then corresponds to voltammetric reduction of the inherent oxygen groups from GO. Chemical vapor deposited graphene functionalized with DNA aptamer in FET biosensor enabled sensitive detection of thrombin at concentrations as low as 30 nM.[974] The presence of DNA aptamer effectively reduced the distance between analytes and the FET surface, thus minimalizing charge screening effects. Label–free biosensing of prostate specific antigen (PSA) in high ionic–strength solutions has been realized using polyethylene glycol (PEG) graphene nanocomposite in FET device.[240] Incorporation of permeable PEG resulted in the increase in Debye screening length adjacent to the surface of FET device, enabling real–time measurements of PSA in in 1 nM – 1000 nM concentration range at physiological conditions.

The advantages of graphene–based nanomaterials that arise from their unique physio–chemical properties, have already contributed to the development of ultrasensitive and selective biosensing technologies.[80, 264, 821] Current advances in this field are primarily govern by the fabrication of hybrid materials by combining graphene and its derivatives with other known electrocatalysts compounds such as metal nanoparticles or ionic liquids.[272, 340] The synergistic effect between the electrical characteristic of graphene and the incorporated constituents allows for the fabrication of electrochemical biosensors with significantly improved analytical performance, and eased integration on the sensing platforms. In particular, the incorporation of novel recognition elements with excellent recognition ability to targeted analytes as in the case of molecularly imprinted polymers (MIPs), on the surface of graphene, may further lead to enhancements in analytical performance. Since the electroanalytical performance of graphene is strongly dictated by the presence of structural defects, edges and functional groups on its surface, novel synthetic methods with large degree of compositional control would have to be developed to further increase its commercial applications in biosensing. Therefore, graphene analogs such as GO and rGO, with large abundance of surface functional groups, are more extensively employed in biosensing applications, due to its remarkable properties such as good water dispersibility and biocompatibility, large surface area, facile surface modification, and low manufacturing cost.

Cellular detection. The detection of circulating tumor cells in patient is crucial for early diagnosis of cancer, highly precise cancer therapy, and monitoring therapeutic outcomes in real time.[895] To endow graphene with biosensing capabilities for cellular detection, it is often required to functionalize its surface with recognition elements that can interact with targeted analytes through specific interactions, and sometimes also participate in signal transduction events.[272]

Feng et al. performed label–free detection of cancer cells with overexpressed nucleolin on plasma membrane, such as breast cancer cells and human cervical carcinoma cells, using graphene functionalized with AS1411 aptamer.[975] The developed electrochemical aptasensor can distinguish between cancer and normal cells at the concentrations as low as one thousand cells. The authors used GO layer modified with 3,4,9,10–perylene tetracarboxylic acid (PTCA) to prevent aggregation of GO sheets on surface of the electrode and subsequently to covalently attach the NH_2–modified nucleolin aptamers with oligonucleotides antibodies acting as the recognition element. The binding interactions of the aptamer with cancer cells enhances the electron transfer resistance for electron transfer of $[Fe(CN)_6]^{3-/4-}$ complexes. Yang et al. developed a cytosensor based on the carboxymethyl chitosan–functionalized graphene enriched with folic acid (FA). Folate receptors found in the cell membrane of FA have a known affinity to HL–60

cancer cells. This label free sensors demonstrated LODs of 500 cells mL^{-1}.[976]

Besides small-molecule modified graphene demonstrated above, complex platforms that incorporate enzyme, aptamer, nanoparticles or their combinations have also been applied in cellular detection. Wu et al. functionalized graphene with laccase (Lac) and 2,2–azino–bis(3–ethylbenzothiazoline–6–sulfonic acid) (ABTS) for biocatalytic reduction of oxygen.[977] ABTS and laccase were integrated on the surface of graphene through the π–π and electrostatic interactions of these components. This bio–platform could sense extracellular oxygen, released from human erythrocytes cells, at concentrations as low as 10 μM. The Guo group monitored triggered cellular release of H_2O_2 from human cells by growing the cells on the surface of layered graphene–artificial peroxidase–protein modified electrodes.[978] Graphene was used as a bio–scaffold with good dimensional compatibility for human cell growth and substantial electrical conductivity for electrical detection. Selectivity to H_2O_2 together with enhanced cell adhesion and growth capability was ensured by incorporating artificial peroxidase (AP) and extracellular matrix protein onto the surface of graphene. The authors showed that through the stimulation of phorbol12–myristate–13–acetate (PMA, 5 μg mL^{-1}), hydrogen peroxide was released from a single MCF–7 cell over 25 s, quantifying the number of extracellularly released H_2O_2 as 10^{11} molecules per cell.

A prostate metastatic cancer cells (Du–145) specific cytosensor was fabricated by Yadegari and co–workers through using anti–CD166 monoclonal antibody–modified gold electrode as a capture and recognition element together with Gr–Au nanoparticle–HRP–conjugated trastuzumab antibody hybrid nanostructure as a nanoprobe for accurate recognition of target cells and efficient amplification of enzymatic signals.[979] The developed biosensor demonstrated high sensitivity and selectivity toward Du–145 cancer cells with LOD of 20 cells mL^{-1}, and an extended linear range from 10^2 to 10^6 cells mL^{-1}. He and co–workers combined together negatively charged GO with poly–l–lysine to improve capacity for leukemia K562 cancer cells adhesion.[980] This cytosensor responded linearly from 10^2 to 10^7 cells mL^{-1}, with the detection limit of 30 cells mL^{-1}. Akhavan et al. further enhanced sensitivity to leukemia cells (LOD of 0.02 cell mL^{-1}) through electrophoretic deposition of chemically exfoliated graphene oxide sheets on graphite rods, which led to the formation of Mg^{2+}–charged graphene composites.[981]

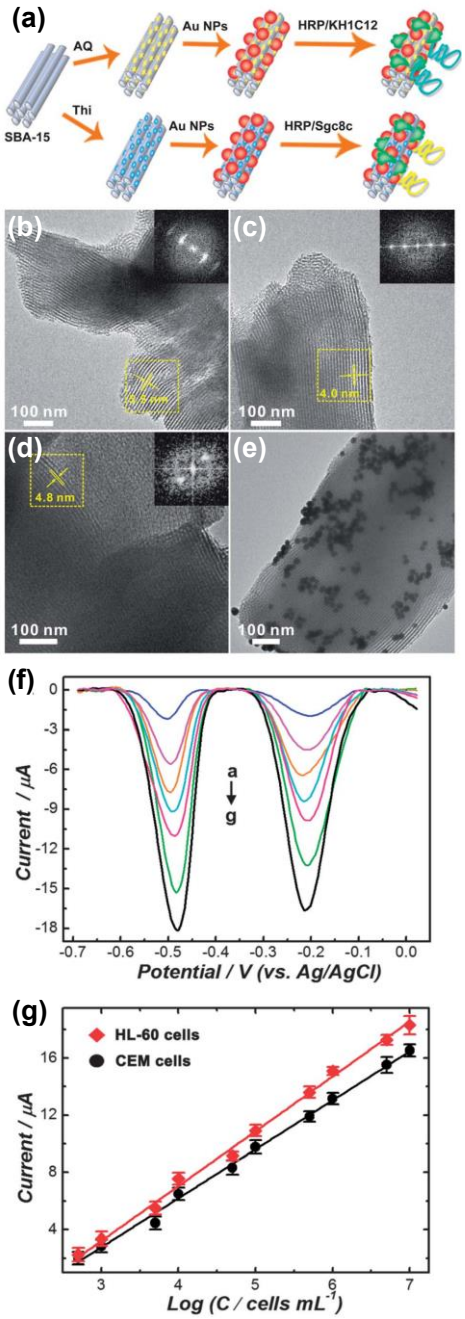

Figure 55. (a) Schemes illustrating the LBL assembly processes for the fabrication of SBA–15 redox–tags–Au NP–HRP–aptamer hybrid electrochemical nanoprobes. The relative sizes of the SBA–15, redox tags, Au NPs, HRP, and aptamers are not to scale. TEM images of SBA–15 (b) before redox tag loading and after loading of (c) Thi and (d) AQ. The insets show the Fourier Transform patterns obtained from the selected regions in the TEM images. (e) TEM image of SBA–15 loaded with Thi and decorated with Au NPs. (f) DPV responses at different HL–60 and CEM cell concentrations (from curve a to g: 5×10^2, 5×10^3, 1×10^4, 5×10^4, 1×10^5, 1×10^6 and 1×10^7 cells mL^{-1} of HL–60 and CEM cells, respectively). (g) Calibration curves for HL–60 and CEM cells in PBS, pH 6.5, containing 1 mM H_2O_2.[982] Reproduced with permission from Ref. [982] Copyright 2013 The Royal Society of Chemistry.

Simultaneous detection of both acute myeloid leukemia and acute lymphocytic leukemia was realized Wang and co–workers performed by cell using dual aptamer–functionalized, multilayered graphene–Au nanoparticle electrodes (**Figure 55a–e**).[982] This biosensor displayed LODs of ~350 cells per mL and wide linear response range of 5×10^{2}–1×10^{7} cells mL^{-1} for both HL–60 and CEM cells, with minimal cross–reactivity and interference from non–targeting cells such as non–leukemia cancer cells, K562 (a chronic leukemia cell line), and normal red blood cells (**Figure 55f–g)**. Free–standing graphene paper electrodes doped with Au nanoparticles allowed sensitive detection of *Escherichia coli* O157:H7.[983] This immunosensor showed good analytical response to the foodborne bacterium in concentration range spanning from 1.5×10^{2} to 1.5×10^{7} cfu mL^{-1} and the device exhibited low detection limit of 1.5×10^{2} cfu mL^{-1}. Khoshfetrat et al. immobilized the thiolated sgc8c aptamer onto Au–coated magnetic Fe_3O_4 nanoparticles with nitrogen–doped graphene nanosheets serving as platform for amplifying the read–out signal.[984] Ethidium bromide could intercalate into the stem of the aptamer hairpin, providing the DPV signal for the quantification of the leukemia cancer cells from 10 to 1×10^{6} cell mL^{-1}.

4.4.2. Black Phosphorous

2D black phosphorous is also considered as alternative materials for the development of electrochemical biosensors due to its inherent bulk conductivity,[985] electrocatalytic properties and biocompatibility.[986] Sofer and co–workers demonstrated large anisotropy in the electrochemical properties of black phosphorous with edge–plane sites exhibiting faster rates of electron transfer to inner and outer sphere redox probes as compared to basal plane sites.[987] They also showed that the edge–plane monocrystal electrodes of BP exhibited over one order of magnitude higher sensitivity to dopamine and ascorbic acid oxidation than BP electrodes with basal sites. Wang et al. utilized BP to develop a non–enzymatic hydrogen peroxide sensor through drop–casting small aliquots of BP directly onto the GCE. The resulting sensors exhibited good sensitivity to H_2O_2 with LODs of 0.1 μM.[988] The same authors observed that BP on the electrode can be oxidized at higher concentrations of H_2O_2, irreversibly diminishing the sensing properties of the sensor. Black phosphorous functionalized with poly–l–lysine and a myoglobin–specific (Mb) aptamer on screen printed electrodes was used as a label–free electrochemical platform for myoglobin detection by Kumar et al. (**Figure 56a)**.[361] CV measurements demonstrated 0.524 pg mL^{-1} sensitivity to myoglobin through oxidation of Fe^{2+}/Fe^{3+} from Mb–heme group in human serum. Mayorga–Martinez and coworkers synthesized BP nanoparticles through electrochemical exfoliation and used them directly as labels for the detection of rabbit immunoglobulin G (IgG).[362] The functionalized BP–IgG nanoparticles were subsequently conjugated with anti–rabbit IgG–magnetic beads and together transferred onto screen printed electrodes. Upon the exposure to strong acid, the BP–IgG nanoparticles detached from the surface of the electrode, and consequently the BP nanoparticles could be detected via electrocatalytic reduction of H^+ by the impact of BP particles with the electrode. The frequency of the impacts was directly related to the concentration of rabbit IgG allowing its determination at 0.98 ng mL^{-1} levels (**Figure 56b)**. Different experimental approach was undertaken by Chen et al. who fabricated a FET device from few–layer BP nanosheets to detect IgG via anti–IgG linked to gold nanoparticles functionalized BP sheets (**Figure 56c)**.[363] The authors observed that IgG molecules induced a negative gate potential on the BP nanosheet consequently increasing the drain–source current due to the p–type semiconducting nature of BP thus permitting human IgG detection at 10 ng mL^{-1} levels. Recently, poly–l–lysine–black phosphorus (pLL–BP) hybrid was used as scaffold for the immobilization of hemoglobin to construct a sensitive H_2O_2 biosensor.[989] The Hb–pLL–BP based enzymatic electrochemical device showed high catalytic activity toward the reduction of oxygen and hydrogen peroxide with linear concentration dependence in the 10 μM to 700 μM range of H_2O_2 and high selectivity against ascorbic and uric acid.

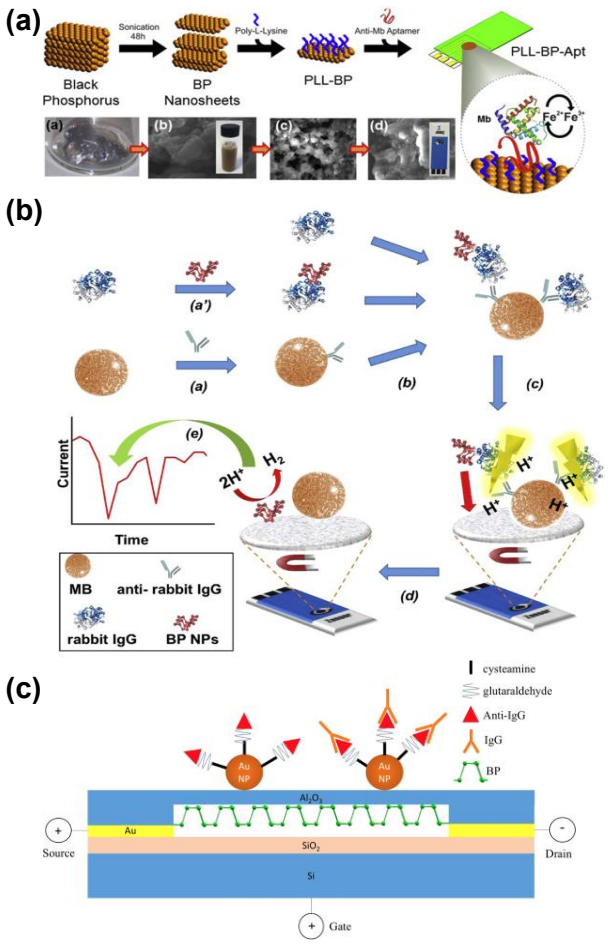

Figure 56. (a) Electrochemical myoglobin sensors.[361] Reproduced from Ref. [361] Copyright 2016 American Chemical Society.(b) 2D nanosheets of black phosphorus as labels for magneto immunoassay for rabbit IgG determination.[362] Reproduced from Ref. [362] Copyright 2016 American Chemical Society.(c) FET transistors based biosensors based on black phosphorus.[363]. Reproduced with permission from Ref. [363] Copyright 2017 Elsevier B.V.

Although 2D black phosphorous has received increasing attention in the field of electroanalytical chemistry, still much remains to be done in discovering the unique properties of this exciting material. The primary limitation of using BP in biosensing applications is its lack of long–term stability induced by the surface oxidation and moisture absorption. A possible approach to address this issue is to use a protective layer (e.g., metal oxide or polymer) that separates BP from the ambient environment, and thus improves its stability in sensing applications. In addition, the presence of structural defects in the form of kinks, or folds strongly influence the kinetics of electron transfer in biosensing applications. Therefore, the rational synthetic and experimental approaches leading to high degree of control over the structure and composition of BP together with detailed studies for understanding the underlying mechanism of BP in electrochemical sensing of bio–analytes are required for its broad implementation in practical applications.

4.4.3. Transition Metal Dichalcogenides

The increasing demand for developing highly sensitive, selective, low power consuming, reliable and portable sensing devices has stimulated active research on implementing novel 2D nanomaterials, after the great success of graphene. The high surface–to–volume ratio in 2D TMDs offers huge potential for the detection of large amounts of target analysts per unit area as well as rapid response and recovery with low power consumptions. On contrary to graphene, 2D TDMs nanosheets also hold a great promise as novel nanomaterial for biomedical applications as they can be readily synthesized on a large scale and can be directly dispersed in aqueous solution without the aid of surfactants.[990-991]

Small biomolecules, hydrogen peroxide, and proteins. Sarkar et al. integrated 2D MoS_2 monolayers onto an oxidized silicon substrate with a streptavidin–functionalized dielectric layer for selective detection of biotin at concentrations as low as 100 fM (**Figure 57a–d**). The authors observed that current signal can be modulated via the gating effect due to biotin interactions in the FET device, indicated that this signal transduction mechanism can be further utilized for the determination of other biomolecule including proteins and nucleic acids (**Figure 57e–f**).[184]

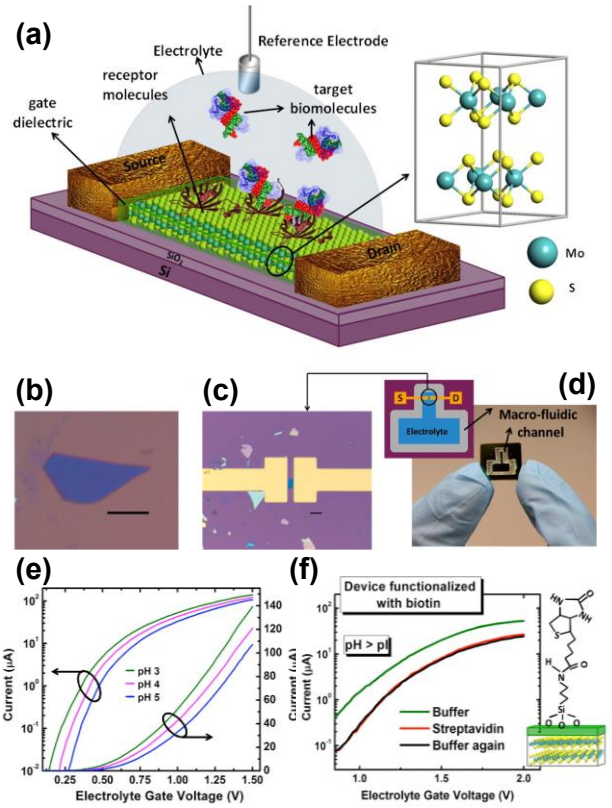

Figure 57. (a) Schematic diagram of MoS_2–based FET biosensor. For biosensing, the dielectric layer, covering the MoS_2 channel, is functionalized with receptors for specifically capturing the target biomolecules. The charged biomolecules, after being captured, induce a gating effect, modulating the device current. An electrolyte gate is in the form of a reference electrode (Ag/AgCl) is used for applying bias to the electrolyte.[184] (b) Optical image of a MoS_2 flake on 270 nm SiO_2 grown on degenerately doped Si substrate. Scale bar, 10 μm. (c) Optical image of the MoS_2 FET biosensor device showing the extended electrodes made of Ti/Au. Scale bar, 10 μm. (d) Image and schematic diagram (inset figure) of the chip with the biosensor device and macrofluidic channel for containing the electrolyte. (e) Linear region for a pH change of 4 to 5 of the electrolyte solution derived from the I_d–V_g curves. (f) A device functionalized with biotin was first measured in pure buffer (0.01 PBS), as shown by the green curve. Addition of streptavidin solution (10 μM in 0.01 PBS) leads to decrease in current (red curve) due to the negative charge of the protein, as the pH of the solution is more than the pI of streptavidin. The device is then measured again in pure buffer, leading to no significant change (black curve).[184] Reproduced from Ref. [184] Copyright 2014 American Chemical Society.

Extending the applicability of TMDCs in electrochemical sensor development, Lee and co–workers fabricated a dielectric layer–free MoS_2–based FET biosensor through incorporating anti–prostate specific antigen (anti–PSA) antibody on the surface of MoS_2 layer. The hydrophobic nature of the MoS_2 improved physical adsorption between the anti–PSA antibodies and the electrode surface.

The authors observed that the selective binding of negatively charged PSA (pH = 7.8), to the immobilized antibodies, modulated the off–state current allowing sensitive detection at concentrations down to 1 pg mL^{-1}.[992] Employing a similar approach, Wang et al. also fabricated a label–free multilayer MoS_2–based FET bio–platform for the sensitive determination of PSA. The drain current alteration in the FET device caused by the antibody–PSA interactions enabled real–time monitoring of cancer marker protein with good sensitivity (LOD of 375 fM), as well as high selectivity by showing no response to Bovine Serum Albumin (BSA).[993] (**Figure 58a–c**).

Using the same device architecture, Nam et al. functionalized the surface of MoS_2 with anti–human–α antibody receptors for detecting TNF–α molecules.[994] The resulting insulating–layer–coated and insulating–layer–free MoS_2 FET biosensors exhibited V_T (threshold voltage) and g_m(ON–state transconductance) modulated responses upon the antigen–antibody interactions, respectively. The observed difference in bio–response was attributed to the effect of insulating layer thickness on the potential disorder in the MoS_2 FET channels. The same research group further lowered the LOD to 60 fM for the detection of TNF–α molecules by utilizing MoS_2 based electrodes functionalized with anti–human TNF–α antibody.[995] Interestingly, the developed sensors, operating in the subthreshold transport regime exhibited even higher current sensitivities in contrast with sensors working in the linear regime. This high operation subthreshold–regime sensitivity may be utilized to further lower the LOD for TNF–determination.

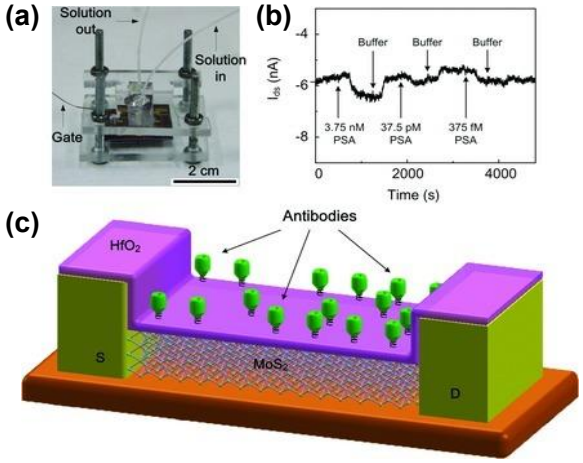

Figure 58. (a) Schematic of the biosensor configuration. (b) Conductance–versus–time data recorded during alternate delivery of PSA and pure buffer solutions; the PSA concentrations were 3.75 nM, 37.5 pM, and 375 fM, respectively. Dashed lines are the local baselines, and the length of the lines with arrows are the ΔI_{ds} (i.e., I_{ds} change in response to the presence of PSA). The buffer solutions used in all measurements were 100 μM phosphate buffer solutions. (c) Schematic of the biofunctionalization layers on the device surface (S: source, D: drain).[993] Reproduced with permission from Ref. [993] Copyright 2014 John Wiley and Sons.

Antibodies, and nucleic acid aptamers have been progressively identified as potential molecular recognition elements for the construction of biosensors capable of detecting various biomolecular targets. Huang et al. developed label–free electrochemical biosensor for 17b–estradiol determination through the immobilization of the selective aptamer on the surface of WS_2 nanosheets decorated with Au nanoparticle on GCE.[996] The resulting biosensor responded linearly to 17b–estradiol in 1.0×10^{-11} to 5.0×10^{-9} M concentration range with the LOD of 2.0×10^{-12} M, and could be used for practical determination of biomolecule in serum and water samples. Huang and co–workers fabricated a bio–platform for immunoglobulin E (IgE) determination based on Au nanoparticle and aptamer functionalized WS_2–graphene nanocomposites.[997] The synergistic effect between WS_2, graphene and Au resulted in significant signal amplification, allowing determination of IgE at concentrations as low as 0.12 pM. Huang et al. constructed an electrochemical sensor for the determination of bisphenol A (BPA) based on MoS_2–chitosan–Au nanoparticles composites modified electrode.[998] A linear correlation between the oxidation peak current and BPA concentration was observed in the concentration range spanning from 0.05 to 100 μM with the LOD of 5.0×10^{-9} M. CEA selective immunosensor was recently fabricated by Wang et al., in which MoS_2–Au was used as the solid support for the immobilization of CEA primary antibody, Ag nanoparticles, GOD, and CEA secondary antibody.[999] The fabricated immunosensor allowed detection of CEA in the range of 1 pg mL^{-1} to 50 ng mL^{-1} with the LODs of 0.27 pg mL^{-1} in human serum albumin samples. In addition, this immunoassay exhibited minimum degree of cross–reactivity with other biomolecules including human chorionic gonadotropin (HCG), α–fetoprotein (AFP), cancer antigen 125 (CA125) and PSA. Jing et al. used a sandwich–type electrochemical assay for sensitive detection of thrombin by using palladium nanoparticles decorated on poly(diallyldimethylammonium chloride)–graphene–MoS_2 surface, which was further functionalized by hemin/G–quadruplex, GOD, and toluidine blue (Tb) serving as redox probes.[1000] The incorporated GOD catalyzed the oxidation of glucose to gluconolactone, which was linked with the reduction of the dissolved oxygen to H_2O_2. Both processes were then catalyzed by PdNPs and hemin/G–quadruplex species acting as hydrogen peroxide (HRP)–mimicking enzymes. This resulted in significant electrochemical signal amplification, allowing thr determination of thrombin at 0.062 pM concentrations.

Pumera et al. incorporated several 2D transition metal dichalcogenides (TMDs) including WS_2, WSe_2, MoS_2, and $MoSe_2$ into the second–generation glucose biosensor through drop–casting each material onto the GCE, followed by immobilization of GOD and glutaraldehyde (GTA) on the electrode surface.[1001] WS_2, and WSe_2 exhibited smaller peak–to–peak separation and faster electron transfer rates than electrodes based on other studied TMDs. The enhanced performance of WX_2 (X = S, Se) modified electrodes was attributed to the presence of metallic 1T phase, which promoted the signal transduction in the developed sensor. The resulting sensors could detect glucose at

concentrations as low as 52 μM. Wang and co–workers achieved comparable sensitivity to glucose (2.8 μM) by functionalizing the surface of MoS_2 with gold nanoparticles and used it as a large capacity scaffold for GOD adsorption.[1002] A non–enzymatic glucose sensor based on the MoS_2 decorated with Cu nanoparticles covered with Nafion binder was developed by Huang et al.[1003] This bio–device exhibited good response (1055 μA mM^{-1} cm^{-2} sensitivity) to glucose in the concentration range of 0.2 mM to 4 mM with high selectivity over DA, UA, and AA.

2D TMDs have also been demonstrated to exhibit appealing properties for the detection of small biological molecules including neurotransmitter, metabolites or vitamins.[394] Narayanan et al. utilized solvent assisted chemical exfoliation to prepare atomically thin sheets of MoS_2 and used it for the determination of DA in the presence of AA.[1004] They reported on the presence of surface negative charges in MoS_2, which eliminated the interference of negatively charged AA, at physiological pH, thus allowing differentiation between AA and DA. Different experimental approach to improve selectivity to DA was adopted by Wu et al., who prepared electrochemically reduced MoS_2 nanosheets on the 3–aminopropyltriethoxysilane modified GCE through irreversible voltammetric cycling of the film in 0.5 M NaCl under N_2 atmosphere.[1005] The formed electrode could differentiate between AA, UA, and DA with the strongest signal observed for DA. The high sensitivity to DA can be explained by the presence of negative charges on the surface of $rMoS_2$ (after electrochemical reduction) which repelled the anionic forms of AA and UA but induced attractive interactions with the cationic form of DA.

Sarkar et al. employed template–free solvothermal method to prepare vanadium sulfide (VS_2)–Nafion modified GCE for a non–enzymatic electrochemical detection of H_2O_2.[1006] The resulting biosensor responded to H_2O_2 in a broad concentration range of 0.5 μM to 3.0 mM, with the LODs of 0.224 μM. Wang et al. further improved sensitivity to H_2O_2 through the incorporation of hydroquinone, as redox mediator, on the surface of MoS_2.[1007] This sensor responded linearly in the concentration range of 1.0×10^{-6} to 9.5×10^{-4} M with the detection limit of 2.6×10^{-7} M, as demonstrated through DPV measurements. Another experimental strategy for sensitive H_2O_2 sensing was shown by Song and co–workers.[1008] The authors, by using horseradish peroxidase immobilized onto the surface of MoS_2–graphene nanocomposite, could sense H_2O_2 with sensitivity of 679.7 μA mM^{-1} cm^{-2}, and nanomolar detection limits 49 nM. In addition, the analytical response was not hindered by the presence of 1 mM interferants such as AA, lysine (Lys), DA, and cysteine (Cys). Yoo et al. performed electrochemical biosensing of H_2O_2 using myoglobin and MoS_2 nanoparticles encapsulated within GO.[1009] The proposed sensor could detect H_2O_2 at 20 nM concentrations, and exhibited good selectivity over AA, $NaNO_2$, and $NaHCO_3$ interferants. The encapsulation of MoS_2 nanoparticles in GO, significantly enhanced the available surface area for myoglobin (Mb) immobilization, consequently improving the measured analytical signal. More recently, the group led by Zhu used GCE modified with MoS_2 nanoparticles for real–time trace amount monitoring of H_2O_2 (LODs 2.5 nM) released from Raw 264.7 cells.[250] The authors attributed good electrocatalytic activity of the developed biosensor, for reduction of H_2O_2, to large fraction of exposed edge sites, and a high surface area of formed nanoparticles.

Nucleic acids. 2D TMDs were also employed to construct electrochemical biosensor not only for detecting small molecules, cells and proteins, but also nucleic acids. Loo and co–workers developed a sensitive DNA sensor based on the disposable electrical printed carbon chip electrodes functionalized with probe DNA molecules by physical adsorption.[1010] MoS_2 nanoflakes were then used as an electroactive label, with the oxidation peak exploited as the analytical signal. The mechanism of detection is based on the different affinity of MoS_2 towards ssDNA and dsDNA. The same research group also investigated the influence of different transition metals (Mo and W) and chalcogens (S and Se) on the interactions between herparin (Hp) and transition metal dichalcogenides.[1011] Se–and Mo–TMDs materials displayed strong interactions with Hp DNA in contrast to WS_2 and WSe_2 TMDs, respectively. Interestingly, upon chemical exfoliation, the difference in the degree of interactions between the immobilized Hp and each TMDs became less significant.

Yang and co–workers electropolymerized xanthurenic acid (XA) directly onto the surface of MoS_2 and used it for direct sensing of guanine and adenine at nanomolar concentrations (LOD of 2.7×10^{-8} M and 3.2×10^{-8} M for adenine and guanine, respectively).[1012] The negatively charged surface of the MoS_2–poly(XA) facilitated the adsorption of positively charge nucleotides on its surface, giving rise to enhanced electrocatalytic effect.[1012] Wang and co–workers exfoliated MoS_2 sheets through sonication in 1–butyl–3–methylimidazolium hexafluorophosphate ionic liquid and thionin to form MoS_2–thionin composites.[1013] The resulting composite film was used as selective biosensor for the detection of dsDNA (0.09 ng mL^{-1} to 1.9 ng mL^{-1}) through intercalation and electrostatic interactions of thionin with DNA. Lee et al. further improved the sensitivity to DNA by immobilization of ssDNA probe molecule onto the surface of MoS_2 in FET device.[1014] The resulting bio–platform responded to targeted ssDNA with high sensitivity of 17 mV dec^{-1}, wide dynamic range of spanning over six orders of magnitude and LOD of 10 fM. The hybridization of target ssDNA with probe molecule in the sensing channel of the biosensor led to the negative shift of the threshold voltage and an increase in the drain current. This observation could be ascribed to electrostatic gating effects induced by the detachment of negatively charged probe DNA molecules from the MoS_2 electrode surface after hybridization.

To further improve adsorption capacity for the loading of probe DNA molecule, Jiao and co–workers electrodeposited free–standing ZnO directly on the surface of MoS_2 scaffold, and consequently used the nanocomposite for the detection of DNA.[1015] The authors reported on high sensitivity of the developed biosensor to DNA with LODs down to 6.6×10^{-16} M concentrations. The good adsorption of probe DNA to MoS_2 surface was attributed to strong

electrostatic interaction between positively charged ZnO and negatively charged DNA. Yang et al. lowered the detection limits to DNA through the fabrication of MoS_2–PANI–DNA nanocomposite modified carbon paste electrode.[1016] MoS_2 was prepared through a liquid exfoliation of bulk MoS_2, while polyaniline–MoS_2 composite was prepared by oxidative polymerization of aniline monomer (ANI) directly on the surface of MoS_2 film. The prepared nanocomposite served as a scaffold for the immobilization of probe DNA. This biosensor exhibited dynamic detection range for the complimentary CaMV35S gene sequence in the concentration range spanning from 1.0×10^{-15} to 1.0×10^{-6} M and the detection limit of 2.0×10^{-16} M. Comparable sensitivity was obtained by Huang et al., who functionalized the surface of WS_2–graphene composite with gold nanoparticles and chitosan, and used it as a support for the immobilization of probe DNA molecules.[1017] The resulting sensor could detect the target DNA at 2.3 fM concentration. Liu and co–workers further lowered the detection limits down to 0.79 fM by incorporating MoS_2–multiwall–carbon nanotubes–Au–GOD onto the surface of GCE. The same sensor could also differentiate between the three–base mismatched DNA and one–base mismatched DNA demonstrating high selectivity for nucleic acid detection.

One of the most sensitive 2D TMDs based sensors for the label–free determination of DNA was fabricated by Jiao and coworkers by using ultrasound exfoliation method to produce a thin–layer of MoS_2.[1018] The thin MoS_2 layers were then used as scaffolds for the immobilization of probe ssDNA molecule, via the van der Waals interactions, between the basal plane of MoS_2 and nucleobases of ssDNA. Upon the hybridization with target ssDNA, the formed dsDNA detached from the MoS_2 surface causing a diminishment in the peak current of methyl blue. The response of this biosensor was linear within the DNA concentration range of 1.0×10^{-10} to 1.0×10^{-4} μM, exhibiting a detection limit of 0.019 fM.[1018] Recently, phosphorodiamidate morpholino oligos DNA functionalized MoS_2 in FET biosensor was used for label–free detection of DNA in serum samples.[1019] High affinity of PMO to bind DNA enabled the detection of target analyte at 6 fM concentrations, which is lower than that of the previously reported MoS_2 FET DNA biosensor based on DNA-DNA hybridization. The resulting MoS_2–based FET sensor demonstrated high sequence selectivity capable of discriminating between the complementary DNA from one-base mismatched DNA, three-base mismatched DNA, and noncomplementary DNA.[1019]

Beyond the DNA analysis, 2D TMDs–based electrodes showed great potential for real–sample RNA and ATP monitoring. For example, the Zhu group fabricated a label free micro–RNA–21 sensor using MoS_2–Au–Thionine composites as transducer and recognition element.[1020] They observed that the formation of the DNA–RNA complex on the surface of electrode hindered the electron transfer of thionine. This bio–platform responded linearly in the 1.0 pM to 10.0 nM concentration range with LODs of 0.26 pM and could detect microRNA–21 in human serum samples. Su et al. immobilized both thrombin and adenosine triphosphate (ATP) specific aptamers on the surface of MoS_2 modified with Au nanoparticles through Au–S bond formation.[1021] This aptasensor could simultaneously detect ATP and thrombin at concentrations as low as 0.74 nM for ATP and 0.0012 nM for thrombin with high selectivity to target molecules over cytidine triphosphate, uridine triphosphate, and guanosine triphosphate, L–lysine, bull serum albumin, Hb, and L–histidine.[1021] The observed signal enhancement was due to the synergy effect between the immobilized aptamer, and the surface of MoS_2–Au modified electrode. The same group also developed a label–free immunosensor based on Au–thionine–MoS_2 composites for carcinoembryonic antigen (CEA) detection.[1022] Under optimal experimental conditions, this bio–platform showed LOD as low as 0.52 pg mL^{-1} and a wide linear response range spanning from 1 pg mL^{-1} to 10 ng mL^{-1}.[1022]

Despite the increasing number of successful demonstrations of 2D TMDCs in biosensing, the fundamental issue lays in the limited understanding of the influence of the structural and compositional defects as well as lateral dimensions/thickness on their sensing properties. In particular, the presence of defects, kinks, and edges contributes to the formation of localized metallic or semi–conductive regions, which similarly to graphene, demonstrate varying catalytic effect for biomolecule sensing.[871, 1023] Therefore, novel synthetic methods, with large degree of structural control, are required to induce desired sensing properties for the engineering of biosensors. The formation of novel hybrid materials through incorporating other electroactive components such as metal oxides, metals, graphene, or conductive polymers may be also of interest for the design of new generation of biosensors. Besides the improvement in the manufacturing of high quality TMDCs, in large area, for biosensor applications, their production at industrial–scale is still challenging. Regardless of these issues, the use of 2D TMDCs is an exciting development, and will provide unique opportunities for biosensing applications.

4.4.4. Metal Oxides

2D metal oxides have recently become recognized as either sensing elements or immobilization scaffolds for the fabrication of biosensors due to their excellent electrical properties arising from the electron confinement effect, high surface–to–volume ratio, high surface reactivity and catalytic activity along with strong adsorption ability for analytes. Impedimetric sensor was developed by Sticker et al., who employed atomic layer deposition to fabricate 15 nm thick coatings of ZrO_2, sandwiched between two Au electrodes, on the PDMS biochip.[1024] The developed bio–platform was then applied for label–free analysis of human lung adenocarcinoma epithelial cell cultures (H441) and human dermal fibroblast cells (NHDF). Vabbina and co–workers immobilized anti–cortisol antibody (Anti–Cab) onto the surface of 2D ZnO modified Au electrodes and used it as label–free cortisol specific immunosensor.[905] The analytical response of these sensors was not affected by the presence of biological interferants in the sample such as PSA, NSE, EGFR and BSA, and the sensor was suitable for cortisol detection at concentrations as low as 1 pM. The improved catalytic performance was attributed to the presence of large

area in polarized (0001) plane in CuO, and high surface charge density that could promote higher loadings of the Anity–Cab antibody on the surface. Tan et al. fabricated a nanocomposite film composed of TiO_2–CH–α–1–fetoprotein antibody, and applied it for the amperometric detection of AFP in real serum samples. The resulting immunosensor responded to AFP within the concentration range of 1.0 to 160.0 ng/mL, and LODs of 0.1 ng mL^{-1}. A nanostructured ZnO film with a wide bandgap (3.37 eV), and a large excitation binding energy (60 eV), prepared using sol–gel process, has been used for the immobilization of ChOx (IEP 4.7) to sense cholesterol with a wide linear range (5.0–400 mg dL^{-1}), low K_m (0.98 mg dL^{-1}), and high sensitivity (59 nA mg^{-1} dL cm^{-2}).[1025] The same research group synthesized ZnO films through radiofrequency magnetron sputtering at 50 mTorr, and also utilized it as a scaffold for ChOx. The fabricated ChOx – ZnO – Au electrode demonstrated high sensitivity and linear responses to cholesterol in the range of 0.65–10.34 mM, and K_m values as low as 2.1 mM. In later study, Solanki et al. immobilized rabbit–immunoglobin antibodies (r–IgGs) together with BSA onto the surface of ZnO for the determination of ochratoxin–A.[1026] The resulting impedimetric sensor showed high sensitivity (189 Ω nM dm^{-3} cm^{-2}) to ochratoxin–A in the concentration range of 0.006–0.01 nM dm^{-3} and LODs of 0.006 nM dm^{-3}. Malhotra and co–workers electrochemically deposited ZrO_2 film onto gold electrode and used it as scaffold for the immobilization of 21–mer ssDNA probe, specific to Mycobacterium tuberculosis. The resulting biosensors exhibited LODs of 65 ng mL^{-1} with response time of less than 60 s.[1027] Solanki et al. also fabricated nanolayers of ZrO_2, through a sol–gel–method, for the immobilization of 17–base ssDNA, identified from the 16s rRNA coding region of Escherichia coli. This biosensor demonstrated high selectivity and sensitivity towards hybridization detection of complementary DNA in the range of 10^{-6} to 10^6 pM.[1028]

FETs based on metal oxides have attracted much attention in biosensing research and related applications due to their high sensitivity and specificity for rapid analyte detection. For example, Balendharm and co–workers incorporated 2D MoO_3 layers, prepared through liquid phase exfoliation, into a FET device for BSA determination with 250 μg mL^{-1} sensitivity.[1029-1030] The exposure of the prepared biosensor induced protein immobilization onto the surface of MoO_3 nanosheets. The negatively charged BSA induced a negative potential on the surface of the sensing layer further resulting in the reduction of the channel conductance. Another strategy to impart selectivity to targeted analytes was demonstrated by Lahav and co–workers, who imprinted (*R*/*S*)–2–methylferrocene carboxylic acids, (*R*/*S*)–2 phenylbutanoic acid, and (*R*/*S*)–2–propanoic acid onto TiO_2 thin film on the gate surface of ISFET devices.[1031] The imprinted sites demonstrated high chiroselectivity and chirospecificity only towards the imprinted target enantiomers. Pogorelova and co–workers fabricated an ISFET device utilizing a molecularly imprinted polymeric membrane containing specific recognition sites for benzylphosphonic acids and thiophenols through the polymerization of titanium(IV) butoxide in the presence of a titanium(IV) phosphonate complexes.[1032] The imprinted TiO_2 films exhibited good sensitivity to different mercaptants and phosphonic acid derivatives in the concentration range of 1×10^{-6} to 5×10^{-4} M.

Mishra et al. employed FTO–coated conducting glass substrate modified with NiO for a non–enzymatic label–free glucose determination.[1033] The biosensor showed good selectivity to glucose over folic acid, AA, and UA, high–specific sensitivity of 3.9 μA μM cm^{-2}, LOD of 1 μM and a response time of less than 1 s. High sensitivity of the NiO coated electrodes to glucose can be attributed to the oxidation of glucose molecules immobilized within larger surface area of the NiO film, catalyzed by the presence of Ni^{3+} sites created by electrochemical cycling. Yang and co–workers observed that the thin layers of CuO–Nafion nanocomposite, deposited on GCE, significantly enhanced sensitivity for non–enzymatic oxidation of glucose.[1034] The authors reported on the LOD of 50 nM, response time under 2 sec, and linear response range spanning from 0.1 to 4.0 mM. The proposed mechanism for the oxidation of glucose on CuO film relied on the deprotonation and isomerization of glucose to its enediol form. This process was then followed by adsorption of glucose onto the electrode surface, and subsequent oxidation by Cu^{II} and Cu^{III}.[1034]

Xu and co–workers fabricated a H_2O_2 biosensor based on ZnO–Au nanoparticles–Nafion–HRP modified GCE.[1035] The observed catalytic current increased linearly with the H_2O_2 concentration in a range of 1.5×10^{-5} to 1.1×10^{-3} M, with the LOD of 9.0×10^{-6} M. Jia et al. further improved sensitivity to H_2O_2 by attaching vertically aligned Co_3O_4 nanowalls, synthesized by directly heating Co foil under ambient conditions, to the surface of GCE using silver paint.[1036] The Co_3O_4 modified electrodes showed good sensitivity to H_2O_2 oxidation (1671 μA $mM^{-1}cm^{-2}$) and the detection limit of 2.8 μM. The improved electrocatalytic performance of Co_3O_4/GCE was due to an increased electro transfer rate between H_2O_2 and Co_3O_4 nanowalls, and enhanced accessibility of many nanoscale transport channels in the composite film. Li and co–workers used benzyltrimethylammonium hydroxide (BTMAH) ionic liquid mediated autoclave reaction to synthesize 2D CuO nanoplates.[1037] The authors suggested that the benzyltrimethylammonium cation preferentially adsorbs onto the (001) planes subsequently blocking the further growth along the [001] direction. This effect led to the growth along the (001) planes giving rise to well–defined 2D nanostructure. The resulting CuO modified electrodes exhibited good electroactivity for the amperometric detection of H_2O_2. Li et al. fabricated 30 nM thick nanosheets of CuO directly onto the surface of Cu foil and applied it for the amperometric sensing of H_2O_2.[1038]

While 2D metal oxides has experienced rapid adoption in the field of biosensing, much remains to be done in exploring the unique features of this exciting materials. Focusing on understanding the nature of biomolecule–transducer interactions using these 2D materials in biosensing applications is also of growing interest. Formation of innovative 2D metal oxides composite materials such as inorganic–organic and metal–semiconductor hybrids, is also being explored as the new approach to harness their

multifunctional properties, resulting from the combination of both nanostructures. For instance, the Schottky barrier formed at the interface between metal oxide and metal nanoparticles can significantly alter the electron transport properties in the material, and thus it may be utilized to enhance charge transfer between redox active enzymes and transducers, consequently improving the performance of bioanalytical devices. Furthermore, surface embedment/immobilization of bioactive molecules with desired bioanalytical properties for facilitating material–analyte interactions as well as improving the charge transfer (e.g., enzymes, MIPs, proteins) should be regarded as a promising strategy for the development of amplified biosensing technologies. Novel synthetic strategies that offer accurate control over the size, morphology and nanostructure of 2D metal oxides, may facilitate their incorporation into integrated bioanalytical devices as well as provide a favorable environment for achieving the oriented immobilization of desired biomolecules on their surface, which can lead to signal amplification. Altogether, still much more should be done for the incorporation of 2D and layered metal oxides for future technological advances.

4.4.5. Other 2D Materials

Boron nitride, consisting of strong sigma bonds and weak van der Waals layered structure, is a material with high thermal conductivity and mechanical stability.[447] 2D *h*–BN has already been utilized as an electrocatalyst in applications such as the oxygen reduction reaction (ORR)[1039] and in metal–free solar energy conversion.[1040] This electrocatalytic performance might beneficial for the development of electrochemical sensors. Khan and co–workers demonstrated that GCE, boron–doped diamond (BDD), and screen–printed graphitic electrodes (SPEs) modified with *h*–BN exhibited electrocatalytic effect to DA oxidation (**Figure 59a–b**).[1041] The electrochemical performance was largely dependent on the mass loading of the *h*–BN, and the nature of the underlying electrode. In particular, *h*–BN drop–cast layer was readily delaminated from the smooth electrode surface as observed for GCE, resulting in higher overpotential required for DA oxidation, and decreased peak current. The resulting electrodes exhibited detection limits of 0.65 μM to DA in the presence of UA. Nonetheless, the simultaneous detection of DA and AA was not possible due to poor peak–to–peak resolution between these biomolecules. The same research group observed that through exfoliation of *h*–BN in surfactant solution the electrochemical performance of the *h*–BN modified SPE to DA oxidation was dominated by the presence of incorporated surfactant e.g., sodium cholate. Such modifications led to diminishment of LODs to 1.57 μM versus pristine *h*–BN.[1042] Li et al. prepared hexagonal *h*–BN flakes through low temperature combustion synthesis, carbothermal reduction and nitridation methods. The synthesized *h*–BN were largely amorphous and possessed layered structure with high density defects and active surface groups. This resulting biosensor could simultaneously differentiate between AA, DA and UA within 30–1000, 0.5–150 and 1–300 μM concentration ranges, with detection limits of 3.77, 0.02 and 0.15 μM for AA, DA and UA, respectively. The enhancement in the electroanalytical response was attributed to high specific surface area together with high density of defects in the *h*–BN.[1043] An amperometric sensor for the detection of indole–3–acetic acid (IAA) using hemin–boron nitride (hemin/BN) nanocomposite modified electrodes was developed by Xu and co–workers.[1044] The hemin–BN nanocomposites were synthesized using a facile hydrothermal method. The sensor responded linearly to changing concentrations of IAA from 0.5 uM to 0.08 mM with a detection limit of 0.1 uM. Seckin and co–workers using polyimide–boron nitride (PI–BN) nanocomposite modified Pt electrodes prepared a DA biosensor. The resulting device exhibited LODs of 4×10^{-8} M to DA oxidation with good selectivity to UA, AA, lactose, urea, and sucrose.[1045] Non–enzymatic glucose sensor has been developed byRanganethan et al. through the use of *h*–BN nanosheets–Cu–BTC MOF composite. Electrochemical measurements demonstrated a sensor sensitivity of 18.1 μA $\mu M^{-1}\,cm^{-2}$, linear response range of 10–900 μM, and LOD of 5.5 μM to glucose. In addition, the biosensor exhibited satisfactory selectivity over dopamine, AA, UA, urea, and nitrate.[1046] Two–dimensional *h*–BN functionalized with graphene quantum dots and molecularly imprinted polymer (MIP) deposited on glassy carbon electrode was capable of detecting serotonin (5–HT) in the 1.0×10^{-12} M to 1.0×10^{-8} M concentration range with LODs of 2.0×10^{-13} M.[1047] The resulting electrodes exhibited high selectivity to serotonin over dopamine, tryptophan, and norepinephrine, and were suitable for direct quantification of this neurotransmitter in urine samples due to high binding affinity of MIP to 5–HT.

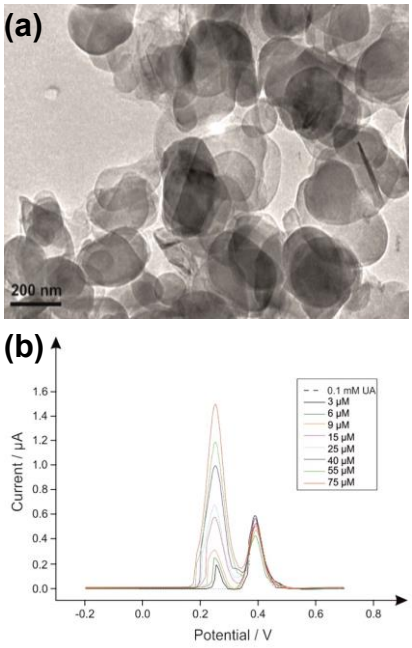

Figure 59. (a) TEM images of 2D–hBN nanosheets. (b) DPVs recorded by adding aliquots of DA at concentrations in the range of 3–75 μM (in 0.1 mM UA in pH 5.0 acetate buffer) utilizing an *h*–BN modified SPEs.[1041] Reproduced from Ref. [1041] Copyright 2016 American Chemical Society.

MXenes have attracted significant research interest in recent years due to their unique properties, such as metallic conductivity, hydrophilic surfaces, and good stability in aqueous environments.[121] This combination of properties makes them suitable candidates for various analytical applications.[1048] Xu and co–workers constructed an ultrathin conductive $Ti_3C_2T_x$ (T: =O, –OH, –F) based FET device, and used it for the monitoring of cultured primary hippocampal neurons as well as the detection of dopamine (**Figure 60a–c**).[1049] The ultrathin $Ti_3C_2T_x$ micropatterns were formed by microcontact printing (μCP) of $Ti_3C_2T_x$ aqueous dispersion directly onto the 3–aminopropyltriethoxysilanecover slips. The resulting devices could detect dopamine through the interaction between DA, and the electrons from the terminal groups (e.g., –OH or–F) of the $Ti_3C_2T_x$ leading to an increase in the number of holes in the material, and subsequently enhancement in the conductance of the FET device. In addition, the same device was used for real–time monitoring of activity of cultured primary hippocampal neurons with excellent biocompatibility even in long term culturing. Wang et al. fabricated a mediator–free biosensor for the detection of H_2O_2 using MXene $Ti_3C_2T_x$ as scaffold for the immobilization of hemoglobin (Hb).[1050] $Ti_3C_2T_x$–Ti_3C_2 sensing layer was prepared by etching Al from Ti_3AlC_2 in HF and subsequently by mixing the synthesized MXene with Hb and Nafion to produce a stable nanocomposite. The resulting biosensors responded linearly to changing concentrations of H_2O_2 in the range of 0.1–260 μM with the LODs of 20 nM. They observed that the enzyme was adsorbed by surface functional groups of the nanolayers, and then is funneled down towards the interior of the MXene nanolayers allowing the immobilization of enzyme on the inner surfaces of the organ–like structure. This effect led to an increased chance of effective collisions between substrate and redox proteins resulting in enhanced performance of the developed sensor. The same research group utilized the special organ–like structure of TiO_2–Ti_3C_2 nanohybrids to entrap Hb on the surface of the electrode and used it as a biosensor for analytical detection of H_2O_2.[1051] The resulting device exhibited wide linear range of response 0.1–380 μM, and detection limits of 14 nM. In addition, the TiO_2–Ti_3C_2 based sensor retained up to 94.6% of the initial response to H_2O_2 after 60–day storage, demonstrating excellent robustness for bioanalytical applications. Lorencova et al. used $Ti_3C_2T_x$ layer drop–cast on GCE as electrocatalyst for reduction of H_2O_2. The fabricated biosensor could detect H_2O_2 amperometrically at the concentrations as low as 0.7 nM with the response time shorter than 10 sec. The same sensor also exhibited sensitivity to direct oxidation of NADH.[1052] An amperometric biosensor platform constructed from $Ti_3C_2T_x$/Au/Nafion/GOD deposited on GCE was recently applied for enzymatic sensing of glucose.[1053] The nanocomposite–based biosensor exhibited a linear amperometric response to glucose in the concentration range from 0.1 to 18 mM with a sensitivity of 4.2 $\mu A mM^{-1} cm^{-2}$ and a detection limit of 5.9 μM. The superior sensing performance of this sensor was attributed to the presence of Au/$Ti_3C_2T_x$, which effectively facilitated electron transfer between the active redox centers of the enzyme and the electrode.

Zhu and co–workers also utilized MXene–Ti_3C_2 and Nafion composite layer as effective scaffold for the immobilization of Hb on the GCE to fabricate a mediator–free biosensor for nitrite determination.[1054] The resulting MXene–based bio–platform displayed a low detection limit of 0.12 μM, and a linear response range spanning from 0.5 to 11800 μM, and was applied for the detection of nitrite in environmental water samples without any other pretreatment. GOD immobilized on the surface of $Ti_3C_2T_x$ nanosheets decorated with Au nanoparticles and Nafion was used to construct an enzymatic glucose biosensor by Rakhi and co–workers.[1055] The fabricated biosensor demonstrated electrocatalytic activity toward the detection of glucose within 0.1 mM to 18 mM concentration range with the LOD of 5.9 μM, and good selectivity over biological interferants including DA, UA, and AA.[1055] $Ti_3C_2T_x$ sheets doped with Pt nanoparticles has been adopted by While Lorencova et al. todevelop biosensor for the detection of AA, DA, UA, acetaminophen, and H_2O_2.[1052] The authors observed that the detection of H_2O_2 (LOD of 448 nM) was not compromised by the presence AA, DA, UA, and acetaminophen, since the applied potential for H_2O_2 catalysis was below the redox potential required to oxidize the interferants. Even though each individual biomolecule could be detected at the nM concentrations, the selectivity of the formed nanohybrid material was largely dictated by the presence of outer membrane e.g., chitosan or Nafion, in particular $Ti_3C_2T_x$–Pt hybrids offer limited resolution between DA and AA, which may create difficulties in the practical application of these sensing devices.

The intriguing properties of 2D nanomaterials such as tunable conductivity, large surface area, biocompatibility, or electronic anisotropy further suggests that future advances in the interdisciplinary research are likely to lead to a new generation of electrochemical biosensors. The most recent progress in this field relies on the synthesis of novel hybrid materials by combining the 2D nanostructures with other compounds such as metal nanoparticles, metal oxides or conductive polymers leading to the fabrication of electrochemical sensors and biosensors with improved analytical performance due to the synergistic combination of their electroanalytical properties. Most of the biosensing experiments reported using 2D materials had to be performed under a controlled environment due to often limited stability to water and air that results in the degradation of the nanostructures. Therefore, novel ways to improve stability of these materials (e.g., through the application of protective coating or careful device engineering) need to be addressed for practical biosensing applications. The evaluation of the toxicity and biocompatibility of each 2D material is also critical for in vivo applications in sensing. The electrical properties of many 2D materials in the context of biosensing also vary significantly with the presence of lattice defects including corner atoms, uncoordinated open sites, kinks, nanoribbons or edges, where the edge sites, in contrast to basal plane, typically exhibit high electrocatalytic transformations for material–analyte interactions. Hence, future work needs to concentrate on obtaining better understanding of the influence of structural and compositional

defects on the sensing properties of 2D materials as well as developing novel synthetic approaches that provide high degree of compositional control over the final structure. In addition, the lack of suitable technology for manufacturing of 2D nanostructures at the industrial scale, with uniform quality and large area, is yet another challenge. Despite these challenges, 2D materials possess numerous attractive properties for biosensors development, thus opening new realm of possibilities for analytical applications that are currently non–accessible using conventional 0D, 1D or 3D materials. In particular, the field of flexible/wearable electronics could significantly benefit from the mechanical compatibility of these 2D nanomaterials with current device fabrication methods, giving rise to a new generation of multifunctional biosensing devices.

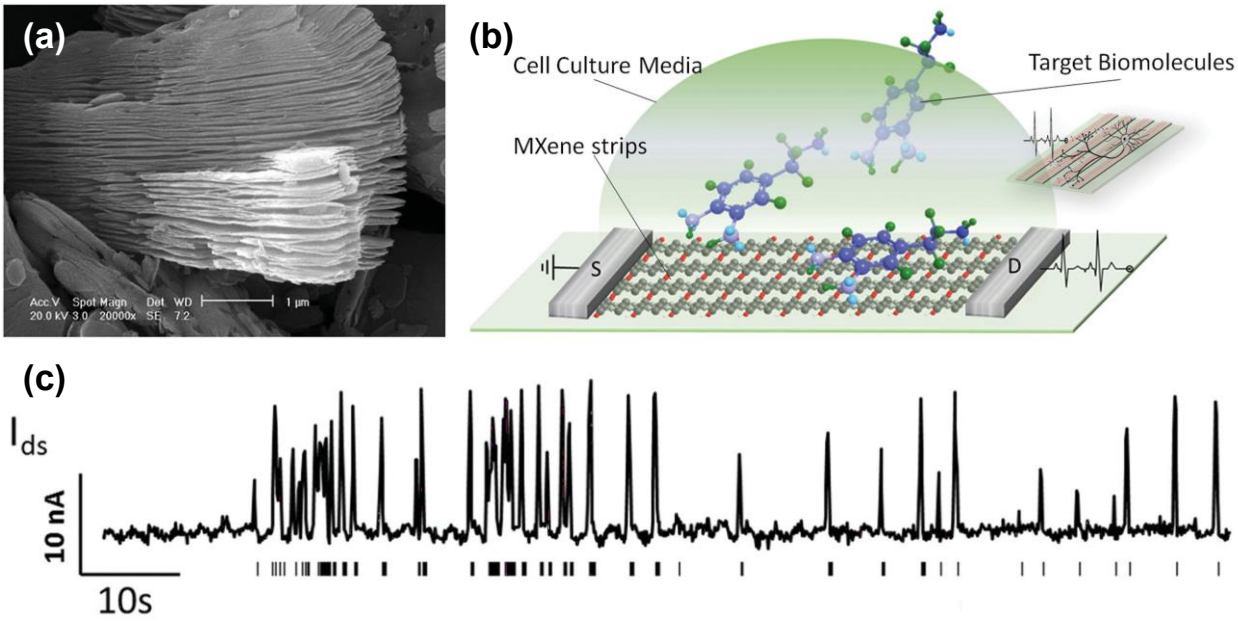

Figure 60. (a) SEM image of the multilayer-structured MXene; (b) Schematic of a biosensing device based on MXene field-effect transistors; (c) The derivation of neuronal spiking activities by using current measurements with the MXene–FET device.[1049] Reproduced with permission from Ref. [1049] Copyright 2016 John Wiley and Sons.

Table 6. Summary of Sensing Performances for Biomolecules by 2D Materials.

Specific Analyte	Material	Architecture	Readout/ Method	LOD	Experimental range	Notes	Ref
(*S*)–2–methylferro–cene carboxylic acids	TiO_2	FET: $Si/SiO_2/TiO_2$	I	0.6 mM	0.125–6.25 mM	(*R*)–2–Methylferro–cene carboxylic acids	1031
(*S*)–2–phenylbutanoic acid	TiO_2	FET: $Si/SiO_2/TiO_2$	I	0.5 mM	0.25–2.5mM	(*R*)–2–phenylbutanoic acid	1031
(*S*)–2–propanoicacid	TiO_2	FET: $Si/SiO_2/TiO_2$	I	0.45 mM	0.3–1.25 mM	(*R*)–2–propanoicacid	1031
17β–estradiol	WS_2–Au NP–AP	WS_2–Au NP–AP/GCE	DPV	2 pM	1.0×10^{-11}–5.0×10^{-9} M	Naphthalene, 1–amino-anthraquinone	996
AA	Gr	Gr/GCE	Amp	6.45 μM	9.00–2314 μM	DA, UA	1056
AA	Gr	Gr/PPF	CV	0.12 mM	0.4–6.0 mM	Glucose	921
AA	Gr–Fe_3O_4–NH_2	Gr–Fe_3O_4–NH_2/GCE	Amp	0.074 μM	5.0–1600 μM	DA, UA	1057
AA	Gr–Pt–Nafion	Gr–Pt–Nafion/GCE	DPV	0.15 μM	0.15–34.4 μM	DA, UA	1058
AA	*h*–BN	*h*–BN/GCE	DPV	3.77 μM	30–1000 μM	DA, UA	1043
AA	rGO	rGO/GCE	DPV	250 μM	0.5–2 mM	K^+, Ca^{2+}, Na^+, Mg^{2+}, Zn^{2+}, NH_4^+, Cl^-, SO_4^{2-}, NO_3^-, HCO_3^-	1059
AA	rGO–Au	rGO–Au/GCE	DPV	5.1×10^{-5} M	2.4×10^{-4}–1.5×10^{-3} M	NaCl, KCl, $NaNO_3$, $CaCl_2$, Glucose, L–cysteine, CA	1060

Specific Analyte	Material	Architecture	Readout/ Method	LOD	Experimental range	Notes	Ref
AFP	Gr–anti–AFP–Thi	Gr–anti–AFP–Thi/GCE	CV	5.77 pg mL^{-1}	0.05–2.00 ng mL^{-1}	IgG, vitamin C, BSA, Glucose	965
AFP	Gr–Au–COOH–Thi–Nafion	Gr–Au–COOH–Nafion–Thi–anti–AFP/GCE	DPV	5.4 pg mL^{-1}	0.016–50 ng mL^{-1}	AFP, CEA, SS2	1061
AFP	Gr–COOH–Au–Pd	Gr–COOH–Au–Pd/GCE	Amp	5 pg mL^{-1}	0.05–30 ng mL^{-1}	N/A	1062
AFP	Gr–CT–HRP–anti–AFP–Au–PTH	Gr–CT–HRP–anti–AFP–Au–PTH/GCE	CV	0.7 ng mL^{-1}	1.0–10 ng mL^{-1}	N/A	963
AFP	rGO–Au NP–PEDOT–PB	rGO–AuNP–PEDOT–PB/GCE	DPV	3.3 pg mL^{-1}	0.01–50 ng mL^{-1}	CEA, PSA, BSA, DA, AA, Glucose	964
aliskiren	rGO–Pt NP–Nafion	rGO–PtNP–Nafion/GCE	DPV	8.2 nM	0.045–0.45 μM; 0.45–2.70 μM	K^+, Na^+, Ca^{2+}, Cl^-, NO_3^-, SO_4^{2-}	971
ATP	Gr–Pr–ATA	Gr–Pr–ATA/GCE	DPV	0.7 nM	2.2 nM–1.3 μM	CTP, GTP, UTP	1063
ATP	MoS_2–Au NP–Aptamer	MoS_2–AuNP–Aptamer /GCE	SQWV	0.74 nM	1 nM–10 mM	CTP, UTP, GTP	1021
biotin–streptavidin	MoS_2	FET: $Si/SiO_2/MoS_2$/ Ti–Au/Ti–Au	I	100 fM	N/A	IgG	184
bisphenol A	MoS_2–Au NP–CS	MoS_2–AuNP–CS/GCE	CV	5 nM	0.05–100 μM	Al^{3+}, Fe^{3+}, Ca^{2+}, Mg^{2+}, Cu^{2+}, Zn^{2+}, SO_4^{2-}, Br^-, Cl^-, F^-, NO_3^-	998
BNP	rGO–Pt NP–anti–BNP	FET: Si/SiO_2/rGO–Pt NP–anti–BNP/Au/Au	I	0.1 pM	100 fM–1 nM	BSA, D–Dimer, HAS	1064
BRCA1 5382	rGO–Au NP–ssDNA	rGO–Au NP–ssDNA/GCE	EIS	1.0×10^{-20} M	3.0×10^{-20}–1.0×10^{-12} M; 1.0×10^{-12}–1.0×10^{-7} M	CT–DNA, NC–DNA	961
BSA	MoO_3	FET: Al_2O_3/MoO_3 /Ag/Ag	R	15 μM	1–25 mg mL^{-1}	N/A	1030
caffeine	rGO	rGO/GCE	DPV	N/A	50–300 μM	Theophylline, Methyl xanthine	943
carbofuran	Gr–COOH–NiO–Nafion	Gr–COOH–NiO–Nafion/GCE	Amp	5×10^{-13} M	1.0×10^{-12}–1×10^{-10} M; 1.0×10^{-10}–1×10^{-8} M	Lucose, CA, OA PO_4^{3-}, SO_4^{2-}, NO_3^-, Cu^{2+}, Pb^{2+}	1065
CEA	Gr–Anti–CEA	FET: Si/SiO_2/Gr–Anti–CEA/Au/Au	I	100 pg L^{-1}	100 pg mL^{-1}–100 ng mL^{-1}	NSE, CYFRE21–1	966
CEA	Gr–Au–COOH–Nafion	Gr–Au–COOH–Nafion/GCE	DPV	2.8 pg mL^{-1}	0.010–50 ng mL^{-1}	AFP, CEA, SS2	1061
CEA	Gr–IL–Nafion	Gr–IL–Nafion/GCE	DPV	0.34 fg mL^{-1}	0.5 fg mL^{-1}–0.5 ng mL^{-1}	CEA, PSA, BSA, MUC1	1066
CEA	MoS_2–Au–Ab	MoS_2–Au–Ab/GCE	DPV	0.27 pg mL^{-1}	1 pg mL^{-1}–50 ng mL^{-1}	HCG, CA125, PSA, AFP	999
CEA	MoS_2–PB	MoS_2–PB/GCE	DPV	0.54 pg mL^{-1}	0.005–10 ng mL^{-1}	AFP, NSE, BSA, IgG.	1046
CEA	MoS_2–Thi–Au NP	MoS_2–Thi–Au NP/GCE	SWVQ	0.52 pg mL^{-1}	1 pg mL^{-1}–10 ng mL^{-1}	NSE, IgG, AFP	1022
CEA	rGO–HRP–Ab_2	rGO–HRP–Ab_2/GCE	EIS	0.64 pg mL^{-1}	1.0 pg mL^{-1}–80 ng mL^{-1}	hIgG, AFP, PSA	967
cells	Gr–AP–Laminin	Gr–AP–Laminin/ITO	Amperometric	0.1×10^{-6} M	0.1×10^{-6} M–100×10^{-6} M	N/A	978
cells (Du–145)	Gr–Au NP–Ab–HRP	Gr–Au NP–Ab–HRP/Au	DPV	20 cells mL^{-1}	10^2–10^6 cells mL^{-1}	MCF–7, 293T, HepG2, L02 cells	979
cells (Hella)	Gr–PTCA–Aptamer	Gr–PTCA–Aptamer/GCE	EIS	794 cells mL^{-1}	1.0×10^3–1.0×10^6 cells mL^{-1}	HeLa cells, K562 cells, MDA–231 cells, Normal cell line, NIH3T3 cells	975
cells (HL–60)	Gr–CMC–PEI–FA	Gr–CMC–PEI–FA/GCE	EIS	500 cells mL^{-1}	5.0×10^2–5.0×10^6 cell mL^{-1}	A549 cells, HL–60 cells	976
cells (Leukemia)	Gr	Gr/GR	DPV	0.02 cell mL–1	1.0×10^5–0.1 cell mL^{-1}	CCRF–CEM, B–CLL	981
cells (Leukemia)	Gr–Au–Aptamer	Gr–Au–Aptamer/GCE	DPV	350 cells mL^{-1}	5.0 x 10^2 to 1.0 x 10^7 cells mL^{-1}	HL–60, CEM, Hela, K562	982
cells (Leukemia)	Gr–N–Aptamer	Gr–N–Aptamer/SPE	DPV	10 cells mL^{-1}	1.0×10^1–1.0×10^6 cell mL^{-1}	CCRF–CEM, Ramos cells	984

Specific Analyte	Material	Architecture	Readout/ Method	LOD	Experimental range	Notes	Ref
cells (Leukemia)	Gr–PLL	Gr–PLL/GCE	EIS	30 cells mL^{-1}	1.0×10^{2}–1.0×10^{7} cells mL^{-1}	MDA–MB–435S, MDA–MB–231, MDA–MB–453, MCF–7, T–47D cell lines	126
cholesterol	Gr–ChOx	Gr–ChOx/GR	Amp	5 μM	50–350 μM	N/A	1067
cholesterol	Gr–CS–Pd–Pt	Gr–CS–Pd–Pt/GCE	Amp	0.75 μM	2.2×10^{-6}–5.2×10^{-4} M	AA, UA, Glucose	1068
cholesterol	Gr–Pt–ChE–ChO	Gr–Pt–ChE–ChO/GCE	Amp	0.2 μM	0.2–35 μM	N/A	926
cholesterol	Gr–PVP–PANI	Gr–PVP–PANI/SPE	Amp	1 μM	50 μM–10 mM	AA, Glucose	1069
cholesterol	Gr–TiO_2–PdPt–ChO	Gr–TiO_2–PdPt–ChOx/GCE	Amp	0.017 μM	5.0×10^{-8} – 5.9×10^{-4} M	AA, DA, UA, Glucose	925
cholesterol	Gr–β–CD–MB	Gr–β–CD–MB/GCE	DPV	1 μM	1–100 μM	NaCl, KCl, $MgCl_2$, Glycine, Tyrosine, Tryptophan, AA, SDS, Lidocaine, Chloropramine, Quinine, Quindine, Piroxicam	924
cholesterol	ZnO–ChOx	ZnO–ChOx/ITO	CV	0.5 mg L^{-1}	5–400 mg L^{-1}	AA, UA, Glucose, LA, Urea, Sodium pyruvate	1025
cocaine	rGO–Au–aptamer	rGO–Au–aptamer/SPE	DPV	1.5 x 10^{-3} pM	1–500 nM	Ecgonine methyl ester, Benzoyl ecgonine	1070
cortisol	ZnO–Anti–C_{ab}–BSA	ZnO–Anti–C_{ab}–BSA/Au	CV/EIS	1 pM	1 pM–100 nM	PSA, NSE, EGFR	1071
DNA	Gr	FET: Si/SiO_2/Gr/Au/Au	I	10 pM	N/A	SNS–DNA	1072
DNA	Gr	Gr/GCE	DPV	N/A	N/A	A, G, C, T	950
DNA	Gr	Gr/GCE	DPV	1 μg mL^{-1}	N/A	A, G, C, T	951
DNA	Gr–Au	Gr–Au/GCE	Amp	3.4 fM	50–5000 fM	MM–DNA, NC–DNA	956
DNA	Gr–Au NP–DNA	Gr–Au NP–DNA/GCE	DPV	8.3×10^{-12} M	2.5×10^{-11}–1.3×10^{-9} M	SBM–DNA, TBM–DNA, NC–DNA	957
DNA	Gr–MoS_2–CT–Au–ssDNA	Gr–MoS_2–CT–Au–ssDNA/GCE	DPV	0.0022 pM	5.0×10^{-14}–5.0×10^{-9} M	SBM–O, C–O, TBM–O	1073
DNA	Gr–MoS_2–DNA	Gr–MoS_2–DNA/GCE	DPV	1.0×10^{-17} M	1.0×10^{-16}–1.0×10^{-13} M	NC–DNA, SBM–DNA, DBM–DNA	953
DNA	Gr–ssDNA	FET: Si/SiO_2/Gr–ssDNA/Cr/Au	I	1 fM	100 pM–100 nM	SBM–DNA, DBM–DNA, Random sequence DNA	959
DNA	MoS_2	MoS_2/DEP	DPV	0.03 nM	0.03 nM–300 nM	C–DNA, SBM–DNA, NC–DNA	1010
DNA	MoS_2	FET: Si/SiO_2/MoS_2/Cr–Au/Cr–Au	I	10 fM	1.0×10^{-14}–1.0×10^{-8}	SS–DNA, C–DNA, NC–DNA, SBM–DNA	1014
DNA	MoS_2–Au	MoS_2–Au/GCE	DPV	11 fM	0.01–100 pM	BSA, IgE, Thrombin, HAS	1074
DNA	MoS_2–PANI–DNA	MoS_2–PANI–DNA/GCE	EIS	2.0×10^{-16} M	1.0×10^{-15}–1.0×10^{-6} M	NC–DNA, SBM–DNA	1016
DNA	MoS_2–ssDNA	MoS_2–ssDNA/CPE	DPV	1.9×10^{-17} M	1.0×10^{-16} M–1.0×10^{-10} M	NC–DNA, SBM–DNA, TBM–DNA	1018
DNA	MoS_2–Thi	MoS_2–Thi /GCE	SQWV	0.09 ng mL^{-1}	0.09 ng mL^{-1}–1.9 ng mL^{-1}	BSA	1013
DNA	MoS_2–ZnO–ssDNA	MoS_2–ZnO–ssDNA/GCE	DPV	6.6×10^{-16} M	1.0×10^{-15} M–1.0×10^{-6} M	N/A	1015
DNA	rGO	rGO/GR	DPV	9.4 zM	0.1 fM–10 mM	A, G, C, T	952
DNA	rGO	rGO/SPE	DPV	30 nM	N/A	Wild–type, Mutant, NC–DNA	958
DNA	rGO–Au	Gr–Au/GCE	DPV	2.0×10^{-7} M	2.0×10^{-7}–1.0×10^{-6} M	Synthetic DNA, SBM–DNA, DBM–DNA	948
DNA	rGO–Au NP–ssDNA	rGO–Au NP–ssDNA/GCE	DPV	5 aM	1×10^{-17}–1×10^{-13} M	SBM–DNA, TBM–DNA	960
DNA	WS_2–Gr–CT–Au NP–ssDNA	WS_2–Gr–CT–Au NP–ssDNA/GCE	DPV	0.0023 pM	0.01–500 pM	NC–DNA, SBM–DNA, TBM–DNA	1017
adenine	Gr–COOH	Gr–COOH/GCE	DPV	2.5×10^{-8} M	0.5–200 μM	N/A	945
adenine	Gr–PPy	Gr–PPy/GCE	LSV	0.02 μM	0.06–100 μM	AA, DA, Glucose, K^+, Na^+, Ca^{2+}, Mg^{2+}, Fe^{3+}, Al^{3+}, Zn^{2+}, NH_4^+, Cl^-, NO_3^-, SO_4^{2-}, CO_3^{2-}, F^-, Br^-	949

Specific Analyte	Material	Architecture	Readout/ Method	LOD	Experimental range	Notes	Ref
adenine	MoS_2–PXA	MoS_2–PXA/CPE	DPV	3.2×10^{-8} M	0.5–10 μM	N/A	1012
guanine	Gr–COOH	Gr–COOH/GCE	DPV	5.0×10^{-8} M	0.5–200 μM	N/A	945
guanine	Gr–PPy	Gr–PPy/GCE	LSV	0.01 μM	0.04–100 μM	AA, DA, Glucose, K^+, Na^+, Ca^{2+}, Mg^{2+}, Fe^{3+}, Al^{3+}, Zn^{2+}, NH_4^+, Cl^-, NO_3^-, SO_4^{2-}, CO_3^{2-}, F^-, Br^-	949
guanine	MoS_2–PXA	MoS_2–PXA/CPE	DPV	2.7×10^{-8} M	0.5–10 μM	N/A	1012
DNA (HBV)	GO–DNA	GO–DNA/PGE	DPV	2.02 μM	20–160 μg mL^{-1}	C–DNA, NC–DNA, MM–DNA	946
DA	GO–Au–polydA	GO–Au–polydA/Au	DPV	0.1 pg mL^{-1}	1.0×10^{1}–1.0×10^{5} cells mL^{-1}	HL7702, HEK293, HeGp2, Hela, MCF–7	1075
DA	GO–Ferulic acid	GO–Ferulic acid/GCE	Amp	0.19 μM	0.6–1000 μM	5–HT, Glucose, AA, H_2O_2, UA	1076
DA	Gr	Gr/Si	DPV	0.17 μM	1–50 μM; 50–100 μM	AA, UA	908
DA	Gr	Gr/GCE	DPV	2.64 μM	4–100 μM	N/A	1077
DA	Gr	Gr/GCE	DPV	1 mM	N/A	AA, HT–5	1078
DA	Gr–CT	Gr–CT/GCE	DPV	5 μM	5–200 μM	AA, UA	909
DA	Gr–EDTA–Nafion	Gr–EDTA–Nafion/GCE	DPV	0.01 μM	0.20–25 μM	AA	910
DA	Gr–Fe_3O_4–NH_2	Gr–Fe_3O_4–NH_2/GCE	Amp	0.13 μM	0.2–38 μM	AA, UA	1057
DA	Gr–LDH	Gr–LDH/GCE	SQWV	0.3 μM	1.0–199 μM	AA, UA	916
DA	Gr–PANI–DA–Aptamer	Gr–PANI–DA–Aptamer/GCE	CV	1.98 pM	0.007–90 nM	Tyramine, AA, Hydroxytyrosine, 3,4–dihydroxyphenylacetic acid, Homovanillic acid	206
DA	Gr–Pt–Nafion	Gr–Pt–Nafion/GCE	DPV	0.03 μM	0.03–8.13 μM	AA, UA	1058
DA	Gr–PVP	Gr–PVP/GCE	Amp	0.2 nM	5.0×10^{-10}–1.1×10^{-3}	AA, UA	912
DA	Gr–SO_3^-	Gr–SO_3^-/GCE	DPV	40 nM	0.20–20 μM	AA, UA	913
DA	Gr–β–CD	Gr–β–CD/GCE	CV	5.0 nM	0.009–12.7 μM	AA	911
DA	*h*–BN	*h*–BN/SPE	DPV	1.57 μM	3–75 μM	AA, UA	1042
DA	*h*–BN	*h*–BN/SPE	DPV	0.65 μM	3–75 μM	AA, UA	1041
DA	*h*–BN	*h*–BN/GCE	DPV	0.02 μM	0.5–150 μM	AA, UA	1043
DA	*h*–BN–PI	*h*–BN–PI/Pt	DPV	4×10^{-8} M	4.0×10^{-8} –52.0×10^{-8} M	AA, UA	1045
DA	MoS_2–APTES	MoS_2–APTES/GCE	DPV	1 μM	1–50 μM	AA, UA	1005
DA	rGO	rGO/GCE	DPV	0.5 μM	0.5–60 μM	K^+, Ca^{2+}, Na^+, Mg^{2+}, Zn^{2+}, NH_4^+, Cl^-, SO_4^{2-}, NO_3^-, HCO_3^-	1059
DA	rGO–Au	rGO–Au/GCE	DPV	1.4×10^{-6} M	6.8×10^{-6}–4.1×10^{-5} M	NaCl, KCl, $NaNO_3$, $CaCl_2$, Glucose, l–cysteine, CA	1060
DA	rGO–Fe_3O_4	rGO–Fe_3O_4/GCE	DPV	0.08 μM	0.4–3.5 μM	AA, UA	914
DA	rGO–nile blue–AuNP	rGO/nile blue/AuNP	SWV	1 nM	10 nM to 0.2 mM	AA, UA, epinephrine, norepinephrine, glucose	897
DA	rGO–Pd NP	rGO–Pd NP/GCE	DPV	0.233 μM	1–150 μM	AA, UA, Glucose	915
DA	rGO–SnO_2–Au NP–PDA	rGO–SnO_2–Au NP–PDA/GCE	DPV	5 nM	0.008–20 μM	AA, UA	917
DA	$Ti_3C_2T_x$	FET: Glass/$Ti_3C_2T_x$/Ag/Ag	I	100×10^{-9} M	100×10^{-9} M–50×10^{-6} M	N/A	1049
erythromycin	Gr–Lac–ABTS/GCE	Gr–Lac–ABTS/GCE	Amp	10 μM	0.05–0.4 mM	AA, UA	977
escherichia coli	ZrO_2–ssDNA	ZrO_2–ssDNA/ITO	DPV	1.0×10^{-6} pM	1.0×10^{-6}–1.0×10^{6} pM	NC–DNA	1028
escherichia coli O157:H7	rGO–Au NP–Ab	rGO–Au NP–Ab/rGO	EIS	1.5×10^{2} cfu mL^{-1}	1.5×10^{2}–1.5×10^{7} cfu mL^{-1}	E. coli DH 5α, S. aureus, L. monocytogenes	983
glucose	CuO–Nafion	CuO–Nafion/GCE	Amp	50	0.1–4.0 mM	AA, UA, NaCl	1034
glucose	GO–Ag NP–SiO_2–GOD	GO–Ag NP–SiO_2–GOD/GCE	CV	0.31 mM	2–12 mM	N/A	892
glucose	GO–CT–Fc–GOD	GO–CT–Fc–GOD/GCE	Amp	7.6 μM	0.02–6.78 mM	N/A	1079

Specific Analyte	Material	Architecture	Readout/ Method	LOD	Experimental range	Notes	Ref
glucose	GO–CuO	GO–CuO/GCE	Amp	0.69 μM	2.79 μM–2.03 mM	AA, UA	1080
glucose	GO–Pt NF	GO–Pt NF/GCE	Amp	2 μM	2 μM–10.3 mM; 10.3–20.3 mM	N/A	897
glucose	Gr–Au–GOD–DNA	Gr–Au–GOD–DNA/GCE	CV	0.3 μM	0.8–50 μM	AA, UA, ACT	890
glucose	Gr–Co_3O_4	Gr–Co_3O_4/GCE	Amp	25 nM	20 μM–80 μM	AA, UA	901
glucose	Gr–Cu	Gr–Cu/GCE	Amp	0.5 μM	0.5 μM–4.5 mM	Lactose, Fructose, Sucrose, AA, DA, UA	1081
glucose	Gr–CuO	Gr–CuO/GCE	Amp	0.23 μM	0.5–5 μM; 10–100 μM	AA, UA, Ethanol	897
glucose	Gr–GOD	FET: Au/PDMS/Gr–GOD /Gr–Ag NW/ Gr–Ag NW	I	0.4 μM	1 μM–10 mM	N/A	894
glucose	rGO-N–Chitosan–GOD	rGO-N–Chitosan–GOD/GCE	Amp	0.01 mM	0.1 to 1.1 mM	AA, UA	885
glucose	Gr–N–CT–GOD	Gr–N–CT–GOD/GCE	Amp	0.01 mM	0.1–1.1 mM	AA, UA	889
glucose	Gr–NiO	Gr–NiO/GCE	Amp	5 μM	5 μM–4.2 mM	AA, DA, UA	1082
glucose	Gr–PDDA–CuO	Gr–PDDA–CuO/GCE	Amp	0.2 μM	0.4–4000 μM	Fructose, Lactose, Sucrose, AA, UA, DA	896
glucose	Gr-Pd	FET: Au/PBS-NaOH/Gr-Pd/Au/Au	I	1 nm	10^{-9} M–10^{-6} M	UA, AA	904
glucose	Gr–Pd NP–CT–GOD	Gr–Pd NP–CT–GOD/GCE	Amp	0.2 μM	1.0 μM–1.0 mM	UA, AA	891
glucose	Gr–Pd NP–Nafion	Gr–Pd NP–Nafion/GCE	Amp	1 μM	10 μM–5 mM	AA, UA, AP	898
glucose	Gr–Pt NP–CT–GOD	Gr–Pt NP–CT–GOD/GCE	Amp	0.6 μM	0.15–5 mM	N/A	888
glucose	*h*–BN–CuBTC–Nafion	*h*–BN–CuBTC–Nafion/GCE	Amp	5.5 μM	10–900 μM	AA, DA, UA, Urea, NaCl, KNO_3	1046
glucose	In_2O_3	FET: Si/SiO_2/In_2O_3/Ti–Au/Ti–Au	I	7 fM	1.0×10^{-11}–1.0×10^{-5} M,	N/A	1083
glucose	MoS_2	MoS_2/GCE	CV, Amp	2 mM	2.00–16.0 mM	N/A	250
glucose	MoS_2–Au–GOD	MoS_2–Au–GOD	Amp	0.042 μM	0.25–13.2 mM	N/A	1084
glucose	MoS_2–Au–GOD–Nafion	MoS_2–Au–GOD–Nafion/GCE	Amp	2.8 μM	10–300 μM	KCl, NaCl, DA, UA	1002
glucose	MoS_2–Cu–Nafion	MoS_2–Cu–Nafion/GCE	Amp	0.2 mM	0.2–4 mM	AA, DA, UA	1003
glucose	MXene–Au–Nafion–GOD	MXene–Au–Nafion–GOD/GCE	Amp	5.9 μM	0.1–18 mM	DA, UA, AA	1055
glucose	NiO	NiO/FTO	Amp	1 μM	0.1–1.1 mM	AA, FA, UA	1033
glucose	rGO–CuS	rGO–CuS/GCE	Amp	0.19 μM	1–2000 μM	Na^+, Ca^{2+}, Al^{3+}, NO_3^-, Cl^-, SO_4^{2-}, FA, DA, OA, AA, UA, Fructose, Maltose, Lactose	893
glucose	rGO–GOD–PPy	rGO–GOD–PPy/GCE	Amp	3 μM	2–40 μM	N/A	886
glucose	rGO–MWCNT	rGO–MWCNT/GCE	Amp	4.7 μM	0.01–6.5 mM	N/A	1085
glucose	rGO–Pt–Ni NP	rGO–Pt–Ni NP/GCE	Amp	0.2 μM	0.05–5.66 mM	AA, DA, UA, GA, LA, Acetaminophen	1086
glucose	rGO–Pt–Ni NP	GO–Pt–Ni NP/GCE	Amp	0.01 mM	0.01 mM–35 mM	AA, UA, Urea, AAP, Fructose	899
glucose	$Ti_3C_2T_x$-Au	$Ti_3C_2T_x$-Au-Nafion-GOD/GCE	Amp	5.9 μM.	0.1 to 18 mM	N/A	1053
glucose	VS_2–Nafion	VS_2–Nafion/GCE	Amp	0.21 μM	0.5 μM–3 mM	UA, AA, L–cysteine	1006
glucose	WS_2–GOD–GTA	WS_2–GOD–GTA/GCE	Amp	52.0 μM	77 – 274 μM; 0.77 – 22.3 mM	AA, DA, UA, Glucose,	1001
glutathione	Gr	Gr/SPE	Amp	3 μM	10–500 μM	AA, UA, L–cysteine Glucose	899
guanosine	Gr–CT–Fe_3O_4	Gr–CT–Fe_3O_4/GCE	DPV	7.5×10^{-7} M	2.0×10^{-6}–3.5×10^{-4} M	A, G	947
H_2O_2	BP	BP/GCE	EIS	1.0×10^{-7}M	1.0×10^{-7}–5.0×10^{-5} M	N/A	988
H_2O_2	BP-pLL	BP-pLL/GCE	CV		10–700 μM	AA, UA	971
H_2O_2	Co_3O_4	Co_3O_4/GCE	Amp	2.8 μM	0–5.35 mM	N/A	1036

Specific Analyte	Material	Architecture	Readout/ Method	LOD	Experimental range	Notes	Ref
H_2O_2	CuO	CuO/Cu	Amp	N/A	N/A	N/A	1038
H_2O_2	CuO–Nafion	CuO–Nafion/GCE	Amp	500 μM	500 μM–50 mM	N/A	1037
H_2O_2	Gr–CT–Hb	Gr–CT–Hb/GCE	Amp	5.1×10^{-7} M	6.5–230 μM	N/A	933
H_2O_2	Gr–CT–MP11	Gr–CT–MP11/Au	Amp	2.0 μM	2.5–135 μM	N/A	936
H_2O_2	Gr–HRP–ADA–CD	Gr–HRP–ADA–CD/GCE	Amp	0.1 μM	0.7–35 μM	Glucose, Ethanol, OA, AA, UA	901
H_2O_2	Gr–Pt	Gr–Pt/GCE	Amp	0.05 μM	0.1 μM–1.0 mM	N/A	900
H_2O_2	Gr–Pt	Gr–Pt/GCE	Amp	80 nM	1 μM–500 μM	AA, UA	937
H_2O_2	Gr–SDBS–HRP	Gr–HRP/GCE	Amp	1.0×10^{-7} M	1.0×10^{-6} M–2.6×10^{-3} M	Glucose, Sucrose, Ethanol, LA, AA, CA	935
H_2O_2	Gr–SO_3^-–Au	Gr–SO_3^-–Au/GCE	Amp	0.20 μM	20 μM–15 mM	Mg^{2+}, Ca^{2+}, Zn^{2+}, Fe^{2+}, Al^{3+}, Cl^-, NO_3^-, SO_4^{2-}, Glucose	902
H_2O_2	Gr–TPA–HRP	Gr–TPA–HRP/GCE	Amp	1.1×10^{-7} M	6.3×10^{-7}–1.68×10^{-5} M	AA	934
H_2O_2	MoS_2	MoS_2/GCE	Amp	2.5 nM	0.100 μM–100 μM	AA, UA	250
H_2O_2	MoS_2–GO–Myoglobin	MoS_2–GO–Myoglobin/GCE	Amp	20 nM	N/A	AA, $NaNO_2$, $NaHCO_3$	1009
H_2O_2	MoS_2–Gr–HRP	MoS_2–Gr–HRP/GCE	Amp	0.049 μM	0.2 μM–1.1 mM	AA, DA, Cysteine, Lys	1009
H_2O_2	MoS_2–HRP	MoS_2–HRP/GCE	DPV	2.6×10^{-7} M	1.0×10^{-6}–9.5×10^{-4} M	N/A	1007
H_2O_2	MXene	MXene/GCE	Amp	0.7 nM	N/A	N/A	1052
H_2O_2	MXene–Nafion–Hb	MXene–Nafion–Hb/GCE	Amp	14 nM	0.1–380 μM	AA, DA, UA, Glucose	1051
H_2O_2	MXene–Nafion–Hb	MXene–Nafion–Hb/GCE	Amp	20 nM	0.1–260 μM	N/A	1050
H_2O_2	rGO–$MnFe_2O_4$–Nafion	rGO–$MnFe_2O_4$–Nafion/GCE	Amp	0.35 μm	1 μM–22 mM	AA, DA, CA, U, AP, UA, NaCl, Glucose	940
H_2O_2	rGO–PB	rGO–PB/GCE	Amp	45 nM	0.05–120 μM	N/A	938
H_2O_2	rGO–Pt–Ni	rGO–Pt–Ni/GCE	Amp	0.3 nM	1 nM–5.3 mM	Fructose, Glucose, AA, UA, Cl^-, SO_4^{2-}	939
H_2O_2	VS_2–Nafion	VS_2–Nafion/GCE	Amp	0.224 μM	0.5 μM–2.5 mM	UA, AA, L–cysteine	1006
H_2O_2	ZnO–Au NP–Nafion–HRP	ZnO–Au NP–Nafion–HRP/GCE	Amp	9.0×10^{-6} M	1.5×10^{-5}–1.1×10^{-3} M	N/A	1035
human growth factor 2	Gr	FET: Au/SiO_2/Graphene/Au/Au	I	60 fM	0.0001–200 ng mL^{-1}	N/A	1087
IAA	rGO–Hemin	rGO–Hemin/GCE	Amp	0.074 μM	0.1–43 μM, 43–183 μM.	AA, SC, CPPU	1044
IgE	Gr–Ag–Ab	Gr–Ag–SA/SPE	SWV	3.6 ng mL^{-1}	10–1000 ng mL^{-1}	N/A	1088
IgE	WS_2–Gr–Au NP–Aptamer	WS_2–Gr–Au NP–Aptamer/GCE	DPV	1.2×10^{-13} M	1.0×10^{-12}–1.0×10^{-8} M	Thrombin, BSA	997
IgG	BP	BP (label)	Amp	0.98 ng mL^{-1}	2–100 ng mL^{-1}	Human Hb	362
IgG	BP	Si/SiO_2/BP/Au/Au	I	2 ng mL^{-1}	10–500 ng mL^{-1}	Avidin	363
IgG	GO–Protein	GO–Protein/GCE	EIS	0.67 nM	3.3–683 nM	Myoglobin	883
IgG	rGO–PDA–Au NP	rGO–PDA–Au NP/GCE	DPV	0.001 ng mL^{-1}	0.1–100 ng mL^{-1} 0.01–100 ng mL^{-1}	BSA, l–cysteine, TYR, PSA	962
interleukin–6	Gr–HRP–Ab_2–Au NP–PDA–CNT	Gr–HRP–Ab_2–Au NP–PDA–CNT–ITO	Amp	0.3 pg mL^{-1}	1–40 pg mL^{-1}	AFP, Human chorionic gonadotropin, PSA	1089
LDL	rGO–NiO–Ab	rGO–NiO–Ab/ITO	EIS	0.07 mg L^{-1}	0–130 mg L^{-1}	Cholesterol, Cholesterol triglyceride	970
listeria monocytogenes	TiO_2	TiO_2/Au	EIS	4.7×10^{2} cfu mL^{-1}	4.7×10^{2}–4.65×10^{7} cfu mL^{-1}	N/A	1090
microRNA–21	MoS_2–Thi–Au NP–DNA	MoS_2–Thi–Au NP–DNA/GCE	SQWV	0.26 pM	1.0 pM–10.0 nM	SBM–miRNA, NC–miRNA	1020
miRNA	rGO–CP–DNA–miRNA	rGO–CP–DNA–miRNA/GCE	SQWV	8 fM	1 fM–1nM	p–DNA29b–1, p–DNA–141, miR29b–, miR–141	955

Specific Analyte	Material	Architecture	Readout/ Method	LOD	Experimental range	Notes	Ref
miRNA	rGO–MWCNT	rGO–MWCNT /GSPE	SQWV	30 fM	10 nM–30 fM	Ab1, HRP–Ab2, Ab1	954
MMP–2	Gr–N–Au NP–Ab	Gr–N–Au NP–Ab/GCE	DPV	0.11 pg mL^{-1}	0.0005–50 ng mL^{-1}	MMP–7, IL–6, CEA, IgG	968
mycobacterium tuberculosis	ZrO_2–ssDNA	ZrO_2–ssDNA/Au	DPV	0.065 ng μL^{-1}	640–0.065 ng μL^{-1}	NC–O, SBM–O	1027
myoglobin	BP–PLL–Aptamer	BP–PLL–Aptamer/SPE	CV	0.524 pg mL^{-1}	1 pg mL^{-1}–16 µg mL^{-1}	Hb, BSA	361
NADH	Gr–DNA–Au NP	Gr–DNA–Au NP/Au	DPV	1 fM	1 fM–10 pM	N/A	931
NADH	rGO	rGO/GCE	Amp	0.6 µM	0–500 µM	AA	929
NADH	rGO–Au	rGO–Au/GCE	Amp	1.13 nM	50 nM–500 µM	Glutathione, Glucose, AA, Guanine	928
nitrite	MXene–Hb–Nafion	MXene–Hb–Nafion/GCE	Amp	0.12 µM	0.5–11800 µM	N/A	1054
ochratoxin–A	ZnO–BSA–r–IgG	ZnO–BSA–r–IgG/ITO	EIS	0.006 nM	0.006–0.01 nM	N/A	1026
octylphenol	Gr–CoNi NP–MIP	Gr–CoNi NP–MIP/CE	DPV	3.6×10^{-11} M	1.0×10^{-10}–1.0×10^{-7} M	OP, PL, NP, 4–AP, NTP, BPA	941
PDGF	GO–Pt–TBA–GOD–HRP–Au–SWCN	rGO–TB–FC–Pt–TBA–GOD–PDGF–HRP–Au–SWCN/GCE	DPV	8 pM	0.01–35 nM	Thrombin	1091
PDGF	Gr–PDDA–Au	Gr–PDDA–Au/GCE	CV	1.7 pM	0.005–60 nM	PDGF–BSA, PDGF–Hb, PDGF–CEA, PDGF AMP	1092
PSA	GO–ssDNA–PLLA	GO–ssDNA–PLLA/Au	DPV	1 ng mL^{-1}	1–100 ng mL^{-1}	IgG, IgM, Glucose, AA, UA, FBS, Human serum protein	1093
PSA	Gr–CT–MB	Gr–CT–MB/GCE	Amp	13 pg mL^{-1}	0.05–5.00 ng mL^{-1}	AFP, BSA, Vitamin C, Glucose	1094
PSA	Gr–HRP–Ab–Au	Gr–HRP–Ab–Au /SPE	LSV	0.46 pg mL^{-1}	0.46 pg mL^{-1}–2.0 µg mL^{-1}	Cancer antigen 125 and 199, AFP, BSA.	1095
PSA	Gr–NH_2–FCA–Ag–NH_2–MCM48	Gr–NH_2–FCA–Ag–NH_2–MCM48/GCE	Amp	2 pg mL^{-1}	0.01–10.0 ng mL^{-1}	PSA, IgG, Lysozyme, AFP	1096
PSA	MoS_2	FET: Si/SiO_2/MoS_2/ Ti–Au/Ti–Au	I	1 pg mL^{-1}	1 pg mL^{-1}–10 ng mL^{-1}	IgG	992
PSA	MoS_2–Ab	FET: Si/SiO_2/MoS_2–Ab/Ti–Au/Ti–Au	I	375 fM	3.75 nM–375 fM	BSA	993
PTH	MoS_2–Au	MoS_2–Au/GCE	DPV	80 nM	0.1–200 µM	KCl, Glucose, AA, UA	1097
PTH	MoS_2–Gr	MoS_2–Gr/Au	CV, EIS	1 pg mL^{-1}	1–50 pg mL^{-1}	N/A	1098
rutin	Gr	Gr/GCE	SDPV	2.1×10^{-8} M	1.0×10^{-7}–1.0×10^{-5} M	AA, Glucose, Ca^{2+}, Fe^{3+}, Cu^{2+}, Na^{+}, K^{+}, PO_4^{3-}, CO_3^{2-}, Cl^{-} and NO_3^{-}, FA, Vitamin B2	1099
serotonin	*h*–BN–Gr QDs	*h*–BN–Gr QDs/GCE	DPV	2.0×10^{-13} M	1.0×10^{-12} – 1.0×10^{-8} M	DA, tryptophan, and norepinephrine	1047
silodosin	Gr–Pt NP–Nafion	Gr–Pt NP–Nafion/GCE	DPV	0.55 nM	1.8–290.0 nM	K^{+}, Na^{+}, Ca^{2+}, Cl^{-}, NO_3^{-}, SO_4^{2-}	972
thiodyglycol	GO–Au	GO–Au/Au	DPV	0.2 uM	1.2×10^{-5} M–0.82×10^{-3} M	N/A	1100
thrombin	Gr–aptamer	FET: Si/SiO_2/Gr–aptamer /Au/Au	I	30 nM	10-300 nM	N/A	974
thrombin	GO-aptamer	GO-aptamer/Carbon	DPV	3 pM	3 pM–0.3 µM	BSA, IgG, avidin	973
thrombin	GO–(Au–ALP)nLBL	GO–(Au–ALP)nLBL/GCE	LSV	2.7 fM	8 fM–15 nM	BSA, HRP, Mouse IgG	1101
thrombin	Gr–CT–TBA	Gr–CT–TBA/GCE	CV, EIS	0.45 fM	0.45–100 fM	BSA, Trypsase	1102
thrombin	Gr–Nafion–NiHCF NP–Au	Gr–Nafion–NiHCF NP–Au/GCE	CV	0.3 pM	1 pM–1 nM; 1 nM–80 nM	Hb, L–cysteine, BSA	1103
thrombin	Gr–O–TBA	Gr–O–TBA/GCE	DPV	0.35 pM	1.0×10^{-12}–4.0×10^{-10} M	BSA, HSA, IgG, Trypsin, Insulin, Transferrin	1104
thrombin	Gr–PAMAM	Gr–PAMAM/GCE	DPV	0.05 pM	0.0001–80 nM	BSA, Hb, PDGF	1105
thrombin	Gr–PAMMA–Th–TBA–Hemin–BSA	Gr–PAMMA–Th–TBA–Hemin–BSA/GCE	DPV	0.1 pM	0.0002–30.0 nM	Lysozyme, IgG, BSA, L–cysteine	1106

Specific Analyte	Material	Architecture	Readout/ Method	LOD	Experimental range	Notes	Ref
thrombin	Gr–PANI–Au–MPTS–GOD–TBA	Gr–PANI–Au–MPTS–GOD–TBA/GCE	CV	0.56 pM	1.0×10^{-12}–3.0×10^{-8} M	AFP, BSA, CEA	1107
thrombin	Gr–Pd–Tb–TBA–Hemin–BSA	Gr–Pd–Tb–TBA–Hemin–BSA/GCE	DPV	0.03 pM	0.1 pM–50 nM	BSA, HB, HAS, IgG, Lysozyme	1108
thrombin	Gr–PTCA	Gr–PTCA/Au	CV	0.2 pM	0.001–40 nM	BSA, BHB, IgG	1109
thrombin	Gr–PTCDA–Au	Gr–PTCDA–Au/Au	Amp	6.5×10^{-16} M	1.0×10^{-15}–1.0×10^{-9} M	BSA, BHB, IgG, Prothrombin, Elastin	1110
thrombin	Gr–ssDNA	Gr–ssDNA/PGE	DPV	0.1 pM	100–500 nM	N/A	1111
thrombin	Gr–Tb–Au	Gr–Tb–Au/GCE	CV	0.33 pM	0.001–80 nM	Hb, BSA, L–cysteine	1112
thrombin	Gr–Tb–Pt–PBA–GOD–HRP	Gr–Tb–Pt–PBA–GOD–HRP/GCE	DPV	11.0 pM	0.02–45 nM	PDGF, Thrombin	1091
thrombin	Gr–Th–Au	Gr–Th–Au/GCE	DPV	0.093 nM	0.5–40 nM	Lysozyme, BSA	1113
thrombin	MoS_2–Au NP–Aptamer	MoS_2–Au NP–Aptamer /GCE	SQWV	0.0012 nM	0.01 nM–10 μM	Hb, L–lysine, BSA, L–hystidine	1021
thrombin	MoS_2–Gr–PDDA–Pd NP–Aptamer	MoS_2–Gr–PDDA–Pd NP–Aptamer/GCE	DPV	0.062 pM	0.0001–40 nM	BSA, l–cysteine, IgG, Hb, CEA, AFP	1000
thrombin	rGO–TBA	GO–TBA/GCE	DPV	500 fM	0.001–50 nM	BSA, IgG, Hb	1114
thrombin	rGO–TB–FC–Pt–TBA–GOD–PDGF–HRP–Au–SWCN	rGO–TB–FC–Pt–TBA–GOD–PDGF–HRP–Au–SWCN/GCE	DPV	11.0 pM	0.02–45 nM	Platelet–derived growth factor	1091
TNF–α	MoS_2–Ab	FET: $Si/SiO_2/MoS_2$–Ab/Ti/Au	I	60 fM	60 fM–6 pM	Interleukin–6 cytokine	995
TNF–α	MoS_2–Ab	FET: $Si/SiO_2/MoS_2$–Ab/Ti–Au/ Ti–Au	I	60 fM	60 fM–6 pM	N/A	994
triclosan	Gr–PDDA–Pd	Gr–PDDA–Pd/GCE	DPV	3.5 nM	9.0 nM–20.0 μM	AA, CA, Glucose, Na^+, K^+, Ca^{2+}, Mg^{2+}, Ni^{2+}, Cl^-, NO_3^-, SO_4^{2-}	1115
tryptamine	Gr–PPy–HAM-WCNTs–MIP	Gr–PPy–HAMWCNTs–MIP/GCE	Amp	7.4×10^{-8} M	9.0×10^{-8}–7.0×10^{-5} M	Tryptamine, Tyramine, DA, Tryptophan	1116
UA	Gr	Gr/GCE	Amp	4.82 μM	6.00–1330 μM	AA, DA	1056
UA	Gr–Fe_3O_4–NH_2	Gr–Fe_3O_4–NH_2/GCE	Amp	0.056 μM	1.0–850 μM	AA, DA	1057
UA	Gr–PBA–Au NP	Gr–PBA–Au NP/GCE	Amp	2.0×10^{-7} M	2.0×10^{-6}–6.2×10^{-5} M	N/A	922
UA	Gr–Pt–Nafion	Gr–Pt–Nafion/GCE	CV/DPV	0.05 μM	0.05–11.85 μM	AA. DA	1058
UA	*h*–BN	*h*–BN/GCE	DPV	0.15 μM	1–300 μM	AA, DA	1043
UA	rGO	rGO/GCE	DPV	0.5 μM	0.5–60 μM	K^+, Ca^{2+}, Na^+, Mg^{2+}, Zn^{2+}, NH_4^+, Cl^-, SO_4^{2-}, NO_3^-, HCO_3^-	1059
UA	rGO–Au	rGO–Au/GCE	DPV	1.8×10^{-6} M	8.8×10^{-6}–5.3×10^{-5} M	NaCl, KCl, $NaNO_3$, $CaCl_2$, Glucose, l–cysteine, CA	1060
VEGF	GO–ssDNA–PLLA	GO–ssDNA–PLLA/Au	DPV	0.05 ng mL^{-1}	0.05–100 ng mL^{-1}	IgG, IgM, Glucose, AA, UA, FBS, Human serum protein	1093
vincristine	rGO–Au–MIP	rGO–AuNP–MIP/GCE	DPV	26 nM	5.0×10^{-8}—5.0×10^{-6} M	Daunorubicin, Vinblastine, Guanine. Ca^{2+}, Mg^{2+}, Zn^{2+}, K^+	1117

Note: FET is described in a way of gate electrode/insulator/channel material/source electrode/drain electrode. N/A, not available.

5. Conclusions and Perspectives

In the last decade, advancements in the development of electrically–transduced sensors have been significantly propelled by the prediction, design and synthesis of 2D materials, the exploration of their remarkable physical and chemical properties, as well as progress in the fabrication technology.[7] The increasing number of experimental strategies for integrating these 2D nanostructures into functional devices, with desired strong interfacial interactions, further advanced the development of this unique

group of materials, which have already found wide applications in areas where their unique physical and chemical properties such as tunable band gap, large surface-to-volume ratio, or excellent mechanical stability can be harnessed.[102, 121]

In this review, we described recent advances in the development of electrically–transduced sensors based on the 2D nanomaterials to provide a concise view of new advances in areas ranging from unique structural features, device engineering, strategies for electrochemical signal amplification and transduction, and the development of novel electroanalytical techniques used in the miniaturization and integration of the sensors. We discussed necessary components, sensing mechanism, and device architectures for the development of electrically–transduced sensing platforms, which highlighted the fundamental detection principles governing their response. We also demonstrated structural and compositional features as well as surface chemistry of 2D nanostructures that dictate their electrical properties, ultimately allowing fascinating applications in the development of electrically–transduced sensors. Specific advances in the application of 2D materials in sensing were illustrated in the context of four major groups of analytes, including gases, volatile compounds, ions, and biomolecules, and then discussed from both a historical and analytical perspective.

With recent advancements in the preparatory methods of 2D nanomaterials, an even greater degree of control over structural features, including size, thickness, crystallinity, engineered defects, doping, and functionalization have been achieved,[73] leading to precise engineering of physicochemical properties. Further improvements in the integration and characterization methods of 2D nanostructures, have allowed structural and compositional features to be effectively probed, thus enhancing the understanding of structure-property relationships within these materials.

The synergy of multifunctional properties in 2D nanostructures with electrochemical methods has already led to significant enhancements in the selectivity, stability, and reproducibility of sensing devices for a diverse range of analytes including small reactive gases,[114] volatile organic compounds,[113] ions[261, 830] and biomolecules.[272] In particular, the inherent presence of a 2D basal plane in this class of materials ensures a large abundance of exposed active sites as well as ultra-short diffusion paths, which together can effectively facilitate interactions with targeted analytes, and consequently enhance the charge transfer processes in electrically–transduced sensing.

Because 2D nanomaterials possess atomic thicknesses, and are readily accessible by chemical synthetic methods,[73, 1118] their sensing properties such as selectivity or sensitivity could be further improved through surface functionalization with guest molecules including nanoparticles, metal oxides or polymers.[72] Generally, four major conceptual and experimental approaches have been demonstrated to obtain functional sensing devices. *First*, molecular engineering of 2D nanomaterials through edge and defect engineering has the potential to incorporate an increased number of active sites for material-analyte interactions.[387] *Second*, the minimization of the thickness of the 2D layer can enhance the surface-to-volume ratio,[73] thus leading to substantial enhancements in sensitivity. *Third*, improvements in the kinetics of charge transfer through strain engineering, doping of heteroatoms, and designing synergetic composites with superior electrical properties (e.g., nanoparticles), which can effectively facilitate charge transfer, can significantly improve signal transduction.[474] *Fourth*, the sensing properties of fabricated devices (e.g., selectivity and sensitivity) can also be tailored towards the detection of specific analytes through the incorporation of known recognition centers including enzymes, or ligands, onto the surface of 2D materials.[80, 282, 573, 1023] These unique properties, which arise from the ultrathin 2D structural characteristics of the nanomaterials, have been already extensively explored for a variety of sensing applications demonstrating excellent electroanalytical performance, as in the case of graphene, with the potential to complement the current commercial sensing systems/technologies.[10, 80, 110, 126-127, 146, 159, 264-265, 272, 347, 412, 475, 573, 883, 991]

Even though significant advances in many key areas related to the design and application of electrically–transduced sensors have been made, there is still an ongoing demand to implement these 2D sensors into real-world applications.[73, 321] Synthetic routes toward high-quality, large area monolayers of most 2D materials are not yet readily accessible, although not all electro-analytical applications require this.[473] Currently many available 2D materials exhibit a large degree of non-homogeneity in their 2D size, which may lead to poor reproducibility in the sensing performance of electroanalytical devices including their sensitivity, stability and reproducibility.[70, 72] The current manufacturing processes of 2D nanomaterials are often limited by low production rates and insufficient quality, and thus do not meet the industrial standards for their commercialization.[1118] The presence of structural defects, produced during synthesis, have a large influence on the electronic properties of 2D materials, and consequently on the electroanalytical performance of sensing technologies.[123, 353, 821, 1119] The mass production of ultrathin epitaxially oriented 2D nanomaterials with desired structural features in a highly controllable manner remains an unresolved challenge in this field, and requires further innovation, research, and development.

The ability to design 2D materials with targeted structure-property relationship remains an unresolved issue due to the limited understanding of their growth mechanism, and possible host-guest interactions within the material. To address these challenges, rigorous computational modelling together with analytical assessment of structure-property relationships through in situ transmission electron microscopy, spectroscopic techniques such as X-ray photoelectron, Raman or infrared spectroscopy, and electron paramagnetic resonance in 2D materials is required. Hybrid 2D nanostructures can provide an efficient avenue for broadening and improvements in the performance of 2D nanomaterials in electrically–transduced sensing

application. However, it can be difficult to control the morphology, and orientation of intrinsic functional groups on their surface. The ability to effectively incorporate receptor molecules for analyte-material interactions on the surface of 2D materials, with control over their spatial distribution needs to be addressed due to its critical importance in enhancing the selectivity of fabricated electrochemical biosensors.

Many 2D nanostructures undergo oxidation in ambient conditions, resulting in structural alterations or even material decomposition, thus significantly limiting their application in functional devices.[81, 321] One critical challenge is finding new strategies to effectively stabilize the synthesized nanomaterials not only during processing and storage but also in practical applications. These challenges may be addressed with the development of novel 2D materials, as recently demonstrated through progress in the synthesis and application of 2D conductive covalent-organic frameworks, which exhibited excellent mechanical, thermal and catalytic stability.

Due to large anisotropic structure, refined chemical control over nanoscale morphology of layered 2D structures is critical for further progress in the field.[1120-1121] Development of methods for selective chemical functionalization of edge sites vs basal planes[84, 331] has the potential to enable improved approaches to creating dispersions of 2D materials that can interface with additive manufacturing technologies such as ink-jet printing, roll-to-roll processing, and 3D printing.[262, 502, 690, 1122]

It is also important to consider whether 2D nanomaterials are more suited as components in the development of sensing devices than current available technologies, such as conductive polymers, in terms of their analytical performance, cost effectiveness, earth abundance, and toxicity. In particular, the biocompatibility of fabricated 2D materials and 2D material interfaces should be investigated to enable their practical implementation into bioanalytical applications.[282, 1123-1124]

Developing effective strategies of interfacing 2D materials with electrical contacts, within functional devices, remain an important consideration for producing high quality sensors that are capable of fully harnessing the unique and multifunctional nature of 2D nanostructures. Current integration methods, such as drop casting or microfabrication, often fail to harness the intrinsic properties of 2D materials. [89, 102, 421] It is thus a significant challenge to develop a facile, effective, and reliable strategy to improve the incorporation of 2D structures into functional devices. This challenge could be addressed by enhancing the current methods of fabrication to ideally couple the synthesis and integration into a device in one step.[102, 1125] The integration of multifunctional 2D materials with unique analyte recognition properties into soft and biocompatible substrates, miniaturized chips, and multiplex platforms for simultaneous detection of targeted analytes needs to be extensively explored to enable the development of portable, wearable, and interconnected devices and networks for addressing environmental monitoring, diagnosis of disease, and health care.[1117-18, 103-104, 124, 324, 334]

In addition to interfacing 2D materials with electrodes, van der Waals heterostructures resulting from interfaces of different 2D materials, holds great promise for improving electrical contacts, material stability, and device performance.[117] Creating new methods for fabricating such heterostructured interfaces in sensing devices has the potential to improve sensitivity, selectivity, and stability of sensors based on 2D materials.[72, 473]

Innovations in 2D material design are also critical to further progress in the field. [70-73] Although the roadmap for 2D material discovery and development has progressed at rapid pace, many new 2D materials have not yet been explored as candidates for chemical sensing. Computational assessment combined with curiosity-driven research can offer many opportunities for fundamental dis-covery of stimuli-responsive 2D materials with promising utility in chemical sensing.[1126]

Finally, synergistic integration of multifunctionality in sensors based on 2D materials is critical for harnessing the multifaced features of these materials in electronic and electrochemical devices. [94, 113, 321, 474] For instance, design of porous conductive mate-rials that enable synergistic coupling of high hydrophobicity, large surface area, high capacitance, and low charge transfer resistance can enhance the functional performance of potentiometric devices.[88-89] Alternatively, coupling electronic and magnetic exachange interactions in 2D materials can enhance purtubations to charge transport caused by interactions with analytes.[1127-1129]

The development of these sensing technologies may lead to significant advances compared to the current analytical technologies, in terms of simplicity, cost, and superior sensing performance. Although, the exploration of new 2D nanostructures is still in the early phases of research, the unprecedented diversity of these materials that arise from their unique physical and chemical structures is likely to further consolidate their position in the field of electrically–transduced sensors and nanoscience, and it is very probable that the commercial and industrial technologies will incorporate them into widespread use in the coming years.

AUTHOR INFORMATION

Corresponding Author

*katherine.a.mirica@dartmouth.edu

Author Contributions

†These authors contributed equally to this work.

The manuscript was written through contributions of all authors. All authors have given approval to the final version of the manuscript.

Notes

The authors declare no competing financial interest.

Biographies

Zheng Meng obtained his B.S. in University of Science and Technology Beijing in 2011. He got his Ph.D. in Institute of Chemistry, Chinese Academy of Sciences under the supervision of Prof. Chuan-Feng Chen in 2016. He then moved to Dartmouth College to work as a postdoctoral researcher with Prof. Mirica. His current interests focus on the developing of new two-dimensional conductive metal–organic frameworks and covalent organic frameworks, and exploring their applications in sensing, catalysis, and electronics.

Robert Stolz is a proud native of Cleveland, Ohio. His passion for chemistry and material science was inspired by undergraduate work in the laboratory of Professor Brian Northrop at Wesleyan University. After graduating with a B.A. in 2012 and an M.A. in 2013, Robert worked as a polymer chemist for Dow Chemical Company's Advanced Materials Division in Philadelphia. He joined the Mirica laboratory in the Spring of 2016 to pursue his doctorate in Chemistry.

Lukasz Mendecki obtained his MSc in Forensic Science from King's College London. He then went on to earn his PhD from Keele University under the supervision of Dr. Aleksandar Radu. His research explored the development of novel strategies for improvements in potentiometric ion selective electrodes. He then moved to Dartmouth College to work with Prof. Mirica on the application of two-dimensional conductive metal–organic frameworks in electrochemical sensors, catalysis, and energy storage.

Katherine Mirica received her BS degree in Chemistry (magna cum laude) in 2004 from Boston College, working in the laboratory of Prof. Lawrence T. Scott. In 2011, she earned her PhD in Chemistry from Harvard University under the guidance of Prof. George M. Whitesides. She completed her postdoctoral training at the Massachusetts Institute of Technology with Prof. Timothy M. Swager during 2011-2015. Prof. Mirica began her independent scientific career as an Assistant Professor in the Department of Chemistry at Dartmouth College in July 2015. Her current research interests include multifunctional materials and self-assembly.

ACKNOWLEDGMENT

The authors acknowledge support from start-up funds provided by Dartmouth College, from Walter and Constance Burke Research Initiation Award, the Army Research Office Young Investigator Program Grant No. W911NF-17-1-0398, Sloan Research Fellowship, and 3M Non-Tenured Faculty Award.

ABBREVIATIONS

1–ethyl–3–(3–dimethylaminopropyl)carbodiimide	EDC
1,6-hexanediamine	HA
2,2–azino–bis(3–ethylbenzothiazoline–6–sulfonic acid	ABTS
3,4,9,10-perylene tetracarboxylic acid	PTCA
3-aminopropyltriethoxysilane	APTES
3-mercapto-propyltrimethox-ysilane	MPTMOS
4-aminopheol	4-AP
Acetaminophen	ACT
Acetic acid	AA
Adenine, guanine, cytosine, and thymine	A, G, C, T
Adenosine triphosphate	ATP
Alpha–fetoprotein	AFP
Aptamer	AP
Aniline monomer	ANI
Anti–cortisol antibody	Anti–Cab
Artificial peroxidase	APO
Ascorbic acid	AA
Benzyltrimethylammonium hydroxide	BTMAH
Bisphenol	BPA
Black phosphorous	BP
Boron–doped diamond	BDD
Bovine serum albumin	BSA
Brain natriuretic peptide	BNP
Cancer antigen 125	CA125
Capacitance	C
Carbon electrode	CE
Carbon nitride	CN
Carbon nanotubes	CNT
Carbon paste electrode	CPE
Carbon sphere	CNSP
Carboxymethyl chitosan	CMC
Carcinoembryonic antigen	CEA
Cetyltrimethylammonium bromide	CTAB
Central nervous system	CNS
Chemical–sensitive	CS
Chemical vapor deposition	CVD
Chitosan	CT
Cholesterol esterase	ChE
Cholesterol oxidase	ChO
Chronic leukemia cell line	K562
Circulating tumor DNA	ctDNA
Citrate buffer	CB
Citric acid	CA
Conductive polymer	CP
Conductivity	σ
Covalent organic framework	COF
Current	I
Cyclic voltammetry	CV
Cyclodextrin	CD
Cysteic acid	CsA
Cytokeratin-19-fragment	CYFRA21
Density functional theory	DFT

Deoxyribonucleic acid	DNA
Differential pulse cathodic stripping voltammetry	DPCSV
Differential pulse voltammetry	DPV
Differential pulse anodic stripping voltammetry	DPASV
Dihydronicotinamide adenine dinucleotide	NADH
Dimethyl acetamide	DMA
Dimethyl methylphosphonate	DMMP
Dinitrotoluene	DNT
Disposable electrical printed carbon chips	DEP
Dopamine	DA
Double base mismatch	DBM
Double stranded deoxyribonucleic acid	dsDNA
Drain current	I_{DS}
Drain-source voltage	V_{DS}
Electrochemical impedance spectroscopy	EIS
Electrochemically reduced graphene oxide	ERGO
Electromotive force	EMF
Electron beam lithography	EBL
Epidermal electronic system	EES
Epidermal growth factor receptor	EGFR
Escherichia coli	*E. coil*
Ethyl acetate	EA
Ethylenediamine	EDA
Ethylenediamine triacetic acid	EDTA
Field-effect transistor	FET
Flexible integrated sensing array	FISA
Flexible printed circuit board	FPCB
Folic acid	FA
Forchlorfenuron	CPPU
Frequency	f
Gate voltage	V_{GS}
Glassy carbon electrode	GCE
Glucose oxidase	GOD
Glutaraldehyde	GTA
Glutaric acid	GA
Gold screen printed electrodes	GSPE
Graphene	Gr
Graphene oxide	GO
Graphite oxide	GPO
Graphite rod	GR
Hemoglobin	Hb
Hepatitis B virus	HBV
Heparin	Hp
Hexagonal boron nitride	*h*-BN
Hexahydroxytriphenylene	HHTP
Hexaiminotriphenylene	HITP
Highest occupied molecular orbital	HOMO
Horseradish peroxidase	HRP
Human breast cancer cell	MCF-7
Human chorionic gonadotropin	HCG
Human dermal fibroblast cells	NHDF
Human embryonic kidney cell	293T
Human interleukin-6	IL-6
Human liver hepatocellular carcinoma	HepG2
Human normal hepatocyte cell	L02
Human prostatic metastatic cancer cell	Du-145
Immunoglobulin	Ig
Immunoglobulin E	IgE
Immunoglobulin G	IgG
Indium tin oxide electrode	ITO
Indole-3-acetic acid	IAA
Inductance	L
Interdigitated electrode	IDE
Ion-selective electrode	ISE
Ion-selective field effect transistor	ISFET
Ion-selective membranes	ISM
Laccase	LACC
Laccase–tyrosinase	LACC-TYR
Layered double hydroxides	LDHs
Layered metal oxides	LMO
L-cysteine	CYS
Limit of detection	LOD
Linear discriminant analysis	LDA
L-leucine	LEU
Low density lipoprotein	LDL
Lowest unoccupied molecular orbital	LUMO
Matrix metalloproteinases-7	MMP-7
Metal-organic framework	MOF
Methylene blue	MB
Microcontact printing	μCP
Microperoxidase-11	MP-11
Molecularly imprinted polymer	MIP
Multilayer graphene nanoflake films	MGNF
Multiwall carbon nanotubes	MWCNT
Myoglobin	Mb
Nanoflower	NF
Nanoparticles	NPs
Nanowire	NW
Neuron specific enolase	NSE
Nicotinamide adenine dinucleotide	NAD
Nitrophenol	NTP
N-methyl-2-pyrrolidone	NMP
N, *N*-dimethylformamide	DMF
Nonylphenol	NP

Octadecylamine	ODA
Octylphenol	OP
Oxalic acid	OA
Oxygen reduction reaction	ORR
Parathyroid hormone	PTH
Parts–per–billion	ppb
Parts–per–million	ppm
Parts–per–quadrillion	ppq
Parts–per–trillion	ppt
Pascal	Pa
Pencil graphite electrode	PGE
Permittivity	ε
Phase	Φ
Phenol	PL
Phorbol12–myristate–13–acetate	PMA
Phosphate buffered saline	PBS
Phosphorodiamidate morpholino oligos	PMO
Photoresist film	PPF
Poly(3,4-ethylenedioxythiophene)	PEDOT
Poly(9-9′-dioctyl-fluorene-co-bithiophene)	F8T2
Poly(acrylic acid)	PAA
Poly(diallylimethyammonium chloride)	PDDA
Poly(ethylene glycol)	PEG
Poly(ethylene terephthalate)	PET
Poly(ethyleneimine)	PEI
Poly(methylmethacrylate)	PMMA
Poly(sodium 4-styrenesulfonate)	PSS
Poly(xanthurenic acid)	PXA
Polyaniline	PANI
Polydopamine	PDA
Polyehtylenetereph-thalate	PETP
Polyethylene naphthalate	PEtN
Polyethylenimine-functionalized ionic liq-uid	PFIL
Polyfuran	PF
Polyimide	PI
Poly-l-lysine	PLL
Polypyrene	PPr
Polypyrrole propylic acid	Ppa
Polypyrrole	PPy
Polythionine	PTH
Polythiophene	PTHP
Polyvinylpyrrolidone	PVP
Porphyrin	Pr
Principle component analysis	PCA
Prostate specific antigen	PSA
Pyrene butyric acid	PBA
Pyrolysed photoresist film	PPF
Pyrrole phosphate buffer solution	PPBS
Ribonucleic acid	RNA
Reduced graphene oxide	rGO
Resistance	R
Response	S
Restless legs syndrome	RLS
Screen printed graphitic electrode	SPE
Serotonin	5-HT
Single base mismatched oligonucleotide	SBM-O
Single stranded deoxyribonucleic acid	ssDNA
Single nucleotide substitution	SNS-DNA
Sodium dodecyl benzene sulfonate	SDBS
Square wave anodic stripping voltammetry	SWASV
Streptococcus suis serotype 2	SS2
Target/mismatch (MM) mixtures	MM-DNA
Tetrasodium 1,3,6,8-pyrenetetrasulfonic acid	TPA
Thiol group tagged	TGT
Thionine	Thi
Three-dimensional	3D
Toluidine blue	Tb
Transient metal dichalcogenides	TMDC
Triethylamine	TEA
Trimesic acid	BTC
Triphosphate aptamer	ATA
Triple base mismatch	TBM
Tumor necrosis factor	TNF
Two-dimensional	2D
Tyrosinase	TYR
Ultra–violet	UV
Urea	U
Uric acid	UA
Vascular endothelial growth factor	VEGF
Volatile organic compounds	VOCs
Voltage	V
Work function	φ
Xanthurenic acid	XA
α-fetoprotein	AFP
β-cyclodextrin	β-CD

REFERENCES

1. Gellman, S. H. Introduction: Molecular Recognition. *Chem. Rev.* **1997,** *97*, 1231-1232.
2. De Marcellis, A.; Ferri, G., Physical and Chemical Sensors. In *Analog Circuits and Systems for Voltage-Mode and Current-Mode Sensor Interfacing Applications*, Springer Netherlands: Dordrecht, 2011; pp 1-35.
3. Janata, J.; Bezegh, A. Chemical Sensors. *Anal. Chem.* **2002,** *60*, 62-74.
4. Bănică, F. G., *Chemical Sensors and Biosensors: Fundamentals and Applications*. 2012.
5. Cammann, K.; Lemke, U.; Rohen, A.; Sander, J.; Wilken, H.; Winter, B. Chemical Sensors and Biosensors—Principles and Applications. *Angew. Chem. Int. Ed.* **1991,** *30*, 516-539.
6. Sekhar, P. K.; Brosha, E. L.; Mukundan, R.; Garzon, F. Chemical Sensors for Environmental Monitoring and Homeland Security. *Electrochem. Soc. Interface.* **2010,** *19*, 35-40.
7. Chandran, G. T.; Li, X.; Ogata, A.; Penner, R. M. Electrically Transduced Sensors Based on Nanomaterials (2012-2016). *Anal. Chem.* **2017,** *89*, 249-275.
8. Windmiller, J. R.; Wang, J. Wearable Electrochemical Sensors and Biosensors: A Review. *Electroanalysis* **2013,** *25*, 29-46.
9. Bakker, E.; Telting-Diaz, M. Electrochemical Sensors. *Anal. Chem.* **2002,** *74*, 2781-2800.
10. Kimmel, D. W.; LeBlanc, G.; Meschievitz, M. E.; Cliffel, D. E. Electrochemical Sensors and Biosensors. *Anal. Chem.* **2012,** *84*, 685-707.
11. Bandodkar, A. J.; Wang, J. Non-Invasive Wearable Electrochemical Sensors: A Review. *Trends Biotechnol.* **2014,** *32*, 363-371.
12. Janata, J.; Josowicz, M. Conducting Polymers in Electronic Chemical Sensors. *Nat. Mater.* **2003,** *2*, 19-24.
13. Willner, I.; Zayats, M. Electronic Aptamer-Based Sensors. *Angew. Chem. Int. Ed.* **2007,** *46*, 6408-6418.
14. Drummond, T. G.; Hill, M. G.; Barton, J. K. Electrochemical DNA Sensors. *Nat. Biotechnol.* **2003,** *21*, 1192-1199.
15. Arshak, K.; Moore, E.; Lyons, G. M.; Harris, J.; Clifford, S. A Review of Gas Sensors Employed in Electronic Nose Applications. *Sensor Rev.* **2004,** *24*, 181-198.
16. Steinhubl, S. R.; Muse, E. D.; Topol, E. J. The Emerging Field of Mobile Health. *Sci. Transl. Med.* **2015,** *7*, 283rv283.
17. Diamond, D.; Coyle, S.; Scarmagnani, S.; Hayes, J. Wireless Sensor Networks and Chemo-/Biosensing. *Chem. Rev.* **2008,** *108*, 652-679.
18. Dieffenderfer, J.; Wilkins, M.; Hood, C.; Beppler, E.; Daniele, M. A.; Bozkurt, A. Towards a Sweat-Based Wireless and Wearable Electrochemical Sensor. *2016 IEEE Sensors* **2016**, 1-3.
19. Kim, D. H.; Lu, N.; Ma, R.; Kim, Y. S.; Kim, R. H.; Wang, S.; Wu, J.; Won, S. M.; Tao, H.; Islam, A.; Yu, K. J.; Kim, T. I.; Chowdhury, R.; Ying, M.; Xu, L.; Li, M.; Chung, H. J.; Keum, H.; McCormick, M.; Liu, P.; Zhang, Y. W.; Omenetto, F. G.; Huang, Y.; Coleman, T.; Rogers, J. A. Epidermal Electronics. *Science* **2011,** *333*, 838-843.
20. Kaltenbrunner, M.; Sekitani, T.; Reeder, J.; Yokota, T.; Kuribara, K.; Tokuhara, T.; Drack, M.; Schwodiauer, R.; Graz, I.; Bauer-Gogonea, S.; Bauer, S.; Someya, T. An Ultra-Lightweight Design for Imperceptible Plastic Electronics. *Nature* **2013,** *499*, 458-463.
21. Gao, W.; Emaminejad, S.; Nyein, H. Y. Y.; Challa, S.; Chen, K.; Peck, A.; Fahad, H. M.; Ota, H.; Shiraki, H.; Kiriya, D.; Lien, D. H.; Brooks, G. A.; Davis, R. W.; Javey, A. Fully Integrated Wearable Sensor Arrays for Multiplexed in Situ Perspiration Analysis. *Nature* **2016,** *529*, 509-514.
22. Kassal, P.; Kim, J.; Kumar, R.; de Araujo, W. R.; Steinberg, I. M.; Steinberg, M. D.; Wang, J. Smart Bandage with Wireless Connectivity for Uric Acid Biosensing as an Indicator of Wound Status. *Electrochem. Commun.* **2015,** *56*, 6-10.
23. Mannoor, M. S.; Tao, H.; Clayton, J. D.; Sengupta, A.; Kaplan, D. L.; Naik, R. R.; Verma, N.; Omenetto, F. G.; McAlpine, M. C. Graphene-Based Wireless Bacteria Detection on Tooth Enamel. *Nat. Commun.* **2012,** *3*, 763.
24. Kalantar-Zadeh, K.; Berean, K. J.; Ha, N.; Chrimes, A. F.; Xu, K.; Grando, D.; Ou, J. Z.; Pillai, N.; Campbell, J. L.; Brkljača, R.; Taylor, K. M.; Burgell, R. E.; Yao, C. K.; Ward, S. A.; McSweeney, C. S.; Muir, J. G.; Gibson, P. R. A Human Pilot Trial of Ingestible Electronic Capsules Capable of Sensing Different Gases in the Gut. *Nat. Electron.* **2018,** *1*, 79-87.
25. Park, J.; Kim, J.; Kim, K.; Kim, S. Y.; Cheong, W. H.; Park, K.; Song, J. H.; Namgoong, G.; Kim, J. J.; Heo, J.; Bien, F.; Park, J. U. Wearable, Wireless Gas Sensors Using Highly Stretchable and Transparent Structures of Nanowires and Graphene. *Nanoscale* **2016,** *8*, 10591-10597.
26. Xu, L.; Gutbrod, S. R.; Bonifas, A. P.; Su, Y.; Sulkin, M. S.; Lu, N.; Chung, H. J.; Jang, K. I.; Liu, Z.; Ying, M.; Lu, C.; Webb, R. C.; Kim, J. S.; Laughner, J. I.; Cheng, H.; Liu, Y.; Ameen, A.; Jeong, J. W.; Kim, G. T.; Huang, Y.; Efimov, I. R.; Rogers, J. A. 3D Multifunctional Integumentary Membranes for Spatiotemporal Cardiac Measurements and Stimulation across the Entire Epicardium. *Nat. Commun.* **2014,** *5*, 3329.
27. Fahad, H. M.; Shiraki, H.; Amani, M.; Zhang, C.; Hebbar, V. S.; Gao, W.; Ota, H.; Hettick, M.; Kiriya, D.; Chen, Y. Z.; Chueh, Y. L.; Javey, A. Room Temperature Multiplexed Gas Sensing Using Chemical-Sensitive 3.5-nm-Thin Silicon Transistors. *Sci. Adv.* **2017,** *3*, e1602557.
28. McEvoy, M. A.; Correll, N. Materials Science. Materials That Couple Sensing, Actuation, Computation, and Communication. *Science* **2015,** *347*, 1261689.
29. Paolesse, R.; Nardis, S.; Monti, D.; Stefanelli, M.; Di Natale, C. Porphyrinoids for Chemical Sensor Applications. *Chem. Rev.* **2017,** *117*, 2517-2583.
30. Watson, J.; Ihokura, K. Gas-Sensing Materials. *MRS Bull.* **2013,** *24*, 14-17.
31. Poghossian, A.; Luth, H.; Schultze, J. W.; Schoning, M. J. (Bio-)Chemical and Physical Microsensor Arrays Using an Identical Transducer Principle. *Electrochim. Acta* **2001,** *47*, 243-249.
32. Schoning, M. J.; Poghossian, A.; Schultze, J. W.; Luth, H. Field-Effect Based Multifunctional Hybrid Sensor Module for the Determination of Both (Bio-)Chemical and Physical Parameters. *Advanced Environmental Sensing Technology II* **2002,** *4576*, 149-159.
33. Xu, S.; Zhang, Y.; Jia, L.; Mathewson, K. E.; Jang, K. I.; Kim, J.; Fu, H.; Huang, X.; Chava, P.; Wang, R.; Bhole, S.; Wang, L.; Na, Y. J.; Guan, Y.; Flavin, M.; Han, Z.; Huang, Y.; Rogers, J. A. Soft Microfluidic Assemblies of Sensors, Circuits, and Radios for the Skin. *Science* **2014,** *344*, 70-74.
34. Kenry; Yeo, J. C.; Lim, C. T. Emerging Flexible and Wearable Physical Sensing Platforms for Healthcare and Biomedical Applications. *Microsyst Nanoeng.* **2016,** *2*, 16043.
35. Wang, P.; Liu, Q., Physical Sensors and Measurement. In *Biomedical Sensors and Measurement*, Springer, Berlin, Heidelberg: 2011; pp 51-115.
36. Bhalla, M. R.; Bhalla, A. V. Comparative Study of Various Touchscreen Technologies. *International Journal of Computer Applications* **2010,** *6*, 12-18.
37. Yacobi, B. G., *Semiconductor Materials*. Springer, Boston, MA: 2003.
38. Pirondini, L.; Dalcanale, E. Molecular Recognition at the Gas-Solid Interface: A Powerful Tool for Chemical Sensing. *Chem. Soc. Rev.* **2007,** *36*, 695-706.

39. Ariga, K.; Hill, J. P.; Endo, H. Developments in Molecular Recognition and Sensing at Interfaces. *International Journal of Molecular Sciences* **2007,** *8*, 864-883.
40. Mu, B.; Zhang, J.; McNicholas, T. P.; Reuel, N. F.; Kruss, S.; Strano, M. S. Recent Advances in Molecular Recognition Based on Nanoengineered Platforms. *Acc. Chem. Res.* **2014,** *47*, 979-988.
41. Fortin, J., Transduction Principles. In *Functional Thin Films and Nanostructures for Sensors*, Springer, Boston, MA: 2009; pp 17-29.
42. Sinclair, I., *Passive Components for Circuit Design*. Elsevier Science: 2000.
43. Wikipedia, S.; Books, L., *Diodes: Diode, Zener Diode, Pin Diode, Back-to-Back Connection, Resonant Tunneling Diode, Cat's-Whisker Detector, Schottky Diode, Impatt Diode*. General Books LLC: 2010.
44. Sevin, L. J., *Field-Effect Transistors*. McGraw-Hill: 1965.
45. Deshpande, R. P., *Capacitors: Technology and Trends*. Tata McGraw Hill Education: 2012.
46. Webster, J. G.; Eren, H., *Measurement, Instrumentation, and Sensors Handbook, Second Edition: Spatial, Mechanical, Thermal, and Radiation Measurement*. Taylor & Francis: 2014.
47. Wring, S. A.; Hart, J. P. Chemically Modified, Carbon-Based Electrodes and Their Application as Electrochemical Sensors for the Analysis of Biologically Important Compounds. A Review. *Analyst* **1992,** *117*, 1215-1229.
48. Jiang, L.; Nelson, G. W.; Abda, J.; Foord, J. S. Novel Modifications to Carbon-Based Electrodes to Improve the Electrochemical Detection of Dopamine. *ACS Appl. Mater. Interfaces* **2016,** *8*, 28338-28348.
49. Macpherson, J. V. A Practical Guide to Using Boron Doped Diamond in Electrochemical Research. *Phys. Chem. Chem. Phys.* **2015,** *17*, 2935-2949.
50. Bai, H.; Shi, G. Q. Gas Sensors Based on Conducting Polymers. *Sensors* **2007,** *7*, 267-307.
51. Synowczyk, A. W.; Heinze, J., Application of Fullerenes as Sensor Materials. In *Electronic Properties of Fullerenes*, Springer, Berlin, Heidelberg: 1993; pp 73-77.
52. Pilehvar, S.; De Wael, K. Recent Advances in Electrochemical Biosensors Based on Fullerene-C60 Nano-Structured Platforms. *Biosensors* **2015,** *5*, 712-735.
53. Fennell, J. F., Jr.; Liu, S. F.; Azzarelli, J. M.; Weis, J. G.; Rochat, S.; Mirica, K. A.; Ravnsbaek, J. B.; Swager, T. M. Nanowire Chemical/Biological Sensors: Status and a Roadmap for the Future. *Angew. Chem. Int. Ed.* **2016,** *55*, 1266-1281.
54. Tang, R.; Shi, Y.; Hou, Z.; Wei, L. Carbon Nanotube-Based Chemiresistive Sensors. *Sensors* **2017,** *17*, 882.
55. Mirica, K. A.; Azzarelli, J. M.; Weis, J. G.; Schnorr, J. M.; Swager, T. M. Rapid Prototyping of Carbon-Based Chemiresistive Gas Sensors on Paper. *Proc. Natl. Acad. Sci. U. S. A.* **2013,** *110*, E3265-3270.
56. Kauffman, D. R.; Star, A. Carbon Nanotube Gas and Vapor Sensors. *Angew. Chem. Int. Ed.* **2008,** *47*, 6550-6570.
57. Howes, P. D.; Chandrawati, R.; Stevens, M. M. Bionanotechnology. Colloidal Nanoparticles as Advanced Biological Sensors. *Science* **2014,** *346*, 1247390.
58. El-Ansary, A.; Faddah, L. M. Nanoparticles as Biochemical Sensors. *Nanotechnol. Sci. Appl.* **2010,** *3*, 65-76.
59. Luo, X.; Morrin, A.; Killard, A. J.; Smyth, M. R. Application of Nanoparticles in Electrochemical Sensors and Biosensors. *Electroanalysis* **2006,** *18*, 319-326.
60. Lange, U.; Roznyatovskaya, N. V.; Mirsky, V. M. Conducting Polymers in Chemical Sensors and Arrays. *Anal. Chim. Acta* **2008,** *614*, 1-26.
61. Guo, L.; Jackman, J. A.; Yang, H.-H.; Chen, P.; Cho, N.-J.; Kim, D.-H. Strategies for Enhancing the Sensitivity of Plasmonic Nanosensors. *Nano Today* **2015,** *10*, 213-239.
62. Xia, F.; Wang, H.; Xiao, D.; Dubey, M.; Ramasubramaniam, A. Two-Dimensional Material Nanophotonics. *Nat. Photonics* **2014,** *8*, 899-907.
63. Dean, C. R.; Young, A. F.; Meric, I.; Lee, C.; Wang, L.; Sorgenfrei, S.; Watanabe, K.; Taniguchi, T.; Kim, P.; Shepard, K. L.; Hone, J. Boron Nitride Substrates for High-Quality Graphene Electronics. *Nat. Nanotechnol.* **2010,** *5*, 722-726.
64. Huang, X.; Sheng, P.; Tu, Z.; Zhang, F.; Wang, J.; Geng, H.; Zou, Y.; Di, C. A.; Yi, Y.; Sun, Y.; Xu, W.; Zhu, D. A Two-Dimensional Pi-D Conjugated Coordination Polymer with Extremely High Electrical Conductivity and Ambipolar Transport Behaviour. *Nat. Commun.* **2015,** *6*, 7408.
65. Bao, W.; Cai, X.; Kim, D.; Sridhara, K.; Fuhrer, M. S. High Mobility Ambipolar MoS_2 Field-Effect Transistors: Substrate and Dielectric Effects. *Appl. Phys. Lett.* **2013,** *102*.
66. Perello, D. J.; Chae, S. H.; Song, S.; Lee, Y. H. High-Performance N-Type Black Phosphorus Transistors with Type Control via Thickness and Contact-Metal Engineering. *Nat. Commun.* **2015,** *6*, 7809.
67. Liu, H.; Neal, A. T.; Zhu, Z.; Luo, Z.; Xu, X.; Tomanek, D.; Ye, P. D. Phosphorene: An Unexplored 2D Semiconductor with a High Hole Mobility. *ACS Nano* **2014,** *8*, 4033-4041.
68. Bolotin, K. I.; Sikes, K. J.; Jiang, Z.; Klima, M.; Fudenberg, G.; Hone, J.; Kim, P.; Stormer, H. L. Ultrahigh Electron Mobility in Suspended Graphene. *Solid State Commun.* **2008,** *146*, 351-355.
69. Wang, Y.; Chen, Y.; Lacey, S. D.; Xu, L.; Xie, H.; Li, T.; Danner, V. A.; Hu, L. Reduced Graphene Oxide Film with Record-High Conductivity and Mobility. *Mater. Today* **2018,** *21*, 186-192.
70. Butler, S. Z.; Hollen, S. M.; Cao, L.; Cui, Y.; Gupta, J. A.; Gutierrez, H. R.; Heinz, T. F.; Hong, S. S.; Huang, J.; Ismach, A. F.; Johnston-Halperin, E.; Kuno, M.; Plashnitsa, V. V.; Robinson, R. D.; Ruoff, R. S.; Salahuddin, S.; Shan, J.; Shi, L.; Spencer, M. G.; Terrones, M.; Windl, W.; Goldberger, J. E. Progress, Challenges, and Opportunities in Two-Dimensional Materials Beyond Graphene. *ACS Nano* **2013,** *7*, 2898-2926.
71. Xu, M.; Liang, T.; Shi, M.; Chen, H. Graphene-Like Two-Dimensional Materials. *Chem. Rev.* **2013,** *113*, 3766-3798.
72. Novoselov, K. S.; Mishchenko, A.; Carvalho, A.; Castro Neto, A. H. 2D Materials and Van Der Waals Heterostructures. *Science* **2016,** *353*, aac9439.
73. Tan, C.; Cao, X.; Wu, X. J.; He, Q.; Yang, J.; Zhang, X.; Chen, J.; Zhao, W.; Han, S.; Nam, G. H.; Sindoro, M.; Zhang, H. Recent Advances in Ultrathin Two-Dimensional Nanomaterials. *Chem. Rev.* **2017,** *117*, 6225-6331.
74. Li, J.; Wang, X.-Y.; Liu, X.-R.; Jin, Z.; Wang, D.; Wan, L.-J. Facile Growth of Centimeter-Sized Single-Crystal Graphene on Copper Foil at Atmospheric Pressure. *J. Mater. Chem. C* **2015,** *3*, 3530-3535.
75. Vlassiouk, I. V.; Stehle, Y.; Pudasaini, P. R.; Unocic, R. R.; Rack, P. D.; Baddorf, A. P.; Ivanov, I. N.; Lavrik, N. V.; List, F.; Gupta, N.; Bets, K. V.; Yakobson, B. I.; Smirnov, S. N. Evolutionary Selection Growth of Two-Dimensional Materials on Polycrystalline Substrates. *Nat. Mater.* **2018,** *17*, 318-322.
76. Novoselov, K. S.; Geim, A. K.; Morozov, S. V.; Jiang, D.; Zhang, Y.; Dubonos, S. V.; Grigorieva, I. V.; Firsov, A. A. Electric Field Effect in Atomically Thin Carbon Films. *Science* **2004,** *306*, 666-669.
77. Castro Neto, A. H.; Guinea, F.; Peres, N. M. R.; Novoselov, K. S.; Geim, A. K. The Electronic Properties of Graphene. *Rev. Mod. Phys* **2009,** *81*, 109-162.
78. He, Q. Y.; Wu, S. X.; Yin, Z. Y.; Zhang, H. Graphene-Based Electronic Sensors. *Chem. Sci.* **2012,** *3*, 1764-1772.

79. Melitz, W.; Shen, J.; Kummel, A. C.; Lee, S. Kelvin Probe Force Microscopy and Its Application. *Surf. Sci. Rep.* **2011,** *66*, 1-27.
80. Pumera, M.; Ambrosi, A.; Bonanni, A.; Chng, E. L. K.; Poh, H. L. Graphene for Electrochemical Sensing and Biosensing. *TrAC, Trends Anal. Chem.* **2010,** *29*, 954-965.
81. Khandelwal, A.; Mani, K.; Karigerasi, M. H.; Lahiri, I. Phosphorene – the Two-Dimensional Black Phosphorous: Properties, Synthesis and Applications. *Mater. Sci. Eng. B* **2017,** *221*, 17-34.
82. Lin, Y.; Williams, T. V.; Connell, J. W. Soluble, Exfoliated Hexagonal Boron Nitride Nanosheets. *J. Phys. Chem. Lett.* **2009,** *1*, 277-283.
83. Li, L. H.; Chen, Y. Atomically Thin Boron Nitride: Unique Properties and Applications. *Adv. Funct. Mater.* **2016,** *26*, 2594-2608.
84. Chhowalla, M.; Shin, H. S.; Eda, G.; Li, L. J.; Loh, K. P.; Zhang, H. The Chemistry of Two-Dimensional Layered Transition Metal Dichalcogenide Nanosheets. *Nat. Chem.* **2013,** *5*, 263-275.
85. Tan, C.; Zhang, H. Two-Dimensional Transition Metal Dichalcogenide Nanosheet-Based Composites. *Chem. Soc. Rev.* **2015,** *44*, 2713-2731.
86. Kalantar-zadeh, K.; Ou, J. Z.; Daeneke, T.; Mitchell, A.; Sasaki, T.; Fuhrer, M. S. Two Dimensional and Layered Transition Metal Oxides. *Appl. Mater. Today* **2016,** *5*, 73-89.
87. Balendhran, S.; Walia, S.; Nili, H.; Ou, J. Z.; Zhuiykov, S.; Kaner, R. B.; Sriram, S.; Bhaskaran, M.; Kalantar-zadeh, K. Two-Dimensional Molybdenum Trioxide and Dichalcogenides. *Adv. Funct. Mater.* **2013,** *23*, 3952-3970.
88. Sun, L.; Campbell, M. G.; Dinca, M. Electrically Conductive Porous Metal-Organic Frameworks. *Angew. Chem. Int. Ed.* **2016,** *55*, 3566-3579.
89. Ko, M.; Mendecki, L.; Mirica, K. A. Conductive Two-Dimensional Metal-Organic Frameworks as Multifunctional Materials. *Chem. Commun.* **2018,** *54*, 7873-7891.
90. Jin, E.; Asada, M.; Xu, Q.; Dalapati, S.; Addicoat, M. A.; Brady, M. A.; Xu, H.; Nakamura, T.; Heine, T.; Chen, Q.; Jiang, D. Two-Dimensional sp^2 Carbon-Conjugated Covalent Organic Frameworks. *Science* **2017,** *357*, 673-676.
91. Yang, H.; Zhang, S.; Han, L.; Zhang, Z.; Xue, Z.; Gao, J.; Li, Y.; Huang, C.; Yi, Y.; Liu, H.; Li, Y. High Conductive Two-Dimensional Covalent Organic Framework for Lithium Storage with Large Capacity. *ACS Appl. Mater. Interfaces* **2016,** *8*, 5366-5375.
92. Rao, C. N.; Sood, A. K.; Subrahmanyam, K. S.; Govindaraj, A. Graphene: The New Two-Dimensional Nanomaterial. *Angew. Chem. Int. Ed.* **2009,** *48*, 7752-7777.
93. Sun, Y.; Lei, F.; Gao, S.; Pan, B.; Zhou, J.; Xie, Y. Atomically Thin Tin Dioxide Sheets for Efficient Catalytic Oxidation of Carbon Monoxide. *Angew. Chem. Int. Ed.* **2013,** *52*, 10569-10572.
94. Varghese, S.; Varghese, S.; Swaminathan, S.; Singh, K.; Mittal, V. Two-Dimensional Materials for Sensing: Graphene and Beyond. *Electronics* **2015,** *4*, 651-687.
95. Li, Z.; Wong, S. L. Functionalization of 2D Transition Metal Dichalcogenides for Biomedical Applications. *Mater. Sci. Eng. C Mater. Biol. Appl.* **2017,** *70*, 1095-1106.
96. Hirsch, A.; Hauke, F. Post-Graphene 2D Chemistry: The Emerging Field of Molybdenum Disulfide and Black Phosphorus Functionalization. *Angew. Chem. Int. Ed.* **2018,** *57*, 4338-4354.
97. Georgakilas, V.; Otyepka, M.; Bourlinos, A. B.; Chandra, V.; Kim, N.; Kemp, K. C.; Hobza, P.; Zboril, R.; Kim, K. S. Functionalization of Graphene: Covalent and Non-Covalent Approaches, Derivatives and Applications. *Chem. Rev.* **2012,** *112*, 6156-6214.
98. Kou, L.; Frauenheim, T.; Chen, C. Phosphorene as a Superior Gas Sensor: Selective Adsorption and Distinct I-V Response. *J. Phys. Chem. Lett.* **2014,** *5*, 2675-2681.
99. Lei, S. Y.; Luan, S.; Yu, H. Co-Doped Phosphorene: Enhanced Sensitivity of CO Gas Sensing. *Int. J. Mod Phys B* **2017**, 1850068.
100. Suvansinpan, N.; Hussain, F.; Zhang, G.; Chiu, C. H.; Cai, Y.; Zhang, Y. W. Substitutionally Doped Phosphorene: Electronic Properties and Gas Sensing. *Nanotechnology* **2016,** *27*, 065708.
101. Late, D. J.; Huang, Y. K.; Liu, B.; Acharya, J.; Shirodkar, S. N.; Luo, J.; Yan, A.; Charles, D.; Waghmare, U. V.; Dravid, V. P.; Rao, C. N. Sensing Behavior of Atomically Thin-Layered MoS_2 Transistors. *ACS Nano* **2013,** *7*, 4879-4891.
102. Zeng, M.; Xiao, Y.; Liu, J.; Yang, K.; Fu, L. Exploring Two-Dimensional Materials toward the Next-Generation Circuits: From Monomer Design to Assembly Control. *Chem. Rev.* **2018,** *118*, 6236-6296.
103. Gao, L. Flexible Device Applications of 2D Semiconductors. *Small* **2017,** *13*, 1603994.
104. Bandodkar, A. J.; Jeerapan, I.; Wang, J. Wearable Chemical Sensors: Present Challenges and Future Prospects. *ACS Sens.* **2016,** *1*, 464-482.
105. Xiang, D.; Wang, X.; Jia, C.; Lee, T.; Guo, X. Molecular-Scale Electronics: From Concept to Function. *Chem. Rev.* **2016,** *116*, 4318-4440.
106. Chuang, C. H.; Brown, P. R.; Bulovic, V.; Bawendi, M. G. Improved Performance and Stability in Quantum Dot Solar Cells through Band Alignment Engineering. *Nat. Mater.* **2014,** *13*, 796-801.
107. Yue, Z.; Lisdat, F.; Parak, W. J.; Hickey, S. G.; Tu, L.; Sabir, N.; Dorfs, D.; Bigall, N. C. Quantum-Dot-Based Photoelectrochemical Sensors for Chemical and Biological Detection. *ACS Appl. Mater. Interfaces* **2013,** *5*, 2800-2814.
108. Pedireddy, S.; Lee, H. K.; Tjiu, W. W.; Phang, I. Y.; Tan, H. R.; Chua, S. Q.; Troadec, C.; Ling, X. Y. One-Step Synthesis of Zero-Dimensional Hollow Nanoporous Gold Nanoparticles with Enhanced Methanol Electrooxidation Performance. *Nat. Commun.* **2014,** *5*, 4947.
109. Yildirimer, L.; Thanh, N. T.; Loizidou, M.; Seifalian, A. M. Toxicology and Clinical Potential of Nanoparticles. *Nano Today* **2011,** *6*, 585-607.
110. Comini, E.; Sberveglieri, G. Metal Oxide Nanowires as Chemical Sensors. *Mater. Today* **2010,** *13*, 28-36.
111. Zhao, X.; Cai, B.; Tang, Q.; Tong, Y.; Liu, Y. One-Dimensional Nanostructure Field-Effect Sensors for Gas Detection. *Sensors* **2014,** *14*, 13999-14020.
112. Choi, K. J.; Jang, H. W. One-Dimensional Oxide Nanostructures as Gas-Sensing Materials: Review and Issues. *Sensors* **2010,** *10*, 4083-4099.
113. Liu, X.; Ma, T.; Pinna, N.; Zhang, J. Two-Dimensional Nanostructured Materials for Gas Sensing. *Adv. Funct. Mater.* **2017,** *27*.
114. Neri, G. Thin 2D: The New Dimensionality in Gas Sensing. *Chemosensors* **2017,** *5*, 21.
115. Kreno, L. E.; Leong, K.; Farha, O. K.; Allendorf, M.; Van Duyne, R. P.; Hupp, J. T. Metal-Organic Framework Materials as Chemical Sensors. *Chem. Rev.* **2012,** *112*, 1105-1125.
116. Xu, S.; Yan, Z.; Jang, K. I.; Huang, W.; Fu, H.; Kim, J.; Wei, Z.; Flavin, M.; McCracken, J.; Wang, R.; Badea, A.; Liu, Y.; Xiao, D.; Zhou, G.; Lee, J.; Chung, H. U.; Cheng, H.; Ren, W.; Banks, A.; Li, X.; Paik, U.; Nuzzo, R. G.; Huang, Y.; Zhang, Y.; Rogers, J. A. Materials Science. Assembly of Micro/Nanomaterials into Complex, Three-Dimensional Architectures by Compressive Buckling. *Science* **2015,** *347*, 154-159.
117. Cai, Z.; Liu, B.; Zou, X.; Cheng, H. M. Chemical Vapor Deposition Growth and Applications of Two-Dimensional

Materials and Their Heterostructures. *Chem. Rev.* **2018,** *118*, 6091-6133.
118. Dong, R.; Zhang, T.; Feng, X. Interface-Assisted Synthesis of 2D Materials: Trend and Challenges. *Chem. Rev.* **2018,** *118*, 6189-6235.
119. Mannix, A. J.; Kiraly, B.; Hersam, M. C.; Guisinger, N. P. Synthesis and Chemistry of Elemental 2D Materials. *Nat. Rev. Chem.* **2017,** *1*, 0014.
120. Chen, Y.; Fan, Z.; Zhang, Z.; Niu, W.; Li, C.; Yang, N.; Chen, B.; Zhang, H. Two-Dimensional Metal Nanomaterials: Synthesis, Properties, and Applications. *Chem. Rev.* **2018,** *118*, 6409-6455.
121. Jin, H.; Guo, C.; Liu, X.; Liu, J.; Vasileff, A.; Jiao, Y.; Zheng, Y.; Qiao, S. Z. Emerging Two-Dimensional Nanomaterials for Electrocatalysis. *Chem. Rev.* **2018,** *118*, 6337-6408.
122. Holzinger, M.; Le Goff, A.; Cosnier, S. Nanomaterials for Biosensing Applications: A Review. *Front Chem* **2014,** *2*, 63.
123. Yuan, W.; Shi, G. Graphene-Based Gas Sensors. *J. Mater. Chem. A* **2013,** *1*, 10078.
124. Singh, E.; Meyyappan, M.; Nalwa, H. S. Flexible Graphene-Based Wearable Gas and Chemical Sensors. *ACS Appl. Mater. Interfaces* **2017,** *9*, 34544-34586.
125. Yavari, F.; Koratkar, N. Graphene-Based Chemical Sensors. *J. Phys. Chem. Lett.* **2012,** *3*, 1746-1753.
126. Wu, S.; He, Q.; Tan, C.; Wang, Y.; Zhang, H. Graphene-Based Electrochemical Sensors. *Small* **2013,** *9*, 1160-1172.
127. Sun, Y. F.; Liu, S. B.; Meng, F. L.; Liu, J. Y.; Jin, Z.; Kong, L. T.; Liu, J. H. Metal Oxide Nanostructures and Their Gas Sensing Properties: A Review. *Sensors* **2012,** *12*, 2610-2631.
128. Zhang, J.; Qin, Z.; Zeng, D.; Xie, C. Metal-Oxide-Semiconductor Based Gas Sensors: Screening, Preparation, and Integration. *Phys. Chem. Chem. Phys.* **2017,** *19*, 6313-6329.
129. Hahn, Y. B.; Ahmad, R.; Tripathy, N. Chemical and Biological Sensors Based on Metal Oxide Nanostructures. *Chem. Commun.* **2012,** *48*, 10369-10385.
130. Marco, S.; Gutierrez-Galvez, A. Signal and Data Processing for Machine Olfaction and Chemical Sensing: A Review. *IEEE Sens. J.* **2012,** *12*, 3189-3214.
131. Göpel, W. New Materials and Transducers for Chemical Sensors. *Sensors Actuators B: Chem.* **1994,** *18*, 1-21.
132. Lu, W.; Lieber, C. M. Nanoelectronics from the Bottom Up. *Nat. Mater.* **2007,** *6*, 841-850.
133. Shimomura, M.; Sawadaishi, T. Bottom-up Strategy of Materials Fabrication: A New Trend in Nanotechnology of Soft Materials. *Curr. Opin. Colloid Interface Sci.* **2001,** *6*, 11-16.
134. Cravotto, G.; Cintas, P. Sonication-Assisted Fabrication and Post-Synthetic Modifications of Graphene-Like Materials. *Chem. Eur. J.* **2010,** *16*, 5246-5259.
135. Wang, Z.; Cohen, S. M. Postsynthetic Modification of Metal-Organic Frameworks. *Chem. Soc. Rev.* **2009,** *38*, 1315-1329.
136. Huang, X.; Qi, X.; Boey, F.; Zhang, H. Graphene-Based Composites. *Chem. Soc. Rev.* **2012,** *41*, 666-686.
137. Liu, Z.; Lau, S. P.; Yan, F. Functionalized Graphene and Other Two-Dimensional Materials for Photovoltaic Devices: Device Design and Processing. *Chem. Soc. Rev.* **2015,** *44*, 5638-5679.
138. Bhimanapati, G. R.; Lin, Z.; Meunier, V.; Jung, Y.; Cha, J.; Das, S.; Xiao, D.; Son, Y.; Strano, M. S.; Cooper, V. R.; Liang, L.; Louie, S. G.; Ringe, E.; Zhou, W.; Kim, S. S.; Naik, R. R.; Sumpter, B. G.; Terrones, H.; Xia, F.; Wang, Y.; Zhu, J.; Akinwande, D.; Alem, N.; Schuller, J. A.; Schaak, R. E.; Terrones, M.; Robinson, J. A. Recent Advances in Two-Dimensional Materials Beyond Graphene. *ACS Nano* **2015,** *9*, 11509-11539.
139. Gupta, A.; Sakthivel, T.; Seal, S. Recent Development in 2D Materials Beyond Graphene. *Prog. Mater Sci.* **2015,** *73*, 44-126.
140. Zeghbroeck, V., *Principles of Semiconductor Devices and Heterojunctions*. Prentice Hall PTR: 2007.
141. Berger, L. I., *Semiconductor Materials*. Taylor & Francis: 1996.
142. Neamen, D., *An Introduction to Semiconductor Devices*. McGraw-Hill, Inc.: 2006; p 720.
143. Kahn, A. Fermi Level, Work Function and Vacuum Level. *Mater. Horizons* **2016,** *3*, 7-10.
144. Tung, R. T. The Physics and Chemistry of the Schottky Barrier Height. *Appl. Phy. Rev.* **2014,** *1*, 011304.
145. Griffiths, D. J., *Introduction to Electrodynamics*. Cambridge University Press: 2017.
146. Yang, S.; Jiang, C.; Wei, S.-h. Gas Sensing in 2D Materials. *Appl. Phy. Rev.* **2017,** *4*, 021304.
147. Wang, T.; Huang, D.; Yang, Z.; Xu, S.; He, G.; Li, X.; Hu, N.; Yin, G.; He, D.; Zhang, L. A Review on Graphene-Based Gas/Vapor Sensors with Unique Properties and Potential Applications. *Nano-Micro Lett.* **2016,** *8*, 95-119.
148. Ishihara, T.; Matsubara, S. Capacitive Type Gas Sensors. *J. Electroceram.* **1998,** *2*, 215-228.
149. Fonollosa, J.; Solorzano, A.; Marco, S. Chemical Sensor Systems and Associated Algorithms for Fire Detection: A Review. *Sensors* **2018,** *18*.
150. Potyrailo, R. A. Multivariable Sensors for Ubiquitous Monitoring of Gases in the Era of Internet of Things and Industrial Internet. *Chem. Rev.* **2016,** *116*, 11877-11923.
151. Shimizu, Y.; Egashira, M. Basic Aspects and Challenges of Semiconductor Gas Sensors. *MRS Bull.* **2013,** *24*, 18-24.
152. Barsan, N.; Weimar, U. Conduction Model of Metal Oxide Gas Sensors. *J. Electroceram.* **2001,** *7*, 143-167.
153. Lee, J. H.; Avsar, A.; Jung, J.; Tan, J. Y.; Watanabe, K.; Taniguchi, T.; Natarajan, S.; Eda, G.; Adam, S.; Castro Neto, A. H.; Ozyilmaz, B. Van Der Waals Force: A Dominant Factor for Reactivity of Graphene. *Nano Lett.* **2015,** *15*, 319-325.
154. Collins, P. G. Extreme Oxygen Sensitivity of Electronic Properties of Carbon Nanotubes. *Science* **2000,** *287*, 1801-1804.
155. Yew, Y. T.; Ambrosi, A.; Pumera, M. Nitroaromatic Explosives Detection Using Electrochemically Exfoliated Graphene. *Sci. Rep.* **2016,** *6*, 33276.
156. Church, J.; Wang, X.; Calderon, J.; Lee, W. H.; Cho, H. J.; Zhai, L. A Graphene-Based Nanosensor for in Situ Monitoring of Polycyclic Aromatic Hydrocarbons (PAHs). *J. Nanosci. Nanotechnol* **2016,** *16*, 1620-1623.
157. Schedin, F.; Geim, A. K.; Morozov, S. V.; Hill, E. W.; Blake, P.; Katsnelson, M. I.; Novoselov, K. S. Detection of Individual Gas Molecules Adsorbed on Graphene. *Nat. Mater.* **2007,** *6*, 652-655.
158. Cui, S.; Pu, H.; Wells, S. A.; Wen, Z.; Mao, S.; Chang, J.; Hersam, M. C.; Chen, J. Ultrahigh Sensitivity and Layer-Dependent Sensing Performance of Phosphorene-Based Gas Sensors. *Nat. Commun.* **2015,** *6*, 8632.
159. Abbas, A. N.; Liu, B.; Chen, L.; Ma, Y.; Cong, S.; Aroonyadet, N.; Kopf, M.; Nilges, T.; Zhou, C. Black Phosphorus Gas Sensors. *ACS Nano* **2015,** *9*, 5618-5624.
160. Donarelli, M.; Ottaviano, L.; Giancaterini, L.; Fioravanti, G.; Perrozzi, F.; Cantalini, C. Exfoliated Black Phosphorus Gas Sensing Properties at Room Temperature. 2D *Mater.* **2016,** *3*, 025002.
161. Hussain, T.; Kaewmaraya, T.; Chakraborty, S.; Ahuja, R. Defect and Substitution-Induced Silicene Sensor to Probe Toxic Gases. *J. Phys. Chem. C* **2016,** *120*, 25256-25262.
162. Gupta, S. K.; Singh, D.; Rajput, K.; Sonvane, Y. Germanene: A New Electronic Gas Sensing Material. *RSC Adv.* **2016,** *6*, 102264-102271.
163. Prasongkit, J.; Amorim, R. G.; Chakraborty, S.; Ahuja, R.; Scheicher, R. H.; Amornkitbamrung, V. Highly Sensitive and

Selective Gas Detection Based on Silicene. *Journal of Physical Chemistry C* **2015,** *119*, 16934-16940.
164. Thomas, R. C. Sensors for Detecting Molecular Hydrogen Based on Pd Metal Alloys. *J. Electrochem. Soc.* **1997,** *144*, 3245-3249.
165. Sen, S.; Muthe, K. P.; Joshi, N.; Gadkari, S. C.; Gupta, S. K.; Jagannath; Roy, M.; Deshpande, S. K.; Yakhmi, J. V. Room Temperature Operating Ammonia Sensor Based on Tellurium Thin Films. *Sensors Actuators B: Chem.* **2004,** *98*, 154-159.
166. Perkins, F. K.; Friedman, A. L.; Cobas, E.; Campbell, P. M.; Jernigan, G. G.; Jonker, B. T. Chemical Vapor Sensing with Monolayer MoS_2. *Nano Lett.* **2013,** *13*, 668-673.
167. Ovcharenko, R.; Dedkov, Y.; Voloshina, E. Adsorption of NO_2 on WSe_2: Dft and Photoelectron Spectroscopy Studies. *J Phys Condens Matter* **2016,** *28*, 364003.
168. Chen, B.; Sahin, H.; Suslu, A.; Ding, L.; Bertoni, M. I.; Peeters, F. M.; Tongay, S. Environmental Changes in $MoTe_2$ Excitonic Dynamics by Defects-Activated Molecular Interaction. *ACS Nano* **2015,** *9*, 5326-5332.
169. Enhanced Sensitivity of $MoTe_2$ Chemical Sensor through Light Illumination. *Micromachines* **2017,** *8*, 155.
170. Cho, B.; Hahm, M. G.; Choi, M.; Yoon, J.; Kim, A. R.; Lee, Y. J.; Park, S. G.; Kwon, J. D.; Kim, C. S.; Song, M.; Jeong, Y.; Nam, K. S.; Lee, S.; Yoo, T. J.; Kang, C. G.; Lee, B. H.; Ko, H. C.; Ajayan, P. M.; Kim, D. H. Charge-Transfer-Based Gas Sensing Using Atomic-Layer MoS_2. *Sci. Rep.* **2015,** *5*, 8052.
171. Shimizu, Y.; Egashira, M. Basic Aspects and Challenges of Semiconductor Gas Sensors. *MRS Bull.* **1999,** *24*, 18-24.
172. Zhang, J.; Liu, X.; Neri, G.; Pinna, N. Nanostructured Materials for Room-Temperature Gas Sensors. *Adv. Mater.* **2016,** *28*, 795-831.
173. Yao, M. S.; Lv, X. J.; Fu, Z. H.; Li, W. H.; Deng, W. H.; Wu, G. D.; Xu, G. Layer-by-Layer Assembled Conductive Metal-Organic Framework Nanofilms for Room-Temperature Chemiresistive Sensing. *Angew. Chem. Int. Ed.* **2017,** *56*, 16510-16514.
174. Campbell, M. G.; Liu, S. F.; Swager, T. M.; Dinca, M. Chemiresistive Sensor Arrays from Conductive 2D Metal-Organic Frameworks. *J. Am. Chem. Soc.* **2015,** *137*, 13780-13783.
175. Rubio-Gimenez, V.; Almora-Barrios, N.; Escorcia-Ariza, G.; Galbiati, M.; Sessolo, M.; Tatay, S.; Marti-Gastaldo, C. Origin of the Chemiresistive Response of Ultrathin Films of Conductive Metal-Organic Frameworks. *Angew. Chem. Int. Ed.* **2018**.
176. Ko, M.; Aykanat, A.; Smith, M. K.; Mirica, K. A. Drawing Sensors with Ball-Milled Blends of Metal-Organic Frameworks and Graphite. *Sensors* **2017,** *17*, 2192.
177. Hong Ng, V. M.; Huang, H.; Zhou, K.; Lee, P. S.; Que, W.; Xu, J. Z.; Kong, L. B. Recent Progress in Layered Transition Metal Carbides and/or Nitrides (MXenes) and Their Composites: Synthesis and Applications. *J. Mater. Chem. A* **2017,** *5*, 3039-3068.
178. Naguib, M.; Kurtoglu, M.; Presser, V.; Lu, J.; Niu, J.; Heon, M.; Hultman, L.; Gogotsi, Y.; Barsoum, M. W. Two-Dimensional Nanocrystals Produced by Exfoliation of Ti_3AlC_2. *Adv. Mater.* **2011,** *23*, 4248-4253.
179. Zhu, J.; Ha, E.; Zhao, G.; Zhou, Y.; Huang, D.; Yue, G.; Hu, L.; Sun, N.; Wang, Y.; Lee, L. Y. S.; Xu, C.; Wong, K.-Y.; Astruc, D.; Zhao, P. Recent Advance in MXenes: A Promising 2D Material for Catalysis, Sensor and Chemical Adsorption. *Coord. Chem. Rev.* **2017,** *352*, 306-327.
180. Kamaraj, M.; Sundar, J. V.; Subramanian, V. Dioxin Sensing Properties of Graphene and Hexagonal Boron Nitride Based Van Der Waals Solids: A First-Principles Study. *RSC Adv.* **2016,** *6*, 107114-107126.
181. Yamini, Y.; Moradi, M. Influence of Topological Defects on the Nitrogen Monoxide-Sensing Characteristics of Graphene-Analogue Bn. *Sensors Actuators B: Chem.* **2014,** *197*, 274-279.
182. Safari, L.; Vessally, E.; Bekhradnia, A.; Hosseinian, A.; Edjlali, L. A Density Functional Theory Study of the Sensitivity of Two-Dimensional Bn Nanosheet to Nerve Agents Cyclosarin and Tabun. *Thin Solid Films* **2017,** *623*, 157-163.
183. Ao, Z. M.; Yang, J.; Li, S.; Jiang, Q. Enhancement of CO Detection in Al Doped Graphene. *Chem. Phys. Lett.* **2008,** *461*, 276-279.
184. Sarkar, D.; Liu, W.; Xie, X.; Anselmo, A. C.; Mitragotri, S.; Banerjee, K. MoS_2 Field-Effect Transistor for Next-Generation Label-Free Biosensors. *ACS Nano* **2014,** *8*, 3992-4003.
185. Blackwood, D.; Josowicz, M. Work Function and Spectroscopic Studies of Interactions between Conducting Polymers and Organic Vapors. *J. Phys. Chem.* **1991,** *95*, 493-502.
186. Potje-Kamloth, K. Semiconductor Junction Gas Sensors. *Chem. Rev.* **2008,** *108*, 367-399.
187. Kong, J.; Javey, A., *Carbon Nanotube Electronics*. Springer US: 2009.
188. Pinto, H.; Markevich, A. Electronic and Electrochemical Doping of Graphene by Surface Adsorbates. *Beilstein J Nanotechnol* **2014,** *5*, 1842-1848.
189. Rhoderick, E. H. The Physics of Schottky Barriers. *J. Phys. D: Appl. Phys.* **1970,** *3*, 1153-1167.
190. The Physics and Chemistry of the Schottky Barrier Height. *Appl. Phy. Rev.* **2014,** *1*, 011304.
191. Liu, B.; Chen, L.; Liu, G.; Abbas, A. N.; Fathi, M.; Zhou, C. High-Performance Chemical Sensing Using Schottky-Contacted Chemical Vapor Deposition Grown Monolayer MoS_2 Transistors. *ACS Nano* **2014,** *8*, 5304-5314.
192. Xu, Y.; Cheng, C.; Du, S. C.; Yang, J. Y.; Yu, B.; Luo, J.; Yin, W. Y.; Li, E. P.; Dong, S. R.; Ye, P. D.; Duan, X. F. Contacts between Two- and Three-Dimensional Materials: Ohmic, Schottky, and P-N Heterojunctions. *Acs Nano* **2016,** *10*, 4895-4919.
193. Ruths, P. F.; Ashok, S.; Fonash, S. J.; Ruths, J. M. A Study of Pd/Si Mis Schottky Barrier Diode Hydrogen Detector. *IEEE Trans. Electron Devices* **1981,** *28*, 1003-1009.
194. Ogawa, H.; Nishikawa, M.; Abe, A. Hall Measurement Studies and an Electrical Conduction Model of Tin Oxide Ultrafine Particle Films. *J. Appl. Phys.* **1982,** *53*, 4448-4455.
195. Xu, C.; Tamaki, J.; Miura, N.; Yamazoe, N. Grain Size Effects on Gas Sensitivity of Porous SnO_2-Based Elements. *Sensors Actuators B: Chem.* **1991,** *3*, 147-155.
196. Sharma, B. L., *Metal-Semiconductor Schottky Barrier Junctions and Their Applications*. Springer, Boston, MA: 1984.
197. Fonash, S. J.; Huston, H.; Ashok, S. Conducting Mis Diode Gas Detectors: The Pd/Siox/Si Hydrogen Sensor. *Sens. Actuators* **1981,** *2*, 363-369.
198. Li, P.; Zhang, D.; Jiang, C.; Zong, X.; Cao, Y. Ultra-Sensitive Suspended Atomically Thin-Layered Black Phosphorus Mercury Sensors. *Biosens. Bioelectron.* **2017,** *98*, 68-75.
199. Vig, J. R.; Walls, F. L. A Review of Sensor Sensitivity and Stability. *Proceedings of the 2000 IEEE/EIA International Frequency Control Symposium & Exhibition* **2000**, 30-33.
200. Loock, H.-P.; Wentzell, P. D. Detection Limits of Chemical Sensors: Applications and Misapplications. *Sensors Actuators B: Chem.* **2012,** *173*, 157-163.
201. Shrivastava, A.; Gupta, V. Methods for the Determination of Limit of Detection and Limit of Quantitation of the Analytical Methods. *Chronicles of Young Scientists* **2011,** *2*, 21-25.
202. Püntener, M.; Vigassy, T.; Baier, E.; Ceresa, A.; Pretsch, E. Improving the Lower Detection Limit of Potentiometric

Sensors by Covalently Binding the Ionophore to a Polymer Backbone. *Anal. Chim. Acta* **2004,** *503*, 187-194.
203. Lee, E.; VahidMohammadi, A.; Prorok, B. C.; Yoon, Y. S.; Beidaghi, M.; Kim, D. J. Room Temperature Gas Sensing of Two-Dimensional Titanium Carbide (MXene). *ACS Appl. Mater. Interfaces* **2017,** *9*, 37184-37190.
204. Harris, D. C., *Quantitative Chemical Analysis*. W. H. Freeman: 2016.
205. Peveler, W. J.; Yazdani, M.; Rotello, V. M. Selectivity and Specificity: Pros and Cons in Sensing. *ACS Sens.* **2016,** *1*, 1282-1285.
206. Liu, S.; Xing, X.; Yu, J.; Lian, W.; Li, J.; Cui, M.; Huang, J. A Novel Label-Free Electrochemical Aptasensor Based on Graphene-Polyaniline Composite Film for Dopamine Determination. *Biosens. Bioelectron.* **2012,** *36*, 186-191.
207. Kalantar-zadeh, K., *Sensors*. Springer: 2013.
208. Varghese, O. K.; Gong, D.; Paulose, M.; Ong, K. G.; Grimes, C. A. Hydrogen Sensing Using Titania Nanotubes. *Sensors Actuators B: Chem.* **2003,** *93*, 338-344.
209. Saaman, A. A.; Bergveld, P. A Note on the Use of the Word 'Reversible'. *Sens. Actuators* **1985,** *7*, 69-71.
210. Valentini, L.; Cantalini, C.; Armentano, I.; Kenny, J. M.; Lozzi, L.; Santucci, S. Highly Sensitive and Selective Sensors Based on Carbon Nanotubes Thin Films for Molecular Detection. *Diamond Relat. Mater.* **2004,** *13*, 1301-1305.
211. Nah, J.; Kumar, S. B.; Fang, H.; Chen, Y.-Z.; Plis, E.; Chueh, Y.-L.; Krishna, S.; Guo, J.; Javey, A. Quantum Size Effects on the Chemical Sensing Performance of Two-Dimensional Semiconductors. *J. Phys. Chem. C* **2012,** *116*, 9750-9754.
212. Williams, D. E. Semiconducting Oxides as Gas-Sensitive Resistors. *Sensors Actuators B: Chem.* **1999,** *57*, 1-16.
213. Romain, A. C.; Nicolas, J. Long Term Stability of Metal Oxide-Based Gas Sensors for E-Nose Environmental Applications: An Overview. *Sensors Actuators B: Chem.* **2010,** *146*, 502-506.
214. Sisk, B. C.; Lewis, N. S. Comparison of Analytical Methods and Calibration Methods for Correction of Detector Response Drift in Arrays of Carbon Black-Polymer Composite Vapor Detectors. *Sensors Actuators B: Chem.* **2005,** *104*, 249-268.
215. Mao, S.; Lu, G.; Chen, J. Nanocarbon-Based Gas Sensors: Progress and Challenges. *J. Mater. Chem. A* **2014,** *2*, 5573-5579.
216. Tongay, S. Preface to a Special Topic: 2D Materials and Applications. *Appl. Phy. Rev.* **2018,** *5*.
217. Chiu, S. W.; Tang, K. T. Towards a Chemiresistive Sensor-Integrated Electronic Nose: A Review. *Sensors* **2013,** *13*, 14214-14247.
218. Neri, G. First Fifty Years of Chemoresistive Gas Sensors. *Chemosensors* **2015,** *3*, 1-20.
219. Salehi-Khojin, A.; Khalili-Araghi, F.; Kuroda, M. A.; Lin, K. Y.; Leburton, J. P.; Masel, R. I. On the Sensing Mechanism in Carbon Nanotube Chemiresistors. *ACS Nano* **2011,** *5*, 153-158.
220. Zhang, T.; Mubeen, S.; Myung, N. V.; Deshusses, M. A. Recent Progress in Carbon Nanotube-Based Gas Sensors. *Nanotechnology* **2008,** *19*, 332001.
221. Hangarter, C. M.; Chartuprayoon, N.; Hernández, S. C.; Choa, Y.; Myung, N. V. Hybridized Conducting Polymer Chemiresistive Nano-Sensors. *Nano Today* **2013,** *8*, 39-55.
222. Agladze, K.; Aliev, R. R.; Yamaguchi, T.; Yoshikawa, K. Chemical Diode. *J. Phys. Chem.* **1996,** *100*, 13895-13897.
223. Di Bartolomeo, A. Graphene Schottky Diodes: An Experimental Review of the Rectifying Graphene/Semiconductor Heterojunction. *Phys. Rep.* **2016,** *606*, 1-58.
224. Ross, J. S.; Klement, P.; Jones, A. M.; Ghimire, N. J.; Yan, J.; Mandrus, D. G.; Taniguchi, T.; Watanabe, K.; Kitamura, K.; Yao, W.; Cobden, D. H.; Xu, X. Electrically Tunable Excitonic Light-Emitting Diodes Based on Monolayer WSe_2 P-N Junctions. *Nat. Nanotechnol.* **2014,** *9*, 268-272.
225. Al Balushi, Z. Y.; Wang, K.; Ghosh, R. K.; Vila, R. A.; Eichfeld, S. M.; Caldwell, J. D.; Qin, X.; Lin, Y. C.; DeSario, P. A.; Stone, G.; Subramanian, S.; Paul, D. F.; Wallace, R. M.; Datta, S.; Redwing, J. M.; Robinson, J. A. Two-Dimensional Gallium Nitride Realized via Graphene Encapsulation. *Nat. Mater.* **2016,** *15*, 1166-1171.
226. Kim, H. Y.; Lee, K.; McEvoy, N.; Yim, C.; Duesberg, G. S. Chemically Modulated Graphene Diodes. *Nano Lett.* **2013,** *13*, 2182-2188.
227. Li, S. J. F. a. Z. Schottky-Barrier Diode and Metal-Oxide-Semiconductor Capacitor Gas Sensors. *ACS Symp. Ser.* **1986,** *309*, 177-202.
228. Yoshizumi, T.; Miyahara, Y., Field-Effect Transistors for Gas Sensing. In *Different Types of Field-Effect Transistors - Theory and Applications*, IntechOpen: 2017.
229. Mao, S.; Chang, J.; Pu, H.; Lu, G.; He, Q.; Zhang, H.; Chen, J. Two-Dimensional Nanomaterial-Based Field-Effect Transistors for Chemical and Biological Sensing. *Chem. Soc. Rev.* **2017,** *46*, 6872-6904.
230. Cervenka, J.; Budi, A.; Dontschuk, N.; Stacey, A.; Tadich, A.; Rietwyk, K. J.; Schenk, A.; Edmonds, M. T.; Yin, Y. F.; Medhekar, N.; Kalbac, M.; Pakes, C. I. Graphene Field Effect Transistor as a Probe of Electronic Structure and Charge Transfer at Organic Molecule-Graphene Interfaces. *Nanoscale* **2015,** *7*, 1471-1478.
231. Torsi, L.; Magliulo, M.; Manoli, K.; Palazzo, G. Organic Field-Effect Transistor Sensors: A Tutorial Review. *Chem. Soc. Rev.* **2013,** *42*, 8612-8628.
232. Stine, R.; Mulvaney, S. P.; Robinson, J. T.; Tamanaha, C. R.; Sheehan, P. E. Fabrication, Optimization, and Use of Graphene Field Effect Sensors. *Anal. Chem.* **2013,** *85*, 509-521.
233. Cramer, T.; Campana, A.; Leonardi, F.; Casalini, S.; Kyndiah, A.; Murgia, M.; Biscarini, F. Water-Gated Organic Field Effect Transistors – Opportunities for Biochemical Sensing and Extracellular Signal Transduction. *J. Mater. Chem. B* **2013,** *1*, 3728-3741.
234. Stern, E.; Wagner, R.; Sigworth, F. J.; Breaker, R.; Fahmy, T. M.; Reed, M. A. Importance of the Debye Screening Length on Nanowire Field Effect Transistor Sensors. *Nano Lett.* **2007,** *7*, 3405-3409.
235. Israelachvili, J. N., *Intermolecular and Surface Forces*. Elsevier Inc.: 2011.
236. Forsyth, R.; Devadoss, A.; Guy, O. J. Graphene Field Effect Transistors for Biomedical Applications: Current Status and Future Prospects. *Diagnostics* **2017,** *7*, 45.
237. Stern, E.; Vacic, A.; Rajan, N. K.; Criscione, J. M.; Park, J.; Ilic, B. R.; Mooney, D. J.; Reed, M. A.; Fahmy, T. M. Label-Free Biomarker Detection from Whole Blood. *Nat. Nanotechnol.* **2010,** *5*, 138-142.
238. Elnathan, R.; Kwiat, M.; Pevzner, A.; Engel, Y.; Burstein, L.; Khatchtourints, A.; Lichtenstein, A.; Kantaev, R.; Patolsky, F. Biorecognition Layer Engineering: Overcoming Screening Limitations of Nanowire-Based FET Devices. *Nano Lett.* **2012,** *12*, 5245-5254.
239. Maehashi, K.; Katsura, T.; Kerman, K.; Takamura, Y.; Matsumoto, K.; Tamiya, E. Label-Free Protein Biosensor Based on Aptamer-Modified Carbon Nanotube Field-Effect Transistors. *Anal. Chem.* **2007,** *79*, 782-787.
240. Gao, N.; Gao, T.; Yang, X.; Dai, X.; Zhou, W.; Zhang, A.; Lieber, C. M. Specific Detection of Biomolecules in Physiological Solutions Using Graphene Transistor Biosensors. *Proc. Natl. Acad. Sci. U. S. A.* **2016,** *113*, 14633-14638.
241. Terzic, E.; Terzic, J.; Nagarajah, R.; Alamgir, M., Capacitive Sensing Technology. In *A Neural Network Approach*

to Fluid Quantity Measurement in Dynamic Environments, 2012; pp 11-37.
242. Kopp, T.; Mannhart, J. Calculation of the Capacitances of Conductors: Perspectives for the Optimization of Electronic Devices. *J. Appl. Phys.* **2009,** *106*, 15753-15757.
243. Zhang, Y.; Ma, R.; Zhen, X. V.; Kudva, Y. C.; Buhlmann, P.; Koester, S. J. Capacitive Sensing of Glucose in Electrolytes Using Graphene Quantum Capacitance Varactors. *ACS Appl. Mater. Interfaces* **2017,** *9*, 38863-38869.
244. Blue, R.; Uttamchandani, D. Chemicapacitors as a Versatile Platform for Miniature Gas and Vapor Sensors. *Meas. Sci. Technol.* **2017,** *28*, 022001.
245. Conductivity Sensors and Capacitive Sensors. In *Chemical Sensors*, 2007; pp 123-132.
246. Sze, S. M.; Ng, K. K., *Physics of Semiconductor Devices*. John Wiley & Sons, Inc.: 2006.
247. Balkus, K. J.; Ball, L. J.; Gnade, B. E.; Anthony, J. M. A Capacitance Type Chemical Sensor Based on $AlPO_4$-5 Molecular Sieves. *Chem. Mater.* **1997,** *9*, 380-386.
248. Bakker, E.; Bühlmann, P.; Pretsch, E. Carrier-Based Ion-Selective Electrodes and Bulk Optodes. 1. General Characteristics. *Chem. Rev.* **1997,** *97*, 3083-3132.
249. Bobacka, J.; Ivaska, A.; Lewenstam, A. Potentiometric Ion Sensors. *Chem. Rev.* **2008,** *108*, 329-351.
250. Wang, T.; Zhu, H.; Zhuo, J.; Zhu, Z.; Papakonstantinou, P.; Lubarsky, G.; Lin, J.; Li, M. Biosensor Based on Ultrasmall MoS_2 Nanoparticles for Electrochemical Detection of H_2O_2 Released by Cells at the Nanomolar Level. *Anal. Chem.* **2013,** *85*, 10289-10295.
251. Bakker, E. Determination of Unbiased Selectivity Coefficients of Neutral Carrier-Based Cation-Selective Electrodes. *Anal. Chem.* **1997,** *69*, 1061-1069.
252. Mikhelson, K. N., *Ion-Selective Electrodes*. Springer Berlin Heidelberg: 2013.
253. Hu, J.; Stein, A.; Bühlmann, P. Rational Design of All-Solid-State Ion-Selective Electrodes and Reference Electrodes. *TrAC, Trends Anal. Chem.* **2016,** *76*, 102-114.
254. Nikolskii, B. P.; Materova, E. A. Solid Contact in Membrane Ion-Selective Electrodes. *In Ion-Selective Electrode Rev.* Elsevier Great Britain: **1985,** *7*, 3-39.
255. Bobacka, J. Conducting Polymer-Based Solid-State Ion-Selective Electrodes. *Electroanalysis* **2006,** *18*, 7-18.
256. Migdalski, J.; Blaz, T.; Lewenstam, A. Conducting Polymer-Based Ion-Selective Electrodes. *Anal. Chim. Acta* **1996,** *322*, 141-149.
257. Hu, J.; Zou, X. U.; Stein, A.; Buhlmann, P. Ion-Selective Electrodes with Colloid-Imprinted Mesoporous Carbon as Solid Contact. *Anal. Chem.* **2014,** *86*, 7111-7118.
258. Lai, C. Z.; Fierke, M. A.; Stein, A.; Buhlmann, P. Ion-Selective Electrodes with Three-Dimensionally Ordered Macroporous Carbon as the Solid Contact. *Anal. Chem.* **2007,** *79*, 4621-4626.
259. Crespo, G. A.; Macho, S.; Rius, F. X. Ion-Selective Electrodes Using Carbon Nanotubes as Ion-to-Electron Transducers. *Anal. Chem.* **2008,** *80*, 1316-1322.
260. Crespo, G. A.; Macho, S.; Bobacka, J.; Rius, F. X. Transduction Mechanism of Carbon Nanotubes in Solid-Contact Ion-Selective Electrodes. *Anal. Chem.* **2009,** *81*, 676-681.
261. Ping, J.; Wang, Y.; Wu, J.; Ying, Y. Development of an All-Solid-State Potassium Ion-Selective Electrode Using Graphene as the Solid-Contact Transducer. *Electrochem. Commun.* **2011,** *13*, 1529-1532.
262. He, Q.; Das, S. R.; Garland, N. T.; Jing, D.; Hondred, J. A.; Cargill, A. A.; Ding, S.; Karunakaran, C.; Claussen, J. C. Enabling Inkjet Printed Graphene for Ion Selective Electrodes with Postprint Thermal Annealing. *ACS Appl. Mater. Interfaces* **2017,** *9*, 12719-12727.
263. Hernández, R.; Riu, J.; Bobacka, J.; Vallés, C.; Jiménez, P.; Benito, A. M.; Maser, W. K.; Rius, F. X. Reduced Graphene Oxide Films as Solid Transducers in Potentiometric All-Solid-State Ion-Selective Electrodes. *J. Phys. Chem. C* **2012,** *116*, 22570-22578.
264. Liu, Y.; Dong, X.; Chen, P. Biological and Chemical Sensors Based on Graphene Materials. *Chem. Soc. Rev.* **2012,** *41*, 2283-2307.
265. Turner, A. P. Biosensors: Sense and Sensibility. *Chem. Soc. Rev.* **2013,** *42*, 3184-3196.
266. Zhang, X.; Ju, H.; Wang, J., *Electrochemical Sensors, Biosensors and Their Biomedical Applications*. Academic Press: 2008.
267. Bard, A. J.; Faulkner, L. R., *Electrochemical Methods: Fundamentals and Applications*. Wiley: 2000.
268. Langhus, D. L. Analytical Electrochemistry, 2nd Edition (Wang, Joseph). *J. Chem. Educ.* **2001,** *78*, 457.
269. Thiyagarajan, N.; Chang, J.-L.; Senthilkumar, K.; Zen, J.-M. Disposable Electrochemical Sensors: A Mini Review. *Electrochem. Commun.* **2014,** *38*, 86-90.
270. Privett, B. J.; Shin, J. H.; Schoenfisch, M. H. Electrochemical Sensors. *Anal. Chem.* **2010,** *82*, 4723-4741.
271. Silwana, B.; Van Der Horst, C.; Iwuoha, E.; Somerset, V. A Brief Review on Recent Developments of Electrochemical Sensors in Environmental Application for Pgms. *Journal of Environmental Science and Health, Part A* **2016,** *51*, 1233-1247.
272. Fang, Y.; Wang, E. Electrochemical Biosensors on Platforms of Graphene. *Chem. Commun.* **2013,** *49*, 9526-9539.
273. Wang, J. Electrochemical Glucose Biosensors. *Chem. Rev.* **2008,** *108*, 814-825.
274. Yogeswaran, U.; Chen, S. M. A Review on the Electrochemical Sensors and Biosensors Composed of Nanowires as Sensing Material. *Sensors* **2008,** *8*, 290-313.
275. Wei, D.; Ivaska, A. Applications of Ionic Liquids in Electrochemical Sensors. *Anal. Chim. Acta* **2008,** *607*, 126-135.
276. Rieger, P. H., *Electrochemistry*. Springer Netherlands: 1993.
277. Thirsk, H. R., *Electrochemistry*. The Chemical Society: **1978**.
278. Stradiotto, N. R.; Yamanaka, H.; Zanoni, M. V. B. Electrochemical Sensors: A Powerful Tool in Analytical Chemistry. *Journal of the Brazilian Chemical Society* **2003,** *14*, 159-173.
279. Grieshaber, D.; MacKenzie, R.; Voros, J.; Reimhult, E. Electrochemical Biosensors - Sensor Principles and Architectures. *Sensors* **2008,** *8*, 1400-1458.
280. Hendry, S. P.; Higgins, I. J.; Bannister, J. V. Amperometric Biosensors. *J. Biotechnol.* **1990,** *15*, 229-238.
281. Zoski, C. G., *Handbook of Electrochemistry*. Elsevier: 2007.
282. Suvarnaphaet, P.; Pechprasarn, S. Graphene-Based Materials for Biosensors: A Review. *Sensors* **2017,** *17*, 2161.
283. Shao, Y.; Wang, J.; Wu, H.; Liu, J.; Aksay, I. A.; Lin, Y. Graphene Based Electrochemical Sensors and Biosensors: A Review. *Electroanalysis* **2010,** *22*, 1027-1036.
284. Lvovich, V. F., *Impedance Spectroscopy: Applications to Electrochemical and Dielectric Phenomena*. Wiley: 2015.
285. Barsoukov, E.; Macdonald, J. R., *Impedance Spectroscopy: Theory, Experiment, and Applications*. Wiley: 2018.
286. Orazem, M. E.; Tribollet, B., *Electrochemical Impedance Spectroscopy*. Wiley: 2017.
287. Lasia, A., *Electrochemical Impedance Spectroscopy and Its Applications*. Springer New York: 2014.

288. Park, S.-M.; Yoo, J.-S. Peer Reviewed: Electrochemical Impedance Spectroscopy for Better Electrochemical Measurements. *Anal. Chem.* **2003,** *75*, 455 A-461 A.
289. Randviir, E. P.; Banks, C. E. Electrochemical Impedance Spectroscopy: An Overview of Bioanalytical Applications. *Anal. Methods* **2013,** *5*, 1098.
290. Park, J. Y.; Park, S. M. DNA Hybridization Sensors Based on Electrochemical Impedance Spectroscopy as a Detection Tool. *Sensors* **2009,** *9*, 9513-9532.
291. Daniels, J. S.; Pourmand, N. Label-Free Impedance Biosensors: Opportunities and Challenges. *Electroanalysis* **2007,** *19*, 1239-1257.
292. Narakathu, B. B.; Wen, G.; Obare, S. O.; Atashbar, M. Z. Electrochemical Impedance Spectroscopy Sensing of Toxic Organophosphorus Compounds. **2010**, 1518-1521.
293. Zourob, M.; Elwary, S.; Turner, A. P. F., *Principles of Bacterial Detection: Biosensors, Recognition Receptors and Microsystems*. Springer New York: 2008.
294. Lisdat, F.; Schafer, D. The Use of Electrochemical Impedance Spectroscopy for Biosensing. *Anal. Bioanal. Chem.* **2008,** *391*, 1555-1567.
295. Bogomolova, A.; Komarova, E.; Reber, K.; Gerasimov, T.; Yavuz, O.; Bhatt, S.; Aldissi, M. Challenges of Electrochemical Impedance Spectroscopy in Protein Biosensing. *Anal. Chem.* **2009,** *81*, 3944-3949.
296. Chao, Y.; Rairigh, D.; Mason, A. On-Chip Electrochemical Impedance Spectroscopy for Biosensor Arrays. **2006**, 93-96.
297. Bissett, M. A.; Worrall, S. D.; Kinloch, I. A.; Dryfe, R. A. W. Comparison of Two-Dimensional Transition Metal Dichalcogenides for Electrochemical Supercapacitors. *Electrochim. Acta* **2016,** *201*, 30-37.
298. Levi, M. D.; Aurbach, D. Diffusion Coefficients of Lithium Ions During Intercalation into Graphite Derived from the Simultaneous Measurements and Modeling of Electrochemical Impedance and Potentiostatic Intermittent Titration Characteristics of Thin Graphite Electrodes. *J Phys. Chem. B* **1997,** *101*, 4641-4647.
299. Geim, A. K.; Novoselov, K. S. The Rise of Graphene. *Nat. Mater.* **2007,** *6*, 183-191.
300. Chen, J. H.; Jang, C.; Xiao, S.; Ishigami, M.; Fuhrer, M. S. Intrinsic and Extrinsic Performance Limits of Graphene Devices on SiO_2. *Nat. Nanotechnol.* **2008,** *3*, 206-209.
301. Akturk, A.; Goldsman, N. Electron Transport and Full-Band Electron-Phonon Interactions in Graphene. *J. Appl. Phys.* **2008,** *103*, 053702.
302. Grüneis, A.; Attaccalite, C.; Wirtz, L.; Shiozawa, H.; Saito, R.; Pichler, T.; Rubio, A. Tight-Binding Description of the Quasiparticle Dispersion of Graphite and Few-Layer Graphene. *Phys. Rev. B* **2008,** *78*.
303. Bonaccorso, F.; Colombo, L.; Yu, G.; Stoller, M.; Tozzini, V.; Ferrari, A. C.; Ruoff, R. S.; Pellegrini, V. 2D Materials. Graphene, Related Two-Dimensional Crystals, and Hybrid Systems for Energy Conversion and Storage. *Science* **2015,** *347*, 1246501.
304. Lee, C.; Wei, X.; Kysar, J. W.; Hone, J. Measurement of the Elastic Properties and Intrinsic Strength of Monolayer Graphene. *Science* **2008,** *321*, 385-388.
305. Lerf, A.; He, H.; Forster, M.; Klinowski, J. Structure of Graphite Oxide Revisitedii. *J. Phys. Chem. B* **1998,** *102*, 4477-4482.
306. Xiao, J.; Zhang, L.; Zhou, K.; Li, J.; Xie, X.; Li, Z. Anisotropic Friction Behaviour of Highly Oriented Pyrolytic Graphite. *Carbon* **2013,** *65*, 53-62.
307. Warner, J. H. The Influence of the Number of Graphene Layers on the Atomic Resolution Images Obtained from Aberration-Corrected High Resolution Transmission Electron Microscopy. *Nanotechnology* **2010,** *21*, 255707.
308. Dave, S. H.; Gong, C.; Robertson, A. W.; Warner, J. H.; Grossman, J. C. Chemistry and Structure of Graphene Oxide Via Direct Imaging. *ACS Nano* **2016,** *10*, 7515-7522.
309. Lotya, M.; Hernandez, Y.; King, P. J.; Smith, R. J.; Nicolosi, V.; Karlsson, L. S.; Blighe, F. M.; De, S.; Wang, Z.; McGovern, I. T.; Duesberg, G. S.; Coleman, J. N. Liquid Phase Production of Graphene by Exfoliation of Graphite in Surfactant/Water Solutions. *J. Am. Chem. Soc.* **2009,** *131*, 3611-3620.
310. Park, S.; Ruoff, R. S. Chemical Methods for the Production of Graphenes. *Nat. Nanotechnol.* **2009,** *4*, 217-224.
311. Kim, K. S.; Zhao, Y.; Jang, H.; Lee, S. Y.; Kim, J. M.; Kim, K. S.; Ahn, J. H.; Kim, P.; Choi, J. Y.; Hong, B. H. Large-Scale Pattern Growth of Graphene Films for Stretchable Transparent Electrodes. *Nature* **2009,** *457*, 706-710.
312. Li, X.; Cai, W.; An, J.; Kim, S.; Nah, J.; Yang, D.; Piner, R.; Velamakanni, A.; Jung, I.; Tutuc, E.; Banerjee, S. K.; Colombo, L.; Ruoff, R. S. Large-Area Synthesis of High-Quality and Uniform Graphene Films on Copper Foils. *Science* **2009,** *324*, 1312-1314.
313. Bae, S.; Kim, H.; Lee, Y.; Xu, X.; Park, J. S.; Zheng, Y.; Balakrishnan, J.; Lei, T.; Kim, H. R.; Song, Y. I.; Kim, Y. J.; Kim, K. S.; Ozyilmaz, B.; Ahn, J. H.; Hong, B. H.; Iijima, S. Roll-to-Roll Production of 30-Inch Graphene Films for Transparent Electrodes. *Nat. Nanotechnol.* **2010,** *5*, 574-578.
314. Sun, Z.; Yan, Z.; Yao, J.; Beitler, E.; Zhu, Y.; Tour, J. M. Growth of Graphene from Solid Carbon Sources. *Nature* **2010,** *468*, 549-552.
315. Tran-Van, A. F.; Wegner, H. A. Strategies in Organic Synthesis for Condensed Arenes, Coronene, and Graphene. *Top. Curr. Chem.* **2014,** *349*, 121-157.
316. Nguyen, G. D.; Tsai, H. Z.; Omrani, A. A.; Marangoni, T.; Wu, M.; Rizzo, D. J.; Rodgers, G. F.; Cloke, R. R.; Durr, R. A.; Sakai, Y.; Liou, F.; Aikawa, A. S.; Chelikowsky, J. R.; Louie, S. G.; Fischer, F. R.; Crommie, M. F. Atomically Precise Graphene Nanoribbon Heterojunctions from a Single Molecular Precursor. *Nat. Nanotechnol.* **2017,** *12*, 1077-1082.
317. Wu, J.; Pisula, W.; Mullen, K. Graphenes as Potential Material for Electronics. *Chem. Rev.* **2007,** *107*, 718-747.
318. Brodie, B. C. On the Atomic Weight of Graphite. *Philosophical Transactions of the Royal Society of London* **1859,** *149*, 249-259.
319. Staudenmaier, L. Verfahren Zur Darstellung Der Graphitsäure. *Berichte der deutschen chemischen Gesellschaft* **1898,** *31*, 1481-1487.
320. Hummers, W. S.; Offeman, R. E. Preparation of Graphitic Oxide. *J. Am. Chem. Soc.* **1958,** *80*, 1339-1339.
321. Zhang, H. Ultrathin Two-Dimensional Nanomaterials. *ACS Nano* **2015,** *9*, 9451-9469.
322. Allen, M. J.; Tung, V. C.; Kaner, R. B. Honeycomb Carbon: A Review of Graphene. *Chem. Rev.* **2010,** *110*, 132-145.
323. Zhang, Y.; Zhang, L.; Zhou, C. Review of Chemical Vapor Deposition of Graphene and Related Applications. *Acc. Chem. Res.* **2013,** *46*, 2329-2339.
324. Yu, X.; Cheng, H.; Zhang, M.; Zhao, Y.; Qu, L.; Shi, G. Graphene-Based Smart Materials. *Nat. Rev. Mater.* **2017,** *2*, 17046.
325. Guo, S.; Dong, S. Graphene and Its Derivative-Based Sensing Materials for Analytical Devices. *J. Mater. Chem.* **2011,** *21*, 18503.
326. Choi, W.; Lahiri, I.; Seelaboyina, R.; Kang, Y. S. Synthesis of Graphene and Its Applications: A Review. *Crit. Rev. Solid State Mater. Sci.* **2010,** *35*, 52-71.

327. Tang, S.; Cao, Z. Adsorption of Nitrogen Oxides on Graphene and Graphene Oxides: Insights from Density Functional Calculations. *J. Chem. Phys.* **2011,** *134*, 044710.
328. Ishii, A.; Yamamoto, M.; Asano, H.; Fujiwara, K. Dft Calculation for Adatom Adsorption on Graphene Sheet as a Prototype of Carbon Nanotube Functionalization. *J. Phys. Conf. Ser* **2008,** *100*, 052087.
329. Qin, W.; Li, X.; Bian, W. W.; Fan, X. J.; Qi, J. Y. Density Functional Theory Calculations and Molecular Dynamics Simulations of the Adsorption of Biomolecules on Graphene Surfaces. *Biomaterials* **2010,** *31*, 1007-1016.
330. Zhang, H.-p.; Luo, X.-g.; Lin, X.-y.; Lu, X.; Leng, Y.; Song, H.-t. Density Functional Theory Calculations on the Adsorption of Formaldehyde and Other Harmful Gases on Pure, Ti-Doped, or N-Doped Graphene Sheets. *Appl. Surf. Sci.* **2013,** *283*, 559-565.
331. Zhou, M.; Zhai, Y.; Dong, S. Electrochemical Sensing and Biosensing Platform Based on Chemically Reduced Graphene Oxide. *Anal. Chem.* **2009,** *81*, 5603-5613.
332. Lin, Y. M.; Avouris, P. Strong Suppression of Electrical Noise in Bilayer Graphene Nanodevices. *Nano Lett.* **2008,** *8*, 2119-2125.
333. Qinghui, S.; Guanxiong, L.; Teweldebrhan, D.; Balandin, A. A.; Rumyantsev, S.; Shur, M. S.; Dong, Y. Flicker Noise in Bilayer Graphene Transistors. *IEEE Electron Device Lett.* **2009,** *30*, 288-290.
334. Jang, H.; Park, Y. J.; Chen, X.; Das, T.; Kim, M. S.; Ahn, J. H. Graphene-Based Flexible and Stretchable Electronics. *Adv. Mater.* **2016,** *28*, 4184-4202.
335. Liu, J. Q.; Liu, Z.; Barrow, C. J.; Yang, W. R. Molecularly Engineered Graphene Surfaces for Sensing Applications: A Review. *Anal. Chim. Acta* **2015,** *859*, 1-19.
336. Zhang, Y. H.; Chen, Y. B.; Zhou, K. G.; Liu, C. H.; Zeng, J.; Zhang, H. L.; Peng, Y. Improving Gas Sensing Properties of Graphene by Introducing Dopants and Defects: A First-Principles Study. *Nanotechnology* **2009,** *20*, 185504.
337. Wei, X. L.; Chen, Y. P.; Liu, W. L.; Zhong, J. X. Enhanced Gas Sensor Based on Nitrogen-Vacancy Graphene Nanoribbons. *Phys. Lett. A* **2012,** *376*, 559-562.
338. Hussain, T.; Panigrahi, P.; Ahuja, R. Enriching Physisorption of H_2S and NH_3 Gases on a Graphane Sheet by Doping with Li Adatoms. *Phys. Chem. Chem. Phys.* **2014,** *16*, 8100-8105.
339. Niu, F.; Liu, J.-M.; Tao, L.-M.; Wang, W.; Song, W.-G. Nitrogen and Silica Co-Doped Graphene Nanosheets for NO_2 Gas Sensing. *J. Mater. Chem. A* **2013,** *1*, 6130.
340. Sundaram, R. S.; Gómez-Navarro, C.; Balasubramanian, K.; Burghard, M.; Kern, K. Electrochemical Modification of Graphene. *Adv. Mater.* **2008,** *20*, 3050-3053.
341. Chu, B. H.; Lo, C. F.; Nicolosi, J.; Chang, C. Y.; Chen, V.; Strupinski, W.; Pearton, S. J.; Ren, F. Hydrogen Detection Using Platinum Coated Graphene Grown on Sic. *Sensors Actuators B: Chem.* **2011,** *157*, 500-503.
342. Yi, J.; Lee, J. M.; Park, W. I. Vertically Aligned ZnO Nanorods and Graphene Hybrid Architectures for High-Sensitive Flexible Gas Sensors. *Sensors Actuators B: Chem.* **2011,** *155*, 264-269.
343. Song, Z.; Wei, Z.; Wang, B.; Luo, Z.; Xu, S.; Zhang, W.; Yu, H.; Li, M.; Huang, Z.; Zang, J.; Yi, F.; Liu, H. Sensitive Room-Temperature H_2S Gas Sensors Employing SnO_2 Quantum Wire/Reduced Graphene Oxide Nanocomposites. *Chem. Mater.* **2016,** *28*, 1205-1212.
344. Choi, S. J.; Choi, C.; Kim, S. J.; Cho, H. J.; Hakim, M.; Jeon, S.; Kim, I. D. Highly Efficient Electronic Sensitization of Non-Oxidized Graphene Flakes on Controlled Pore-Loaded WO_3 Nanofibers for Selective Detection of H_2S Molecules. *Sci. Rep.* **2015,** *5*, 8067.
345. Konkena, B.; Vasudevan, S. Covalently Linked, Water-Dispersible, Cyclodextrin: Reduced-Graphene Oxide Sheets. *Langmuir* **2012,** *28*, 12432-12437.
346. Konwer, S.; Guha, A. K.; Dolui, S. K. Graphene Oxide-Filled Conducting Polyaniline Composites as Methanol-Sensing Materials. *J. Mater. Sci.* **2012,** *48*, 1729-1739.
347. Wu, J.; Tao, K.; Miao, J.; Norford, L. K., Graphene for Future High-Performance Gas Sensing. In *Outlook and Challenges of Nano Devices, Sensors, and Mems*, 2017; pp 347-363.
348. Lei, W.; Si, W.; Xu, Y.; Gu, Z.; Hao, Q. Conducting Polymer Composites with Graphene for Use in Chemical Sensors and Biosensors. *Microchimica Acta* **2014,** *181*, 707-722.
349. Liu, Y.; Yu, D.; Zeng, C.; Miao, Z.; Dai, L. Biocompatible Graphene Oxide-Based Glucose Biosensors. *Langmuir* **2010,** *26*, 6158-6160.
350. Bridgman, P. W. Two New Modifications of Phosphorus. *J. Am. Chem. Soc.* **1914,** *36*, 1344-1363.
351. Li, L.; Yu, Y.; Ye, G. J.; Ge, Q.; Ou, X.; Wu, H.; Feng, D.; Chen, X. H.; Zhang, Y. Black Phosphorus Field-Effect Transistors. *Nat. Nanotechnol.* **2014,** *9*, 372-377.
352. Rodin, A. S.; Carvalho, A.; Castro Neto, A. H. Strain-Induced Gap Modification in Black Phosphorus. *Phys. Rev. Lett.* **2014,** *112*, 176801.
353. Gusmao, R.; Sofer, Z.; Pumera, M. Black Phosphorus Rediscovered: From Bulk Material to Monolayers. *Angew. Chem. Int. Ed.* **2017,** *56*, 8052-8072.
354. Cartz, L.; Srinivasa, S. R.; Riedner, R. J.; Jorgensen, J. D.; Worlton, T. G. Effect of Pressure on Bonding in Black Phosphorus. *J. Chem. Phys.* **1979,** *71*, 1718-1721.
355. Zhang, C. D.; Lian, J. C.; Yi, W.; Jiang, Y. H.; Liu, L. W.; Hu, H.; Xiao, W. D.; Du, S. X.; Sun, L. L.; Gao, H. J. Surface Structures of Black Phosphorus Investigated with Scanning Tunneling Microscopy. *J. Phys. Chem. C* **2009,** *113*, 18823-18826.
356. Tran, V.; Soklaski, R.; Liang, Y.; Yang, L. Layer-Controlled Band Gap and Anisotropic Excitons in Few-Layer Black Phosphorus. *Phys. Rev. B* **2014,** *89*, 235319.
357. Kim, J.; Baik, S. S.; Ryu, S. H.; Sohn, Y.; Park, S.; Park, B. G.; Denlinger, J.; Yi, Y.; Choi, H. J.; Kim, K. S. 2D Materials. Observation of Tunable Band Gap and Anisotropic Dirac Semimetal State in Black Phosphorus. *Science* **2015,** *349*, 723-726.
358. Tran, V.; Yang, L. Scaling Laws for the Band Gap and Optical Response of Phosphorene Nanoribbons. *Phys. Rev. B* **2014,** *89*, 548-555.
359. Peng, X.; Copple, A.; Wei, Q. Edge Effects on the Electronic Properties of Phosphorene Nanoribbons. *J. Appl. Phys.* **2014,** *116*, 2994-2998.
360. Kistanov, A. A.; Cai, Y.; Zhou, K.; Dmitriev, S. V.; Zhang, Y.-W. Large Electronic Anisotropy and Enhanced Chemical Activity of Highly Rippled Phosphorene. *J. Phys. Chem. C* **2016,** *120*, 6876-6884.
361. Kumar, V.; Brent, J. R.; Shorie, M.; Kaur, H.; Chadha, G.; Thomas, A. G.; Lewis, E. A.; Rooney, A. P.; Nguyen, L.; Zhong, X. L.; Burke, M. G.; Haigh, S. J.; Walton, A.; McNaughter, P. D.; Tedstone, A. A.; Savjani, N.; Muryn, C. A.; O'Brien, P.; Ganguli, A. K.; Lewis, D. J.; Sabherwal, P. Nanostructured Aptamer-Functionalized Black Phosphorus Sensing Platform for Label-Free Detection of Myoglobin, a Cardiovascular Disease Biomarker. *ACS Appl. Mater. Interfaces* **2016,** *8*, 22860-22868.
362. Mayorga-Martinez, C. C.; Mohamad Latiff, N.; Eng, A. Y.; Sofer, Z.; Pumera, M. Black Phosphorus Nanoparticle Labels for Immunoassays via Hydrogen Evolution Reaction Mediation. *Anal. Chem.* **2016**, 10074–10079.

363. Chen, Y.; Ren, R.; Pu, H.; Chang, J.; Mao, S.; Chen, J. Field-Effect Transistor Biosensors with Two-Dimensional Black Phosphorus Nanosheets. *Biosens. Bioelectron.* **2017,** *89*, 505-510.
364. Ben Aziza, Z.; Zhang, K.; Baillargeat, D.; Zhang, Q. Enhancement of Humidity Sensitivity of Graphene through Functionalization with Polyethylenimine. *Appl. Phys. Lett.* **2015,** *107*, 134102.
365. Kuriakose, S.; Ahmed, T.; Balendhran, S.; Bansal, V.; Sriram, S.; Bhaskaran, M.; Walia, S. Black Phosphorus: Ambient Degradation and Strategies for Protection. 2D *Mater.* **2018,** *5*, 032001.
366. Choi, J. R.; Yong, K. W.; Choi, J. Y.; Nilghaz, A.; Lin, Y.; Xu, J.; Lu, X. Black Phosphorus and Its Biomedical Applications. *Theranostics* **2018,** *8*, 1005-1026.
367. Abellan, G.; Wild, S.; Lloret, V.; Scheuschner, N.; Gillen, R.; Mundloch, U.; Maultzsch, J.; Varela, M.; Hauke, F.; Hirsch, A. Fundamental Insights into the Degradation and Stabilization of Thin Layer Black Phosphorus. *J. Am. Chem. Soc.* **2017,** *139*, 10432-10440.
368. Wang, Q. H.; Kalantar-Zadeh, K.; Kis, A.; Coleman, J. N.; Strano, M. S. Electronics and Optoelectronics of Two-Dimensional Transition Metal Dichalcogenides. *Nat. Nanotechnol.* **2012,** *7*, 699-712.
369. Joensen, P.; Frindt, R. F.; Morrison, S. R. Single-Layer MoS_2. *Mater. Res. Bull.* **1986,** *21*, 457-461.
370. Mak, K. F.; Lee, C.; Hone, J.; Shan, J.; Heinz, T. F. Atomically Thin MoS_2: A New Direct-Gap Semiconductor. *Phys. Rev. Lett.* **2010,** *105*, 136805.
371. Kolobov, A. V.; Tominaga, J., Bulk Tmdcs: Review of Structure and Properties. In *Two-Dimensional Transition-Metal Dichalcogenides*, Springer, Cham: 2016; pp 29-77.
372. Yoshida, M.; Ye, J.; Zhang, Y.; Imai, Y.; Kimura, S.; Fujiwara, A.; Nishizaki, T.; Kobayashi, N.; Nakano, M.; Iwasa, Y. Extended Polymorphism of Two-Dimensional Material. *Nano Lett.* **2017,** *17*, 5567-5571.
373. Voiry, D.; Mohite, A.; Chhowalla, M. Phase Engineering of Transition Metal Dichalcogenides. *Chem. Soc. Rev.* **2015,** *44*, 2702-2712.
374. Wilson, J. A.; Yoffe, A. D. The Transition Metal Dichalcogenides Discussion and Interpretation of the Observed Optical, Electrical and Structural Properties. *Adv. Phys.* **1969,** *18*, 193-335.
375. Li, H.; Lu, G.; Yin, Z.; He, Q.; Li, H.; Zhang, Q.; Zhang, H. Optical Identification of Single- and Few-Layer MoS_2 Sheets. *Small* **2012,** *8*, 682-686.
376. Castellanos-Gomez, A.; Barkelid, M.; Goossens, A. M.; Calado, V. E.; van der Zant, H. S.; Steele, G. A. Laser-Thinning of MoS_2: On Demand Generation of a Single-Layer Semiconductor. *Nano Lett.* **2012,** *12*, 3187-3192.
377. Eda, G.; Yamaguchi, H.; Voiry, D.; Fujita, T.; Chen, M.; Chhowalla, M. Photoluminescence from Chemically Exfoliated MoS_2. *Nano Lett.* **2011,** *11*, 5111-5116.
378. Eda, G.; Fujita, T.; Yamaguchi, H.; Voiry, D.; Chen, M.; Chhowalla, M. Coherent Atomic and Electronic Heterostructures of Single-Layer MoS_2. *ACS Nano* **2012,** *6*, 7311-7317.
379. Coleman, J. N.; Lotya, M.; O'Neill, A.; Bergin, S. D.; King, P. J.; Khan, U.; Young, K.; Gaucher, A.; De, S.; Smith, R. J.; Shvets, I. V.; Arora, S. K.; Stanton, G.; Kim, H. Y.; Lee, K.; Kim, G. T.; Duesberg, G. S.; Hallam, T.; Boland, J. J.; Wang, J. J.; Donegan, J. F.; Grunlan, J. C.; Moriarty, G.; Shmeliov, A.; Nicholls, R. J.; Perkins, J. M.; Grieveson, E. M.; Theuwissen, K.; McComb, D. W.; Nellist, P. D.; Nicolosi, V. Two-Dimensional Nanosheets Produced by Liquid Exfoliation of Layered Materials. *Science* **2011,** *331*, 568-571.
380. Cunningham, G.; Lotya, M.; Cucinotta, C. S.; Sanvito, S.; Bergin, S. D.; Menzel, R.; Shaffer, M. S.; Coleman, J. N. Solvent Exfoliation of Transition Metal Dichalcogenides: Dispersibility of Exfoliated Nanosheets Varies Only Weakly between Compounds. *ACS Nano* **2012,** *6*, 3468-3480.
381. Liu, K. K.; Zhang, W.; Lee, Y. H.; Lin, Y. C.; Chang, M. T.; Su, C. Y.; Chang, C. S.; Li, H.; Shi, Y.; Zhang, H.; Lai, C. S.; Li, L. J. Growth of Large-Area and Highly Crystalline MoS_2 Thin Layers on Insulating Substrates. *Nano Lett.* **2012,** *12*, 1538-1544.
382. Lee, H. S.; Min, S. W.; Chang, Y. G.; Park, M. K.; Nam, T.; Kim, H.; Kim, J. H.; Ryu, S.; Im, S. MoS_2 Nanosheet Phototransistors with Thickness-Modulated Optical Energy Gap. *Nano Lett.* **2012,** *12*, 3695-3700.
383. Lee, Y. H.; Zhang, X. Q.; Zhang, W.; Chang, M. T.; Lin, C. T.; Chang, K. D.; Yu, Y. C.; Wang, J. T.; Chang, C. S.; Li, L. J.; Lin, T. W. Synthesis of Large-Area MoS_2 Atomic Layers with Chemical Vapor Deposition. *Adv. Mater.* **2012,** *24*, 2320-2325.
384. Vancso, P.; Magda, G. Z.; Peto, J.; Noh, J. Y.; Kim, Y. S.; Hwang, C.; Biro, L. P.; Tapaszto, L. The Intrinsic Defect Structure of Exfoliated MoS_2 Single Layers Revealed by Scanning Tunneling Microscopy. *Sci. Rep.* **2016,** *6*, 29726.
385. Hong, J.; Hu, Z.; Probert, M.; Li, K.; Lv, D.; Yang, X.; Gu, L.; Mao, N.; Feng, Q.; Xie, L.; Zhang, J.; Wu, D.; Zhang, Z.; Jin, C.; Ji, W.; Zhang, X.; Yuan, J.; Zhang, Z. Exploring Atomic Defects in Molybdenum Disulphide Monolayers. *Nat. Commun.* **2015,** *6*, 6293.
386. Manzeli, S.; Ovchinnikov, D.; Pasquier, D.; Yazyev, O. V.; Kis, A. 2D Transition Metal Dichalcogenides. *Nat. Rev. Mater.* **2017,** *2*, 17033.
387. Hu, Z.; Wu, Z.; Han, C.; He, J.; Ni, Z.; Chen, W. Two-Dimensional Transition Metal Dichalcogenides: Interface and Defect Engineering. *Chem. Soc. Rev.* **2018,** *47*, 3100-3128.
388. Li, X.; Zhu, H. Two-Dimensional MoS_2: Properties, Preparation, and Applications. *Journal of Materiomics* **2015,** *1*, 33-44.
389. Lauritsen, J. V.; Kibsgaard, J.; Helveg, S.; Topsoe, H.; Clausen, B. S.; Laegsgaard, E.; Besenbacher, F. Size-Dependent Structure of MoS_2 Nanocrystals. *Nat. Nanotechnol.* **2007,** *2*, 53-58.
390. Tuxen, A.; Kibsgaard, J.; Gobel, H.; Laegsgaard, E.; Topsoe, H.; Lauritsen, J. V.; Besenbacher, F. Size Threshold in the Dibenzothiophene Adsorption on MoS_2 Nanoclusters. *ACS Nano* **2010,** *4*, 4677-4682.
391. Ou, J. Z.; Ge, W.; Carey, B.; Daeneke, T.; Rotbart, A.; Shan, W.; Wang, Y.; Fu, Z.; Chrimes, A. F.; Wlodarski, W.; Russo, S. P.; Li, Y. X.; Kalantar-Zadeh, K. Physisorption-Based Charge Transfer in Two-Dimensional SnS_2 for Selective and Reversible NO_2 Gas Sensing. *ACS Nano* **2015,** *9*, 10313-10323.
392. Li, Y.; Leonardi, S. G.; Bonavita, A.; Neri, G.; Wlodarski, W. Two-Dimensional (2D) Sns 2 -Based Oxygen Sensor. *Procedia Eng.* **2016,** *168*, 1102-1105.
393. Bharatula, L. D.; Erande, M. B.; Mulla, I. S.; Rout, C. S.; Late, D. J. Sns2 Nanoflakes for Efficient Humidity and Alcohol Sensing at Room Temperature. *RSC Adv.* **2016,** *6*, 105421-105427.
394. Hu, Y.; Huang, Y.; Tan, C.; Zhang, X.; Lu, Q.; Sindoro, M.; Huang, X.; Huang, W.; Wang, L.; Zhang, H. Two-Dimensional Transition Metal Dichalcogenide Nanomaterials for Biosensing Applications. *Mater. Chem. Front.* **2017,** *1*, 24-36.
395. Rao, C. N. R. Transition Metal Oxides. *Annu. Rev. Phys. Chem.* **1989,** *40*, 291-326.
396. Ray, C.; Pal, T. Recent Advances of Metal–Metal Oxide Nanocomposites and Their Tailored Nanostructures in Numerous Catalytic Applications. *J. Mater. Chem. A* **2017,** *5*, 9465-9487.
397. Kalantar-zadeh, K.; Tang, J.; Wang, M.; Wang, K. L.; Shailos, A.; Galatsis, K.; Kojima, R.; Strong, V.; Lech, A.;

Wlodarski, W.; Kaner, R. B. Synthesis of Nanometre-Thick MoO_3 Sheets. *Nanoscale* **2010,** *2*, 429-433.
398. Kalantar-zadeh, K.; Vijayaraghavan, A.; Ham, M.-H.; Zheng, H.; Breedon, M.; Strano, M. S. Synthesis of Atomically Thin WO_3 sheets from Hydrated Tungsten Trioxide. *Chem. Mater.* **2010,** *22*, 5660-5666.
399. Sun, Z.; Liao, T.; Dou, Y.; Hwang, S. M.; Park, M. S.; Jiang, L.; Kim, J. H.; Dou, S. X. Generalized Self-Assembly of Scalable Two-Dimensional Transition Metal Oxide Nanosheets. *Nat. Commun.* **2014,** *5*, 3813.
400. Xiao, X.; Song, H.; Lin, S.; Zhou, Y.; Zhan, X.; Hu, Z.; Zhang, Q.; Sun, J.; Yang, B.; Li, T.; Jiao, L.; Zhou, J.; Tang, J.; Gogotsi, Y. Scalable Salt-Templated Synthesis of Two-Dimensional Transition Metal Oxides. *Nat. Commun.* **2016,** *7*, 11296.
401. ten Elshof, J. E.; Yuan, H.; Gonzalez Rodriguez, P. Two-Dimensional Metal Oxide and Metal Hydroxide Nanosheets: Synthesis, Controlled Assembly and Applications in Energy Conversion and Storage. *Adv. Energy Mater.* **2016,** *6*, 1600355.
402. Biener, M. M.; Biener, J.; Schalek, R.; Friend, C. M. Growth of Nanocrystalline MoO_3 on Au(111) Studied by in Situ Scanning Tunneling Microscopy. *J. Chem. Phys.* **2004,** *121*, 12010-12016.
403. Mannhart, J.; Schlom, D. G. Oxide Interfaces--an Opportunity for Electronics. *Science* **2010,** *327*, 1607-1611.
404. Campbell, C. T.; Sauer, J. Introduction: Surface Chemistry of Oxides. *Chem. Rev.* **2013,** *113*, 3859-3862.
405. Pacchioni, G.; Freund, H. Electron Transfer at Oxide Surfaces. The MgO Paradigm: From Defects to Ultrathin Films. *Chem. Rev.* **2013,** *113*, 4035-4072.
406. Kuhlenbeck, H.; Shaikhutdinov, S.; Freund, H. J. Well-Ordered Transition Metal Oxide Layers in Model Catalysis--a Series of Case Studies. *Chem. Rev.* **2013,** *113*, 3986-4034.
407. Helander, M. G.; Wang, Z. B.; Qiu, J.; Lu, Z. H. Band Alignment at Metal/Organic and Metal/Oxide/Organic Interfaces. *Appl. Phys. Lett.* **2008,** *93*, 193310.
408. Hwang, H. Y.; Iwasa, Y.; Kawasaki, M.; Keimer, B.; Nagaosa, N.; Tokura, Y. Emergent Phenomena at Oxide Interfaces. *Nat. Mater.* **2012,** *11*, 103-113.
409. Bielaski, A. Adsorption Species of Oxygen on the Surfaces of Transition Metal Oxides. *J. Catal.* **1972,** *25*, 398-406.
410. Kanan, S. M.; El-Kadri, O. M.; Abu-Yousef, I. A.; Kanan, M. C. Semiconducting Metal Oxide Based Sensors for Selective Gas Pollutant Detection. *Sensors* **2009,** *9*, 8158-8196.
411. Tomchenko, A. A.; Harmer, G. P.; Marquis, B. T.; Allen, J. W. Semiconducting Metal Oxide Sensor Array for the Selective Detection of Combustion Gases. *Sensors Actuators B: Chem.* **2003,** *93*, 126-134.
412. Wang, C.; Yin, L.; Zhang, L.; Xiang, D.; Gao, R. Metal Oxide Gas Sensors: Sensitivity and Influencing Factors. *Sensors* **2010,** *10*, 2088-2106.
413. Gardon, M.; Guilemany, J. M. A Review on Fabrication, Sensing Mechanisms and Performance of Metal Oxide Gas Sensors. *J. Mater. Sci. Mater. Electron.* **2012,** *24*, 1410-1421.
414. Yaghi, O. M.; Li, H. L. Hydrothermal Synthesis of a Metal-Organic Framework Containing Large Rectangular Channels. *J. Am. Chem. Soc.* **1995,** *117*, 10401-10402.
415. Batten, S. R.; Champness, N. R.; Chen, X.-M.; Garcia-Martinez, J.; Kitagawa, S.; Öhrström, L.; O'Keeffe, M.; Paik Suh, M.; Reedijk, J. Terminology of Metal–Organic Frameworks and Coordination Polymers (Iupac Recommendations 2013). *Pure Appl. Chem.* **2013,** *85*, 1715-1724.
416. Stassen, I.; Burtch, N.; Talin, A.; Falcaro, P.; Allendorf, M.; Ameloot, R. An Updated Roadmap for the Integration of Metal-Organic Frameworks with Electronic Devices and Chemical Sensors. *Chem. Soc. Rev.* **2017,** *46*, 3185-3241.
417. Morozan, A.; Jaouen, F. Metal Organic Frameworks for Electrochemical Applications. *Energy Environ. Sci* **2012,** *5*, 9269.
418. Campbell, M. G.; Sheberla, D.; Liu, S. F.; Swager, T. M.; Dinca, M. Cu_3(Hexaiminotriphenylene)$_2$: An Electrically Conductive 2D Metal-Organic Framework for Chemiresistive Sensing. *Angew. Chem. Int. Ed.* **2015,** *54*, 4349-4352.
419. Hendon, C. H.; Rieth, A. J.; Korzynski, M. D.; Dinca, M. Grand Challenges and Future Opportunities for Metal-Organic Frameworks. *ACS Cent Sci* **2017,** *3*, 554-563.
420. Arvand, M.; Abbasnejad, S.; Ghodsi, N. Graphene Quantum Dots Decorated with Fe_3O_4 Nanoparticles/Functionalized Multiwalled Carbon Nanotubes as a New Sensing Platform for Electrochemical Determination of L-Dopa in Agricultural Products. *Anal. Methods* **2016,** *8*, 5861-5868.
421. Campbell, M. G.; Dinca, M. Metal-Organic Frameworks as Active Materials in Electronic Sensor Devices. *Sensors* **2017,** *17*, 1108.
422. Hmadeh, M.; Lu, Z.; Liu, Z.; Gandara, F.; Furukawa, H.; Wan, S.; Augustyn, V.; Chang, R.; Liao, L.; Zhou, F.; Perre, E.; Ozolins, V.; Suenaga, K.; Duan, X. F.; Dunn, B.; Yamamto, Y.; Terasaki, O.; Yaghi, O. M. New Porous Crystals of Extended Metal-Catecholates. *Chem. Mater.* **2012,** *24*, 3511-3513.
423. Hu, Z.; Zhao, D. Metal–Organic Frameworks with Lewis Acidity: Synthesis, Characterization, and Catalytic Applications. *CrystEngComm* **2017,** *19*, 4066-4081.
424. Liu, H.; Li, X.; Chen, L.; Wang, X.; Pan, H.; Zhang, X.; Zhao, M. Gas Adsorption Effects on the Electronic Properties of Two-Dimensional Nickel Bis(dithiolene) Complex. *J. Phys. Chem. C* **2016,** *120*, 3846-3852.
425. Miner, E. M.; Gul, S.; Ricke, N. D.; Pastor, E.; Yano, J.; Yachandra, V. K.; Van Voorhis, T.; Dincă, M. Mechanistic Evidence for Ligand-Centered Electrocatalytic Oxygen Reduction with the Conductive MOF Ni_3(Hexaiminotriphenylene)$_2$. *ACS Catal.* **2017,** *7*, 7726-7731.
426. Miner, E. M.; Fukushima, T.; Sheberla, D.; Sun, L.; Surendranath, Y.; Dinca, M. Electrochemical Oxygen Reduction Catalysed by Ni_3(Hexaiminotriphenylene)$_2$. *Nat. Commun.* **2016,** *7*, 10942.
427. Furukawa, H.; Cordova, K. E.; O'Keeffe, M.; Yaghi, O. M. The Chemistry and Applications of Metal-Organic Frameworks. *Science* **2013,** *341*, 1230444.
428. James, S. L. Metal-Organic Frameworks. *Chem. Soc. Rev.* **2003,** *32*, 276.
429. Sheberla, D.; Sun, L.; Blood-Forsythe, M. A.; Er, S.; Wade, C. R.; Brozek, C. K.; Aspuru-Guzik, A.; Dinca, M. High Electrical Conductivity in Ni_3(2,3,6,7,10,11-Hexaiminotriphenylene)$_2$, a Semiconducting Metal-Organic Graphene Analogue. *J. Am. Chem. Soc.* **2014,** *136*, 8859-8862.
430. Zhao, J.; Liu, H.; Yu, Z.; Quhe, R.; Zhou, S.; Wang, Y.; Liu, C. C.; Zhong, H.; Han, N.; Lu, J.; Yao, Y.; Wu, K. Rise of Silicene: A Competitive 2D Material. *Prog. Mater Sci.* **2016,** *83*, 24-151.
431. Molle, A.; Goldberger, J.; Houssa, M.; Xu, Y.; Zhang, S. C.; Akinwande, D. Buckled Two-Dimensional Xene Sheets. *Nat. Mater.* **2017,** *16*, 163-169.
432. Molle, A. Xenes: A New Emerging Two-Dimensional Materials Platform for Nanoelectronics. *Semiconductors, Dielectrics, and Metals for Nanoelectronics 14* **2016,** *75*, 163-173.
433. Chen, X. P.; Tan, C. J.; Yang, Q.; Meng, R. S.; Liang, Q. H.; Cai, M.; Zhang, S. L.; Jiang, J. K. Ab Initio Study of the Adsorption of Small Molecules on Stanene. *J. Phys. Chem. C* **2016,** *120*, 13987-13994.
434. Wang, T. X.; Zhao, R. M.; Zhao, M. Y.; Zhao, X.; An, Y. P.; Dai, X. Q.; Xia, C. X. Effects of Applied Strain and Electric Field

on Small-Molecule Sensing by Stanene Monolayers. *J. Mater. Sci.* **2017,** *52*, 5083-5096.
435. Daniel, M. C.; Astruc, D. Gold Nanoparticles: Assembly, Supramolecular Chemistry, Quantum-Size-Related Properties, and Applications toward Biology, Catalysis, and Nanotechnology. *Chem. Rev.* **2004,** *104*, 293-346.
436. Fan, Z.; Huang, X.; Tan, C.; Zhang, H. Thin Metal Nanostructures: Synthesis, Properties and Applications. *Chem. Sci.* **2015,** *6*, 95-111.
437. Niu, J.; Wang, D.; Qin, H.; Xiong, X.; Tan, P.; Li, Y.; Liu, R.; Lu, X.; Wu, J.; Zhang, T.; Ni, W.; Jin, J. Novel Polymer-Free Iridescent Lamellar Hydrogel for Two-Dimensional Confined Growth of Ultrathin Gold Membranes. *Nat. Commun.* **2014,** *5*, 3313.
438. Huang, X.; Tang, S.; Mu, X.; Dai, Y.; Chen, G.; Zhou, Z.; Ruan, F.; Yang, Z.; Zheng, N. Freestanding Palladium Nanosheets with Plasmonic and Catalytic Properties. *Nat. Nanotechnol.* **2011,** *6*, 28-32.
439. Duan, H.; Yan, N.; Yu, R.; Chang, C. R.; Zhou, G.; Hu, H. S.; Rong, H.; Niu, Z.; Mao, J.; Asakura, H.; Tanaka, T.; Dyson, P. J.; Li, J.; Li, Y. Ultrathin Rhodium Nanosheets. *Nat. Commun.* **2014,** *5*, 3093.
440. Wang, L.; Zhu, Y.; Wang, J. Q.; Liu, F.; Huang, J.; Meng, X.; Basset, J. M.; Han, Y.; Xiao, F. S. Two-Dimensional Gold Nanostructures with High Activity for Selective Oxidation of Carbon-Hydrogen Bonds. *Nat. Commun.* **2015,** *6*, 6957.
441. Puntes, V. F.; Krishnan, K. M.; Alivisatos, A. P. Colloidal Nanocrystal Shape and Size Control: The Case of Cobalt. *Science* **2001,** *291*, 2115-2117.
442. Favier, F.; Walter, E. C.; Zach, M. P.; Benter, T.; Penner, R. M. Hydrogen Sensors and Switches from Electrodeposited Palladium Mesowire Arrays. *Science* **2001,** *293*, 2227-2231.
443. Hakkinen, H. The Gold-Sulfur Interface at the Nanoscale. *Nat. Chem.* **2012,** *4*, 443-455.
444. Campbell, C. T. Ultrathin Metal Films and Particles on Oxide Surfaces: Structural, Electronic and Chemisorptive Properties. *Surf. Sci. Rep.* **1997,** *27*, 1-111.
445. Paggel, J. J. Quantum-Well States as Fabry-PÉRot Modes in a Thin-Film Electron Interferometer. *Science* **1999,** *283*, 1709-1711.
446. Qin, S.; Kim, J.; Niu, Q.; Shih, C. K. Superconductivity at the Two-Dimensional Limit. *Science* **2009,** *324*, 1314-1317.
447. Zhang, K.; Feng, Y.; Wang, F.; Yang, Z.; Wang, J. Two Dimensional Hexagonal Boron Nitride (2D-*h*BN): Synthesis, Properties and Applications. *J. Mater. Chem. C* **2017,** *5*, 11992-12022.
448. Li, L. H.; Chen, Y. Atomically Thin Boron Nitride: Unique Properties and Applications. *Advanced Functional Materials* **2016,** *26*, 2594-2608.
449. Weng, Q.; Wang, X.; Wang, X.; Bando, Y.; Golberg, D. Functionalized Hexagonal Boron Nitride Nanomaterials: Emerging Properties and Applications. *Chem. Soc. Rev.* **2016,** *45*, 3989-4012.
450. Vogt, P.; De Padova, P.; Quaresima, C.; Avila, J.; Frantzeskakis, E.; Asensio, M. C.; Resta, A.; Ealet, B.; Le Lay, G. Silicene: Compelling Experimental Evidence for Graphenelike Two-Dimensional Silicon. *Phys. Rev. Lett.* **2012,** *108*, 155501.
451. Wang, J.; Ma, F.; Sun, M. Graphene, Hexagonal Boron Nitride, and Their Heterostructures: Properties and Applications. *RSC Adv.* **2017,** *7*, 16801-16822.
452. Ryu, G. H.; Park, H. J.; Ryou, J.; Park, J.; Lee, J.; Kim, G.; Shin, H. S.; Bielawski, C. W.; Ruoff, R. S.; Hong, S.; Lee, Z. Atomic-Scale Dynamics of Triangular Hole Growth in Monolayer Hexagonal Boron Nitride under Electron Irradiation. *Nanoscale* **2015,** *7*, 10600-10605.
453. Thomas, A.; Fischer, A.; Goettmann, F.; Antonietti, M.; Müller, J.-O.; Schlögl, R.; Carlsson, J. M. Graphitic Carbon Nitride Materials: Variation of Structure and Morphology and Their Use as Metal-Free Catalysts. *J. Mater. Chem.* **2008,** *18*.
454. Algara-Siller, G.; Severin, N.; Chong, S. Y.; Bjorkman, T.; Palgrave, R. G.; Laybourn, A.; Antonietti, M.; Khimyak, Y. Z.; Krasheninnikov, A. V.; Rabe, J. P.; Kaiser, U.; Cooper, A. I.; Thomas, A.; Bojdys, M. J. Triazine-Based Graphitic Carbon Nitride: A Two-Dimensional Semiconductor. *Angew. Chem. Int. Ed.* **2014,** *53*, 7450-7455.
455. Anasori, B.; Xie, Y.; Beidaghi, M.; Lu, J.; Hosler, B. C.; Hultman, L.; Kent, P. R.; Gogotsi, Y.; Barsoum, M. W. Two-Dimensional, Ordered, Double Transition Metals Carbides (MXenes). *ACS Nano* **2015,** *9*, 9507-9516.
456. Wang, C.; Yang, S.; Cai, H.; Ataca, C.; Chen, H.; Zhang, X.; Xu, J.; Chen, B.; Wu, K.; Zhang, H.; Liu, L.; Li, J.; Grossman, J. C.; Tongay, S.; Liu, Q. Enhancing Light Emission Efficiency without Color Change in Post-Transition Metal Chalcogenides. *Nanoscale* **2016,** *8*, 5820-5825.
457. Miller, T. S.; Jorge, A. B.; Suter, T. M.; Sella, A.; Cora, F.; McMillan, P. F. Carbon Nitrides: Synthesis and Characterization of a New Class of Functional Materials. *Phys. Chem. Chem. Phys.* **2017,** *19*, 15613-15638.
458. Kroke, E. Novel Group 14 Nitrides. *Coord. Chem. Rev.* **2004,** *248*, 493-532.
459. Zhu, J.; Xiao, P.; Li, H.; Carabineiro, S. A. Graphitic Carbon Nitride: Synthesis, Properties, and Applications in Catalysis. *ACS Appl. Mater. Interfaces* **2014,** *6*, 16449-16465.
460. Barsoum, M. W., *Max Phases: Properties of Machinable Ternary Carbides and Nitrides*. Wiley: 2013.
461. Tang, Q.; Zhou, Z.; Shen, P. Are MXenes Promising Anode Materials for Li Ion Batteries? Computational Studies on Electronic Properties and Li Storage Capability of Ti_3C_2 and $Ti_3C_2X_2$ (X = F, OH) Monolayer. *J. Am. Chem. Soc.* **2012,** *134*, 16909-16916.
462. Xie, Y.; Kent, P. R. C. Hybrid Density Functional Study of Structural and Electronic Properties of Functionalized $Ti_{n+1}X_n$(X=C, N) Monolayers. *Phys. Rev. B* **2013,** *87*, 235441.
463. Yu, X. F.; Li, Y. C.; Cheng, J. B.; Liu, Z. B.; Li, Q. Z.; Li, W. Z.; Yang, X.; Xiao, B. Monolayer Ti_2Co_2: A Promising Candidate for NH_3 Sensor or Capturer with High Sensitivity and Selectivity. *ACS Appl. Mater. Interfaces* **2015,** *7*, 13707-13713.
464. Junkaew, A.; Arroyave, R. Enhancement of the Selectivity of MXenes (M_2C, M = Ti, V, Nb, Mo) via Oxygen-Functionalization: Promising Materials for Gas-Sensing and -Separation. *Phys. Chem. Chem. Phys.* **2018,** *20*, 6073-6082.
465. Afzaal, M.; O'Brien, P. Recent Developments in II–VI and III–VI Semiconductors and Their Applications in Solar Cells. *J. Mater. Chem.* **2006,** *16*, 1597-1602.
466. Gouskov, A.; Camassel, J.; Gouskov, L. Growth and Characterization of III–VI Layered Crystals Like Gase, Gate, Inse, Gase1-Xtex and Gaxin1-Xse. *Prog. Cryst. Growth Charact. Mater.* **1982,** *5*, 323-413.
467. Chen, Z.; Biscaras, J.; Shukla, A. A High Performance Graphene/Few-Layer Inse Photo-Detector. *Nanoscale* **2015,** *7*, 5981-5986.
468. Ma, D.; Li, T.; Yuan, D.; He, C.; Lu, Z.; Lu, Z.; Yang, Z.; Wang, Y. The Role of the Intrinsic Se and in Vacancies in the Interaction of O_2 and H_2O Molecules with the Inse Monolayer. *Appl. Surf. Sci.* **2018,** *434*, 215-227.
469. Politano, A.; Chiarello, G.; Samnakay, R.; Liu, G.; Gurbulak, B.; Duman, S.; Balandin, A. A.; Boukhvalov, D. W. The Influence of Chemical Reactivity of Surface Defects on Ambient-Stable Inse-Based Nanodevices. *Nanoscale* **2016,** *8*, 8474-8479.
470. Balakrishnan, N.; Kudrynskyi, Z. R.; Smith, E. F.; Fay, M. W.; Makarovsky, O.; Kovalyuk, Z. D.; Eaves, L.; Beton, P. H.; Patanè, A. Engineering P–N Junctions and Bandgap Tuning of Inse Nanolayers by Controlled Oxidation. *2D Mater.* **2017,** *4*, 025043.

471. Cai, Y.; Zhang, G.; Zhang, Y.-W. Charge Transfer and Functionalization of Monolayer Inse by Physisorption of Small Molecules for Gas Sensing. *J. Phys. Chem. C* **2017,** *121*, 10182-10193.
472. Bandurin, D. A.; Tyurnina, A. V.; Yu, G. L.; Mishchenko, A.; Zolyomi, V.; Morozov, S. V.; Kumar, R. K.; Gorbachev, R. V.; Kudrynskyi, Z. R.; Pezzini, S.; Kovalyuk, Z. D.; Zeitler, U.; Novoselov, K. S.; Patane, A.; Eaves, L.; Grigorieva, I. V.; Fal'ko, V. I.; Geim, A. K.; Cao, Y. High Electron Mobility, Quantum Hall Effect and Anomalous Optical Response in Atomically Thin Inse. *Nat. Nanotechnol.* **2017,** *12*, 223-227.
473. Lin, Z.; McCreary, A.; Briggs, N.; Subramanian, S.; Zhang, K.; Sun, Y.; Li, X.; Borys, N. J.; Yuan, H.; Fullerton-Shirey, S. K.; Chernikov, A.; Zhao, H.; McDonnell, S.; Lindenberg, A. M.; Xiao, K.; LeRoy, B. J.; Drndić, M.; Hwang, J. C. M.; Park, J.; Chhowalla, M.; Schaak, R. E.; Javey, A.; Hersam, M. C.; Robinson, J.; Terrones, M. 2D Materials Advances: From Large Scale Synthesis and Controlled Heterostructures to Improved Characterization Techniques, Defects and Applications. *2D Mater.* **2016,** *3*, 042001.
474. Fiori, G.; Bonaccorso, F.; Iannaccone, G.; Palacios, T.; Neumaier, D.; Seabaugh, A.; Banerjee, S. K.; Colombo, L. Electronics Based on Two-Dimensional Materials. *Nat. Nanotechnol.* **2014,** *9*, 768-779.
475. Varghese, S. S.; Lonkar, S.; Singh, K. K.; Swaminathan, S.; Abdala, A. Recent Advances in Graphene Based Gas Sensors. *Sensors Actuators B: Chem.* **2015,** *218*, 160-183.
476. Dos Santos-Alves, J. S. G.; Patier, R. F. The Environmental Control of Atmospheric Pollution. The Framework Directive and Its Development. The New European Approach. *Sensors Actuators B: Chem.* **1999,** *59*, 69-74.
477. Xu, K.; Fu, C.; Gao, Z.; Wei, F.; Ying, Y.; Xu, C.; Fu, G. Nanomaterial-Based Gas Sensors: A Review. *Instrum Sci. Technol.* **2017,** *46*, 115-145.
478. Sutariya, B. B.; Penney, D. G.; Nallamothu, B. G. Hypothermia Following Acute Carbon-Monoxide Poisoning Increases Mortality. *Toxicol. Lett.* **1990,** *52*, 201-208.
479. Atkinson, R. Atmospheric Chemistry of VOCs and Nox. *Atmos. Environ.* **2000,** *34*, 2063-2101.
480. Savel'ev, A. M.; Starik, A. M.; Titova, N. S. Formation Kinetics of Sulfur-Bearing Compounds in Combustion of Hydrocarbon Fuels in Air. *Combustion, Explosion, and Shock Waves* **2002,** *38*, 609-621.
481. Timmer, B.; Olthuis, W.; Berg, A. v. d. Ammonia Sensors and Their Applications—a Review. *Sensors Actuators B: Chem.* **2005,** *107*, 666-677.
482. Mustafa, A. K.; Gadalla, M. M.; Snyder, S. H. Signaling by Gasotransmitters. *Sci Signal.* **2009,** *2*, re2.
483. Takahashi, N.; Kozai, D.; Mori, Y. Trp Channels: Sensors and Transducers of Gasotransmitter Signals. *Front. Physiol.* **2012,** *3*, 324.
484. Zhou, X.; Lee, S.; Xu, Z.; Yoon, J. Recent Progress on the Development of Chemosensors for Gases. *Chem. Rev.* **2015,** *115*, 7944-8000.
485. Tricoli, A.; Righettoni, M.; Teleki, A. Semiconductor Gas Sensors: Dry Synthesis and Application. *Angew. Chem. Int. Ed.* **2010,** *49*, 7632-7659.
486. Wehling, T. O.; Novoselov, K. S.; Morozov, S. V.; Vdovin, E. E.; Katsnelson, M. I.; Geim, A. K.; Lichtenstein, A. I. Molecular Doping of Graphene. *Nano Lett.* **2008,** *8*, 173-177.
487. Leenaerts, O.; Partoens, B.; Peeters, F. M. Adsorption of Small Molecules on Graphene. *Microelectron. J.* **2009,** *40*, 860-862.
488. Bunch, J. S.; van der Zande, A. M.; Verbridge, S. S.; Frank, I. W.; Tanenbaum, D. M.; Parpia, J. M.; Craighead, H. G.; McEuen, P. L. Electromechanical Resonators from Graphene Sheets. *Science* **2007,** *315*, 490-493.
489. Kong, J.; Franklin, N. R.; Zhou, C. W.; Chapline, M. G.; Peng, S.; Cho, K. J.; Dai, H. J. Nanotube Molecular Wires as Chemical Sensors. *Science* **2000,** *287*, 622-625.
490. Chen, G.; Paronyan, T. M.; Harutyunyan, A. R. Sub-ppt Gas Detection with Pristine Graphene. *Appl. Phys. Lett.* **2012,** *101*, 053119.
491. Lin, J.; Zhong, J.; Kyle, J. R.; Penchev, M.; Ozkan, M.; Ozkan, C. S. Molecular Absorption and Photodesorption in Pristine and Functionalized Large-Area Graphene Layers. *Nanotechnology* **2011,** *22*, 355701.
492. Singh, A.; Uddin, A.; Sudarshan, T.; Koley, G. Tunable Reverse-Biased Graphene/Silicon Heterojunction Schottky Diode Sensor. *Small* **2014,** *10*, 1555-1565.
493. Dan, Y.; Lu, Y.; Kybert, N. J.; Luo, Z.; Johnson, A. T. Intrinsic Response of Graphene Vapor Sensors. *Nano Lett.* **2009,** *9*, 1472-1475.
494. Li, D.; Muller, M. B.; Gilje, S.; Kaner, R. B.; Wallace, G. G. Processable Aqueous Dispersions of Graphene Nanosheets. *Nat. Nanotechnol.* **2008,** *3*, 101-105.
495. Gilje, S.; Han, S.; Wang, M.; Wang, K. L.; Kaner, R. B. A Chemical Route to Graphene for Device Applications. *Nano Lett.* **2007,** *7*, 3394-3398.
496. Stankovich, S.; Dikin, D. A.; Piner, R. D.; Kohlhaas, K. A.; Kleinhammes, A.; Jia, Y.; Wu, Y.; Nguyen, S. T.; Ruoff, R. S. Synthesis of Graphene-Based Nanosheets via Chemical Reduction of Exfoliated Graphite Oxide. *Carbon* **2007,** *45*, 1558-1565.
497. Tung, V. C.; Allen, M. J.; Yang, Y.; Kaner, R. B. High-Throughput Solution Processing of Large-Scale Graphene. *Nat. Nanotechnol.* **2009,** *4*, 25-29.
498. Fowler, J. D.; Allen, M. J.; Tung, V. C.; Yang, Y.; Kaner, R. B.; Weiller, B. H. Practical Chemical Sensors from Chemically Derived Graphene. *ACS Nano* **2009,** *3*, 301-306.
499. Lu, G.; Ocola, L. E.; Chen, J. Gas Detection Using Low-Temperature Reduced Graphene Oxide Sheets. *Appl. Phys. Lett.* **2009,** *94*, 083111.
500. Lu, G.; Ocola, L. E.; Chen, J. Reduced Graphene Oxide for Room-Temperature Gas Sensors. *Nanotechnology* **2009,** *20*, 445502.
501. Ghosh, R.; Midya, A.; Santra, S.; Ray, S. K.; Guha, P. K. Chemically Reduced Graphene Oxide for Ammonia Detection at Room Temperature. *ACS Appl. Mater. Interfaces* **2013,** *5*, 7599-7603.
502. Dua, V.; Surwade, S. P.; Ammu, S.; Agnihotra, S. R.; Jain, S.; Roberts, K. E.; Park, S.; Ruoff, R. S.; Manohar, S. K. All-Organic Vapor Sensor Using Inkjet-Printed Reduced Graphene Oxide. *Angew. Chem. Int. Ed.* **2010,** *49*, 2154-2157.
503. Wang, D. H.; Hu, Y.; Zhao, J. J.; Zeng, L. L.; Tao, X. M.; Chen, W. Holey Reduced Graphene Oxide Nanosheets for High Performance Room Temperature Gas Sensing. *J. Mater. Chem. A* **2014,** *2*, 17415-17420.
504. Zhang, Y.; Guo, L.; Wei, S.; He, Y.; Xia, H.; Chen, Q.; Sun, H.-B.; Xiao, F.-S. Direct Imprinting of Microcircuits on Graphene Oxides Film by Femtosecond Laser Reduction. *Nano Today* **2010,** *5*, 15-20.
505. Lin, J.; Peng, Z.; Liu, Y.; Ruiz-Zepeda, F.; Ye, R.; Samuel, E. L.; Yacaman, M. J.; Yakobson, B. I.; Tour, J. M. Laser-Induced Porous Graphene Films from Commercial Polymers. *Nat. Commun.* **2014,** *5*, 5714.
506. Strong, V.; Dubin, S.; El-Kady, M. F.; Lech, A.; Wang, Y.; Weiller, B. H.; Kaner, R. B. Patterning and Electronic Tuning of Laser Scribed Graphene for Flexible All-Carbon Devices. *ACS Nano* **2012,** *6*, 1395-1403.
507. Yuan, W.; Liu, A.; Huang, L.; Li, C.; Shi, G. High-Performance NO_2 Sensors Based on Chemically Modified Graphene. *Adv. Mater.* **2013,** *25*, 766-771.

508. Yin, P. T.; Shah, S.; Chhowalla, M.; Lee, K. B. Design, Synthesis, and Characterization of Graphene-Nanoparticle Hybrid Materials for Bioapplications. *Chem. Rev.* **2015,** *115*, 2483-2531.
509. Li, W.; Geng, X.; Guo, Y.; Rong, J.; Gong, Y.; Wu, L.; Zhang, X.; Li, P.; Xu, J.; Cheng, G.; Sun, M.; Liu, L. Reduced Graphene Oxide Electrically Contacted Graphene Sensor for Highly Sensitive Nitric Oxide Detection. *ACS Nano* **2011,** *5*, 6955-6961.
510. Chen, Z.; Umar, A.; Wang, S.; Wang, Y.; Tian, T.; Shang, Y.; Fan, Y.; Qi, Q.; Xu, D.; Jiang, L. Supramolecular Fabrication of Multilevel Graphene-Based Gas Sensors with High NO_2 Sensibility. *Nanoscale* **2015,** *7*, 10259-10266.
511. Deng, S.; Tjoa, V.; Fan, H. M.; Tan, H. R.; Sayle, D. C.; Olivo, M.; Mhaisalkar, S.; Wei, J.; Sow, C. H. Reduced Graphene Oxide Conjugated Cu2o Nanowire Mesocrystals for High-Performance NO_2 Gas Sensor. *J. Am. Chem. Soc.* **2012,** *134*, 4905-4917.
512. Yang, W.; Wan, P.; Zhou, X.; Hu, J.; Guan, Y.; Feng, L. Additive-Free Synthesis of In_2O_3 Cubes Embedded into Graphene Sheets and Their Enhanced NO_2 Sensing Performance at Room Temperature. *ACS Appl. Mater. Interfaces* **2014,** *6*, 21093-21100.
513. An, X.; Yu, J. C.; Wang, Y.; Hu, Y.; Yu, X.; Zhang, G. WO_3 Nanorods/Graphene Nanocomposites for High-Efficiency Visible-Light-Driven Photocatalysis and NO_2 Gas Sensing. *J. Mater. Chem.* **2012,** *22*, 8525.
514. Yang, S.; Song, X.; Zhang, P.; Sun, J.; Gao, L. Self-Assembled α-Fe_2O_3 Mesocrystals/Graphene Nanohybrid for Enhanced Electrochemical Capacitors. *Small* **2014,** *10*, 2270-2279.
515. Kang, I.-S.; So, H.-M.; Bang, G.-S.; Kwak, J.-H.; Lee, J.-O.; Won Ahn, C. Recovery Improvement of Graphene-Based Gas Sensors Functionalized with Nanoscale Heterojunctions. *Appl. Phys. Lett.* **2012,** *101*, 123504.
516. Lin, Q.; Li, Y.; Yang, M. Tin Oxide/Graphene Composite Fabricated via a Hydrothermal Method for Gas Sensors Working at Room Temperature. *Sensors Actuators B: Chem.* **2012,** *173*, 139-147.
517. Lu, G.; Ocola, L. E.; Chen, J. Room-Temperature Gas Sensing Based on Electron Transfer between Discrete Tin Oxide Nanocrystals and Multiwalled Carbon Nanotubes. *Adv. Mater.* **2009,** *21*, 2487-2491.
518. Mao, S.; Cui, S.; Yu, K.; Wen, Z.; Lu, G.; Chen, J. Ultrafast Hydrogen Sensing through Hybrids of Semiconducting Single-Walled Carbon Nanotubes and Tin Oxide Nanocrystals. *Nanoscale* **2012,** *4*, 1275-1279.
519. Liu, S.; Yu, B.; Zhang, H.; Fei, T.; Zhang, T. Enhancing NO_2 Gas Sensing Performances at Room Temperature Based on Reduced Graphene Oxide-ZnO Nanoparticles Hybrids. *Sensors Actuators B: Chem.* **2014,** *202*, 272-278.
520. Huang, X.; Hu, N.; Gao, R.; Yu, Y.; Wang, Y.; Yang, Z.; Siu-Wai Kong, E.; Wei, H.; Zhang, Y. Reduced Graphene Oxide–Polyaniline Hybrid: Preparation, Characterization and Its Applications for Ammonia Gas Sensing. *J. Mater. Chem.* **2012,** *22*, 22488.
521. Seekaew, Y.; Lokavee, S.; Phokharatkul, D.; Wisitsoraat, A.; Kerdcharoen, T.; Wongchoosuk, C. Low-Cost and Flexible Printed Graphene–PEDOT:PSS Gas Sensor for Ammonia Detection. *Org. Electron.* **2014,** *15*, 2971-2981.
522. Yang, Y.; Li, S.; Yang, W.; Yuan, W.; Xu, J.; Jiang, Y. In Situ Polymerization Deposition of Porous Conducting Polymer on Reduced Graphene Oxide for Gas Sensor. *ACS Appl. Mater. Interfaces* **2014,** *6*, 13807-13814.
523. Wu, Z.; Chen, X.; Zhu, S.; Zhou, Z.; Yao, Y.; Quan, W.; Liu, B. Enhanced Sensitivity of Ammonia Sensor Using Graphene/Polyaniline Nanocomposite. *Sensors Actuators B: Chem.* **2013,** *178*, 485-493.
524. Bai, H.; Sheng, K.; Zhang, P.; Li, C.; Shi, G. Graphene Oxide/Conducting Polymer Composite Hydrogels. *J. Mater. Chem.* **2011,** *21*, 18653.
525. Yuan, W.; Huang, L.; Zhou, Q.; Shi, G. Ultrasensitive and Selective Nitrogen Dioxide Sensor Based on Self-Assembled Graphene/Polymer Composite Nanofibers. *ACS Appl. Mater. Interfaces* **2014,** *6*, 17003-17008.
526. Huang, J.; Virji, S.; Weiller, B. H.; Kaner, R. B. Polyaniline Nanofibers: Facile Synthesis and Chemical Sensors. *J. Am. Chem. Soc.* **2003,** *125*, 314-315.
527. Zhang, T.; Nix, M. B.; Yoo, B.-Y.; Deshusses, M. A.; Myung, N. V. Electrochemically Functionalized Single-Walled Carbon Nanotube Gas Sensor. *Electroanalysis* **2006,** *18*, 1153-1158.
528. Ding, M.; Tang, Y.; Gou, P.; Reber, M. J.; Star, A. Chemical Sensing with Polyaniline Coated Single-Walled Carbon Nanotubes. *Adv. Mater.* **2011,** *23*, 536-540.
529. Hübert, T.; Boon-Brett, L.; Black, G.; Banach, U. Hydrogen Sensors – a Review. *Sensors Actuators B: Chem.* **2011,** *157*, 329-352.
530. Ma, J.; Michaelides, A.; Alfe, D. Binding of Hydrogen on Benzene, Coronene, and Graphene from Quantum Monte Carlo Calculations. *J. Chem. Phys.* **2011,** *134*, 134701.
531. Johnson, J. L.; Behnam, A.; Pearton, S. J.; Ural, A. Hydrogen Sensing Using Pd-Functionalized Multi-Layer Graphene Nanoribbon Networks. *Adv. Mater.* **2010,** *22*, 4877-4880.
532. Shin, D. H.; Lee, J. S.; Jun, J.; An, J. H.; Kim, S. G.; Cho, K. H.; Jang, J. Flower-Like Palladium Nanoclusters Decorated Graphene Electrodes for Ultrasensitive and Flexible Hydrogen Gas Sensing. *Sci. Rep.* **2015,** *5*, 12294.
533. Hong, J.; Lee, S.; Seo, J.; Pyo, S.; Kim, J.; Lee, T. A Highly Sensitive Hydrogen Sensor with Gas Selectivity Using a Pmma Membrane-Coated Pd Nanoparticle/Single-Layer Graphene Hybrid. *ACS Appl. Mater. Interfaces* **2015,** *7*, 3554-3561.
534. Lee, J. S.; Oh, J.; Jun, J.; Jang, J. Wireless Hydrogen Smart Sensor Based on Pt/Graphene-Immobilized Radio-Frequency Identification Tag. *ACS Nano* **2015,** *9*, 7783-7790.
535. Vedala, H.; Sorescu, D. C.; Kotchey, G. P.; Star, A. Chemical Sensitivity of Graphene Edges Decorated with Metal Nanoparticles. *Nano Lett.* **2011,** *11*, 2342-2347.
536. Mishra, R. K.; Upadhyay, S. B.; Kushwaha, A.; Kim, T. H.; Murali, G.; Verma, R.; Srivastava, M.; Singh, J.; Sahay, P. P.; Lee, S. H. SnO_2 Quantum Dots Decorated on rGO: A Superior Sensitive, Selective and Reproducible Performance for a H_2 and Lpg Sensor. *Nanoscale* **2015,** *7*, 11971-11979.
537. Anand, K.; Singh, O.; Singh, M. P.; Kaur, J.; Singh, R. C. Hydrogen Sensor Based on Graphene/ZnO Nanocomposite. *Sensors Actuators B: Chem.* **2014,** *195*, 409-415.
538. Al-Mashat, L.; Shin, K.; Kalantar-zadeh, K.; Plessis, J. D.; Han, S. H.; Kojima, R. W.; Kaner, R. B.; Li, D.; Gou, X.; Ippolito, S. J.; Wlodarski, W. Graphene/Polyaniline Nanocomposite for Hydrogen Sensing. *J. Phys. Chem. C* **2010,** *114*, 16168-16173.
539. Zheng, Y.; Lee, D.; Koo, H. Y.; Maeng, S. Chemically Modified Graphene/PEDOT:PSS Nanocomposite Films for Hydrogen Gas Sensing. *Carbon* **2015,** *81*, 54-62.
540. Panda, D.; Nandi, A.; Datta, S. K.; Saha, H.; Majumdar, S. Selective Detection of Carbon Monoxide (CO) Gas by Reduced Graphene Oxide (rGO) at Room Temperature. *RSC Adv.* **2016,** *6*, 47337-47348.
541. Kim, J. H.; Katoch, A.; Kim, H. W.; Kim, S. S. Realization of ppm-Level CO Detection with Exceptionally High Sensitivity Using Reduced Graphene Oxide-Loaded SnO_2 Nanofibers with Simultaneous Au Functionalization. *Chem. Commun.* **2016,** *52*, 3832-3835.

542. Zhang, D.; Jiang, C.; Liu, J.; Cao, Y. Carbon Monoxide Gas Sensing at Room Temperature Using Copper Oxide-Decorated Graphene Hybrid Nanocomposite Prepared by Layer-by-Layer Self-Assembly. *Sensors Actuators B: Chem.* **2017,** *247*, 875-882.
543. Nemade, K. R.; Waghuley, S. A. Carbon Dioxide Gas Sensing Application of Graphene/Y_2O_3 Quantum Dots Composite. *Int. J. Mod. Phys. Conf. Ser.* **2013,** *22*, 380-384.
544. Nemade, K. R.; Waghuley, S. A. Role of Defects Concentration on Optical and Carbon Dioxide Gas Sensing Properties of Sb_2O_3/Graphene Composites. *Opt. Mater.* **2014,** *36*, 712-716.
545. Nemade, K. R.; Waghuley, S. A. Highly Responsive Carbon Dioxide Sensing by Graphene/Al_2O_3 Quantum Dots Composites at Low Operable Temperature. *Indian J. Phys* **2014,** *88*, 577-583.
546. Zhang, Y.-H.; Han, L.-F.; Xiao, Y.-H.; Jia, D.-Z.; Guo, Z.-H.; Li, F. Understanding Dopant and Defect Effect on H_2S Sensing Performances of Graphene: A First-Principles Study. *Comput Mater Sci* **2013,** *69*, 222-228.
547. Liu, X.-Y.; Zhang, J.-M.; Xu, K.-W.; Ji, V. Improving SO_2 Gas Sensing Properties of Graphene by Introducing Dopant and Defect: A First-Principles Study. *Appl. Surf. Sci.* **2014,** *313*, 405-410.
548. Shao, L.; Chen, G.; Ye, H.; Niu, H.; Wu, Y.; Zhu, Y.; Ding, B. Sulfur Dioxide Molecule Sensors Based on Zigzag Graphene Nanoribbons with and without Cr Dopant. *Phys. Lett. A* **2014,** *378*, 667-671.
549. Qin, X.; Meng, Q.; Feng, Y. P. Strain Effects on Enhanced Hydrogen Sulphide Detection Capability of Ag-Decorated Defective Graphene: A First-Principles Investigation. *Mod. Phys. Lett. B* **2012,** *26*.
550. Berahman, M.; Sheikhi, M. H. Hydrogen Sulfide Gas Sensor Based on Decorated Zigzag Graphene Nanoribbon with Copper. *Sensors Actuators B: Chem.* **2015,** *219*, 338-345.
551. Abdulkader Tawfik, S.; Cui, X. Y.; Carter, D. J.; Ringer, S. P.; Stampfl, C. Sensing Sulfur-Containing Gases Using Titanium and Tin Decorated Zigzag Graphene Nanoribbons from First-Principles. *Phys. Chem. Chem. Phys.* **2015,** *17*, 6925-6932.
552. Shen, F.; Wang, D.; Liu, R.; Pei, X.; Zhang, T.; Jin, J. Edge-Tailored Graphene Oxide Nanosheet-Based Field Effect Transistors for Fast and Reversible Electronic Detection of Sulfur Dioxide. *Nanoscale* **2013,** *5*, 537-540.
553. Ren, Y. J.; Zhu, C. F.; Cai, W. W.; Li, H. F.; Ji, H. X.; Kholmanov, I.; Wu, Y. P.; Piner, R. D.; Ruoff, R. S. Detection of Sulfur Dioxide Gas with Graphene Field Effect Transistor. *Appl. Phys. Lett.* **2012,** *100*, 163114.
554. Zhou, L.; Shen, F.; Tian, X.; Wang, D.; Zhang, T.; Chen, W. Stable Cu_2O Nanocrystals Grown on Functionalized Graphene Sheets and Room Temperature H_2S Gas Sensing with Ultrahigh Sensitivity. *Nanoscale* **2013,** *5*, 1564-1569.
555. Cuong, T. V.; Pham, V. H.; Chung, J. S.; Shin, E. W.; Yoo, D. H.; Hahn, S. H.; Huh, J. S.; Rue, G. H.; Kim, E. J.; Hur, S. H.; Kohl, P. A. Solution-Processed ZnO-Chemically Converted Graphene Gas Sensor. *Mater. Lett.* **2010,** *64*, 2479-2482.
556. Zhang, Z.; Zou, R.; Song, G.; Yu, L.; Chen, Z.; Hu, J. Highly Aligned SnO_2 Nanorods on Graphene Sheets for Gas Sensors. *J. Mater. Chem.* **2011,** *21*, 17360.
557. Jiang, Z.; Li, J.; Aslan, H.; Li, Q.; Li, Y.; Chen, M.; Huang, Y.; Froning, J. P.; Otyepka, M.; Zbořil, R.; Besenbacher, F.; Dong, M. A High Efficiency H_2S Gas Sensor Material: Paper Like Fe_2O_3/Graphene Nanosheets and Structural Alignment Dependency of Device Efficiency. *J. Mater. Chem. A* **2014,** *2*, 6714-6717.
558. Choi, S. J.; Jang, B. H.; Lee, S. J.; Min, B. K.; Rothschild, A.; Kim, I. D. Selective Detection of Acetone and Hydrogen Sulfide for the Diagnosis of Diabetes and Halitosis Using SnO_2 Nanofibers Functionalized with Reduced Graphene Oxide Nanosheets. *ACS Appl. Mater. Interfaces* **2014,** *6*, 2588-2597.
559. Cho, S.; Lee, J. S.; Jun, J.; Kim, S. G.; Jang, J. Fabrication of Water-Dispersible and Highly Conductive PSS-Doped Pani/Graphene Nanocomposites Using a High-Molecular Weight PSS Dopant and Their Application in H_2S Detection. *Nanoscale* **2014,** *6*, 15181-15195.
560. Choi, S.-J.; Kim, S.-J.; Kim, I.-D. Ultrafast Optical Reduction of Graphene Oxide Sheets on Colorless Polyimide Film for Wearable Chemical Sensors. *NPG Asia Mater.* **2016,** *8*, e315-e315.
561. Rodriguez, J. A.; Chaturvedi, S.; Kuhn, M.; Hrbek, J. Reaction of H_2S and S2 with Metal/Oxide Surfaces: Band-Gap Size and Chemical Reactivity. *J. Phys. Chem. B* **1998,** *102*, 5511-5519.
562. Rodriguez, J. A.; Maiti, A. Adsorption and Decomposition of H_2S on MgO(100), NiMgO(100), and ZnO(0001) Surfaces: A First-Principles Density Functional Study. *J. Phys. Chem. B* **2000,** *104*, 3630-3638.
563. Fattah, A.; Khatami, S. Selective H_2S Gas Sensing with a Graphene/N-Si Schottky Diode. *IEEE Sens. J.* **2014,** *14*, 4104-4108.
564. Ramamoorthy, R.; Dutta, P. K.; Akbar, S. A. Oxygen Sensors: Materials, Methods, Designs and Applications. *J. Mater. Sci.* **2003,** *38*, 4271-4282.
565. Chen, C. W.; Hung, S. C.; Yang, M. D.; Yeh, C. W.; Wu, C. H.; Chi, G. C.; Ren, F.; Pearton, S. J. Oxygen Sensors Made by Monolayer Graphene under Room Temperature. *Appl. Phys. Lett.* **2011,** *99*, 243502.
566. Zhang, J.; Zhao, C.; Hu, P. A.; Fu, Y. Q.; Wang, Z.; Cao, W.; Yang, B.; Placido, F. A UV Light Enhanced TiO_2/Graphene Device for Oxygen Sensing at Room Temperature. *RSC Adv.* **2013,** *3*, 22185-22190.
567. Wang, Q.; Guo, X.; Cai, L.; Cao, Y.; Gan, L.; Liu, S.; Wang, Z.; Zhang, H.; Li, L. TiO_2-Decorated Graphenes as Efficient Photoswitches with High Oxygen Sensitivity. *Chem. Sci.* **2011,** *2*, 1860-1864.
568. Ellis, J. E.; Sorescu, D. C.; Burkert, S. C.; White, D. L.; Star, A. Uncondensed Graphitic Carbon Nitride on Reduced Graphene Oxide for Oxygen Sensing via a Photoredox Mechanism. *ACS Appl. Mater. Interfaces* **2017,** *9*, 27142-27151.
569. Cho, S.-Y.; Koh, H.-J.; Yoo, H.-W.; Jung, H.-T. Tunable Chemical Sensing Performance of Black Phosphorus by Controlled Functionalization with Noble Metals. *Chem. Mater.* **2017,** *29*, 7197-7205.
570. Lei, S. Y.; Yu, Z. Y.; Shen, H. Y.; Sun, X. L.; Wan, N.; Yu, H. CO Adsorption on Metal-Decorated Phosphorene. *ACS Omega* **2018,** *3*, 3957-3965.
571. Island, J. O.; Steele, G. A.; Zant, H. S. J. v. d.; Castellanos-Gomez, A. Environmental Instability of Few-Layer Black Phosphorus. *2D Mater.* **2015,** *2*, 011002.
572. Irshad, R.; Tahir, K.; Li, B.; Sher, Z.; Ali, J.; Nazir, S. A Revival of 2D Materials, Phosphorene: Its Application as Sensors. *Journal of Industrial and Engineering Chemistry* **2018,** *64*, 60-69.
573. Pumera, M. Phosphorene and Black Phosphorus for Sensing and Biosensing. *TrAC, Trends Anal. Chem.* **2017,** *93*, 1-6.
574. Carvalho, A.; Wang, M.; Zhu, X.; Rodin, A. S.; Su, H.; Castro Neto, A. H. Phosphorene: From Theory to Applications. *Nat. Rev. Mater.* **2016,** *1*, 16061.
575. Kang, M.; Kim, B.; Ryu, S. H.; Jung, S. W.; Kim, J.; Moreschini, L.; Jozwiak, C.; Rotenberg, E.; Bostwick, A.; Kim, K. S. Universal Mechanism of Band-Gap Engineering in Transition-Metal Dichalcogenides. *Nano Lett.* **2017,** *17*, 1610-1615.

576. Lin, Z.; Carvalho, B. R.; Kahn, E.; Lv, R.; Rao, R.; Terrones, H.; Pimenta, M. A.; Terrones, M. Defect Engineering of Two-Dimensional Transition Metal Dichalcogenides. *2D Mater.* **2016,** *3*, 022002.
577. Huang, X.; Zeng, Z.; Zhang, H. Metal Dichalcogenide Nanosheets: Preparation, Properties and Applications. *Chem. Soc. Rev.* **2013,** *42*, 1934-1946.
578. Li, H.; Yin, Z.; He, Q.; Li, H.; Huang, X.; Lu, G.; Fam, D. W.; Tok, A. I.; Zhang, Q.; Zhang, H. Fabrication of Single- and Multilayer MoS_2 Film-Based Field-Effect Transistors for Sensing No at Room Temperature. *Small* **2012,** *8*, 63-67.
579. Kim, Y. H.; Kim, K. Y.; Choi, Y. R.; Shim, Y.-S.; Jeon, J.-M.; Lee, J.-H.; Kim, S. Y.; Han, S.; Jang, H. W. Ultrasensitive Reversible Oxygen Sensing by Using Liquid-Exfoliated MoS_2 Nanoparticles. *J. Mater. Chem. A* **2016,** *4*, 6070-6076.
580. Late, D. J.; Doneux, T.; Bougouma, M. Single-Layer $MoSe_2$ Based NH_3 Gas Sensor. *Appl. Phys. Lett.* **2014,** *105*, 233103.
581. Sarkar, D.; Xie, X.; Kang, J.; Zhang, H.; Liu, W.; Navarrete, J.; Moskovits, M.; Banerjee, K. Functionalization of Transition Metal Dichalcogenides with Metallic Nanoparticles: Implications for Doping and Gas-Sensing. *Nano Lett.* **2015,** *15*, 2852-2862.
582. Choi, S. Y.; Kim, Y.; Chung, H. S.; Kim, A. R.; Kwon, J. D.; Park, J.; Kim, Y. L.; Kwon, S. H.; Hahm, M. G.; Cho, B. Effect of Nb Doping on Chemical Sensing Performance of Two-Dimensional Layered $MoSe_2$. *ACS Appl. Mater. Interfaces* **2017,** *9*, 3817-3823.
583. Ruiz, A.; Calleja, A.; Espiell, F.; Cornet, A.; Morante, J. R. Nanosized Nb-Tio/Sub2/ Gas Sensors Derived from Alkoxides Hydrolization. *IEEE Sens. J.* **2003,** *3*, 189-194.
584. Cho, B.; Kim, A. R.; Kim, D. J.; Chung, H. S.; Choi, S. Y.; Kwon, J. D.; Park, S. W.; Kim, Y.; Lee, B. H.; Lee, K. H.; Kim, D. H.; Nam, J.; Hahm, M. G. Two-Dimensional Atomic-Layered Alloy Junctions for High-Performance Wearable Chemical Sensor. *ACS Appl. Mater. Interfaces* **2016,** *8*, 19635-19642.
585. Feng, Z.; Xie, Y.; Chen, J.; Yu, Y.; Zheng, S.; Zhang, R.; Li, Q.; Chen, X.; Sun, C.; Zhang, H.; Pang, W.; Liu, J.; Zhang, D. Highly Sensitive $MoTe_2$ Chemical Sensor with Fast Recovery Rate through Gate Biasing. *2D Mater.* **2017,** *4*, 025018.
586. O'Brien, M.; Lee, K.; Morrish, R.; Berner, N. C.; McEvoy, N.; Wolden, C. A.; Duesberg, G. S. Plasma Assisted Synthesis of WS_2 for Gas Sensing Applications. *Chem. Phys. Lett.* **2014,** *615*, 6-10.
587. Ko, K. Y.; Song, J. G.; Kim, Y.; Choi, T.; Shin, S.; Lee, C. W.; Lee, K.; Koo, J.; Lee, H.; Kim, J.; Lee, T.; Park, J.; Kim, H. Improvement of Gas-Sensing Performance of Large-Area Tungsten Disulfide Nanosheets by Surface Functionalization. *ACS Nano* **2016**, 9287–9296.
588. Xu, Y.; Schoonen, M. A. A. The Absolute Energy Positions of Conduction and Valence Bands of Selected Semiconducting Minerals. *Am. Mineral.* **2000,** *85*, 543-556.
589. Patil, S. G.; Tredgold, R. H. Electrical and Photoconductive Properties of SnS_2 Crystals. *J. Phys. D: Appl. Phys.* **1971,** *4*, 718-722.
590. Zappa, D. Molybdenum Dichalcogenides for Environmental Chemical Sensing. *Materials* **2017,** *10*, 1418.
591. Hsu, L. C.; Newman, J.; Ativanichayaphong, T.; Cao, H.; Sin, J.; Graff, M.; Stephanou, H. E.; Chiao, J. C. Evaluation of Commercial Metal-Oxide Based NO_2 Sensors. *Sensor Rev.* **2007,** *27*, 121-131.
592. Leonardi, S. Two-Dimensional Zinc Oxide Nanostructures for Gas Sensor Applications. *Chemosensors* **2017,** *5*, 17.
593. Chen, M.; Wang, Z.; Han, D.; Gu, F.; Guo, G. Porous ZnO Polygonal Nanoflakes: Synthesis, Use in High-Sensitivity NO_2 Gas Sensor, and Proposed Mechanism of Gas Sensing. *J. Phys. Chem. C* **2011,** *115*, 12763-12773.
594. Yu, L.; Wei, J.; Luo, Y.; Tao, Y.; Lei, M.; Fan, X.; Yan, W.; Peng, P. Dependence of Al^{3+} on the Growth Mechanism of Vertical Standing ZnO Nanowalls and Their NO_2 Gas Sensing Properties. *Sensors Actuators B: Chem.* **2014,** *204*, 96-101.
595. Yu, L.; Guo, F.; Liu, S.; Yang, B.; Jiang, Y.; Qi, L.; Fan, X. Both Oxygen Vacancies Defects and Porosity Facilitated NO_2 Gas Sensing Response in 2D ZnO Nanowalls at Room Temperature. *J. Alloys Compd.* **2016,** *682*, 352-356.
596. Xiao, C.; Yang, T.; Chuai, M.; Xiao, B.; Zhang, M. Synthesis of ZnO Nanosheet Arrays with Exposed (100) Facets for Gas Sensing Applications. *Phys. Chem. Chem. Phys.* **2016,** *18*, 325-330.
597. Mun, Y.; Park, S.; An, S.; Lee, C.; Kim, H. W. NO_2 Gas Sensing Properties of Au-Functionalized Porous ZnO Nanosheets Enhanced by UV Irradiation. *Ceram. Int.* **2013,** *39*, 8615-8622.
598. Wang, J.; Li, X.; Xia, Y.; Komarneni, S.; Chen, H.; Xu, J.; Xiang, L.; Xie, D. Hierarchical ZnO Nanosheet-Nanorod Architectures for Fabrication of Poly(3-Hexylthiophene)/ZnO Hybrid NO_2 Sensor. *ACS Appl. Mater. Interfaces* **2016,** *8*, 8600-8607.
599. Song, X.; Gao, L. Facile Synthesis and Hierarchical Assembly of Hollow Nickel Oxide Architectures Bearing Enhanced Photocatalytic Properties. *J. Phys. Chem. C* **2008,** *112*, 15299-15305.
600. Nguyen, D. H.; El-Safty, S. A. Synthesis of Mesoporous Nio Nanosheets for the Detection of Toxic NO_2 Gas. *Chem. Eur. J.* **2011,** *17*, 12896-12901.
601. Bao, M.; Chen, Y.; Li, F.; Ma, J.; Lv, T.; Tang, Y.; Chen, L.; Xu, Z.; Wang, T. Plate-Like P-N Heterogeneous NiO/WO_3 Nanocomposites for High Performance Room Temperature NO_2 Sensors. *Nanoscale* **2014,** *6*, 4063-4066.
602. Liu, J.; Guo, Z.; Meng, F.; Luo, T.; Li, M.; Liu, J. Novel Porous Single-Crystalline ZnO Nanosheets Fabricated by Annealing $ZnS(en)_{0.5}$ (en = ethylenediamine) Precursor. Application in a Gas Sensor for Indoor Air Contaminant Detection. *Nanotechnology* **2009,** *20*, 125501.
603. Nguyen, D. D.; Do, D. T.; Vu, X. H.; Dang, D. V.; Nguyen, D. C. ZnO Nanoplates Surfaced-Decorated by WO_3 Nanorods for NH_3 Gas Sensing Application. *Adv. Nat. Sci: Nanosci. Nanotechnol.* **2016,** *7*, 015004.
604. Li, Y.; Jiao, M.; Yang, M. In-Situ Grown Nanostructured ZnO via a Green Approach and Gas Sensing Properties of Polypyrrole/ZnO Nanohybrids. *Sensors Actuators B: Chem.* **2017,** *238*, 596-604.
605. Wang, J.; Yang, P.; Wei, X.; Zhou, Z. Preparation of Nio Two-Dimensional Grainy Films and Their High-Performance Gas Sensors for Ammonia Detection. *Nanoscale Res. Lett.* **2015,** *10*, 119.
606. Li, X.; Chen, N.; Lin, S.; Wang, J.; Zhang, J. Nio-Wrapped Mesoporous TiO_2 Microspheres Based Selective Ammonia Sensor at Room Temperature. *Sensors Actuators B: Chem.* **2015,** *209*, 729-734.
607. Zhang, F.; Zhu, A.; Luo, Y.; Tian, Y.; Yang, J.; Qin, Y. CuO Nanosheets for Sensitive and Selective Determination of H_2S with High Recovery Ability. *J. Phys. Chem. C* **2010,** *114*, 19214-19219.
608. Li, Z.; Wang, N.; Lin, Z.; Wang, J.; Liu, W.; Sun, K.; Fu, Y. Q.; Wang, Z. Room-Temperature High-Performance H_2S Sensor Based on Porous CuO Nanosheets Prepared by Hydrothermal Method. *ACS Appl. Mater. Interfaces* **2016,** *8*, 20962-20968.
609. Yu, T.; Cheng, X.; Zhang, X.; Sui, L.; Xu, Y.; Gao, S.; Zhao, H.; Huo, L. Highly Sensitive H_2S Detection Sensors at Low Temperature Based on Hierarchically Structured Nio Porous Nanowall Arrays. *J. Mater. Chem. A* **2015,** *3*, 11991-11999.

610. Urasinska-Wojcik, B.; Vincent, T. A.; Gardner, J. W. H 2 S Sensing Properties of Wo 3 Based Gas Sensor. *Procedia Eng.* **2016,** *168*, 255-258.
611. Li, H.-Y.; Huang, L.; Wang, X.-X.; Lee, C.-S.; Yoon, J.-W.; Zhou, J.; Guo, X.; Lee, J.-H. Molybdenum Trioxide Nanopaper as a Dual Gas Sensor for Detecting Trimethylamine and Hydrogen Sulfide. *RSC Adv.* **2017,** *7*, 3680-3685.
612. Hu, J.; Sun, Y.; Wang, X.; Chen, L.; Zhang, W.; Chen, Y. Synthesis and Gas Sensing Properties of Molybdenum Oxide Modified Tungsten Oxide Microstructures for ppb-Level Hydrogen Sulphide Detection. *RSC Adv.* **2017,** *7*, 28542-28547.
613. Moon, C. S.; Kim, H.-R.; Auchterlonie, G.; Drennan, J.; Lee, J.-H. Highly Sensitive and Fast Responding CO Sensor Using SnO_2 Nanosheets. *Sensors Actuators B: Chem.* **2008,** *131*, 556-564.
614. Jones, D. R.; Maffeïs, T. G. G. Analysis of the Kinetics of Surface Reactions on a Zinc Oxide Nanosheet-Based Carbon Monoxide Sensor Using an Eley–Rideal Model. *Sensors Actuators B: Chem.* **2015,** *218*, 16-24.
615. Zeng, Y.; Qiao, L.; Bing, Y.; Wen, M.; Zou, B.; Zheng, W.; Zhang, T.; Zou, G. Development of Microstructure CO Sensor Based on Hierarchically Porous ZnO Nanosheet Thin Films. *Sensors Actuators B: Chem.* **2012,** *173*, 897-902.
616. Chang, S.-P.; Wen, C.-H.; Chang, S.-J. Two-Dimensional ZnO Nanowalls for Gas Sensor and Photoelectrochemical Applications. *Electron. Mater. Lett.* **2014,** *10*, 693-697.
617. Chen, T. P.; Chang, S. P.; Chang, S. J. Fabrication of ZnO Nanowall-Based Hydrogen Gas Nanosensor. *Adv. Mater. Res.* **2013,** *684*, 21-25.
618. Chen, T. P.; Chang, S. P.; Hung, F. Y.; Chang, S. J.; Hu, Z. S.; Chen, K. J. Simple Fabrication Process for 2D ZnO Nanowalls and Their Potential Application as a Methane Sensor. *Sensors* **2013,** *13*, 3941-3950.
619. Alsaif, M. M. Y. A.; Balendhran, S.; Field, M. R.; Latham, K.; Wlodarski, W.; Ou, J. Z.; Kalantar-zadeh, K. Two Dimensional A-MoO_3 Nanoflakes Obtained Using Solvent-Assisted Grinding and Sonication Method: Application for H_2 Gas Sensing. *Sensors Actuators B: Chem.* **2014,** *192*, 196-204.
620. Yang, S.; Wang, Z.; Hu, Y.; Luo, X.; Lei, J.; Zhou, D.; Fei, L.; Wang, Y.; Gu, H. Highly Responsive Room-Temperature Hydrogen Sensing of α-MoO_3 Nanoribbon Membranes. *ACS Appl. Mater. Interfaces* **2015,** *7*, 9247-9253.
621. Smith, M. K.; Jensen, K. E.; Pivak, P. A.; Mirica, K. A. Direct Self-Assembly of Conductive Nanorods of Metal Organic Frameworks into Chemiresistive Devices on Shrinkable Polymer Films. *Chem. Mater.* **2016,** *28*, 5264-5268.
622. Smith, M. K.; Mirica, K. A. Self-Organized Frameworks on Textiles (SOFT): Conductive Fabrics for Simultaneous Sensing, Capture, and Filtration of Gases. *J. Am. Chem. Soc.* **2017,** *139*, 16759-16767.
623. Kim, S. J.; Koh, H. J.; Ren, C. E.; Kwon, O.; Maleski, K.; Cho, S. Y.; Anasori, B.; Kim, C. K.; Choi, Y. K.; Kim, J.; Gogotsi, Y.; Jung, H. T. Metallic Ti_3C_2Tx MXene Gas Sensors with Ultrahigh Signal-to-Noise Ratio. *ACS Nano* **2018,** *12*, 986-993.
624. Shukla, V.; Wärnå, J.; Jena, N. K.; Grigoriev, A.; Ahuja, R. Toward the Realization of 2D Borophene Based Gas Sensor. *J. Phys. Chem. C* **2017,** *121*, 26869-26876.
625. Yong, Y.; Su, X.; Cui, H.; Zhou, Q.; Kuang, Y.; Li, X. Two-Dimensional Tetragonal Gan as Potential Molecule Sensors for No and NO_2 Detection: A First-Principle Study. *ACS Omega* **2017,** *2*, 8888-8895.
626. Bhattacharyya, K.; Pratik, S. M.; Datta, A. Controlled Pore Sizes in Monolayer C2n Act as Ultrasensitive Probes for Detection of Gaseous Pollutants (HF, HCN, and H_2S). *J. Phys. Chem. C* **2018,** *122*, 2248-2258.
627. Wang, D.; Gu, W.; Zhang, Y.; Hu, Y.; Zhang, T.; Tao, X.; Chen, W. Novel C-Rich Carbon Nitride for Room Temperature NO_2 Gas Sensors. *RSC Adv.* **2014,** *4*, 18003-18006.
628. Li, S.; Wang, Z.; Wang, X.; Sun, F.; Gao, K.; Hao, N.; Zhang, Z.; Ma, Z.; Li, H.; Huang, X.; Huang, W. Orientation Controlled Preparation of Nanoporous Carbon Nitride Fibers and Related Composite for Gas Sensing under Ambient Conditions. *Nano Res.* **2017,** *10*, 1710-1719.
629. Zhang, S.; Hang, N. T.; Zhang, Z.; Yue, H.; Yang, W. Preparation of G-C_3N_4/Graphene Composite for Detecting NO_2 at Room Temperature. *Nanomaterials* **2017,** *7*, 12.
630. Tian, H.; Fan, H.; Ma, J.; Liu, Z.; Ma, L.; Lei, S.; Fang, J.; Long, C. Pt-Decorated Zinc Oxide Nanorod Arrays with Graphitic Carbon Nitride Nanosheets for Highly Efficient Dual-Functional Gas Sensing. *J. Hazard. Mater.* **2018,** *341*, 102-111.
631. S, R.; P.N, S.; S, R. Nanostructured Palladium Modified Graphitic Carbon Nitride – High Performance Room Temperature Hydrogen Sensor. *Int. J. Hydrogen Energy* **2016,** *41*, 20779-20786.
632. Soltani, A.; Thévenin, P.; Bakhtiar, H.; Bath, A. Humidity Effects on the Electrical Properties of Hexagonal Boron Nitride Thin Films. *Thin Solid Films* **2005,** *471*, 277-286.
633. Lin, L.; Liu, T.; Zhang, Y.; Sun, R.; Zeng, W.; Wang, Z. Synthesis of Boron Nitride Nanosheets with a Few Atomic Layers and Their Gas-Sensing Performance. *Ceram. Int.* **2016,** *42*, 971-975.
634. Ayari, T.; Bishop, C.; Jordan, M. B.; Sundaram, S.; Li, X.; Alam, S.; ElGmili, Y.; Patriarche, G.; Voss, P. L.; Salvestrini, J. P.; Ougazzaden, A. Gas Sensors Boosted by Two-Dimensional H-Bn Enabled Transfer on Thin Substrate Foils: Towards Wearable and Portable Applications. *Sci. Rep.* **2017,** *7*, 15212.
635. Fang, H.; Battaglia, C.; Carraro, C.; Nemsak, S.; Ozdol, B.; Kang, J. S.; Bechtel, H. A.; Desai, S. B.; Kronast, F.; Unal, A. A.; Conti, G.; Conlon, C.; Palsson, G. K.; Martin, M. C.; Minor, A. M.; Fadley, C. S.; Yablonovitch, E.; Maboudian, R.; Javey, A. Strong Interlayer Coupling in Van Der Waals Heterostructures Built from Single-Layer Chalcogenides. *Proc. Natl. Acad. Sci. U. S. A.* **2014,** *111*, 6198-6202.
636. Jariwala, D.; Sangwan, V. K.; Lauhon, L. J.; Marks, T. J.; Hersam, M. C. Emerging Device Applications for Semiconducting Two-Dimensional Transition Metal Dichalcogenides. *ACS Nano* **2014,** *8*, 1102-1120.
637. Niu, Y.; Wang, R.; Jiao, W.; Ding, G.; Hao, L.; Yang, F.; He, X. MoS_2 Graphene Fiber Based Gas Sensing Devices. *Carbon* **2015,** *95*, 34-41.
638. Xu, Z.; Liu, Z.; Sun, H.; Gao, C. Highly Electrically Conductive Ag-Doped Graphene Fibers as Stretchable Conductors. *Adv. Mater.* **2013,** *25*, 3249-3253.
639. Zhou, Y.; Liu, G.; Zhu, X.; Guo, Y. Ultrasensitive NO_2 Gas Sensing Based on rGO/MoS_2 Nanocomposite Film at Low Temperature. *Sensors Actuators B: Chem.* **2017,** *251*, 280-290.
640. Feng, Z. H.; Chen, B. Y.; Qian, S. B.; Xu, L. Y.; Feng, L. F.; Yu, Y. Y.; Zhang, R.; Chen, J. C.; Li, Q. Q.; Li, Q. N.; Sun, C. L.; Zhang, H.; Liu, J.; Pang, W.; Zhang, D. H. Chemical Sensing by Band Modulation of a Black Phosphorus/Molybdenum Diselenide Van Der Waals Hetero-Structure. *2D Mater.* **2016,** *3*, 035021.
641. Nemade, K. R.; Waghuley, S. A. Chemiresistive Gas Sensing by Few-Layered Graphene. *J. Electron. Mater.* **2013,** *42*, 2857-2866.
642. Yoon, H. J.; Jun, D. H.; Yang, J. H.; Zhou, Z.; Yang, S. S.; Cheng, M. M.-C. Carbon Dioxide Gas Sensor Using a Graphene Sheet. *Sensors Actuators B: Chem.* **2011,** *157*, 310-313.
643. Chung, M. G.; Kim, D.-H.; Seo, D. K.; Kim, T.; Im, H. U.; Lee, H. M.; Yoo, J.-B.; Hong, S.-H.; Kang, T. J.; Kim, Y. H. Flexible Hydrogen Sensors Using Graphene with Palladium Nanoparticle Decoration. *Sensors Actuators B: Chem.* **2012,** *169*, 387-392.

644. Phan, D.-T.; Chung, G.-S. Effects of Pd Nanocube Size of Pd Nanocube-Graphene Hybrid on Hydrogen Sensing Properties. *Sensors Actuators B: Chem.* **2014,** *204*, 437-444.
645. Chen, X.; Yasin, F. M.; Eggers, P. K.; Boulos, R. A.; Duan, X.; Lamb, R. N.; Iyer, K. S.; Raston, C. L. Non-Covalently Modified Graphene Supported Ultrafine Nanoparticles of Palladium for Hydrogen Gas Sensing. *RSC Adv.* **2013,** *3*, 3213.
646. Kaniyoor, A.; Imran Jafri, R.; Arockiadoss, T.; Ramaprabhu, S. Nanostructured Pt Decorated Graphene and Multi Walled Carbon Nanotube Based Room Temperature Hydrogen Gas Sensor. *Nanoscale* **2009,** *1*, 382-386.
647. Chu, B. H.; Nicolosi, J.; Lo, C. F.; Strupinski, W.; Pearton, S. J.; Ren, F. Effect of Coated Platinum Thickness on Hydrogen Detection Sensitivity of Graphene-Based Sensors. *Electrochem. Solid-State Lett.* **2011,** *14*, K43.
648. Zhang, Z.; Zou, X.; Xu, L.; Liao, L.; Liu, W.; Ho, J.; Xiao, X.; Jiang, C.; Li, J. Hydrogen Gas Sensor Based on Metal Oxide Nanoparticles Decorated Graphene Transistor. *Nanoscale* **2015,** *7*, 10078-10084.
649. Paul, R. K.; Badhulika, S.; Saucedo, N. M.; Mulchandani, A. Graphene Nanomesh as Highly Sensitive Chemiresistor Gas Sensor. *Anal. Chem.* **2012,** *84*, 8171-8178.
650. Ben Aziza, Z.; Zhang, Q.; Baillargeat, D. Graphene/Mica Based Ammonia Gas Sensors. *Appl. Phys. Lett.* **2014,** *105*, 254102.
651. Cho, B.; Yoon, J.; Lim, S. K.; Kim, A. R.; Kim, D. H.; Park, S. G.; Kwon, J. D.; Lee, Y. J.; Lee, K. H.; Lee, B. H.; Ko, H. C.; Hahm, M. G. Chemical Sensing of 2D Graphene/ MoS_2 Heterostructure Device. *ACS Appl. Mater. Interfaces* **2015,** *7*, 16775-16780.
652. Lee, K.; Gatensby, R.; McEvoy, N.; Hallam, T.; Duesberg, G. S. High-Performance Sensors Based on Molybdenum Disulfide Thin Films. *Adv. Mater.* **2013,** *25*, 6699-6702.
653. Huang, X.; Hu, N.; Zhang, L.; Wei, L.; Wei, H.; Zhang, Y. The NH_3 Sensing Properties of Gas Sensors Based on Aniline Reduced Graphene Oxide. *Synth. Met.* **2013,** *185-186*, 25-30.
654. Hu, N.; Yang, Z.; Wang, Y.; Zhang, L.; Wang, Y.; Huang, X.; Wei, H.; Wei, L.; Zhang, Y. Ultrafast and Sensitive Room Temperature NH_3 Gas Sensors Based on Chemically Reduced Graphene Oxide. *Nanotechnology* **2014,** *25*, 025502.
655. Meng, H.; Yang, W.; Ding, K.; Feng, L.; Guan, Y. Cu2o Nanorods Modified by Reduced Graphene Oxide for NH_3 Sensing at Room Temperature. *J. Mater. Chem. A* **2015,** *3*, 1174-1181.
656. Ye, Z.; Jiang, Y.; Tai, H.; Yuan, Z. The Investigation of Reduced Graphene Oxide/P3HT Composite Films for Ammonia Detection. *Integr. Ferroelectr.* **2014,** *154*, 73-81.
657. Wang, Y.; Zhang, L.; Hu, N.; Wang, Y.; Zhang, Y.; Zhou, Z.; Liu, Y.; Shen, S.; Peng, C. Ammonia Gas Sensors Based on Chemically Reduced Graphene Oxide Sheets Self-Assembled on Au Electrodes. *Nanoscale Res. Lett.* **2014,** *9*, 251.
658. Xu, K.; Li, N.; Zeng, D.; Tian, S.; Zhang, S.; Hu, D.; Xie, C. Interface Bonds Determined Gas-Sensing of SnO_2-SnS_2 Hybrids to Ammonia at Room Temperature. *ACS Appl. Mater. Interfaces* **2015,** *7*, 11359-11368.
659. Chung, M. G.; Kim, D. H.; Lee, H. M.; Kim, T.; Choi, J. H.; Seo, D. k.; Yoo, J.-B.; Hong, S.-H.; Kang, T. J.; Kim, Y. H. Highly Sensitive NO_2 Gas Sensor Based on Ozone Treated Graphene. *Sensors Actuators B: Chem.* **2012,** *166-167*, 172-176.
660. Hoa, L. T.; Tien, H. N.; Luan, V. H.; Chung, J. S.; Hur, S. H. Fabrication of a Novel 2D-Graphene/2D-Nio Nanosheet-Based Hybrid Nanostructure and Its Use in Highly Sensitive NO_2 Sensors. *Sensors Actuators B: Chem.* **2013,** *185*, 701-705.
661. Lee, C.; Ahn, J.; Lee, K. B.; Kim, D.; Kim, J. Graphene-Based Flexible NO_2 Chemical Sensors. *Thin Solid Films* **2012,** *520*, 5459-5462.
662. Srivastava, S.; Jain, K.; Singh, V. N.; Singh, S.; Vijayan, N.; Dilawar, N.; Gupta, G.; Senguttuvan, T. D. Faster Response of NO_2 Sensing in Graphene-WO_3 Nanocomposites. *Nanotechnology* **2012,** *23*, 205501.
663. He, Q.; Zeng, Z.; Yin, Z.; Li, H.; Wu, S.; Huang, X.; Zhang, H. Fabrication of Flexible MoS_2 Thin-Film Transistor Arrays for Practical Gas-Sensing Applications. *Small* **2012,** *8*, 2994-2999.
664. Cui, S.; Wen, Z.; Huang, X.; Chang, J.; Chen, J. Stabilizing MoS_2 Nanosheets through SnO_2 Nanocrystal Decoration for High-Performance Gas Sensing in Air. *Small* **2015,** *11*, 2305-2313.
665. Su, P.-G.; Shieh, H.-C. Flexible NO_2 Sensors Fabricated by Layer-by-Layer Covalent Anchoring and in Situ Reduction of Graphene Oxide. *Sensors Actuators B: Chem.* **2014,** *190*, 865-872.
666. Dong, Y.-l.; Zhang, X.-f.; Cheng, X.-l.; Xu, Y.-m.; Gao, S.; Zhao, H.; Huo, L.-h. Highly Selective NO_2 Sensor at Room Temperature Based on Nanocomposites of Hierarchical Nanosphere-Like A-Fe_2O_3 and Reduced Graphene Oxide. *RSC Adv.* **2014,** *4*, 57493-57500.
667. Huang, L.; Wang, Z.; Zhang, J.; Pu, J.; Lin, Y.; Xu, S.; Shen, L.; Chen, Q.; Shi, W. Fully Printed, Rapid-Response Sensors Based on Chemically Modified Graphene for Detecting NO_2 at Room Temperature. *ACS Appl. Mater. Interfaces* **2014,** *6*, 7426-7433.
668. Farahani, H.; Wagiran, R.; Hamidon, M. N. Humidity Sensors Principle, Mechanism, and Fabrication Technologies: A Comprehensive Review. *Sensors* **2014,** *14*, 7881-7939.
669. Mirzaei, A.; Leonardi, S. G.; Neri, G. Detection of Hazardous Volatile Organic Compounds (VOCs) by Metal Oxide Nanostructures-Based Gas Sensors: A Review. *Ceram. Int.* **2016,** *42*, 15119-15141.
670. Li, B.; Sauve, G.; Iovu, M. C.; Jeffries-El, M.; Zhang, R.; Cooper, J.; Santhanam, S.; Schultz, L.; Revelli, J. C.; Kusne, A. G.; Kowalewski, T.; Snyder, J. L.; Weiss, L. E.; Fedder, G. K.; McCullough, R. D.; Lambeth, D. N. Volatile Organic Compound Detection Using Nanostructured Copolymers. *Nano Lett.* **2006,** *6*, 1598-1602.
671. Europe, W. R. O. f., *Selected Pollutants*. Copenhagen: 2010.
672. Chung, P. R.; Tzeng, C. T.; Ke, M. T.; Lee, C. Y. Formaldehyde Gas Sensors: A Review. *Sensors* **2013,** *13*, 4468-4484.
673. Yavari, F.; Kritzinger, C.; Gaire, C.; Song, L.; Gulapalli, H.; Borca-Tasciuc, T.; Ajayan, P. M.; Koratkar, N. Tunable Bandgap in Graphene by the Controlled Adsorption of Water Molecules. *Small* **2010,** *6*, 2535-2538.
674. Dimiev, A. M.; Alemany, L. B.; Tour, J. M. Graphene Oxide. Origin of Acidity, Its Instability in Water, and a New Dynamic Structural Model. *ACS Nano* **2013,** *7*, 576-588.
675. Yao, Y.; Chen, X.; Zhu, J.; Zeng, B.; Wu, Z.; Li, X. The Effect of Ambient Humidity on the Electrical Properties of Graphene Oxide Films. *Nanoscale Res. Lett.* **2012,** *7*, 363.
676. Zhao, F.; Cheng, H.; Zhang, Z.; Jiang, L.; Qu, L. Direct Power Generation from a Graphene Oxide Film under Moisture. *Adv. Mater.* **2015,** *27*, 4351-4357.
677. Nair, R. R.; Wu, H. A.; Jayaram, P. N.; Grigorieva, I. V.; Geim, A. K. Unimpeded Permeation of Water through Helium-Leak-Tight Graphene-Based Membranes. *Science* **2012,** *335*, 442-444.
678. Borini, S.; White, R.; Wei, D.; Astley, M.; Haque, S.; Spigone, E.; Harris, N.; Kivioja, J.; Ryhanen, T. Ultrafast Graphene Oxide Humidity Sensors. *ACS Nano* **2013,** *7*, 11166-11173.
679. Bi, H.; Yin, K.; Xie, X.; Ji, J.; Wan, S.; Sun, L.; Terrones, M.; Dresselhaus, M. S. Ultrahigh Humidity Sensitivity of Graphene Oxide. *Sci. Rep.* **2013,** *3*, 2714.

680. Chen, W. P.; Zhao, Z. G.; Liu, X. W.; Zhang, Z. X.; Suo, C. G. A Capacitive Humidity Sensor Based on Multi-Wall Carbon Nanotubes (MWCTNs). *Sensors* **2009,** *9*, 7431-7444.
681. Chen, X.; Zhang, J.; Wang, Z.; Yan, Q.; Hui, S. Humidity Sensing Behavior of Silicon Nanowires with Hexamethyldisilazane Modification. *Sensors Actuators B: Chem.* **2011,** *156*, 631-636.
682. Wang, Y.; Park, S.; Yeow, J. T. W.; Langner, A.; Müller, F. A Capacitive Humidity Sensor Based on Ordered Macroporous Silicon with Thin Film Surface Coating. *Sensors Actuators B: Chem.* **2010,** *149*, 136-142.
683. Wang, Z.; Shi, L.; Wu, F.; Yuan, S.; Zhao, Y.; Zhang, M. The Sol-Gel Template Synthesis of Porous TiO_2 for a High Performance Humidity Sensor. *Nanotechnology* **2011,** *22*, 275502.
684. Kim, Y.; Jung, B.; Lee, H.; Kim, H.; Lee, K.; Park, H. Capacitive Humidity Sensor Design Based on Anodic Aluminum Oxide. *Sensors Actuators B: Chem.* **2009,** *141*, 441-446.
685. Su, P.-G.; Chiou, C.-F. Electrical and Humidity-Sensing Properties of Reduced Graphene Oxide Thin Film Fabricated by Layer-by-Layer with Covalent Anchoring on Flexible Substrate. *Sensors Actuators B: Chem.* **2014,** *200*, 9-18.
686. Zhang, D.; Tong, J.; Xia, B. Humidity-Sensing Properties of Chemically Reduced Graphene Oxide/Polymer Nanocomposite Film Sensor Based on Layer-by-Layer Nano Self-Assembly. *Sensors Actuators B: Chem.* **2014,** *197*, 66-72.
687. Guo, L.; Jiang, H.-B.; Shao, R.-Q.; Zhang, Y.-L.; Xie, S.-Y.; Wang, J.-N.; Li, X.-B.; Jiang, F.; Chen, Q.-D.; Zhang, T.; Sun, H.-B. Two-Beam-Laser Interference Mediated Reduction, Patterning and Nanostructuring of Graphene Oxide for the Production of a Flexible Humidity Sensing Device. *Carbon* **2012,** *50*, 1667-1673.
688. Ma, R.; Tsukruk, V. V. Seriography-Guided Reduction of Graphene Oxide Biopapers for Wearable Sensory Electronics. *Adv. Funct. Mater.* **2017,** *27*, 1604802.
689. Sinar, D.; Knopf, G. K. Printed Graphene Interdigitated Capacitive Sensors on Flexible Polyimide Substrates. *2014 IEEE 14th International Conference on Nanotechnology (IEEE-Nano)* **2014**, 538-542.
690. Yuan, Y.; Peng, B.; Chi, H.; Li, C.; Liu, R.; Liu, X. Layer-by-Layer Inkjet Printing Sps:Pedot NP/rGO Composite Film for Flexible Humidity Sensors. *RSC Adv.* **2016,** *6*, 113298-113306.
691. Deen, D. A.; Olson, E. J.; Ebrish, M. A.; Koester, S. J. Graphene-Based Quantum Capacitance Wireless Vapor Sensors. *IEEE Sens. J.* **2014,** *14*, 1459-1466.
692. Kumar, B.; Min, K.; Bashirzadeh, M.; Farimani, A. B.; Bae, M. H.; Estrada, D.; Kim, Y. D.; Yasaei, P.; Park, Y. D.; Pop, E.; Aluru, N. R.; Salehi-Khojin, A. The Role of External Defects in Chemical Sensing of Graphene Field-Effect Transistors. *Nano Lett.* **2013,** *13*, 1962-1968.
693. Xu, K.; Cao, P.; Heath, J. R. Graphene Visualizes the First Water Adlayers on Mica at Ambient Conditions. *Science* **2010,** *329*, 1188-1191.
694. Temmen, M.; Ochedowski, O.; Schleberger, M.; Reichling, M.; Bollmann, T. R. J. Hydration Layers Trapped between Graphene and a Hydrophilic Substrate. *New J. Phys.* **2014,** *16*, 053039.
695. Olson, E. J.; Ma, R.; Sun, T.; Ebrish, M. A.; Haratipour, N.; Min, K.; Aluru, N. R.; Koester, S. J. Capacitive Sensing of Intercalated H_2O Molecules Using Graphene. *ACS Appl. Mater. Interfaces* **2015,** *7*, 25804-25812.
696. Shehzad, K.; Shi, T.; Qadir, A.; Wan, X.; Guo, H.; Ali, A.; Xuan, W.; Xu, H.; Gu, Z.; Peng, X.; Xie, J.; Sun, L.; He, Q.; Xu, Z.; Gao, C.; Rim, Y.-S.; Dan, Y.; Hasan, T.; Tan, P.; Li, E.; Yin, W.; Cheng, Z.; Yu, B.; Xu, Y.; Luo, J.; Duan, X. Designing an Efficient Multimode Environmental Sensor Based on Graphene-Silicon Heterojunction. *Adv. Mater. Technol.* **2017,** *2*, 1600262.
697. Smith, A. D.; Elgammal, K.; Niklaus, F.; Delin, A.; Fischer, A. C.; Vaziri, S.; Forsberg, F.; Rasander, M.; Hugosson, H.; Bergqvist, L.; Schroder, S.; Kataria, S.; Ostling, M.; Lemme, M. C. Resistive Graphene Humidity Sensors with Rapid and Direct Electrical Readout. *Nanoscale* **2015,** *7*, 19099-19109.
698. Yu, H. W.; Kim, H. K.; Kim, T.; Bae, K. M.; Seo, S. M.; Kim, J. M.; Kang, T. J.; Kim, Y. H. Self-Powered Humidity Sensor Based on Graphene Oxide Composite Film Intercalated by Poly(Sodium 4-Styrenesulfonate). *ACS Appl. Mater. Interfaces* **2014,** *6*, 8320-8326.
699. Lin, W.-D.; Chang, H.-M.; Wu, R.-J. Applied Novel Sensing Material Graphene/Polypyrrole for Humidity Sensor. *Sensors Actuators B: Chem.* **2013,** *181*, 326-331.
700. Su, P.-G.; Lu, Z.-M. Flexibility and Electrical and Humidity-Sensing Properties of Diamine-Functionalized Graphene Oxide Films. *Sensors Actuators B: Chem.* **2015,** *211*, 157-163.
701. Porter, T. L.; Vail, T. L.; Eastman, M. P.; Stewart, R.; Reed, J.; Venedam, R.; Delinger, W. A Solid-State Sensor Platform for the Detection of Hydrogen Cyanide Gas. *Sensors Actuators B: Chem.* **2007,** *123*, 313-317.
702. Robinson, J. T.; Perkins, F. K.; Snow, E. S.; Wei, Z.; Sheehan, P. E. Reduced Graphene Oxide Molecular Sensors. *Nano Lett.* **2008,** *8*, 3137-3140.
703. Zhou, S.; Xu, H.; Gan, W.; Yuan, Q. Graphene Quantum Dots: Recent Progress in Preparation and Fluorescence Sensing Applications. *RSC Adv.* **2016,** *6*, 110775-110788.
704. Sreeprasad, T. S.; Rodriguez, A. A.; Colston, J.; Graham, A.; Shishkin, E.; Pallem, V.; Berry, V. Electron-Tunneling Modulation in Percolating Network of Graphene Quantum Dots: Fabrication, Phenomenological Understanding, and Humidity/Pressure Sensing Applications. *Nano Lett.* **2013,** *13*, 1757-1763.
705. Alizadeh, T.; Shokri, M.; Hanifehpour, Y.; Joo, S. W. A New Hydrogen Cyanide Chemiresistor Gas Sensor Based on Graphene Quantum Dots. *Int. J. Environ. Anal. Chem.* **2016,** *96*, 763-775.
706. Yang, M.; He, J.; Hu, X.; Yan, C.; Cheng, Z. CuO Nanostructures as Quartz Crystal Microbalance Sensing Layers for Detection of Trace Hydrogen Cyanide Gas. *Environ. Sci. Technol.* **2011,** *45*, 6088-6094.
707. Dong, Y.; Shao, J.; Chen, C.; Li, H.; Wang, R.; Chi, Y.; Lin, X.; Chen, G. Blue Luminescent Graphene Quantum Dots and Graphene Oxide Prepared by Tuning the Carbonization Degree of Citric Acid. *Carbon* **2012,** *50*, 4738-4743.
708. Mlsna, T. E.; Cemalovic, S.; Warburton, M.; Hobson, S. T.; Mlsna, D. A.; Patel, S. V. Chemicapacitive Microsensors for Chemical Warfare Agent and Toxic Industrial Chemical Detection. *Sensors Actuators B: Chem.* **2006,** *116*, 192-201.
709. Legako, J. A.; White, B. J.; Harmon, H. J. Detection of Cyanide Using Immobilized Porphyrin and Myoglobin Surfaces. *Sensors Actuators B: Chem.* **2003,** *91*, 128-132.
710. Roerecke, M.; Rehm, J. Alcohol Use Disorders and Mortality: A Systematic Review and Meta-Analysis. *Addiction* **2013,** *108*, 1562-1578.
711. Selvam, A. P.; Muthukumar, S.; Kamakoti, V.; Prasad, S. A Wearable Biochemical Sensor for Monitoring Alcohol Consumption Lifestyle through Ethyl Glucuronide (EtG) Detection in Human Sweat. *Sci. Rep.* **2016,** *6*, 23111.
712. McPherson, S.; Lucey, M. R.; Moriarty, K. J. Decompensated Alcohol Related Liver Disease: Acute Management. *BMJ* **2016,** *352*, i124.
713. Chen, B. D.; Liu, H. Z.; Li, X.; Lu, C. X.; Ding, Y. C.; Lu, B. H. Fabrication of a Graphene Field Effect Transistor Array on Microchannels for Ethanol Sensing. *Appl. Surf. Sci.* **2012,** *258*, 1971-1975.

714. Kim, Y.; An, T. K.; Kim, J.; Hwang, J.; Park, S.; Nam, S.; Cha, H.; Park, W. J.; Baik, J. M.; Park, C. E. A Composite of a Graphene Oxide Derivative as a Novel Sensing Layer in an Organic Field-Effect Transistor. *J. Mater. Chem. C* **2014,** *2*, 4539-4544.
715. Liang, S. M.; Zhu, J. W.; Wang, C.; Yu, S. T.; Bi, H. P.; Liu, X. H.; Wang, X. Fabrication of α-Fe_2O_3@Graphene Nanostructures for Enhanced Gas-Sensing Property to Ethanol. *Appl. Surf. Sci.* **2014,** *292*, 278-284.
716. Liu, Y.; Lin, S.; Lin, L. A Versatile Gas Sensor with Selectivity Using a Single Graphene Transistor. *2015 Transducers - 2015 18th International Conference on Solid-State Sensors, Actuators and Microsystems (Transducers)* **2015**, 961-964.
717. Korpan, Y. I.; Gonchar, M. V.; Sibirny, A. A.; Martelet, C.; El'skaya, A. V.; Gibson, T. D.; Soldatkin, A. P. Development of Highly Selective and Stable Potentiometric Sensors for Formaldehyde Determination. *Biosens. Bioelectron.* **2000,** *15*, 77-83.
718. Alizadeh, T.; Soltani, L. H. Graphene/Poly(Methyl Methacrylate) Chemiresistor Sensor for Formaldehyde Odor Sensing. *J. Hazard. Mater.* **2013,** *248*, 401-406.
719. Minh Triet, N.; Thai Duy, L.; Hwang, B. U.; Hanif, A.; Siddiqui, S.; Park, K. H.; Cho, C. Y.; Lee, N. E. High-Performance Schottky Diode Gas Sensor Based on the Heterojunction of Three-Dimensional Nanohybrids of Reduced Graphene Oxide-Vertical ZnO Nanorods on an Algan/Gan Layer. *ACS Appl. Mater. Interfaces* **2017,** *9*, 30722-30732.
720. Dong, L.; Shen, X.; Deng, C. Development of Gas Chromatography–Mass Spectrometry Following Headspace Single-Drop Microextraction and Simultaneous Derivatization for Fast Determination of the Diabetes Biomarker, Acetone in Human Blood Samples. *Anal. Chim. Acta* **2006,** *569*, 91-96.
721. Li, X.; Xu, Z.; Lu, X.; Yang, X.; Yin, P.; Kong, H.; Yu, Y.; Xu, G. Comprehensive Two-Dimensional Gas Chromatography/Time-of-Flight Mass Spectrometry for Metabonomics: Biomarker Discovery for Diabetes Mellitus. *Anal. Chim. Acta* **2009,** *633*, 257-262.
722. Shin, J.; Choi, S.-J.; Lee, I.; Youn, D.-Y.; Park, C. O.; Lee, J.-H.; Tuller, H. L.; Kim, I.-D. Thin-Wall Assembled SnO_2 fibers Functionalized by Catalytic Pt Nanoparticles and Their Superior Exhaled-Breath-Sensing Properties for the Diagnosis of Diabetes. *Adv. Funct. Mater.* **2013,** *23*, 2357-2367.
723. Choi, S.-J.; Ryu, W.-H.; Kim, S.-J.; Cho, H.-J.; Kim, I.-D. Bi-Functional Co-Sensitization of Graphene Oxide Sheets and Ir Nanoparticles on P-Type Co_3O_4 Nanofibers for Selective Acetone Detection. *J. Mater. Chem. B* **2014,** *2*, 7160-7167.
724. Liu, F.; Chu, X.; Dong, Y.; Zhang, W.; Sun, W.; Shen, L. Acetone Gas Sensors Based on Graphene-$ZnFe_2O_4$ Composite Prepared by Solvothermal Method. *Sensors Actuators B: Chem.* **2013,** *188*, 469-474.
725. Kehayias, C. E.; MacNaughton, S.; Sonkusale, S.; Staii, C. Kelvin Probe Microscopy and Electronic Transport Measurements in Reduced Graphene Oxide Chemical Sensors. *Nanotechnology* **2013,** *24*, 245502.
726. Myers, M.; Cooper, J.; Pejcic, B.; Baker, M.; Raguse, B.; Wieczorek, L. Functionalized Graphene as an Aqueous Phase Chemiresistor Sensing Material. *Sensors Actuators B: Chem.* **2011,** *155*, 154-158.
727. Duesberg, G. S.; Kim, H. Y.; Lee, K.; McEvoy, N.; Winters, S.; Yim, C. Investigation of Carbon-Silicon Schottky Diodes and Their Use as Chemical Sensors. *2013 Proceedings of the European Solid-State Device Research Conference (Essderc)* **2013**, 85-90.
728. Zheng, Q.; Fu, Y.-c.; Xu, J.-q. Advances in the Chemical Sensors for the Detection of DMMP — a Simulant for Nerve Agent Sarin. *Procedia Eng.* **2010,** *7*, 179-184.
729. Alizadeh, T.; Soltani, L. H. Reduced Graphene Oxide-Based Gas Sensor Array for Pattern Recognition of DMMP Vapor. *Sensors Actuators B: Chem.* **2016,** *234*, 361-370.
730. Hu, N.; Wang, Y.; Chai, J.; Gao, R.; Yang, Z.; Kong, E. S.-W.; Zhang, Y. Gas Sensor Based on P-Phenylenediamine Reduced Graphene Oxide. *Sensors Actuators B: Chem.* **2012,** *163*, 107-114.
731. Na, K.; Ma, H.; Park, J.; Yeo, J.; Park, J. U.; Bien, F. Graphene-Based Wireless Environmental Gas Sensor on Pet Substrate. *IEEE Sens. J.* **2016,** *16*, 5003-5009.
732. Salehi-Khojin, A.; Estrada, D.; Lin, K. Y.; Bae, M. H.; Xiong, F.; Pop, E.; Masel, R. I. Polycrystalline Graphene Ribbons as Chemiresistors. *Adv. Mater.* **2012,** *24*, 53-57, 52.
733. Nagareddy, V. K.; Goss, J. P.; Wright, N. G.; Horsfall, A. B.; Hernandez, S. C.; Wheeler, V. D.; Nyakiti, L. O.; Myers-Ward, R. L.; Eddy, C. R., Jr.; Walton, S. G.; Gaskill, D. K.; *IEEE*, Oxygen Functionalised Epitaxial Graphene Sensors for Enhanced Polar Organic Chemical Vapour Detection. In *2012 IEEE Sensors Proceedings*, 2012; pp 2126-2129.
734. Pan, B.; Xing, B. Adsorption Mechanisms of Organic Chemicals on Carbon Nanotubes. *Environ. Sci. Technol.* **2008,** *42*, 9005-9013.
735. Hutchison, G. R.; Ratner, M. A.; Marks, T. J.; Naaman, R. Adsorption of Polar Molecules on a Molecular Surface. *J. Phys. Chem. B* **2001,** *105*, 2881-2884.
736. Nallon, E. C.; Schnee, V. P.; Bright, C.; Polcha, M. P.; Li, Q. Chemical Discrimination with an Unmodified Graphene Chemical Sensor. *ACS Sens.* **2016,** *1*, 26-31.
737. Fattah, A.; Khatami, S.; Mayorga-Martinez, C. C.; Medina-Sanchez, M.; Baptista-Pires, L.; Merkoci, A. Graphene/Silicon Heterojunction Schottky Diode for Vapors Sensing Using Impedance Spectroscopy. *Small* **2014,** *10*, 4193-4199.
738. Hasani, A.; Dehsari, H. S.; Gavgani, J. N.; Shalamzari, E. K.; Salehi, A.; Taromi, F. A.; Mahyari, M. Sensor for Volatile Organic Compounds Using an Interdigitated Gold Electrode Modified with a Nanocomposite Made from Poly(3,4-Ethylenedioxythiophene)-Poly(Styrenesulfonate) and Ultra-Large Graphene Oxide. *Microchimica Acta* **2015,** *182*, 1551-1559.
739. Teradal, N. L.; Marx, S.; Morag, A.; Jelinek, R. Porous Graphene Oxide Chemi-Capacitor Vapor Sensor Array. *J. Mater. Chem. C* **2017,** *5*, 1128-1135.
740. Kulkarni, G. S.; Reddy, K.; Zhong, Z. H.; Fan, X. D. Graphene Nanoelectronic Heterodyne Sensor for Rapid and Sensitive Vapour Detection. *Nat. Commun.* **2014,** *5*, 4376.
741. Kybert, N. J.; Han, G. H.; Lerner, M. B.; Dattoli, E. N.; Esfandiar, A.; Johnson, A. T. C. Scalable Arrays of Chemical Vapor Sensors Based on DNA-Decorated Graphene. *Nano Res.* **2014,** *7*, 95-103.
742. Gautam, M.; Jayatissa, A. H. Detection of Organic Vapors by Graphene Films Functionalized with Metallic Nanoparticles. *J. Appl. Phys.* **2012,** *112*, 114326.
743. Nemade, K. R.; Waghuley, S. A. Lpg Sensing Application of Graphene/CeO_2 Quantum Dots Composite. *Aip Conf Proc* **2013,** *1536*, 1258-1259.
744. Majumder, D.; Roy, S. Development of Low-ppm CO Sensors Using Pristine CeO_2 Nanospheres with High Surface Area. *ACS Omega* **2018,** *3*, 4433-4440.
745. Ranola, R. A. G.; Kalaw, J. M.; Sevilla, F. B., III Surface Adsorbed Reduced Graphene Oxide on Nylon-6 via Vacuum-Assisted Self-Assembly for Chemiresistor Sensing of Trimethylamine. *IEEE Sens. J.* **2016,** *16*, 1880-1886.
746. Ranola, R. A. G.; Kalaw, J. M.; Sevilla, F. B., III, Graphene/Nylon-6 Chemiresistor Sensor for Trimethylamine Gas Sensing. In *Power and Energy Systems III*, Leeprechanon, N., Ed. 2014; Vol. 492, pp 321-325.

747. Wood, J. D.; Wells, S. A.; Jariwala, D.; Chen, K. S.; Cho, E.; Sangwan, V. K.; Liu, X.; Lauhon, L. J.; Marks, T. J.; Hersam, M. C. Effective Passivation of Exfoliated Black Phosphorus Transistors against Ambient Degradation. *Nano Lett.* **2014,** *14*, 6964-6970.
748. Hanlon, D.; Backes, C.; Doherty, E.; Cucinotta, C. S.; Berner, N. C.; Boland, C.; Lee, K.; Harvey, A.; Lynch, P.; Gholamvand, Z.; Zhang, S.; Wang, K.; Moynihan, G.; Pokle, A.; Ramasse, Q. M.; McEvoy, N.; Blau, W. J.; Wang, J.; Abellan, G.; Hauke, F.; Hirsch, A.; Sanvito, S.; O'Regan, D. D.; Duesberg, G. S.; Nicolosi, V.; Coleman, J. N. Liquid Exfoliation of Solvent-Stabilized Few-Layer Black Phosphorus for Applications Beyond Electronics. *Nat. Commun.* **2015,** *6*, 8563.
749. Yasaei, P.; Behranginia, A.; Foroozan, T.; Asadi, M.; Kim, K.; Khalili-Araghi, F.; Salehi-Khojin, A. Stable and Selective Humidity Sensing Using Stacked Black Phosphorus Flakes. *Acs Nano* **2015,** *9*, 9898-9905.
750. Erande, M. B.; Pawar, M. S.; Late, D. J. Humidity Sensing and Photodetection Behavior of Electrochemically Exfoliated Atomically Thin-Layered Black Phosphorus Nanosheets. *ACS Appl. Mater. Interfaces* **2016,** *8*, 11548-11556.
751. Late, D. J. Liquid Exfoliation of Black Phosphorus Nanosheets and Its Application as Humidity Sensor. *Microporous Mesoporous Mater.* **2016,** *225*, 494-503.
752. Miao, J.; Cai, L.; Zhang, S.; Nah, J.; Yeom, J.; Wang, C. Air-Stable Humidity Sensor Using Few-Layer Black Phosphorus. *ACS Appl. Mater. Interfaces* **2017,** *9*, 10019-10026.
753. Walia, S.; Sabri, Y.; Ahmed, T.; Field, M. R.; Ramanathan, R.; Arash, A.; Bhargava, S. K.; Sriram, S.; Bhaskaran, M.; Bansal, V.; Balendhran, S. Defining the Role of Humidity in the Ambient Degradation of Few-Layer Black Phosphorus. *2D Mater.* **2017,** *4*, 015025.
754. Kruse, J. A. Methanol Poisoning. *Intensive Care Med.* **1992,** *18*, 391-397.
755. Mayorga-Martinez, C. C.; Sofer, Z.; Pumera, M. Layered Black Phosphorus as a Selective Vapor Sensor. *Angew. Chem. Int. Ed.* **2015,** *54*, 14317-14320.
756. Feng, J.; Peng, L.; Wu, C.; Sun, X.; Hu, S.; Lin, C.; Dai, J.; Yang, J.; Xie, Y. Giant Moisture Responsiveness of VS_2 Ultrathin Nanosheets for Novel Touchless Positioning Interface. *Adv. Mater.* **2012,** *24*, 1969-1974.
757. Zhang, S.-L.; Choi, H.-H.; Yue, H.-Y.; Yang, W.-C. Controlled Exfoliation of Molybdenum Disulfide for Developing Thin Film Humidity Sensor. *Curr. Appl. Phys.* **2014,** *14*, 264-268.
758. Tahir, M. N.; Zink, N.; Eberhardt, M.; Therese, H. A.; Kolb, U.; Theato, P.; Tremel, W. Overcoming the Insolubility of Molybdenum Disulfide Nanoparticles through a High Degree of Sidewall Functionalization Using Polymeric Chelating Ligands. *Angew. Chem. Int. Ed.* **2006,** *45*, 4809-4815.
759. Pawbake, A. S.; Waykar, R. G.; Late, D. J.; Jadkar, S. R. Highly Transparent Wafer-Scale Synthesis of Crystalline WS_2 Nanoparticle Thin Film for Photodetector and Humidity-Sensing Applications. *ACS Appl. Mater. Interfaces* **2016,** *8*, 3359-3365.
760. Guo, H. Y.; Lan, C. Y.; Zhou, Z. F.; Sun, P. H.; Wei, D. P.; Li, C. Transparent, Flexible, and Stretchable WS_2 Based Humidity Sensors for Electronic Skin. *Nanoscale* **2017,** *9*, 6246-6253.
761. Selin, N. E. Global Biogeochemical Cycling of Mercury: A Review. *Annual Review of Environment and Resources* **2009,** *34*, 43-63.
762. https://www.osha.gov/SLTC/etools/hospital/hazards/mercury/mercury.html.
763. Wang, D.; Zhou, K.; Sun, M.; Fang, Z.; Liu, X.; Sun, X. Room Temperature Elemental Mercury Sensor Using MoS_2-Pani Nano-Sheet-Flowers Composite. *Anal. Methods* **2013,** *5*, 6576.
764. Friedman, A. L.; Keith Perkins, F.; Cobas, E.; Jernigan, G. G.; Campbell, P. M.; Hanbicki, A. T.; Jonker, B. T. Chemical Vapor Sensing of Two-Dimensional MoS_2 Field Effect Transistor Devices. *Solid-State Electron.* **2014,** *101*, 2-7.
765. Zonnevylle, M. C.; Hoffmann, R.; Harris, S. Thiophene Hydrodesulfurization on MoS_2; Theoretical Aspects. *Surf. Sci.* **1988,** *199*, 320-360.
766. Galvan, D. H.; Antúnez-García, J.; Moyado, S. F. Electronic Properties of $NbSe_2$ over Graphene: A Meticulous Theoretical Analysis. *OALib* **2017,** *04*, 1-9.
767. Yan, H.; Song, P.; Zhang, S.; Yang, Z.; Wang, Q. Dispersed SnO_2 Nanoparticles on MoS_2 Nanosheets for Superior Gas-Sensing Performances to Ethanol. *RSC Adv.* **2015,** *5*, 79593-79599.
768. Huo, N.; Yang, S.; Wei, Z.; Li, S. S.; Xia, J. B.; Li, J. Photoresponsive and Gas Sensing Field-Effect Transistors Based on Multilayer WS_2 Nanoflakes. *Sci. Rep.* **2014,** *4*, 5209.
769. Dwivedi, P.; Das, S.; Dhanekar, S. Wafer-Scale Synthesized MoS_2/Porous Silicon Nanostructures for Efficient and Selective Ethanol Sensing at Room Temperature. *ACS Appl. Mater. Interfaces* **2017,** *9*, 21017-21024.
770. Shur, M.; Rumyantsev, S.; Jiang, C.; Samnakay, R.; Renteria, J.; Balandin, A. A. Selective Gas Sensing with MoS_2 Thin Film Transistors. *2014 IEEE Sensors* **2014**, 55-57.
771. Samnakay, R.; Jiang, C.; Rumyantsev, S. L.; Shur, M. S.; Balandin, A. A. Selective Chemical Vapor Sensing with Few-Layer MoS_2 Thin-Film Transistors: Comparison with Graphene Devices. *Appl. Phys. Lett.* **2015,** *106*, 023115.
772. Kim, J. S.; Yoo, H. W.; Choi, H. O.; Jung, H. T. Tunable Volatile Organic Compounds Sensor by Using Thiolated Ligand Conjugation on MoS_2. *Nano Lett.* **2014,** *14*, 5941-5947.
773. Sreeprasad, T. S.; Nguyen, P.; Kim, N.; Berry, V. Controlled, Defect-Guided, Metal-Nanoparticle Incorporation onto MoS_2 via Chemical and Microwave Routes: Electrical, Thermal, and Structural Properties. *Nano Lett.* **2013,** *13*, 4434-4441.
774. Cho, S. Y.; Koh, H. J.; Yoo, H. W.; Kim, J. S.; Jung, H. T. Tunable Volatile-Organic-Compound Sensor by Using Au Nanoparticle Incorporation on MoS_2. *ACS Sens.* **2017,** *2*, 183-189.
775. Hong, X.; Liu, J.; Zheng, B.; Huang, X.; Zhang, X.; Tan, C.; Chen, J.; Fan, Z.; Zhang, H. A Universal Method for Preparation of Noble Metal Nanoparticle-Decorated Transition Metal Dichalcogenide Nanobelts. *Adv. Mater.* **2014,** *26*, 6250-6254.
776. Umar, A.; Akhtar, M. S.; Dar, G. N.; Abaker, M.; Al-Hajry, A.; Baskoutas, S. Visible-Light-Driven Photocatalytic and Chemical Sensing Properties of SnS_2 Nanoflakes. *Talanta* **2013,** *114*, 183-190.
777. Jing, Z.; Zhan, J. Fabrication and Gas-Sensing Properties of Porous ZnO Nanoplates. *Adv. Mater.* **2008,** *20*, 4547-4551.
778. Zhang, J.; Liu, X.; Wu, S.; Cao, B.; Zheng, S. One-Pot Synthesis of Au-Supported ZnO Nanoplates with Enhanced Gas Sensor Performance. *Sensors Actuators B: Chem.* **2012,** *169*, 61-66.
779. Zhang, L.; Zhao, J.; Lu, H.; Li, L.; Zheng, J.; Li, H.; Zhu, Z. Facile Synthesis and Ultrahigh Ethanol Response of Hierarchically Porous ZnO Nanosheets. *Sensors Actuators B: Chem.* **2012,** *161*, 209-215.
780. Meng, F.; Hou, N.; Ge, S.; Sun, B.; Jin, Z.; Shen, W.; Kong, L.; Guo, Z.; Sun, Y.; Wu, H.; Wang, C.; Li, M. Flower-Like Hierarchical Structures Consisting of Porous Single-Crystalline ZnO Nanosheets and Their Gas Sensing Properties to Volatile Organic Compounds (VOCs). *J. Alloys Compd.* **2015,** *626*, 124-130.

781. Li, K.-M.; Li, Y.-J.; Lu, M.-Y.; Kuo, C.-I.; Chen, L.-J. Direct Conversion of Single-Layer SnO Nanoplates to Multi-Layer SnO_2 nanoplates with Enhanced Ethanol Sensing Properties. *Adv. Funct. Mater.* **2009,** *19*, 2453-2456.
782. Sun, P.; Cao, Y.; Liu, J.; Sun, Y.; Ma, J.; Lu, G. Dispersive SnO_2 Nanosheets: Hydrothermal Synthesis and Gas-Sensing Properties. *Sensors Actuators B: Chem.* **2011,** *156*, 779-783.
783. Zhang, L.; Yin, Y. Hierarchically Mesoporous SnO_2 Nanosheets: Hydrothermal Synthesis and Highly Ethanol-Sensitive Properties Operated at Low Temperature. *Sensors Actuators B: Chem.* **2013,** *185*, 594-601.
784. Sun, P.; Zhao, W.; Cao, Y.; Guan, Y.; Sun, Y.; Lu, G. Porous SnO_2 Hierarchical Nanosheets: Hydrothermal Preparation, Growth Mechanism, and Gas Sensing Properties. *CrystEngComm* **2011,** *13*, 3718.
785. Lou, Z.; Wang, L.; Wang, R.; Fei, T.; Zhang, T. Synthesis and Ethanol Sensing Properties of SnO_2 Nanosheets via a Simple Hydrothermal Route. *Solid-State Electron.* **2012,** *76*, 91-94.
786. Guo, J.; Zhang, J.; Ju, D.; Xu, H.; Cao, B. Three-Dimensional SnO_2 Microstructures Assembled by Porous Nanosheets and Their Superior Performance for Gas Sensing. *Powder Technol.* **2013,** *250*, 40-45.
787. Zhou, Q.; Chen, W.; Li, J.; Tang, C.; Zhang, H. Nanosheet-Assembled Flower-Like SnO_2 Hierarchical Structures with Enhanced Gas-Sensing Performance. *Mater. Lett.* **2015,** *161*, 499-502.
788. Li, T.; Zeng, W.; Long, H.; Wang, Z. Nanosheet-Assembled Hierarchical SnO_2 Nanostructures for Efficient Gas-Sensing Applications. *Sensors Actuators B: Chem.* **2016,** *231*, 120-128.
789. Liu, Y.; Jiao, Y.; Zhang, Z.; Qu, F.; Umar, A.; Wu, X. Hierarchical SnO_2 Nanostructures Made of Intermingled Ultrathin Nanosheets for Environmental Remediation, Smart Gas Sensor, and Supercapacitor Applications. *ACS Appl. Mater. Interfaces* **2014,** *6*, 2174-2184.
790. Zhao, C.; Fu, J.; Zhang, Z.; Xie, E. Enhanced Ethanol Sensing Performance of Porous Ultrathin Nio Nanosheets with Neck-Connected Networks. *RSC Adv.* **2013,** *3*, 4018.
791. Wang, J.; Zeng, W.; Wang, Z. Assembly of 2D Nanosheets into 3D Flower-Like Nio: Synthesis and the Influence of Petal Thickness on Gas-Sensing Properties. *Ceram. Int.* **2016,** *42*, 4567-4573.
792. Jia, X.; Fan, H.; Yang, W. Hydrothermal Synthesis and Primary Gas Sensing Properties of CuO Nanosheets. *J. Dispersion Sci. Technol.* **2010,** *31*, 866-869.
793. Che, H.; Liu, A.; Zhang, X.; Hou, J.; Mu, J.; He, H. Two-Dimensional Nanosheets-Assembled Flower-Like Co_3O_4 Microspheres and Their Gas Sensing Performanc. *Nano* **2014,** *09*, 1450071.
794. Chen, D.; Hou, X.; Wen, H.; Wang, Y.; Wang, H.; Li, X.; Zhang, R.; Lu, H.; Xu, H.; Guan, S.; Sun, J.; Gao, L. The Enhanced Alcohol-Sensing Response of Ultrathin WO_3 Nanoplates. *Nanotechnology* **2010,** *21*, 035501.
795. Ji, F.; Ren, X.; Zheng, X.; Liu, Y.; Pang, L.; Jiang, J.; Liu, S. F. 2D -MoO_3 Nanosheets for Superior Gas Sensors. *Nanoscale* **2016,** *8*, 8696-8703.
796. Liu, C.; Lu, H.; Zhang, J.; Yang, Z.; Zhu, G.; Yin, F.; Gao, J.; Chen, C.; Xin, X. Abnormal P-Type Sensing Response of Tio 2 Nanosheets with Exposed {001} Facets. *J. Alloys Compd.* **2017,** *705*, 112-117.
797. Guo, W.; Fu, M.; Zhai, C.; Wang, Z. Hydrothermal Synthesis and Gas-Sensing Properties of Ultrathin Hexagonal ZnO Nanosheets. *Ceram. Int.* **2014,** *40*, 2295-2298.
798. Li, G.; Wang, X.; Ding, H.; Zhang, T. A Facile Synthesis Method for $Ni(OH)_2$ Ultrathin Nanosheets and Their Conversion to Porous Nio Nanosheets Used for Formaldehyde Sensing. *RSC Adv.* **2012,** *2*, 13018.
799. Zhang, Z.; Wen, Z.; Ye, Z.; Zhu, L. Gas Sensors Based on Ultrathin Porous Co_3O_4 Nanosheets to Detect Acetone at Low Temperature. *RSC Adv.* **2015,** *5*, 59976-59982.
800. Yang, C.; Xiao, F.; Wang, J.; Su, X. 3D Flower- and 2D Sheet-Like CuO Nanostructures: Microwave-Assisted Synthesis and Application in Gas Sensors. *Sensors Actuators B: Chem.* **2015,** *207*, 177-185.
801. Wan, W.; Li, Y.; Ren, X.; Zhao, Y.; Gao, F.; Zhao, H. 2D SnO_2 Nanosheets: Synthesis, Characterization, Structures, and Excellent Sensing Performance to Ethylene Glycol. *Nanomaterials* **2018,** *8*, 112.
802. Xu, J. Q.; Xue, Z. G.; Qin, N.; Cheng, Z. X.; Xiang, Q. The Crystal Facet-Dependent Gas Sensing Properties of ZnO Nanosheets: Experimental and Computational Study. *Sensors Actuators B: Chem.* **2017,** *242*, 148-157.
803. Stassen, I.; Bueken, B.; Reinsch, H.; Oudenhoven, J. F. M.; Wouters, D.; Hajek, J.; Van Speybroeck, V.; Stock, N.; Vereecken, P. M.; Van Schaijk, R.; De Vos, D.; Ameloot, R. Towards Metal–Organic Framework Based Field Effect Chemical Sensors: Uio-66-Nh2 for Nerve Agent Detection. *Chem. Sci.* **2016,** *7*, 5827-5832.
804. Hoppe, B.; Hindricks, K. D. J.; Warwas, D. P.; Schulze, H. A.; Mohmeyer, A.; Pinkvos, T. J.; Zailskas, S.; Krey, M. R.; Belke, C.; König, S.; Fröba, M.; Haug, R. J.; Behrens, P. Graphene-Like Metal–Organic Frameworks: Morphology Control, Optimization of Thin Film Electrical Conductivity and Fast Sensing Applications. *CrystEngComm* **2018**.
805. Tomer, V. K.; Thangaraj, N.; Gahlot, S.; Kailasam, K. Cubic Mesoporous Ag@Cn: A High Performance Humidity Sensor. *Nanoscale* **2016,** *8*, 19794-19803.
806. Tomer, V. K.; Duhan, S.; Sharma, A. K.; Malik, R.; Nehra, S. P.; Devi, S. One Pot Synthesis of Mesoporous ZnO–Sio 2 Nanocomposite as High Performance Humidity Sensor. *Colloids Surf. Physicochem. Eng. Aspects* **2015,** *483*, 121-128.
807. Zhang, Z.; Huang, J.; Yuan, Q.; Dong, B. Intercalated Graphitic Carbon Nitride: A Fascinating Two-Dimensional Nanomaterial for an Ultra-Sensitive Humidity Nanosensor. *Nanoscale* **2014,** *6*, 9250-9256.
808. Sajid, M.; Kim, H. B.; Lim, J. H.; Choi, K. H. Liquid-Assisted Exfoliation of 2D *h*BN Flakes and Their Dispersion in Peo to Fabricate Highly Specific and Stable Linear Humidity Sensors. *J. Mater. Chem. C* **2018,** *6*, 1421-1432.
809. Chung, Y.; Park, H.; Lee, E.; Kim, S.-H.; Kim, D.-J. Communication—Gas Sensing Behaviors of Electrophoretically Deposited Nickel Oxide Films from Morphologically Tailored Particles. *J. Electrochem. Soc.* **2016,** *163*, B624-B626.
810. Kim, H.-J.; Lee, J.-H. Highly Sensitive and Selective Gas Sensors Using P-Type Oxide Semiconductors: Overview. *Sensors Actuators B: Chem.* **2014,** *192*, 607-627.
811. Shahzad, F.; Alhabeb, M.; Hatter, C. B.; Anasori, B.; Man Hong, S.; Koo, C. M.; Gogotsi, Y. Electromagnetic Interference Shielding with 2D Transition Metal Carbides (MXenes). *Science* **2016,** *353*, 1137-1140.
812. Zhang, H.; Kulkarni, A.; Kim, H.; Woo, D.; Kim, Y.-J.; Hong, B. H.; Choi, J.-B.; Kim, T. Detection of Acetone Vapor Using Graphene on Polymer Optical Fiber. *J. Nanosci. Nanotechnol* **2011,** *11*, 5939-5943.
813. Kim, N.-H.; Choi, S.-J.; Kim, S.-J.; Cho, H.-J.; Jang, J.-S.; Koo, W.-T.; Kim, M.; Kim, I.-D. Highly Sensitive and Selective Acetone Sensing Performance of WO_3 Nanofibers Functionalized by Rh_2O_3 Nanoparticles. *Sensors Actuators B: Chem.* **2016,** *224*, 185-192.
814. Koo, W. T.; Yu, S.; Choi, S. J.; Jang, J. S.; Cheong, J. Y.; Kim, I. D. Nanoscale Pdo Catalyst Functionalized Co_3O_4 Hollow Nanocages Using MOF Templates for Selective Detection of

Acetone Molecules in Exhaled Breath. *ACS Appl. Mater. Interfaces* **2017,** *9*, 8201-8210.
815. Chen, W.; Qin, Z.; Liu, Y.; Zhang, Y.; Li, Y.; Shen, S.; Wang, Z. M.; Song, H. Z. Promotion on Acetone Sensing of Single SnO_2 Nanobelt by Eu Doping. *Nanoscale Res. Lett.* **2017,** *12*, 405.
816. Zhang, L.; Li, C.; Liu, A. R.; Shi, G. Q. Electrosynthesis of Graphene Oxide/Polypyrene Composite Films and Their Applications for Sensing Organic Vapors. *J. Mater. Chem.* **2012,** *22*, 8438-8443.
817. Zhu, C.; Xu, F.; Zhang, L.; Li, M.; Chen, J.; Xu, S.; Huang, G.; Chen, W.; Sun, L. Ultrafast Preparation of Black Phosphorus Quantum Dots for Efficient Humidity Sensing. *Chem. Eur. J.* **2016,** *22*, 7357-7362.
818. Lavine, M. S. Popping Materials and Devices from 2D into 3D. *Science* **2015,** *347*, 141-143.
819. Mauter, M. S.; Elimelech, M. Environmental Applications of Carbon-Based Nanomaterials. *Environ. Sci. Technol.* **2008,** *42*, 5843-5859.
820. Perreault, F.; Fonseca de Faria, A.; Elimelech, M. Environmental Applications of Graphene-Based Nanomaterials. *Chem. Soc. Rev.* **2015,** *44*, 5861-5896.
821. Ambrosi, A.; Chua, C. K.; Bonanni, A.; Pumera, M. Electrochemistry of Graphene and Related Materials. *Chem. Rev.* **2014,** *114*, 7150-7188.
822. Blake, P.; Brimicombe, P. D.; Nair, R. R.; Booth, T. J.; Jiang, D.; Schedin, F.; Ponomarenko, L. A.; Morozov, S. V.; Gleeson, H. F.; Hill, E. W.; Geim, A. K.; Novoselov, K. S. Graphene-Based Liquid Crystal Device. *Nano Lett.* **2008,** *8*, 1704-1708.
823. Aragay, G.; Merkoçi, A. Nanomaterials Application in Electrochemical Detection of Heavy Metals. *Electrochim. Acta* **2012,** *84*, 49-61.
824. Gong, X.; Liu, G.; Li, Y.; Yu, D. Y. W.; Teoh, W. Y. Functionalized-Graphene Composites: Fabrication and Applications in Sustainable Energy and Environment. *Chem. Mater.* **2016,** *28*, 8082-8118.
825. Gumpu, M. B.; Sethuraman, S.; Krishnan, U. M.; Rayappan, J. B. B. A Review on Detection of Heavy Metal Ions in Water – an Electrochemical Approach. *Sensors Actuators B: Chem.* **2015,** *213*, 515-533.
826. Zhu, L.; Xu, L.; Huang, B.; Jia, N.; Tan, L.; Yao, S. Simultaneous Determination of Cd(II) and Pb(II) Using Square Wave Anodic Stripping Voltammetry at a Gold Nanoparticle-Graphene-Cysteine Composite Modified Bismuth Film Electrode. *Electrochim. Acta* **2014,** *115*, 471-477.
827. Wen, Y.; Li, F. Y.; Dong, X.; Zhang, J.; Xiong, Q.; Chen, P. The Electrical Detection of Lead Ions Using Gold-Nanoparticle- and DNAzyme-Functionalized Graphene Device. *Adv Healthc Mater* **2013,** *2*, 271-274.
828. Xuan, X.; Hossain, M. F.; Park, J. Y. A Fully Integrated and Miniaturized Heavy-Metal-Detection Sensor Based on Micro-Patterned Reduced Graphene Oxide. *Sci. Rep.* **2016,** *6*, 33125.
829. Li, J.; Guo, S.; Zhai, Y.; Wang, E. High-Sensitivity Determination of Lead and Cadmium Based on the Nafion-Graphene Composite Film. *Anal. Chim. Acta* **2009,** *649*, 196-201.
830. Willemse, C. M.; Tlhomelang, K.; Jahed, N.; Baker, P. G.; Iwuoha, E. I. Metallo-Graphene Nanocomposite Electrocatalytic Platform for the Determination of Toxic Metal Ions. *Sensors* **2011,** *11*, 3970-3987.
831. Kong, N.; Liu, J.; Kong, Q.; Wang, R.; Barrow, C. J.; Yang, W. Graphene Modified Gold Electrode via π– π Stacking Interaction for Analysis of Cu^{2+} and Pb^{2+}. *Sensors Actuators B: Chem.* **2013,** *178*, 426-433.
832. Gong, X.; Bi, Y.; Zhao, Y.; Liu, G.; Teoh, W. Y. Graphene Oxide-Based Electrochemical Sensor: A Platform for Ultrasensitive Detection of Heavy Metal Ions. *RSC Adv.* **2014,** *4*, 24653-24657.
833. Zhang, Y.; Qi, M.; Liu, G. C⍰C Bonding of Graphene Oxide on 4-Aminophenyl Modified Gold Electrodes Towards Simultaneous Detection of Heavy Metal Ions. *Electroanalysis* **2015,** *27*, 1110-1118.
834. Liu, J.; Fu, S.; Yuan, B.; Li, Y.; Deng, Z. Toward a Universal "Adhesive Nanosheet" for the Assembly of Multiple Nanoparticles Based on a Protein-Induced Reduction/Decoration of Graphene Oxide. *J. Am. Chem. Soc.* **2010,** *132*, 7279-7281.
835. Williams, G.; Seger, B.; Kamat, P. V. TiO_2-Graphene Nanocomposites. UV-Assisted Photocatalytic Reduction of Graphene Oxide. *ACS Nano* **2008,** *2*, 1487-1491.
836. Gong, J.; Zhou, T.; Song, D.; Zhang, L. Monodispersed Au Nanoparticles Decorated Graphene as an Enhanced Sensing Platform for Ultrasensitive Stripping Voltammetric Detection of Mercury(II). *Sensors Actuators B: Chem.* **2010,** *150*, 491-497.
837. Wei, Y.; Gao, C.; Meng, F.-L.; Li, H.-H.; Wang, L.; Liu, J.-H.; Huang, X.-J. SnO_2/Reduced Graphene Oxide Nanocomposite for the Simultaneous Electrochemical Detection of Cadmium(II), Lead(II), Copper(II), and Mercury(II): An Interesting Favorable Mutual Interference. *J. Phys. Chem. C* **2011,** *116*, 1034-1041.
838. Park, J. W.; Park, S. J.; Kwon, O. S.; Lee, C.; Jang, J. High-Performance Hg^{2+} FET -Type Sensors Based on Reduced Graphene Oxide-Polyfuran Nanohybrids. *Analyst* **2014,** *139*, 3852-3855.
839. Zhang, Y.; Xie, J.; Liu, Y.; Pang, P.; Feng, L.; Wang, H.; Wu, Z.; Yang, W. Simple and Signal-Off Electrochemical Biosensor for Mercury(II) Based on Thymine-Mercury-Thymine Hybridization Directly on Graphene. *Electrochim. Acta* **2015,** *170*, 210-217.
840. Yu, C.; Guo, Y.; Liu, H.; Yan, N.; Xu, Z.; Yu, G.; Fang, Y.; Liu, Y. Ultrasensitive and Selective Sensing of Heavy Metal Ions with Modified Graphene. *Chem. Commun.* **2013,** *49*, 6492-6494.
841. Tan, F.; Cong, L.; Saucedo, N. M.; Gao, J.; Li, X.; Mulchandani, A. An Electrochemically Reduced Graphene Oxide Chemiresistive Sensor for Sensitive Detection of Hg^{2+} Ion in Water Samples. *J. Hazard. Mater.* **2016,** *320*, 226-233.
842. Zhang, T.; Cheng, Z.; Wang, Y.; Li, Z.; Wang, C.; Li, Y.; Fang, Y. Self-Assembled 1-Octadecanethiol Monolayers on Graphene for Mercury Detection. *Nano Lett.* **2010,** *10*, 4738-4741.
843. Afsharimani, N.; Uluutku, B.; Saygin, V.; Baykara, M. Z. Self-Assembled Molecular Films of Alkanethiols on Graphene for Heavy Metal Sensing. *J. Phys. Chem. C* **2017,** *122*, 474-480.
844. Liu, L.; Wang, C.; Wang, G. Novel Cysteic Acid/Reduced Graphene Oxide Composite Film Modified Electrode for the Selective Detection of Trace Silver Ions in Natural Waters. *Anal. Methods* **2013,** *5*, 5812.
845. Wonsawat, W.; Chuanuwatanakul, S.; Dungchai, W.; Punrat, E.; Motomizu, S.; Chailapakul, O. Graphene-Carbon Paste Electrode for Cadmium and Lead Ion Monitoring in a Flow-Based System. *Talanta* **2012,** *100*, 282-289.
846. Zhao, Z.-Q.; Chen, X.; Yang, Q.; Liu, J.-H.; Huang, X.-J. Beyond the Selective Adsorption of Polypyrrole-Reduced Graphene Oxide Nanocomposite toward Hg^{2+}: Ultra-Sensitive and -Selective Sensing Pb^{2+} by Stripping Voltammetry. *Electrochem. Commun.* **2012,** *23*, 21-24.
847. Gao, C.; Yu, X. Y.; Xu, R. X.; Liu, J. H.; Huang, X. J. Alooh-Reduced Graphene Oxide Nanocomposites: One-Pot Hydrothermal Synthesis and Their Enhanced Electrochemical Activity for Heavy Metal Ions. *ACS Appl. Mater. Interfaces* **2012,** *4*, 4672-4682.
848. Silwana, B.; van der Horst, C.; Iwuoha, E.; Somerset, V. Reduced Graphene Oxide Impregnated Antimony Nanoparticle

Sensor for Electroanalysis of Platinum Group Metals. *Electroanalysis* **2016,** *28*, 1597-1607.
849. Ziółkowski, R.; Górski, Ł.; Malinowska, E. Carboxylated Graphene as a Sensing Material for Electrochemical Uranyl Ion Detection. *Sensors Actuators B: Chem.* **2017,** *238*, 540-547.
850. Wu, Q. Y.; Lan, J. H.; Wang, C. Z.; Xiao, C. L.; Zhao, Y. L.; Wei, Y. Z.; Chai, Z. F.; Shi, W. Q. Understanding the Bonding Nature of Uranyl Ion and Functionalized Graphene: A Theoretical Study. *J. Phys. Chem. A* **2014,** *118*, 2149-2158.
851. Kumar, S.; Bhanjana, G.; Dilbaghi, N.; Kumar, R.; Umar, A. Fabrication and Characterization of Highly Sensitive and Selective Arsenic Sensor Based on Ultra-Thin Graphene Oxide Nanosheets. *Sensors Actuators B: Chem.* **2016,** *227*, 29-34.
852. Li, F.; Ye, J.; Zhou, M.; Gan, S.; Zhang, Q.; Han, D.; Niu, L. All-Solid-State Potassium-Selective Electrode Using Graphene as the Solid Contact. *Analyst* **2012,** *137*, 618-623.
853. Dutta, J. C. In *Ion Sensitive Field Effect Transistor for Applications in Bioelectronic Sensors: A Research Review*, 2012 2nd National Conference on Computational Intelligence and Signal Processing (CISP), 2012; pp 185-191.
854. Patil, A. V.; Fernandes, F. B.; Bueno, P. R.; Davis, J. J. Graphene-Based Protein Biomarker Detection. *Bioanalysis* **2015,** *7*, 725-742.
855. Fu, W.; Jiang, L.; van Geest, E. P.; Lima, L. M.; Schneider, G. F. Sensing at the Surface of Graphene Field-Effect Transistors. *Adv. Mater.* **2017,** *29*, 1603610.
856. Fu, W.; Nef, C.; Tarasov, A.; Wipf, M.; Stoop, R.; Knopfmacher, O.; Weiss, M.; Calame, M.; Schonenberger, C. High Mobility Graphene Ion-Sensitive Field-Effect Transistors by Noncovalent Functionalization. *Nanoscale* **2013,** *5*, 12104-12110.
857. Dankerl, M.; Hauf, M. V.; Lippert, A.; Hess, L. H.; Birner, S.; Sharp, I. D.; Mahmood, A.; Mallet, P.; Veuillen, J.-Y.; Stutzmann, M.; Garrido, J. A. Graphene Solution-Gated Field-Effect Transistor Array for Sensing Applications. *Adv. Funct. Mater.* **2010,** *20*, 3117-3124.
858. Zhan, B.; Li, C.; Yang, J.; Jenkins, G.; Huang, W.; Dong, X. Graphene Field-Effect Transistor and Its Application for Electronic Sensing. *Small* **2014,** *10*, 4042-4065.
859. Li, H.; Zhu, Y.; Islam, M. S.; Rahman, M. A.; Walsh, K. B.; Koley, G. Graphene Field Effect Transistors for Highly Sensitive and Selective Detection of K^+ Ions. *Sensors Actuators B: Chem.* **2017,** *253*, 759-765.
860. Mao, S.; Pu, H.; Chang, J.; Sui, X.; Zhou, G.; Ren, R.; Chen, Y.; Chen, J. Ultrasensitive Detection of Orthophosphate Ions with Reduced Graphene Oxide/Ferritin Field-Effect Transistor Sensors. *Environmental Science: Nano* **2017,** *4*, 856-863.
861. Sudibya, H. G.; He, Q.; Zhang, H.; Chen, P. Electrical Detection of Metal Ions Using Field-Effect Transistors Based on Micropatterned Reduced Graphene Oxide Films. *ACS Nano* **2011,** *5*, 1990-1994.
862. Sofue, Y.; Ohno, Y.; Maehashi, K.; Inoue, K.; Matsumoto, K. Highly Sensitive Electrical Detection of Sodium Ions Based on Graphene Field-Effect Transistors. *Jpn. J. Appl. Phys.* **2011,** *50*, 06GE07.
863. Liu, X.; Ye, C.; Li, X.; Cui, N.; Wu, T.; Du, S.; Wei, Q.; Fu, L.; Yin, J.; Lin, C. T. Highly Sensitive and Selective Potassium Ion Detection Based on Graphene Hall Effect Biosensors. *Materials* **2018,** *11*, 399.
864. Du, Y.; Liu, H.; Deng, Y.; Ye, P. D. Device Perspective for Black Phosphorus Field-Effect Transistors: Contact Resistance, Ambipolar Behavior, and Scaling. *ACS Nano* **2014,** *8*, 10035-10042.
865. Xia, F.; Wang, H.; Jia, Y. Rediscovering Black Phosphorus as an Anisotropic Layered Material for Optoelectronics and Electronics. *Nat. Commun.* **2014,** *5*, 4458.
866. Saito, Y.; Iwasa, Y. Ambipolar Insulator-to-Metal Transition in Black Phosphorus by Ionic-Liquid Gating. *ACS Nano* **2015,** *9*, 3192-3198.
867. Koenig, S. P.; Doganov, R. A.; Schmidt, H.; Castro Neto, A. H.; Özyilmaz, B. Electric Field Effect in Ultrathin Black Phosphorus. *Appl. Phys. Lett.* **2014,** *104*, 103106.
868. Li, P.; Zhang, D.; Liu, J.; Chang, H.; Sun, Y.; Yin, N. Air-Stable Black Phosphorus Devices for Ion Sensing. *ACS Appl. Mater. Interfaces* **2015,** *7*, 24396-24402.
869. Kou, L.; Fu, M.; Liang, R. Solid-Contact Ca^{2+}-Selective Electrodes Based on Two-Dimensional Black Phosphorus as Ion-to-Electron Transducers. *RSC Adv.* **2017,** *7*, 43905-43908.
870. Li, P.; Zhang, D.; Wu, J.; Cao, Y.; Wu, Z. Flexible Integrated Black Phosphorus Sensor Arrays for High Performance Ion Sensing. *Sensors Actuators B: Chem.* **2018,** *273*, 358-364.
871. Ping, J.; Fan, Z.; Sindoro, M.; Ying, Y.; Zhang, H. Recent Advances in Sensing Applications of Two-Dimensional Transition Metal Dichalcogenide Nanosheets and Their Composites. *Adv. Funct. Mater.* **2017,** *27*, 1605817.
872. Zhou, G.; Chang, J.; Pu, H.; Shi, K.; Mao, S.; Sui, X.; Ren, R.; Cui, S.; Chen, J. Ultrasensitive Mercury Ion Detection Using DNA-Functionalized Molybdenum Disulfide Nanosheet/Gold Nanoparticle Hybrid Field-Effect Transistor Device. *ACS Sens.* **2016,** *1*, 295-302.
873. Jiang, S.; Cheng, R.; Ng, R.; Huang, Y.; Duan, X. Highly Sensitive Detection of Mercury(II) Ions with Few-Layer Molybdenum Disulfide. *Nano Res.* **2015,** *8*, 257-262.
874. Ghanei-Motlagh, M.; Taher, M. A. A Novel Electrochemical Sensor Based on Silver/Halloysite Nanotube/Molybdenum Disulfide Nanocomposite for Efficient Nitrite Sensing. *Biosens. Bioelectron.* **2018,** *109*, 279-285.
875. Waheed, A.; Mansha, M.; Ullah, N. Nanomaterials-Based Electrochemical Detection of Heavy Metals in Water: Current Status, Challenges and Future Direction. *TrAC, Trends Anal. Chem.* **2018,** *105*, 37-51.
876. Liu, Z.-G.; Chen, X.; Liu, J.-H.; Huang, X.-J. Well-Arranged Porous Co_3O_4 Microsheets for Electrochemistry of Pb(II) Revealed by Stripping Voltammetry. *Electrochem. Commun.* **2013,** *30*, 59-62.
877. Yu, L.; Zhang, P.; Dai, H.; Chen, L.; Ma, H.; Lin, M.; Shen, D. An Electrochemical Sensor Based on Co_3O_4 Nanosheets for Lead Ions Determination. *RSC Adv.* **2017,** *7*, 39611-39616.
878. Zhang, J.; Liao, J.; Yang, F.; Xu, M.; Lin, S. Regulation of the Electroanalytical Performance of Ultrathin Titanium Dioxide Nanosheets toward Lead Ions by Non-Metal Doping. *Nanomaterials* **2017,** *7*, 327.
879. Mendecki, L.; Mirica, K. A. Conductive Metal-Organic Frameworks as Ion-to-Electron Transducers in Potentiometric Sensors. *ACS Appl. Mater. Interfaces* **2018,** *10*, 19248-19257.
880. Chen, Y.; Tan, C.; Zhang, H.; Wang, L. Two-Dimensional Graphene Analogues for Biomedical Applications. *Chem. Soc. Rev.* **2015,** *44*, 2681-2701.
881. Chimene, D.; Alge, D. L.; Gaharwar, A. K. Two-Dimensional Nanomaterials for Biomedical Applications: Emerging Trends and Future Prospects. *Adv. Mater.* **2015,** *27*, 7261-7284.
882. Khin, M. M.; Nair, A. S.; Babu, V. J.; Murugan, R.; Ramakrishna, S. A Review on Nanomaterials for Environmental Remediation. *Energy Environ. Sci* **2012,** *5*, 8075-8109.
883. Roy, S.; Soin, N.; Bajpai, R.; Misra, D. S.; McLaughlin, J. A.; Roy, S. S. Graphene Oxide for Electrochemical Sensing Applications. *J. Mater. Chem.* **2011,** *21*, 14725.
884. Kang, X.; Wang, J.; Wu, H.; Aksay, I. A.; Liu, J.; Lin, Y. Glucose Oxidase-Graphene-Chitosan Modified Electrode for Direct Electrochemistry and Glucose Sensing. *Biosens. Bioelectron.* **2009,** *25*, 901-905.

885. Wang, Y.; Shao, Y.; Matson, D. W.; Li, J.; Lin, Y. Nitrogen-Doped Graphene and Its Application in Electrochemical Biosensing. *ACS Nano* **2010,** *4*, 1790-1798.
886. Alwarappan, S.; Liu, C.; Kumar, A.; Li, C.-Z. Enzyme-Doped Graphene Nanosheets for Enhanced Glucose Biosensing. *J. Phys. Chem. C* **2010,** *114*, 12920-12924.
887. Zeng, G.; Xing, Y.; Gao, J.; Wang, Z.; Zhang, X. Unconventional Layer-by-Layer Assembly of Graphene Multilayer Films for Enzyme-Based Glucose and Maltose Biosensing. *Langmuir* **2010,** *26*, 15022-15026.
888. Shan, C.; Yang, H.; Song, J.; Han, D.; Ivaska, A.; Niu, L. Direct Electrochemistry of Glucose Oxidase and Biosensing for Glucose Based on Graphene. *Anal. Chem.* **2009,** *81*, 2378-2382.
889. Chen, Y.; Li, Y.; Sun, D.; Tian, D.; Zhang, J.; Zhu, J.-J. Fabrication of Gold Nanoparticles on Bilayer Graphene for Glucose Electrochemical Biosensing. *J. Mater. Chem.* **2011,** *21*, 7604.
890. Zheng, J.; He, Y.; Sheng, Q.; Zhang, H. DNA as a Linker for Biocatalytic Deposition of Au Nanoparticles on Graphene and Its Application in Glucose Detection. *J. Mater. Chem.* **2011,** *21*, 12873.
891. Zeng, Q.; Cheng, J. S.; Liu, X. F.; Bai, H. T.; Jiang, J. H. Palladium Nanoparticle/Chitosan-Grafted Graphene Nanocomposites for Construction of a Glucose Biosensor. *Biosens. Bioelectron.* **2011,** *26*, 3456-3463.
892. Lu, W.; Luo, Y.; Chang, G.; Sun, X. Synthesis of Functional SiO_2-Coated Graphene Oxide Nanosheets Decorated with Ag Nanoparticles for H_2O_2 and Glucose Detection. *Biosens. Bioelectron.* **2011,** *26*, 4791-4797.
893. Wu, H.; Wang, J.; Kang, X.; Wang, C.; Wang, D.; Liu, J.; Aksay, I. A.; Lin, Y. Glucose Biosensor Based on Immobilization of Glucose Oxidase in Platinum Nanoparticles/Graphene/Chitosan Nanocomposite Film. *Talanta* **2009,** *80*, 403-406.
894. Kim, J.; Kim, M.; Lee, M. S.; Kim, K.; Ji, S.; Kim, Y. T.; Park, J.; Na, K.; Bae, K. H.; Kyun Kim, H.; Bien, F.; Young Lee, C.; Park, J. U. Wearable Smart Sensor Systems Integrated on Soft Contact Lenses for Wireless Ocular Diagnostics. *Nat. Commun.* **2017,** *8*, 14997.
895. Bohunicky, B.; Mousa, S. A. Biosensors: The New Wave in Cancer Diagnosis. *Nanotechnol. Sci. Appl.* **2010,** *4*, 1-10.
896. Yang, J.; Lin, Q.; Yin, W.; Jiang, T.; Zhao, D.; Jiang, L. A Novel Nonenzymatic Glucose Sensor Based on Functionalized Pdda-Graphene/CuO Nanocomposites. *Sensors Actuators B: Chem.* **2017,** *253*, 1087-1095.
897. Liu, S.; Wang, Z.; Wang, F.; Yu, B.; Zhang, T. High Surface Area Mesoporous CuO: A High-Performance Electrocatalyst for Non-Enzymatic Glucose Biosensing. *RSC Adv.* **2014,** *4*, 33327-33331.
898. Yan, X.; Gu, Y.; Li, C.; Zheng, B.; Li, Y.; Zhang, T.; Zhang, Z.; Yang, M. A Non-Enzymatic Glucose Sensor Based on the Cus Nanoflakes–Reduced Graphene Oxide Nanocomposite. *Anal. Methods* **2018,** *10*, 381-388.
899. Gao, H.; Xiao, F.; Ching, C. B.; Duan, H. One-Step Electrochemical Synthesis of PtNi Nanoparticle-Graphene Nanocomposites for Nonenzymatic Amperometric Glucose Detection. *ACS Appl. Mater. Interfaces* **2011,** *3*, 3049-3057.
900. Zhu, X.; Jiao, Q.; Zhang, C.; Zuo, X.; Xiao, X.; Liang, Y.; Nan, J. Amperometric Nonenzymatic Determination of Glucose Based on a Glassy Carbon Electrode Modified with Nickel(II) Oxides and Graphene. *Microchimica Acta* **2013,** *180*, 477-483.
901. Dong, X. C.; Xu, H.; Wang, X. W.; Huang, Y. X.; Chan-Park, M. B.; Zhang, H.; Wang, L. H.; Huang, W.; Chen, P. 3D Graphene-Cobalt Oxide Electrode for High-Performance Supercapacitor and Enzymeless Glucose Detection. *ACS Nano* **2012,** *6*, 3206-3213.
902. Wu, G. H.; Song, X. H.; Wu, Y. F.; Chen, X. M.; Luo, F.; Chen, X. Non-Enzymatic Electrochemical Glucose Sensor Based on Platinum Nanoflowers Supported on Graphene Oxide. *Talanta* **2013,** *105*, 379-385.
903. Lu, L. M.; Li, H. B.; Qu, F.; Zhang, X. B.; Shen, G. L.; Yu, R. Q. In Situ Synthesis of Palladium Nanoparticle-Graphene Nanohybrids and Their Application in Nonenzymatic Glucose Biosensors. *Biosens. Bioelectron.* **2011,** *26*, 3500-3504.
904. Shin, D. H.; Kim, W.; Jun, J.; Lee, J. S.; Kim, J. H.; Jang, J. Highly Selective FET-Type Glucose Sensor Based on Shape-Controlled Palladium Nanoflower-Decorated Graphene. *Sensors Actuators B: Chem.* **2018,** *264*, 216-223.
905. Beaulieu, J. M.; Gainetdinov, R. R. The Physiology, Signaling, and Pharmacology of Dopamine Receptors. *Pharmacol. Rev.* **2011,** *63*, 182-217.
906. Jackowska, K.; Krysinski, P. New Trends in the Electrochemical Sensing of Dopamine. *Anal. Bioanal. Chem.* **2013,** *405*, 3753-3771.
907. McCreery, R. L. Advanced Carbon Electrode Materials for Molecular Electrochemistry. *Chem. Rev.* **2008,** *108*, 2646-2687.
908. Shang, N. G.; Papakonstantinou, P.; McMullan, M.; Chu, M.; Stamboulis, A.; Potenza, A.; Dhesi, S. S.; Marchetto, H. Catalyst-Free Efficient Growth, Orientation and Biosensing Properties of Multilayer Graphene Nanoflake Films with Sharp Edge Planes. *Adv. Funct. Mater.* **2008,** *18*, 3506-3514.
909. Wang, Y.; Li, Y.; Tang, L.; Lu, J.; Li, J. Application of Graphene-Modified Electrode for Selective Detection of Dopamine. *Electrochem. Commun.* **2009,** *11*, 889-892.
910. Hou, S.; Kasner, M. L.; Su, S.; Patel, K.; Cuellari, R. Highly Sensitive and Selective Dopamine Biosensor Fabricated with Silanized Graphene. *J. Phys. Chem. C* **2010,** *114*, 14915-14921.
911. Tan, L.; Zhou, K.-G.; Zhang, Y.-H.; Wang, H.-X.; Wang, X.-D.; Guo, Y.-F.; Zhang, H.-L. Nanomolar Detection of Dopamine in the Presence of Ascorbic Acid at β-Cyclodextrin/Graphene Nanocomposite Platform. *Electrochem. Commun.* **2010,** *12*, 557-560.
912. Liu, Q.; Zhu, X.; Huo, Z.; He, X.; Liang, Y.; Xu, M. Electrochemical Detection of Dopamine in the Presence of Ascorbic Acid Using Pvp/Graphene Modified Electrodes. *Talanta* **2012,** *97*, 557-562.
913. Li, S.-J.; He, J.-Z.; Zhang, M.-J.; Zhang, R.-X.; Lv, X.-L.; Li, S.-H.; Pang, H. Electrochemical Detection of Dopamine Using Water-Soluble Sulfonated Graphene. *Electrochim. Acta* **2013,** *102*, 58-65.
914. Teymourian, H.; Salimi, A.; Khezrian, S. Fe_3O_4 Magnetic Nanoparticles/Reduced Graphene Oxide Nanosheets as a Novel Electrochemical and Bioeletrochemical Sensing Platform. *Biosens. Bioelectron.* **2013,** *49*, 1-8.
915. Palanisamy, S.; Ku, S.; Chen, S.-M. Dopamine Sensor Based on a Glassy Carbon Electrode Modified with a Reduced Graphene Oxide and Palladium Nanoparticles Composite. *Microchimica Acta* **2013,** *180*, 1037-1042.
916. Wang, Y.; Peng, W.; Liu, L.; Tang, M.; Gao, F.; Li, M. Enhanced Conductivity of a Glassy Carbon Electrode Modified with a Graphene-Doped Film of Layered Double Hydroxides for Selectively Sensing of Dopamine. *Microchimica Acta* **2011,** *174*, 41-46.
917. Cui, X.; Fang, X.; Zhao, H.; Li, Z.; Ren, H. An Electrochemical Sensor for Dopamine Based on Polydopamine Modified Reduced Graphene Oxide Anchored with Tin Dioxide and Gold Nanoparticles. *Anal. Methods* **2017,** *9*, 5322-5332.
918. Jin, H.; Zhao, C.; Gui, R.; Gao, X.; Wang, Z. Reduced Graphene Oxide/Nile Blue/Gold Nanoparticles Complex-Modified Glassy Carbon Electrode Used as a Sensitive and

Label-Free Aptasensor for Ratiometric Electrochemical Sensing of Dopamine. *Anal. Chim. Acta* **2018,** *1025*, 154-162.
919. Duarte, T. L.; Lunec, J. Review: When Is an Antioxidant Not an Antioxidant? A Review of Novel Actions and Reactions of Vitamin C. *Free Radic. Res.* **2005,** *39*, 671-686.
920. Brownson, D. A. C.; Munro, L. J.; Kampouris, D. K.; Banks, C. E. Electrochemistry of Graphene: Not Such a Beneficial Electrode Material? *RSC Adv.* **2011,** *1*, 978.
921. Keeley, G. P.; O'Neill, A.; McEvoy, N.; Peltekis, N.; Coleman, J. N.; Duesberg, G. S. Electrochemical Ascorbic Acid Sensor Based on Dmf-Exfoliated Graphene. *J. Mater. Chem.* **2010,** *20*, 7864.
922. Hong, W.; Bai, H.; Xu, Y.; Yao, Z.; Gu, Z.; Shi, G. Preparation of Gold Nanoparticle/Graphene Composites with Controlled Weight Contents and Their Application in Biosensors. *J. Phys. Chem. C* **2010,** *114*, 1822-1826.
923. Dietschy, J. M.; Turley, S. D. Thematic Review Series: Brain Lipids. Cholesterol Metabolism in the Central Nervous System During Early Development and in the Mature Animal. *J. Lipid Res.* **2004,** *45*, 1375-1397.
924. Agnihotri, N.; Chowdhury, A. D.; De, A. Non-Enzymatic Electrochemical Detection of Cholesterol Using β-Cyclodextrin Functionalized Graphene. *Biosens. Bioelectron.* **2015,** *63*, 212-217.
925. Cao, S.; Zhang, L.; Chai, Y.; Yuan, R. An Integrated Sensing System for Detection of Cholesterol Based on TiO_2-Graphene-Pt-Pd Hybrid Nanocomposites. *Biosens. Bioelectron.* **2013,** *42*, 532-538.
926. Dey, R. S.; Raj, C. R. Development of an Amperometric Cholesterol Biosensor Based on Graphene−Pt Nanoparticle Hybrid Material. *J. Phys. Chem. C* **2010,** *114*, 21427-21433.
927. Radoi, A.; Compagnone, D. Recent Advances in NADH Electrochemical Sensing Design. *Bioelectrochemistry* **2009,** *76*, 126-134.
928. Govindhan, M.; Amiri, M.; Chen, A. Au Nanoparticle/Graphene Nanocomposite as a Platform for the Sensitive Detection of NADH in Human Urine. *Biosens. Bioelectron.* **2015,** *66*, 474-480.
929. Tabrizi, M. A.; Zand, Z. A Facile One-Step Method for the Synthesis of Reduced Graphene Oxide Nanocomposites by NADH as Reducing Agent and Its Application in NADH Sensing. *Electroanalysis* **2014,** *26*, 171-177.
930. Li, Z.; Huang, Y.; Chen, L.; Qin, X.; Huang, Z.; Zhou, Y.; Meng, Y.; Li, J.; Huang, S.; Liu, Y.; Wang, W.; Xie, Q.; Yao, S. Amperometric Biosensor for NADH and Ethanol Based on Electroreduced Graphene Oxide–Polythionine Nanocomposite Film. *Sensors Actuators B: Chem.* **2013,** *181*, 280-287.
931. Li, Z.; Su, W.; Liu, S.; Ding, X. An Electrochemical Biosensor Based on DNA Tetrahedron/Graphene Composite Film for Highly Sensitive Detection of NADH. *Biosens. Bioelectron.* **2015,** *69*, 287-293.
932. Jones, C. W., *Applications of Hydrogen Peroxide and Derivatives*. 1999; Vol. 122, p 6339-6340.
933. Xu, H.; Dai, H.; Chen, G. Direct Electrochemistry and Electrocatalysis of Hemoglobin Protein Entrapped in Graphene and Chitosan Composite Film. *Talanta* **2010,** *81*, 334-338.
934. Lu, Q.; Dong, X.; Li, L. J.; Hu, X. Direct Electrochemistry-Based Hydrogen Peroxide Biosensor Formed from Single-Layer Graphene Nanoplatelet-Enzyme Composite Film. *Talanta* **2010,** *82*, 1344-1348.
935. Zeng, Q.; Cheng, J.; Tang, L.; Liu, X.; Liu, Y.; Li, J.; Jiang, J. Self-Assembled Graphene-Enzyme Hierarchical Nanostructures for Electrochemical Biosensing. *Adv. Funct. Mater.* **2010,** *20*, 3366-3372.
936. Zhou, Y.; Liu, S.; Jiang, H.-J.; Yang, H.; Chen, H.-Y. Direct Electrochemistry and Bioelectrocatalysis of Microperoxidase-11 Immobilized on Chitosan-Graphene Nanocomposite. *Electroanalysis* **2010,** *22*, 1323-1328.
937. Guo, S.; Wen, D.; Zhai, Y.; Dong, S.; Wang, E. Platinum Nanoparticle Ensemble-on-Graphene Hybrid Nanosheet: One-Pot, Rapid Synthesis, and Used as New Electrode Material for Electrochemical Sensing. *ACS Nano* **2010,** *4*, 3959-3968.
938. Cao, L.; Liu, Y.; Zhang, B.; Lu, L. In Situ Controllable Growth of Prussian Blue Nanocubes on Reduced Graphene Oxide: Facile Synthesis and Their Application as Enhanced Nanoelectrocatalyst for H_2O_2 Reduction. *ACS Appl. Mater. Interfaces* **2010,** *2*, 2339-2346.
939. Sun, Y.; Luo, M.; Qin, Y.; Zhu, S.; Li, Y.; Xu, N.; Meng, X.; Ren, Q.; Wang, L.; Guo, S. Atomic-Thick PtNi Nanowires Assembled on Graphene for High-Sensitivity Extracellular Hydrogen Peroxide Sensors. *ACS Appl. Mater. Interfaces* **2017,** *9*, 34715-34721.
940. Rani, G. P. J.; Saravanan, J.; Sheet, S.; Rajan, M. A. J.; Lee, Y. S.; Balasubramani, A.; kumar, G. G. The Sensitive and Selective Enzyme-Free Electrochemical H_2O_2 Sensor Based on rGO/$MnFe_2O_4$ Nanocomposite. *Electrocatalysis* **2017,** *9*, 102-112.
941. Long, F.; Zhang, Z.; Wang, J.; Yan, L.; Zhou, B. Cobalt-Nickel Bimetallic Nanoparticles Decorated Graphene Sensitized Imprinted Electrochemical Sensor for Determination of Octylphenol. *Electrochim. Acta* **2015,** *168*, 337-345.
942. Oliveira, T. M.; Barroso, M. F.; Morais, S.; Araujo, M.; Freire, C.; de Lima-Neto, P.; Correia, A. N.; Oliveira, M. B.; Delerue-Matos, C. Sensitive Bi-Enzymatic Biosensor Based on Polyphenoloxidases-Gold Nanoparticles-Chitosan Hybrid Film-Graphene Doped Carbon Paste Electrode for Carbamates Detection. *Bioelectrochemistry* **2014,** *98*, 20-29.
943. Khoo, W. Y.; Pumera, M.; Bonanni, A. Graphene Platforms for the Detection of Caffeine in Real Samples. *Anal. Chim. Acta* **2013,** *804*, 92-97.
944. Liu, J.; Cao, Z.; Lu, Y. Functional Nucleic Acid Sensors. *Chem. Rev.* **2009,** *109*, 1948-1998.
945. Huang, K. J.; Niu, D. J.; Sun, J. Y.; Han, C. H.; Wu, Z. W.; Li, Y. L.; Xiong, X. Q. Novel Electrochemical Sensor Based on Functionalized Graphene for Simultaneous Determination of Adenine and Guanine in DNA. *Colloids Surf. B. Biointerfaces* **2011,** *82*, 543-549.
946. Muti, M.; Sharma, S.; Erdem, A.; Papakonstantinou, P. Electrochemical Monitoring of Nucleic Acid Hybridization by Single-Use Graphene Oxide-Based Sensor. *Electroanalysis* **2011,** *23*, 272-279.
947. Yin, H.; Zhou, Y.; Ma, Q.; Ai, S.; Chen, Q.; Zhu, L. Electrocatalytic Oxidation Behavior of Guanosine at Graphene, Chitosan and Fe_3O_4 Nanoparticles Modified Glassy Carbon Electrode and Its Determination. *Talanta* **2010,** *82*, 1193-1199.
948. Du, M.; Yang, T.; Jiao, K. Immobilization-Free Direct Electrochemical Detection for DNA Specific Sequences Based on Electrochemically Converted Gold Nanoparticles/Graphene Composite Film. *J. Mater. Chem.* **2010,** *20*, 9253.
949. Gao, Y. S.; Xu, J. K.; Lu, L. M.; Wu, L. P.; Zhang, K. X.; Nie, T.; Zhu, X. F.; Wu, Y. Overoxidized Polypyrrole/Graphene Nanocomposite with Good Electrochemical Performance as Novel Electrode Material for the Detection of Adenine and Guanine. *Biosens. Bioelectron.* **2014,** *62*, 261-267.
950. Ambrosi, A.; Pumera, M. Stacked Graphene Nanofibers for Electrochemical Oxidation of DNA Bases. *Phys. Chem. Chem. Phys.* **2010,** *12*, 8943-8947.
951. Lim, C. X.; Hoh, H. Y.; Ang, P. K.; Loh, K. P. Direct Voltammetric Detection of DNA and pH Sensing on Epitaxial Graphene: An Insight into the Role of Oxygenated Defects. *Anal. Chem.* **2010,** *82*, 7387-7393.

952. Akhavan, O.; Ghaderi, E.; Rahighi, R. Toward Single-DNA Electrochemical Biosensing by Graphene Nanowalls. *ACS Nano* **2012,** *6*, 2904-2916.
953. Chu, Y.; Cai, B.; Ma, Y.; Zhao, M.; Ye, Z.; Huang, J. Highly Sensitive Electrochemical Detection of Circulating Tumor DNA Based on Thin-Layer MoS_2/Graphene Composites. *RSC Adv.* **2016,** *6*, 22673-22678.
954. Tran, H. V.; Piro, B.; Reisberg, S.; Huy Nguyen, L.; Dung Nguyen, T.; Duc, H. T.; Pham, M. C. An Electrochemical Elisa-Like Immunosensor for Mirnas Detection Based on Screen-Printed Gold Electrodes Modified with Reduced Graphene Oxide and Carbon Nanotubes. *Biosens. Bioelectron.* **2014,** *62*, 25-30.
955. Tran, H. V.; Piro, B.; Reisberg, S.; Duc, H. T.; Pham, M. C. Antibodies Directed to Rna/DNA Hybrids: An Electrochemical Immunosensor for Micrornas Detection Using Graphene-Composite Electrodes. *Anal. Chem.* **2013,** *85*, 8469-8474.
956. Liu, A. L.; Zhong, G. X.; Chen, J. Y.; Weng, S. H.; Huang, H. N.; Chen, W.; Lin, L. Q.; Lei, Y.; Fu, F. H.; Sun, Z. L.; Lin, X. H.; Lin, J. H.; Yang, S. Y. A Sandwich-Type DNA Biosensor Based on Electrochemical Co-Reduction Synthesis of Graphene-Three Dimensional Nanostructure Gold Nanocomposite Films. *Anal. Chim. Acta* **2013,** *767*, 50-58.
957. Niu, S.; Sun, J.; Nan, C.; Lin, J. Sensitive DNA Biosensor Improved by 1,10-Phenanthroline Cobalt Complex as Indicator Based on the Electrode Modified by Gold Nanoparticles and Graphene. *Sensors Actuators B: Chem.* **2013,** *176*, 58-63.
958. Bonanni, A.; Chua, C. K.; Zhao, G.; Sofer, Z.; Pumera, M. Inherently Electroactive Graphene Oxide Nanoplatelets as Labels for Single Nucleotide Polymorphism Detection. *ACS Nano* **2012,** *6*, 8546-8551.
959. Ping, J.; Vishnubhotla, R.; Vrudhula, A.; Johnson, A. T. Scalable Production of High-Sensitivity, Label-Free DNA Biosensors Based on Back-Gated Graphene Field Effect Transistors. *ACS Nano* **2016,** *10*, 8700-8704.
960. Dong, H.; Zhu, Z.; Ju, H.; Yan, F. Triplex Signal Amplification for Electrochemical DNA Biosensing by Coupling Probe-Gold Nanoparticles-Graphene Modified Electrode with Enzyme Functionalized Carbon Sphere as Tracer. *Biosens. Bioelectron.* **2012,** *33*, 228-232.
961. Benvidi, A.; Firouzabadi, A. D.; Moshtaghiun, S. M.; Mazloum-Ardakani, M.; Tezerjani, M. D. Ultrasensitive DNA Sensor Based on Gold Nanoparticles/Reduced Graphene Oxide/Glassy Carbon Electrode. *Anal. Biochem.* **2015,** *484*, 24-30.
962. Zhang, S.; Huang, N.; Lu, Q.; Liu, M.; Li, H.; Zhang, Y.; Yao, S. A Double Signal Electrochemical Human Immunoglobulin G Immunosensor Based on Gold Nanoparticles-Polydopamine Functionalized Reduced Graphene Oxide as a Sensor Platform and Agnps/Carbon Nanocomposite as Signal Probe and Catalytic Substrate. *Biosens. Bioelectron.* **2016,** *77*, 1078-1085.
963. Su, B.; Tang, J.; Huang, J.; Yang, H.; Qiu, B.; Chen, G.; Tang, D. Graphene and Nanogold-Functionalized Immunosensing Interface with Enhanced Sensitivity for One-Step Electrochemical Immunoassay of α-Fetoprotein in Human Serum. *Electroanalysis* **2010,** *22*, 2720-2728.
964. Yang, T. T.; Jia, H. Y.; Liu, Z.; Qiu, X. L.; Gao, Y. S.; Xu, J. K.; Lu, L. M.; Yu, Y. F. Label-Free Electrochemical Immunoassay for α-Fetoprotein Based on a Redox Matrix of Prussian Blue-Reduced Graphene Oxide/Gold Nanoparticles-Poly(3, 4-Ethylenedioxythiophene) Composite. *J. Electroanal. Chem.* **2017,** *799*, 625-633.
965. Wei, Q.; Mao, K.; Wu, D.; Dai, Y.; Yang, J.; Du, B.; Yang, M.; Li, H. A Novel Label-Free Electrochemical Immunosensor Based on Graphene and Thionine Nanocomposite. *Sensors Actuators B: Chem.* **2010,** *149*, 314-318.
966. Zhou, L.; Mao, H.; Wu, C.; Tang, L.; Wu, Z.; Sun, H.; Zhang, H.; Zhou, H.; Jia, C.; Jin, Q.; Chen, X.; Zhao, J. Label-Free Graphene Biosensor Targeting Cancer Molecules Based on Non-Covalent Modification. *Biosens. Bioelectron.* **2017,** *87*, 701-707.
967. Hou, L.; Cui, Y.; Xu, M.; Gao, Z.; Huang, J.; Tang, D. Graphene Oxide-Labeled Sandwich-Type Impedimetric Immunoassay with Sensitive Enhancement Based on Enzymatic 4-Chloro-1-Naphthol Oxidation. *Biosens. Bioelectron.* **2013,** *47*, 149-156.
968. Yang, G.; Li, L.; Rana, R. K.; Zhu, J.-J. Assembled Gold Nanoparticles on Nitrogen-Doped Graphene for Ultrasensitive Electrochemical Detection of Matrix Metalloproteinase-2. *Carbon* **2013,** *61*, 357-366.
969. Chen, H.; Zhang, J.; Gao, Y.; Liu, S.; Koh, K.; Zhu, X.; Yin, Y. Sensitive Cell Apoptosis Assay Based on Caspase-3 Activity Detection with Graphene Oxide-Assisted Electrochemical Signal Amplification. *Biosens. Bioelectron.* **2015,** *68*, 777-782.
970. Ali, M. A.; Singh, C.; Mondal, K.; Srivastava, S.; Sharma, A.; Malhotra, B. D. Mesoporous Few-Layer Graphene Platform for Affinity Biosensing Application. *ACS Appl. Mater. Interfaces* **2016,** *8*, 7646-7656.
971. Ateş, A. K.; Er, E.; Çelikkan, H.; Erk, N. Reduced Graphene Oxide/Platinum Nanoparticles/Nafion Nanocomposite as a Novel 2D Electrochemical Sensor for Voltammetric Determination of Aliskiren. *New J. Chem.* **2017,** *41*, 15320-15326.
972. Er, E.; Çelikkan, H.; Erk, N. An Ultra-Sensitive 2D Electrochemical Sensor Based on a Ptnps@Graphene/Nafion Nanocomposite for Determination of A1-Ar Antagonist Silodosin in Human Plasma. *Anal. Methods* **2017,** *9*, 3782-3789.
973. Loo, A. H.; Bonanni, A.; Pumera, M. Thrombin Aptasensing with Inherently Electroactive Graphene Oxide Nanoplatelets as Labels. *Nanoscale* **2013,** *5*, 4758-4762.
974. Saltzgaber, G.; Wojcik, P.; Sharf, T.; Leyden, M. R.; Wardini, J. L.; Heist, C. A.; Adenuga, A. A.; Remcho, V. T.; Minot, E. D. Scalable Graphene Field-Effect Sensors for Specific Protein Detection. *Nanotechnology* **2013,** *24*, 355502.
975. Feng, L.; Chen, Y.; Ren, J.; Qu, X. A Graphene Functionalized Electrochemical Aptasensor for Selective Label-Free Detection of Cancer Cells. *Biomaterials* **2011,** *32*, 2930-2937.
976. Yang, G.; Cao, J.; Li, L.; Rana, R. K.; Zhu, J.-J. Carboxymethyl Chitosan-Functionalized Graphene for Label-Free Electrochemical Cytosensing. *Carbon* **2013,** *51*, 124-133.
977. Wu, X.; Hu, Y.; Jin, J.; Zhou, N.; Wu, P.; Zhang, H.; Cai, C. Electrochemical Approach for Detection of Extracellular Oxygen Released from Erythrocytes Based on Graphene Film Integrated with Laccase and 2,2-Azino-Bis(3-Ethylbenzothiazoline-6-Sulfonic Acid). *Anal. Chem.* **2010,** *82*, 3588-3596.
978. Guo, C. X.; Zheng, X. T.; Lu, Z. S.; Lou, X. W.; Li, C. M. Biointerface by Cell Growth on Layered Graphene-Artificial Peroxidase-Protein Nanostructure for in Situ Quantitative Molecular Detection. *Adv. Mater.* **2010,** *22*, 5164-5167.
979. Yadegari, A.; Omidi, M.; Yazdian, F.; Zali, H.; Tayebi, L. An Electrochemical Cytosensor for Ultrasensitive Detection of Cancer Cells Using Modified Graphene–Gold Nanostructures. *RSC Adv.* **2017,** *7*, 2365-2372.
980. Zhang, D.; Zhang, Y.; Zheng, L.; Zhan, Y.; He, L. Graphene Oxide/Poly-L-Lysine Assembled Layer for Adhesion and Electrochemical Impedance Detection of Leukemia K562 Cancer Cells. *Biosens. Bioelectron.* **2013,** *42*, 112-118.

981. Akhavan, O.; Ghaderi, E.; Rahighi, R.; Abdolahad, M. Spongy Graphene Electrode in Electrochemical Detection of Leukemia at Single-Cell Levels. *Carbon* **2014,** *79*, 654-663.
982. Zheng, T.; Tan, T.; Zhang, Q.; Fu, J. J.; Wu, J. J.; Zhang, K.; Zhu, J. J.; Wang, H. Multiplex Acute Leukemia Cytosensing Using Multifunctional Hybrid Electrochemical Nanoprobes at a Hierarchically Nanoarchitectured Electrode Interface. *Nanoscale* **2013,** *5*, 10360-10368.
983. Wang, Y.; Ping, J.; Ye, Z.; Wu, J.; Ying, Y. Impedimetric Immunosensor Based on Gold Nanoparticles Modified Graphene Paper for Label-Free Detection of Escherichia Coli O157:H7. *Biosens. Bioelectron.* **2013,** *49*, 492-498.
984. Khoshfetrat, S. M.; Mehrgardi, M. A. Amplified Detection of Leukemia Cancer Cells Using an Aptamer-Conjugated Gold-Coated Magnetic Nanoparticles on a Nitrogen-Doped Graphene Modified Electrode. *Bioelectrochemistry* **2017,** *114*, 24-32.
985. Wang, L.; Sofer, Z.; Pumera, M. Voltammetry of Layered Black Phosphorus: Electrochemistry of Multilayer Phosphorene. *ChemElectroChem* **2015,** *2*, 324-327.
986. Latiff, N. M.; Teo, W. Z.; Sofer, Z.; Fisher, A. C.; Pumera, M. The Cytotoxicity of Layered Black Phosphorus. *Chem. Eur. J.* **2015,** *21*, 13991-13995.
987. Sofer, Z.; Sedmidubsky, D.; Huber, S.; Luxa, J.; Bousa, D.; Boothroyd, C.; Pumera, M. Layered Black Phosphorus: Strongly Anisotropic Magnetic, Electronic, and Electron-Transfer Properties. *Angew. Chem. Int. Ed.* **2016,** *55*, 3382-3386.
988. Yan, S.; Wang, B.; Wang, Z.; Hu, D.; Xu, X.; Wang, J.; Shi, Y. Supercritical Carbon Dioxide-Assisted Rapid Synthesis of Few-Layer Black Phosphorus for Hydrogen Peroxide Sensing. *Biosens. Bioelectron.* **2016,** *80*, 34-38.
989. Zhao, Y.; Zhang, Y. H.; Zhuge, Z.; Tang, Y. H.; Tao, J. W.; Chen, Y. Synthesis of a Poly-L-Lysine/Black Phosphorus Hybrid for Biosensors. *Anal. Chem.* **2018,** *90*, 3149-3155.
990. Huang, Y.; Guo, J.; Kang, Y.; Ai, Y.; Li, C. M. Two Dimensional Atomically Thin MoS_2 Nanosheets and Their Sensing Applications. *Nanoscale* **2015,** *7*, 19358-19376.
991. Kalantar-zadeh, K.; Ou, J. Z. Biosensors Based on Two-Dimensional MoS_2. *ACS Sens.* **2016,** *1*, 5-16.
992. Lee, J.; Dak, P.; Lee, Y.; Park, H.; Choi, W.; Alam, M. A.; Kim, S. Two-Dimensional Layered MoS_2 Biosensors Enable Highly Sensitive Detection of Biomolecules. *Sci. Rep.* **2014,** *4*, 7352.
993. Wang, L.; Wang, Y.; Wong, J. I.; Palacios, T.; Kong, J.; Yang, H. Y. Functionalized MoS_2 Nanosheet-Based Field-Effect Biosensor for Label-Free Sensitive Detection of Cancer Marker Proteins in Solution. *Small* **2014,** *10*, 1101-1105.
994. Nam, H.; Oh, B.-R.; Chen, P.; Yoon, J. S.; Wi, S.; Chen, M.; Kurabayashi, K.; Liang, X. Two Different Device Physics Principles for Operating MoS_2 Transistor Biosensors with Femtomolar-Level Detection Limits. *Appl. Phys. Lett.* **2015,** *107*, 012105.
995. Nam, H.; Oh, B. R.; Chen, P.; Chen, M.; Wi, S.; Wan, W.; Kurabayashi, K.; Liang, X. Multiple MoS_2 Transistors for Sensing Molecule Interaction Kinetics. *Sci. Rep.* **2015,** *5*, 10546.
996. Huang, K.-J.; Liu, Y.-J.; Zhang, J.-Z.; Liu, Y.-M. A Novel Aptamer Sensor Based on Layered Tungsten Disulfide Nanosheets and Au Nanoparticles Amplification for 17β-Estradiol Detection. *Anal. Methods* **2014,** *6*, 8011-8017.
997. Huang, K.-J.; Liu, Y.-J.; Cao, J.-T.; Wang, H.-B. An Aptamer Electrochemical Assay for Sensitive Detection of Immunoglobulin E Based on Tungsten Disulfide–Graphene Composites and Gold Nanoparticles. *RSC Adv.* **2014,** *4*, 36742.
998. Huang, K. J.; Liu, Y. J.; Liu, Y. M.; Wang, L. L. Molybdenum Disulfide Nanoflower-Chitosan-Au Nanoparticles Composites Based Electrochemical Sensing Platform for Bisphenol a Determination. *J. Hazard. Mater.* **2014,** *276*, 207-215.
999. Fu, L.; Zheng, Y. H.; Wang, A. W.; Cai, W.; Lin, H. T. Sensitive Determination of Quinoline Yellow Using Poly (Diallyldimethylammonium Chloride) Functionalized Reduced Graphene Oxide Modified Grassy Carbon Electrode. *Food Chem.* **2015,** *181*, 127-132.
1000. Jing, P.; Yi, H.; Xue, S.; Chai, Y.; Yuan, R.; Xu, W. A Sensitive Electrochemical Aptasensor Based on Palladium Nanoparticles Decorated Graphene-Molybdenum Disulfide Flower-Like Nanocomposites and Enzymatic Signal Amplification. *Anal. Chim. Acta* **2015,** *853*, 234-241.
1001. Rohaizad, N.; Mayorga-Martinez, C. C.; Sofer, Z.; Pumera, M. 1t-Phase Transition Metal Dichalcogenides (MoS_2, $MoSe_2$, WS_2, and WSe_2) with Fast Heterogeneous Electron Transfer: Application on Second-Generation Enzyme-Based Biosensor. *ACS Appl. Mater. Interfaces* **2017,** *9*, 40697-40706.
1002. Su, S.; Sun, H.; Xu, F.; Yuwen, L.; Fan, C.; Wang, L. Direct Electrochemistry of Glucose Oxidase and a Biosensor for Glucose Based on a Glass Carbon Electrode Modified with MoS_2 Nanosheets Decorated with Gold Nanoparticles. *Microchimica Acta* **2014,** *181*, 1497-1503.
1003. Huang, J.; Dong, Z.; Li, Y.; Li, J.; Tang, W.; Yang, H.; Wang, J.; Bao, Y.; Jin, J.; Li, R. MoS_2 Nanosheet Functionalized with Cu Nanoparticles and Its Application for Glucose Detection. *Mater. Res. Bull.* **2013,** *48*, 4544-4547.
1004. Narayanan, T. N.; Vusa, C. S.; Alwarappan, S. Selective and Efficient Electrochemical Biosensing of Ultrathin Molybdenum Disulfide Sheets. *Nanotechnology* **2014,** *25*, 335702.
1005. Wu, S.; Zeng, Z.; He, Q.; Wang, Z.; Wang, S. J.; Du, Y.; Yin, Z.; Sun, X.; Chen, W.; Zhang, H. Electrochemically Reduced Single-Layer MoS_2 Nanosheets: Characterization, Properties, and Sensing Applications. *Small* **2012,** *8*, 2264-2270.
1006. Sarkar, A.; Ghosh, A. B.; Saha, N.; Bhadu, G. R.; Adhikary, B. Newly Designed Amperometric Biosensor for Hydrogen Peroxide and Glucose Based on Vanadium Sulfide Nanoparticles. *ACS Appl. Nano Mater.* **2018,** *1*, 1339-1347.
1007. Wang, G.-X.; Bao, W.-J.; Wang, J.; Lu, Q.-Q.; Xia, X.-H. Immobilization and Catalytic Activity of Horseradish Peroxidase on Molybdenum Disulfide Nanosheets Modified Electrode. *Electrochem. Commun.* **2013,** *35*, 146-148.
1008. Song, H.; Ni, Y.; Kokot, S. Investigations of an Electrochemical Platform Based on the Layered MoS_2-Graphene and Horseradish Peroxidase Nanocomposite for Direct Electrochemistry and Electrocatalysis. *Biosens. Bioelectron.* **2014,** *56*, 137-143.
1009. Yoon, J.; Lee, T.; Bapurao, G. B.; Jo, J.; Oh, B. K.; Choi, J. W. Electrochemical H_2O_2 Biosensor Composed of Myoglobin on MoS_2 Nanoparticle-Graphene Oxide Hybrid Structure. *Biosens. Bioelectron.* **2017,** *93*, 14-20.
1010. Loo, A. H.; Bonanni, A.; Ambrosi, A.; Pumera, M. Molybdenum Disulfide (MoS_2) Nanoflakes as Inherently Electroactive Labels for DNA Hybridization Detection. *Nanoscale* **2014,** *6*, 11971-11975.
1011. Loo, A. H.; Bonanni, A.; Sofer, Z.; Pumera, M. Transitional Metal/Chalcogen Dependant Interactions of Hairpin DNA with Transition Metal Dichalcogenides, Mx2. *Chemphyschem* **2015,** *16*, 2304-2306.
1012. Yang, T.; Chen, M.; Nan, F.; Chen, L.; Luo, X.; Jiao, K. Enhanced Electropolymerization of Poly(Xanthurenic Acid)–MoS_2 Film for Specific Electrocatalytic Detection of Guanine and Adenine. *J. Mater. Chem. B* **2015,** *3*, 4884-4891.
1013. Wang, T.; Zhu, R.; Zhuo, J.; Zhu, Z.; Shao, Y.; Li, M. Direct Detection of DNA Below ppb Level Based on Thionin-Functionalized Layered MoS_2 Electrochemical Sensors. *Anal. Chem.* **2014,** *86*, 12064-12069.

1014. Lee, D.-W.; Lee, J.; Sohn, I. Y.; Kim, B.-Y.; Son, Y. M.; Bark, H.; Jung, J.; Choi, M.; Kim, T. H.; Lee, C.; Lee, N.-E. Field-Effect Transistor with a Chemically Synthesized MoS_2 Sensing Channel for Label-Free and Highly Sensitive Electrical Detection of DNA Hybridization. *Nano Res.* **2015,** *8*, 2340-2350.
1015. Yang, T.; Chen, M.; Kong, Q.; Luo, X.; Jiao, K. Toward DNA Electrochemical Sensing by Free-Standing ZnO Nanosheets Grown on 2D Thin-Layered MoS_2. *Biosens. Bioelectron.* **2017,** *89*, 538-544.
1016. Yang, J.; Kwak, T. J.; Zhang, X.; McClain, R.; Chang, W. J.; Gunasekaran, S. Iridium Oxide-Reduced Graphene Oxide Nanohybrid Thin Film Modified Screen-Printed Electrodes as Disposable Electrochemical Paper Microfluidic pH Sensors. *J. Vis. Exp.* **2016**, e53339
1017. Huang, K.-J.; Liu, Y.-J.; Wang, H.-B.; Gan, T.; Liu, Y.-M.; Wang, L.-L. Signal Amplification for Electrochemical DNA Biosensor Based on Two-Dimensional Graphene Analogue Tungsten Sulfide–Graphene Composites and Gold Nanoparticles. *Sensors Actuators B: Chem.* **2014,** *191*, 828-836.
1018. Wang, X.; Nan, F.; Zhao, J.; Yang, T.; Ge, T.; Jiao, K. A Label-Free Ultrasensitive Electrochemical DNA Sensor Based on Thin-Layer MoS_2 Nanosheets with High Electrochemical Activity. *Biosens. Bioelectron.* **2015,** *64*, 386-391.
1019. Mei, J.; Li, Y. T.; Zhang, H.; Xiao, M. M.; Ning, Y.; Zhang, Z. Y.; Zhang, G. J. Molybdenum Disulfide Field-Effect Transistor Biosensor for Ultrasensitive Detection of DNA by Employing Morpholino as Probe. *Biosens. Bioelectron.* **2018,** *110*, 71-77.
1020. Zhu, D.; Liu, W.; Zhao, D.; Hao, Q.; Li, J.; Huang, J.; Shi, J.; Chao, J.; Su, S.; Wang, L. Label-Free Electrochemical Sensing Platform for Microrna-21 Detection Using Thionine and Gold Nanoparticles Co-Functionalized MoS_2 Nanosheet. *ACS Appl. Mater. Interfaces* **2017,** *9*, 35597-35603.
1021. Su, S.; Sun, H.; Cao, W.; Chao, J.; Peng, H.; Zuo, X.; Yuwen, L.; Fan, C.; Wang, L. Dual-Target Electrochemical Biosensing Based on DNA Structural Switching on Gold Nanoparticle-Decorated MoS_2 Nanosheets. *ACS Appl. Mater. Interfaces* **2016,** *8*, 6826-6833.
1022. Su, S.; Zou, M.; Zhao, H.; Yuan, C.; Xu, Y.; Zhang, C.; Wang, L.; Fan, C.; Wang, L. Shape-Controlled Gold Nanoparticles Supported on MoS_2 Nanosheets: Synergistic Effect of Thionine and MoS_2 and Their Application for Electrochemical Label-Free Immunosensing. *Nanoscale* **2015,** *7*, 19129-19135.
1023. Wang, Y. H.; Huang, K. J.; Wu, X. Recent Advances in Transition-Metal Dichalcogenides Based Electrochemical Biosensors: A Review. *Biosens. Bioelectron.* **2017,** *97*, 305-316.
1024. Sticker, D.; Rothbauer, M.; Charwat, V.; Steinkühler, J.; Bethge, O.; Bertagnolli, E.; Wanzenboeck, H. D.; Ertl, P. Zirconium Dioxide Nanolayer Passivated Impedimetric Sensors for Cell-Based Assays. *Sensors Actuators B: Chem.* **2015,** *213*, 35-44.
1025. Solanki, P. R.; Kaushik, A.; Ansari, A. A.; Malhotra, B. D. Nanostructured Zinc Oxide Platform for Cholesterol Sensor. *Appl. Phys. Lett.* **2009,** *94*, 143901. MoS_2
1026. Ansari, A. A.; Kaushik, A.; Solanki, P. R.; Malhotra, B. D. Nanostructured Zinc Oxide Platform for Mycotoxin Detection. *Bioelectrochemistry* **2010,** *77*, 75-81.
1027. Das, M.; Sumana, G.; Nagarajan, R.; Malhotra, B. D. Zirconia Based Nucleic Acid Sensor for Mycobacterium Tuberculosis Detection. *Appl. Phys. Lett.* **2010,** *96*, 133703.
1028. Solanki, P. R.; Kaushik, A.; Chavhan, P. M.; Maheshwari, S. N.; Malhotra, B. D. Nanostructured Zirconium Oxide Based Genosensor for Escherichia Coli Detection. *Electrochem. Commun.* **2009,** *11*, 2272-2277.
1029. Chu, Y. M.; Lin, C. C.; Chang, H. C.; Li, C.; Guo, C. TiO_2 Nanowire FET Device: Encapsulation of Biomolecules by Electro Polymerized Pyrrole Propylic Acid. *Biosens. Bioelectron.* **2011,** *26*, 2334-2340.
1030. Balendhran, S.; Walia, S.; Alsaif, M.; Nguyen, E. P.; Ou, J. Z.; Zhuiykov, S.; Sriram, S.; Bhaskaran, M.; Kalantar-Zadeh, K. Field Effect Biosensing Platform Based on 2D α -MoO_3. *ACS Nano* **2013,** *7*, 9753-9760.
1031. Lahav, M.; Kharitonov, A. B.; Willner, I. Imprinting of Chiral Molecular Recognition Sites in Thin TiO_2 Films Associated with Field-Effect Transistors: Novel Functionalized Devices for Chiroselective and Chirospecific Analyses. *Chem. Eur. J.* **2001,** *7*, 3992-3997.
1032. Pogorelova, S. P.; Kharitonov, A. B.; Willner, I.; Sukenik, C. N.; Pizem, H.; Bayer, T. Development of Ion-Sensitive Field-Effect Transistor-Based Sensors for Benzylphosphonic Acids and Thiophenols Using Molecularly Imprinted TiO_2 Films. *Anal. Chim. Acta* **2004,** *504*, 113-122.
1033. Mishra, S.; Yogi, P.; Sagdeo, P. R.; Kumar, R. Mesoporous Nickel Oxide (NiO) Nanopetals for Ultrasensitive Glucose Sensing. *Nanoscale Res. Lett.* **2018,** *13*, 16.
1034. Sun, S.; Sun, Y.; Chen, A.; Zhang, X.; Yang, Z. Nanoporous Copper Oxide Ribbon Assembly of Free-Standing Nanoneedles as Biosensors for Glucose. *Analyst* **2015,** *140*, 5205-5215.
1035. Xiang, C.; Zou, Y.; Sun, L.-X.; Xu, F. Direct Electrochemistry and Enhanced Electrocatalysis of Horseradish Peroxidase Based on Flowerlike ZnO–Gold Nanoparticle–Nafion Nanocomposite. *Sensors Actuators B: Chem.* **2009,** *136*, 158-162.
1036. Jia, W.; Guo, M.; Zheng, Z.; Yu, T.; Rodriguez, E. G.; Wang, Y.; Lei, Y. Electrocatalytic Oxidation and Reduction of H_2O_2 on Vertically Aligned Co_3O_4 Nanowalls Electrode: Toward H_2O_2 Detection. *J. Electroanal. Chem.* **2009,** *625*, 27-32.
1037. Li, R.; Du, J.; Luan, Y.; Xue, Y.; Zou, H.; Zhuang, G.; Li, Z. Ionic Liquid Precursor-Based Synthesis of CuO Nanoplates for Gas Sensing and Amperometric Sensing Applications. *Sensors Actuators B: Chem.* **2012,** *168*, 156-164.
1038. Li, Y.; Cao, D.; Liu, Y.; Liu, R.; Yang, F.; Yin, J.; Wang, G. CuO Nanosheets Grown on Cupper Foil as the Catalyst for H_2O_2 Electroreduction in Alkaline Medium. *Int. J. Hydrogen Energy* **2012,** *37*, 13611-13615.
1039. Khan, A. F.; Randviir, E. P.; Brownson, D. A. C.; Ji, X.; Smith, G. C.; Banks, C. E. 2D Hexagonal Boron Nitride (2D - *h*BN) Explored as a Potential Electrocatalyst for the Oxygen Reduction Reaction. *Electroanalysis* **2017,** *29*, 622-634.
1040. Huang, C.; Chen, C.; Zhang, M.; Lin, L.; Ye, X.; Lin, S.; Antonietti, M.; Wang, X. Carbon-Doped Bn Nanosheets for Metal-Free Photoredox Catalysis. *Nat. Commun.* **2015,** *6*, 7698.
1041. Khan, A. F.; Brownson, D. A.; Randviir, E. P.; Smith, G. C.; Banks, C. E. 2D Hexagonal Boron Nitride (2D - *h*BN) Explored for the Electrochemical Sensing of Dopamine. *Anal. Chem.* **2016,** *88*, 9729-9737.
1042. Khan, A. F.; Brownson, D. A. C.; Foster, C. W.; Smith, G. C.; Banks, C. E. Surfactant Exfoliated 2D Hexagonal Boron Nitride (2D - *h*BN) Explored as a Potential Electrochemical Sensor for Dopamine: Surfactants Significantly Influence Sensor Capabilities. *Analyst* **2017,** *142*, 1756-1764.
1043. Li, Q.; Huo, C.; Yi, K.; Zhou, L.; Su, L.; Hou, X. Preparation of Flake Hexagonal Bn and Its Application in Electrochemical Detection of Ascorbic Acid, Dopamine and Uric Acid. *Sensors Actuators B: Chem.* **2018,** *260*, 346-356.
1044. Liu, F.; Tang, J.; Xu, J.; Shu, Y.; Xu, Q.; Wang, H.; Hu, X. Low Potential Detection of Indole-3-Acetic Acid Based on the Peroxidase-Like Activity of Hemin/Reduced Graphene Oxide Nanocomposite. *Biosens. Bioelectron.* **2016,** *86*, 871-878.
1045. Aksoy, B.; Paşahan, A.; Güngör, Ö.; Köytepe, S.; Seçkin, T. A Novel Electrochemical Biosensor Based on Polyimide-Boron Nitride Composite Membranes. *Int. J. Polym. Mater. Polym. Biomater.* **2016,** *66*, 203-212.

1046. Ranganethan, S.; Lee, S.-M.; Lee, J.; Chang, S.-C. Electrochemical Non-Enzymatic Glucose Sensor Based on Hexagonal Boron Nitride with Metal-Organic Framework Composite. *J. Sensor Sci. & Tech.* **2017,** *26*, 379-385.
1047. Yola, M. L.; Atar, N. A Novel Detection Approach for Serotonin by Graphene Quantum Dots/Two-Dimensional (2D) Hexagonal Boron Nitride Nanosheets with Molecularly Imprinted Polymer. *Appl. Surf. Sci.* **2018,** *458*, 648-655.
1048. Naguib, M.; Mashtalir, O.; Carle, J.; Presser, V.; Lu, J.; Hultman, L.; Gogotsi, Y.; Barsoum, M. W. Two-Dimensional Transition Metal Carbides. *ACS Nano* **2012,** *6*, 1322-1331.
1049. Xu, B.; Zhu, M.; Zhang, W.; Zhen, X.; Pei, Z.; Xue, Q.; Zhi, C.; Shi, P. Ultrathin MXene-Micropattern-Based Field-Effect Transistor for Probing Neural Activity. *Adv. Mater.* **2016,** *28*, 3333-3339.
1050. Wang, F.; Yang, C.; Duan, C.; Xiao, D.; Tang, Y.; Zhu, J. An Organ-Like Titanium Carbide Material (MXene) with Multilayer Structure Encapsulating Hemoglobin for a Mediator-Free Biosensor. *J. Electrochem. Soc.* **2014,** *162*, B16-B21.
1051. Wang, F.; Yang, C.; Duan, M.; Tang, Y.; Zhu, J. TiO_2 Nanoparticle Modified Organ-Like Ti_3C_2 MXene Nanocomposite Encapsulating Hemoglobin for a Mediator-Free Biosensor with Excellent Performances. *Biosens. Bioelectron.* **2015,** *74*, 1022-1028.
1052. Lorencova, L.; Bertok, T.; Dosekova, E.; Holazova, A.; Paprckova, D.; Vikartovska, A.; Sasinkova, V.; Filip, J.; Kasak, P.; Jerigova, M.; Velic, D.; Mahmoud, K. A.; Tkac, J. Electrochemical Performance of $Ti_3C_2T_x$ MXene in Aqueous Media: Towards Ultrasensitive H_2O_2 Sensing. *Electrochim. Acta* **2017,** *235*, 471-479.
1053. Rakhi, R. B.; Nayak, P.; Xia, C.; Alshareef, H. N. Novel Amperometric Glucose Biosensor Based on MXene Nanocomposite. *Sci. Rep.* **2016,** *6*, 36422.
1054. Liu, H.; Duan, C.; Yang, C.; Shen, W.; Wang, F.; Zhu, Z. A Novel Nitrite Biosensor Based on the Direct Electrochemistry of Hemoglobin Immobilized on MXene-Ti_3C_2. *Sensors Actuators B: Chem.* **2015,** *218*, 60-66.
1055. Rakhi, R. B.; Nayuk, P.; Xia, C.; Alshareef, H. N. Novel Amperometric Glucose Biosensor Based on MXene Nanocomposite. *Sci. Rep.* **2016,** *6*, 36422.
1056. Qi, S.; Zhao, B.; Tang, H.; Jiang, X. Determination of Ascorbic Acid, Dopamine, and Uric Acid by a Novel Electrochemical Sensor Based on Pristine Graphene. *Electrochim. Acta* **2015,** *161*, 395-402.
1057. Wu, D.; Li, Y.; Zhang, Y.; Wang, P.; Wei, Q.; Du, B. Sensitive Electrochemical Sensor for Simultaneous Determination of Dopamine, Ascorbic Acid, and Uric Acid Enhanced by Amino-Group Functionalized Mesoporous Fe_3O_4@Graphene Sheets. *Electrochim. Acta* **2014,** *116*, 244-249.
1058. Sun, C. L.; Lee, H. H.; Yang, J. M.; Wu, C. C. The Simultaneous Electrochemical Detection of Ascorbic Acid, Dopamine, and Uric Acid Using Graphene/Size-Selected Pt Nanocomposites. *Biosens. Bioelectron.* **2011,** *26*, 3450-3455.
1059. Yang, L.; Liu, D.; Huang, J.; You, T. Simultaneous Determination of Dopamine, Ascorbic Acid and Uric Acid at Electrochemically Reduced Graphene Oxide Modified Electrode. *Sensors Actuators B: Chem.* **2014,** *193*, 166-172.
1060. Wang, C.; Du, J.; Wang, H.; Zou, C. e.; Jiang, F.; Yang, P.; Du, Y. A Facile Electrochemical Sensor Based on Reduced Graphene Oxide and Au Nanoplates Modified Glassy Carbon Electrode for Simultaneous Detection of Ascorbic Acid, Dopamine and Uric Acid. *Sensors Actuators B: Chem.* **2014,** *204*, 302-309.
1061. Zhu, Q.; Chai, Y.; Yuan, R.; Zhuo, Y.; Han, J.; Li, Y.; Liao, N. Amperometric Immunosensor for Simultaneous Detection of Three Analytes in One Interface Using Dual Functionalized Graphene Sheets Integrated with Redox-Probes as Tracer Matrixes. *Biosens. Bioelectron.* **2013,** *43*, 440-445.
1062. Zhao, L.; Li, S.; He, J.; Tian, G.; Wei, Q.; Li, H. Enzyme-Free Electrochemical Immunosensor Configured with Au-Pd Nanocrystals and N-Doped Graphene Sheets for Sensitive Detection of Afp. *Biosens. Bioelectron.* **2013,** *49*, 222-225.
1063. Zhang, H.; Han, Y.; Guo, Y.; Dong, C. Porphyrin Functionalized Graphene Nanosheets-Based Electrochemical Aptasensor for Label-Free Atp Detection. *J. Mater. Chem.* **2012,** *22*, 23900.
1064. Lei, Y. M.; Xiao, M. M.; Li, Y. T.; Xu, L.; Zhang, H.; Zhang, Z. Y.; Zhang, G. J. Detection of Heart Failure-Related Biomarker in Whole Blood with Graphene Field Effect Transistor Biosensor. *Biosens. Bioelectron.* **2017,** *91*, 1-7.
1065. Yang, L.; Wang, G.; Liu, Y.; Wang, M. Development of a Biosensor Based on Immobilization of Acetylcholinesterase on Nio Nanoparticles-Carboxylic Graphene-Nafion Modified Electrode for Detection of Pesticides. *Talanta* **2013,** *113*, 135-141.
1066. Huang, J. Y.; Zhao, L.; Lei, W.; Wen, W.; Wang, Y. J.; Bao, T.; Xiong, H. Y.; Zhang, X. H.; Wang, S. F. A High-Sensitivity Electrochemical Aptasensor of Carcinoembryonic Antigen Based on Graphene Quantum Dots-Ionic Liquid-Nafion Nanomatrix and Dnazyme-Assisted Signal Amplification Strategy. *Biosens. Bioelectron.* **2018,** *99*, 28-33.
1067. Manjunatha, R.; Shivappa Suresh, G.; Melo, J. S.; D'Souza, S. F.; Venkatesha, T. V. An Amperometric Bienzymatic Cholesterol Biosensor Based on Functionalized Graphene Modified Electrode and Its Electrocatalytic Activity Towards Total Cholesterol Determination. *Talanta* **2012,** *99*, 302-309.
1068. Cao, S.; Zhang, L.; Chai, Y.; Yuan, R. Electrochemistry of Cholesterol Biosensor Based on a Novel Pt-Pd Bimetallic Nanoparticle Decorated Graphene Catalyst. *Talanta* **2013,** *109*, 167-172.
1069. Ruecha, N.; Rangkupan, R.; Rodthongkum, N.; Chailapakul, O. Novel Paper-Based Cholesterol Biosensor Using Graphene/Polyvinylpyrrolidone/Polyaniline Nanocomposite. *Biosens. Bioelectron.* **2014,** *52*, 13-19.
1070. Jiang, B.; Wang, M.; Chen, Y.; Xie, J.; Xiang, Y. Highly Sensitive Electrochemical Detection of Cocaine on Graphene/Aunp Modified Electrode via Catalytic Redox-Recycling Amplification. *Biosens. Bioelectron.* **2012,** *32*, 305-308.
1071. Vabbina, P. K.; Kaushik, A.; Pokhrel, N.; Bhansali, S.; Pala, N. Electrochemical Cortisol Immunosensors Based on Sonochemically Synthesized Zinc Oxide 1D Nanorods and 2D Nanoflakes. *Biosens. Bioelectron.* **2015,** *63*, 124-130.
1072. Xu, S.; Zhan, J.; Man, B.; Jiang, S.; Yue, W.; Gao, S.; Guo, C.; Liu, H.; Li, Z.; Wang, J.; Zhou, Y. Real-Time Reliable Determination of Binding Kinetics of DNA Hybridization Using a Multi-Channel Graphene Biosensor. *Nat. Commun.* **2017,** *8*, 14902.
1073. Cao, X. Ultra-Sensitive Electrochemical DNA Biosensor Based on Signal Amplification Using Gold Nanoparticles Modified with Molybdenum Disulfide, Graphene and Horseradish Peroxidase. *Microchimica Acta* **2014,** *181*, 1133-1141.
1074. Liu, Y.-M.; Zhou, M.; Liu, Y.-Y.; Shi, G.-F.; Zhang, J.-J.; Cao, J.-T.; Huang, K.-J.; Chen, Y.-H. Fabrication of Electrochemiluminescence Aptasensor Based on in Situ Growth of Gold Nanoparticles on Layered Molybdenum Disulfide for Sensitive Detection of Platelet-Derived Growth Factor-Bb. *RSC Adv.* **2014,** *4*, 22888.
1075. Wang, K.; He, M. Q.; Zhai, F. H.; He, R. H.; Yu, Y. L. A Novel Electrochemical Biosensor Based on Polyadenine

Modified Aptamer for Label-Free and Ultrasensitive Detection of Human Breast Cancer Cells. *Talanta* **2017,** *166*, 87-92.
1076. Han, H. S.; Seol, H.; Kang, D. H.; Ahmed, M. S.; You, J.-M.; Jeon, S. Electrochemical Oxidation and Determination of Dopamine in the Presence of Aa Using Ferulic Acid Functionalized Electrochemically Reduced Graphene. *Sensors Actuators B: Chem.* **2014,** *204*, 289-296.
1077. Kim, Y. R.; Bong, S.; Kang, Y. J.; Yang, Y.; Mahajan, R. K.; Kim, J. S.; Kim, H. Electrochemical Detection of Dopamine in the Presence of Ascorbic Acid Using Graphene Modified Electrodes. *Biosens. Bioelectron.* **2010,** *25*, 2366-2369.
1078. Alwarappan, S.; Erdem, A.; Liu, C.; Li, C.-Z. Probing the Electrochemical Properties of Graphene Nanosheets for Biosensing Applications. *J. Phys. Chem. C* **2009,** *113*, 8853-8857.
1079. Qiu, J.-D.; Huang, J.; Liang, R.-P. Nanocomposite Film Based on Graphene Oxide for High Performance Flexible Glucose Biosensor. *Sensors Actuators B: Chem.* **2011,** *160*, 287-294.
1080. Song, J.; Xu, L.; Zhou, C.; Xing, R.; Dai, Q.; Liu, D.; Song, H. Synthesis of Graphene Oxide Based CuO Nanoparticles Composite Electrode for Highly Enhanced Nonenzymatic Glucose Detection. *ACS Appl. Mater. Interfaces* **2013,** *5*, 12928-12934.
1081. Luo, J.; Jiang, S.; Zhang, H.; Jiang, J.; Liu, X. A Novel Non-Enzymatic Glucose Sensor Based on Cu Nanoparticle Modified Graphene Sheets Electrode. *Anal. Chim. Acta* **2012,** *709*, 47-53.
1082. Zeng, G.; Li, W.; Ci, S.; Jia, J.; Wen, Z. Highly Dispersed Nio Nanoparticles Decorating Graphene Nanosheets for Non-Enzymatic Glucose Sensor and Biofuel Cell. *Sci. Rep.* **2016,** *6*, 36454.
1083. Chen, H.; Rim, Y. S.; Wang, I. C.; Li, C.; Zhu, B.; Sun, M.; Goorsky, M. S.; He, X.; Yang, Y. Quasi-Two-Dimensional Metal Oxide Semiconductors Based Ultrasensitive Potentiometric Biosensors. *ACS Nano* **2017,** *11*, 4710-4718.
1084. Parlak, O.; Incel, A.; Uzun, L.; Turner, A. P. F.; Tiwari, A. Structuring Au Nanoparticles on Two-Dimensional MoS_2 Nanosheets for Electrochemical Glucose Biosensors. *Biosens. Bioelectron.* **2017,** *89*, 545-550.
1085. Mani, V.; Devadas, B.; Chen, S. M. Direct Electrochemistry of Glucose Oxidase at Electrochemically Reduced Graphene Oxide-Multiwalled Carbon Nanotubes Hybrid Material Modified Electrode for Glucose Biosensor. *Biosens. Bioelectron.* **2013,** *41*, 309-315.
1086. Huang, K. J.; Zhang, J. Z.; Liu, Y. J.; Wang, L. L. Novel Electrochemical Sensing Platform Based on Molybdenum Disulfide Nanosheets-Polyaniline Composites and Au Nanoparticles. *Sensors Actuators B: Chem.* **2014,** *194*, 303-310.
1087. Yang, Y.; Yang, X.; Zou, X.; Wu, S.; Wan, D.; Cao, A.; Liao, L.; Yuan, Q.; Duan, X. Ultrafine Graphene Nanomesh with Large on/Off Ratio for High-Performance Flexible Biosensors. *Adv. Funct. Mater.* **2017,** *27*, 1604096.
1088. Song, W.; Li, H.; Liu, H.; Wu, Z.; Qiang, W.; Xu, D. Fabrication of Streptavidin Functionalized Silver Nanoparticle Decorated Graphene and Its Application in Disposable Electrochemical Sensor for Immunoglobulin E. *Electrochem. Commun.* **2013,** *31*, 16-19.
1089. Wang, G.; He, X.; Chen, L.; Zhu, Y.; Zhang, X. Ultrasensitive Il-6 Electrochemical Immunosensor Based on Au Nanoparticles-Graphene-Silica Biointerface. *Colloids Surf. B. Biointerfaces* **2014,** *116*, 714-719.
1090. Wang, R.; Dong, W.; Ruan, C.; Kanayeva, D.; Tian, R.; Lassiter, K.; Li, Y. TiO_2 Nanowire Bundle Microelectrode Based Impedance Immunosensor for Rapid and Sensitive Detection of Listeria Monocytogenes. *Nano Lett.* **2008,** *8*, 2625-2631.
1091. Bai, L.; Yuan, R.; Chai, Y.; Zhuo, Y.; Yuan, Y.; Wang, Y. Simultaneous Electrochemical Detection of Multiple Analytes Based on Dual Signal Amplification of Single-Walled Carbon Nanotubes and Multi-Labeled Graphene Sheets. *Biomaterials* **2012,** *33*, 1090-1096.
1092. Deng, K.; Xiang, Y.; Zhang, L.; Chen, Q.; Fu, W. An Aptamer-Based Biosensing Platform for Highly Sensitive Detection of Platelet-Derived Growth Factor via Enzyme-Mediated Direct Electrochemistry. *Anal. Chim. Acta* **2013,** *759*, 61-65.
1093. Pan, L. H.; Kuo, S. H.; Lin, T. Y.; Lin, C. W.; Fang, P. Y.; Yang, H. W. An Electrochemical Biosensor to Simultaneously Detect Vegf and Psa for Early Prostate Cancer Diagnosis Based on Graphene Oxide/ssDNA/Plla Nanoparticles. *Biosens. Bioelectron.* **2017,** *89*, 598-605.
1094. Mao, K.; Wu, D.; Li, Y.; Ma, H.; Ni, Z.; Yu, H.; Luo, C.; Wei, Q.; Du, B. Label-Free Electrochemical Immunosensor Based on Graphene/Methylene Blue Nanocomposite. *Anal. Biochem.* **2012,** *422*, 22-27.
1095. Yan, M.; Zang, D.; Ge, S.; Ge, L.; Yu, J. A Disposable Electrochemical Immunosensor Based on Carbon Screen-Printed Electrodes for the Detection of Prostate Specific Antigen. *Biosens. Bioelectron.* **2012,** *38*, 355-361.
1096. Li, Y.; Han, J.; Chen, R.; Ren, X.; Wei, Q. Label Electrochemical Immunosensor for Prostate-Specific Antigen Based on Graphene and Silver Hybridized Mesoporous Silica. *Anal. Biochem.* **2015,** *469*, 76-82.
1097. Su, S.; Sun, H.; Xu, F.; Yuwen, L.; Wang, L. Highly Sensitive and Selective Determination of Dopamine in the Presence of Ascorbic Acid Using Gold Nanoparticles-Decorated MoS_2nanosheets Modified Electrode. *Electroanalysis* **2013,** *25*, 2523-2529.
1098. Kim, H. U.; Kim, H. Y.; Kulkarni, A.; Ahn, C.; Jin, Y.; Kim, Y.; Lee, K. N.; Lee, M. H.; Kim, T. A Sensitive Electrochemical Sensor for in Vitro Detection of Parathyroid Hormone Based on a MoS_2-Graphene Composite. *Sci. Rep.* **2016,** *6*, 34587.
1099. Du, H.; Ye, J.; Zhang, J.; Huang, X.; Yu, C. Graphene Nanosheets Modified Glassy Carbon Electrode as a Highly Sensitive and Selective Voltammetric Sensor for Rutin. *Electroanalysis* **2010,** *22*, 2399-2406.
1100. Singh, V. V.; Nigam, A. K.; Yadav, S. S.; Tripathi, B. K.; Srivastava, A.; Boopathi, M.; Singh, B. Graphene Oxide as Carboelectrocatalyst for in Situ Electrochemical Oxidation and Sensing of Chemical Warfare Agent Simulant. *Sensors Actuators B: Chem.* **2013,** *188*, 1218-1224.
1101. Wang, Y.; Yuan, R.; Chai, Y.; Yuan, Y.; Bai, L. In Situ Enzymatic Silver Enhancement Based on Functionalized Graphene Oxide and Layer-by-Layer Assembled Gold Nanoparticles for Ultrasensitive Detection of Thrombin. *Biosens. Bioelectron.* **2012,** *38*, 50-54.
1102. Wang, Y.; Xiao, Y.; Ma, X.; Li, N.; Yang, X. Label-Free and Sensitive Thrombin Sensing on a Molecularly Grafted Aptamer on Graphene. *Chem. Commun.* **2012,** *48*, 738-740.
1103. Jiang, L.; Yuan, R.; Chai, Y.; Yuan, Y.; Bai, L.; Wang, Y. Aptamer-Based Highly Sensitive Electrochemical Detection of Thrombin via the Amplification of Graphene. *Analyst* **2012,** *137*, 2415-2420.
1104. Guo, Y.; Han, Y.; Guo, Y.; Dong, C. Graphene-Orange II Composite Nanosheets with Electroactive Functions as Label-Free Aptasensing Platform for "Signal-on" Detection of Protein. *Biosens. Bioelectron.* **2013,** *45*, 95-101.
1105. Zhang, J.; Chai, Y.; Yuan, R.; Yuan, Y.; Bai, L.; Xie, S. A Highly Sensitive Electrochemical Aptasensor for Thrombin Detection Using Functionalized Mesoporous Silica@Multiwalled Carbon Nanotubes as Signal Tags and DNAzyme Signal Amplification. *Analyst* **2013,** *138*, 6938-6945.
1106. Yuan, Y.; Liu, G.; Yuan, R.; Chai, Y.; Gan, X.; Bai, L. Dendrimer Functionalized Reduced Graphene Oxide as Nanocarrier for Sensitive Pseudobienzyme Electrochemical Aptasensor. *Biosens. Bioelectron.* **2013,** *42*, 474-480.

1107. Bai, L.; Yan, B.; Chai, Y.; Yuan, R.; Yuan, Y.; Xie, S.; Jiang, L.; He, Y. An Electrochemical Aptasensor for Thrombin Detection Based on Direct Electrochemistry of Glucose Oxidase Using a Functionalized Graphene Hybrid for Amplification. *Analyst* **2013,** *138*, 6595-6599.
1108. Xie, S.; Chai, Y.; Yuan, R.; Bai, L.; Yuan, Y.; Wang, Y. A Dual-Amplification Aptasensor for Highly Sensitive Detection of Thrombin Based on the Functionalized Graphene-Pd Nanoparticles Composites and the Hemin/G-Quadruplex. *Anal. Chim. Acta* **2012,** *755*, 46-53.
1109. Yuan, Y.; Gou, X.; Yuan, R.; Chai, Y.; Zhuo, Y.; Ye, X.; Gan, X. Graphene-Promoted 3,4,9,10-Perylenetetracarboxylic Acid Nanocomposite as Redox Probe in Label-Free Electrochemical Aptasensor. *Biosens. Bioelectron.* **2011,** *30*, 123-127.
1110. Peng, K.; Zhao, H.; Wu, X.; Yuan, Y.; Yuan, R. Ultrasensitive Aptasensor Based on Graphene-3,4,9,10-Perylenetetracarboxylic Dianhydride as Platform and Functionalized Hollow Ptco Nanochains as Enhancers. *Sensors Actuators B: Chem.* **2012,** *169*, 88-95.
1111. Zhao, J.; Chen, G.; Zhu, L.; Li, G. Graphene Quantum Dots-Based Platform for the Fabrication of Electrochemical Biosensors. *Electrochem. Commun.* **2011,** *13*, 31-33.
1112. Xie, S.; Yuan, R.; Chai, Y.; Bai, L.; Yuan, Y.; Wang, Y. Label-Free Electrochemical Aptasensor for Sensitive Thrombin Detection Using Layer-by-Layer Self-Assembled Multilayers with Toluidine Blue-Graphene Composites and Gold Nanoparticles. *Talanta* **2012,** *98*, 7-13.
1113. Zhang, Z.; Luo, L.; Zhu, L.; Ding, Y.; Deng, D.; Wang, Z. Aptamer-Linked Biosensor for Thrombin Based on Aunps/Thionine-Graphene Nanocomposite. *Analyst* **2013,** *138*, 5365-5370.
1114. Xu, Z.; He, C.; Sun, T.; Wang, L. Sensitive Electrochemical Aptasensor for Thrombin Detection with Platinum Nanoparticles, Blocking Reagent-Horseradish Peroxidase and Graphene Oxide as Enhancers. *Electroanalysis* **2013**, 2339-2344.
1115. Wu, T.; Li, T.; Liu, Z.; Guo, Y.; Dong, C. Electrochemical Sensor for Sensitive Detection of Triclosan Based on Graphene/Palladium Nanoparticles Hybrids. *Talanta* **2017,** *164*, 556-562.
1116. Xing, X.; Liu, S.; Yu, J.; Lian, W.; Huang, J. Electrochemical Sensor Based on Molecularly Imprinted Film at Polypyrrole-Sulfonated Graphene/Hyaluronic Acid-Multiwalled Carbon Nanotubes Modified Electrode for Determination of Tryptamine. *Biosens. Bioelectron.* **2012,** *31*, 277-283.
1117. Zhang, Y.; Zheng, J.; Guo, M. Preparation of Molecularly Imprinted Electrochemical Sensor for Detection of Vincristine Based on Reduced Graphene Oxide/Gold Nanoparticle Composite Film. *Chin. J. Chem .* **2016,** *34*, 1268-1276.
1118. Duong, D. L.; Yun, S. J.; Lee, Y. H. Van Der Waals Layered Materials: Opportunities and Challenges. *ACS Nano* **2017,** *11*, 11803-11830.
1119. Chia, X.; Eng, A. Y.; Ambrosi, A.; Tan, S. M.; Pumera, M. Electrochemistry of Nanostructured Layered Transition-Metal Dichalcogenides. *Chem. Rev.* **2015,** *115*, 11941-11966.
1120. Eredia, M.; Bertolazzi, S.; Leydecker, T.; El Garah, M.; Janica, I.; Melinte, G.; Ersen, O.; Ciesielski, A.; Samori, P. Morphology and Electronic Properties of Electrochemically Exfoliated Graphene. *J. Phys. Chem. Lett.* **2017,** *8*, 3347-3355.
1121. Choi, W.; Choudhary, N.; Han, G. H.; Park, J.; Akinwande, D.; Lee, Y. H. Recent Development of Two-Dimensional Transition Metal Dichalcogenides and Their Applications. *Mater. Today* **2017,** *20*, 116-130.
1122. McManus, D.; Vranic, S.; Withers, F.; Sanchez-Romaguera, V.; Macucci, M.; Yang, H.; Sorrentino, R.; Parvez, K.; Son, S. K.; Iannaccone, G.; Kostarelos, K.; Fiori, G.; Casiraghi, C. Water-Based and Biocompatible 2D Crystal Inks for All-Inkjet-Printed Heterostructures. *Nat. Nanotechnol.* **2017,** *12*, 343-350.
1123. Shavanova, K.; Bakakina, Y.; Burkova, I.; Shtepliuk, I.; Viter, R.; Ubelis, A.; Beni, V.; Starodub, N.; Yakimova, R.; Khranovskyy, V. Application of 2D Non-Graphene Materials and 2D Oxide Nanostructures for Biosensing Technology. *Sensors* **2016,** *16*, 223.
1124. Kenry; Lim, C. T. Biocompatibility and Nanotoxicity of Layered Two-Dimensional Nanomaterials. *ChemNanoMat* **2017,** *3*, 5-16.
1125. Seo, H.-K.; Kim, K.; Min, S.-Y.; Lee, Y.; Park, C. E.; Raj, R.; Lee, T.-W. Direct Growth of Graphene-Dielectric Bi-Layer Structure on Device Substrates from Si-Based Polymer. *2D Mater.* **2017,** *4*.
1126. Haastrup, S.; Strange, M.; Pandey, M.; Deilmann, T.; Schmidt, P. S.; Hinsche, N. F.; Gjerding, M. N.; Torelli, D.; Larsen, P. M.; Riis-Jensen, A. C.; Gath, J.; Jacobsen, K. W.; Jørgen Mortensen, J.; Olsen, T.; Thygesen, K. S. The Computational 2D Materials Database: High-Throughput Modeling and Discovery of Atomically Thin Crystals. *2D Mater.* **2018,** *5*.
1127. Burch, K. S. Electric Switching of Magnetism in 2D. *Nat. Nanotechnol.* **2018,** *13*, 532.
1128. Hellman, F.; Hoffmann, A.; Tserkovnyak, Y.; Beach, G. S. D.; Fullerton, E. E.; Leighton, C.; MacDonald, A. H.; Ralph, D. C.; Arena, D. A.; Durr, H. A.; Fischer, P.; Grollier, J.; Heremans, J. P.; Jungwirth, T.; Kimel, A. V.; Koopmans, B.; Krivorotov, I. N.; May, S. J.; Petford-Long, A. K.; Rondinelli, J. M.; Samarth, N.; Schuller, I. K.; Slavin, A. N.; Stiles, M. D.; Tchernyshyov, O.; Thiaville, A.; Zink, B. L. Interface-Induced Phenomena in Magnetism. *Rev. Mod. Phys* **2017,** *89*.
1129. Bartual-Murgui, C.; Akou, A.; Thibault, C.; Molnár, G.; Vieu, C.; Salmon, L.; Bousseksou, A. Spin-Crossover Metal–Organic Frameworks: Promising Materials for Designing Gas Sensors. *J. Mater. Chem. C* **2015,** *3*, 1277-1285.

Insert Table of Contents artwork here